

D3.3



BEACON - Bentonite Mechanical Evolution

Description of the constitutive models developed in the project. Conceptual bases, mathematical description and model capabilities. Assessment of predictive power

DELIVERABLE (D3.3)

Author: Antonio Gens

With contributions by V. Kumar, S. Beese, D. Mašín G. Scaringi, J. Kruis, T. Krejčí, T. Koudelka, Z. Sun, J. Najser, J. Svoboda, O. Kristensson, M. Åkesson, D. Malmberg, A. Spetz, J. A. Bosch, Al. Ferrari, L. Laloui, L. Zdravkovic, G. Ghiadistri, G. Pedone, D. Potts, K. Tsiampousi, A. Narkuniene, P. Poskas, D. Justinavicius, R. Newson, K. Thatcher, S. Benbow, N. Chittenden, R. B. Vasconcelos, C. E. Rodríguez, R. Charlier, F. Collin, B. Dardé, L. Gramegna

Reporting period: 01/06/20 – 31/05/22

Date of issue of this report: 31/10/21

Start date of project: **01/06/17**

Duration: 60 Months

This project receives funding from the Euratom research and training programme 2014-2018 under grant agreement No 745 942		
Dissemination Level		
PU	Public	X
RE	Restricted to a group specified by the partners of the Beacon project	
CO	Confidential, only for partners of the Beacon project	

REVIEW

Name	Internal/Project/External	Comments
All Beacon partners	Project internal	

DISTRIBUTION LIST

Name	Number of copies	Comments
Seifallah BEN HADJ HASSINE (EC)	Digital	
Beacon partners	Digital	

Abstract

Deliverable 3.3 contains the final account of the activities performed in Work Package 3 (WP3) during the project. It includes a summary description of the final state of the constitutive models developed in the project (conceptual bases, mathematical description and model capabilities) with particular attention to the improvements achieved during the project. The results of a verification exercise (Task 3.3) based on the modelling of a set of oedometer tests following two different stress paths are also presented.

The Deliverable shows that important and substantial advances have been achieved in the framework of BEACON's WP3 regarding the development and improvement of constitutive models and their implementation in computer codes. The models encompass a wide range of approaches and can deal with an extensive combination of simulation conditions. The models developed are able to reproduce what are considered to be key features of behaviour underlying homogenization processes such as stress path dependency, strain irreversibility, and others. As a result, modelling capabilities in this area have been enhanced very significantly as a result of the project. The performance of the models when applied to the simulation of relevant problems is assessed in Work Package 5.

In the context of these advances, several modelling teams have also identified areas of further constitutive model developments that are deemed necessary to improve simulation capabilities. In addition, outstanding uncertainties remain concerning the detailed knowledge of some of the individual phenomena underlying homogenization, the precise role of different components and parameters of specific models.

Content

1	Introduction	5
2	Work Package 3: general overview	6
3	Constitutive models: description and capabilities	9
3.1	Bundesanstalt fuer Geowissenschaften und Rohstoffe (BGR)	9
3.2	Charles University – Czech Technical University (CU-CTU)	11
3.3	Clay Technology (ClayTech)	14
3.4	Ecole Polytechnique Federale de Lausanne (EPFL)	16
3.5	Imperial College London (ICL)	19
3.6	Lietuvos Energetikos Institutas (LEI)	22
3.7	Quintessa.....	24
3.8	Universitat Politècnica de Catalunya (UPC).....	27
3.9	Université de Liège (ULg)	30
3.10	Main model developments and improvements	33
4	Task 3.3: verification	35
4.1	Definition of the Task.....	35
4.2	Modelling results	39
5	General comments on model development and capabilities	44
6	Outstanding uncertainties and predictive power of the models	46
7	Concluding remarks	47
	Appendix. Modelling specifications for Task 3.3	48

Annexes. Contributions to Deliverable 3.3

Annex A	Bundesanstalt fuer Geowissenschaften und Rohstoffe (BGR)
Annex B	Charles University – Czech Technical University (CU-CTU)
Annex C	Clay Technology (ClayTech)
Annex D	Ecole Polytechnique federale de Lausanne (EPFL)
Annex E	Imperial College London (ICL)
Annex F	Lietuvos Energetikos Institutas (LEI)
Annex G	Quintessa (Quintessa)
Annex H	Universitat Politècnica de Catalunya (UPC)
Annex I	Université de Liège (ULg)

1 Introduction

According to the proposal, the driver for this project is repository safety, and the demands of waste management organizations to verify that the material selection and initial state design fulfil the long-term performance expectations. Bentonite-based barriers and seals are significant contributors to the repository safety. In that respect, the state of the barriers and seals when they become saturated at the end of the transient period is an aspect of key importance. Recent dismantlings of a number of large-scale in situ tests performed in a number of Underground Research Laboratories have revealed that barriers and seals may not exhibit complete homogenisation at the end of the transient period. Average properties are therefore not sufficient to characterize the state of the barrier/seal and tested and reliable predictive tools to anticipate the evolution of the barriers and seals are therefore required.

Consequently, the overall objective of the project is to develop and test the tools necessary for the assessment of the mechanical evolution of an installed bentonite barrier or seal and their resulting performance. The goal is to verify the performance of current designs for buffers, backfills, seals and plugs. Figure 1-1 shows the general structure of the project in terms of Work Packages (WPs) Within the project, WP3 is devoted to the development of the constitutive models for describing the hydro-mechanical and thermo-hydro-mechanical behaviour of bentonite-based highly-swelling materials in an appropriate manner. As Figure 1-1 indicates WP3 occupies a central position in the project and it is closely related to WP5.

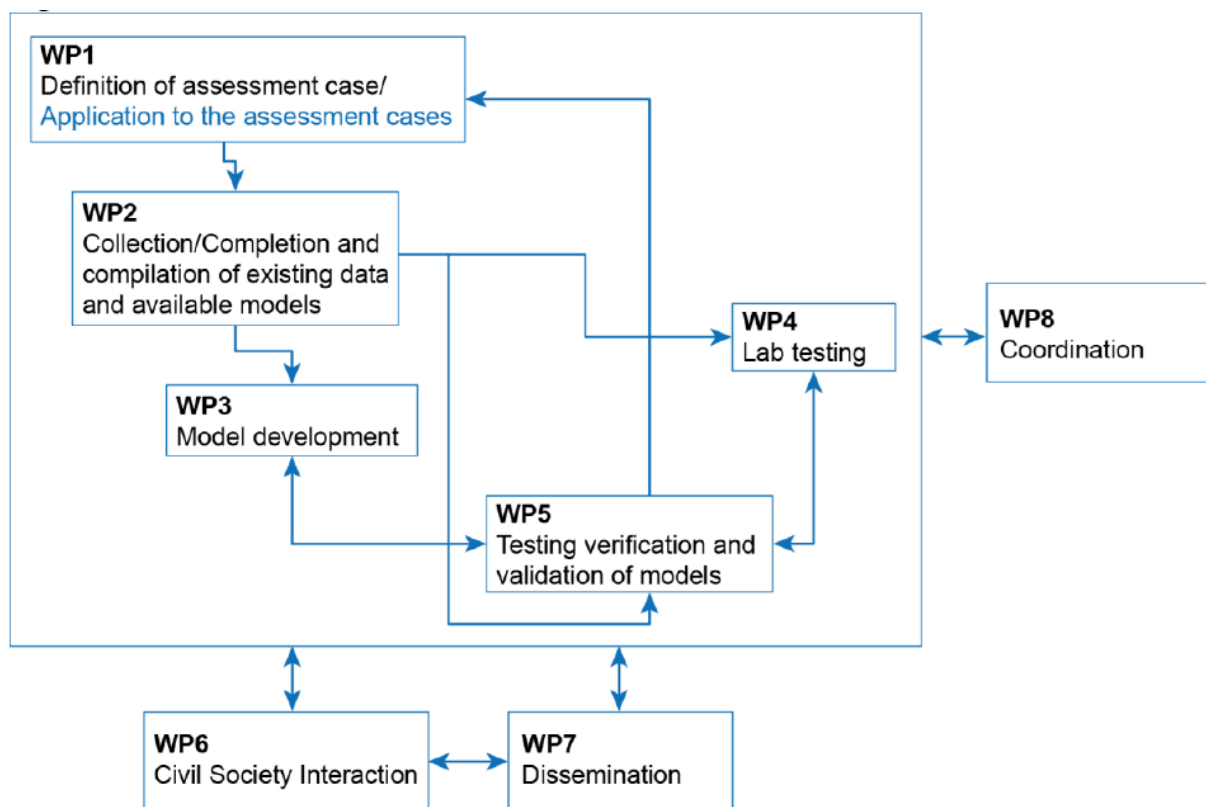


Figure 1-1. Structure of the BEACON project in terms of Work Packages. The arrows indicate one-way or two-ways relationships between Work Packages. The central location of Work Package 3 is apparent in the diagram.

This Deliverable 3.3 contains the final account of the activities performed in WP3 during the project. The state of the constitutive models at the start of the project was reported in Deliverable 3.1 whereas Deliverable 3.2 contained the developments carried out up to the half-point of the project (2 years). Deliverable 3.3 contains a summary description of the final

state of the constitutive models developed in the project (conceptual bases, mathematical description and model capabilities) as well as some assessment of their predictive power. Particular focus is placed on the improvements achieved during the course of the project.

It is important to note that the development of the constitutive models that constitute the subject of WP3 has been driven and influenced in large measure by their performance in the simulation of the benchmarks defined in WP5. Therefore, a proper understanding of the WP3 work can only be achieved by simultaneously considering the WP5 activities and results that are the subject matter of other Deliverables.

This document is structured as follows. After the introduction, a general overview of Work Package 3 is offered followed by a description of the models developed in the project and their capabilities. Afterwards, a verification Task is presented and the corresponding modelling results are reported and discussed. Finally, some general comments on model development and capabilities are put forward followed by a number of considerations concerning some outstanding uncertainties and the predictive power of the models. The Deliverable closes with a concluding remarks section.

An integral part of this Deliverable is the set of Annexes, from A to I, that contain the full details of the work carried out by the various modelling teams. The contents of the main body of this report should always be interpreted taking into account the information provided in those Annexes.

2 Work Package 3: general overview

The main goal of Work Package 3 is the development of constitutive models for the description of the mechanical, hydromechanical (HM) and, optionally, thermo-hydro-mechanical (THM) behaviour of bentonite-based materials with the aim of introducing them into numerical tools capable of analysing problems of engineering significance. In particular, the project BEACON is especially focused on the processes of homogenization or, conversely, the development of heterogeneity throughout the transient phase of engineered barriers and seals. The proposed scope of potential developments is wide: saturated and unsaturated materials, isothermal and non-isothermal conditions and different types of materials (e.g. compacted blocks, pellets-based granular bentonite).

Nine teams have performed model development activities:

- Bundesanstalt fuer Geowissenschaften und Rohstoffe (BGR), DE
- Charles University – Czech Technical University (CU-CTU, CZ Consortium)
- Clay Technology (ClayTech), SE
- Ecole Polytechnique Federale de Lausanne (EPFL), CH
- Imperial College London (ICL), UK
- Lietuvos Energetikos Institutas (LEI), LT
- Quintessa (Quintessa), UK
- Universitat Politècnica de Catalunya (UPC), ES
- Université de Liège (ULg), BE

Five other teams have provided support in various ways:

- Centro de Investigaciones Energeticas, Medioambientales y Tecnologicas (CIEMAT), ES
- Gesellschaft fur Anlagen und Reaktorsicherheit (GRS), DE

- Karlsruher Institut fuer Technologie (KIT), DE
- Posiva (POSIVA), FI
- Teknologian tutkimuskeskus (VTT), FI

The work in WP3 has included not only the development and improvement of constitutive models but also tasks of model implementation into computer codes to be used in the solution of boundary value problems at different scales. A variety of codes have been used for this purpose: Code_Bright (UPC), Comsol Multiphysics (Clay Tech., LEI, Quintessa), ICFEP (ICL), Lagamine (EPFL, ULg), OpenGeoSys (BGR), QPAC (Quintessa), SIFEL (CU-CTU). This variety of codes makes evident the wide scope of the numerical implementation work performed.

At the start of the project, the modelling teams were asked about the capabilities of the models were examined with respect to a number of general features of behaviour:

Mechanical behaviour:

- Dependence of swelling strain on applied stress
- Dependence of swelling strain on dry density
- Irreversibility of strains in wetting/drying cycles
- Dependence of swelling pressure on dry density
- Stress path dependence from an unsaturated to a saturated state
- Stress path dependence from a saturated to an unsaturated state
- Use of a double structure/porosity model
- Consideration of temperature effects
- Dependence of strains developed in a temperature cycle (increase/decrease) on OCR (or stress)

Hydraulic behaviour

- Consideration of hysteresis in retention curve
- Dependence of void ratio of the retention curve
- Use of a double structure/porosity model

Those features were considered to be the key characteristics of behaviour underlying the homogenization processes. The answers were collected in a series of Tables of capabilities that were included in Deliverable 3.1. Updated Tables of capabilities (Table 2-1) are incorporated in this Deliverable thus providing a summary view of the developments carried out in the project. It should be stressed, though, that those Tables indicate only major overhauls of the models, there have been many significant improvements and advances that do not get reflected there.

In addition, and in accordance with the project plan, a Task has been proposed in the WP (Task 3.3) for the verification of the basic features of the models against simple benchmarks. It has involved the simulation a set of oedometric tests on compacted MX-80 bentonite performed and made available by EPFL. The results of this Task are summarised in this Deliverable and described in detail in the Annexes.

Table 2-1. Updated Table of capabilities

Name of the constitutive law:			
Behaviour feature	D3.1	D3.3	Remarks
Mechanical behaviour			
Dependence of swelling strain on applied stress (at the same dry density) (Figure 1)			
Dependence of swelling stress on dry density (at the same stress) (Figure 1)			
Irreversibility of strains in wetting/drying cycles (Figure 2)			
Dependence of swelling pressure on dry density (Figure 4)			
Stress path dependence from an unsaturated to a saturated state (Figure 5)			
Stress path dependence from a saturated to an unsaturated state (Figure 6)			
Double structure/porosity considered?			
Are temperature effects considered in the model?			
Dependence of strains developed in a temperature cycle (increase/decrease) on OCR (or stress) (Figure 7)			
Hydraulic behaviour (retention curve)			
Hysteresis			
Dependence on void ratio			
Double structure/porosity considered?			

3 Constitutive models: description and capabilities

This section contains a summary account of the main features and the general capabilities of the constitutive models developed and used in the project. Full descriptions are provided in Annexes A to I from which the material that follows has been extracted and condensed.

3.1 Bundesanstalt fuer Geowissenschaften und Rohstoffe (BGR)

The mechanical constitutive law is based on a Modified Cam model that incorporates effects such as softening or hardening in an elasto-plastic framework. It allows the simulation of stress-path dependency and irreversibility in the mechanical behaviour. In the current state, the elastic parameters are held constant so there is no saturation-dependent elastic stiffness. The lack of cohesion in the model means that the mechanical model cannot start in a stress-free state. Also, under large dilatancy the yield surface collapses to a point, causing softening and localization. This is mitigated by limiting the evolution of the pre-consolidation pressure to a pre-determined minimum value. The model used is a simplified small strain variant.

A double structure model has been developed in which total porosity is additively split into macro and micro porosity. Both porosities co-exist at each material point and their evolutions are derived from the governing equations valid at the respective scale. The main assumptions made in the derivation of the micro scale balance equation are that fluid density is constant, there are no spatial flow terms and strains are purely swelling strains and fully reversible. With those assumptions the micro variables are updated at constitutive level and the number of global unknowns does not increase. The hydraulic model allows for a non-monotonic evolution of the stresses and it allows a delay in the evolution of the swelling stresses. To prevent unrealistic results under high suction values, the potential responsible for water uptake is uncoupled from the capillary pressure used to define the effective stress principle.

In the current model, the macro-porosity does not contribute to the coupled hydro-mechanical behaviour in partially saturated conditions and therefore, some complexity in the saturation process is lost. However, it is a simple and effective approach to capture major trends in the swelling pressure evolution and it is well suited to applications in confined conditions. Previous test cases simulated in the project have demonstrated consistent applicability of this definition of the swelling law to fully-confined or nearly-confined cases.

A newer simulation environment (OpenGeoSys⁶) has been used for the modelling performed in WP3. A non-isothermal extension of the model is currently planned. Other ongoing developments include the reformulation of the mode of water uptake and its effects on the volumetric deformation in unconfined conditions and the incorporation of mercury intrusion porosimetry data.

Table 3-1 contain the updated Table of capabilities for this model.

Table 3-1. Updated capability Table for the BGR model (DSM)

Name of the constitutive law: Elastoplasticity, linear swelling and double structure hydraulics (DSM)			
Behaviour feature	D3.1	D3.3	Remarks
Mechanical behaviour			
Dependence of swelling strain on applied stress (at the same dry density) (Figure 1)	Y	Y	
Dependence of swelling stress on dry density (at the same stress) (Figure 1)	Y	Y	Max. swelling pressure is a constant input parameter
Irreversibility of strains in wetting/drying cycles (Figure 2)	N	Y	Modified CamClay elastoplasticity
Dependence of swelling pressure on dry density (Figure 4)	N	N	Maximum swelling pressure is a constant input parameter. It does not depend on DD changes during simulation
Stress path dependence from an unsaturated to a saturated state (Figure 5)	N	Y	Covered by HM coupled elastoplastic model.
Stress path dependence from a saturated to an unsaturated state (Figure 6)	N	-	Testing of this feature not covered in modelling of Task 3.3
Double structure/porosity considered?	N	Y	Currently only for the hydraulic model
Are temperature effects considered in the model?	Y	N	Currently used model formulation for Task 3.3 does not have temperature yet.
Dependence of strains developed in a temperature cycle (increase/decrease) on OCR (or stress) (Figure 7)	Y	N	Currently used model formulation for Task 3.3 does not have temperature yet.
Hydraulic behaviour (retention curve)			
Hysteresis	N	N	
Dependence on void ratio	N	N	
Double structure/porosity considered?	N	Y	

3.2 Charles University – Czech Technical University (CU-CTU)

The model is a double structure formulation developed within the framework of hypoplasticity that includes the effects of temperature. It is based on the assumption that it is possible to distinguish two levels of structure a macrostructure, which represents an assembly of silt-size aggregates of the clay particles, and a microstructure, which represents the internal structure of these aggregates. A conceptual sketch of these two levels of structure is shown in Figure 3-1.

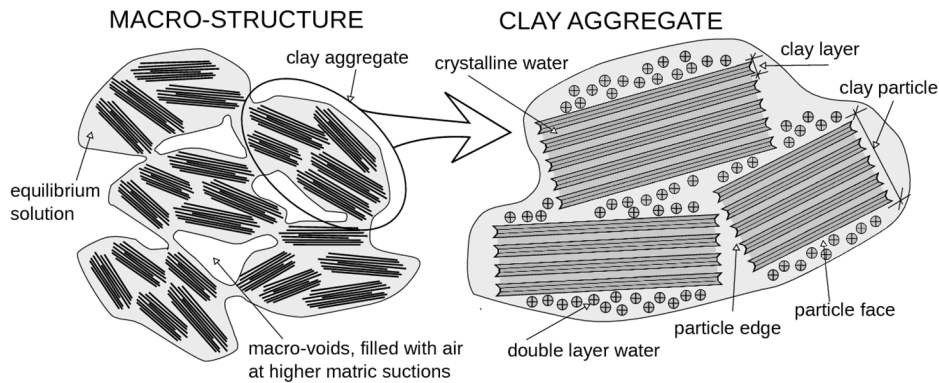


Figure 3-1. Schematic representation of the double structure concept

Figure 3-2 presents a scheme illustrating the hydromechanical coupling between the two structural levels. The individual models are denoted as G^M , G^m , H^M , and H^m , respectively. The mechanical behaviour of the macrostructure (G^M) is described using a hypoplastic model for unsaturated soils). The hydraulic response of the macrostructure (H^M) is based on a void ratio–dependent water retention model. The microstructure has been considered as fully saturated (simple H^m model), with its mechanical behaviour (G^m) reversible and volumetric, governed by the Terzaghi effective stress principle. The $G^M H^M$ coupling is accomplished by the dependency of H^M on volume change and by the dependency of the effective stress on degree of saturation of the macrostructure. The $G^m H^m$ coupling is introduced through the adoption of the Terzaghi effective stress for the mechanical behaviour of the microstructure. Finally, the double-structure coupling was controlled by a function of relative void ratio. An additional thermal dependency has been introduced for water retention curves, volumetric behaviour of microstructure and normal compression behaviour of the macrostructure.

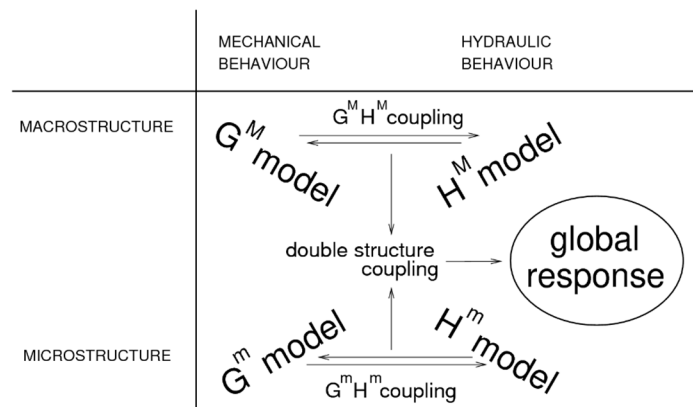


Figure 3-2. Scheme of the double structure coupling concept adopted in the hypoplastic model

The major focus of development within BEACON has been related to numerical aspects of the model implementation within the SIFEL finite element software. A significant improvement was the reformulation of the water retention model for macrostructure

This improvement focuses on the reformulation of the water retention model for macrostructure in order to have continuous first derivatives and thus to improve the numerical performance of the model. A comparison between the original and the new smoothed water retention curves is shown in Figure 3-3. It should be noted that hysteresis is incorporated in the water retention model. Other developments include the replacement of the effective stress of the macrostructural part of the model by an alternative formulation, and the introduction of suction-dependency of the quasi-elastic stiffness to allow the prediction of the higher swelling capacity of the saturated samples.

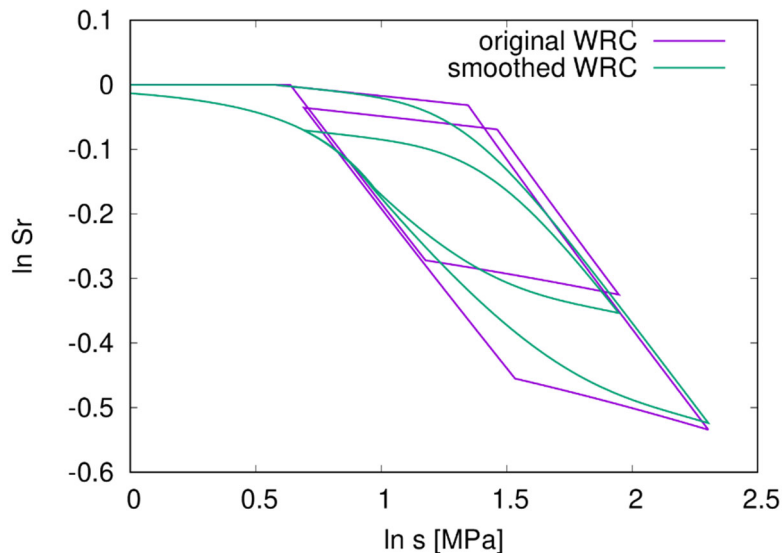


Figure 3-3. Comparison between the original and the new smoothed water retention curves

The THM hypoplastic model has been fully calibrated and validated with a comprehensive set of experimental data on the Czech BCV bentonite obtained within BEACON project, with the aim to be used in finite element simulations of experiments performed on this material. The potential of the model is further demonstrated in a comprehensive analysis, including sensitivity calculations, of the CRT experiment using parameters independently calibrated from laboratory results.

The updated Table of capabilities is presented in Table 3-2. It is evident that from the qualitative point of view, the original model already included all the listed capabilities but, of course, significant improvements have been introduced to achieve better quantitative agreement with observations.

Future developments are intended to address issues in the constitutive model (such as microstructural stress path dependency or behaviour at low water content) as well as introducing modifications in the numerical procedures to increase robustness.

Table 3-2. Updated capability Table for the CU-CTU model

Name of the constitutive law:			
Behaviour feature	D3.1	D3.3	Remarks
Mechanical behaviour			
Dependence of swelling strain on applied stress (at the same dry density) (Figure1)	Y	Y	
Dependence of swelling stress on dry density (at the same stress) (Figure 1)	Y	Y	
Irreversibility of strains in wetting/drying cycles (Figure 2)	Y	Y	
Dependence of swelling pressure on dry density (Figure 4)	Y	Y	
Stress path dependence from an unsaturated to a saturated state (Figure 5)	Y	Y	
Stress path dependence from a saturated to an unsaturated state (Figure 6)	Y	Y	
Double structure/porosity considered?	Y	Y	
Are temperature effects considered in the model?	Y	Y	
Dependence of strains developed in a temperature cycle (increase/decrease) on OCR (or stress) (Figure 7)	Y	Y	
Hydraulic behaviour (retention curve)			
Hysteresis	Y	Y	
Dependence on void ratio	Y	Y	
Double structure/porosity considered?	Y	Y	

3.3 Clay Technology (ClayTech)

In WP3 the formulation of the Hysteresis Based Material (HBM) model has been extended from a state where it only was only valid for isotropic and fully saturated conditions to the present state where it is valid for general stress states and general degrees of saturation. In addition, vapour and vapor transport have been included.

As described in Annex C, the basis of the mechanical part of the model is a thermodynamic relation for the chemical potential of the interlayer water in the clay. This relation couples the stress at full saturation to the chemical potential difference between the interlayer water and a reference water (suction) by a quantity denoted clay potential. The clay potential incorporates dry density dependence and path dependency, i.e. hysteresis. The unsaturated regime is introduced by incorporating a gas phase in addition to the phase consisting of saturated clay grains. This results in definitions of a micro void ratio, present in the saturated clay grains only, and a total void ratio. The total stress for the unsaturated clay is then defined by scaling the stress in the saturated clay grains with a contact area function, expressed in terms of the two void ratios. Finally, an interaction function, in terms of an evolution law for the micro void ratio, completes the model. Figure 3-4 illustrates the adopted material structure. It has been demonstrated that the new formulation is able to simulate the dependence of swelling strains on applied stress and void ratio, the irreversibility of strains in wetting/drying cycles, the dependence of swelling stress on dry density and the stress path dependency when moving from an unsaturated to a saturated state and vice-versa.

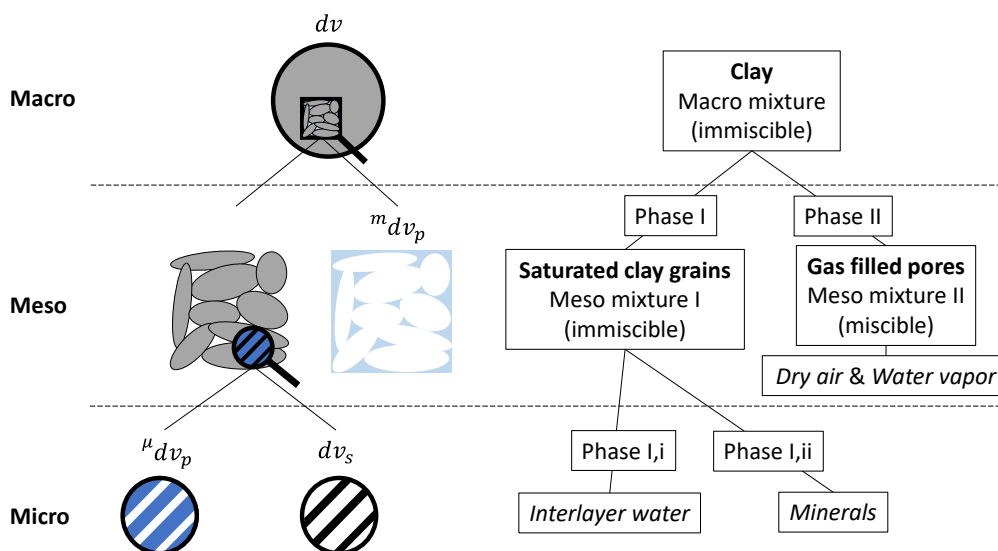


Figure 3-4. Conceptual scheme of the adopted material structure

The model is able, using a single set of parameters, to produce representative solutions for a wide range of problems. The model is versatile in the sense that material characteristics such as retention, swelling pressure and deviatoric stress at failure always are consistent with each other. Basing the model on a thermomechanical framework is also a strength when assessing the capabilities to make predictions. Another strength is that the model is not unduly flexible in the sense that excessive tweaking of the parameters is limited and they cannot be varied in an arbitrary manner.

Obviously, the clay potential function, which is dependent on the void ratio and the path dependent variable, lies at the very heart of HBM and governs much of the fundamental behaviour of the model. Therefore, it is essential to define, from experimental data, this function as accurately as possible. Limits to the generality of the original HBM formulation became evident when bentonite buffer components in other forms than compacted blocks are present, such as pellet filled gaps or granular bentonite. The simulation of these materials has

required a modification of the original contact area function although it may be necessary to revisit the material structure assumptions and thereby reformulate the material model. The implementation of the model into the Comsol Multiphysics code is still under development.

Finally, the updated Table of capabilities is shown in Table 3-3.

Table 3-3. Updated capability Table for the Clay Tech model (HBM)

Name of the constitutive law:		Hysteresis Based Material model	
Behaviour feature	D3.1	D3.3	Remarks
Mechanical behaviour			
Dependence of swelling strain on applied stress (at the same dry density) (Figure 1)	Y	Y	New calculations performed with developed model.
Dependence of swelling stress on dry density (at the same stress) (Figure 1)	Y	Y	New calculations performed with developed model.
Irreversibility of strains in wetting/drying cycles (Figure 2)	Y	Y	New calculations performed with developed model.
Dependence of swelling pressure on dry density (Figure 4)	Y	Y	New calculations performed with developed model.
Stress path dependence from an unsaturated to a saturated state (Figure 5)	-	Y	No analysis was performed in D3.1. New calculations performed with developed model.
Stress path dependence from a saturated to an unsaturated state (Figure 6)	N	Y	Analysis in D3.1 was treated as water-saturated throughout the changing state. New calculations performed with developed model.
Double structure/porosity considered?	Y	Y	For unsaturated conditions there are two pore spaces.
Are temperature effects considered in the model?	Y	Y	First and foremost, through the thermal expansion of water.
Dependence of strains developed in a temperature cycle (increase/decrease) on OCR (or stress) (Figure 7)	Y	Y	No new calculation apart from one in the D3.1 report.
Hydraulic behaviour (retention curve)			
Hysteresis	Y	Y	Inherent from the HBM model
Dependence on void ratio	Y	Y	Inherent from the HBM model
Double structure/porosity considered?	Y	Y	Micro pores water-filled and meso pores gas-filled at unsaturated states.

3.4 Ecole Polytechnique Federale de Lausanne (EPFL)

The model ACMEG-TS, capable to simulate the behaviour of non-isothermal and unsaturated soil conditions, was the starting point for the work performed in BEACON intended to extend the applicability of the model to highly expansive bentonite-based materials.

The water retention curve and the loading collapse curve have been the object of major modifications. Similarly to the original model, Bishop effective stress using the degree of saturation as the pore pressure averaging parameter is used as the variable conjugated to elastic strains, but now the degree of saturation is used as the variable that expresses the increase of yield stress with suction, defining a loading collapse curve such as that shown in Figure 3-5.

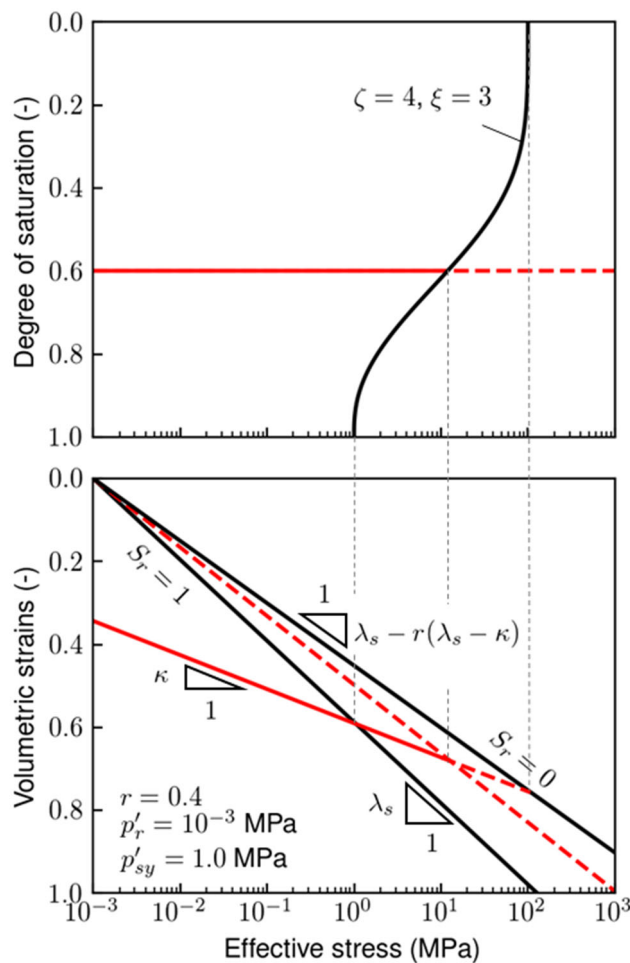


Figure 3-5. LC curve depending on degree of saturation and mechanical parameters for volume change behaviour

A new water retention model has been developed that takes explicitly into account the existence of adsorbed water and the dependency of free water on dry density. In addition, a non-isothermal extension is introduced where the elastic domain is expressed as a function of temperature to allow the consideration of thermo-plastic behaviour. The constitutive model developed has been implemented in the finite element code Lagamine.

The model has been calibrated using a series of laboratory tests on Febex bentonite (e.g. Figure 3-6) The model parameters, independently evaluated, have been successfully used in

the application of the model to the analysis of the Febex test (Step 2 in WP5) indicating a significant predictive potential.

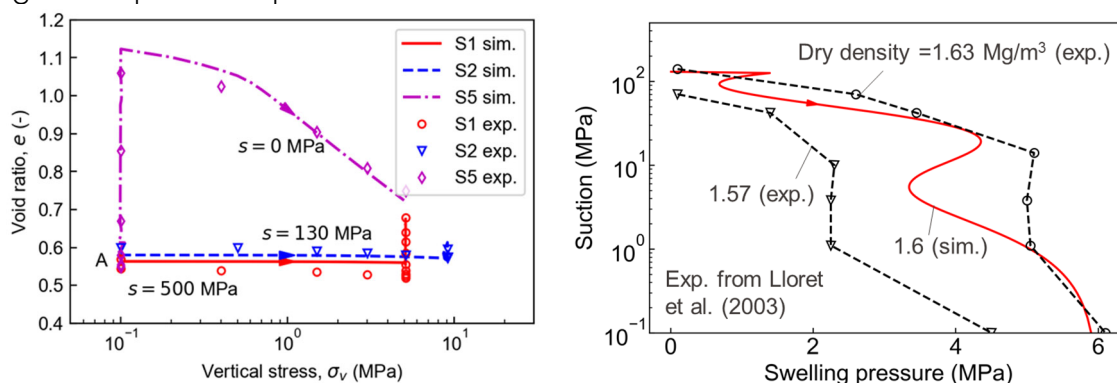


Figure 3-6. Examples of model calibration against results of laboratory tests on Febex bentonite

The main limitation of the model refers to the representation of the behaviour of low-density pellets materials where an excessive collapse is computed; further development may be required in this area as well as in the incorporation of hysteresis in the new water retention model.

Table 3-4 contains the updated Table of capabilities for this enhanced ACMEG-TS model.

Table 3-4. Updated capability Table for the EPFL model (ACMEG-TS)

Name of the constitutive law: ACMEG-TS			
Behaviour feature	D3.1	D3.3	Remarks
Mechanical behaviour			
Dependence of swelling strain on applied stress (at the same dry density)	Yes	Yes	Swelling strain under low stress is more consistent with experimental evidence in the new version
Dependence of swelling strain on dry density (at the same stress)	Yes	Yes	
Irreversibility of strains in wetting/drying cycles	Yes/no	Yes	Previous version: Final state not consistent with initial OCR New version: Consistent with experimental evidence
Dependence of swelling pressure on dry density	Yes	Yes	In the new version the stress collapse during swelling pressure can be controlled through specific input parameters
Stress path dependence from an unsaturated to a saturated state	Yes	Yes	In the new version the stress path dependence is an effect of different radial stress development during wetting
Stress path dependence from a saturated to an unsaturated state	Yes	Yes	
Double structure/porosity considered?	No	No	
Are temperature effects considered in the model?	Yes	Yes	
Dependence of strains developed in a temperature cycle (increase/decrease) on OCR (or stress)	Yes	Yes	
Hydraulic behaviour (retention curve)			
Hysteresis	Yes	No	
Dependence on void ratio	Yes	Yes	The dependency has been revised in the new model to better predict bentonite behaviour
Double structure/porosity considered?	No	Yes	In the new model: division between free water and adsorbed water

3.5 Imperial College London (ICL)

A double-structure model for unsaturated highly expansive clays, ICDSM, has been developed in the framework of elasto-plasticity and critical state-based soil mechanics. The model is an extension of a single structure model, ICSSM, developed for unsaturated moderately expansive clays. The ICDSM model adopts the conceptual basis of the Barcelona Expansive Model (BExM) but it incorporates a significant number of distinctive features

As described in Annex E, the ICDSM adopts the concept of double porosity typical of the structure of compacted clays (Figure 3-7). One level of porosity is the void space between the clay aggregates, defined as macro- or inter-aggregate porosity. The second level of porosity is the void space within an aggregate, defined as micro- or intra-aggregate porosity. Macro-porosity is associated with the evolution of negative pore water pressures (suctions) in the clay, while micro-porosity governs the physico-chemical processes associated with the clay mineralogy.

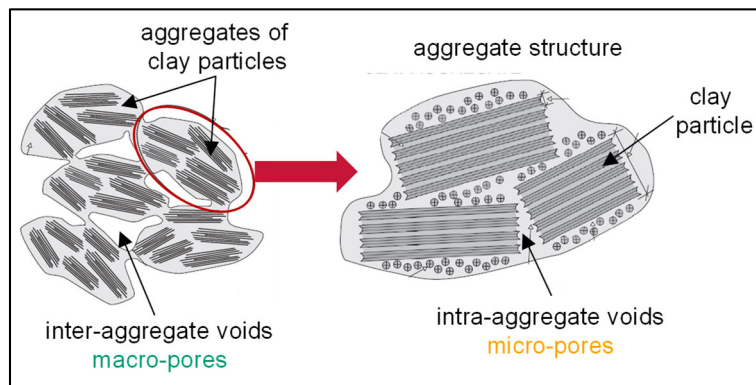


Figure 3-7. Conceptual scheme of a double-porosity structure

To enable the modelling of highly expansive materials, the pre-failure behaviour of the material is no longer purely elastic. Although the micro-structural volumetric deformation is elastic, it is assumed to contribute to the macro-structural volumetric plastic strains, introducing an additional plastic mechanism via suitable interaction functions (Figure 3-8). Finally, the ICDSM formulation introduces the void factor parameter that allows the quantification of the micro-structural evolution. It is defined as the ratio of the micro-void ratio to the total void ratio; this parameter expresses the degree of dominance of each structural level in the overall clay fabric. On the hydraulic side, a Van Genuchten-type soil water retention model and a variable permeability model have been adopted. Permeability is assumed to vary linearly with matric suction between two set values (Figure 3-9).

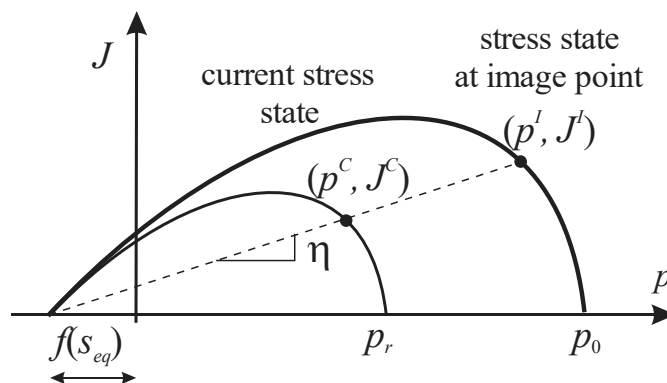


Figure 3-8. Definition of parameters describing structural interaction

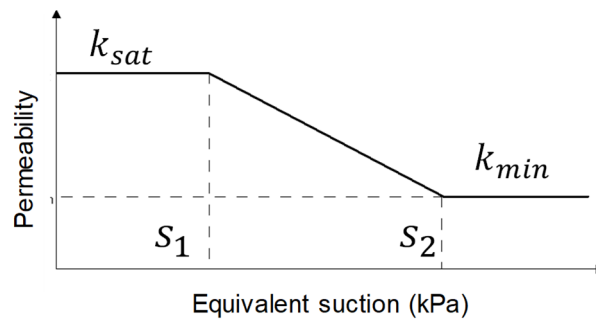


Figure 3-9. Variable permeability model

The hydro-mechanical model was mainly developed before the start of BEACON. While small numerical adjustments were made to the mechanical ICDSM model, its formulation remained the same throughout the project, as well as the formulations of retention curve and permeability models. Both mechanical and hydraulic models were calibrated from experimental evidence found in the literature for two types of bentonite. Two sets of model parameters were derived, one for MX80 and one for Febex materials. Those parameters sets were used throughout the project thus indicating a significant amount of predictive power. Adjustments were made mainly to micro-structural parameters and water retention curves in some simulations, to reflect the changes in the initial dry density. There is, however, still scope for more robust tuning and development of the modelling framework.

By means of suitable single-element analyses, it has been demonstrated that the ICDSM model reproduces correctly the dependence of swelling strains on applied stress and void ratio, the irreversibility of strains in wetting/drying cycles, the dependence of swelling stress on dry density and the stress path dependency when moving from an unsaturated to a saturated state and vice-versa. The updates capabilities of the model are shown in Table 3-5.

Table 3-5. Updated capability Table for the ICL model (ICDSM)

Name of the constitutive law: Imperial College Double Structure Model			
Behaviour feature	D3.1	D3.3	Remarks
Mechanical behaviour			
Dependence of swelling strain on applied stress (at the same dry density)	Y	Y	
Dependence of swelling strain on dry density (at the same stress)	Y	Y	
Irreversibility of strains in wetting/drying cycles	Y	Y	
Dependence of swelling pressure on dry density	Y	Y	
Stress path dependence from an unsaturated to a saturated state	Y	Y	
Stress path dependence from a saturated to an unsaturated state	Y	Y	
Double structure/porosity considered?	Y	Y	
Are temperature effects considered in the model?	N	N	
Dependence of strains developed in a temperature cycle (increase/decrease) on OCR (or stress) (Figure 7)	N	N	
Hydraulic behaviour (retention curve)			
Hysteresis	Y	Y	
Dependence on void ratio	Y	Y	
Double structure/porosity considered?	N	N	

3.6 Lietuvos Energetikos Institutas (LEI)

The hydro-mechanical (HM) formulation is based on Richards equation to represent water flow through unsaturated material and on elastic deformation to represent wetting-induced swelling. The retention curve proposed by EPFL that differentiates between capillary and absorbed water in a double porosity framework is adopted (Figure 3-10). The model also includes a dependence of the air-entry value on void ratio. The mechanical behaviour of bentonite has been represented by an elastic constitutive model based on the generalized Hooke's law complemented with hydration-induced swelling strains considered in an analogous manner as thermally-induced strains. Plastic deformations of bentonite are not considered in the current model.

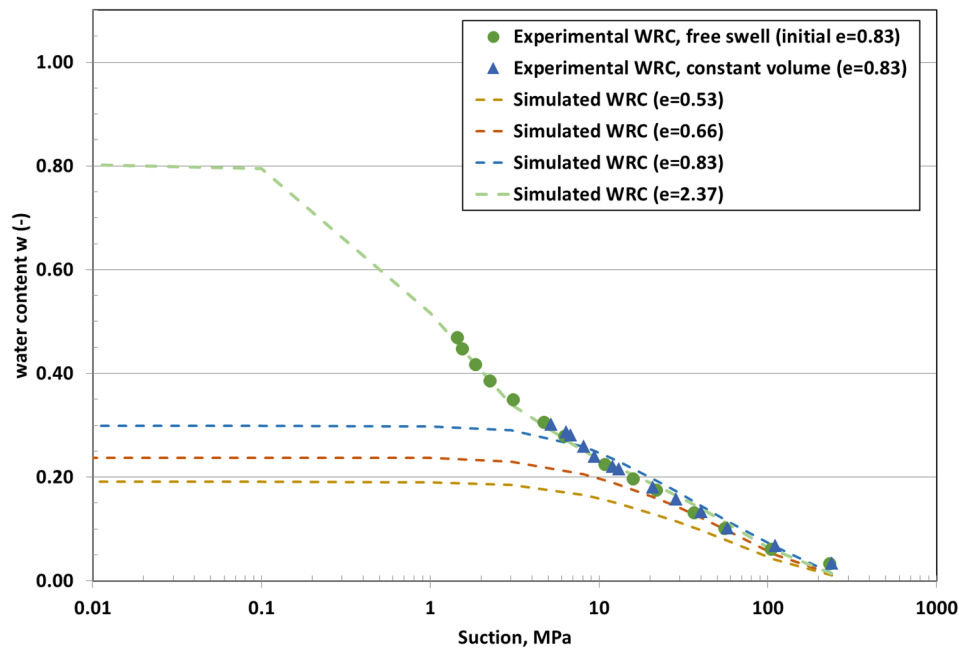


Figure 3-10. Water retention curves for MX-80 bentonite using the EPFL retention curve model

The model includes key couplings to consider the impact of mechanical deformations on porosity change and thereby on change of water balance, specific moisture capacity, storage coefficient and permeability. The non-linear elastic HM model was implemented in the numerical tool COMSOL Multiphysics.

From the analyses of boundary value problems, it has been found that the predictive power of the model is still somewhat limited in some cases. The model output could be considered more as an indicator of trends but not as a predictor for absolute values. The current model formulation includes some parameters such as swelling coefficient which depend on bentonite type, sample form, density, porewater composition and experimental conditions that require an experimental database covering the full range of these aspects. Further model developments are intended to incorporate the representation of irreversible strains.

In order to increase the predictive capacity of the model, the hydromechanical behaviour of bentonite under different material layouts, hydration conditions should be explored further experimentally and numerically. Further model developments are also needed with the main focus of the consideration of friction (for laboratory scale experiments) and the representation of irreversible strains.

The updated Table of capabilities (Table 3-6) shows that, in this case, there has been a very significant advance in the incorporation of major features of behaviour.

Table 3-6. Updated capability Table for the LEI model (HM)

Name of the constitutive law: Behaviour feature	Simplified Hydromechanical Model		
	D3.1	D3.3	Remarks
Mechanical behaviour			
Dependence of swelling strain on applied stress (at the same dry density)	-	yes	
Dependence of swelling stress on dry density (at the same stress)	-	Yes	Swelling strains depend on swelling coefficient which differ for samples of different dry density and is calibrated
Irreversibility of strains in wetting/drying cycles	-	No	Due to elasticity, strains are reversible
Dependence of swelling pressure on dry density	-	Yes	Swelling pressure is dependent on mechanical properties (bulk modulus), which defined as a function of void ratio (dry density)
Stress path dependence from an unsaturated to a saturated state	-	No	
Stress path dependence from a saturated to an unsaturated state	-	No	
Double structure/porosity considered?	-	-	Not implemented yet
Are temperature effects considered in the model?	-	-	Not implemented yet
Dependence of strains developed in a temperature cycle (increase/decrease) on OCR (or stress)	-	-	Not implemented yet
Hydraulic behaviour (retention curve)			
Hysteresis	No	No	
Dependence on void ratio	No	Yes	For water retention curve based on van Genuchten model, the dependence of air entry pressure on total void ratio is prescribed
Double structure/porosity considered?	No	Yes, partially	For water retention curve based on EPFL WRC model, capillary and absorbed water ratio could be related to macro and microporosity

3.7 Quintessa

Initially, Quintessa had available the Internal Limit Model (ILM) developed as part of the DECOVALEX-2015 project. It is a fully coupled thermo-hydro-mechanical model based on Richards' equation for the hydraulics, momentum balance for the mechanics and the Modified Cam Clay model to represent plastic deformation.

The model is based on an experimental empirical observation; i.e. the fact that three important relationships: the swelling pressure of the bentonite versus dry density, the suction versus water content and the void ratio versus vertical stress for loading and unloading (oedometer tests) can be described by a single exponential equation. The curves corresponding to those relationships constitute Internal Limit Curves, ILCs (Figure 3-11 to Figure 3-13). They suggest that, for a given dry density of the bentonite, there is a limiting stress that the material can support due to swelling, compaction or suction. In addition, it is assumed that suction is related to the difference between free swelling suction and stress. Observations from laboratory data are used to define the ILCs, which are used to parameterise both mechanical and hydraulic properties of the bentonite. In some case (retention curve) the ILC is considered dependent on temperature. The model is implemented in the multi-physics code QPAC.

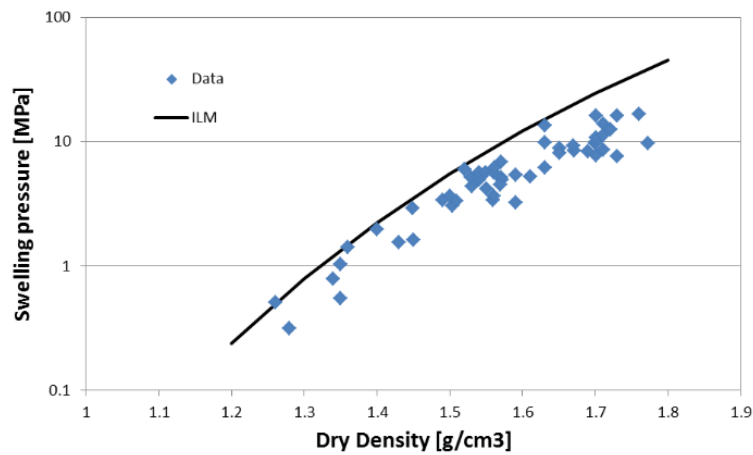


Figure 3-11. Example of ILC. Swelling pressure vs dry density data fitted exponential curve

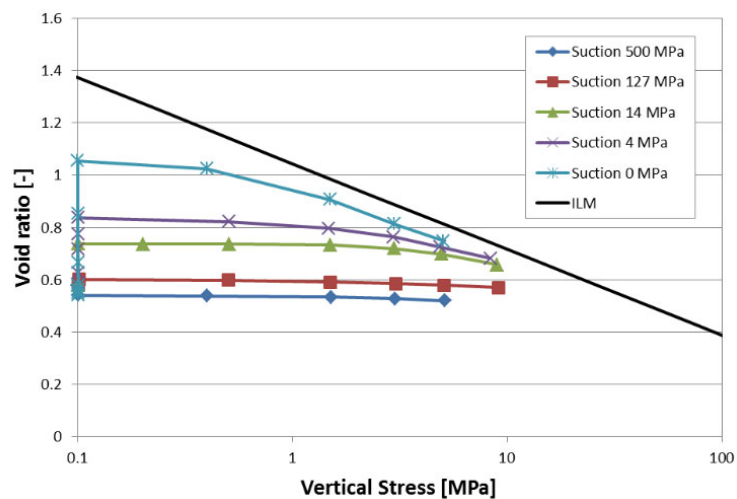


Figure 3-12. Example of ILC. Oedometer test data with fitted exponential curve

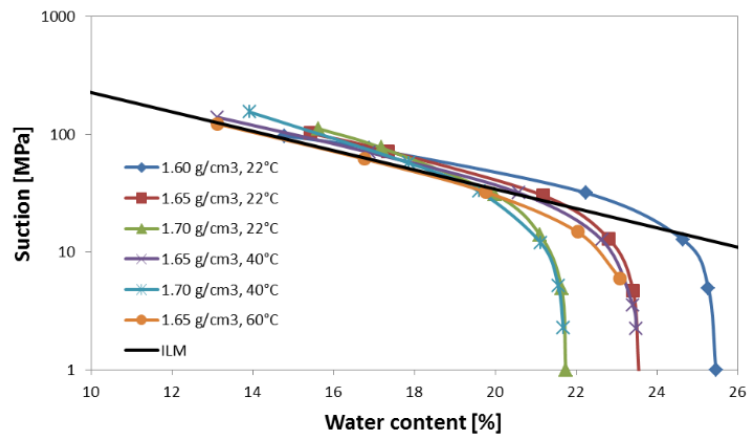


Figure 3-13. Example of ILC. Confined water retention data at different dry densities and temperatures compared with the ILM suction curve

The ILM is a single-porosity model. Although a double-porosity model may be more physically representative of the bentonite structure, it has been decided not to introduce this additional complexity in the model to avoid requiring additional parameters which are not always directly available from experimental measurements. During the BEACON project, the main focus has been on applying the existing ILM model for bentonite to new experiments and testing its validity, including its predictive capabilities. These applications have necessitated the development of improved material property models, development of friction boundary conditions, and developments to the QPAC code to enable representation of more complex geometries. Alongside this work, capabilities have been developed for modelling bentonite in COMSOL Multiphysics.

A major advantage of Quintessa's model is that it requires only a few parameters that are mostly directly measurable in experiments. The Internal Limit Curve can be parameterised using oedometer data and applied to parameterise water retention and swelling pressure curves. This greatly strengthens the predictive capabilities of the model, since it requires minimal calibration to each experiment. However, because of the exponential curve used, the model is particularly sensitive to uncertainties in measurements of dry density. The model has been successfully applied to a wide range of bentonite-based materials.

Although the full assessment of the predictive power has to be made within WP5, it can be stated that, similarly to other models, Quintessa's model is able to predict the final values of variables such as saturation and swelling pressure better than transient behaviour. This is true for both laboratory experiments and full-scale experiments.

The list of updated capabilities are presented in Table 3-7.

Table 3-7. Updated capability Table for Quintessa's model (ILM)

Name of the constitutive law:		ILM	
Behaviour feature	D3.1	D3.3	Remarks
Mechanical behaviour			
Dependence of swelling strain on applied stress (at the same dry density) (Figure 1)	✓	✓	
Dependence of swelling stress on dry density (at the same stress) (Figure 1)	✓	✓	
Irreversibility of strains in wetting/drying cycles (Figure 2)	✓	✓	
Dependence of swelling pressure on dry density (Figure 4)	✓	✓	
Stress path dependence from an unsaturated to a saturated state (Figure 5)	✓	✓	
Stress path dependence from a saturated to an unsaturated state (Figure 6)	✓	✓	
Double structure/porosity considered?	X	X	
Are temperature effects considered in the model?	✓	✓	
Dependence of strains developed in a temperature cycle (increase/decrease) on OCR (or stress) (Figure 7)	✓	✓	
Hydraulic behaviour (retention curve)			
Hysteresis	X	X	
Dependence on void ratio	✓	✓	
Double structure/porosity considered?	X	X	

3.8 Universitat Politècnica de Catalunya (UPC)

A double structure/porosity model (BExM) has been adopted as the main mechanical constitutive law to represent the behaviour of bentonite-based materials in the project. The model distinguishes between two structural levels: macro and micro. The basic physicochemical phenomena that underlie the swelling properties of the bentonite correspond to the microstructure leading to a behaviour that is assumed reversible but nonlinear. The macrostructural level corresponds to the overall arrangement of the larger components of the medium such as aggregates. The macro level is influenced by the microstructural strains, often in an irreversible manner. The relationship between the two structural levels is defined by two interaction functions, one for wetting paths and another one for drying paths (Figure 3-14). A feature of the model is the possibility of tracking the evolution of macro and micro porosities throughout the analysis, thus yielding results that can be related to microstructural experimental observations.

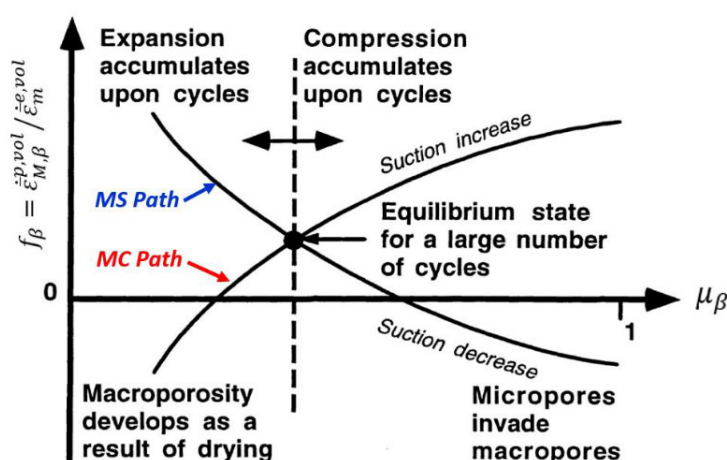


Figure 3-14. Interaction functions

In the initial stages of the project, a number of significant modifications were introduced in the existing constitutive model formulation. The most salient ones are: a more consistent definition of porosity and volume fractions, the fact that the microstructure may be unsaturated, and it is not assumed that there is hydraulic equilibrium between microstructure and macrostructure. The micro-macro transfer of liquid (or, sometimes, gas) is governed by a linear law between flow and micro-macro potential difference at a rate controlled by a newly introduced leakage parameter. Subsequent developments have included the clarification of the physical meaning of the interaction functions via DEM simulations and the examination of the relationship between the micro and macro elastic components that lead to a direct relationship between the two sets of elastic parameters.

In the later part of the project, the main activity has been related to the incorporation of thermal effects into the double structure constitutive law in a rigorous manner. This has required the modification of a large proportion of the model formulation (BExM-T). The work is still ongoing but a first version incorporating the thermal expansion of constituents and of the overall medium is available and has been used to perform the analysis of a non-isothermal assessment case.

Model developments have also involved the hydraulic component of the formulation. Variations of permeability depend only on the macro porosity, a more realistic assumption that, in addition, allows to examine the effect of evolving microstructure. This is consistent with the assumption that advective flow takes place in the macrostructure. The exchange of water (or gas) between micro and macro levels occurs at a local level only; this has the added

advantage that the potential (or suction) at micro level becomes a local variable, reducing in this way the number of global degrees of freedom. Also, separate retention curves are defined for each structural level, as the microstructure may now be unsaturated (Figure 3-15)

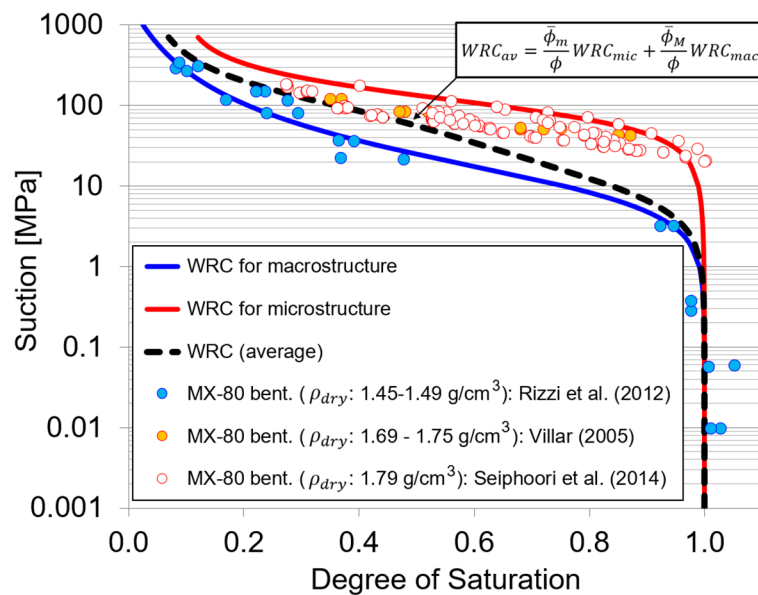


Figure 3-15. Water retention curves for the macro- and micro-structural domains of compacted samples of MX-80 bentonite

Finally, there has been continuous work on the BExM-T model implementation in the computer code (that it is still ongoing) to improve the convergence performance of the calculations. Special attention has been given to the precise calculation of the Jacobian under a variety of conditions. The numerical algorithm requires still improvements for the non-isothermal model.

It has also been possible to identify some shortcomings of the model that may require further developments: the adoption of Bishop effective stress for the microstructural behaviour that links too closely the effects of suction and stress changes, a more constrained manner to determine and calibrate the interaction functions is required, the variation of permeability with fabric changes should be reviewed. In addition, the use of a double structural model introduces a considerable level of complexity in the analyses and requires more computing power. The need for such an approach should be carefully evaluated for each particular case analysed. This appears to be especially relevant in non-isothermal problems. Although the model has been successfully applied to a wide range of cases, It should also be mentioned that, within WP3, the predictive power of the model is largely unproven.

Table 3-8 shows the updated list of model capabilities with some clarifying remarks

Table 3-8. Updated capability Table for the UPC model (BExM-T)

Name of the constitutive law:		Enhanced Double Porosity Model (BExM-T)	
Behaviour feature	D3.1	D3.3	Remarks
Mechanical behaviour			
Dependence of swelling strain on applied stress (at the same dry density)	YES	YES	The location of the stress state respect to the LC curve generates this dependence.
Dependence of swelling strain on dry density (at the same stress)	YES	YES	Swelling strain is implicitly dependent on the dry density. This dependence is modelled by a suitable choice of the saturated pre-consolidation pressure
Irreversibility of strains in wetting/drying cycles	YES	YES	The irreversible strains are generated in wetting/drying paths that cross the current LC curve.
Dependence of swelling pressure on dry density	YES	YES	At the same initial conditions, stress state and suction, different values of the isotropic yield stress for saturated conditions are used
Stress path dependence from an unsaturated to a saturated state	YES	YES	This feature comes from the HM constitutive formulation. The transition of saturated to unsaturated (or vice-versa) is not a trivial issue with the net stress as stress variable.
Stress path dependence from a saturated to an unsaturated state	YES	YES	
Double structure/porosity considered?	YES	YES	The expansive clay is considered as a multi-phase porous media composed by arrangement of clay aggregates and micro- and macro-pores.
Are temperature effects considered in the model?	NO	YES	Elastic thermal expansion/contraction is considered. Plastic thermal collapse can be introduced by the activation of the dependence of p_0^* on thermal changes. The dependence of the macro- and micro-structural water properties on temperature are also included in the current double-porosity model.
Dependence of strains developed in a temperature cycle (increase/decrease) on OCR (or stress)	NO	NO	Irreversible thermal strains arising from the structural coupling between micro and macro media are not taken into account. However, structural changes might occur during a temperature cycle because of the fully coupled THM formulation
Hydraulic behaviour (retention curve)			
Hysteresis	NO	NO	
Dependence on void ratio	NO	NO	It has not been considered so far. However, an explicit dependence of the pore-air entry value could be easily implemented into the present double-porosity formulation.
Double structure/porosity considered?	YES	YES	Macro- and micro-structural hydraulic responses are related to different WRC, each of them associated with a distinct pore level.

3.9 Université de Liège (ULg)

ULg has used two different constitutive models for bentonite-based materials in the project. The first one is an improved BBM, that was, to a large extent, available at the start of the project and it has been extensively used. The second model has been developed during the final stages of the project has only been applied to a benchmark. The second model will be subject to wide-ranging validation in the immediate future.

The classical BBM has been adopted as the basic initial model in the project (Figure 3-16). ULg has then performed a comprehensive (and very valuable) exercise of calibration of BBM parameters for a wide range of bentonite-based materials: Compacted Febex bentonite, Febex bentonite pellets, mixture of sand and MX-80 bentonite, MX-80 bentonite pellets and compacted MX-80 bentonite at two different dry densities. The work has been usefully extended to the estimation of the variation of BBM parameters with dry density(e.g. Figure 3-17).

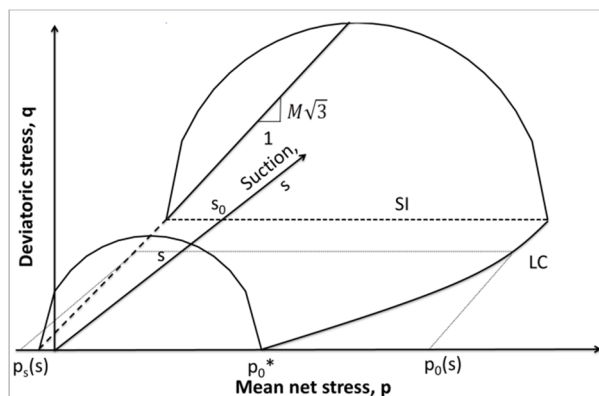


Figure 3-16. Three-dimensional view of the BBM yield surface

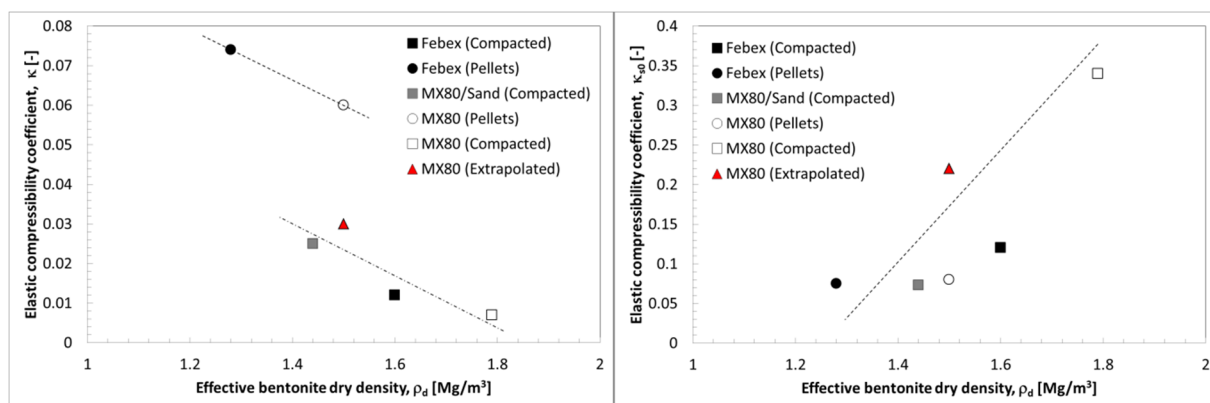


Figure 3-17. Calibrated variation of elastic compressibility coefficients with dry density

A significant drawback of the BBM model is the significant swelling pressure overestimation when isochoric wetting tests are modelled. In order to clarify this issue, the effect of the compressibility parameter for suction changes has been evaluated for three different cases: i) constant elastic compressibility coefficient, ii) constant elastic compressibility coefficient for saturation values below a given threshold, and iii) pressure-dependent elastic compressibility coefficient. It is concluded that, although option iii) requires back analysis calibration for the determination of two parameters, it provides a more accurate results for a larger range of phenomena and stress paths conditions.

For some benchmarks, ULg has also used an interface finite element and constitutive model, that allows taking into account both unilateral contact and friction. This has helped to improve significantly their modelling capabilities.

The updated capabilities of the model based on BBM are shown in Table 3-9.

Table 3-9. Updated capability Table for the ULg model (BBM-ULiege)

Name of the constitutive law:		BBM-ULiege
Behaviour feature	D3.3	Remarks
Mechanical behaviour		
Dependence of swelling strain on applied stress (at the same dry density)	Y	
Dependence of swelling stress on dry density (at the same stress)	Y	
Irreversibility of strains in wetting/drying cycles	N	
Dependence of swelling pressure on dry density	Y	
Stress path dependence from an unsaturated to a saturated state	Y	
Stress path dependence from a saturated to an unsaturated state	Y	
Double structure/porosity considered?	N	
Are temperature effects considered in the model?	N	
Dependence of strains developed in a temperature cycle (increase/decrease) on OCR (or stress)	-	Temperature effects not considered
Hydraulic behaviour (retention curve)		
Hysteresis	N	Only if irreversible change in void ratio occurs
Dependence on void ratio	Y	
Double structure/porosity considered?	Y	

In addition, ULg has developed a brand new constitutive model: Mohymar. It is a double-structure model (both mechanical and hydraulic) for unsaturated clays developed in the framework of hardening plasticity. The model is formulated using two independent stress variables: Bishop effective stress and a corrected suction pressure.

The model is able to reproduce the essential aspects of the behaviour of unsaturated clays: swelling/shrinkage upon hydration/drying; macrostructural swelling resulting from

Beacon

microstructural swelling; evolution of strength and stiffness with suction; plastic collapse upon wetting. Original features of the model include: consideration of distinct effects of capillary and adsorption suction; smooth transition to saturated state; ability to reach a minimum void ratio; transmission of macrostructural stress to microstructure related to soil fabric and yielding governed by microstructural phenomena.

The model has proved able to satisfactorily reproduce the evolutions of void ratio and microstructural void ratio during various hydration/loading paths, using a single set of parameters. Future work on the model will include: the design of an experimental program for the determination of the model parameters, the improvement of the hydraulic model to consider hysteresis and the incorporation of temperature effects.

The capabilities of the new model are presented in Table 3-10.

Table 3-10. Updated capability Table for the ULg model (Mothymar-ULiege)

Name of the constitutive law:		Mothymar-ULiege
Behaviour feature	D3.3	Remarks
Mechanical behaviour		
Dependence of swelling strain on applied stress (at the same dry density)	Y	
Dependence of swelling stress on dry density (at the same stress)	Y	
Irreversibility of strains in wetting/drying cycles	N	
Dependence of swelling pressure on dry density	Y	
Stress path dependence from an unsaturated to a saturated state	Y	
Stress path dependence from a saturated to an unsaturated state	Y	
Double structure/porosity considered?	Y	
Are temperature effects considered in the model?	N	
Dependence of strains developed in a temperature cycle (increase/decrease) on OCR (or stress)	-	Temperature effects not considered
Hydraulic behaviour (retention curve)		
Hysteresis	N	Only if irreversible change in void ratio occurs
Dependence on void ratio	Y	
Double structure/porosity considered?	Y	

Beacon

3.10 Main model developments and improvements

The main model developments and improvements carried out during the project by the different teams are:

- Bundesanstalt fuer Geowissenschaften und Rohstoffe (BGR)
 - Development of a double structure model (hydraulic model)
 - Incorporation of the elasto-plastic Modified Cam-Clay model for mechanical behaviour allowing for Irreversibility and stress path dependency.
 - Incorporation of a newer simulation environment (OpenGeoSys6)
- Charles University – Czech Technical University (CU-CTU, CZ Consortium)
 - Calibration/verification/validation of a double structure hypoplastic model (hydraulic and mechanical)
 - Advanced water retention model with a smooth transition between saturated and unsaturated states
 - Alternative formulation of the effective stress for the macrostructure and incorporation of suction dependence of the quasi-elastic stiffness
 - Development of finite element models using partially-coupled and fully-coupled algorithms
- Clay Technology (ClayTech)
 - Development of the Hysteresis Based Material (HBM) model for general stress states and general degrees of saturation
 - Incorporation of vapour transport
 - Modification of the original version of HBM to represent granular bentonite
 - Implementation of HBM into COMSOL Multiphysics (ongoing)
- Ecole Polytechnique Federale de Lausanne (EPFL)
 - Development of a new constitutive model based on a hydro-mechanical coupling framework
 - New water retention curve considering adsorbed and free water
 - Modified loading collapse curve function of degree of saturation instead of suction
 - Implementation of the new model in the Lagamine computer code
- Imperial College London (ICI)
 - Double-porosity structure mechanical model (ICDSM)
 - Van Genuchten-type soil water retention (SWR) model
 - Variable permeability model dependent on suction
 - Small numerical adjustments of the ICDSM model in the ICFEP computer code
- Lietuvos Energetikos Institutas (LEI)
 - Development of a hydro-mechanical model
 - Coupling of the two-phase formulation with heat transfer
 - Formulation of a nonlinear elastic hydro-mechanical model
 - Van Genuchten water retention curve with void ratio-dependent air entry
 - Implementation of the models in COMSOL Multiphysics
- Quintessa
 - Coupled hydro-mechanical Internal Limit Model (ILM)
 - Development of a friction boundary condition
 - Inclusion of thermal dependency (vapour diffusion, thermal expansion, and temperature-dependent water retention).
 - Implementation of the ILM in COMSOL Multiphysics (ongoing)

- Universitat Politècnica de Catalunya (UPC)
 - Hydraulic non-equilibrium between structural levels
 - Separate micro and macro water retention curves as the microstructure may be unsaturated
 - Incorporation of thermal effects, first stage (BExM-T)
 - Implementation of the BExM-T in CODE_BRIGTH (ongoing)

- Université de Liège (ULg)
 - Development and calibration of an enhanced BBM (mechanical)
 - Examination of the dependence on degree of saturation and pressure of the elastic compressibility coefficient for suction changes
 - Use of an interface element to simulate friction
 - Development of a new double structure hydromechanical model (Mohymar)

4 Task 3.3: verification

The project plan for WP3 includes the performance of a Task (Task 3.3) for the verification of the basic features of the models against simple benchmarks. After discussion within the WP, it was decided to use for the Task a set of oedometric tests carried out and made available by EPFL (Appendix 1).

4.1 Definition of the Task

The Task is based on a series of oedometer tests on granular MX-80 bentonite using the equipment depicted in Figure 4-1. The oedometric ring in the apparatus is 12.5 mm high and 35.0 mm in diameter. For the tests in which saturation was performed under isochoric conditions, the vertical stress was adjusted to minimize the occurrence of vertical strains (the maximum vertical deformation recorded was 0.6%).

The grading curve of the granular MX-80 bentonite tested is shown in Figure 4-2. All samples were initially prepared by pouring the granular material in the oedometric ring. The initial state of the samples corresponded to the as-poured and hygroscopic condition, with void ratios in the range 0.83-0.85 (corresponding to a dry density of 1.48-1.50 Mg/m³), water content in the range of 6-7% and a total suction between 90 MPa and 110 MPa. Figure 4-3 shows the Pore Size Distribution (PSD) obtained by Mercury Intrusion Porosimetry (MIP) of an as-poured sample with a void ratio of 0.83.

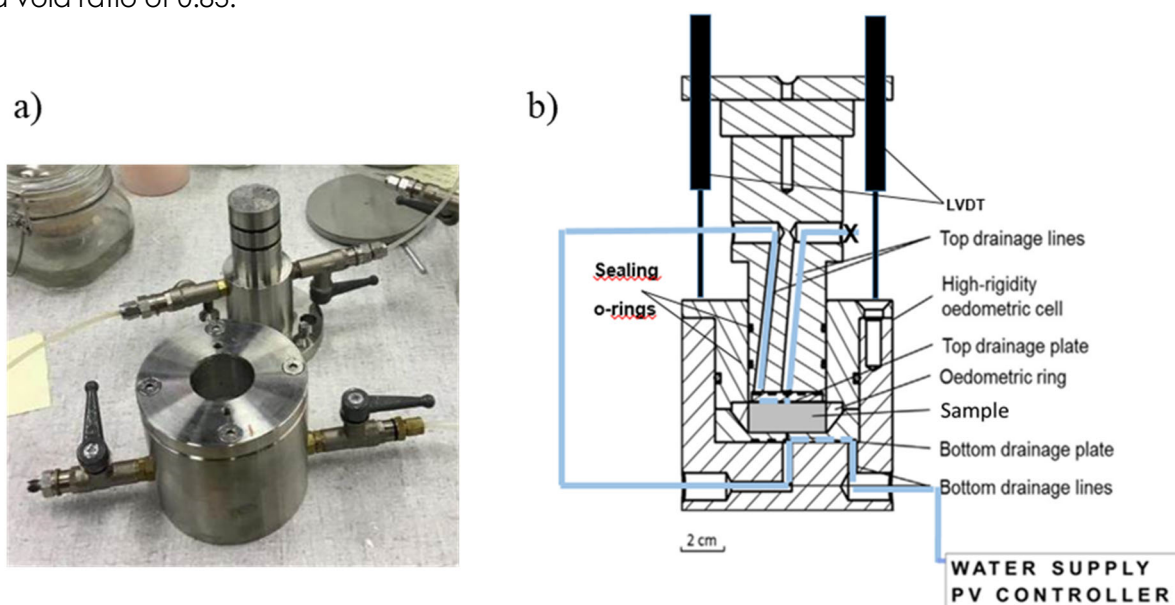


Figure 4-1. a) Oedometer apparatus used in the Task tests, b) Schematic layout of the equipment used to perform the Task tests

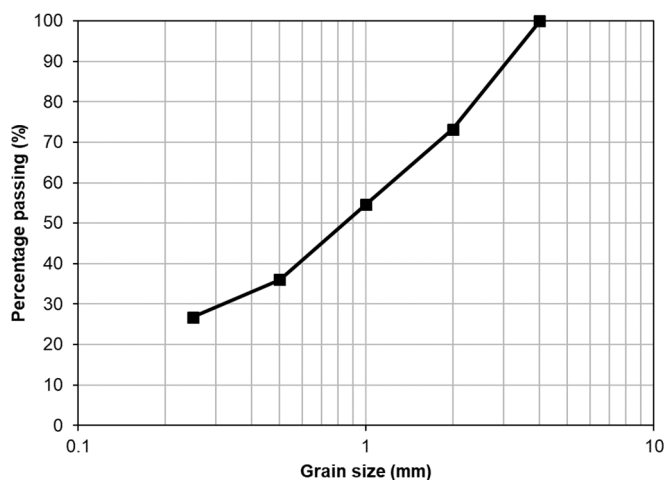


Figure 4-2. Grading curve of the granular MX-80 bentonite used in the Task tests

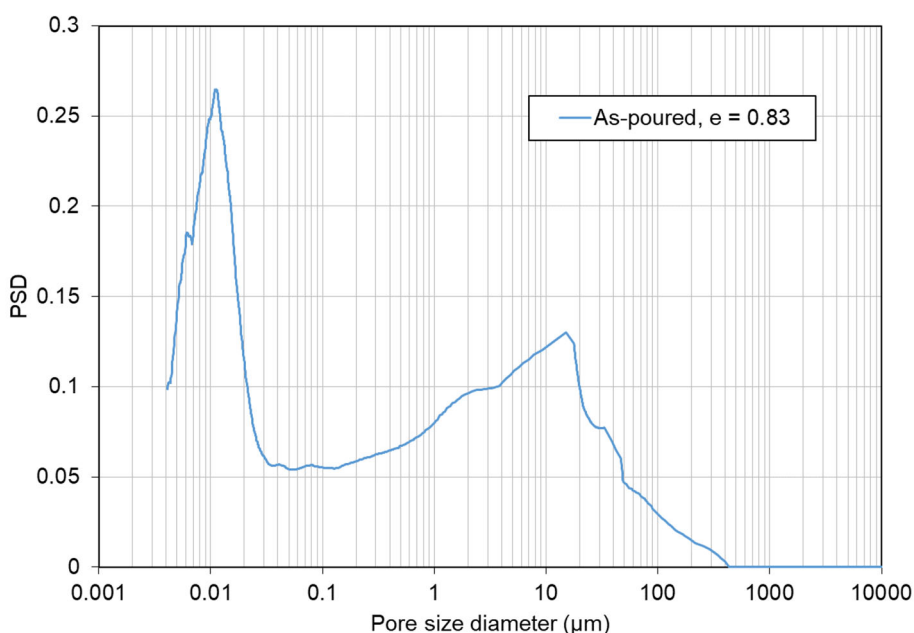


Figure 4-3. Pore size distribution of the as-poured sample, determined by MIP

The stress paths followed in the tests are schematically shown in Figure 4-4. Stress path 1 consists of a swelling by saturation under low applied vertical stress of 21kPa (path A- B) followed by loading of the saturated sample to a very large stress, about 20 MPa (path B-C-D). Stress path 2 started with a swelling pressure stage by saturation under isochoric conditions (path A-B') followed again by loading to a similar large stress (path B'-C'). Comparison of the void ratio at points C and B' gives information of the stress path dependency of the material at that point. Figure 4-4 also shows where MIP pore size observations were performed: A, B, C and B'. Three samples were prepared for each of the two paths; this allowed to perform MIP analyses at intermediate states of the hydro-mechanical loadings. Vertical strain and vertical stress were monitored throughout.

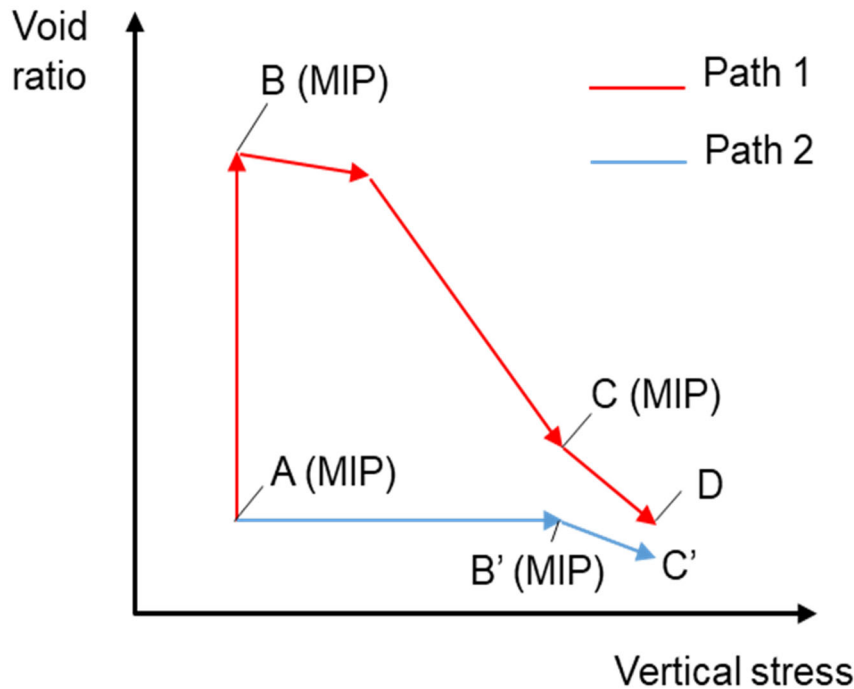


Figure 4-4. Stress paths followed in the testing programme. The points where MIP determinations were performed are indicated.

Figure 4-5 shows the results of the tests in terms of the evolution of vertical stresses with time (stress path A-B) and of the evolution of vertical swelling pressure with time in the isochoric test (path A-B'). It can be noted that the swelling strains under low applied pressure are very large (about 80 %) as corresponds to a highly expansive clay. The observed swelling pressure, 3.1 - 3.5 MPa, lies in the typical range of MX-80 bentonite at the dry density of the sample (2.5 - 4 MPa) obtained in previous investigations. The results of the experiments in terms of void ratio - vertical stress are plotted in Figure 4-6. It can be observed that the stress path dependency results in a void ratio difference of about 0.26 between points B' and C. This difference corresponds to a change of dry density from 1.30 g/cm³ (point C) to 1.50 g/cm³ (point B'), a significant amount.

The results of the pore size MIP determinations are presented in Figure 4-7. It is apparent that the pore size distribution experiences large changes as a result of the saturation and stress changes that occur during the tests. It should be noted that two MIP determinations were performed at each point of interest with very similar results.

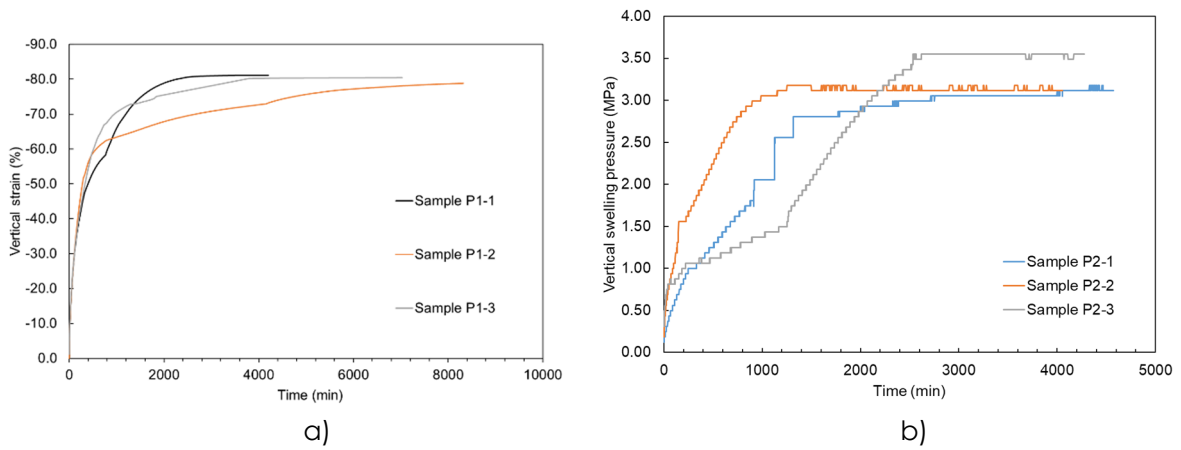


Figure 4-5. a) Evolution of vertical strain with time (path A-B), b) Evolution of vertical swelling pressure with time (path A-B')

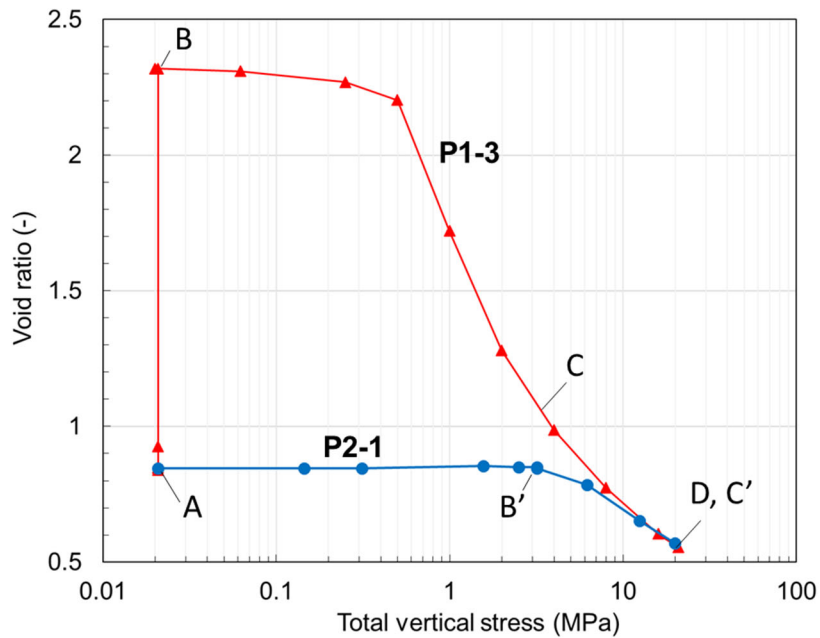


Figure 4-6. Void ratio – vertical stress results of two tests (P1-3 and P2-1) following different stress paths

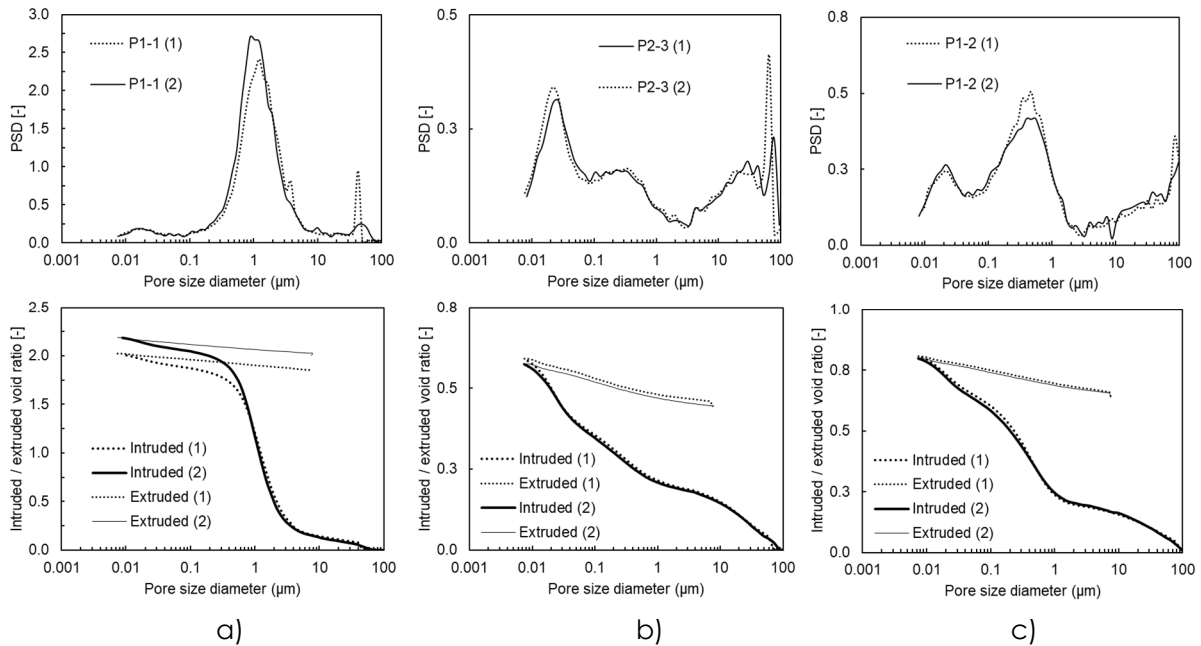


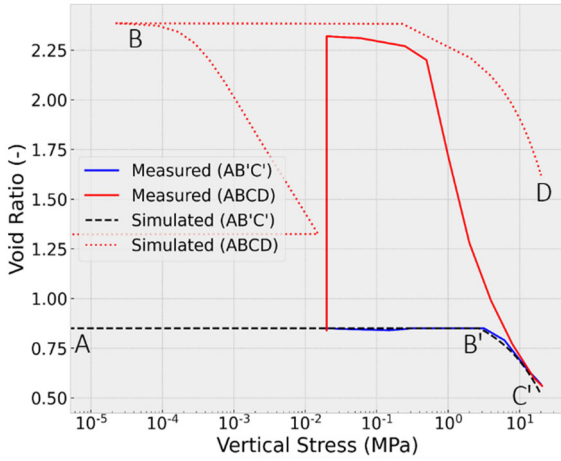
Figure 4-7. MIP results. Top row: pore size distribution, bottom row: intruded and extruded void ratios. a) at point B, b) at point B', c) at point C.

A full description of the experimental work carried out by EPFL is presented in Appendix 1.

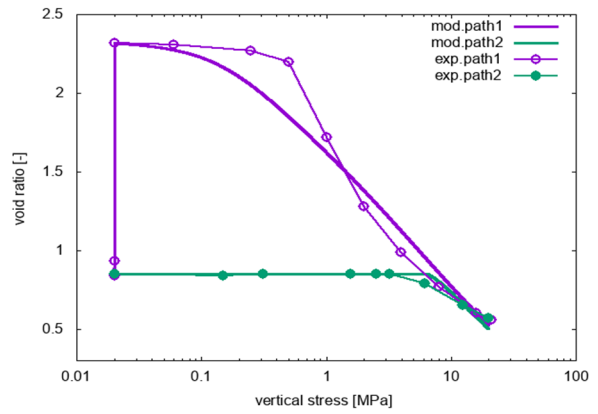
4.2 Modelling results

There were two options for simulating the EPFL tests: as a single element test (i.e. addressing only the constitutive behaviour) or as a boundary value problem modelling the actual laboratory test. BGR, ICL, LEI and ULg performed boundary value analyses whereas EPFL and UPC carried out Single Element analyses. CU-CTU, Cay Tech and Quintessa employed the two approaches. It appears that the same results were obtained with either approach.

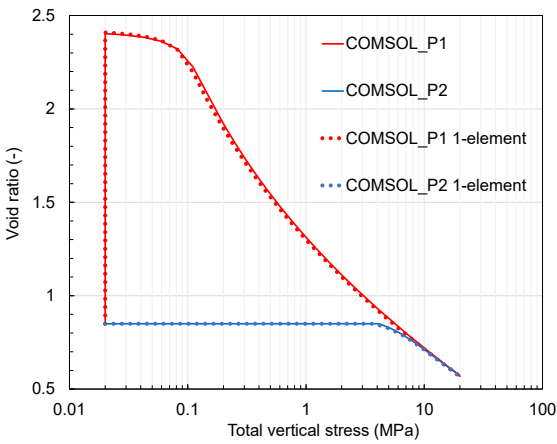
The modelling results of the various teams are summarised in the plots shown in Figure 4-8, extracted from the individual team reports. Some quantitative metrics are collected in Table 4-1.



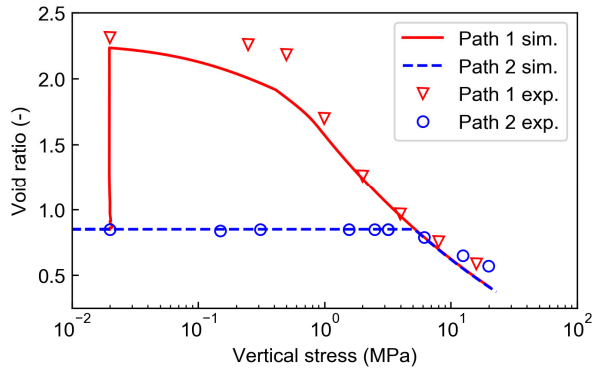
a)



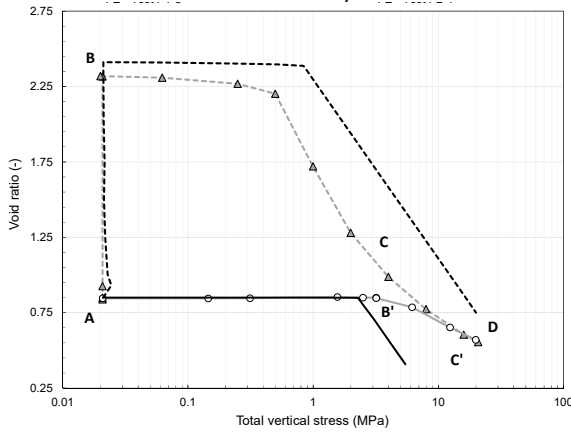
b)



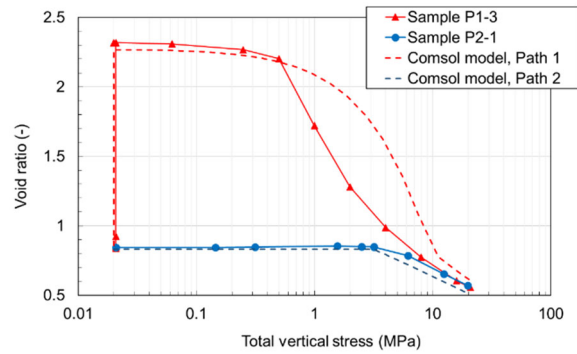
c)



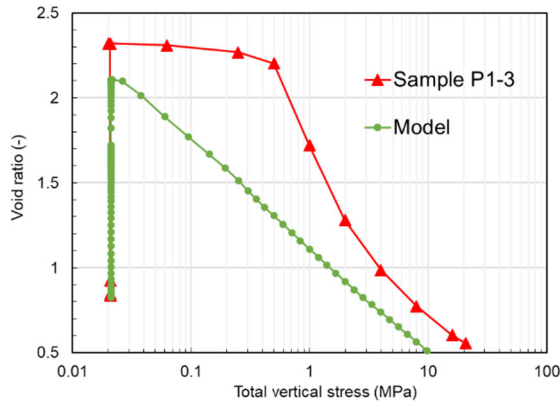
d)



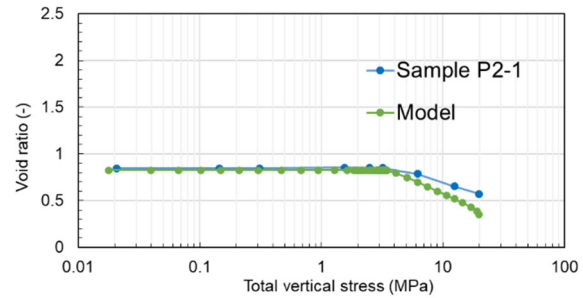
e)



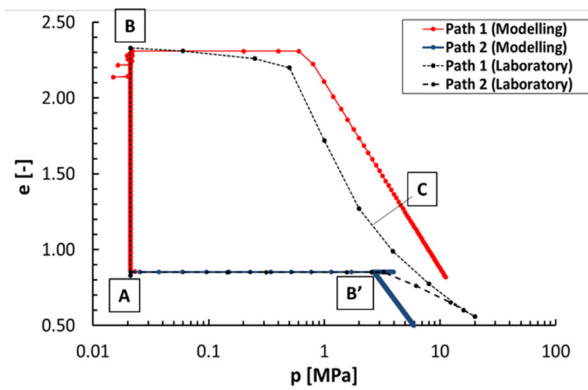
f)



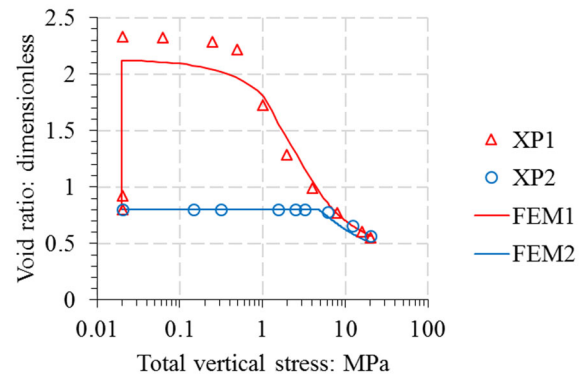
g)



h)



i)



j)

Figure 4-8. Modelling results of Task 3.3. a) BGR, b) CU-CTU, c)Clay Tech, d) EPFL, e) ICL, f) LEI, g) Quintessa, path 1, h) Quintessa, path 2, i) UPC, j) ULg.

Table 4-1. Task 3.3. Experimental and modelling results

	Type of analysis ¹	Void ratio (A)	Void ratio (B)	Swelling pressure, MPa (B')	Void ratio difference ²	Void ratio (C')	Void ratio (D)
Experiment	-	0.83-0.85	2.31-2.37	3.12 – 3.55	0.26	0.57	0.56
BGR	BV	0.85	2.39	2.71	1.33	0.52	1.62
CU-CTU ³	BV/SE	0.85	2.31	6.0	0.14	0.50	0.52
Clay Tech ³	BV/SE	0.85	2.40	3.72	0.09	0.58	0.57
EPFL	SE	0.85	2.23	5.0	0.02	0.41	0.41
ICL	BV	0.85	2.41	2.28	1.04	0.41 ⁶	0.75
LEI	BV	0.83-0.84	2.27	3.15	0.90	0.55	0.61
Quintessa ⁴	BV/SE	0.83	2.11	3.29	0.01	0.34	0.41
UPC	SE	0.85	2.32	2.78	0.69	0.48 ⁶	0.81 ⁶
ULg ⁵	BV	0.83	2.11	4.80	0.18	0.55	0.50

¹ BV: Boundary value analysis, SE: Single point analysis

² Void ratio difference between stress path 1 and stress path 2 at the value of the swelling pressure

³ Results from the Single Element analysis

⁴ Results from the Boundary Value analysis

⁵ Results from the Mohymar model

⁶ The vertical stress of 20 MPa was not reached

Quantitative evaluations, however, are not necessarily very informative as the Task was not a blind prediction exercise and, in principle, there were no constraints in the selection of parameters. It is probably more useful to identify some significant features of behaviour to be used as reference for the evaluation of modelling. The following features have been selected for this purpose (Figure 4-9):

- A) Development of large swelling strains under low applied stresses
- B) Sharp yield point when loading after swelling
- C) Magnitude of swelling pressure within or close to a reasonable range of values (2.5 - 4 MPa)
- D) Stress path dependency at the value of swelling pressure
- E) Convergence of the compression lines at large applied vertical stresses

Features A, C and D are probably the most relevant references in connection with the behaviour of barriers and seals. The large swelling strains under low applied stresses (A) is related to the behaviour of the bentonite when sealing voids, the value of swelling pressure (B) is relevant to the saturation-induced behaviour of the bentonite placed between rigid boundaries and stress path dependency (D) is related to the development of heterogeneities inside the barrier or seal. In contrast, the existence of a yield point (B) should have only a limited effect during the transient period and it is unlikely that the bentonite stresses will go much beyond the swelling pressure value (E). The results of this approximate qualitative evaluation are presented in Table 4-2.

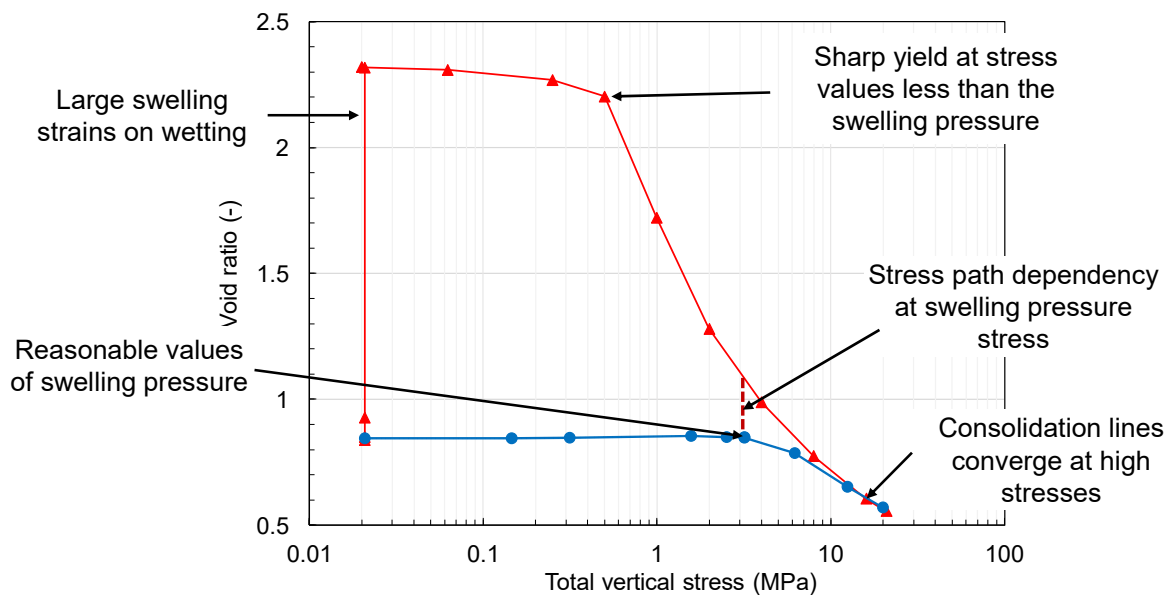


Figure 4-9. Features of behaviour for evaluation references

Table 4-2. Qualitative evaluation of Task 3.3 modelling

	A. Large swelling strains	B. Yield point	C. Swelling pressure	D. Stress path dependency	E. Convergence comp. lines
BGR	Yes	No	Yes	Yes ⁴	No
CU-CTU ¹	Yes	No	Yes	Yes	Yes
Clay Tech	Yes	Yes	Yes	Yes	Yes
EPFL	Yes	Yes	Yes	No	Yes
ICL	Yes	Yes	Yes	Yes ⁴	No
LEI	Yes	Yes	Yes	Yes ⁴	Yes
Quintessa ²	Yes	No	Yes	No	No
UPC	Yes	Yes	Yes	Yes ⁴	No
ULg ³	Yes	Yes	Yes	Yes	Yes

¹ Results from the Single Element analysis

² Results from the Boundary Value analysis

³ Results from the Mohymar model

⁴ Stress path dependency severely overestimated

Although many of the models used in the Task are based on a double structure formulation, only two teams (CU-CTU and UPC) have made an explicit comparison of the model results with experimental observations. Although significant quantitative differences were observed, UPC reported that experimental observations and model calculations were quite consistent: in path A-B there is a large increase of micro void ratio but, also, an even larger one of the macro void ratio, loading (path B-C) results in mainly a reduction of macro void ratio, and the swelling pressure test (path A-B') exhibits a quite limited variation of micro and macro void ratios. However, using a different pore size value to distinguish the two porosity levels, CU-CTU reported more mixed results. It is evident that significant uncertainties remain regarding the criterion to separate micro and macro porosity.

Summarising the Task, it can be asserted that, by and large, the various models are able to follow the main trends obtained in the laboratory tests and they are mostly able to reproduce the most important features of behaviour. It is apparent that some models may benefit from additional work, but their current state appears to be quite suitable to simulate the expansive clay behaviour typical of bentonite-based materials.

5 General comments on model development and capabilities

The development and improvement of the models by the different modelling teams have been extensive and varied. They have been driven by a variety of reasons including the widening the scope of applications, the desire to include fabric and microstructural considerations, the need to improve their performance when applied to the WP5 benchmarks and the requirement to move to non-isothermal problems. The extent of the modifications has depended strongly on the state of the model at the start of the projects; some teams have only needed to carry out minor modifications whereas other teams have had to develop a constitutive model starting from a very basic formulation. In spite of the wide range of model developments and improvements, specific to each modelling team, it is possible to derive some general observations:

- As the updated Tables of capabilities illustrate, it can be stated that the models developed are able to reproduce what are considered to be the key features of behaviour underlying the homogenization processes such as stress path dependency and strain irreversibility. This is confirmed by the satisfactory performance of all the models in conceptual stress path modelling and in the reproduction of Task 3.3 experiments.
- Most models are developed within an elastoplastic framework. One model adopts a hypoplastic formulation whereas another one uses a swelling nonlinear elastic model. Two models (HBM and ILM) are based on a fundamental backbone curve, experimentally determined.
- Double structure models have become dominant in WP3 developments. Sometimes both hydraulic and mechanical models are based on a double structure formulation (5 teams) and, in other cases, only one of the components includes a double structure approach (3 teams). Those double structure developments try to incorporate in the model information on the fabric and microstructure of the material. However, it has not been demonstrated that the improved model results (if identified) compensate for the added complexity and the need to determine a higher number of parameter and initial conditions.
- Most water retention curves are based on the Van Genuchten original expression or on a slightly modified form. Water retention hysteresis is largely ignored (only three teams incorporate it) whereas most teams (7) consider some dependence on void ratio.
- Only three teams have developed a thermo-mechanical model that include explicitly the effects of temperature on mechanical behaviour. It appears, however, that the simple inclusion of an overall thermal expansion of the material is sufficient to achieve satisfactory modelling results in non-isothermal problems at least up to the temperatures contemplated in the BEACON project. It is unknown whether the same conclusion applies to higher temperatures.
- In spite of the prevalence of the double structure models, only two teams have reported the predicted evolution of micro and macro void ratios and has compared it to experimental MIP results. Some predictions appears to be rather consistent with observations. The criterion to distinguish between the two porosity levels remains an issue, though.
- Although it has been proved that lateral friction has an important influence on some laboratory results, only three teams report explicitly the development of appropriate formulations for inclusion in the analyses.



The proper evaluation of the performance of the constitutive models developed in WP3 must be based on their applications to the proposed WP5 benchmarks and, therefore, it is a matter for the corresponding report. Those benchmarks will also provide the information required to identify the learning points acquired from the modelling of experiments involving mechanical evolution and homogenization of the bentonite.

6 Outstanding uncertainties and predictive power of the models

A source of uncertainty identified by practically all modellers is the scarcity of experimental data to determine all the parameters required by the constitutive models. This is especially valid for the modelling of granular bentonite; the situation for compacted bentonite is somewhat better. Against that observation, it must be admitted that the number of parameters in many of the models used in the project is very large. Another common remark is the scarce information on the repeatability and reliability of the experimental results in the proposed benchmarks that may underlie some of the modelling difficulties encountered by various teams.

A general observation is that the final state of the bentonite (in terms of swelling pressure and/or dry density distribution) is more robustly predicted than the transient behaviour; the comparison of the time variation of the various relevant parameters with experimental results is sometimes rather poor. This may be due to the inherent sensitivity of the transient phenomena to small changes in parameters and initial and boundary conditions but the difficulty in determining precisely the required parameters with available information may also play a role.

There is general agreement that there are still limitations in the fundamental knowledge of the basic processes underlying homogenization and other related mechanical phenomena. In this respect, the performance of simple well-designed small-scale laboratory tests addressing individual relevant phenomena is likely to be the most efficient way to advance knowledge. Large field scale tests, though useful to bring all the relevant phenomena together in a realistic setting, are less convenient for enhancing fundamental knowledge. Naturally, the relevant phenomena have to be selected based on the requirements of end-users.

The corresponding activity in terms of constitutive model development would be the performance of sensitivity analyses to establish unambiguously the role and effects of each parameter or group of parameters in relation to different basic behaviour features and phenomena. Because of the large number of cases that had to be modelled in the project (in order to increase the scope of the work), the sensitivity analyses performed have been limited.

Another uncertainty involves the way of incorporating microstructural information in modelling and to decide in which circumstances it is advisable to resort to the unavoidable higher complexity of double structure models. In any case, experimental fabric determination should become a standard feature of laboratory testing. It is unclear at present whether the same model can be used for compacted bentonite and granular bentonite by simply changing the parameters. It is likely, however, that the variation of hydraulic parameters is quite sensitive to the evolution of fabric that is bound to be quite different in the two types of materials.

The consideration in the models of thermal effects on the mechanical behaviour of compacted and granular bentonite is also limited at present, beyond the consideration of a simple thermal expansion coefficient. It appears that this has been sufficient for a successful modelling of non-isothermal problems so far, but it is unknown whether better knowledge and enhanced models are required when moving to higher temperatures. Finally, it is imperative that friction is introduced in the simulation and interpretation of at least some laboratory experiments.

There have been no predictive exercises performed within WP3, the results of Task 3.3. were known to the modelling teams. Therefore, there are no objective bases to evaluate the predictive power of the different models within the WP. In WP5, however, there has been a prediction exercise in Step 3 involving calibration tests quite similar to the experiment selected for blind prediction. Some teams have also reported good quantitative predictions of large-scale tests where many of the parameters have been determined independently from

laboratory tests. Although they are not strictly predictive tasks, they provide further confidence in the potential of the models. Overall, it is undoubted that the predictive power of the models developed has increased significantly as a result of the project. However, more efforts are still required to achieve a wider evidence-based assessment of the predictive capabilities of the models and their range of applicability.

7 Concluding remarks

Important and substantial advances have been performed in the framework of BEACON's WP3 regarding the development and improvement of constitutive models and their implementation in computer codes. The models encompass a wide range of approaches and can deal with an extensive combination of simulation conditions. The models developed are able to reproduce what are considered to be key features of behaviour underlying the homogenization processes such as stress path dependency, strain irreversibility, and others. As a result, modelling capabilities in this area have been enhanced very significantly as a result of the project. The performance of the models when applied to the simulation of relevant problems is assessed in WP5.

In the context of these advances, several modelling teams have also identified areas of further constitutive model developments that are deemed necessary to improve simulation capabilities. In addition, outstanding uncertainties remain concerning the detailed knowledge of some of the individual phenomena underlying homogenization, the precise role of different components and parameters of specific models and the actual predictive power of the formulations developed in the project.

Appendix. Modelling specifications for Task 3.3



MODELLING SPECIFICATIONS FOR TASK 3.3: PERFORMANCE OF CONSTITUTIVE MODELS DEVELOPED IN THE PROJECT

Authors:

Jose A. Bosch, Patrycja Baryla and Alessio Ferrari*

*Contact: alessio.ferrari@epfl.ch

03/07/2019

Contents

1	Introduction	2
2	Tests description	2
2.1	Tested material	2
2.2	Testing set – up	4
2.3	Description of the HM oedometric tests.....	5
3	Test results	6
3.1	Vertical swelling (path 1, stage A–B).....	6
3.2	Swelling pressure test (Path 2, stage A–B').....	7
3.3	Oedometric compression (stages B–C–D and B–C').....	8
3.4	MIP results.....	8
4	Task description	9
5	References.....	9

1 Introduction

This task focuses on the influence of two different hydro-mechanical (HM) stress paths on the final state of granular MX80 bentonite. The task is based on laboratory tests in which two different hydration procedures (free-swelling and constant-volume) were applied; both tests continued with compression to a similar value of vertical total stress. All tests were performed in oedometric conditions.

Microstructural analyses by means of mercury intrusion porosimetry (MIP) were performed in order to assess the evolution of the microstructural features of the material along the different HM loadings.

The description of the tests and the obtained results are given in the following sections. Data are provided in the attached spreadsheets.

2 Tests description

2.1 Tested material

The tested material is granular MX-80 bentonite. Some basic and index properties are reported in Table 1 (after Seiphoori et al. 2014). Dry density of the grains is approximately equal to 2.1 Mg/m³.

The apparent grain size distribution (i.e. distribution of the size of the bentonite grains at the beginning of the tests) is depicted in Figure 1. All samples were initially prepared by pouring the granular material in the oedometric ring. The dry density of the poured material is in the range of 1.48-1.50 Mg/m³; the corresponding values of void ratio are in the range of 0.83-0.85.

Table 1. Basic properties of the MX80 bentonite used in the tests

Smectite content	Specific surface	Specific gravity	Liquid limit	Plastic limit
85%	523 m ² /g	2.74	420%	65%

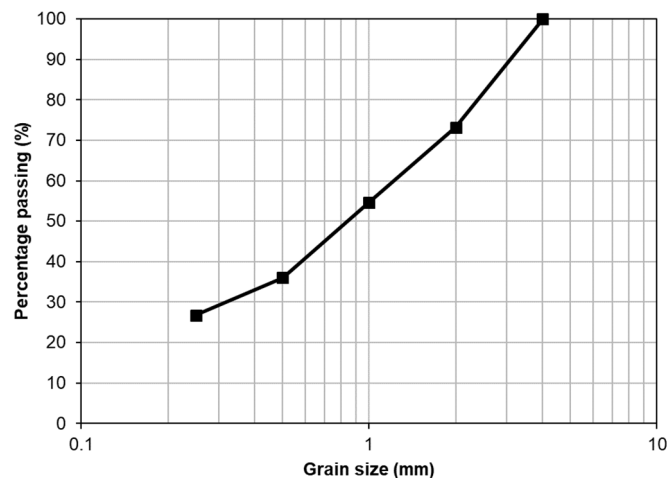


Figure 1. Apparent granulometry of the tested samples

In Figure 2 the Pore Size Distribution (PSD) obtained by MIP of an as-poured sample with a void ratio of 0.83 is reported (data from Seiphoori (2014)).

The water retention behaviour of the MX80 granular bentonite is shown in Figure 3 (data from Seiphoori et al. (2014)) for samples initially prepared at a void ratio of 0.83. The water retention curves refer to free-swelling and constant-volume conditions. Wetting and drying branches are depicted. Seiphoori et al. (2014) discussed the evolutions of the MX80 microstructure associated with the wetting and drying cycles.

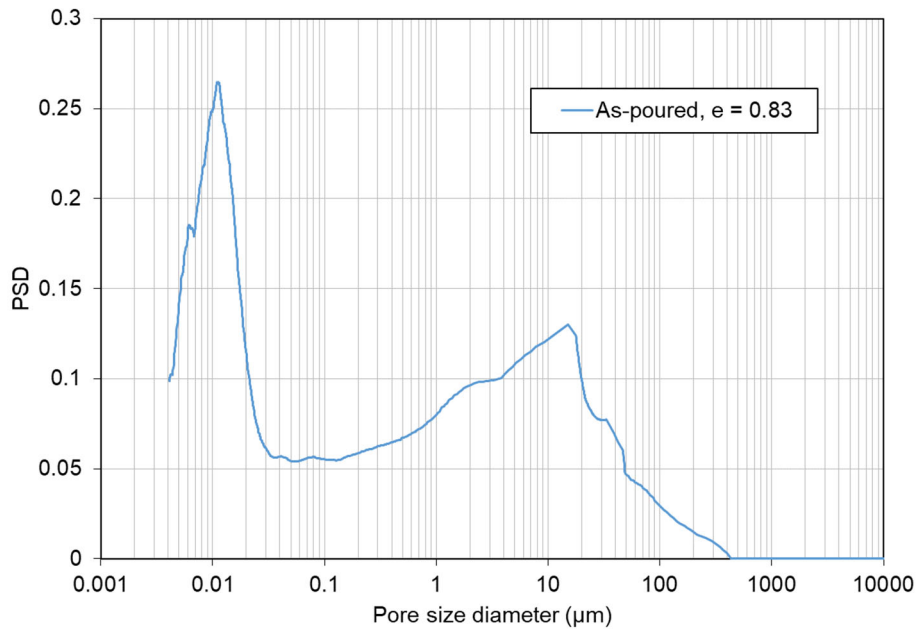


Figure 2. Pore size distribution of an as-poured sample.

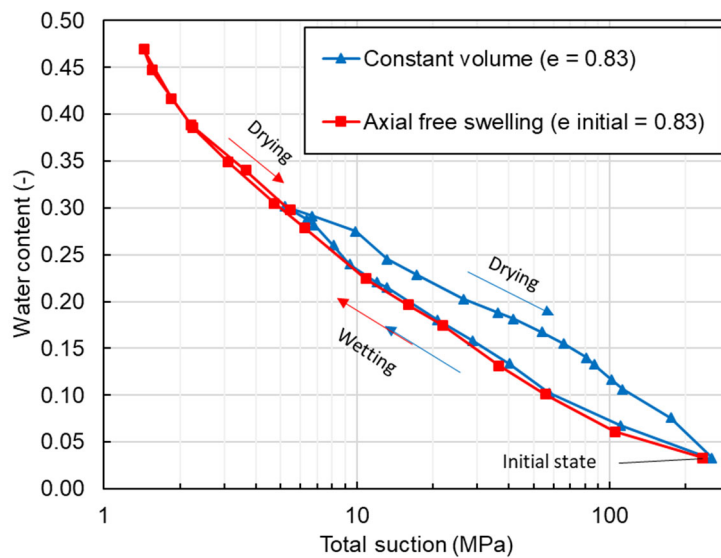


Figure 3. Water retention upon wetting and drying under free-volume and constant-volume conditions.

2.2 Testing set – up

Tests were performed using a high-pressure oedometric cell. A complete description of the apparatus is provided in Ferrari et al. (2016). The cell is made of stainless steel and holds an oedometric ring with height of 12.5 mm and diameter of 35.0 mm. This ring is inserted into a high-rigidity cylindrical cell (Figure 4.a). The top and the bottom of the sample are in contact with metallic porous plates, which are connected to the drainage lines (Figure 4.b).

The cell is placed in a high-stiffness frame equipped with a hydraulic jack, which allows to control the vertical total stress up to 100 MPa (resolution of 0.06 MPa) (Figure 5). The vertical displacement is measured by LVDTs (resolution of 1 μm) fixed on the upper part of the oedometric cell.

Water is supplied with a Pressure/Volume (PV) controller (resolution of pressure control of 1kPa), from the bottom and top bases of the oedometric cell (Figure 4.b).

For the tests in which saturation was carried out in isochoric conditions, the vertical stress was adjusted in order to minimize the development of the swelling strain (maximum registered vertical deformation equal to 0.6%).

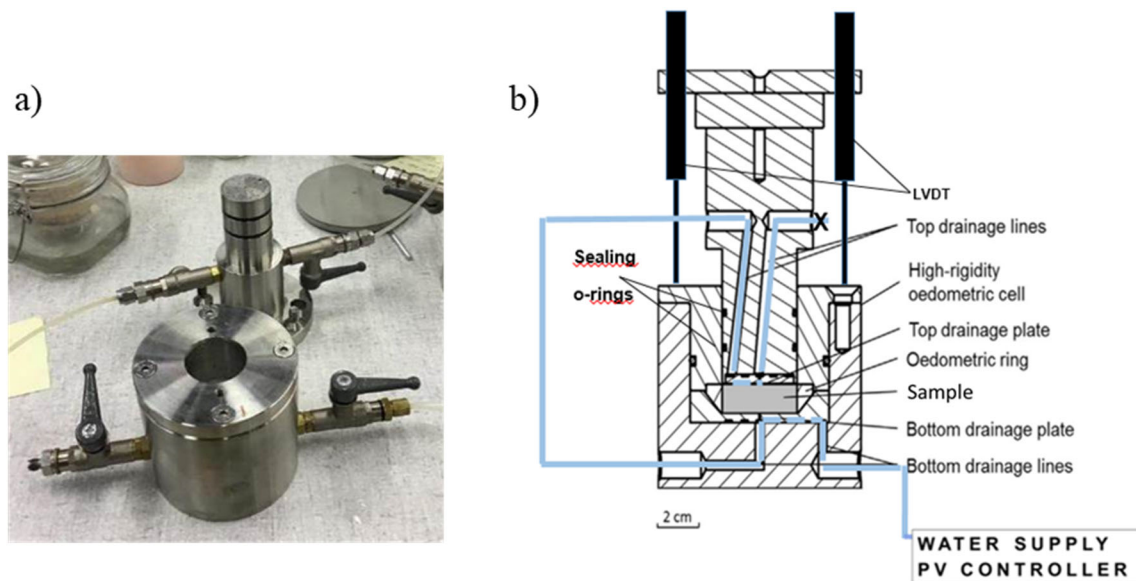


Figure 4. (a) High-rigidity oedometric cell. (b) Schematic layout of the cell showing the drainage system.

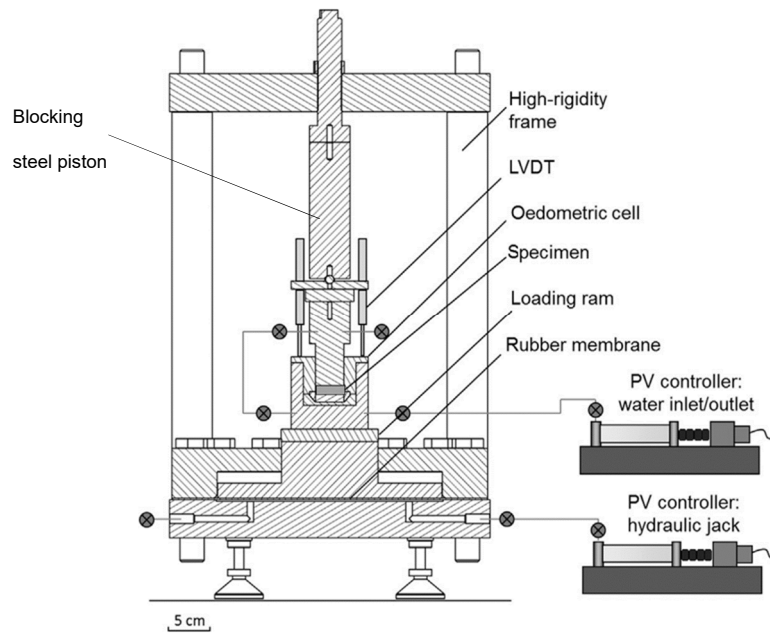


Figure 5. Schematic layout of the test for saturating the sample with liquid water in isochoric conditions.

2.3 Description of the HM oedometric tests

A schematic view of the followed testing paths is shown in the “void ratio – vertical stress” plane in Figure 6, including the points at which microstructural information from MIP is available.

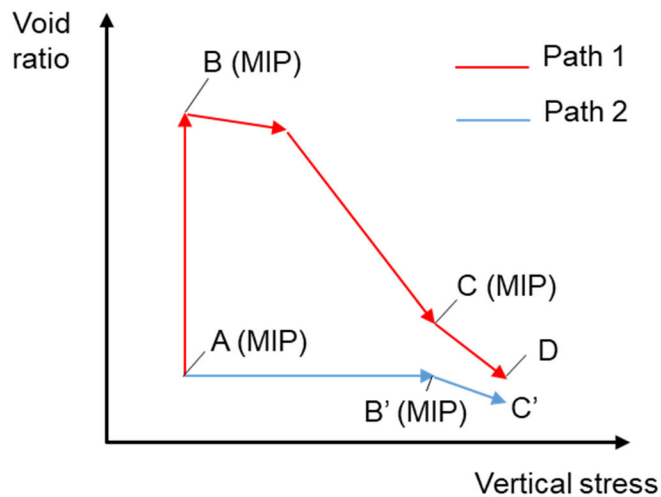


Figure 6. Schematic view of the testing program in terms of void ratio and vertical stress. Initial point is in both cases denoted by A and corresponds to the as-poured, hygroscopic state. The points at which MIP tests observations are available are also shown.

The initial state of the samples corresponded to the as-poured and hygroscopic condition, with void ratios around 0.85, water content in the range of 0.06-0.07 and a total suction between 90

MPa and 110 MPa; the specific initial conditions of the tested samples are given in the corresponding spreadsheets.

Deaerated, deionized water at a constant pore water pressure of 20 kPa was applied in all the stages of the experiments (saturation and loading).

Path 1 (A–B–C–D) consisted in the following two stages:

- **A–B**: Hydration under a constant vertical stress of 21 kPa. The stage finished once swelling strains stabilized with time.
- **B–C–D**: Increase of vertical stress in steps up to 20 MPa.

Path 2 (A–B’–C’) consisted in following two stages:

- **A–B’**: Hydration in constant-volume conditions. Vertical stress was increased according to the observed displacements in order to maintain as much as possible isochoric conditions. This stage finished once swelling pressure stabilized with time.
- **B’–C’**: Increase of vertical stress in steps up to 20 MPa.

Three samples were prepared for each of the two paths; this allowed to perform MIP analyses at intermediate states of the hydro-mechanical loadings. The applied sequence for each sample is summarised in Table 2.

Table 2. Nomenclature for the samples involved in the experimental program.

	Sample	Sequence (see Fig. 6)	MIP
Path 1	P1-1	A-B	At point B
	P1-2	A-B-C	At point C
	P1-3	A-B-C-D	No
Path 2	P2-1	A-B’-C’	No
	P2-2	A-B’	No
	P2-3	A-B’	At point B’

3 Test results

3.1 Vertical swelling (path 1, stage A–B)

The results of the three samples subjected to hydration under constant vertical stress are shown in Figure 7. In spite of some differences in the evolution of the vertical strain with time, the final attained deformation was similar for the three samples (average swelling strain equal to 80.1%, average final void ratio equal to 2.34).

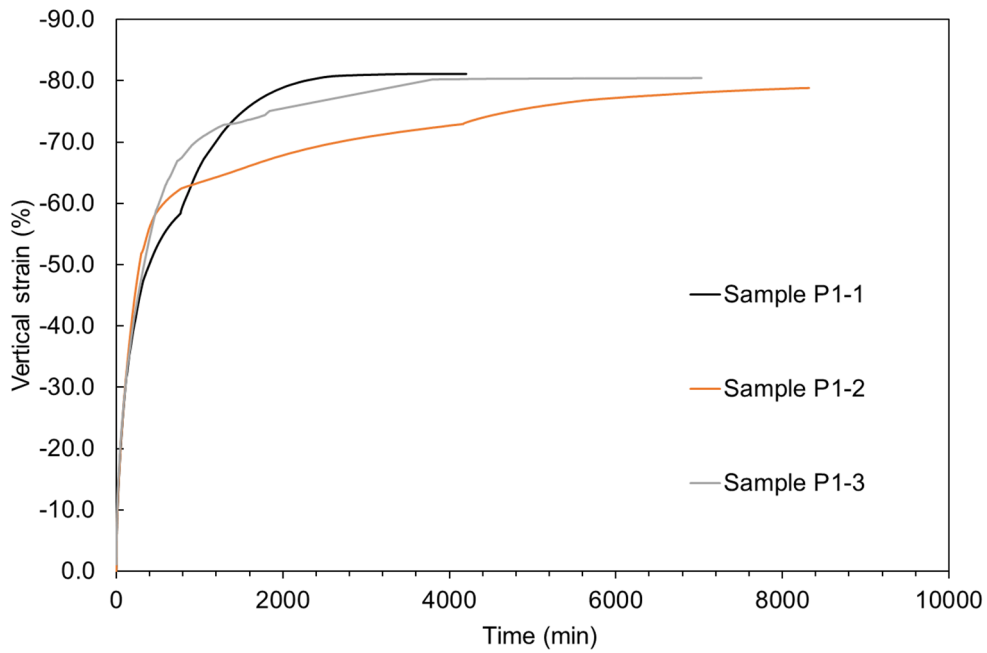


Figure 7. Path 1, stage A-B: evolution of vertical strains with time.

3.2 Swelling pressure test (Path 2, stage A-B')

The results of the swelling pressure tests are shown in Figure 8 in terms of evolution of swelling pressure with time. A small vertical total stress (0.12-0.31 MPa) was applied initially to ensure good contact of the samples with the piston. Manual increase of the vertical stress was performed in order to minimize the unwanted swelling deformations (vertical strain evolutions are provided in the corresponding spreadsheet).

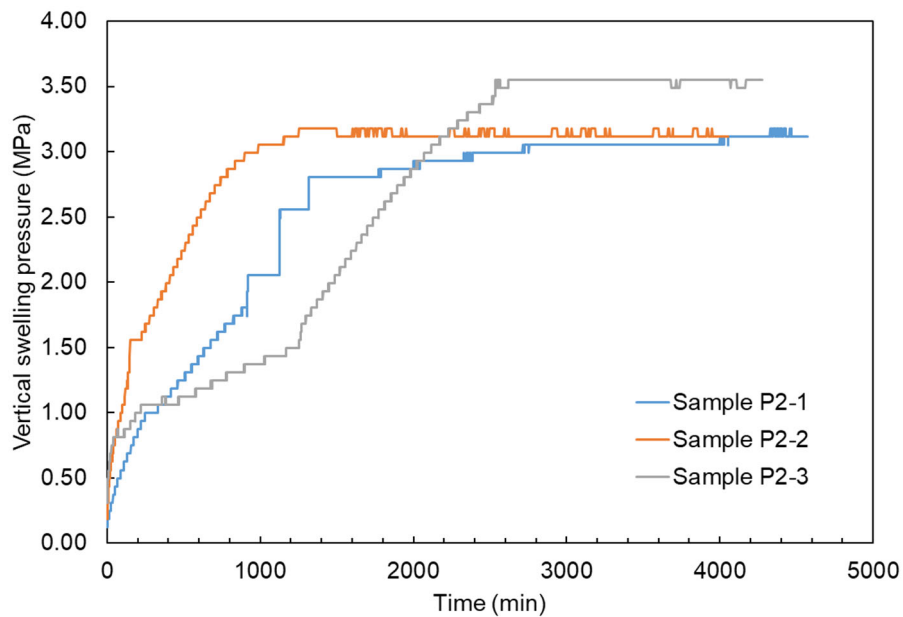


Figure 8. Path 2, stage A-B': evolution of swelling pressure with time.

3.3 Oedometric compression (stages B–C–D and B–C')

The results of the two paths in terms of void ratio and total vertical stress are shown in Figure 9 for the samples P1-3 and P2-1. The evolutions of void ratio (Path 1, stage A-B) and vertical stress (Path 2, stage A-B') during the previous stages are also shown in the figure. Void ratios are computed accounting for the displacement recorded for each load increment, corrected to take into account the deformation of the set-up. Vertical effective stress can be computed considering that a constant back-pressure of 20 kPa was maintained during all the experiments.

MIP is available at point C (vertical stress of 3.24 MPa) from sample P1-2.

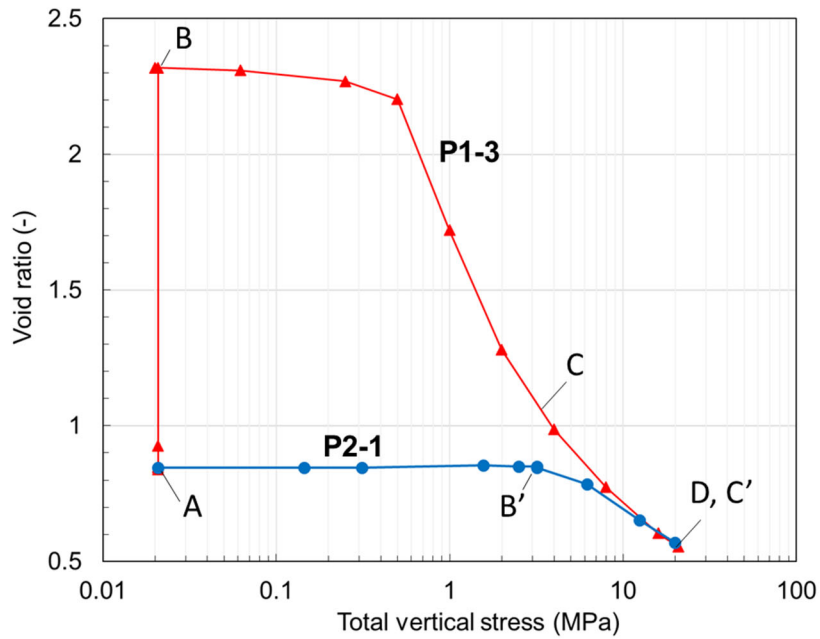


Figure 9. Results of the oedometric compression tests after saturation under constant axial stress (P1-3) and constant volume conditions (P2-1).

3.4 MIP results

MIP results are summarised in Figure 10 in terms of cumulative intruded and extruded volumes and the pore size distribution. For each sample, two MIP tests were performed in order to check repeatability. For completeness, both results are shown in Figure 10.

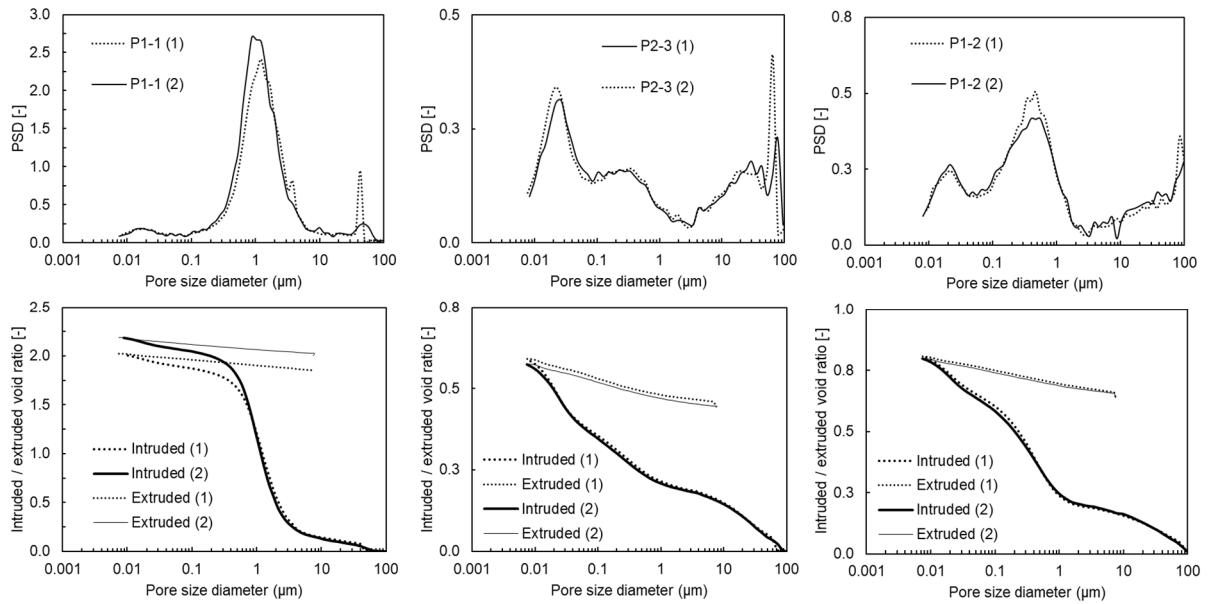


Figure 10. MIP results in terms of pore size distribution (upper row) and intruded - extruded void ratios (lower row). Left column: after axial swelling (P1-1, point B). Central column: After isochoric wetting up to saturation (P2-3, point B'). Right column: After axial swelling and subsequent compression under saturated states at 3.24 MPa (P1-2, point C). For each sample, two MIP tests were performed, indicated in the legends by (1) and (2).

4 Task description

The task consists in simulating with a single set of model parameters the observed hydro-mechanical response of the samples P1-3 (Path 1: A-B-C-D) and P2-1 (Path 2: A-B'-C') as depicted in Figure 9.

For each path, the teams have to provide the evolution of void ratio as a function of total stress (as shown in Figure 9).

MIP results can be used to calibrate/verify the microstructural behaviour of models based on a multi-porosity framework.

5 References

Ferrari, A., Favero, V., Laloui, L., 2016. One-dimensional compression and consolidation of shales. *International Journal of Rock Mechanics and Mining Sciences* 88, 286–300.

Seiphoori, A., 2014. Thermo-hydro-mechanical characterisation and modelling of MX-80 granular bentonite. PhD dissertation, École Polytechnique Fédérale de Lausanne.

Seiphoori, A., Ferrari, A. and Laloui, L., 2014. Water retention behaviour and microstructural evolution of MX-80 bentonite during wetting and drying cycles. *Géotechnique*, 64(9), pp.721-734.

D3.3



Annex A

Contribution to Deliverable 3.3

Contribution to DELIVERABLE (D3.3) BGR Report

Authors: Vinay Kumar, Steffen Beese

Reporting period: 01/06/20 – 31/05/22

Date of issue of this report: **08/09/2021**

Start date of project: **01/06/17**

Duration: 60 Months

This project receives funding from the Euratom research and training programme 2014-2018 under grant agreement No 745 942		
Dissemination Level		
PU	Public	X
RE	Restricted to a group specified by the partners of the Beacon project	
CO	Confidential, only for partners of the Beacon project	

REVIEW

Name	Internal/Project/External	Comments
All Beacon partners	Project internal	

DISTRIBUTION LIST

Name	Number of copies	Comments
Seifallah BEN HADJ HASSINE (EC)	Digital	
Beacon partners	Digital	

Content

1	Introduction	4
2	Description of the model.....	4
3	Basic capabilities of the model	8
4	Task 3.3	8
5	Performance of the model and assessment of predictive power	13
6	Conclusion.....	14
	References	15

1 Introduction

The initial test cases of the BEACON project were modelled with a linear elastic, single structure constitutive model. Over the course of the project, new hydraulic and mechanical models have been implemented in a newer version of OpenGeoSys. In the hydraulic model, a double structure approach is considered. In the mechanical model, the modified Cam-clay plasticity model is implemented. These are used in the simulation of task 3.3. The simulation results are compared to the available measurement data. Limitations of the model and an outlook for further development are also documented.

2 Description of the model

A double structure hydraulic model (DSM) is developed and coupled to a modified Cam-clay plasticity model (MCC) in a monolithic scheme in OpenGeoSys-6. The salient features and important assumptions of this model are documented in this section.

Nomenclature

The nomenclature of the equations described in the subsequent sections is given below

Sub- and superscripts

α : Phase, arbitrary

L : Liquid phase

S : Solid phase

LR : Liquid phase, real

SR : Solid phase, real

M : Macro structure level

m : Micro structure level

eff : Effective

sw : Swelling

mech : Mechanical

vol : Volumetric

dev : Deviatoric

el: Elastic

pl: Plastic

Properties

- \tilde{n}_r (kg/m³): Density
 ϕ (-): Porosity
 S (-): Saturation
 α_B (-): Biot's coefficient
 $\bar{\alpha}$ (-): Mass exchange coefficient
 μ_{LR} (Pa · s): Viscosity of fluid
 μ (Pa): Shear modulus
 K (Pa): Bulk modulus
 p_c (Pa): Preconsolidation pressure
 M (-): Slope of the critical state line
 κ_c (-): Slope of the swelling line
 λ_{sw} (-): Swelling law exponent
 λ_c (-): Slope of virgin consolidation line
 λ_{pl} (-): Plastic multiplier

Variables

- ψ (Pa): Water uptake potential
 p_{LR} (Pa): Liquid (wetting) phase pressure
 p_{FR} (Pa): Mechanically active fluid phase pressure
 e (-): Volumetric strains
 \mathbf{u} (m): Deformation vector
 $\boldsymbol{\sigma}$ (Pa): Stress tensor
 $\boldsymbol{\varepsilon}$ (-): Strain tensor
 \mathbf{w} (m/s): Darcy flow vector

The Double Structure Hydraulic Model (DSM)

The total porosity is additively split into macro and micro porosity. Both porosities co-exist at each material point. The porosity evolution is written in the rate form as (material derivatives are implicitly implied)

$$\dot{\phi} = \dot{\phi}^M + \dot{\phi}^m \quad (1.1)$$

Accordingly two different porosity evolutions are derived from the governing equations valid at the respective scale.

The starting point is the general coupled mass balance equation (cf. Lewis & Schrefler 1998) for phase α in deforming porous media, by

$$\phi_\alpha \tilde{n}_{\alpha R} (\dot{S}_\alpha) + S_\alpha \phi_\alpha (\tilde{n}_{\alpha R}) + S_\alpha \tilde{n}_{\alpha R} (\dot{\phi}_\alpha) + \nabla \cdot (\tilde{n}_{\alpha R} \tilde{\mathbf{w}}_\alpha) + \tilde{n}_\alpha \nabla \cdot (\dot{\mathbf{u}}) = 0 \quad (1.2)$$

For the case of the solid phase (subscript $\alpha = S$) in eq. (1.2), the porosity evolution of the solid phase is the evolution of the volume fraction of the solid phase, expressed as the function of the change in solid phase density and the deformation rate as:

$$\dot{\phi}_S = -\frac{1}{\tilde{n}_{SR}} \phi_S (\tilde{n}_{SR}) - \phi_S \nabla \cdot (\dot{\mathbf{u}}) \quad (1.3)$$

Here ϕ_S is the volume fraction of the solid phase and defined in the rate form as $\dot{\phi}_S = (1 - \dot{\phi})$ where ϕ is the volume fraction of all constituent fluid phases, i.e., the porosity. Substituting this and the following constitutive assumption for the density evolution of the solid phase in eq. (1.3)

$$\frac{\tilde{n}_{SR}}{\tilde{n}_{SR}} = \frac{1}{\tilde{n}_{SR}} \frac{\partial \tilde{n}_{SR}}{\partial p_{FR}} \dot{p}_{FR} + \frac{1}{\tilde{n}_{SR}} \frac{\partial \tilde{n}_{SR}}{\partial \sigma_{eff,m}} \dot{\sigma}_{eff} \quad (1.4)$$

And defining the Biot coefficient as $\alpha_B = 1 - \frac{K_S}{K_{SR}}$, the porosity evolution eq. (1.3) is expanded

as

$$\begin{aligned} \dot{\phi} &= (1-\phi) \left[\frac{1}{\tilde{n}_{SR}} \frac{\partial \tilde{n}_{SR}}{\partial p_{FR}} \dot{p}_{FR} + \frac{1}{\tilde{n}_{SR}} \frac{\partial \tilde{n}_{SR}}{\partial \sigma_{eff,m}} \dot{\sigma}_{eff} \right] + (1-\phi) \nabla \cdot (\dot{\mathbf{u}}) \\ \dot{\phi} &= (1-\phi) \left[\frac{1}{K_{SR}} \dot{p}_{FR} - \frac{1}{(1-\phi)K_{SR}} K_S \left(\dot{\epsilon}_{vol} + \frac{1}{K_{SR}} \dot{p}_{FR} \right) \right] + (1-\phi) \dot{\epsilon}_{vol} \\ \dot{\phi} &= (\alpha_B - \phi) \left[\frac{1}{K_{SR}} \dot{p}_{FR} + \dot{\epsilon}_{vol} \right] \end{aligned} \quad (1.5)$$

A detailed derivation in the context of a THM model is found in Parisio et al. (2019).

In the double structure framework, for the macro scale porosity evolution only the mechanical volumetric strains are considered. The above equation is then rewritten as.

$$\dot{\phi}^M = (\alpha_B - \phi) \left[\frac{1}{K_{SR}} \dot{p}_{FR} + \dot{\epsilon}_{mech} \right] \quad (1.6)$$

Rewriting the balance equation for the macro scale (superscript M) and accounting for the exchange term (Choo et al. 2016) between the two porosity levels on the right hand side, which is expressed generally as a function of the difference in water uptake potential between the two levels, we get the following

$$\tilde{n}_{LR}^M \dot{\phi}^M \dot{S}_L^M + \phi^M S_L^M \tilde{n}_{LR}^M + \tilde{n}_{LR}^M S_L^M \dot{\phi}^M + \nabla \cdot (\tilde{n}_{LR}^M \tilde{\mathbf{w}}_{LS}^M) + \phi^M S_L^M \tilde{n}_{LR}^M \dot{\epsilon} = \frac{\bar{\alpha}}{\mu_{LR}} (\psi_S^M - \psi_S^m) \quad (1.7)$$

And substituting the porosity evolution eq. (1.6) and grouping the terms we arrive at the macro-scale mass balance equation as

$$\begin{aligned} \tilde{n}_{LR}^M \left[\dot{\phi}^M + \frac{\alpha_B - \phi}{K_{SR}} \dot{p}_{FR} S_L^M \right] \dot{S}_L^M + S_L^M \tilde{n}_{LR}^M \left[\frac{\dot{\phi}^M}{K_{LR}} + S_L^M \frac{\alpha_B - \phi}{K_{SR}} \right] \dot{p}_{LR}^M \\ + \nabla \cdot (\tilde{n}_{LR}^M \tilde{\mathbf{w}}_{LS}^M) + \tilde{n}_{LR}^M S_L^M \alpha_B \dot{\epsilon} = -\frac{\bar{\alpha}}{\mu_{LR}} (\psi_S^m - \psi_S^M) \end{aligned} \quad (1.8)$$

The swelling law is valid only on the micro scale and is defined as a function of the micro effective saturation

$$\begin{aligned} \boldsymbol{\sigma}_{sw} &= -\sum_{i=1}^3 \hat{p}_{sw,i} \left(S_{eff,sw}^{\lambda_{sw,i,m}} - S_{eff,sw0}^{\lambda_{sw,i,m}} \right) \mathbf{n}_i \otimes \mathbf{n}_i \\ \boldsymbol{\epsilon}_{sw} &= \mathbf{C}_{el}^{-1} : \boldsymbol{\sigma}_{sw} \end{aligned} \quad (1.9)$$

With this definition, the porosity evolution on the micro scale is derived as a function of the swelling strains

$$\dot{\phi}^m = (\alpha_B - \phi) [\dot{\boldsymbol{\epsilon}}_{sw}] \quad (1.10)$$

The change in the micro porosity is therefore expressed as function of the change in saturation. The balance equation (1.2) is rewritten for the micro structure and coupled to the macrostructure balance equation through the exchange term as

$$\tilde{n}_{LR}^m \dot{\phi}^m \dot{S}_L^m + \tilde{n}_{LR}^m S_L^m \dot{\phi}^m + \tilde{n}_{LR}^m \phi^m S_L^m \dot{\epsilon}_{sw} = \frac{\bar{\alpha}}{\mu_{LR}} (\psi_S^m - \psi_S^M) \quad (1.11)$$

The assumptions made in the derivation of the micro scale balance equation are

- No changes in fluid density

- No spatial flow terms
- Strains are purely swelling strains

Substituting the micro porosity evolution (1.10) and definition of swelling strains, the micro-scale balance equation is expressed below with only the micro scale saturation.

$$\tilde{n}_{LR} \phi^m \dot{S}_L^m + \tilde{n}_{LR} S_L^m (\alpha_B - \phi) [\beta(S_L^m) \dot{S}_L^m] + \phi^m S_L^m \tilde{n}_{LR} \beta(S_L^m) \dot{S}_L^m = \frac{\bar{\alpha}}{\mu_{LR}} (\psi_S^m - \psi_S^M) \quad (1.12)$$

The primary variables of the system are micro and macro fluid pressures. Therefore, the potentials are set equal to the respective fluid phase pressures, which follow the sign conventions generally used in the Richards' assumption.

$$\begin{aligned} \psi_S^m &= -p_{LR,m} \\ \psi_S^M &= -p_{LR,M} \end{aligned} \quad (1.13)$$

The micro and macro saturations are defined by two van Genuchten like functions of the micro and macro pressure respectively.

$$\begin{aligned} S_L^m &= \hat{S}_L^m(-p_{LR}^m) \\ S_L^M &= \hat{S}_L^M(-p_{LR}^M) \end{aligned} \quad (1.14)$$

From the coupled equation system ((1.12),(1.14),(1.10)(1.9)) the quantities S_L^m , ϕ^m , p_{LR}^m , σ_{sw} are solved. For a given increment in the macro scale pressure and displacement, the increments in these constitutive quantities are computed.

The Modified Cam-Clay Model (MCC)

The MCC model describes elasto-plastic behavior of cohesive soils. It is able to consider material effects such as softening or hardening in an elasto-plastic framework. The model presented here is a simplified small strain variant of the model described in Callari et al. (1998). The constitutive equations are implemented in the MFront Framework, see e.g. Helfer et al. (2015). For the sake of a self consistent model description the main equations will be outlined in the following. The salient features of the model are:

- The mechanical strains $\boldsymbol{\varepsilon}_{mech}$ are additively split into an elastic and a plastic contribution in a small-strain framework:

$$\boldsymbol{\varepsilon}_{mech} = \boldsymbol{\varepsilon} - \underbrace{\mathbf{C}_{el}^{-1} : \boldsymbol{\sigma}_{sw}}_{\boldsymbol{\varepsilon}_{sw}} = \boldsymbol{\varepsilon}_{el} + \boldsymbol{\varepsilon}_{pl}. \quad (1.15)$$

- The elastic behavior of the material is assumed to be isotropic following the constitutive equation:

$$\boldsymbol{\sigma}_{eff} = K_S \text{tr}(\boldsymbol{\varepsilon}_{el}) \mathbf{1} + \mu \boldsymbol{\varepsilon}_{el}^{dev}. \quad (1.16)$$

This model is restricted to a constant elastic stiffness neglecting the observed pressure dependency for bentonite.

- Decomposition of the stress tensor into volumetric and deviatoric parts and the subsequent definition of the von-Mises equivalent stress and hydrostatic pressure as

$$\begin{aligned} q &:= \sqrt{\frac{3}{2} \boldsymbol{\sigma}^{dev} : \boldsymbol{\sigma}^{dev}} \\ p &:= -\frac{1}{3} \text{tr}(\boldsymbol{\sigma}) \end{aligned} \quad (1.17)$$

- The yield function is defined as a function of the von-Mises stress q and the hydrostatic pressure p :

$$\Phi := q^2 + M^2 p(p - p_c) \leq 0. \quad (1.18)$$

In (1.18) the parameter M represents the slope of the critical state line and the parameter p_c the preconsolidation pressure. With the evolution of p_c the elastic

domain grows or shrinks, reflecting strain hardening or softening respectively. The evolution is inversely proportional to the total porosity and directly proportional to the rate of permanent compaction $\text{tr}(\dot{\boldsymbol{\epsilon}}_{\text{pl}})$ and the pre-consolidation pressure itself:

$$\dot{p}_c = -\text{tr}(\dot{\boldsymbol{\epsilon}}_{\text{pl}}) \left(\frac{1}{(\lambda_c - \kappa_c)(1 - \phi)} \right) p_c. \quad (1.19)$$

- The plastic strain evolution is defined by the associative flow rule:

$$\dot{\boldsymbol{\epsilon}}_{\text{pl}} = \lambda_{\text{pl}} \mathbf{M}, \quad \text{with } \mathbf{M} = \left(\left\| \frac{\partial \Phi}{\partial \boldsymbol{\sigma}_{\text{eff}}} \right\| \right)^{-1} \frac{\partial \Phi}{\partial \boldsymbol{\sigma}_{\text{eff}}}. \quad (1.20)$$

- With the Karush-Kuhn-Tucker and the consistency conditions:

$$\lambda_{\text{pl}} \geq 0 \quad \Phi \leq 0 \quad \lambda_{\text{pl}} \cdot \Phi = 0 \quad \text{and} \quad \dot{\lambda}_{\text{pl}} \cdot \dot{\Phi} = 0, \quad (1.21)$$

the set of equations is complete.

3 Basic capabilities of the model

The new double structure hydraulic model formulation and the modified Cam-clay plasticity model brings primarily two key capabilities to the simulation of isothermal processes in bentonite.

The hydraulic model allows for a non-monotonic evolution of the stresses. Based on the value of the mass exchange term $\bar{\alpha}$, the evolution of the micro saturation compared to the macro saturation changes thus allowing for a delay in the evolution of the swelling stresses. In materials like Bentonite the assumed equivalence of the capillary pressure to the matrix potential (1.13) in the Richards' model has implications in the mechanical model, leading to unrealistically high stresses in case of a strong HM coupling through the Biot coefficient and the effective stress principle (cf. (1.13)). Therefore, until a model formulation is available that considers both the matrix potential, which is responsible for water uptake, and the capillary pressure, which is used in the effective stress principle, the Biot HM coupling is turned off in partial saturation using a switch-like Bishop's function and is instead controlled only by the swelling law.

The modified Cam-clay model allows for the inclusion of stress-path dependency and irreversibility in the mechanical process. In the current state of the model used to simulate the test case, the elastic parameters are held constant due to which no load-path-dependent elastic stiffness can be simulated. Additional to the above assumption, known shortcomings of the mechanical model are in two aspects. Firstly, the lack of cohesion means that the mechanical model cannot start in a stress-free state. Secondly, under large dilatancy the yield surface collapses to a point, causing softening and localization. This is mitigated by limiting the evolution of the pre-consolidation pressure p_c to a pre-determined minimum value in eq. (1.19).

4 Task 3.3

The DSM model requires some additional steps in the model setup compared to previous test cases. The experimentally determined void ratio is split into micro and macro porosities. Two sets of van Genuchten function parameters (entry pressures, shape factors) are required which in their sum approximate the measured water retention behavior of the experimental specimen. The functions should also ensure (due to the nature of model formulation), that for a given initial suction value (in the Richards' model, the negative liquid phase pressure) the micro and macro structures should be in hydraulic equilibrium with the micro saturation at a much higher value than the macro saturation. The determination of the van Genuchten

shape factor was done by an optimization algorithm under an assumption of the ratio between the micro and macro entry pressures and an assumed initial water distribution between micro and macro pore space that is in equilibrium with each other for the given initial suction value. The values are documented in Table 1 and the resulting functions are shown as plots in Figure 1.

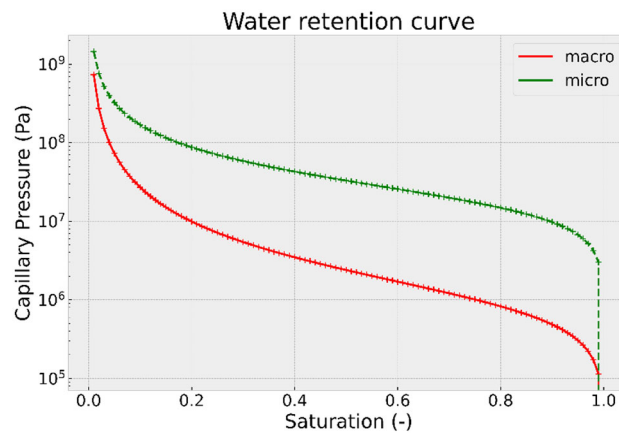


Figure 1: The optimized van Genuchten capillary pressure – Saturation relationships used in the simulation.

Table 1: The optimized van Genuchten function parameters used in the simulation (truncated at 4th decimal place).

Parameter	Entry pressure (MPa)	Shape factor (-)	Porosity (-)	Initial Pressure (MPa)	Initial Saturation (-)
Micro structure	20.0	0.5181	0.3103	-100.0	0.1740
Macro structure	1.0	0.4109	0.1491	-100.0	0.0402

The mechanical parameters used in the simulations of the two stress paths are based on values stated in Åkesson et al. 2010. They are documented in Table 2.

Table 2: Mechanical parameters

Parameter	Value	Unit
Young's Modulus (E)	180	MPa
Poisson's Ratio (ν)	0.2	(-)
Initial Pre-consolidation pressure (p_c)	2.0	MPa
Slope of virgin consolidation line (λ_c)	0.15	(-)
Slope of swelling line (κ)	0.12	(-)
Slope of critical state line (M)	0.24	(-)

The swelling pressures used are given in Table 3 and the choice of values will be explained subsequently. For the hydraulic flow model, an exponential porosity dependent permeability

model based on that described by Verma and Pruess (1986) was used with an initial permeability (based on Åkesson et al. 2010) of $9e-19 \text{ m}^2$.

Table 3: Swelling pressures used along the two stress paths

Parameter	Value	Unit
Swelling pressure (AB'C')	4.0	MPa
Swelling Pressure (ABCD)	50.0	MPa

The swelling part of the model setup is done by defining the swelling law. The model deviates from the task description in defining the maximum swelling pressure used in eq. (1.9). Here two different swelling pressures are used, one for each path. For the confined case, the swelling pressure of 4 MPa for MX-80 is taken directly from characterization curves from given in the BEACON D5.2.1 for the specified dry density of 1.5 Mg/m^3 . For the unconfined case, a significantly higher swelling pressure was chosen which was calibrated to the measured vertical deformation along the path AB. This is necessary due to the current formulation of the swelling model, which accepts the maximum swelling pressure as an input parameter. The limitations of this formulation and possible improvements are discussed in subsequent sections.

The simulation of the two stress paths are done as initial-boundary-value problems in an axisymmetric model domain (Figure 2) as currently the open source code OpenGeoSys-6 (Bilke et al. 2019) cannot handle such coupled problems as single element tests. The models are run in two simulations in the following sequence:

- The fully-confined path AB' is run till a steady axial (swelling) stress is reached, the model is then uniaxially compressed at the top with a linear ramp to 20 MPa (B'C').
- The uniaxially unconfined path AB is run until a steady axial strain is reached, the model is then uniaxially compressed at the top with a linear ramp to 20 MPa (BCD).

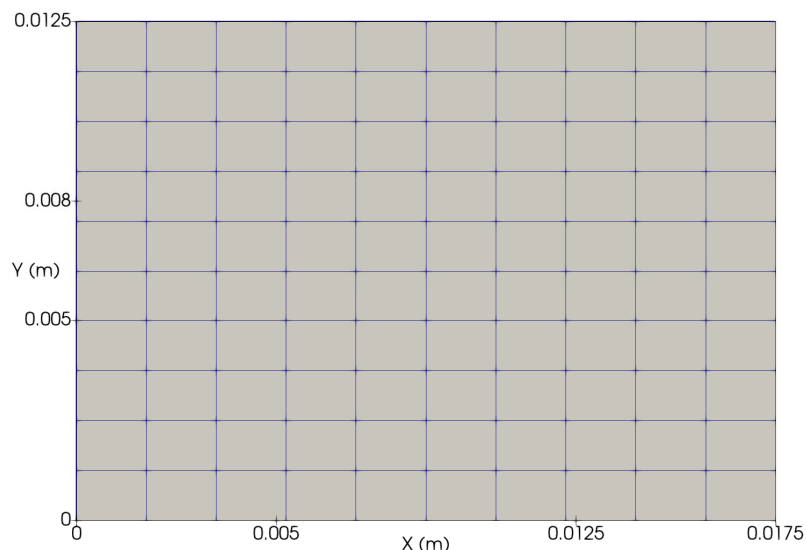


Figure 2: Geometry and Finite element mesh used in the simulations.

During the simulations, no explicit effort was made to match the measured temporal evolution of quantities. Only the steady-state values and their comparison to the measurements are the focus of this modelling exercise. In retrospect, the temporal evolution of quantities are comparable to measurements (whenever available) and have also been documented. The evolution of the simulated strains, stresses and their comparison to

available measured values are shown in

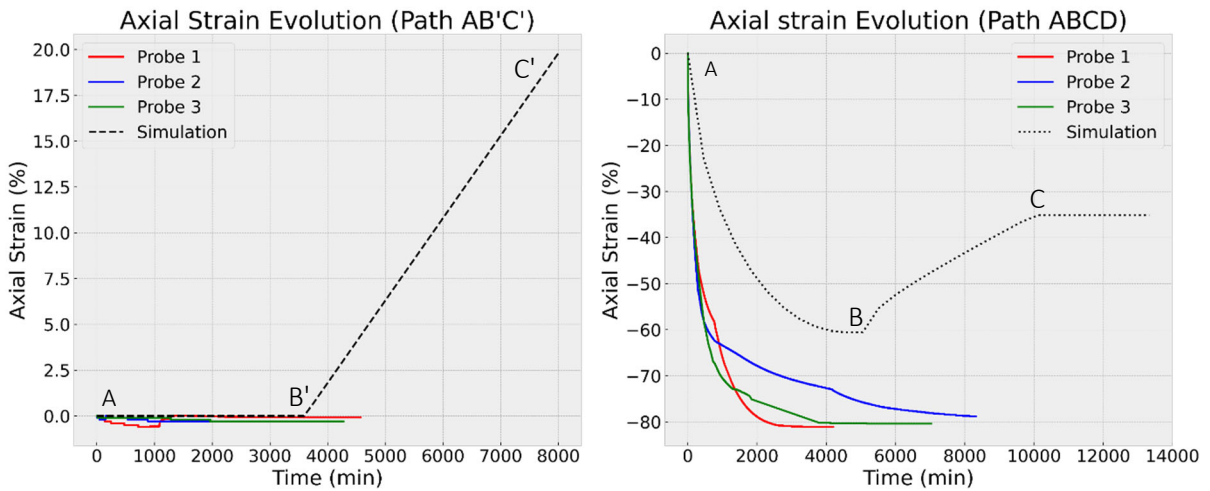


Figure 3 and Figure 4.

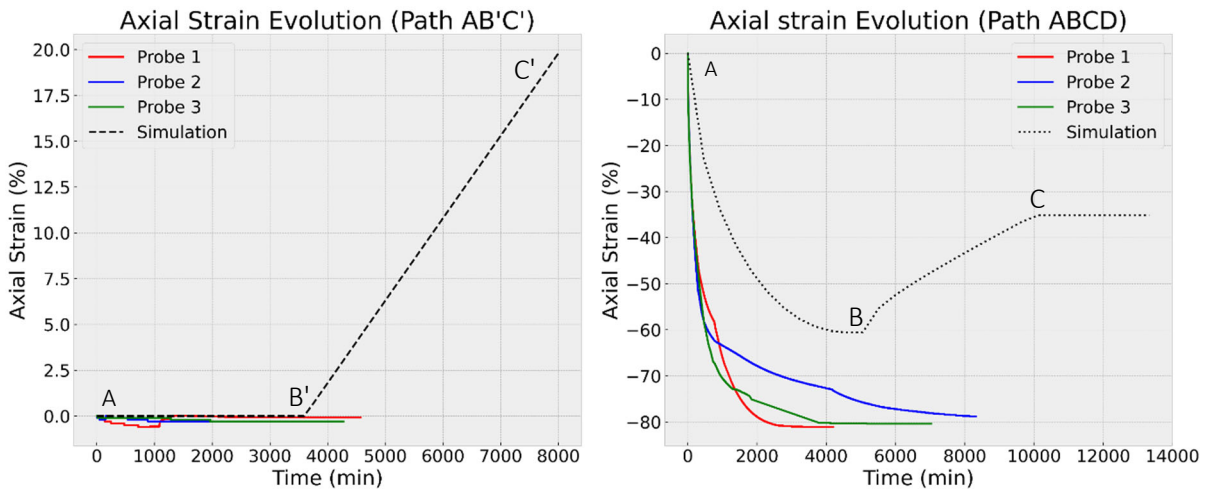


Figure 3: Evolution of axial strains along path AB'C' (l) and path ABCD (r).

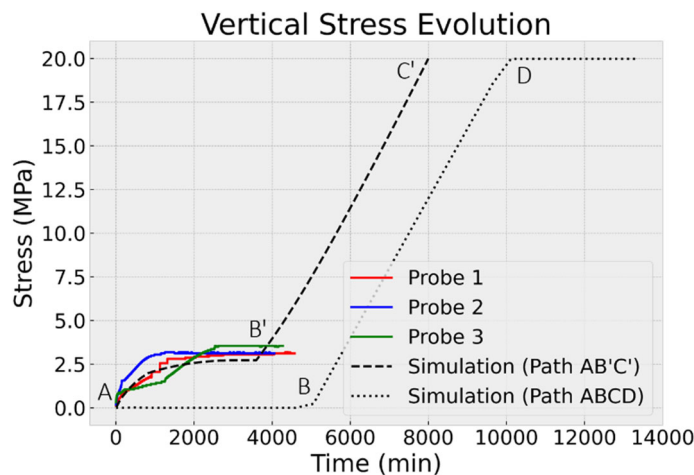


Figure 4: Evolution of vertical stresses along both stress paths.

The saturation along the paths AB' and AB cause changes in the micro and in the macro void ratios (Figure 5). The resulting evolution of porosities is shown in Figure 6. The figures show that along path AB' the micro-porosity increases and results in a decrease in macro porosity.

But along the path B'C' and BCD the micro porosity remains constant. This behavior is directly related to the model formulation and will be discussed in the model assessment section.

Along the free swelling path AB, the saturation results in an increase of porosities, primarily a very large increase of the micro porosity due to the large value of the chosen swelling pressure. However, as in the previous case, the compressive path BCD results only in a reduction of the macro porosity. This behavior limits the final porosities the model can currently reach along compressive loading paths.

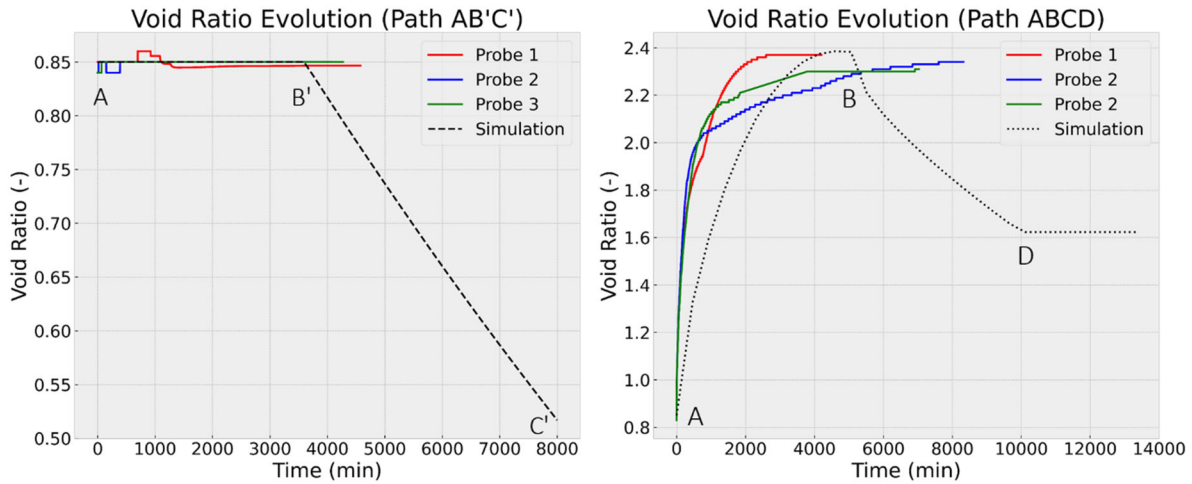


Figure 5: Evolution of void ratios along path AB'C' (l) and path ABCD (r).

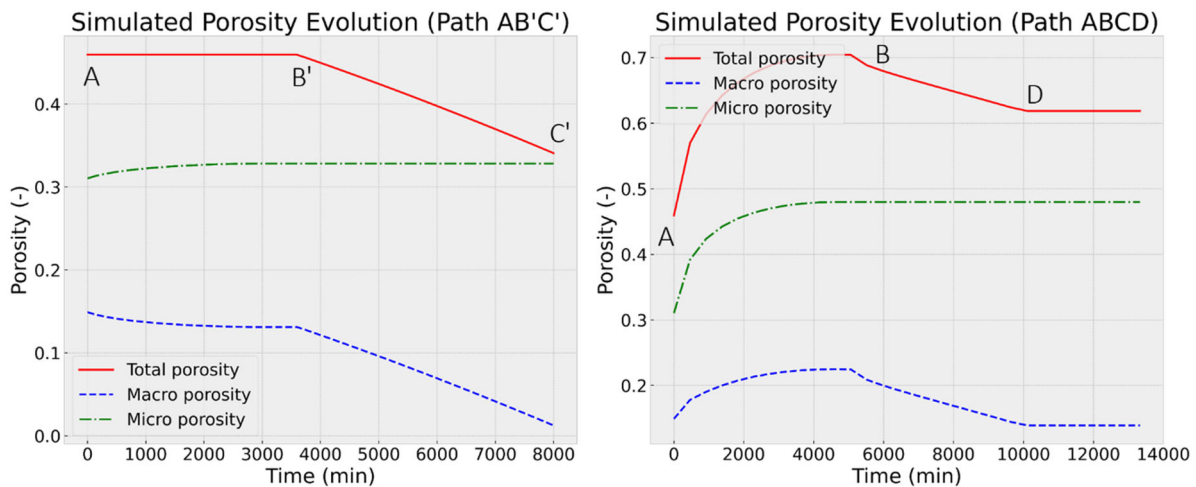


Figure 6: Evolution of porosities along path AB'C' (l) and path ABCD (r).

The void ratio as a function of vertical stress is one of the specified outputs of the model. The functional dependency derived from the simulation and its comparison to the measured values is shown in Figure 7 along with a comparative evolution of void ratios along both paths.

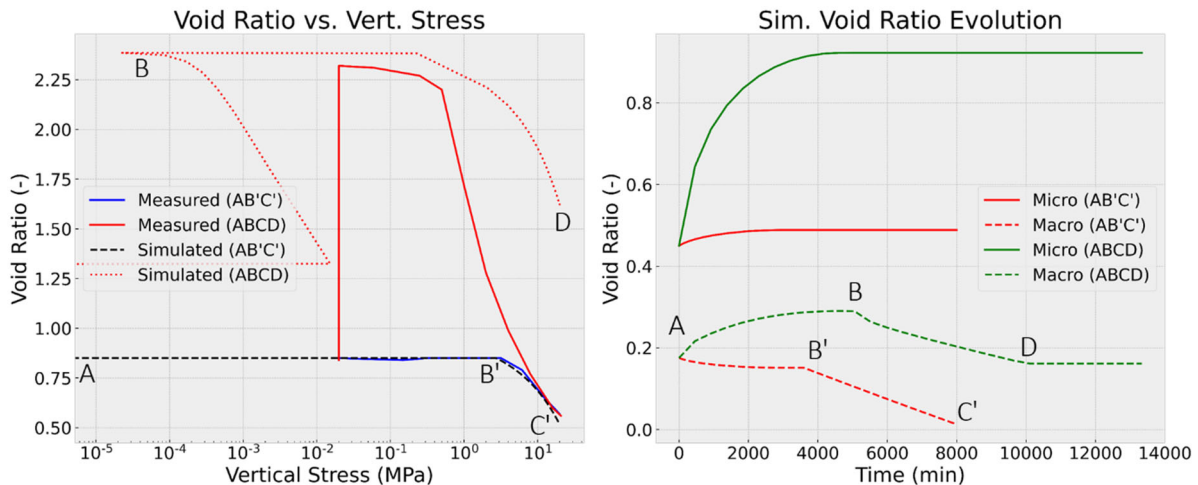


Figure 7: Comparison of simulated stress paths to the experimental stress paths in the vertical stress – void ratio plane (l). Evolution of void ratios along both stress paths (r).

The results show that the model can reproduce the saturation and loading behavior along the entire path AB'C' with good agreement to the measured values. However, limitations, especially along Path ABCD and potential scope for development have been identified and will be discussed in the following section.

5 Performance of the model and assessment of predictive power

The newly introduced DSM model uses two van Genuchten functions to describe the water retention behavior of bentonite one each at the micro and macro porosity level. This compounds the already known sensitivity of the model to the functions describing the water retention behavior. The Richards' approximation of the two-phase flow equation used in the current model assigns the entire water retention behavior to purely capillary forces. This often results in unphysical HM initial conditions in high-suction systems because of the direct coupling of a high suction value to the mechanical model through the Terzaghi effective stresses. This interpretation of suction (in general the water uptake potential) as capillary pressure causes a large deviation in the estimation of the mechanically active liquid (or wetting phase) pressure in high-suction materials. This is overcome by switching off the HM coupling in partially saturated conditions choosing an appropriate switch-like Bishop's function in the effective stress principle. The swelling pressure (in DSM acting only at the micro-porosity level) instead solely controls the HM behavior in partial saturation conditions.

In the current model, because of this model formulation, the macro-porosity does not contribute to the coupled hydro-mechanical behavior in partially saturated conditions and therefore, some complexity in the saturation process is lost. However, this is a simple and effective approach to capture major trends in the swelling pressure evolution and is well suited to applications in confined conditions. Under confined conditions, the system resembles the experimental characterization of swelling pressure closer, therefore the parameters from such swelling pressure characterization curves yield agreeable results in simulations. Additionally, previous test cases simulated in the project have demonstrated (considering the uncertainty in certain mechanical material parameters) consistent applicability of this definition of the swelling law to fully-confined or nearly-confined cases. Such cases are expected to form the majority of practical applications of the model.

The previously mentioned aspects of the model formulation, parametrization and applicability are equally motivating factors for the model usage and a limitation of the model in its applicability to unconfined conditions. The implemented functional (for the current case, linear) dependency of the swelling pressure to the saturation greatly

underestimates water uptake in simulations of free swelling and hence underestimates the strains. Therefore, the simulation of both stress paths with a single parameter set was not possible. The chosen fictive swelling pressure was only a proxy to emulate greater water uptake in Path AB due to which simulation of larger strains was possible. The reformulation of the mode of water uptake and its effects on the volumetric deformation in unconfined conditions is a part of ongoing research.

The DSM's first attempt in modelling a test case was also focused on understanding model behavior. It was however not possible to use the mercury intrusion porosimetry data entirely. This forms a central part of ongoing research. In course of model development, similar test cases will be revisited with improved model formulations, which can better take advantage of MIP data.

Similar to the hydraulic DSM, the current test case is also one of the first applications of the MCC model. The model is better suited to simulate of elastoplastic, path-dependent material behavior of bentonite. The model captures the path dependency and trends in the elastoplastic material behavior. The results are agreeable with measured values along path AB'C', along path ABCD however, there is a strong overestimation of the void ratios in the void ratio vs. vertical stress plane as seen in Figure 7.

6 Conclusion

The test case was one of the first applications of the DSM in which simulations were compared to experimental data. The DSM together with the MCC model was capable of showing path dependency and irreversibility, the two central foci of model development in WP3. The DSM in itself is currently a purely hydraulic model but it provides a more physically motivated process description in bimodal porous materials such as bentonite. In the context of this test case it also alleviates some of the problems occurring in the MCC model (e.g. localization). The stress paths could be simulated with a single parameter set except for the mentioned deviation of the swelling pressure between confined and unconfined paths.

References

Åkesson, M.; Börgesson, L.; Kristensson, O. (2010): SR-Site Data report. THM modelling of buffer, backfill and other system component. Svensk Kärnbränslehantering AB (Technical Report, TR-10-44).

Bilke, L.; Flemisch, B.; Kalbacher, T.; Kolditz, O.; Helmig, R.; and Nagel, T. (2019): Development of Open-Source Porous Media Simulators: Principles and Experiences. *Transport in Porous Media*, vol. 130, p. 337-361, Springer, DOI:10.1007/s11242-019-01310-1.

Callari, C.; Auricchio, F. and Sacco, E. (1998): A finite-strain Cam–Clay model in the framework of multiplicative elasto–plasticity. *International Journal of Plasticity*. vol. 14, p. 1155-87. DOI: 10.1016/S0749-6419(98)00050-3

Choo, J; White, J. A. and Borja, R. I. (2016): Hydromechanical Modeling of Unsaturated Flow in Double Porosity Media. *International Journal of Geomechanics*. Vol. 16, issue 6, p. D4016002. DOI:10.1061/(ASCE)GM.1943-5622.0000558

Helfer, T.; Michel, B.; Proix, J.; Salvo, M.; Sercombe, J. and Casella, M. (2015): Introducing the open-source mfront code generator: Application to mechanical behaviours and material knowledge management within the PLEIADES fuel element modelling platform. *Comput Math Appl*. 70:994-1023. DOI:10.1016/j.camwa.2015.06.027

Lewis, R.W. & Schrefler, B.A. (1998): *The Finite Element Method in the Static and Dynamic Deformation and Consolidation of Porous Media*. John Wiley, Chichester, 2nd ed. 1998, XIII, 492 pp., ISBN: 0-471-94362-2.

Parisio, F.; Vilarrasa, V.; Wang, W.; Kolditz, O. and Nagel, T. (2019): The risks of long-term re-injection in supercritical geothermal systems. *Nature Communications* 10, 4391. <https://doi.org/10.1038/s41467-019-12146-0>

Verma, A. & Pruess, K. (1986): Thermohydrological conditions and silica redistribution near high-level nuclear wastes emplaced in saturated geological formations. Lawrence Berkeley National Laboratory. LBNL Report #: LBL-21613.

D3.3



Annex B

Contribution to Deliverable 3.3

DELIVERABLE (D3.3)
CU-CTU Report

Author: **David Mašín**

Contributors: **Gianvito Scaringi, Jaroslav Kruis, Tomáš Krejčí, Tomáš Koudelka, Zhao Sun, Jan Najser, Jiří Svoboda**

Charles University & Czech Technical University

Reporting period: 01/06/20 – 31/05/22

Date of issue of this report: **31/08/21**

Start date of project: **01/06/17**

Duration: 60 Months

This project receives funding from the Euratom research and training programme 2014-2018 under grant agreement No 745 942		
Dissemination Level		
PU	Public	X
RE	Restricted to a group specified by the partners of the Beacon project	
CO	Confidential, only for partners of the Beacon project	

Content

1	Introduction	3
2	Description of the model.....	4
2.1	Background and basic hypotheses	4
2.2	Mathematical description	5
2.2.1	Theoretical framework.....	5
2.2.2	Mathematical formulation of the original THM model (basic equations, before BEACON development)	7
2.2.3	Input parameters.....	8
2.3	Model developments within BEACON project.....	9
3	Basic capabilities of the model	15
4	Task 3.3	17
4.1	Task 3.3 Water retention modelling.....	17
4.2	Task 3.3 oedometric compression test modelling (path 1 and path 2)	18
4.3	Task 3.3: Comparison of modelling void ratios and MIP results.....	19
5	Performance of the model and assessment of predictive power	22
5.1	Simulations of laboratory experiments on BCV bentonite performed within BEACON project	22
5.2	Modelling of large-scale CRT experiment (task 5.2).....	30
6	Concluding remarks	42
	References	43
	Appendix 1.....	44

1 Introduction

In this report, we present a development of the constitutive model for bentonite by the Czech teams (Charles University and Czech Technical University) undertaken within the project BEACON. The model is a coupled thermo-hydro-mechanical model based on hypoplasticity principles combined with the concept of double structure.

The model has been developed by Mašín (2017) by a hierarchical enhancement of the earlier model by Mašín (2013), which did not consider the effects of temperature. That model, in turn, was a double structure enhancement of earlier models for unsaturated and saturated soils.

The structure of this report is as follows. First, the background of the model, basic equations of its mathematical formulation and improvements within BEACON project are described in Sec. 2. Basic capabilities of the model are described in Sec. 3 continuing with predictions of BEACON benchmark test (task 3.3) done by all BEACON partners. Subsequently, detailed model calibration and validation on BCV bentonite data obtained within BEACON and other projects is described in Sec. 5.1. Finally, Sec. 5.2 describes model validation using large-scale CRT test.

2 Description of the model

2.1 Background and basic hypotheses

The model has been developed using a double-structure framework originally proposed by Gens and Alonso (1992), who introduced the double structure concept, and Alonso et al. (1999), who developed a complete constitutive model. The model is based on the hydro-mechanical double structure hypoplastic model proposed by Mašín (2013), which has been enhanced by the effects of temperature. Background and basic hypotheses of this model is briefly described in this section.

The hypoplastic double-structure model, and double-structure models in general, are based on the assumption supported by various micro-mechanical studies that in expansive soils one can identify two levels of structure: a macrostructure, which represents an assembly of silt-size aggregates of the clay particles, and a microstructure, which represents the internal structure of these aggregates. A conceptual sketch of these two levels of structure is shown in Figure 1.

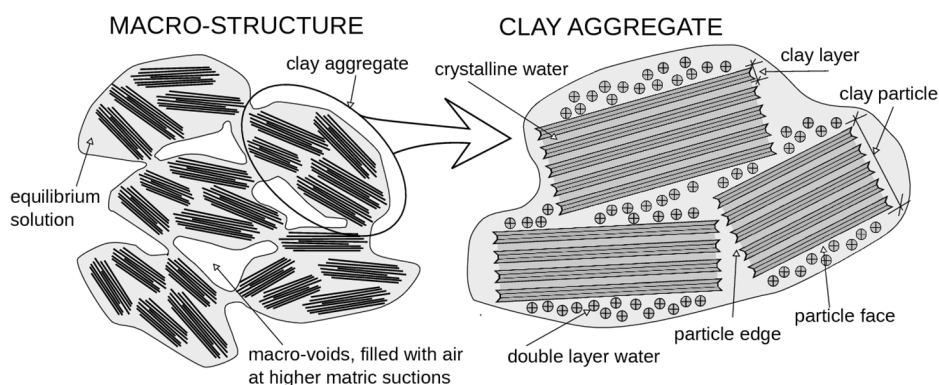


Figure 1: Schematic representation of double structure concept (Mašín, 2013 & 2017).

In Mašín (2013), separate models are considered for the mechanical and hydraulic responses of the microstructure and of the macrostructure. These responses are coupled at each structural level, and the behavior of the two structural levels is linked through the double-structure coupling function. A schematic of the adopted modeling approach is in Figure 2. The individual models are denoted as G^M , G^m , H^M , and H^m , respectively.

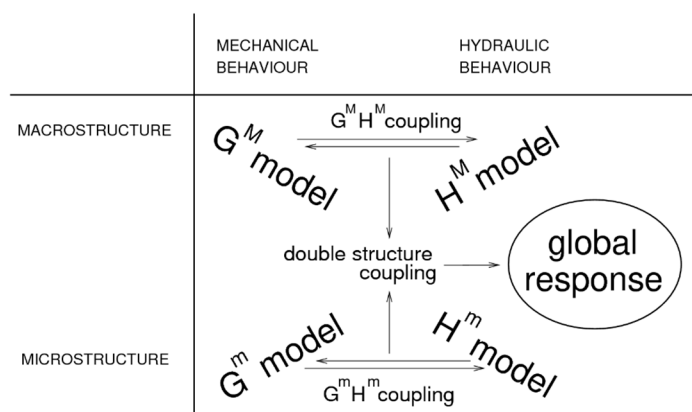


Figure 2: Schematic representation of the double structure coupling concept adopted in the hypoplastic model (Mašín, 2013 & 2017).

In the double-structure model from Mašín (2013), the mechanical behavior of the macrostructure (G^M) was described using the model for unsaturated soils developed by Mašín and Khalili (2008), which itself was based on a hypoplastic model for saturated clays from Mašín (2005). The hydraulic response of the macrostructure (H^M) was based on the void ratio–

dependent water retention model from Mašín (2010). The microstructure has always been considered as fully saturated (simple H^m model), with its mechanical behavior (G^m) reversible volumetric, governed by the Terzaghi effective stress principle (see Mašín and Khalili 2016 for a thorough discussion). The $G^m H^m$ coupling was accomplished by the dependency of H^m on volume change and by the dependency of the effective stress on degree of saturation of the macrostructure S_r^m . The $G^m H^m$ coupling was introduced through the adoption of the Terzaghi effective stress for the mechanical behavior of the microstructure. Finally, the double-structure coupling was controlled by a function of relative void ratio, which evolved from the original proposition by Alonso et al. (1999).

The model by Mašín (2017), adopted in BEACON simulations, evolved from the Mašín (2013) by including the thermal component. To accomplish this task, additional thermal dependency has been introduced for water retention curves, volumetric behaviour of microstructure and normal compression behaviour of macrostructure. The final model is a comprehensive model capable of predicting complex THM behaviour of bentonites, as demonstrated in Sec. 5.

2.2 Mathematical description

2.2.1 Theoretical framework

Hypoplasticity is an approach to non-linear constitutive modelling of geomaterials. In its general form (Gudehus 1996) it may be written as

$$\dot{\boldsymbol{\sigma}} = f_s(\mathcal{L} : \dot{\boldsymbol{\epsilon}} + f_d \mathbf{N} \|\dot{\boldsymbol{\epsilon}}\|) \quad (1)$$

where $\dot{\boldsymbol{\sigma}}$ and $\dot{\boldsymbol{\epsilon}}$ represent the objective (Zaremba-Jaumann) stress rate and the Euler stretching tensor respectively, \mathcal{L} and \mathbf{N} are fourth- and second-order constitutive tensors, and f_s and f_d are two scalar factors. In hypoplasticity, stiffness predicted by the model is controlled by the tensor \mathcal{L} , while strength (and asymptotic response in general, is governed by a combination of \mathcal{L} and \mathbf{N} . Earlier hypoplastic models (such as the model by von Wolffersdorff 1996 and Mašín 2005) did not allow to change the \mathcal{L} formulation arbitrarily, as any modification of the tensor \mathcal{L} undesirably influenced the predicted asymptotic states. This hypoplasticity limitation was overcome by Mašín (2012). He developed an approach enabling to specify the asymptotic state boundary surface independently of the tensor \mathcal{L} and demonstrated it by proposing a simple hypoplastic equivalent of the Modified Cam-clay model. Based this approach, Mašín (2014) developed an advanced hypoplastic model for clays, which is adopted in the the THM model used in this work.

The basic hypoplastic model requires five material parameters φ_c , N , λ^* , κ^* and v . The parameters have the same physical interpretation as parameters of the Modified Cam clay model, and they are thus easy to calibrate based on standard laboratory experiments. The model parameters N and λ^* define the position and the slope of the isotropic normal compression line in the $\ln(1+e)$ vs. $\ln(p/p_r)$ plane. The isotropic normal compression line is described using equation

$$\ln(1+e) = N - \lambda^* \ln\left(\frac{p}{p_r}\right) \quad (2)$$

where $p_r = 1$ kPa is a reference stress. Parameter κ^* controls the slope of the isotropic unloading line in the same plane and also of the isotropic compression line of overconsolidated soil. φ_c is the critical state friction angle, with identical meaning with any other critical state soil mechanics – based model. Finally, the parameter v controls shear modulus.

Apart from stress, the most important state variable controlling the response of the model is void ratio e , or, equivalently, overconsolidation ratio OCR . The OCR is in hypoplasticity defined as:

$$OCR = \frac{p_e}{p} \quad (3)$$

where p_e is the Hvorslev equivalent pressure; that is, mean effective stress at the isotropic normal compression line calculated using Eq. (2) at the current void ratio.

The principle of hypoplasticity can best be demonstrated using a simple one-dimensional model. 1D version of hypoplastic model for shear reads:

$$d\tau = Ld\gamma + N|d\gamma| \quad (4)$$

where $d\tau$ is increment of shear stress (note that compression negative sign convention is adopted), $|X|$ represents absolute value of X and L and N are two moduli. In hypoplasticity, neither the switch function distinguishing between loading and unloading, as in elasto-plastic model, nor strain decomposition into elastic and plastic parts, are needed. A scalar "modulus" N may be defined as

$$N = LY \quad (5)$$

with

$$Y = \frac{\tau}{\tau_{yield}} \quad (6)$$

The modulus L may be specified using a parameter such that $L = E_n$. This simple 1D hypoplastic model thus requires two parameters τ_{yield} and E_n . Predictions of this 1D model are shown in Figure 3, where they are compared with predictions of model elasto-plastic.

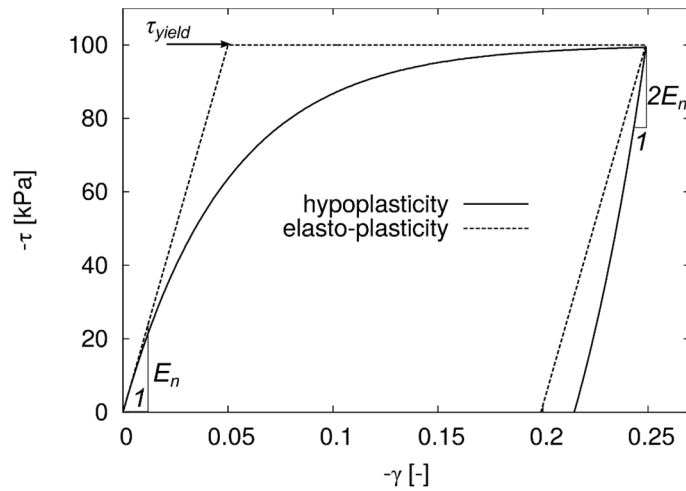


Figure 3: Demonstration of hypoplasticity principles using a simple one-dimensional model.

Let us now consider the Equation (4) and evaluate the stiffness predicted by the hypoplastic model. First of all, the stiffness depends on loading direction (as in elasto-plasticity), thanks to the absolute value appearing in Eq. (4). The following two cases are important for clarifying the model performance:

1. When $\tau = 0$, Y calculated using Eq. (4) is equal to zero. Therefore, $N = 0$ and thus

$$d\tau = Ld\gamma \quad (7)$$

L thus specifies the initial modulus for loading from the state $\tau = 0$.

2. When $\tau = \tau_{yield}$, Y is equal to one. Therefore, $N = L$ and the hypoplastic equation reads

$$d\tau = L(d\gamma + |d\gamma|) \quad (8)$$

In loading, $d\gamma < 0$ and therefore $d\tau = 0$, similar as in elasto-plasticity. During unloading, $d\gamma > 0$ and hypoplasticity predicts

$$d\tau = 2Ld\gamma \quad (9)$$

It follows from the above that for the special cases of $\tau = 0$ and $\tau = \tau_{yield}$ the hypoplastic model predicts similar response as the elasto-plastic model (apart from the unloading modulus at $\tau = \tau_{yield}$, which is twice as high as the loading modulus at $\tau = 0$). The most important difference in predictions of the two models is in the intermediate states $\tau_{yield} < \tau < 0$. While elasto-plasticity

predicts constant stiffness E_n , hypoplasticity predicts gradual decrease of stiffness, starting from the initial modulus E_n and ending with the fully plastic state with stiffness equal to zero. The stiffness decrease is caused by the definition of Y , whose value gradually increases from 0 to 1 and thus forces the modulus N to vary between zero and L .

2.2.2 Mathematical formulation of the original THM model (basic equations, before BEACON development)

The primary equation of the THM hypoplastic model reads

$$\dot{\sigma}^M = f_s[\mathcal{L} : (\dot{\epsilon} - f_m \dot{\epsilon}^m)] + f_d \mathbf{N} \|\dot{\epsilon} - f_m \dot{\epsilon}^m\| + f_u(\mathbf{H}_s + \mathbf{H}_T) \quad (10)$$

For description of the complete mathematical formulation of the model, interested reader is referred to Mašin (2017). Complete model formulation is also given in Appendix of this report. In the following, the main components of Eq. (10) are described:

- Behaviour of *macrostructure* is defined using the hypoplastic approach. Thus, Eq. (10) defines the effective stress rate of macrostructure $\dot{\sigma}^M$. It is defined using Bishop equation, in which the factor χ is equal to the degree of saturation of macrostructure.

$$\sigma^M = \sigma^{net} - \mathbf{1} S_r^M s \quad (11)$$

where σ^{net} is net stress, s is suction and S_r^M is degree of saturation of macrostructure defined using a hysteretic macrostructural void ratio-dependent water retention model of Brooks and Corey (1964) type. The water retention model for macrostructure is sketched in Figure 4.

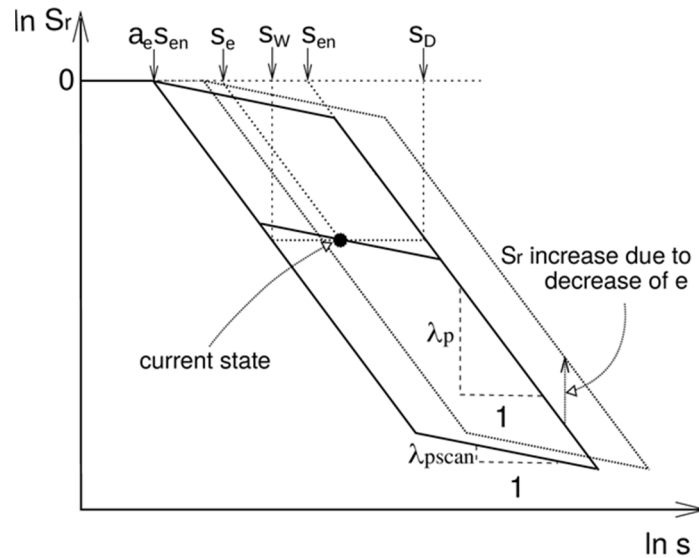


Figure 4: Hysteretic water retention model for macrostructure adopted in hypoplastic THM model for expansive soils

- Behaviour of *microstructure* is defined using elastic volumetric model, which can be written as

$$\dot{\epsilon}^m = \frac{1}{3} \left(\alpha_s \dot{T} - \frac{\kappa_m}{p^m} \dot{p}^m \right) \quad (12)$$

where $\dot{\epsilon}^m$ is microstructural strain, \dot{T} is temperature rate, p^m is microstructural mean effective stress and α_s and κ_m are parameters. Microstructure is always assumed to be fully saturated and its behaviour governed by the Terzaghi effective stress, that is

$$\sigma^m = \sigma^{net} - \mathbf{1} s \quad (13)$$

- The double structure coupling is accomplished through the factor f_m appearing in Eq. (10). This factor depends on relative density, such that for the most dense state $f_m = 1$ and for the most loose state $f_m = 0$. These values mean that at the loose state microstructural strain does not cause any macrostructural deformation, because microstructural units (aggregates) swell into the macrovoids. Contrary, at the densest

possible state macrostructure is basically closed, and any microstructural strain causes equivalent strain macrostructural. The factor f_m is defined as

$$f_m = 1 - (r_{em})^m \quad (14)$$

where m is a parameter and r_{em} is relative void ratio defined as

$$r_{em} = \frac{e - e_d}{e_i - e_d} \quad (15)$$

where e_d is minimum void ratio (equal to microstructural void ratio) and e_i is maximum void ratio (equal to the void ratio at the isotropic normal compression line).

- Eq. (10) contains two tensors \mathbf{H}_s and \mathbf{H}_T and a scalar factor f_u . The factors \mathbf{H}_s and \mathbf{H}_T are denoted as wetting- and heating-induced collapse factors, calculated to ensure that during wetting and heating of specimen whose state is close to the isotropic normal compression line (NCL), its state remains at NCL and thus wetting- and heating-induced collapse is predicted. The factor f_u depends on relative density and decreases the effect of \mathbf{H}_s and \mathbf{H}_T for higher overconsolidation ratios.
- Last, Eq. (10) contains two scalar factors f_s and f_d . These are denoted as barotropy- and pyknotropy factors and they control the effect of stress and void ratio on macrostructural soil stiffness. They were taken over from the basic hypoplastic model for clays from Mašín (2014).

The complete mathematical formulation of the THM hypoplastic model is in Appendix.

2.2.3 Input parameters

Model parameters and their description is summarised in Table 1.

Table 1: Model parameters and their description (from Mašín, 2017).

Parameter	Description
φ_c	Critical state friction angle of macrostructure in a standard soil-mechanics context
λ^*	Slope of isotropic normal compression line in $\ln(p^M/p_r)$ versus $\ln(1 + e)$ space
κ^*	Macrostructural volume strain in p^M unloading
N	Position of isotropic normal compression line in $\ln(p^M/p_r)$ versus $\ln(1 + e)$ space
ν	Stiffness in shear
n_s	Dependency of position of isotropic normal compression line on suction
l_s	Dependency of slope of isotropic normal compression line on suction
n_T	Dependency of position of isotropic normal compression line on temperature
l_T	Dependency of slope of isotropic normal compression line on temperature
m	(1) Control of f_u and thus dependency of wetting-/heating-induced compaction on distance from state boundary surface; (2) control of double-structure coupling function and thus response to wetting-drying and heating-cooling cycles (Mašín 2013b)
α_s	Dependency of microstructural volume strains on temperature
κ_m	Dependency of microstructural volume strains on p^m
e_{r0}^m	Reference microstructural void ratio for reference temperature T_r , reference suction s_r , and zero total stress
c_{sh}	Value of f_m for compression
s_{e0}	Air-entry value of suction for reference macrostructural void ratio e_0^M
a	Dependency of macrostructural air-entry value of suction on temperature
b	Dependency of macrostructural air-entry value of suction on temperature
a_e	Ratio of air entry and air expulsion values of suction for macrostructure water retention model
s_r	Reference suction for e^m
e_0^M	Reference macrostructural void ratio for air-entry value of suction of macrostructure
T_r	Reference temperature

2.3 Model developments within BEACON project

Model development during BEACON project was driven by the need to improve predictive capabilities of the model, in particular when the newly available experimental data showed different behaviour than the experimental data sets used for development of the original model and when this change of behaviour could not be represented by the model through the variation of its parameters. Some model updates were further motivated by numerical reasons, as it was found that abrupt changes of derivatives within the model (for example, slope of water retention curve in its bi-linear logarithmic formulation) may lead to numerical instabilities. The main modification was an update of the macrostructural water retention curve formulation from bi-linear to smooth.

It is to be pointed out that major focus of development within BEACON was related to numerical aspects of the model implementation within SIFEL finite element software, like definition of consistent or partially consistent stiffness matrix, exception and unphysical state handling, robust solution of the implicit part of the model formulation, etc. These developments do not change the actual predictions of the model on the element level, but increase model robustness in finite element simulations.

The improvement focuses on reformulation of the water retention model for macrostructure. In the basic model by Mašín (2017), which follows Mašín (2013) and Wong and Mašín (2013), bi-linear formulation of water retention curve of Brooks and Corey (1964) type is used. The resulting water retention curve is sketched in Figure 4. It is clear that the water retention curve is C-0 continuous only, which means that derivatives $\partial S_r^M / \partial s$ change abruptly at the intersection of the main wetting/drying curves with the scanning curve and at the air

entry/expulsion value of suction. These discontinuities are by-products of the simplification adopted while defining the model equations, as real soil shows indeed non-linear dependency of S_r^M on suction. In addition, they lead to problems in numerical performance of the model when implemented into a finite element code. Last, this bi-linear formulation, which resembles response of elasto-plastic constitutive model, is in contrast to the general formulation of the THM constitutive model, which is hypoplastic and thus inherently non-linear.

In redefining the water retention curve to be C-1 continuous, we adopt with advantage the r_λ formulation proposed by Wong and Mašín (2013). Using this approach, the complete bi-linear water retention curve (not only the main wetting and drying curves) is defined using

$$S_r^M = \begin{cases} 1 & \text{for } s \leq a_e s_{en} \\ \left(\frac{s_e}{s}\right)^{\lambda_p} & \text{for } s > a_e s_{en} \end{cases} \quad (1)$$

where the meaning of variable s_e is clear from Figure 4. It is calculated using

$$s_e = s_{en}(a_e + a_{scan} + a_e a_{scan}) \quad (2)$$

where a_{scan} defines the position of current state along scanning curve, such that $a_{scan} = 0$ on the main drying curve and $a_{scan} = 1$ on the main wetting curve:

$$s_D = \frac{s - s_W}{s - s_D} \quad (3)$$

For meanings of s_W and s_D see Figure 4. Rate of variable a_{scan} is given by

$$\dot{a}_{scan} = \frac{1 - r_\lambda}{s_D(1 - a_e)} \dot{s} \quad (4)$$

Here, r_λ represents ratio of scanning curve slope (in $\ln s$ vs. $\ln S_r$ plane) and slope of the main drying and wetting curves. For the original model, this ratio is given by

$$r_\lambda = \begin{cases} 1 & \text{for } s = s_D \text{ and } \dot{s} > 0 \\ 1 & \text{for } s = a_e s_D \text{ and } \dot{s} < 0 \\ \frac{\lambda_{pscan}}{\lambda_p} = 0.1 & \text{otherwise} \end{cases} \quad (5)$$

Slopes λ_p and λ_{pscan} are indicated in Figure 4.

In the improved model, the discrete value of r_λ from Eq. (5) was modified such that the slope of scanning curve smoothly varies between the main drying and wetting curves. The modification uses three parameters, which are aimed to be internal (hidden from the user and hard-coded in the model implementation) such that the parameters of the complete THM model to be user-calibrated do not change between the two formulations. These internal parameters are denoted as $p_{scan} = 3$, $S_{lim} = 0.75$ and $p_{wett} = 1.1$. In the formulation, new factor f_{scan} is used, defined as

$$f_{scan} = \begin{cases} a_{scan} & \text{for } \dot{s} > 0 \\ 1 - a_{scan} & \text{for } \dot{s} < 0 \end{cases} \quad (6)$$

Smoothed WRC formulation is then achieved by redefining r_λ from Eq. (5) to

$$r_\lambda = \begin{cases} 0 & \text{for } s < a_e s_{en} \text{ and } \dot{s} > 0 \\ \left(\frac{1 - S_r^M}{1 - S_{lim}}\right)^{p_{wett}} & \text{for } S_r^M > S_{lim} \text{ and } \dot{s} < 0 \\ f_{scan}^{p_{scan}} & \text{otherwise} \end{cases} \quad (7)$$

Comparison of predicted water retention curves with the original and redefined models is in Figure 5. Clearly, the updated model provides smooth WRC curve while keeping the reference main wetting and drying curves as asymptotic targets. Subsequent figures present results of constant volume cyclic wetting-drying test expressed in terms of various state variables adopted in the THM hypoplastic model. These figures demonstrate that, apart of smoothing of the WRC formulation, other properties of the model (in this case evolution of the proportion of

microstructural and macrostructural void ratios and their effect on the position of the main drying and wetting branches of water retention curve) are not compromised.

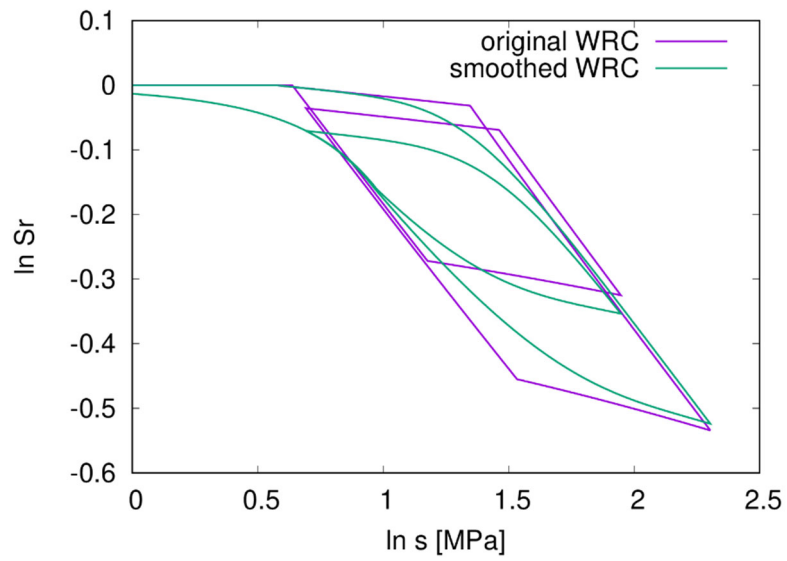
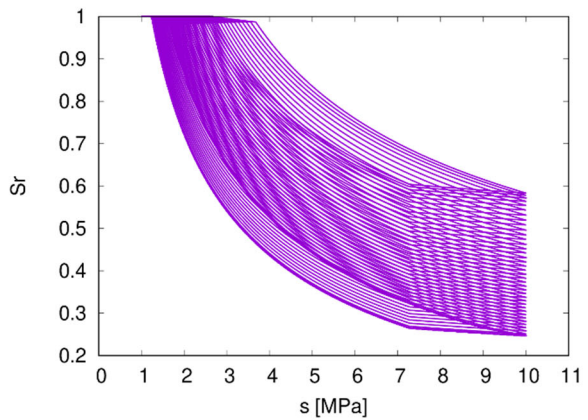
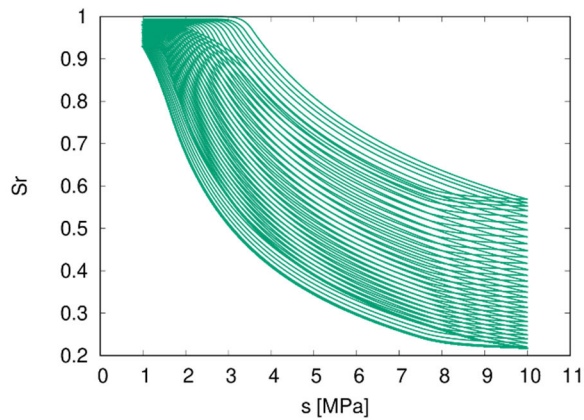
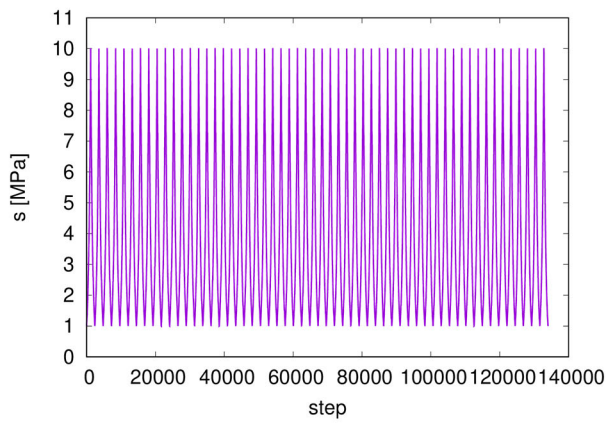
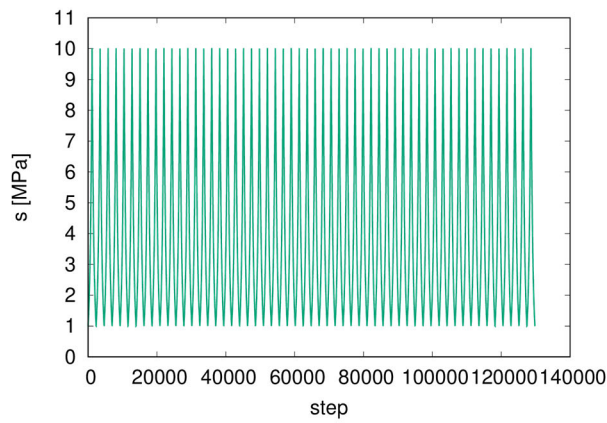
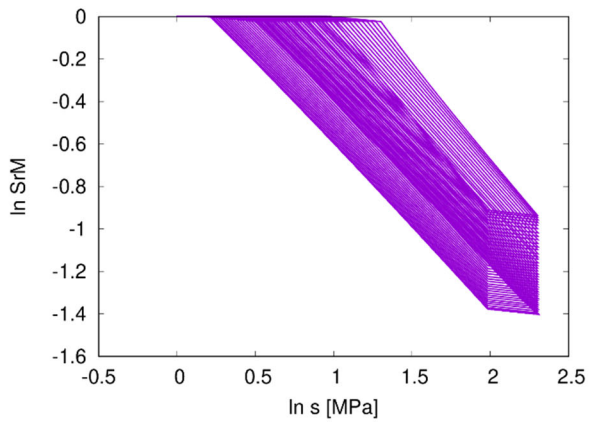
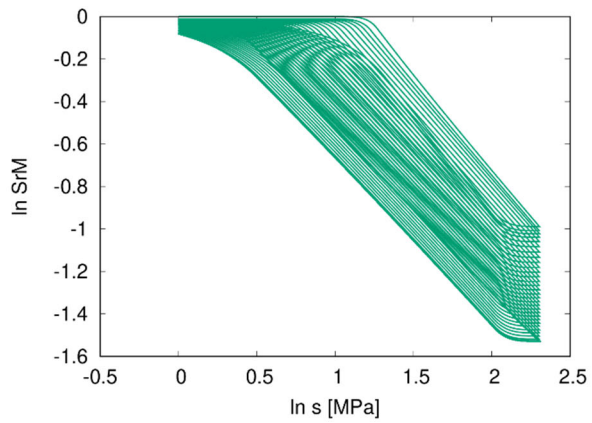
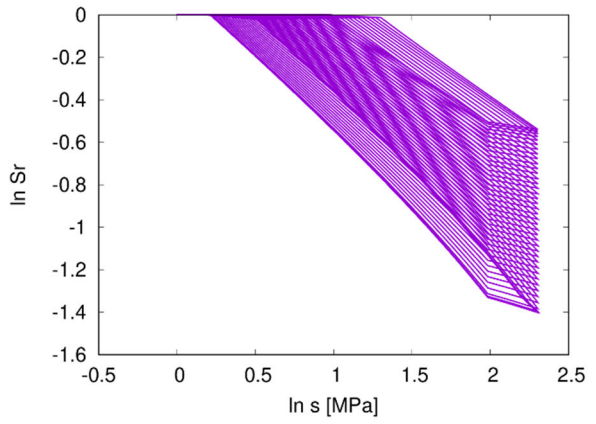
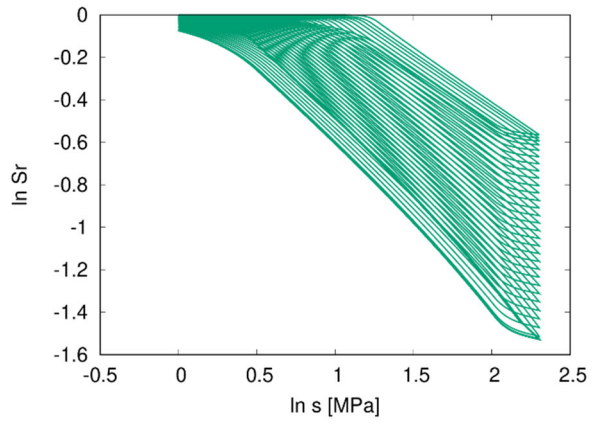
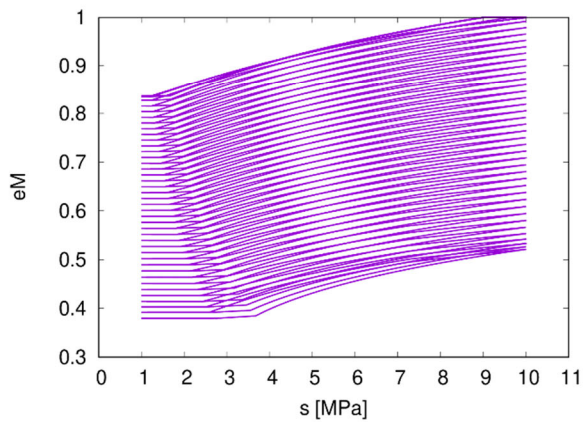
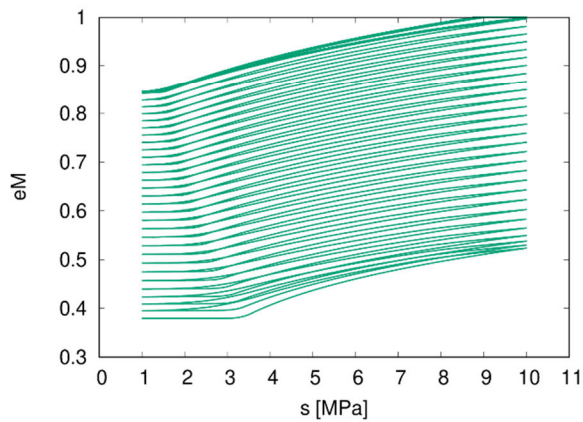
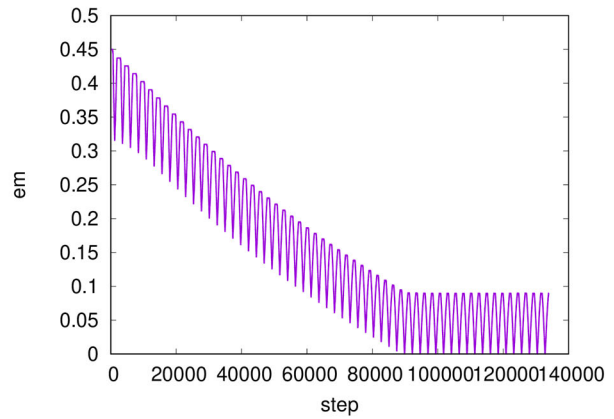
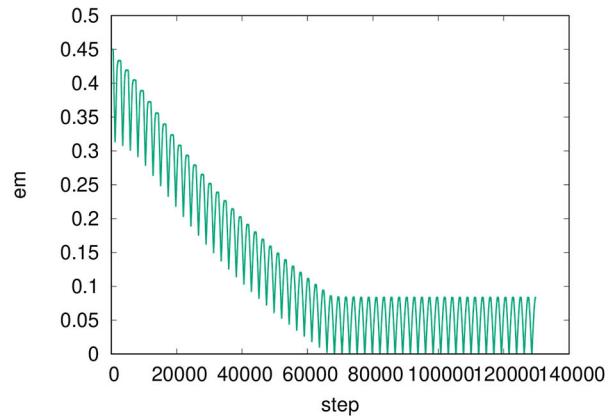
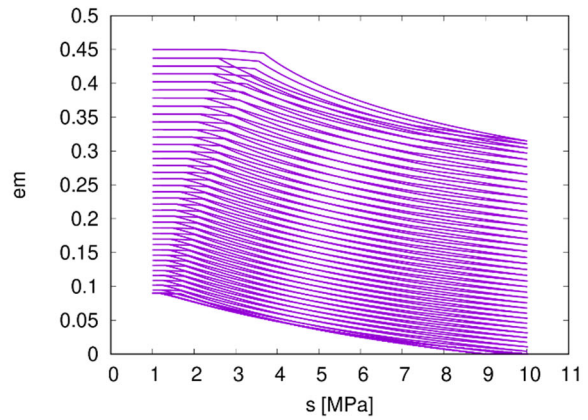
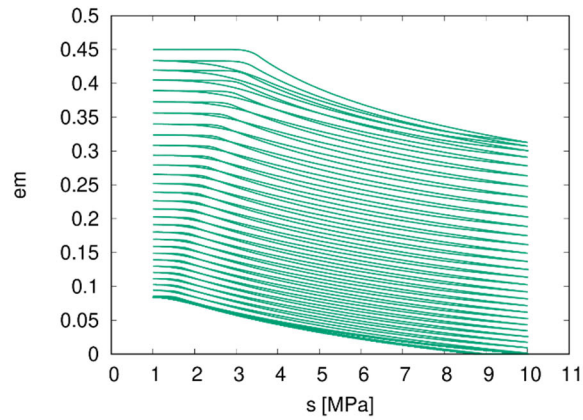
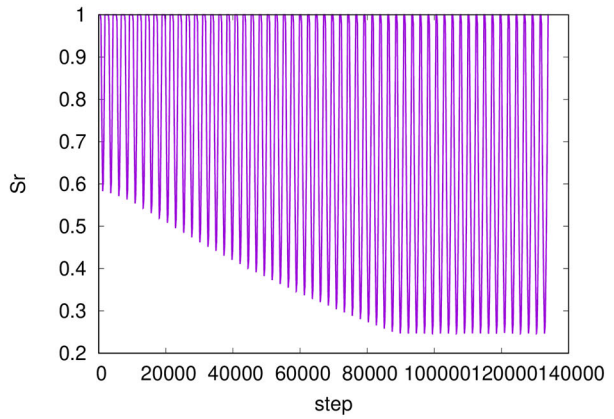
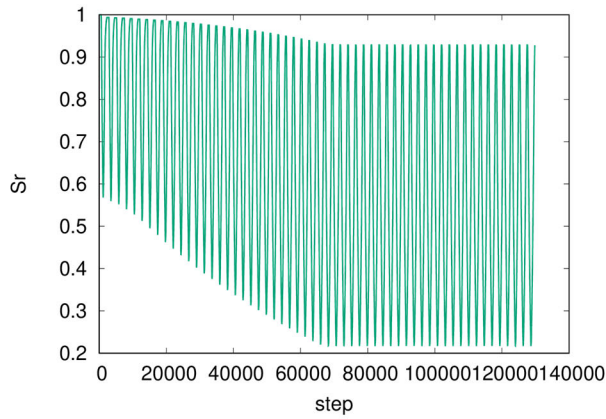


Figure 5: Comparison of water retention curves predicted with the original and modified macrostructural WRC formulations.





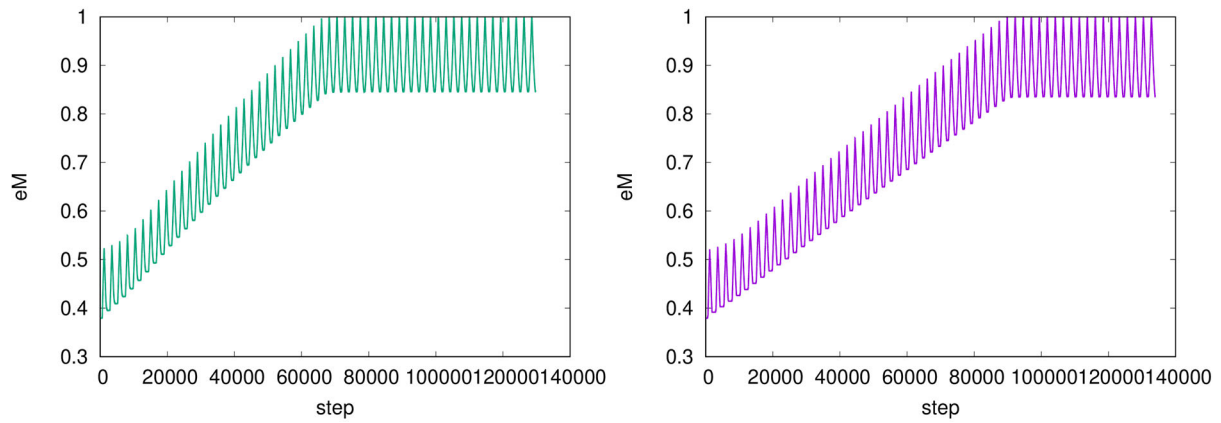


Figure 6: Evolution of various state variables involved in the THM hypoplastic model in cyclic water retention test. Comparison of the original bi-linear logarithmic formulation (right figures) with the new smooth formulation (left figures).

3 Basic capabilities of the model

The table of formal capabilities of the original and updated model is in Table 2.

Table 2: Capabilities of the original and updated model

Name of the constitutive law:			
Behaviour feature	D3.1	D3.3	Remarks
Mechanical behaviour			
Dependence of swelling strain on applied stress (at the same dry density) (Figure 1)	Y	Y	
Dependence of swelling stress on dry density (at the same stress) (Figure 1)	Y	Y	
Irreversibility of strains in wetting/drying cycles (Figure 2)	Y	Y	
Dependence of swelling pressure on dry density (Figure 4)	Y	Y	
Stress path dependence from an unsaturated to a saturated state (Figure 5)	Y	Y	
Stress path dependence from a saturated to an unsaturated state (Figure 6)	Y	Y	
Double structure/porosity considered?	Y	Y	
Are temperature effects considered in the model?	Y	Y	
Dependence of strains developed in a temperature cycle (increase/decrease) on OCR (or stress) (Figure 7)	Y	Y	
Hydraulic behaviour (retention curve)			
Hysteresis	Y	Y	
Dependence on void ratio	Y	Y	
Double structure/porosity considered?	Y	Y	

It is clear from Table 2 that formally, that is from the qualitative point of view, even the original model considered all the tested capabilities and so also the updated model does, figures demonstrating these qualitative features presented in Deliverable 3.1 report will thus not be repeated at this point for the new model. Of course, qualitative consideration of the aspects does not necessarily imply good quantitative performance of the model. Features of the

bentonite behaviour which have not been predicted perfectly from the quantitative point of view using the original model were target of the updates, as described in Sec. 2.3.

4 Task 3.3

The THM hypoplastic model has been evaluated with respect to simulations of experiments on MX80 bentonite. These tests were performed under oedometric conditions and differed in confinement during the wetting phase – test at “path 1” was wetted under constant vertical stress of 21 MPa and subsequently loaded up to vertical stress of 20 MPa, whereas the test with “path 2” was first wetted under constant volume conditions and loaded subsequently up to vertical stress of 20 MPa.

All samples were initially prepared by pouring the granular material in the oedometric ring with dry density of 1.48-1.50 Mg/m³. The corresponding void ratio is in the range of 0.83-0.86, as shown in Table 3 along with initial values of other state variables.

Table 3: Initial values for state variables

Vertical stress (MPa)	Void ratio	Water content (%)	Degree of saturation (%)	Dry density (g/cm ³)	Density of the solid phase (g/cm ³)	Suction (MPa)
0.02	0.85	6.93	22.35	1.48	2.74	150

The description of model parameters is summarized in Table 1 and parameter values used in simulations is in Table 4.

Table 4: The parameters used to simulate the test data on MX-80 bentonite

Parameter	Value	Parameter	Value
Φ_c	25	K_m	0.12
λ	0.23	S_m^*	-2700
κ	0.055	e_{ro}^m	0.9
N	2.7	C_{sh}	0.002
ν	0.25	S_{ref}	-1000
n_s	0.02	e_{ref}^M	0.1
l_s	0	T_{ref}	294
n_T	-0.07	α_T	0.118
l_T	0	b_T	-0.000154
m	0.2	α_{er}	0.5
α_s	0.00015	λ_{p0}	0.55

4.1 Task 3.3 Water retention modelling

The water retention behaviour of the MX80 granular bentonite is shown in Figure 7 (data from Seiphoori et al. (2014)) for samples initially prepared at a void ratio of 0.83. The water retention curves refer to free-swelling and constant-volume conditions. Wetting and drying branches are depicted. Seiphoori et al. (2014) discussed the evolutions of the MX80 microstructure associated with the wetting and drying cycles.

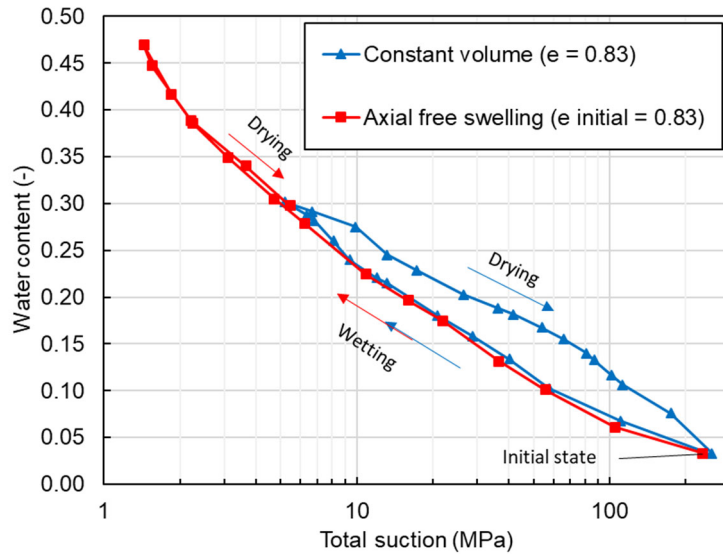


Figure 7: Water retention upon wetting and drying under free-volume and constant-volume conditions

The simulated results of water retention curves under axial free swelling and constant-volume conditions are in Figure 8 using parameters listed in Table 4.

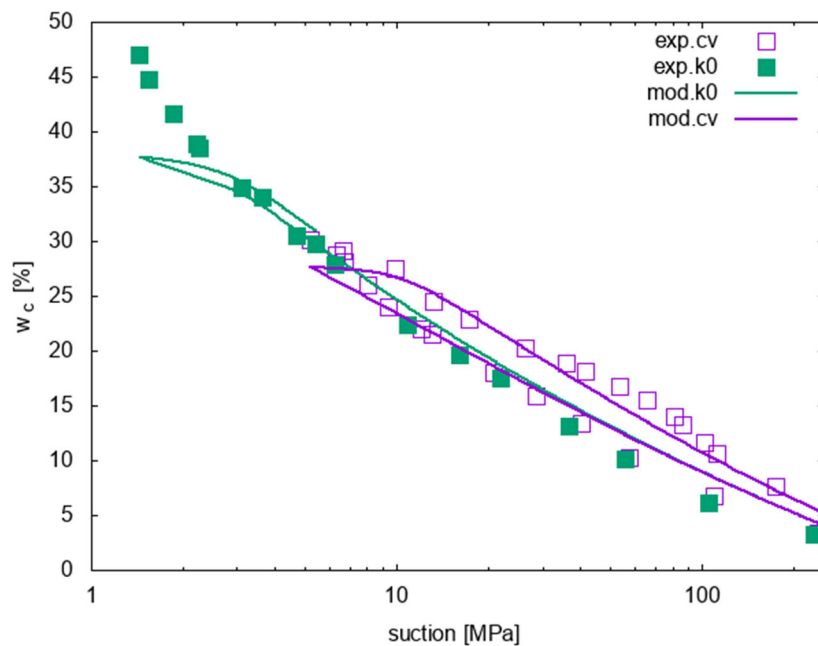


Figure 8: Water retention upon wetting and drying under free-volume and constant-volume conditions simulated using hypoplastic model

It is interesting to observe that, consistently with experiment, the model predicts negligible hysteresis loop for axial free swelling sample and more remarkable hysteresis for constant volume sample. Overall, the water retention behaviour is predicted correctly.

4.2 Task 3.3 oedometric compression test modelling (path 1 and path 2)

A schematic view of the followed testing paths is shown in the “void ratio – vertical stress” plane in Figure 9. Figure 10 shows the simulated results calculated by the THM hypoplastic model.

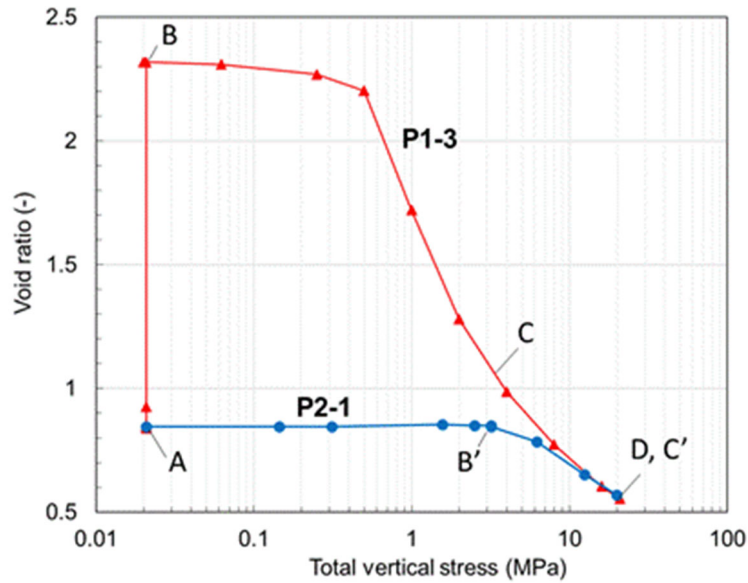


Figure 9: Experimental results of the testing program in terms of void ratio and vertical stress. Initial point is in both cases denoted by A and corresponds to the as-poured, hygroscopic state

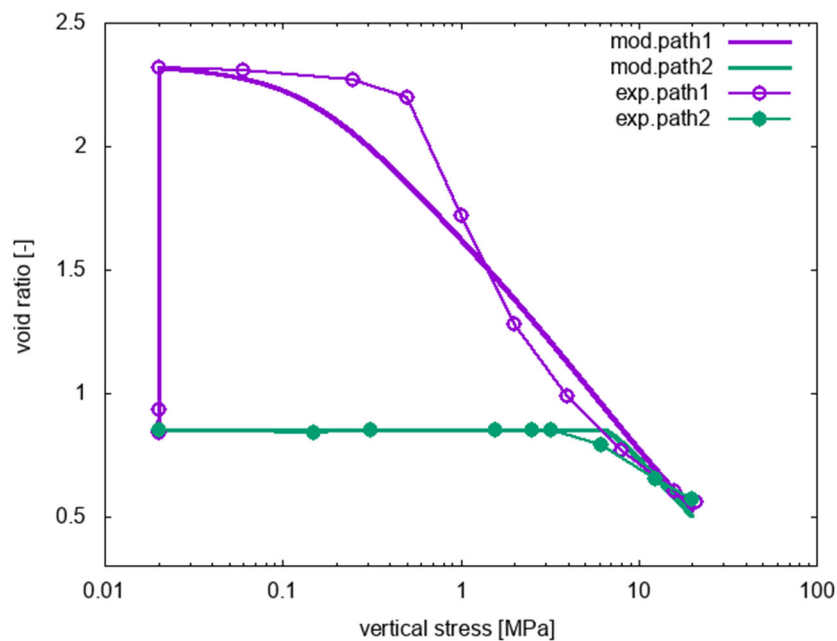


Figure 10: The testing results of void ratio and vertical stress simulated by Triax using hypoplastic model

The model predicts well swelling magnitude of both swelling under constant load and swelling under constant volume tests, although swelling pressures in path 2 are somewhat overestimated. Subsequently, both paths follow a unique normal compression line. The line is consistent with the experiment, the model just does not reproduce the non-linear shape of normal compression line when plotted in log vertical stress vs. void ratio plane.

4.3 Task 3.3: Comparison of modelling void ratios and MIP results

In this model, the calculation of void ratio considers the coupling of micropores and macropores, so it is a nonlinear relationship. The modelling results of total void ratio, micro-void ratio (e^m) and macro-void ratio (e^M) for path 1 and path 2 are presented in Fig. 7.

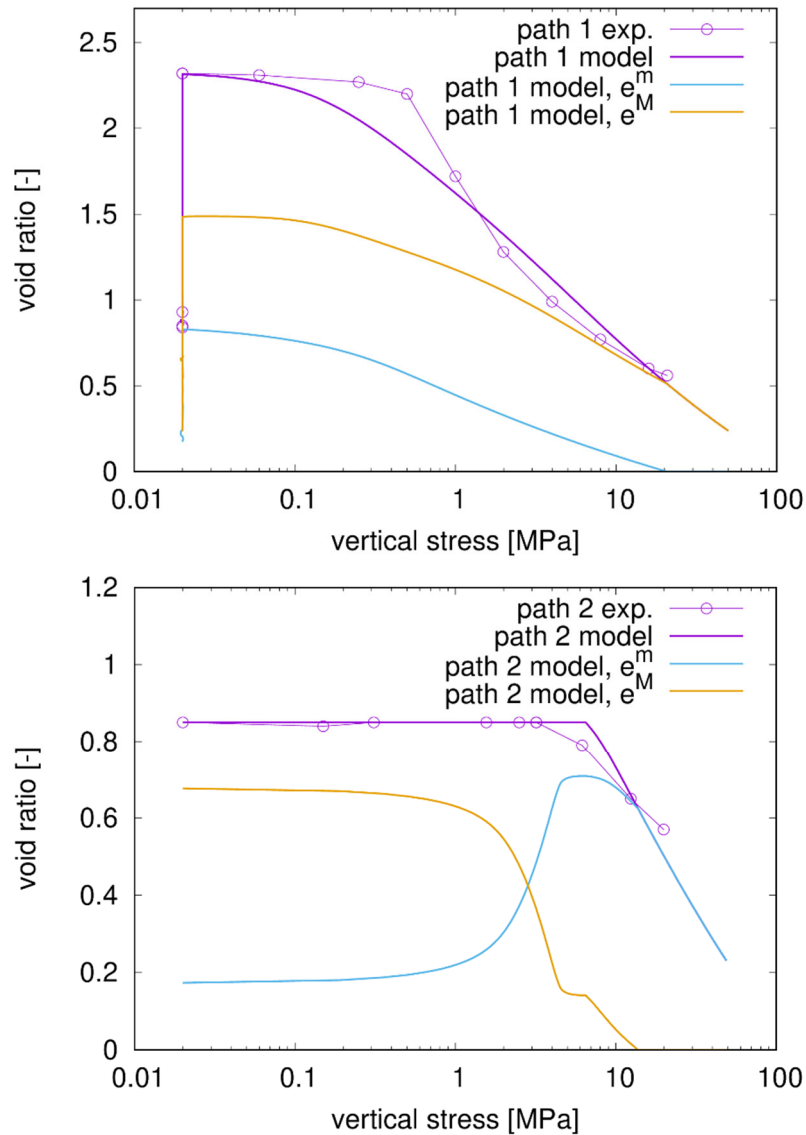


Figure 11: The results in terms of macro- and micro-void ratios calculated by hypoplasticity

The void ratio that results from experiments and modeling are listed in Table 5. Among them, the total void ratio e is collected from the compression testing results. The micro-void ratio e^m and macro-void ratio e^M are calculated from MIP results. The distinguish pore size of macro- and micro- pores is selected at the minima of PSD peaks (around 60 nm). Macro-void ratio is calculated from the cumulative PSD curve, micro-void ratio is assumed as the difference between total void ratio and macro-void ratio. It is to be noted that the PSD of samples often show more complex patterns than a simple double-peak structure, which makes their interpretation using double-porosity concept difficult. For the model, the reported macro-void ratio is defined as volume of voids in aggregates over solid volume, which differs from e^M definition within the model (volume of voids in aggregates over aggregate volume).

For the initial state (point A), the model does not correctly represent proportion of micro- and macro-void ratio. These tests have, however, been performed using different samples than the rest of the measurements and, in our opinion, it may be questionable whether the measurements are consistent with the rest of the experiments (micro-void ratio 0.624 is, at a high suction, higher than micro-void ratios of the other experiments after swelling).

After oedometric swelling (point B) and after constant volume swelling (point B'), the total void ratio is represented correctly, it is also correctly predicted that macro-void ratio is higher than the micro-void ratio. However, micro-void ratio magnitude is higher than experimental in both

cases, the model thus overpredicts microstructural swelling over the swelling of macrostructure. After oedometric loading of constant-load swelled sample (point C), relative magnitude of micro- and macro-void ratios is again predicted correctly (micro being smaller than macro). Modelling however predicts that micro-void ratio decreased significantly during loading (between points B-C), which is not reflected in experimental data (micro-void ratio was almost intact to mechanical loading). This might be partially caused by possible microstructural changes during the process of sampling for MIP testing.

As mentioned above, in all cases, question arises whether double-porosity interpretation of complex PSD curves was relevant.

Table 5: Void ratio results from experiments and modeling

Point	Vertical stress(MPa)	Void ratio from test			Void ratio from modeling		
		e	e ^m	e ^M	e	e ^m	e ^M
A	0.02	0.83	0.624	0.206	0.850	0.174	0.676
B	0.02	2.32	0.426	1.894	2.314	0.829	1.485
			0.256	2.064			
C	3.24	1.1	0.462	0.638	1.201	0.251	0.950
			0.476	0.624			
B'	3.19	0.85	0.475	0.375	0.850	0.709	0.141
			0.468	0.382			

5 Performance of the model and assessment of predictive power

5.1 Simulations of laboratory experiments on BCV bentonite performed within BEACON project

The THM hypoplastic model has been calibrated and validated to a comprehensive set of experimental data on BCV bentonite obtained within BEACON project, to be further used in finite element simulations of Mock-up experiments and of experiments related to homogenisation (dual density samples).

Figure 12 (left) shows predictions of oedometric loading-unloading experiments on saturated BCV bentonite performed at CU demonstrating good representation of loading-unloading behaviour. The samples have been prepared by powder compaction to dry density of 1270 kg/m^3 , swelled in oedometric conditions at a constant load of 10 kPa and subject to oedometric loading-unloading subsequently. Only the saturated loading-unloading phase has been simulated in this case (comparison of predictions of swelling-loading-unloading oedometric tests at various paths combinations is presented later in Figure 20). Although highly preconsolidated initially, the samples reach almost immediately normal compression line, demonstrating that the swelling process led to a decrease of apparent preconsolidation. The model represents well both the loading and unloading stiffness.

Figure 12 (right) shows predictions of uniaxial compression experiments on unsaturated compacted bentonite. In this single case, data are not available for BCV bentonite so experimental results on B75 bentonite tested at CTU have been simulated. It is presumed that unconfined compression strength for the two bentonite types (both coming from the same deposit) would not differ substantially. The cylindrical samples with aspect ratio of 1:1 were tested at different dry densities and initial water content of 6%, corresponding to a suction of 100 MPa for B75 bentonite (see Figure 26). The experiments have been simulated with BCV parameters and initial suction value of 100 MPa. The unconfined strength is represented well for lower dry density sample and is slightly underestimated for higher dry density samples.

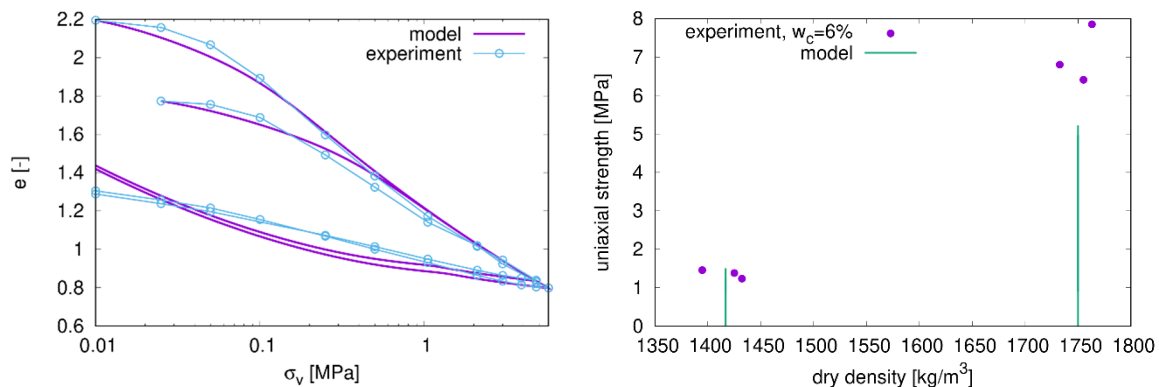


Figure 12: Predictions of oedometric loading-unloading tests on saturated BCV bentonite (left) and uniaxial loading experiments on unsaturated compacted B75 bentonite at water content of 6% (right).

Correct predictions of high uniaxial compressive strength can be explained with the aid of predictions of water retention curves. Compacted bentonite at three different initial dry densities (1200 , 1600 and 1900 kg/m^3) has been tested at constant volume (Figure 13) and unconfined (Figure 14) conditions. At unconfined conditions, the model slightly underpredicts water content and degree of saturation, the trends in the effect of dry density is predicted well otherwise, including lower water content at low suctions for high dry density samples than in the case of the other two tests. Less satisfactory predictions may be seen in the case of the free swelling experiments, where drying curves are represented reasonably well, but water content

is significantly underestimated in wetting curves. The reason for this discrepancy is as follows. As macrostructural water content is relatively low (Figure 15), the behaviour is predominantly affected by the behaviour of microstructure and because microstructure is considered as fully saturated, water retention curves are mainly affected by microstructural void ratio. Microstructural response is in the model considered as reversible and so also water retention curves should show little hysteresis, only coming from the macrostructural part (Figure 15). However, as BCV is highly swelling bentonite, to represent correctly the swelling characteristics, microstructural swelling stiffness is very high, it is actually close to the slope of the normal compression line. As, in addition, the macrostructural effective stress is non-negligible to make sure the uniaxial compression strength is predicted correctly (Figure 12), the state approaches normal compression line during wetting-drying process, which is in the model considered as a boundary of microstructural swelling, breaking thus reversibility of microstructural deformation. This is demonstrated in Figure 16 showing the value of state variable relative void ratio r_e , where value of 1 means that the state at normal compression line has been reached. Predictions of irreversible microstructural deformation is a consequence of high swelling properties of BCV bentonite and is not pronounced in model calibration to other bentonites, it is however indeed incorrect and should be corrected in future versions of the model.

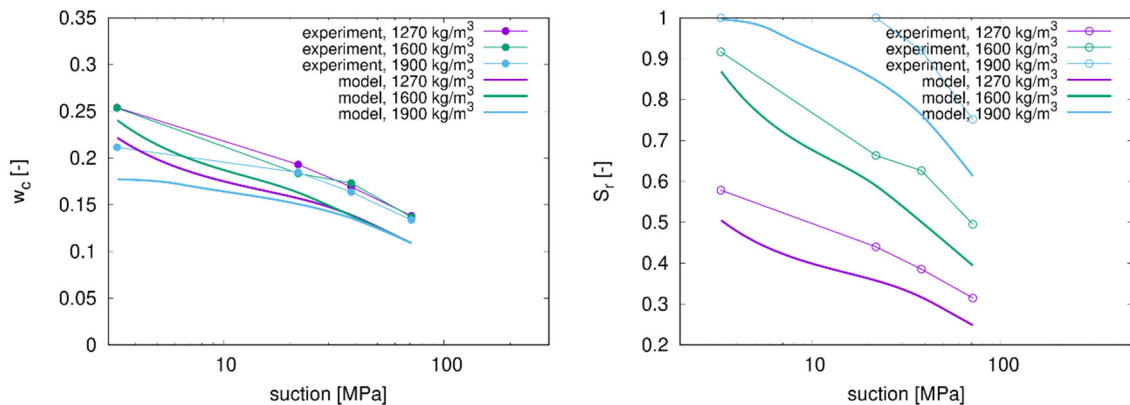


Figure 13: Predictions of water retention tests at compacted BCV bentonite under constant volume conditions at three different initial dry densities of 1200, 1600 and 1900 kg/m³.

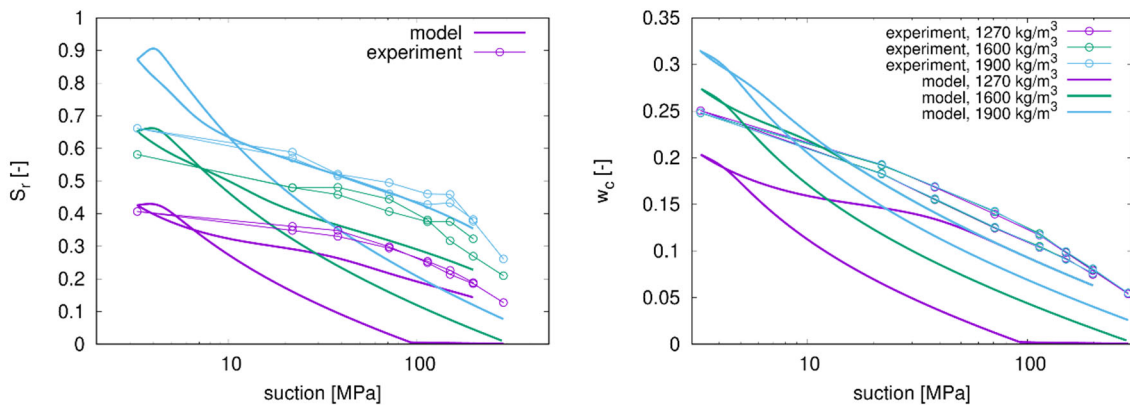


Figure 14: Predictions of water retention tests at compacted BCV bentonite under free swelling conditions at three different initial dry densities of 1200, 1600 and 1900 kg/m³.

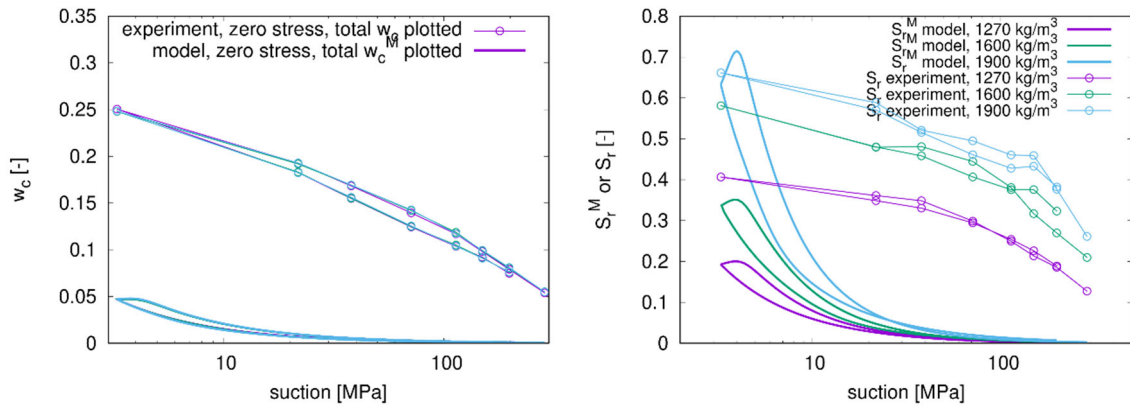


Figure 15: Predictions of macrostructural quantities (macrostructural water content and macrostructural degree of saturation) for water retention tests at compacted BCV bentonite under free swelling conditions at three different initial dry densities of 1200, 1600 and 1900 kg/m³.

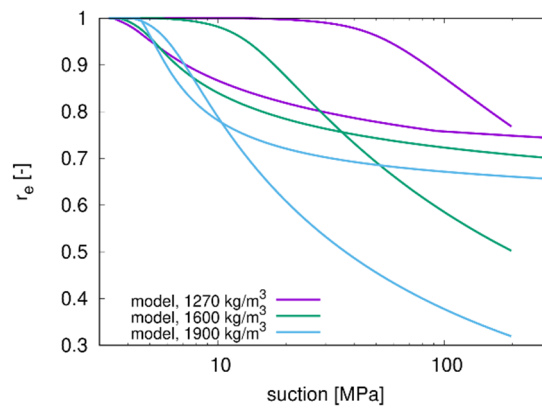


Figure 16: Predictions of relative void ratio for water retention tests at compacted BCV bentonite under free swelling conditions at three different initial dry densities of 1200, 1600 and 1900 kg/m³.

Another model characteristic to be discussed is macrostructural effective stress. In the model, Bishop effective stress equation is adopted for macrostructure, with factor χ equal to macrostructural degree of saturation S_r^M . As already pointed out, to predict high uniaxial compressive strength of compacted bentonite, S_r^M must have non-negligible (albeit low value even for high suctions (see Figure 15)). This non-negligible effective stress is contributing to irreversibility of microstructural void ratio (increased effective stress shifts the state towards normal compression line which subsequently limits microstructural swelling) and it also limits swelling potential, which is predicted reasonably well by the model (Figure 17), but swelling tests under constant load at low vertical loads are by a small fraction underestimated. It is to be pointed out at this point that experimental evidence indicates dry macrostructure for higher suctions, which is clear from both ESEM images (Sun et al., 2019) and from the fact that water content of bentonite at higher suctions is known to be independent of dry density (e.g., Romero et al., 2011). Relating high strength of compacted bentonite with macrostructural degree of saturation S_r^M , which is a concept originating from the idea of matric suction strengthening the inter-aggregate contacts through water meniscy, thus seem to be a simplification of reality as other physico-chemical phenomena play a role at inter-aggregate contacts. This model components should be carefully reconsidered in future model versions.

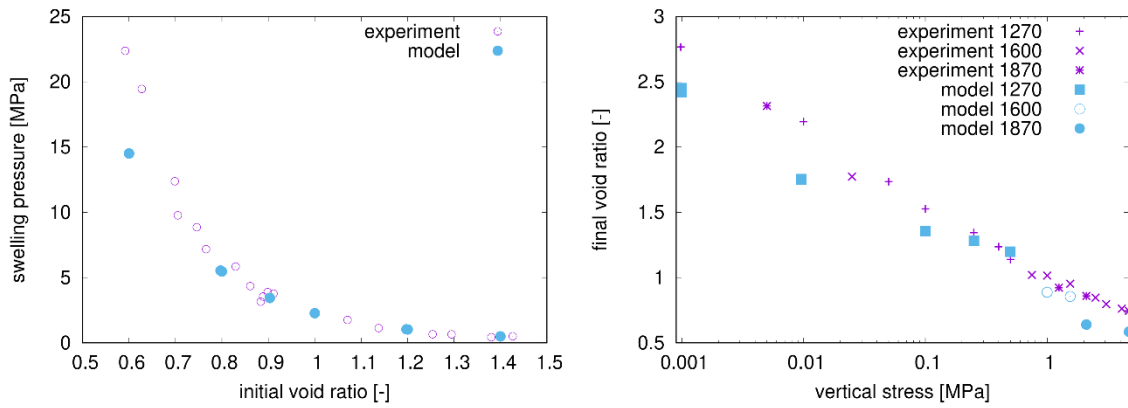


Figure 17: Predictions of swelling pressure tests (left) and oedometric swelling under constant load experiments at three different initial dry densities (right) of unsaturated compacted BCV bentonite.

Regardless the fact that swelling strain in constant vertical load oedometric swelling tests is slightly underpredicted by the model, the model swelling characteristics are predicted very well. This is also clear from Figure 18, which shows both the experiment types plotted in the same graph. The model, consistently with the experimental data, predicts constant load swelling tests consistently lower in pressure vs. dry density graph than for constant volume swelling pressure tests.

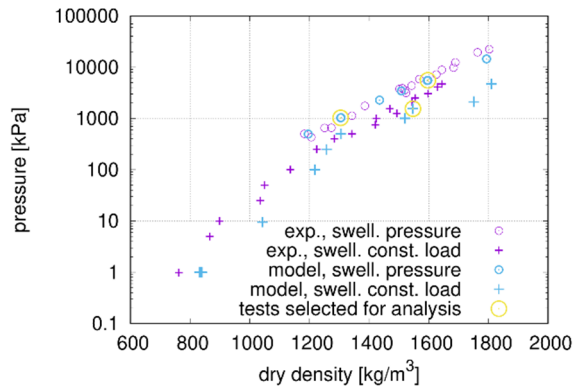


Figure 18: Comparison of predictions of swelling pressure tests and oedometric swelling under constant load experiments of unsaturated compacted BCV bentonite for both model and experiment.

The reason for these predictive capabilities is demonstrated in Figure 19 for selected tests marked using yellow circle in Figure 18. Figure 19 (left) shows evolution of radial and axial stresses. Obviously, they are identical for swelling pressure tests as no inherent anisotropy has been considered in the model. Contrary, in swelling under constant load test, radial stresses develop substantially above axial stress, which remains constant through experiment boundary conditions. As a consequence, the swelling under constant load test runs at high stress obliquity, meaning that the state boundary surface is reached much earlier than in swelling pressure tests (see Figure 19 right, where the value of mean stress normalised by mean stress at the state boundary surface for the given stress ratio is plotted). As discussed above, swelling becomes limited when state boundary surface is reached, which is the reason for the observed difference of swelling pressure and swelling under constant load results. Further, swelling pressures in graph at Figure 18 would be higher if radial stress or mean stress would be plotted rather than vertical stress, which would however still not be sufficient to yield identical results for the two test types.

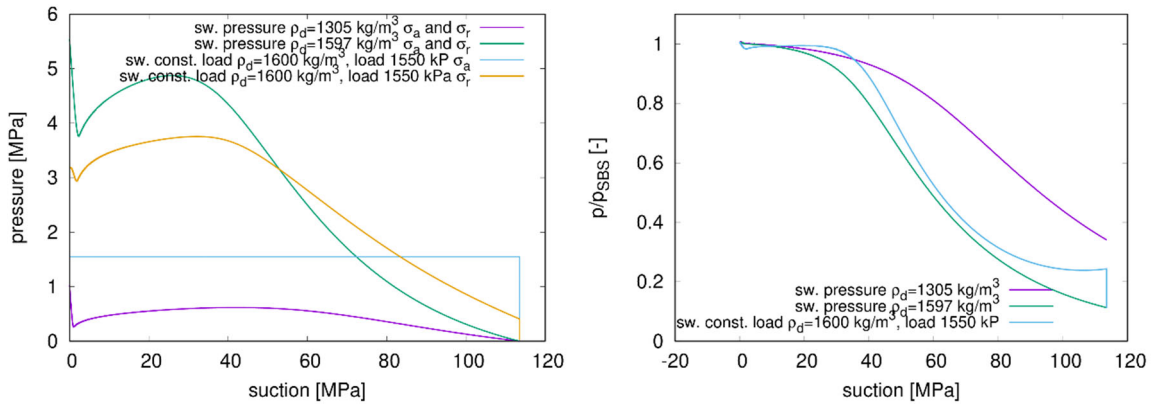


Figure 19: Comparison of predictions of selected swelling pressure tests and oedometric swelling under constant load tests. The selected tests marked using yellow circle in Figure 18.

An interesting experimental data set for model evaluation performed at CTU is shown in Figure 20, representing oedometric swelling-loading-unloading tests at different paths combinations. The graphs also show trend line through experimentally obtained swelling pressure test results. It is clear that this trend line forms a limit for loading parts of the tests (it thus coincides with the normal compression line), which is well predicted by the models. The model also predicts other important phenomena, such as swelling potential of sample at low load when compared with much lower swelling potential of loaded sample. Also, much higher loading stiffness of unsaturated sample when compared with saturated sample is predicted well.

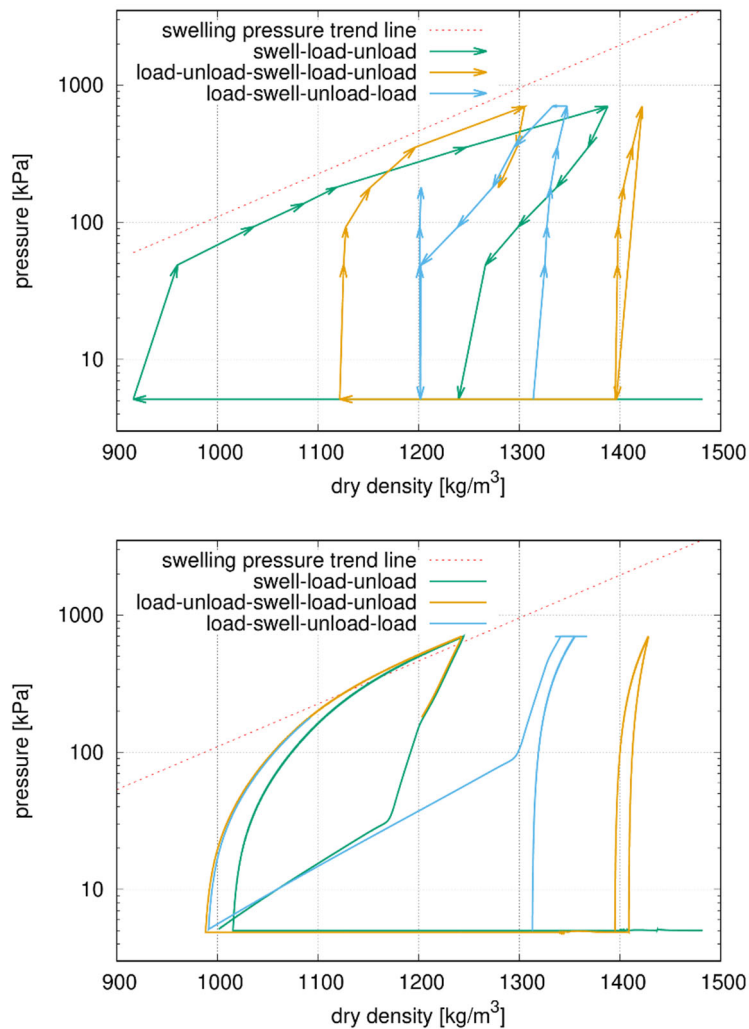


Figure 20: Swelling-loading-unloading oedometric tests at different paths combinations.

The model, in contrast with experiment, predicts high swelling during last phase of unloading. Also, it does not distinguish between swelling potential of pre-loaded and unloaded sample when compared with directly swelled sample. These experimental results were, however, unexpected and more tests would be needed for confirmation of this phenomenon.

Last tests predicted are swelling pressure tests at samples with three different dry densities performed at 20 mm high samples under elevated bottom pore water pressure of approx. 1 MPa with free drainage at the top. The tests have been performed with monitored evolution of pore water pressure with time as water infiltrates the sample. In addition, the experiment at dry density of 1600 kg/m³ has been repeated several times, the sample was dismantled at different times and water content was investigated across the sample length. To predict this test, the experiments must be simulated as boundary value problems using finite element method. The models have been set up within SIFEL finite element code of CTU. Wall friction has not been considered in the simulations.

Time evolution of swelling pressure is shown in in Figure 20. The figure also shows value of swelling pressure as obtained in swelling pressure tests. Consistently with Figure 17, swelling pressures are somewhat underpredicted, for high dry density in particular, but predictions are still considered as satisfactory. The model also overpredicts the initial rate of swelling pressure increase, which may be however caused that constant permeability independent of suction has been used.

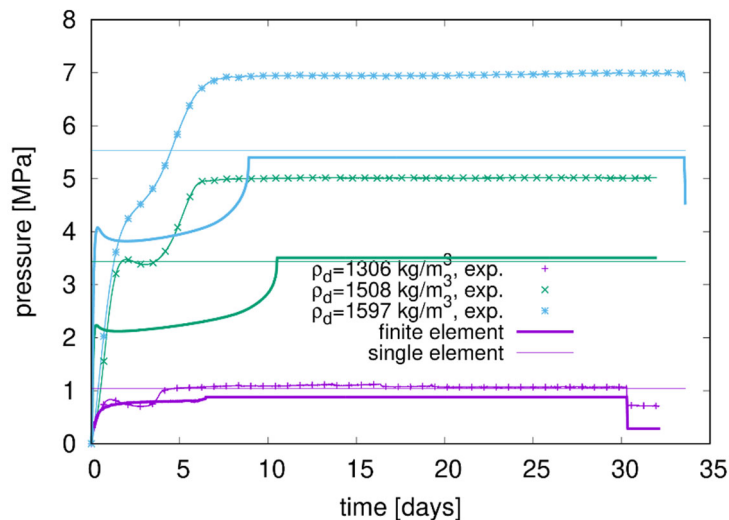


Figure 21: Experimental and predicted evolution of swelling pressures in swelling pressure tests at elevated bottom water pressures of approx. 1 MPa.

The evolution of water content within the sample in several time intervals after the start of the test is shown in Figure 22 for the experiment with dry density of 1597 kN/m³ (the experimental data were obtained on several samples with target dry density of 1600 kN/m³). Water content is overpredicted initially and underpredicted at the end of the test, the trends in water content distribution and evolution is however predicted correctly.

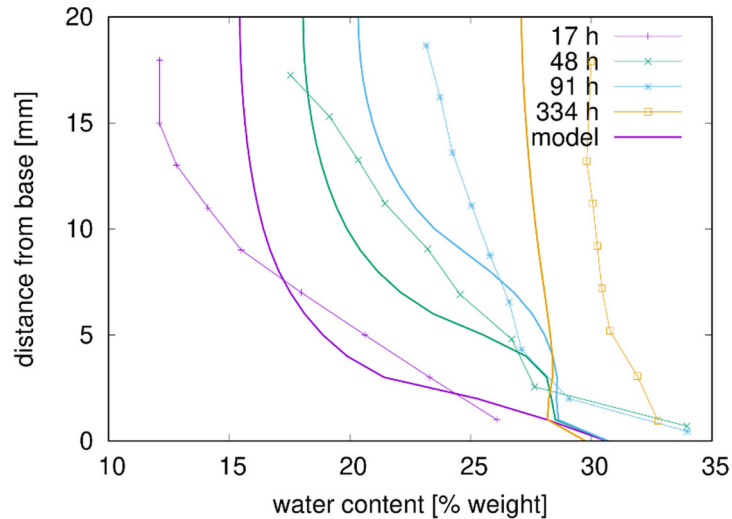


Figure 22: Water content distribution across the sample for several time intervals after the beginning of the test.

It is interesting to point out that water content is not homogeneous across the sample in the time 334, where the sample is practically saturated already. Also, Figure 21 shows that swelling pressures predicted by the finite element model are actually lower than swelling pressures predicted by the single element program. Note that bottom water pressure adds-up to the swelling pressure and the actual swelling pressure corresponds to the pressure predicted at the end of the test, where in two out of three cases pore water pressure was reduced to zero just before the end of the test. Both these observations can be explained with the aid of Figure 23 showing void ratio and degree of saturation distribution for simulations from Figure 22. It is clear that by the time 334 h the sample is fully saturated, however, void ratio is not uniform across the sample which implies non-uniform distribution of water content. The non-uniform distribution of void ratio, which actually originated at the onset of the test and did not change substantially since then (all void ratio curves in Figure 23 practically coincide), implies that the sample is not homogeneous. This means that adopting single element approach to swelling pressure calculation and model calibration, adopted by most of the researchers, is actually not entirely correct.

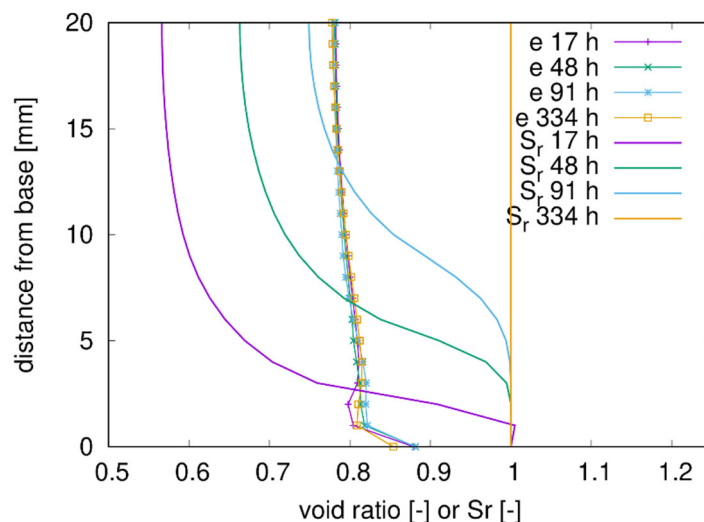


Figure 23: Void ratio and degree of saturation distribution across the sample for several time intervals after the beginning of the test.

To investigate whether the observation described above of non-uniform state within the sample tested for swelling pressures has not been caused by the elevated bottom water pressure of approx. 1 MPa, the simulations have been repeated with a low water pressure of 1 kPa, results of which are in Figure 24. The lowered saturation pressure leads to a slower increase

of swelling pressure (Figure 24 left), while the final swelling pressure is still lower than the one calculated using element test assumption. The distribution of void ratio (Figure 24 right) is practically identical for the two bottom pressures.

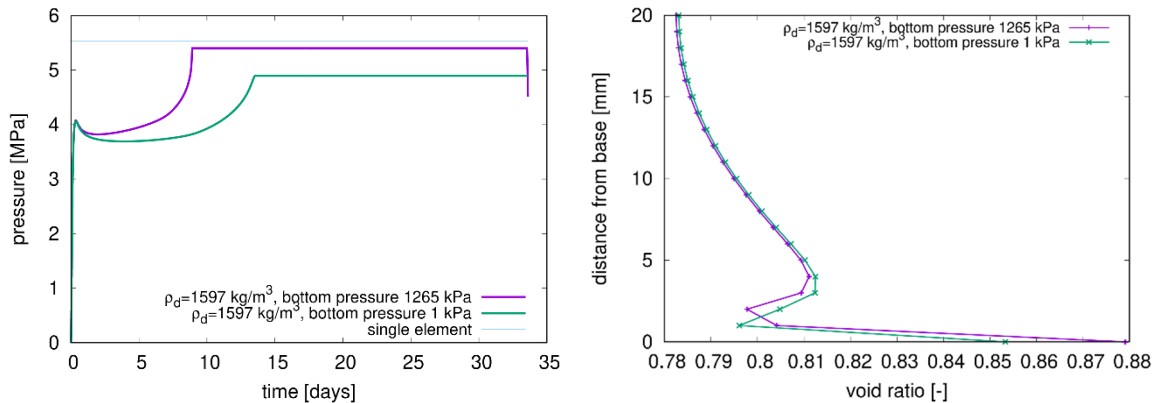


Figure 24: Swelling pressure experiment at a dry density of 1597 kN/m³ from Figure 21 compared with identical experiment with bottom saturation pressure of 1 kPa.

Model parameters adopted in BCV simulations in this section are summarized in Table 6. Simulations have been performed with dry density dependent intrinsic permeability, equal to $3 \times 10^{-20} \text{ m}^2$ for $\rho_d = 1306 \text{ kg/m}^3$, $1 \times 10^{-20} \text{ m}^2$ for $\rho_d = 1508 \text{ kg/m}^3$ and $8 \times 10^{-21} \text{ m}^2$ for $\rho_d = 1597 \text{ kg/m}^3$.

Table 6: Values of the parameters of the THM hypoplastic model for BCV bentonite

Parameter	Unit	Value
φ_c	°	25
λ^*	—	0.12
κ^*	—	0.02
N	—	1.62
v	—	0.24
n_s	—	0.01
l_s	—	0.0
n_T	—	-0.07
l_T	—	0
m	—	10
α_s	1/K	0.00015
κ_m	—	0.1
s_r	kPa	-1000
e_{r0}^m	—	1.0
c_{sh}	—	0.1
s_{e0}	kPa	-2,700
e_0^M	—	0.50
T_r	K	294
a	N/m	0.118
b	N/(mK)	-0.000154
a_e	—	0.75
λ_{p0}	—	1.0

5.2 Modelling of large-scale CRT experiment (task 5.2)

5.2.1 Geometry and discretization

The CU/CTU team constructed a finite-element geometry in SIFEL according to the specifications of the CRT reference case (deliverable D.5.2.1§4.6), i.e. the entire buffer was simulated. Rotational symmetry was assumed, so that the simulation could be carried out in axisymmetric mode. The resulting finite-element mesh had rectangular elements with ~2 cm side and secondary nodes (>5000 nodes, >1500 elements). Four different regions – and material types/characteristics – were used, corresponding to the ring-shaped bentonite blocks, the cylinder-shaped bentonite blocks, the bentonite bricks, and the bentonite pellets loosely installed in the outer gap, between the blocks and the host rock (Figure 25). The prescribed inner gap, between the ring-shaped blocks and the cannister was not considered in the simulation. To simulate the anchors holding the plug on top of the cylinder-shaped blocks, a spring element was introduced with appropriate stiffness, so as to simulate the volume increase of the bentonite during the experiment.

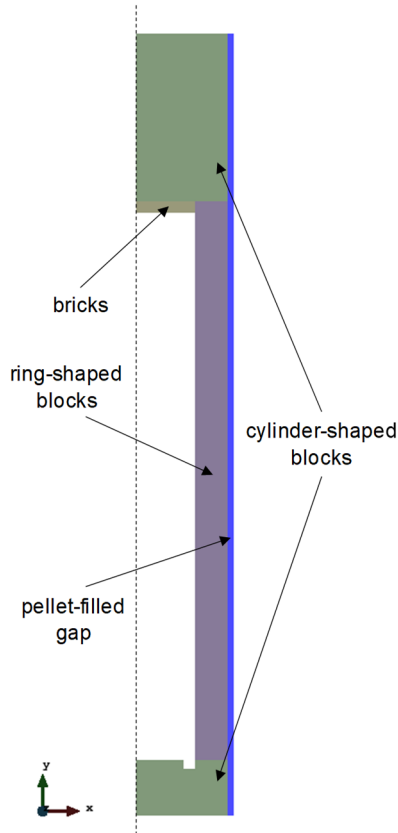


Figure 25: Scheme of the numerical model in SIFEL with indication of the materials. The dashed line indicates the axis of rotational symmetry

5.2.2 Input parameters

The model parameters were calibrated from experimental results relative to the MX-80 bentonite. Experiments on the Czech B75 bentonite were also used, as it was shown that its behaviour is reasonably similar to that of the MX-80 bentonite. The experimental data have been described by Sun et al. (2021). Comparison of experimental data with model predictions is in Figure 26 to Figure 28 Further details on calibration of parameters for which B75 data have not been available (thermal parameters, in particular) can be found in Mašín (2013a) and Mašín (2017).

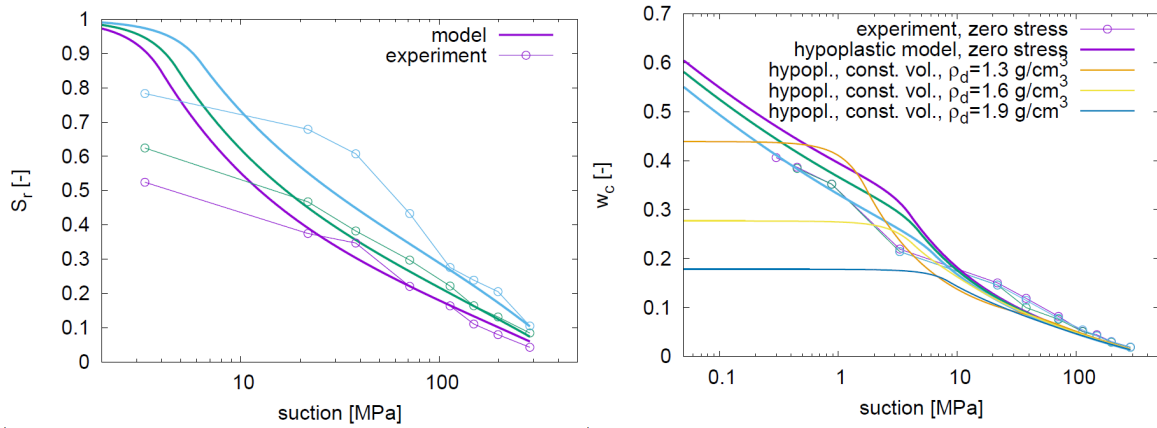


Figure 26: Water retention tests at unconfined conditions at various initial dry densities (1.2, 1.6 and 1.9 kg/m³) in terms of degree of saturation (left) and water content (right). The graphs in terms of water content are also simulated with the model under constant volume conditions (experimental data are not available).

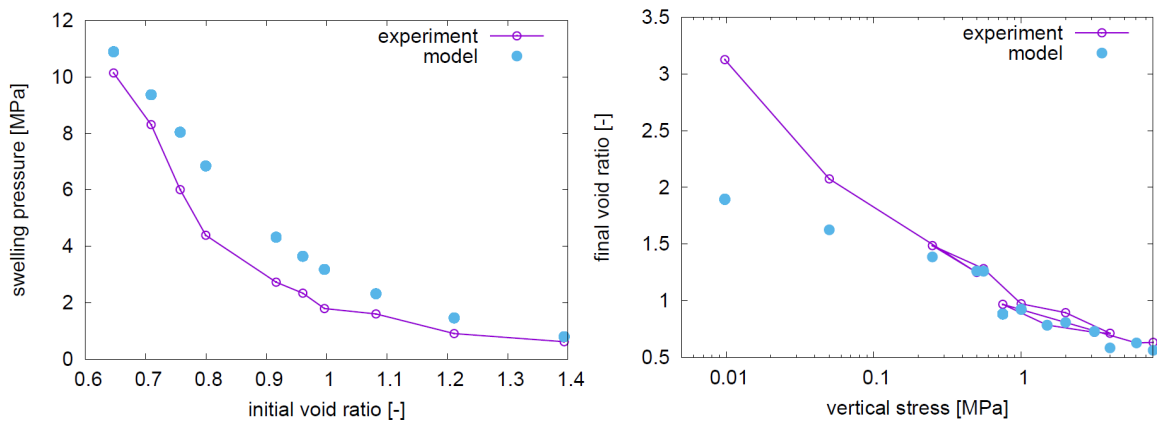


Figure 27: Predictions of swelling pressures (left) and swelling strain under constant load (right) tests.

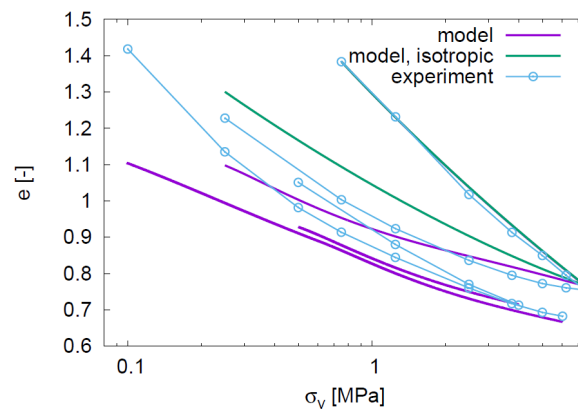


Figure 28: Predictions of oedometric loading and unloading tests. Model predictions also repeated for isotropic conditions (corresponding data not available).

The calibration of most of the THM hypoplastic model parameters was performed using the element test driver TRIAX. Reasonable values of φ_c and ν were assumed, and the reference values s_r , e_0^m , and T_r were chosen to be in the range relevant to the experiments. In fact, these values can be selected arbitrarily, together with e_{r0}^m , which can be adjusted to optimise the water retention behaviour. The parameter κ_m was chosen so as the swelling behaviour could be predicted. The results of isotropic compression tests were used to calibrate the parameters

of the basic hypoplastic model λ^* and κ^* ; then, N , n_s , n_T , and l_T were corrected to predict the INCL correctly, as well as of heating-induced volume changes. The parameter α_s was calibrated from heating tests under high suction, while s_{e0} and a_e , having little effect on the behaviour under high suction, were simply assumed. The values of a and b also were assumed under the simplification that the effect of T on water retention capacity is caused only by changes of surface tension of water.

The values of the single-element parameters (hypoplastic model parameters) used in the CRT simulation are reported in Table 7. As for the macroscopic parameters (finite-element model parameters), these are reported in Table 8. A Lewis and Schrefler's model with mechanical coupling (simplified two-phase transport, i.e. neglecting transport through gas) was adopted in the simulations.

Table 7: Values of the parameters of the THM hypoplastic model for the bentonite used in CRT simulations

Parameter	Unit	Value
φ_c	°	25
λ^*	–	0.130
κ^*	–	0.060
N	–	1.73
ν	–	0.25
n_s	–	0.012
l_s	–	-0.0050
n_T	–	-0.07
l_T	–	0
m	–	1
α_s	1/K	0.00015
κ_m	–	0.07
s_r	kPa	-2,000
e_{r0}^m	–	0.45
c_{sh}	–	0.002
s_{e0}	kPa	-2,700
e_0^M	–	0.50
T_r	K	294
a	N/m	0.118
b	N/(mK)	-0.000154
a_e	–	1.00
λ_{p0}	–	0.7

Table 8: Values of the parameters of the finite-element model for the bentonite

Parameter	Unit	Value
compressible grains		yes
Biot's constant	–	1
E_{solid}	MPa	2.2
n_0	–	0.36–0.49*
$k_{intr,0}$	m ²	2·10 ⁻¹⁹ **
$\beta_{s,0}$	1/K	10 ⁻⁷
$\rho_{s,0}$	kg m ⁻³	1000-1700*
$c_{p,s,0}$	J/(kg K)	830
λ_{dry}	W/(m K)	0.4
λ_{wet}	W/(m K)	1.3
$S_{r,dry}$	–	0.01
$S_{r,wet}$	–	1

* according to the specifications. ** the permeability of the pellet-filled gap was assumed to be 10 times this value

5.2.3 Initial and boundary conditions

The initial conditions were assigned to the model according to the specifications that were provided, as reported in Table 9. The only adjustment that had to be made concerned the porosity of the pellet-filled gap. In fact, while the pellets themselves were made of well-compacted bentonite, they were installed in the gap loosely, resulting in an overall very low dry density and hence high porosity. The model does not feature a third level of structure to account for the pellets-macropore structure; instead, an equivalent double-structure homogeneous material is considered. The chosen value of porosity ($n = 0.49$) was found through preliminary testing to be the maximum allowed by the THM hypoplastic model to run successfully, as for higher values the state surpasses normal compression line defined by parameters from Table 7. Obviously, this introduced some differences compared to the experiments, as the dry mass of the pellets is overestimated, with resulting overestimation of the possible swelling of the layer.

Table 9: Initial conditions

Region	Type of process		
	Thermal	Hydraulic	Mechanical
Cylinder-shaped bentonite blocks	$T = 20\text{ °C}$	$S_r = 0.751$	$\sigma = 0\text{ MPa}, n = 0.39$
Ring-shaped bentonite blocks	$T = 20\text{ °C}$	$S_r = 0.859$	$\sigma = 0\text{ MPa}, n = 0.36$
Pellet-filled gap	$T = 20\text{ °C}$	$S_r = 0.895$	$\sigma = 0\text{ MPa}, n = 0.49^*$
Bentonite bricks	$T = 20\text{ °C}$	$S_r = 0.637$	$\sigma = 0\text{ MPa}, n = 0.42$

* the value in the specifications was $n = 0.64$, but it could not be used in the model.

As for the boundary conditions, the water pressure protocol, provided in the specifications, was used as the hydraulic boundary condition (Table 10), while the heater power protocol was not used as the thermal boundary condition. Instead, experimental values of some of the temperature sensors were used to set the thermal boundaries at the interfaces with the canister and with the host rock (Table 10). This solution was preferred as it was simpler to implement than by setting an energy flux.

Table 10: Hydraulic boundary condition assigned to the outer boundary (pellet-filled gap)

Day	Water pressure (MPa)	Comment
0	0	
679	0	Gradual increase of pressure
714	0.8	Final value after the increase
770	0.1	
805	0.4	
819	0.8	
1598	0	
1877	0	Air flushed (end of simulation)

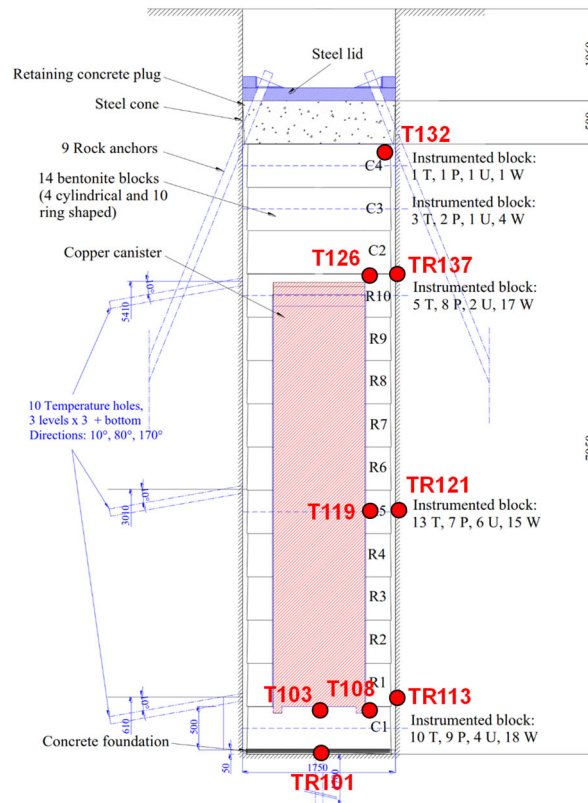


Figure 29: Locations of the temperature sensors used to set the thermal boundary conditions

5.2.4 Results/discussion

In general, the numerical simulation was running smooth, with only some adjustments in the solver parameters to ensure better and faster convergence of the iterative processes. A time step up to 1 day could be used, ensuring completion of the 1877 days-long simulation in 12-24 hours on a 12-core desktop computer. Some challenges were brought by the spring element simulating the anchors, which in some cases caused numerical convergence issues. However, it was found that the value of the stiffness and hence the swelling allowed could be changed in a reasonable range without causing significant changes in the results, but at the same time improving the numerical performance significantly.

Some key results are reported in the charts below (Figure 30, Figure 31, Figure 32), where trends of simulated values are compared with experimentally measured quantities (swelling pressure, suction, temperature) at various locations within the modelled domain. In addition, the evolution of degree of saturation and dry density at various locations, as well as water content and dry density profiles in selected cross sections are shown (Figure 33, Figure 34). In Figure 35, the vertical displacement at the top is also shown.

The results of the simulation are generally in good agreement with the experimentally measured quantities. The trend of swelling pressure development (Figure 30) is well captured, both in terms of temporal evolution (shape of the curve over time) and absolute values. This suggests that the swelling parameters of the bentonite, as well as the hydraulic conductivity were calibrated reasonably well. Nonetheless, the sensors in the experiment seem to have been much more responsive to changes in the hydraulic and thermal boundaries than the numerical simulation, where these signals are almost completely damped at the monitored locations, resulting in rather smooth curves. With reference to the results in R5 (2.75 m above the bottom of the domain, i.e. at mid-height of the canister), it can also be seen that, while the simulation provides similar values of swelling pressure along the cross section at the end of the experiment (~4.5 MPa), the experimentally measured values decrease significantly from the inner to the outer boundary. This suggest that the thermal (inner) boundary exerted a

stronger control than the hydraulic (outer) boundary on the development of swelling pressures, whereas the numerical model shows more or less equal importance of the two boundaries.

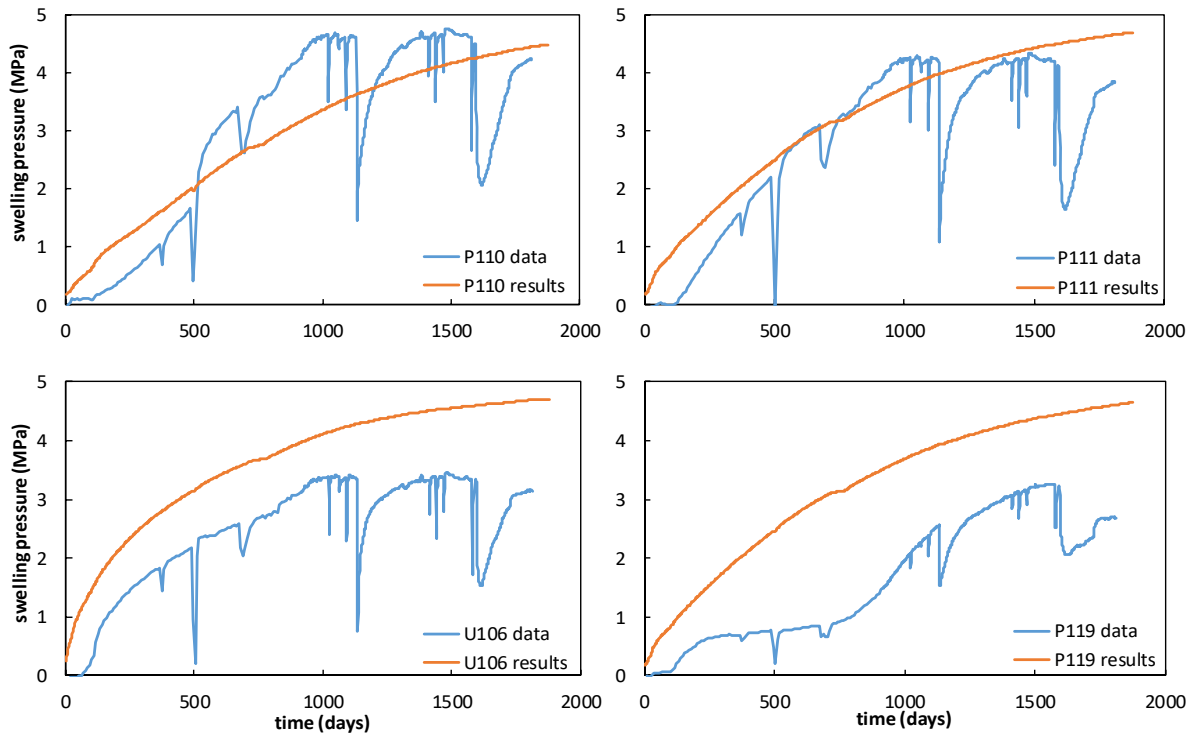


Figure 30: Simulated (results) and experimental (data) values of swelling pressure at four locations in the simulated domain. The sensors P110, P111, and U106 were located in the ring-shaped bentonite block n.5 (R5), at 2.75 m of height from the bottom of the domain, at radii 0.585, 0.685, and 0.785 m, respectively; P119 was located in the ring-shaped bentonite block n.10 (R10), at 5.25 m of height from the bottom of the domain, at 0.685 m radius.

As for the trend of suction (Figure 31), the model captures it reasonably, albeit with a general overestimation of the values. Possibly, the actual air-entry value of the used bentonite was lower than that considered in the simulations (2.7 MPa), or the hydraulic conductivity was somewhat underestimated. It is worth noting, however, that improving the fit with the suction measurements through fine-tuning of the calibrated parameters would have probably resulted in a worse fit with the swelling pressures (Figure 30).

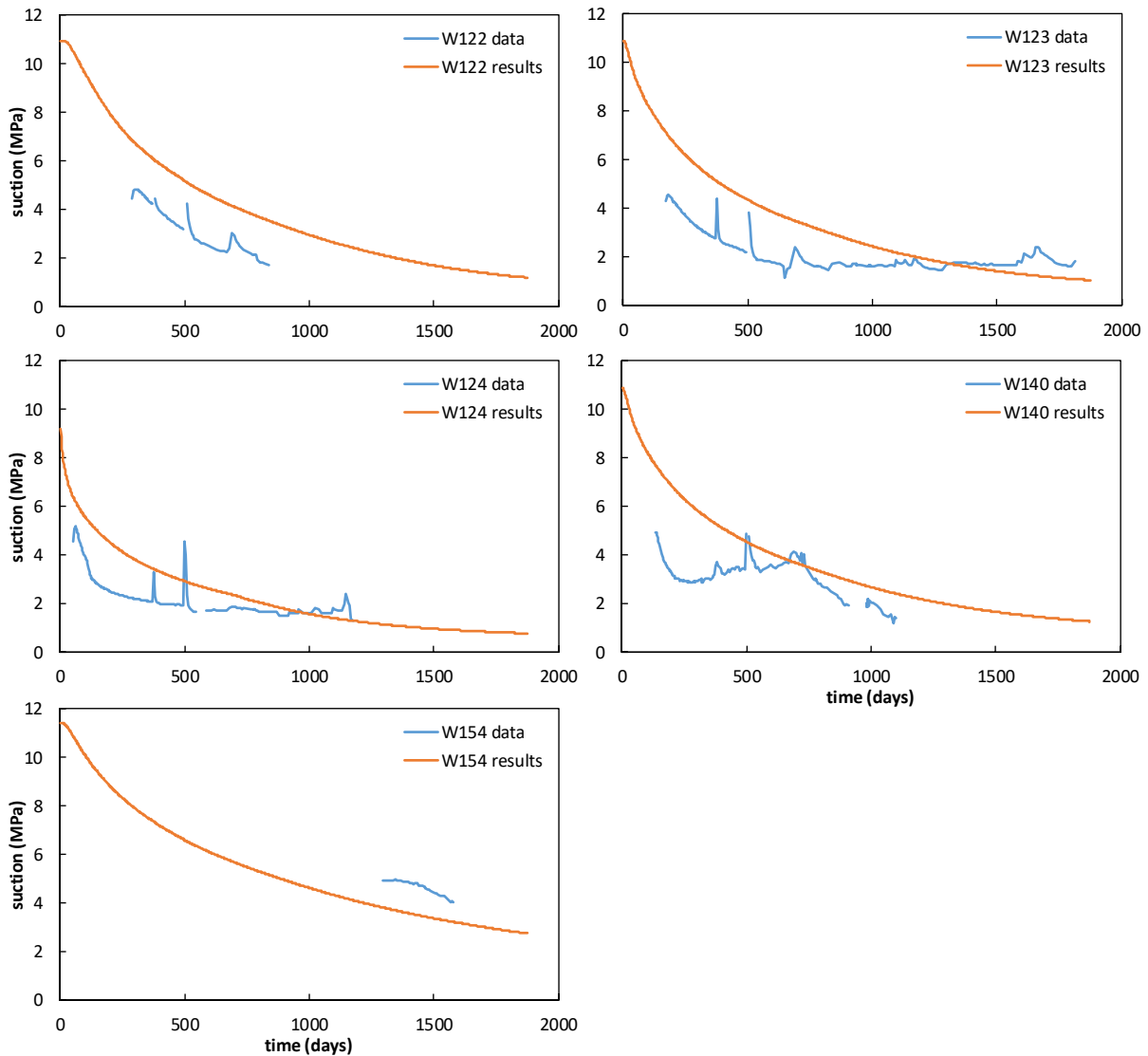


Figure 31: Simulated (results) and experimental (data) values of suction at five locations in the simulated domain. The sensors W122, W123, and W124 were located in the ring-shaped bentonite block n.5 (R5), at 2.75 m of height from the bottom of the domain, at radii 0.585, 0.685, and 0.785 m, respectively; W140 was located in the ring-shaped bentonite block n.10 (R10), at 5.25 m of height from the bottom of the domain, at 0.685 m radius; W154 was located in the cylinder-shaped bentonite block n.3 (C3), at 6.25 m of height from the bottom of the domain, at 0.585 m radius.

In Figure 32, the simulated and measured trends of temperature are compared. The fit is generally very good, which is an expected result since the thermal boundary was assigned in terms of temperatures at the boundaries rather than as an energy flux. Nonetheless, it can be seen from the figure that the model underestimated the temperatures by some degrees in C3, above the cannister, close to the outer boundary.

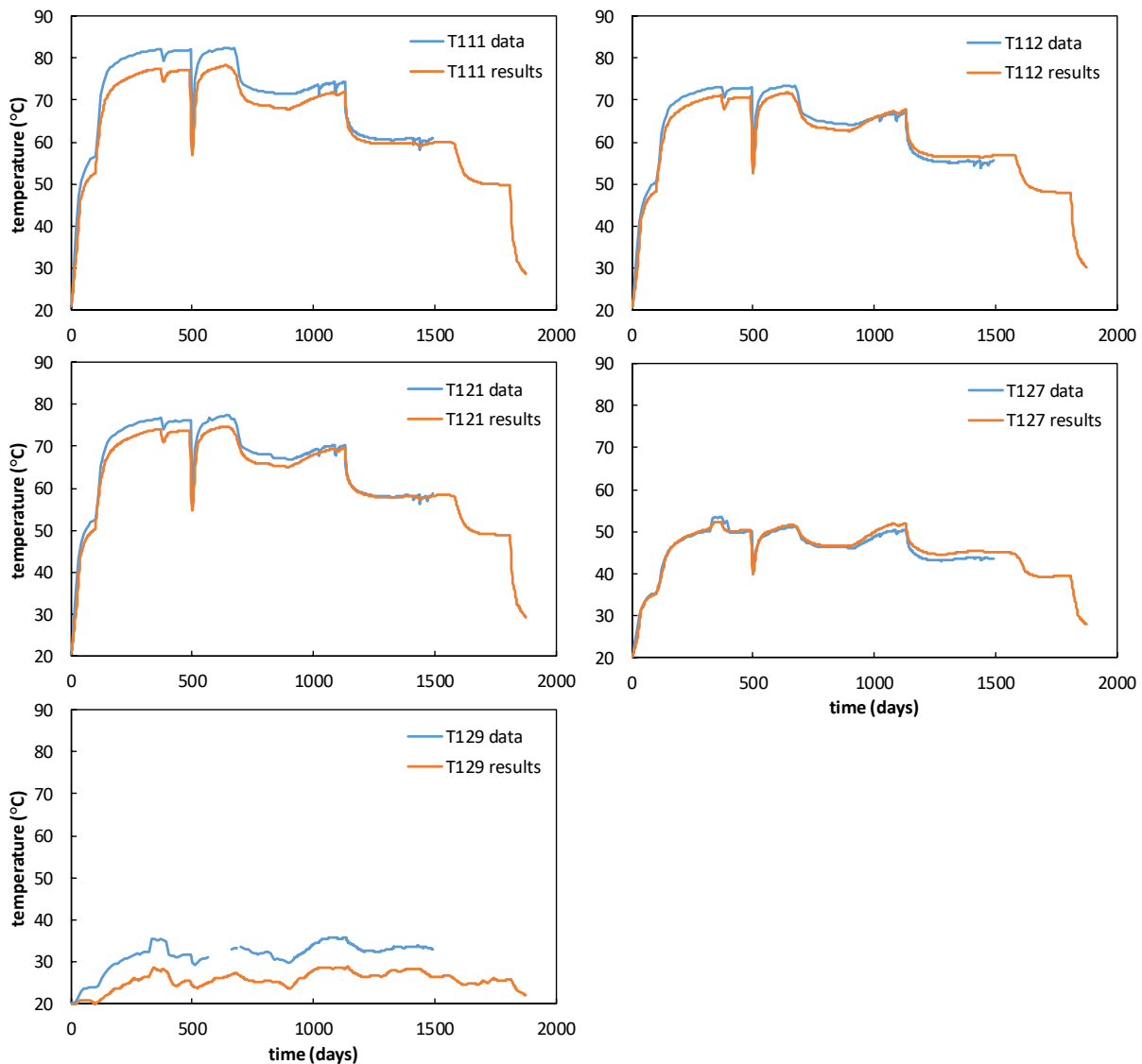


Figure 32: Simulated (results) and experimental (data) values of temperature at five locations in the simulated domain. The sensors T111, T112, and T121 were located in the ring-shaped bentonite block n.5 (R5), at 2.75 m of height from the bottom of the domain, at radii 0.635, 0.735, and 0.685 m, respectively; T127 was located in the ring-shaped bentonite block n.10 (R10), at 5.25 m of height from the bottom of the domain, at 0.685 m radius; T129 was located in the cylinder-shaped bentonite block n.3 (C3), at 6.25 m of height from the bottom of the domain, at 0.785 m radius.

The plots in Figure 33 and Figure 34 show the temporal evolution of degree of saturation, water content, and dry density in some well-instrumented cross sections (i.e. R5, R10, and C3). It can be seen clearly (Figure 33) how the saturation of the bentonite proceeded from the outer boundary towards the centre. It can also be noticed that the dry density generally decreased over time, consistently with the slight volume increase of the domain (at the expenses of a compression of the pellet-filled layer and a slight swelling of the top cap). However, in the innermost regions the dry density increased at first, as an effect of the compression caused by the expansion of the outer regions, and began to decrease only in a later stage.

The model does not show much homogenization of the bentonite (Figure 34). While most of the domain reaches saturation or near-saturation by the end of the simulation, the dry density crystallises during the last year of simulation (note the small differences between the values at 1400 days and those at 1877 days) while significant gradients are still present. The case of section C3 is rather emblematic, as it shows that the differences in dry density along the section

remained almost unchanged throughout the simulation. In this respect, the model underestimates the homogenization which, even though it was incomplete, it did take place in a more significant way in the actual experiment.

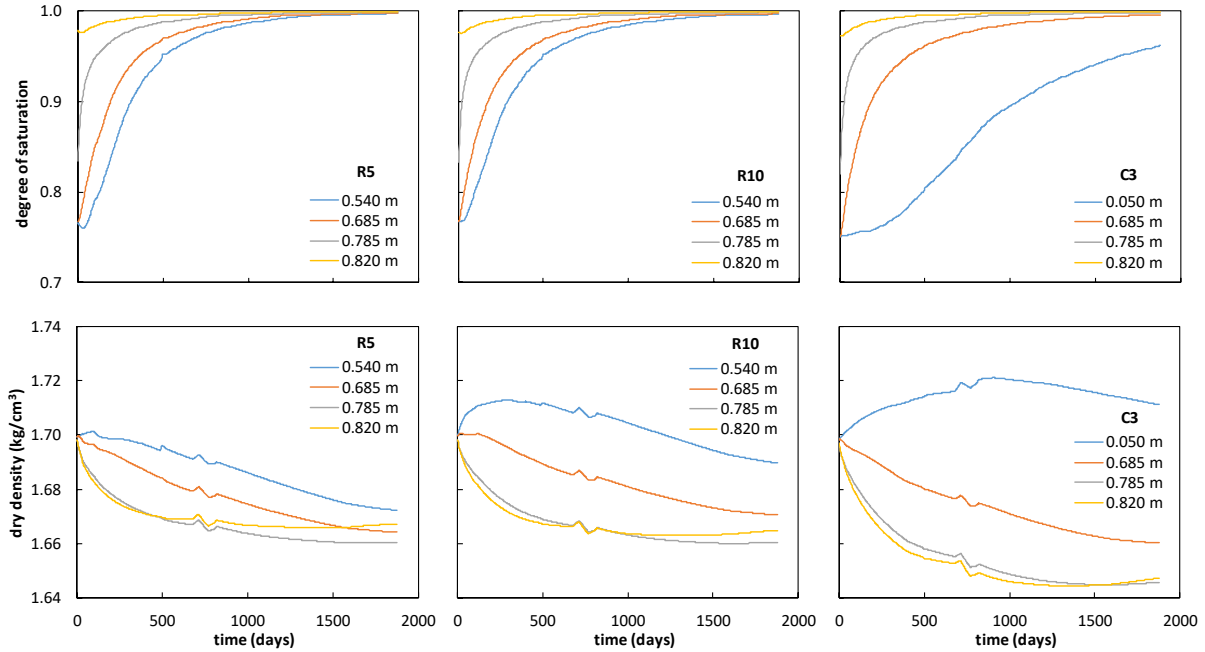


Figure 33: Simulated values of degree of saturation (top) and dry density (bottom) over time in three sections of the experimental domain (R5 – 2.75 m, R10 – 5.25 m, C3 – 6.25 m from the bottom) at various radial distances from the centre.

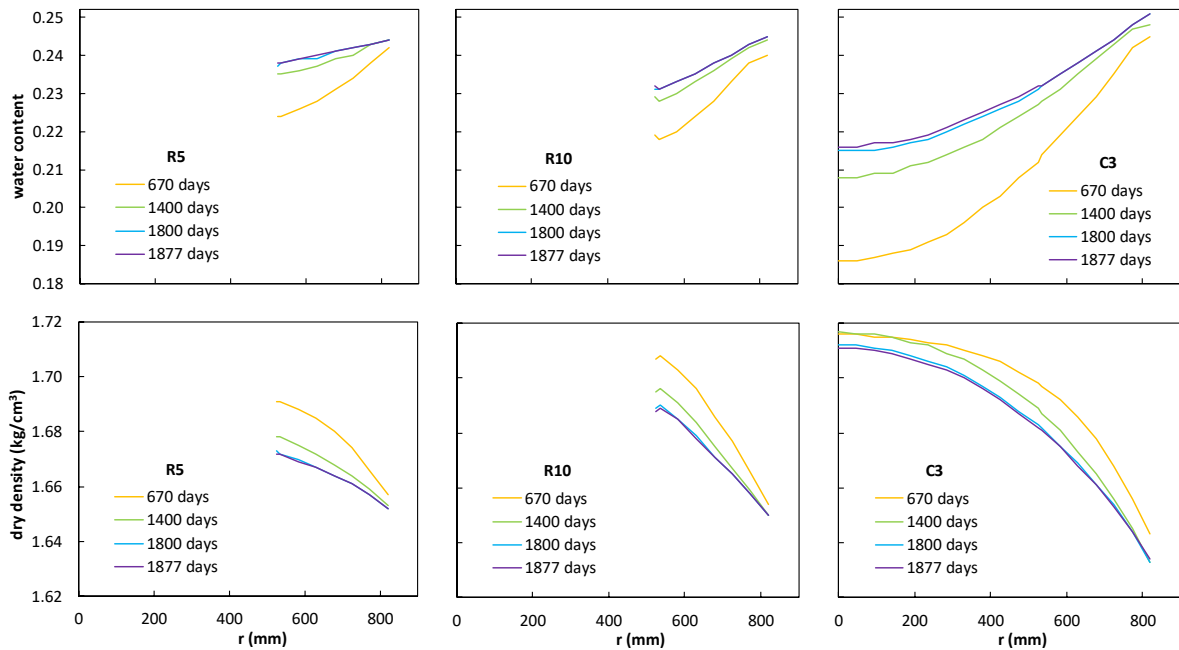


Figure 34: Simulated values of water content (top) and dry density (bottom) across three sections of the experimental domain (R5 – 2.75 m, R10 – 5.25 m, C3 – 6.25 m from the bottom) at various times during the simulation.

Concerning the vertical displacement recorded at the top of the domain, in response to the finite value of stiffness of the anchors, the result of the simulation shown in Figure 35 can be considered acceptable. However, while the magnitude of the displacement is well captured, the same cannot be said for the trend, which appears more regular in the experiments than in

the simulation. The latter, in fact, shows a faster progression of the displacements initially, followed by a very slow increase. In the model, a linear spring was used; the linearity of the behaviour of the actual anchors was demonstrated by plotting the displacements together with the recorded forces. Therefore, the different trend observed in the simulation compared with the experiment must be attributed the behaviour of the bentonite (possibly to the insufficient homogenization achieved during saturation), or to simplifications (higher initial dry density of the pellet-filled gap, resulting in somewhat higher initial stiffness of the domain; absence of the inner gap between the cannister and the bentonite blocks).

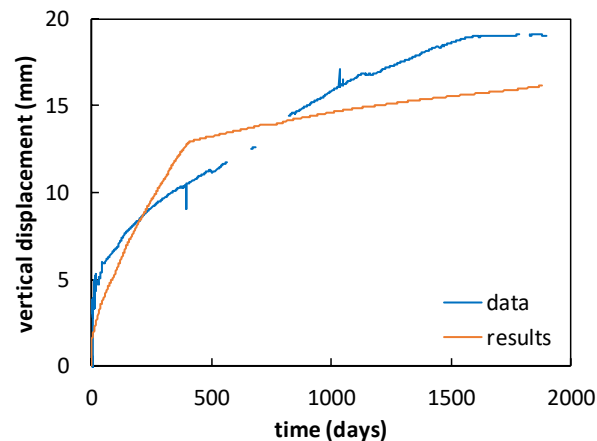


Figure 35: Vertical displacement at the top of the domain due to the finite value of stiffness of the anchors: experimental data vs. numerical simulation results.

In order to obtain some insight into the sensitivity of the numerical model to some of the parameters, additional simulations were carried out. In particular, it was decided to explore three values of air-entry value (s_{e0} parameter in the hypoplastic models), i.e. 1, 2.7, and 6 MPa. The intrinsic permeability of the bentonite blocks and bricks was changed in the range $0.5-10 \cdot 10^{-19} \text{ m}^2$, keeping a ratio of 10 between the (equivalent) permeability of the pellet-filled gap and that of the blocks. The stiffness of the anchors also was changed, as it was found that it can affect the convergence and success of the simulation even though it does not affect the results in terms of swelling pressures and suctions significantly. Most of the successful simulations were obtained using comparatively high values of stiffness, corresponding to very little swelling of the top cap. On the other hand, more realistic values, providing values of swelling in line with the experimental result, often resulted in numerical issues, that are being addressed in current work. An overview of all the simulations that were conducted is provided in Figure 36, which shows all the successful simulations (100% on the horizontal axis), as well as all the simulations that were interrupted at some point due to numerical issues.

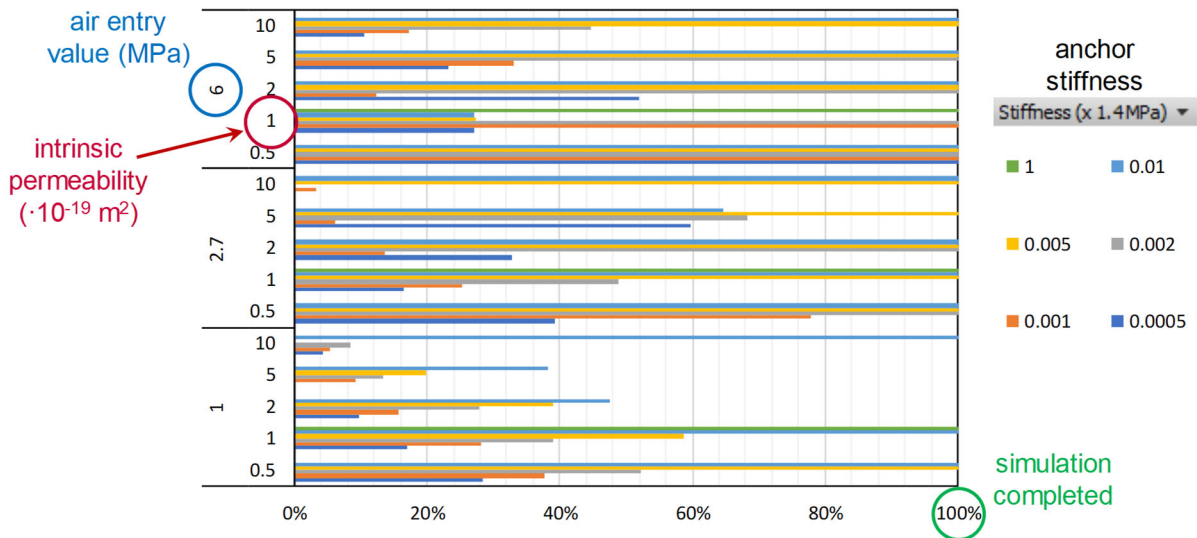


Figure 36: Sensitivity analyses – completed and unsuccessful simulations according to the choice of parameters.

For a quantitative comparison of the results of the various simulations, the normalised mean error (NME) and the normalised root mean square error (NRMSE) were used as the error metrics because of their simplicity:

$$NME = \frac{\frac{1}{n} \sum_i^n (S_i - E_i)}{\frac{1}{n} \sum_i^n E_i}; \quad NRMSE = \frac{\sqrt{\frac{1}{n} \sum_i^n (S_i - E_i)^2}}{\frac{1}{n} \sum_i^n E_i}$$

where S_i and E_i represent simulated and experimental values at corresponding times (i), respectively, and n is the number of experimental observations that were considered.

These error metrics were computed in relation to data series of 9 sensors: 4 swelling pressure sensors (P110, P111, U106, P119) and 5 suction sensors (W122, W123, W124, W140, W154). To obtain comprehensive metrics, the data series were combined assigning weights corresponding to their degree of completeness. For instance, if a sensor was functional during 75% of the experiment, a weight of 0.75 was assigned to the data series.

In Figure 37, groups of vertical bars indicate successful simulations performed with the same set of parameters except for the stiffness of the anchors, which is confirmed to not play a significant role in the investigated range. On the other hand, the figure shows that the trends of NRMSE are not monotonic with respect the intrinsic permeability, while they are less affected by the choice of air-entry value. By looking at the results in terms of NRMSE and NME comprehensively, it is possible to identify some sets of parameters that provide the best performance (smaller square error, smaller over/underestimation). It is clear, however, that there is not a unique set of parameters that optimises the simulation results both in terms of suctions and swelling pressures, and a trade-off is therefore necessary. This is the reason why, earlier in this section, the simulation with air-entry value of 2.7 MPa and intrinsic permeability of $2 \cdot 10^{-19} \text{ m}^2$ was chosen as the representative one, even though it provides some overestimation of suctions and, in smaller proportion, also of swelling pressures. By choosing a smaller value of permeability, for instance, the error in terms of swelling pressures would have been minimised, but at the expenses of a much larger overestimation of suctions.

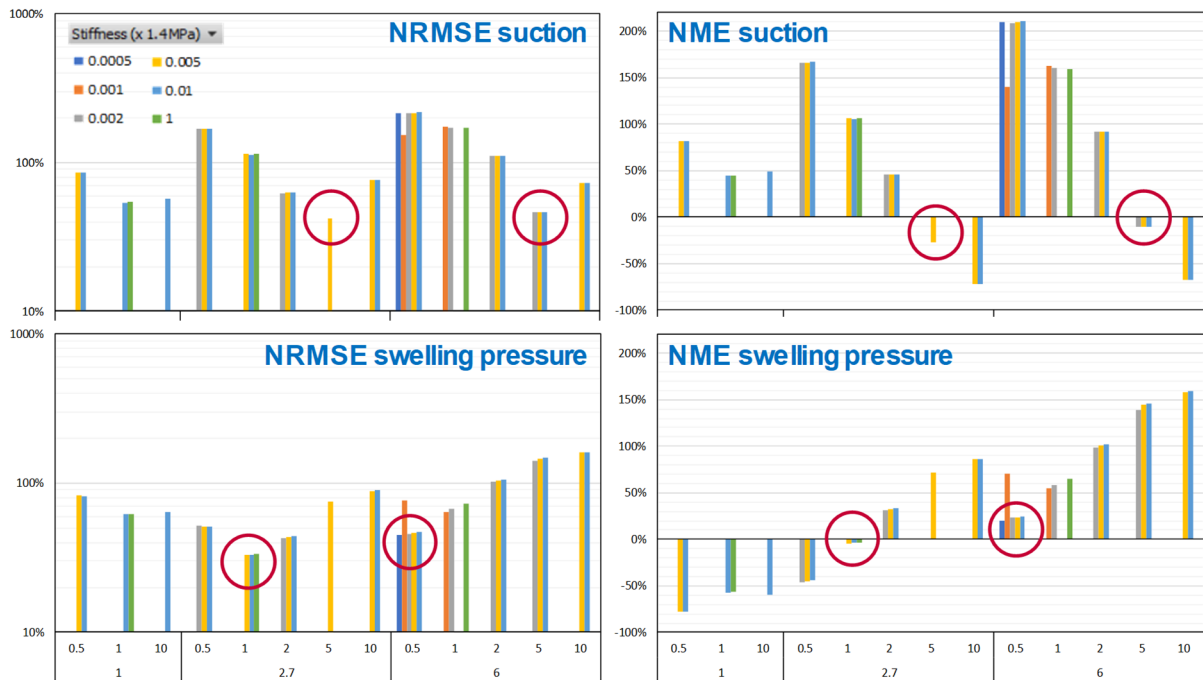


Figure 37: Normalised root mean square error (NRMSE) and normalised mean error (NME) relative to experimental data from suction and swelling pressure sensors for all successful simulations (100% completed, cf. Figure 36) as a function of the chosen air-entry value of suction (1, 2.7, 6 MPa), intrinsic permeability ($0.5\text{--}10 \cdot 10^{-19}$ m²), and anchor stiffness ($0.0005\text{--}1 \cdot 1.4$ MPa). Red circles indicate the simulation or group of simulations with the lowest NRMSE or NME values.

6 Concluding remarks

This report described the THM hypoplastic model for bentonite, which has been within BEACON project further developed and thoroughly evaluated. Most of the developments were focused on numerical aspects of the model, though some developments were also done on the constitutive model level. The model has been evaluated using experimental data on Task 3.3, where satisfactory predictions were obtained.

As the critical task for the Czech partners, the model has been calibrated and evaluated using comprehensive experimental dataset on BCV bentonite. In general, very good predictions of the model for various stress paths and states have been demonstrated. For example, the model predicted correctly the difference in results of swelling pressure and swelling under constant load tests, which could be interpreted through investigation of the model state quantities. Also, the model was successful in predicting complex oedometric swelling-loading-unloading tests with different stress path combinations. Still, some shortcomings have been identified, such as unpretended path dependency of microstructural deformations. Also, adopting macrostructural degree of saturation as a means to predict high strength of compacted bentonite at low water contents appear to be questionable. These observations can be reinspected in future model versions. In our opinion, the BCV dataset through its comprehensiveness can form an interesting benchmark for bentonite model evaluation also for other teams.

Finally, model evaluation through predictions of large-scale CRT test have been presented. The model lead to good representation of the experiment in terms of temperatures, displacements, swelling pressures and suctions. It is to be pointed out that the model has not been specifically calibrated to fit the response of bentonite used in the test, an alternative parameter set obtained through calibration using B75 bentonite, having similar behaviour to the adopted MX80 bentonite, have been used. Further improvement of predictions could thus be expected during fine-tuning of the model parameters. It has also been demonstrated that regardless significant progress of the numerical model implementation and computational stability, the simulations cannot be run for arbitrary combination of the finite element and constitutive model parameters, simulations ending up in divergence in some cases. Future developments are thus still needed to improve model robustness.

References

- Brooks, R., Corey, A., 1964.** Hydraulic properties of porous media. Hydrology paper no. 3. Colorado State University.
- Mašín, D., 2013.** Double structure hydromechanical coupling formalism and a model for unsaturated expansive clays. *Engineering Geology* 165, 73-88.
- Mašín, D., 2017.** Coupled thermohydromechanical double structure model for expansive soils. *ASCE Journal of Engineering Mechanics* 143, No. 9.
- Mašín, D., and Khalili, N., 2016.** Swelling phenomena and effective stress in compacted expansive clays. *Can. Geotech. J.*, 53(1), 134–147.
- Romero, E., G. Della Vecchia, and C. Jommi, 2011.** An insight into the water retention properties of compacted clayey soils. *Géotechnique* 61(4), 313–328.
- Seiphoori, A., Ferrari, A. and Laloui, L., 2014.** Water retention behaviour and microstructural evolution of MX-80 bentonite during wetting and drying cycles. *Géotechnique*, 64(9), pp.721-734.
- Sun, H., Mašín, D., Najser, J., Neděla, V. and Navrátilová, E., 2019.** Bentonite microstructure and saturation evolution in wetting-drying cycles evaluated using ESEM, MIP and WRC measurements. *Géotechnique* 69, No. 8, 713-726
- Sun, H., Scaringi, G., Mašín, D. and Najser, J., 2021.** An experimental investigation on the swelling behavior of compacted B75 bentonite (under review)
- Wong, K. S. and Mašín, D., 2014.** Coupled hydro-mechanical model for partially saturated soils predicting small strain stiffness. *Computers and Geotechnics* 61, 355-369.

Appendix 1

Complete mathematical formulation of the THM hypoplastic model, as has been published in Mašín (2017), it thus describes the original hypoplastic model before BEACON development.

The mathematical formulation of the proposed model for expansive soils is summarized in the following. The behavior of two structural levels is linked through

$$\dot{\epsilon} = \dot{\epsilon}^M + f_m \dot{\epsilon}^m \quad (30)$$

with the following void ratio measures and their relationships:

$$\begin{aligned} \frac{\dot{\epsilon}}{1+e} &= \text{tr} \dot{\epsilon} \\ \frac{\dot{\epsilon}^M}{1+e^M} &= \text{tr}[\dot{\epsilon}^M + (f_m - 1)\dot{\epsilon}^m] \\ \frac{\dot{\epsilon}^m}{1+e^m} &= \text{tr} \dot{\epsilon}^m \end{aligned} \quad (31)$$

$$e = e^M + e^m + e^M e^m \quad (32)$$

$$S_r = S_r^M + \frac{e^m}{e} (S_r^m - S_r^M) \quad (33)$$

The mechanical behavior of the macrostructure is governed by

$$\overset{\circ}{\sigma}^M = f_s (\mathcal{L} : \dot{\epsilon}^M + f_d \mathbf{N} \|\dot{\epsilon}^M\|) + f_u (\mathbf{H}_s + \mathbf{H}_T) \quad (34)$$

where $\overset{\circ}{\sigma}^M$ = macrostructural effective stress defined by

$$\overset{\circ}{\sigma}^M = \overset{\circ}{\sigma}^{\text{net}} - \chi^M s \mathbf{1} \quad (35)$$

The macrostructural effective stress parameter χ^M coincides with the macrostructural degree of saturation S_r^M :

$$S_r^M = \chi^M = \begin{cases} 1 & \text{for } s < s_e \\ \left(\frac{s_e}{s}\right)^\gamma & \text{for } s \geq s_e \end{cases} \quad (36)$$

where

$$s_e = s_{en} (a_e + a_{\text{scan}} - a_e a_{\text{scan}}) \quad (37)$$

with parameter a_e and state variable a_{scan} defined as

$$a_{\text{scan}} = \frac{s - s_W}{s_D - s_W} \quad (38)$$

where s_D = suction at the main drying curve; and s_W at the main wetting curve = current S_r^M .

It follows that

$$s_D = \frac{s_{en}}{s_e} s \quad (39)$$

with

$$s_{en} = s_{e0} \frac{e_0^M}{e^M} \left(\frac{a + bT}{a + bT_r} \right) \quad (40)$$

where a , b , and T_r = parameters.

The rate equation for a_{scan} reads for $s > a_e s_{en}$

$$\dot{a}_{\text{scan}} = \frac{1 - r_\lambda}{s_D(1 - a_e)} \dot{s} \quad (41)$$

Here r_λ is defined as

$$r_\lambda = \begin{cases} 1 & \text{for } s = s_D \text{ and } \dot{s} > 0 \\ 1 & \text{for } s = a_e s_D \text{ and } \dot{s} < 0 \\ \frac{\gamma_{\text{scan}}}{\gamma} & \text{otherwise} \end{cases} \quad (42)$$

where $\gamma = 0.55$ and $\gamma_{\text{scan}} = \gamma/10$ = slopes of the main wetting-drying and scanning curves respectively. If $s \leq a_e s_{en}$, then $a_{\text{scan}} = 0$. The macrostructural effective stress rate from Eq. (34) is given by

$$\dot{\boldsymbol{\sigma}}^M = \dot{\boldsymbol{\sigma}}^{\text{net}} + \mathbf{1}\chi^M \left[(1 - r_\lambda \gamma) \dot{s} - \gamma s \frac{\dot{e}^M}{e^M} + \frac{\gamma s b \dot{T}}{a + bT} \right] \quad (43)$$

with \dot{e}^M calculated using Eq. (31). The hypoplastic tensor \mathcal{L} , which assumes transversely isotropic material (Mašín 2014), is calculated from

$$\mathcal{L} = \frac{1}{2} a_1 \mathbf{1}\mathbf{1} + a_2 \mathbf{1} \otimes \mathbf{1} + a_3 (\mathbf{p} \otimes \mathbf{1} + \mathbf{1} \otimes \mathbf{p}) + a_4 \mathbf{p}\mathbf{1} + a_5 \mathbf{p} \otimes \mathbf{p} \quad (44)$$

where $\mathbf{p} = p_{ij} = n_i n_j$, with n_i a unit vector normal to the plane of symmetry $\mathbf{X}\mathbf{Y} = 1/2(X_{ik}Y_{jl} + X_{il}Y_{jk} + X_{jl}Y_{ik} + X_{jk}Y_{il})$

$$a_1 = \alpha_E \left(1 - \nu_{pp} - 2 \frac{\alpha_E}{\alpha_\nu^2} \nu_{pp}^2 \right) \quad (45)$$

$$a_2 = \alpha_E \nu_{pp} \left(1 + \frac{\alpha_E}{\alpha_\nu^2} \nu_{pp} \right) \quad (46)$$

$$a_3 = \alpha_E \nu_{pp} \left(\frac{1}{\alpha_\nu} + \frac{\nu_{pp}}{\alpha_\nu} - 1 - \frac{\alpha_E}{\alpha_\nu^2} \nu_{pp} \right) \quad (47)$$

$$a_4 = \alpha_E \left(1 - \nu_{pp} - 2 \frac{\alpha_E}{\alpha_\nu^2} \nu_{pp}^2 \right) \frac{1 - \alpha_G}{\alpha_G} \quad (48)$$

$$a_5 = \alpha_E \left(1 - \frac{\alpha_E}{\alpha_\nu^2} \nu_{pp}^2 \right) + 1 - \nu_{pp}^2 - 2 \frac{\alpha_E}{\alpha_\nu} \nu_{pp} (1 + \nu_{pp}) - \frac{2\alpha_E}{\alpha_G} \left(1 - \nu_{pp} - 2 \frac{\alpha_E}{\alpha_\nu^2} \nu_{pp}^2 \right) \quad (49)$$

The hypoplastic barotropy factor f_s is

$$f_s = -\frac{3\text{tr}\boldsymbol{\sigma}^M}{2A_m} \left(\frac{1}{\lambda_{\text{act}}^*} + \frac{1}{\kappa^*} \right) \quad (50)$$

with λ_{act}^* calculated from (for derivation of λ_{act}^* , see Appendix II)

$$\lambda_{\text{act}}^* = \frac{\lambda^*(s, T) e^M (1 + e^m) - \kappa_m (1 + e^m) (p^M / p^m) \{ (1 + e^M) [n_s - l_s \ln(p^M / p_r)] + f_m e^M \}}{e^M (1 + e^m) - (1 + e) [n_s - l_s \ln(p^M / p_r)]} \quad (51)$$

and scalar A_m calculated as

$$A_m = \nu_{pp}^2 \left(\frac{4\alpha_E}{\alpha_\nu} - 2\alpha_E^2 + 2 \frac{\alpha_E^2}{\alpha_\nu^2} - 1 \right) + \nu_{pp} \left(\frac{4\alpha_E}{\alpha_\nu} + 2\alpha_E \right) + 2\alpha_E + 1 \quad (52)$$

The anisotropy coefficients can be calculated from

$$\alpha_E = \alpha_G^{(1/x_{GE})} \quad (53)$$

$$\alpha_\nu = \alpha_G^{(1/x_{G\nu})} \quad (54)$$

$$x_{GE} = 0.8 \quad (55)$$

$$x_{G\nu} = 1 \quad (56)$$

However, in the case of assumed elastic isotropy, α_G from Eq. (45) is equal to 1, and thus also α_E and α_ν . The hypoplastic nonlinear term is governed by

$$\mathbf{N} = -\frac{\mathcal{A}:\mathbf{d}}{f_s f_d^A} \quad (57)$$

with the fourth-order tensor \mathcal{A}

$$\mathcal{A} = f_s \mathcal{L} + \frac{\boldsymbol{\sigma}^M}{\lambda_{\text{act}}^*} \otimes \mathbf{1} \quad (58)$$

and the pyknotropy factor

$$f_d = \left(\frac{2p^M}{p_e} \right)^{\alpha_f} \quad (59)$$

Factor f_d^A controls the shape of the asymptotic state boundary surface:

$$f_d^A = 2^{\alpha_f} (1 - F_m)^{\alpha_f / \omega} \quad (60)$$

The Matuoka-Nakai factor F_m reads

$$F_m = \frac{9I_3 + I_1 I_2}{I_3 + I_1 I_2} \quad (61)$$

and the scalar ω from Eq. (60) is

$$\omega = -\frac{\ln(\cos^2 \varphi_c)}{\ln 2} + a_f (F_m - \sin^2 \varphi_c) \quad (62)$$

with default value of a_f

$$a_f = 0.3 \quad (63)$$

Stress invariants I_1 , I_2 , and I_3 are calculated from

$$I_1 = \text{tr} \boldsymbol{\sigma}^M \quad (64)$$

$$I_2 = \frac{1}{2} [\boldsymbol{\sigma}^M : \boldsymbol{\sigma}^M - (I_1)^2] \quad (65)$$

$$I_3 = \det \boldsymbol{\sigma}^M \quad (66)$$

Asymptotic strain rate direction \mathbf{d} is given by

$$\mathbf{d} = \frac{\mathbf{d}^A}{\|\mathbf{d}^A\|} \quad (67)$$

with

$$\mathbf{d}^A = -\hat{\boldsymbol{\sigma}}^{*M} + \mathbf{1} \left[\frac{2}{3} - \frac{\cos 3\theta + 1}{4} F_m^{1/4} \right] \frac{F_m^{\xi/2} - \sin^{\xi} \varphi_c}{1 - \sin^{\xi} \varphi_c} \quad (68)$$

Lode angle function $\cos 3\theta$ is given by

$$\cos 3\theta = -\sqrt{6} \frac{\text{tr}(\hat{\boldsymbol{\sigma}}^{*M} \cdot \hat{\boldsymbol{\sigma}}^{*M} \cdot \hat{\boldsymbol{\sigma}}^{*M})}{[\hat{\boldsymbol{\sigma}}^{*M} : \hat{\boldsymbol{\sigma}}^{*M}]^{3/2}} \quad (69)$$

and

$$\xi = 1.7 + 3.9 \sin^2 \varphi_c \quad (70)$$

Normalized deviator stress $\hat{\boldsymbol{\sigma}}^{*M}$ reads

$$\hat{\boldsymbol{\sigma}}^{*M} = \frac{\boldsymbol{\sigma}^{*M}}{\text{tr} \boldsymbol{\sigma}^{*M}} - \frac{\mathbf{1}}{3} \quad (71)$$

Nonlinear response inside the asymptotic state boundary surface is controlled by

$$\alpha_f = \frac{\ln \left[\frac{\lambda^* - \kappa^*}{\lambda^* + \kappa^*} \left(\frac{3+a_f^2}{a_f \sqrt{3}} \right) \right]}{\ln 2} \quad (72)$$

with

$$a_f = \frac{\sqrt{3}(3 - \sin \varphi_c)}{2\sqrt{2} \sin \varphi_c} \quad (73)$$

Hvorslev equivalent pressure is calculated from

$$p_e = p_r \exp \left[\frac{N(s, T) - \ln(1 + e)}{\lambda(s, T)^*(s)} \right] \quad (74)$$

where $p_r = 1$ = reference stress (kPa). Values of $N(s, T)$ and $\lambda^*(s, T)$ are represented by

$$\begin{aligned} N(s, T) &= N + n_s \left\langle \ln \frac{s}{s_e} \right\rangle + n_T \ln \left(\frac{T}{T_r} \right) \\ \lambda^*(s, T) &= \lambda^* + l_s \left\langle \ln \frac{s}{s_e} \right\rangle + l_T \ln \left(\frac{T}{T_r} \right) \end{aligned} \quad (75)$$

The variables N , λ^* , n_s , l_s , n_T , and l_T are model parameters. The tensorial terms \mathbf{H}_s and \mathbf{H}_T from Eq. (34) read

$$\mathbf{H}_s = -\frac{c_i r \lambda \boldsymbol{\sigma}^M}{s \lambda_{\text{act}}^*} \left(n_s - l_s \ln \frac{p_e}{p_r} \right) \langle -\dot{s} \rangle \quad (76)$$

$$\mathbf{H}_T = \frac{c_i \boldsymbol{\sigma}^M}{T \lambda_{\text{act}}^*} \left(n_T - l_T \ln \frac{p_e}{p_r} \right) \langle \dot{T} \rangle \quad (77)$$

for $s > a_e s_{en}$ and $\mathbf{H}_s = \mathbf{0}$ otherwise. The factor c_i reads

$$c_i = \frac{(\lambda_{\text{act}}^* + \kappa^*)(2^{\alpha_f} - f_d) + 2\kappa^* f_d}{(\lambda_{\text{act}}^* + \kappa^*)(2^{\alpha_f} - f_d^A) + 2\kappa^* f_d^A} \quad (78)$$

The factor controlling the collapsible behavior f_u is defined by

$$f_u = \begin{cases} \left(\frac{p^M}{p^{MA}} \right)^m & \text{for } p^M \leq p^{MA} \\ \left(\frac{p^M}{p^{MA}} \right)^{100} & \text{for } p^M > p^{MA} \end{cases} \quad (79)$$

where p^{MA} = value of the macrostructural effective stress corresponding to the current stress ratio at the asymptotic state boundary surface, which may be calculated as

$$p^{MA} = \frac{p_e}{2} (f_d^A)^{1/\alpha_f} \quad (80)$$

with m being a model parameter.

The behavior of the microstructure is governed by

$$\dot{\boldsymbol{\epsilon}}_{\text{nom}} = \frac{1}{3} \left(\alpha_s \dot{T} - \frac{\kappa_m}{p^m} \dot{p}^m \right) \quad (81)$$

$$\dot{\boldsymbol{\epsilon}}^m = (1 - f_{ul}) \dot{\boldsymbol{\epsilon}}_{\text{nom}}^m \quad (82)$$

with parameter κ_m . The expression for the factor f_{ul} reads

$$f_{ul} = \begin{cases} \left(\frac{p^M}{p^{MA}} \right)^m & \text{for } p^M \leq p^{MA} \text{ and } \dot{\boldsymbol{\epsilon}}_{\text{nom}}^m > 0 \\ 1 & \text{for } p^M > p^{MA} \text{ and } \dot{\boldsymbol{\epsilon}}_{\text{nom}}^m > 0 \\ 0 & \text{for } \dot{\boldsymbol{\epsilon}}_{\text{nom}}^m \leq 0 \end{cases} \quad (83)$$

The value $\boldsymbol{\sigma}^m$ is the microstructural effective stress given by

$$\boldsymbol{\sigma}^m = \boldsymbol{\sigma}^{\text{net}} - s = \boldsymbol{\sigma}^{\text{tot}} + u_w \quad (84)$$

The value e^m may be initialized through

$$e^m = \exp \left[\kappa_m \ln \frac{s_r}{p^m} + \ln(1 + e_{r0}^m) + \alpha_s (T - T_r) \right] - 1 \quad (85)$$

with parameters e_{r0}^m , s_r , and T_r .

Finally, the double-structure coupling function f_m reads

$$f_m = \begin{cases} 1 - (r_{em})^m & \text{for } \dot{p}^m \leq 0 \\ \left\langle \frac{c_{sh} s}{s_e} \right\rangle & \text{for } \dot{p}^m > 0 \end{cases} \quad (86)$$

whereas $f_m = 1$ if Eq. (86) leads to $f_m > 1$. The value r_{em} is the relative void ratio

$$r_{em} = \frac{e - e_d}{e_i - e_d} \quad (87)$$

with

$$e_i = \exp[N(s, T) - \lambda^*(s, T) \ln p^M] - 1 \quad (88)$$

and

$$e_d = e_m \quad (89)$$

D3.3



Annex C

Contribution to Deliverable 3.3

DELIVERABLE (D3.3) Clay Technology Report

Author(s): Ola Kristensson, Mattias Åkesson, Daniel Malmberg, Alex Spetz

Reporting period: 01/06/20 – 31/05/22

Date of issue of this report: **31/08/21**

Start date of project: **01/06/17**

Duration: 60 Months

This project receives funding from the Euratom research and training programme 2014-2018 under grant agreement No 745 942		
Dissemination Level		
PU	Public	X
RE	Restricted to a group specified by the partners of the Beacon project	
CO	Confidential, only for partners of the Beacon project	

REVIEW

Name	Internal/Project/External	Comments
All Beacon partners	Project internal	

DISTRIBUTION LIST

Name	Number of copies	Comments
Seifallah BEN HADJ HASSINE (EC)	Digital	
Beacon partners	Digital	

Abstract

This report describe work regarding the Hysteresis Based Material (HBM) model performed by Clay Technology and SKB within WP3 of the Beacon project. The main focus of WP3 has been to develop, improve and study the performance of constitutive models and in this final deliverable the present state of HBM and assessments of its capabilities are presented.

A full, but brief, description of the current version of the HBM model are first presented. In connection to this an outline of the development and improvement process is given together with descriptions of important parts of the framework.

At the start of the project, basic capabilities of the model were studied by solving several proposed one-element tests. An updated study, using the current version of the material model, is here reported. A comparison between the studies indicates results obtained from the development process.

When it comes to modelling of Task 3 within WP3, the models generally agree well with the requested output from the experiments. When looking at details, however, there is some differences, especially so for the evolution of variables. There also seems to be an uncertainty in the experimental data when compared to similar tests.

The work carried out in WP3 and WP5 indicates that HBM can accurately model bentonite buffers when subjected to very different conditions only using a single set of parameters. The parameter set, however, has to be accurately fitted to proper experimental material data. There are still work to be done to get better numerical performance from the implementation.

Content

1	Introduction	5
2	Description of the model	5
2.1	Balance equations	6
2.2	Constitutive equations	7
2.3	Developments and improvements during the Beacon project.....	9
3	Basic capabilities of the model	13
3.1	Dependence of swelling strain on applied stress and on dry density	14
3.2	Irreversibility of strains in wetting/drying cycles	15
3.3	Behaviour during swelling stress test. Dependence of swelling pressure on the dry density.	16
3.4	Stress path dependence from an unsaturated to a saturated state.....	17
3.5	Stress path dependence from a saturated to an unsaturated state.....	18
3.6	Feature table	19
4	Task 3.3	20
4.1	Model description	20
4.1.1	Initial conditions, boundary conditions, and parameter values.....	20
4.2	Results and discussion	22
5	Performance of the model and assessment of predictive power	26
6	Concluding remarks	27
	References	29

1 Introduction

In WP3 the development of the Hysteresis Based Material (HBM) model has been taken from a state where it only was valid for isotropic and fully water saturated conditions to the present state where it is valid for general stress states, general degrees of saturation, and vapor transport is included. Much work has gone into development/generalization of the formulation of the model, recasting the developed formulation into a format suitable for implementation into Comsol Mutiphysics and carrying out the implementation.

Within WP3, one element tests, where different aspects of the model come into play, have been performed and show that the model is very promising in that it is capable to give realistic responses using a single set of parameter values for very different scenarios.

The basis of the mechanical part of the model is a thermodynamic relation for the chemical potential of the interlayer water in the clay. This relation couples the stress at full saturation to the chemical potential difference between the interlayer water and a reference water (suction) by a quantity denoted clay potential. The clay potential incorporates dry density dependence and path dependency, i.e. representation of hysteresis. The unsaturated regime is introduced by introducing a gas phase in addition to the phase consisting of saturated clay grains. This results in definitions of a micro void ratio, present in the saturated clay grains only, and a total void ratio. The total stress, for the unsaturated clay, is then defined by scaling the stress in the saturated clay grains with a contact area function, expressed in terms of the two void ratios. Finally, an interaction function, in terms of an evolution law for the micro void ratio, completes the model.

2 Description of the model

The description of the model starts with the adopted material structure from which definitions of quantities enable formulations of balance equations. Thereafter the constitutive equations of the liquid phase, gas phase and mechanics are described.

In Figure 2-1 a sketch of the assumed material structure is given to the left and a diagram to the right. The adopted clay material structure can be described using a tree diagram which visualize the hierarchical nature of the model. The top-level, denoted macroscale, is populated by the 'clay' which can be saturated or unsaturated. The clay is an immiscible mixture of two phases populating the mid-level, the mesoscale. The first phase on the mesoscale is 'saturated clay grains' and the second 'gas filled pores'. The 'saturated clay grains' is an immiscible mixture of two phases populating the low-level, the microscale. The 'gas filled pores' is a miscible mixture of dry air and water vapor. The two phases at the microscale, the building blocks of the 'saturated clay grains', are 'interlayer water' and 'minerals'.

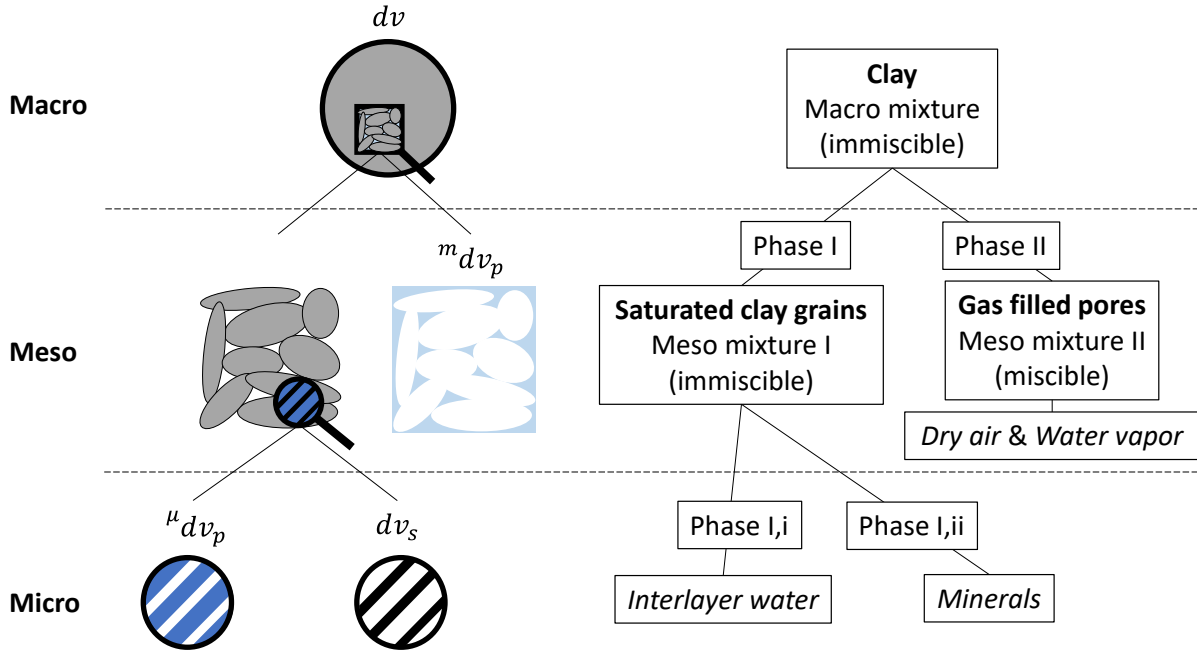


Figure 2-1. Description of the adopted material structure.

To the left in Figure 2-1, volume elements needed for the formulation are defined. From using these, different void ratios can be formulated. The total void ratio is defined by,

$$e = \frac{dv_p}{dv - dv_p} = \frac{{}^\mu dv_p + {}^m dv_p}{dv - ({}^\mu dv_p + {}^m dv_p)}. \quad (2-1)$$

The immiscibility of phases at the micro scale makes it possible to define a corresponding void ratio,

$$e_\mu = \frac{{}^\mu dv_p}{dv_s}. \quad (2-2)$$

As indicated in the right diagram of Figure 2-1 volumes in the structure are allotted specific constituents (mineral, water and air):

- The meso pore space contains dry air and water vapor: ${}^m dm_p = dm_g^a + dm_g^w$
- The micro pore space contains interlayer water: ${}^\mu dm_p = dm_l^w$
- The solid volume contains minerals: $dm_s = dm_m$

2.1 Balance equations

Using what is defined above, balance equations of solid mass, water mass and force can be formulated. To simplify the description somewhat the energy balance and thermal constitutive equations have not been included here even though the thermal process has been addressed within WP5.

The solid mass balance,

$$\frac{\partial e}{\partial t} = (1 + e) \frac{\partial \varepsilon_v}{\partial t}, \quad (2-3)$$

is expressed in terms of total void ratio and the volumetric strain invariant $\varepsilon_v = \text{tr} \boldsymbol{\varepsilon}$, where the small strain tensor $\boldsymbol{\varepsilon} = 0.5(\nabla \mathbf{u} + (\nabla \mathbf{u})^T)$ is given by displacement gradients $\nabla \mathbf{u}$.

The water mass balance,

$$\frac{1}{1 + e} \frac{\partial}{\partial t} [\rho_l e_\mu] + \frac{1}{1 + e} \frac{\partial}{\partial t} [\theta_g^w (e - e_\mu)] + \nabla \cdot (\rho_l \mathbf{q}_l) + \nabla \cdot \mathbf{i}_g^w = f_l^w + f_g^w, \quad (2-4)$$

is given by total and micro void ratio, liquid water density $\rho_l = \frac{dm_l^w}{dv_l^w}$, vapor mass per gas phase $\theta_g^w = \frac{dm_g^w}{dv_g}$, liquid water flux \mathbf{q}_l , vapor flux \mathbf{i}_g^w , and source terms f_l^w and f_g^w .

The force balance,

$$\nabla \cdot \boldsymbol{\sigma} + \mathbf{b} = \mathbf{0}, \quad (2-5)$$

is expressed in terms of the stress tensor $\boldsymbol{\sigma}$, and the body force \mathbf{b} .

2.2 Constitutive equations

The independent variables for which the balance equations are solved for are chosen as displacements, \mathbf{u} , suction, s , and temperature, T . Suction is related to the difference in chemical potential between the water inside a material and some chosen referential state

To complete the formulation material specific, constitutive, relations are specified for the remaining, dependent, variables. In the equations below pressures are given in Pa and temperatures in K. A uniform gas pore pressure field, where $p_g = 0.1$ MPa, has been used. A tilde above a character indicate that it is a function and the same character without a tilde indicates a parameter given by that function, i.e. $a = \tilde{a}(x)$.

The interlayer water is specified by the density,

$$\tilde{\rho}_l(s) = \rho_l^0 \exp(-\alpha s), \quad (2-6)$$

with reference value ρ_l^0 and a compressibility α , and the flux,

$$\tilde{\mathbf{q}}_l(e, e_\mu, s) = \frac{\tilde{\kappa}(e, e_\mu)}{\mu} \nabla s, \quad (2-7)$$

driven by gradients in chemical potential. μ denotes the viscosity and $\tilde{\kappa}(e, e_\mu)$ the permeability function given by,

$$\tilde{\kappa}(e, e_\mu) = \kappa_0 \left(\frac{e}{e_{ref}} \right)^\beta \left(\frac{e_\mu}{e} \right)^\lambda, \quad (2-8)$$

where κ_0 is a reference value, β determines the dependence on void ratio, and λ the water saturation dependence.

The gas phase is assumed to be a mixture of two ideal gases, vapor and dry air, $p_g = p_g^w + p_g^a$, where p_g^w and p_g^a denote the partial gas pressures for the water and air constituents, respectively. The gas density, ρ_g , can be expressed in terms of the two constituents' "relative" densities, vapor mass per gas phase, θ_g^w , and dry air mass per gas phase, θ_g^a , i.e.,

$$\tilde{\rho}_g(s, T) = \tilde{\theta}_g^w(s, T) + \tilde{\theta}_g^a(s, T). \quad (2-9)$$

where the constituents' relative densities are given by,

$$\tilde{\theta}_g^w(s, T) = \frac{M_w}{RT} \tilde{p}_{g\ sat}^w(T) \tilde{RH}(s, T), \quad (2-10)$$

$$\tilde{\theta}_g^a(s, T) = \frac{M_a}{RT} \left(p_g - \tilde{p}_{g\ sat}^w(T) \tilde{RH}(s, T) \right), \quad (2-11)$$

$$\tilde{p}_{g\ sat}^w(T) = 136075 \cdot 10^6 \exp\left(\frac{-5239.7}{T}\right), \quad (2-12)$$

$$\tilde{RH}(s, T) = \exp\left(\frac{-sM_w}{RT\tilde{\rho}_l(s)}\right), \quad (2-13)$$

where $M_w = 0.018$ mol/kg, $M_a = 0.029$ mol/kg and $R = 8.314472$ J/mol/K. The vapor diffusion flux \mathbf{i}_g^w is driven by a gradient in vapor mass concentration ∇c ,

$$\mathbf{i}_g^w = -\tilde{\mathbf{D}}(e, e_\mu, s, T) \nabla c. \quad (2-14)$$

$\tilde{\mathbf{D}}(e, e_\mu, s, T)$, the diffusion coefficient function, is given by,

$$\tilde{\mathbf{D}}(e, e_\mu, s, T) = \tau \phi \tilde{\rho}_g(s, T) \left(1 - \frac{e_\mu}{e}\right) D \frac{T^{2.3}}{p_g} \mathbf{1}, \quad (2-15)$$

where τ denotes the tortuosity, ϕ the porosity, and D the diffusion coefficient of vapor. Since the vapor mass concentration can be formulated using the expressions for the densities θ_g^w and ρ_g ,

$$\tilde{c}(s, T) = \left[\frac{\tilde{\theta}_g^w(s, T)}{\tilde{\rho}_g(s, T)} \right], \quad (2-16)$$

the gradient can be expressed in terms of gradients in suction and temperature,

$$\nabla c = \frac{\partial \tilde{c}(s, T)}{\partial s} \nabla s + \frac{\partial \tilde{c}(s, T)}{\partial T} \nabla T. \quad (2-17)$$

The mechanical material model relates stress to deformation (strain) and chemical potentials (suction). The total stress $\boldsymbol{\sigma}$ for unsaturated/saturated states is given by scaling the saturated grain stress $\boldsymbol{\sigma}^I$ by a contact area function α ,

$$\boldsymbol{\sigma} = \alpha \boldsymbol{\sigma}^I. \quad (2-18)$$

The contact area function is thought of as being defined by the ratio between the contact area between saturated grains and total area for a given representative volume element. In the formulation it is approximated by the function,

$$\alpha = \tilde{\alpha}(e, e_\mu) = \left(\frac{1 + e_\mu}{1 + e} \right)^\gamma, \quad (2-19)$$

where γ defines the shape of the function. Expressing the balance of chemical potential between clay water and referential water gives the thermodynamical basis which HBM rests upon. The obtained expression,

$$-\boldsymbol{\sigma}^I = \boldsymbol{\Psi} - s \mathbf{1}, \quad (2-20)$$

relates the stress in the saturated grain to the difference in clay water and referential water chemical potential (suction) by a quantity which is here called clay potential, $\boldsymbol{\Psi}$. Thus, the clay potential bridges the mechanical and chemical ("hydraulic") processes. Experimentally determined retention and swelling pressure curves show a dependency on void ratio and the path which the state has been arrived at. The clay potential is therefore made dependent on void ratio and a path dependent variable \mathbf{f} ,

$$\boldsymbol{\Psi} = \tilde{\Psi}_M(e_\mu) \mathbf{1} + \tilde{\Psi}_\Delta(e_\mu) \mathbf{f}, \quad (2-21)$$

to enabling representation of what has been observed in the laboratory. The present formulation uses two functions dependent on the micro void ratio, $\tilde{\Psi}_M(e_\mu)$ and $\tilde{\Psi}_\Delta(e_\mu)$. The first one being a "mean" function and the second a "deviation" function multiplied to the path dependent variable. The path dependent variable is governed by an evolution law,

$$\mathbf{f}: d\mathbf{f} = \frac{\partial \mathbf{f}}{\partial \boldsymbol{\varepsilon}} d\boldsymbol{\varepsilon}, \quad (2-22)$$

dependent on the strain path, where the partial derivative components $\frac{\partial f_{ij}}{\partial \varepsilon_{kl}} \neq 0$ when $i = k$ & $j = l$, are specified according to,

$$\frac{\partial f_{ij}}{\partial \varepsilon_{kl}} = -K_{\alpha\beta} \left(f_{ij} - f^{lim}_{ij} \right) \text{sgn}(\dot{\varepsilon}_{kl}). \quad (2-23)$$

$K_{\alpha\beta}$ specifies the slope at $f_{ij} = 0$ and has different values when $i = j$ or $i \neq j$. f_{ij}^{lim} specifies the limits of f_{ij} and sgn denotes the sign function,

$$\text{sgn}(x) = \begin{cases} -1 & \text{if } x < 0 \\ 0 & \text{if } x = 0, \\ 1 & \text{if } x > 0 \end{cases} \quad (2-24)$$

here operating on the components of the strain rate. Symmetry in stress ($\sigma_{ij} = \sigma_{ji}$) gives that \mathbf{f} and $\frac{\partial f_{ij}}{\partial \varepsilon_{kl}} = \frac{\partial f_{ji}}{\partial \varepsilon_{kl}}$ are symmetric. Symmetry in strain gives that $\frac{\partial f_{ij}}{\partial \varepsilon_{kl}} = \frac{\partial f_{ij}}{\partial \varepsilon_{lk}}$. \mathbf{f}^{lim} is determined from an additional limiting condition placed on \mathbf{f} ,

$$f_p^2 + f_q^2 = R^2, \quad (2-25)$$

where the parameter R modifies the restriction. The spherical invariant f_p and deviatoric invariant f_q are defined by,

$$f_p = \frac{1}{3} \text{tr} \mathbf{f}, \quad (2-26)$$

$$f_q^2 = \frac{3}{2} \mathbf{f}^{dev} \cdot \mathbf{f}^{dev} \quad (2-27)$$

\mathbf{f}^{lim} is calculated as follows. For each component f_{ij} , construct a new path variable tensor \mathbf{f}' using \mathbf{f} but where component f_{ij} is replaced with an unknown f'_{ij} ,

$$\mathbf{f}' = \mathbf{f} + (f'_{ij} - f_{ij}) \mathbf{e}_i \otimes \mathbf{e}_j \quad (2-28)$$

Then find f'_{ij}^{\pm} from inserting \mathbf{f}' in the limiting condition and, depending on the sign of df_{ij} (i.e. $\dot{\varepsilon}_{kl}$), identify the limit value f_{ij}^{lim} as f'_{ij}^+ (if $\dot{\varepsilon}_{kl} < 0$) or f'_{ij}^- (if $\dot{\varepsilon}_{kl} > 0$).

The final part of the mechanical constitutive relations is the evolution equation of the micro void ratio,

$$e_{\mu} \cdot de_{\mu} = \frac{\partial e_{\mu}}{\partial e} de + \frac{\partial e_{\mu}}{\partial s} ds, \quad (2-29)$$

The first of the differentials describes a kinematical coupling to the macroscopic variable and the second describe the swelling of the saturated clay grains at the micro scale in terms of suction. The first differential is chosen as being given by the contact area function,

$$\frac{\partial e_{\mu}}{\partial e} = \tilde{\alpha}(e, e_{\mu}), \quad (2-30)$$

and the second differential by the expressions,

$$\frac{\partial e_{\mu}}{\partial s} = \text{smooth_step}(s) \left(\frac{\partial e_{\mu}}{\partial s} \right)^* \quad (2-31)$$

$$\left(\frac{\partial e_{\mu}}{\partial s} \right)^* = \begin{cases} \frac{(e - e_{\mu}) \tilde{\Psi}_M(e_{\mu})}{s} \frac{1}{(e - e_{\mu}) \frac{\partial \tilde{\Psi}_M}{\partial e_{\mu}} - \tilde{\Psi}_M(e_{\mu})} & \text{if } \dot{s} < 0 \\ \frac{-e_{step}}{|s - \tilde{\Psi}_M(e_{\mu} - e_{step})|} & \text{otherwise} \end{cases} \quad (2-32)$$

2.3 Developments and improvements during the Beacon project

During the Beacon project the material model has been both developed and improved, an overview of this process is given below. The mechanical material model is given special attention, changes to other parts are only briefly discussed at the end.

An important improvement was the generalisation of the mechanical model to unrestricted mechanical states. At the start of the development process only isotropic stress conditions were handled using the scalar thermodynamic basis equation,

$$p = \Psi - s. \quad (2-33)$$

This was first improved upon by allowing for cases where the principal mechanical directions were known and did not change during the simulation. In the current version general mechanical states without any restrictions are allowed. This generalisation was achieved by including all dimensions in the thermodynamical basis relation,

$$-\sigma^I = \Psi - s\mathbf{1}, \quad (2-34)$$

which called for full tensorial representation of the clay potential and the path dependent variable together with its evolution law and limiting condition.

Another significant step was achieved when the unsaturated representation was developed. The gas phase was then introduced in the material structure which enabled definitions of total and micro void ratios. Total stress, for the unsaturated/saturated clay, was given by the stress for the saturated clay grains scaled by a contact area function,

$$\sigma = \left(\frac{1 + e_\mu}{1 + e} \right)^\gamma \sigma^I. \quad (2-35)$$

The contact area function is representing the ratio between the contact area between saturated clay grains and the area for a corresponding representative volume element. It is here given by a power law of the fraction between saturated volume ($1 + e_\mu$) and total volume ($1 + e$).

When enabling unsaturated conditions, an “interaction function” was introduced. In D3.1 (in which an isotropic version of HBM was used) the interaction function was defined as an evolution equation for the total pressure. This was specified as partial differentials of void ratio and water content.

$$dp = \frac{\partial p}{\partial e} de + \frac{\partial p}{\partial w} dw. \quad (2-36)$$

When formulating a “principal direction” version of HBM in D3.2 a generalised interaction function, based on the isotropic version, was used. In the principal direction version, the evolution of principal stresses was determined by differentials of principal strain and “principal” water contents.

Finally, when modelling the Febex test in WP5.2 the currently used format of the interaction function,

$$de_\mu = \frac{\partial e_\mu}{\partial e} de + \frac{\partial e_\mu}{\partial s} ds, \quad (2-37)$$

the micro void ratio evolution, was developed to fit into the Comsol formulation/implementation and to achieve a better performance of the model. The micro void ratio is here dependent on total void ratio and suction. The contact area function couples the micro void ratio to the total void ratio,

$$\frac{\partial e_\mu}{\partial e} = \left(\frac{1 + e_\mu}{1 + e} \right)^\gamma, \quad (2-38)$$

and the differential with respect to suction describes the swelling of the saturated clay grains. The suction differential is different for different sign of the suction rate. The expression active for drying conditions was developed to account for a shrinkage limit, observed in experiments. Below follows a description of how the suction differential was formulated.

For negative suction rates, the properties of $\partial e_\mu / \partial s$ is illustrated in the left panel of Figure 2-2. The derivative is defined so that: i) the suction decreases faster than the Ψ_M -function for increasing e_μ -values; and ii) so that saturated conditions (i.e. $e_\mu = e_{tot}$) is reached precisely when $s = 0$. The first condition implies that a stress which corresponds to $f = 0$, ($f = f1$) will display an increasing trend. This is achieved with the condition that the s/Ψ_M -ratio displays a linear decrease with an increasing e_μ -value (Figure 2-2, left panel, right graph). The introduction of this ratio (r) means that:

$$s = r\Psi_M \tag{2-39}$$

Taking the derivative of the expression above with respect to e_μ results in the first relation in the equation below.

$$\frac{\partial s}{\partial e_\mu} = \frac{\partial r}{\partial e_\mu} \Psi_M + r \frac{\partial \Psi_M}{\partial e_\mu} = \frac{-s}{\Psi_M} \frac{1}{e_{tot} - e_\mu} \Psi_M + \frac{s}{\Psi_M} \frac{\partial \Psi_M}{\partial e_\mu} \tag{2-40}$$

This expression is obtained by identifying $\partial r / \partial e_\mu$ as a straight line from the point (e_μ, r) to point $(e_{tot}, 0)$ in Figure 2-2 (left panel, right graph), and by substituting r with s/Ψ_M . Inverting the relation above gives the sought reciprocal partial derivative.

For positive suction rates, the properties of the corresponding derivative are illustrated in the right panel of Figure 2-2. The derivative is defined so that the suction value changes asymptotically towards the Ψ_M -function. This implies that a stress (with $f = 0$) will display an asymptotic trend towards zero.

For this purpose, a parameter e_{step} is introduced. The derivative is defined so that a stress path in each point (e_μ, s) is directed towards the point $(e_\mu - e_{step}, \tilde{\Psi}_M(e_\mu - e_{step}))$ which yields the following expression:

$$\frac{\partial e_\mu}{\partial s} = \frac{-e_{step}}{|s - \tilde{\Psi}_M(e_\mu - e_{step})|} \tag{2-41}$$

Since e_{step} is constant, this means that the point of direction will change with decreasing e_μ values. The absolute value is introduced so that the derivative will yield a negative value regardless of the relative magnitude of s and Ψ_M .

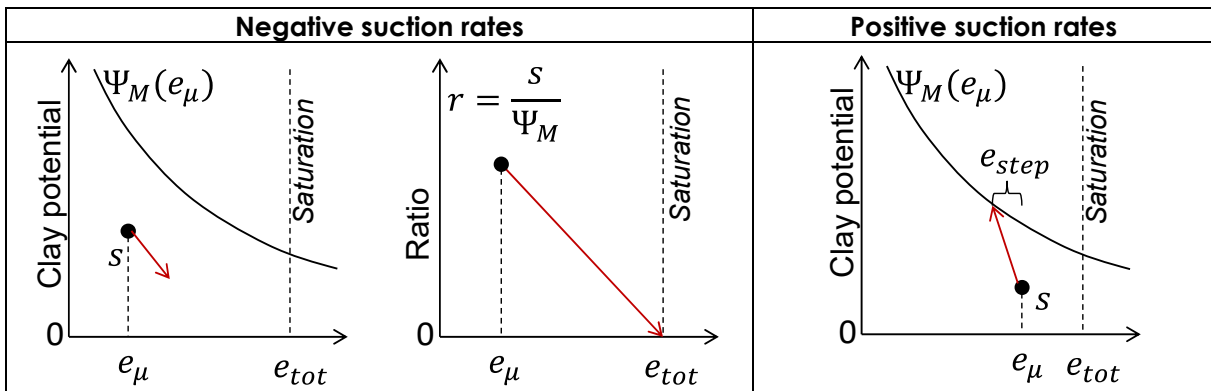


Figure 2-2. Definition of $\partial e_\mu / \partial s$. Left panel: Negative suction rates, $\tilde{\Psi}_M$ and s vs e_μ (left); $s/\tilde{\Psi}_M$ -ratio vs. e_μ (right). Right panel: Positive suction rates, $\tilde{\Psi}_M$ and s vs. e_μ .

When carrying out the modelling tasks in Beacon it soon became obvious that the parametrisation of the clay potential function was an essential part in achieving solutions that provide a good representation of the experimental behaviour of the clay. In particular, models which simulated unsaturated conditions require a clay potential with a very good fit to experimental data over a large interval of void ratios. This is due to the large range in micro

void ratio during such simulations, especially so when starting out from very dry conditions (or if the material undergo significant drying).

As described above in the theory section, the clay potential bridges the mechanical and hydraulic processes in the core relation of the model. A well-designed clay potential function should therefore enable the model to produce both the characteristic mechanical and hydraulic behaviour. This must be kept in mind when selecting the data to match the clay potential and when selecting a suitable parametrisation and performing the fitting. To establish a link from experimental data to the clay potential several characteristic quantities are defined in the theoretical framework. These are the swelling pressure p_s , the deviator stress at failure, q_f , the wetting retention, s_w , and the drying retention, s_d . The clay potential curves, Ψ_M and Ψ_Δ , are then identified in terms of these characteristic quantities. For the mechanical regime, the swelling pressure, p_s , is defined as the minimum pressure attained at full saturation and when suction is zero, and the deviator stress at failure, q_f , (also at full saturation) is defined as the maximum attainable deviator stress,

$$p_s \equiv \min(p) \text{ when } s = 0, \quad (2-42)$$

$$q_f \equiv \max(q). \quad (2-43)$$

With these definitions the clay potential contributions Ψ_M and Ψ_Δ can be identified as,

$$\Psi_M = p_s + q_f \text{ and } \Psi_\Delta = \frac{1}{R} q_f. \quad (2-44)$$

For the hydraulic regime, the wetting retention, s_w , is defined as the minimum suction obtained under unconfined conditions, and the drying retention, s_d , is defined as the maximum suction obtained under unconfined conditions,

$$s_w \equiv \min(s) \text{ when } \sigma = 0, \quad (2-45)$$

$$s_d \equiv \max(s) \text{ when } \sigma = 0. \quad (2-46)$$

With the given definitions the clay potential contributions Ψ_M and Ψ_Δ can be identified as,

$$\Psi_M = \frac{s_d + s_w}{2} \text{ and } \Psi_\Delta = \frac{s_d - s_w}{2R}. \quad (2-47)$$

Thus, to achieve proper representations in both regimes (mechanical and hydraulic) both data sets $\{p_s, q_f\}$ and $\{s_d, s_w\}$ must be considered and these must be well suited and consistent when fitting Ψ_M and Ψ_Δ .

Early in the development of the unsaturated model a micro strain variable was defined using a relation to the total strain. The path dependent variable was given by an evolution relation expressed in this micro strain variable. The use of micro strain was, however, abandoned when the model was implemented in Comsol and the updated interaction function was used.

The hydraulic formulation has also been developed during the Beacon project. Initially, the implementation in Comsol Multiphysics did not simulate hydraulic processes at all, changes in suction and/or water content were prescribed directly. In the first implementations where the unsaturated regime could be represented by the mechanical model, only the wetting direction was allowed for. A big step was taken by including the water mass balance and simulating the suction evolution. The mechanical coupling in the water mass balance has been corrected and the Darcy flux has been introduced in a proper way in the water mass balance. The dry density dependency of the permeability, entering the description of the Darcy flux, was changed to correspond with that used in Code_Bright. WP5.2 called for an introduction of vapor transport which necessitated an expansion of the water mass balance and required the inclusion of the energy balance and new constitutive laws.

3 Basic capabilities of the model

The Hysteresis Based Material (HBM) model was developed during the course of the Beacon project and an updated assessment of the capabilities of this model is presented in this chapter.

Models in which the test conditions were treated as isotropic were solved as single element problems with simple programs written in MathCad spreadsheets. The most significant development of the model for isotropic problems (in relation to the version analysed in D3.1 report) was the definition of the evolution equation of the micro void ratio (see section 2.2 for details):

$$de_{\mu} = \frac{\partial e_{\mu}}{\partial e} de + \frac{\partial e_{\mu}}{\partial s} ds \quad (3-1)$$

This equation largely defines the behaviour of the model for unsaturated conditions. Together with the thermodynamic relation for the chemical potential of the clay water (isotropic version in which p is the pressure):

$$s + \frac{p}{\alpha} = \Psi_M + f \cdot \Psi_{\Delta} \quad (3-2)$$

these two expressions can be developed as derivatives for conditions in which either one of the three variables (s , p or e) is held constant. For conditions with constant pressure ($dp = 0$) this yields:

$$\frac{de}{ds} = \frac{\left[1 - \left(\frac{d\Psi_M}{de_{\mu}} + f \frac{d\Psi_{\Delta}}{de_{\mu}} + \frac{p}{\alpha^2} \frac{\partial \alpha}{\partial e_{\mu}} \right) \frac{\partial e_{\mu}}{\partial s} \right]}{\left[\left(\frac{d\Psi_M}{de_{\mu}} + f \frac{d\Psi_{\Delta}}{de_{\mu}} \right) \frac{\partial e_{\mu}}{\partial e} + \Psi_{\Delta} \frac{df}{de} + \frac{p}{\alpha^2} \left[\frac{\partial \alpha}{\partial e_{\mu}} \frac{\partial e_{\mu}}{\partial e} + \frac{\partial \alpha}{\partial e} \right] \right]} \quad (3-3)$$

Similarly, for conditions with constant void ratio ($de = 0$) this yields:

$$\frac{dp}{ds} = \alpha \left[\left(\frac{d\Psi_M}{de_{\mu}} + f \frac{d\Psi_{\Delta}}{de_{\mu}} + \frac{p}{\alpha^2} \frac{\partial \alpha}{\partial e_{\mu}} \right) \frac{\partial e_{\mu}}{\partial s} - 1 \right] \quad (3-4)$$

Finally, the condition with constant suction ($ds = 0$) gives the following derivative:

$$\frac{dp}{de} = \alpha \left[\left(\frac{d\Psi_M}{de_{\mu}} + f \frac{d\Psi_{\Delta}}{de_{\mu}} \right) \frac{\partial e_{\mu}}{\partial e} + \Psi_{\Delta} \frac{df}{de} + \frac{p}{\alpha^2} \left[\frac{\partial \alpha}{\partial e_{\mu}} \frac{\partial e_{\mu}}{\partial e} + \frac{\partial \alpha}{\partial e} \right] \right] \quad (3-5)$$

Concerning the path variable f for isotropic conditions, this is here treated as a scalar, and the variation of this is defined as a derivative with respect to the void ratio:

$$\frac{df}{de} = -\frac{K}{1 + e_0} (1 + \text{sgn}(\dot{e})f). \quad (3-6)$$

These equations can readily be used to calculate any stress path for isotropic conditions. And essentially all proposed paths described in the D3.1 instructions were analysed in this way. The case with temperature cycles was defined for saturated conditions (see Table 3-1), and since the behaviour of the model regarding such conditions was not changed since the D3.1 report, this case was not re-analysed in the study presented here.

The parameter setting was essentially the same as the one used for the test 1b case in D5.1.2 report. The clay potential functions were adopted on the following form:

$$\Psi = \exp(c_3 e^3 + c_2 e^2 + c_1 e + c_0) \quad (3-7)$$

With the following coefficients used for the lower curve (Ψ_L): $c_3 = -0.0838$; $c_2 = 1.1904$; $c_1 = -6.3234$; and $c_0 = 5.7035$, and the corresponding coefficients for the higher curve (Ψ_H): $c_3 = -0.1463$; $c_2 = 1.6239$; $c_1 = -6.6382$; $c_0 = 6.6008$. The mid-line and the half-allowed span were

calculated as: $\Psi_M = (\Psi_H + \Psi_L)/2$ and $\Psi_\Delta = (\Psi_H - \Psi_L)/2$, respectively. The K parameter was set to 40, and the γ parameter in the contact area function was set to 7. Finally, the parameter used for the dehydration path in the $\partial e_\mu / \partial s$ -derivative (e_{step}) was set to 0.05.

3.1 Dependence of swelling strain on applied stress and on dry density

These tests were performed from initially unsaturated conditions. Six tests were performed, either with one initial void ratio (0.55) and three different pressures (0.2, 9 and 15 MPa), or with one pressure (1 MPa) and three different initial void ratios (0.55, 0.75 and 0.95). In all cases the initial suction value was set to 100 MPa and the initial f value was set to zero. The void ratio evolution, shown in Figure 3-1, was calculated by keeping p constant, by decreasing s , and successively integrating e with Eq (3-3), e_μ with Eq (3-1), and f with Eq (3-6). These results show that the model displays a behaviour in which the swelling strain is influence by the applied load as well as by the dry density.

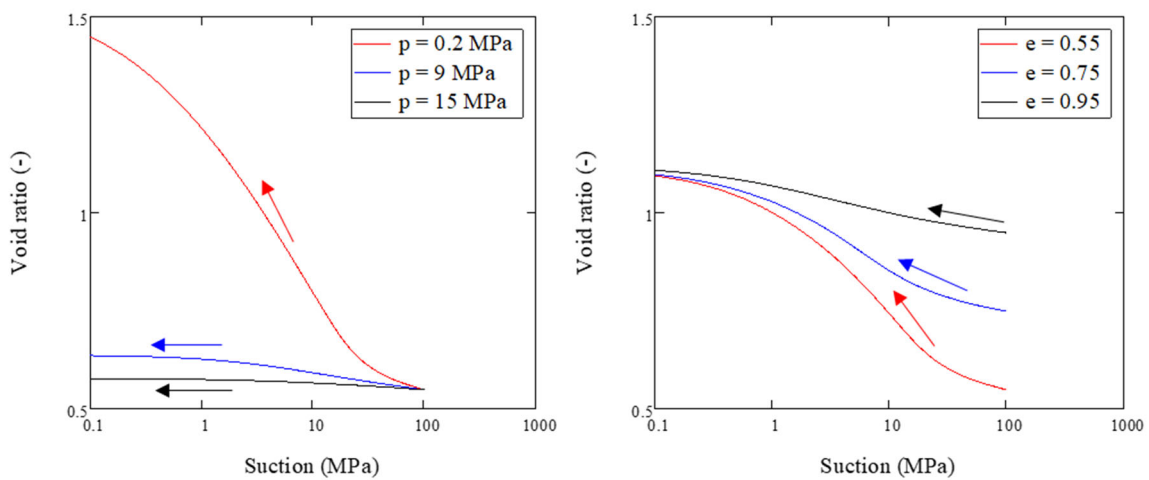


Figure 3-1. Swelling behaviour for different pressures (left) or with different initial void ratio (right).

3.2 Irreversibility of strains in wetting/drying cycles

These tests were performed from initially unsaturated conditions. Three void ratios were chosen (0.7, 0.65 and 0.6). The initial value of the path variable (f) was set to zero. The initial suction value was set to 10 MPa for all test cases whereas the loads were set to 2, 5 and 10 MPa, respectively.

The calculation was performed by integrating Eq (3-3), Eq (3-1), and Eq (3-6), by keeping the pressure constant and changing the suction from the initial value down to zero, after which the suction value was increased to the initial value. Stress paths for these cycles are shown in Figure 3-2. The void ratio evolutions demonstrate that the model displays a behaviour with irreversible strains during these cycles.

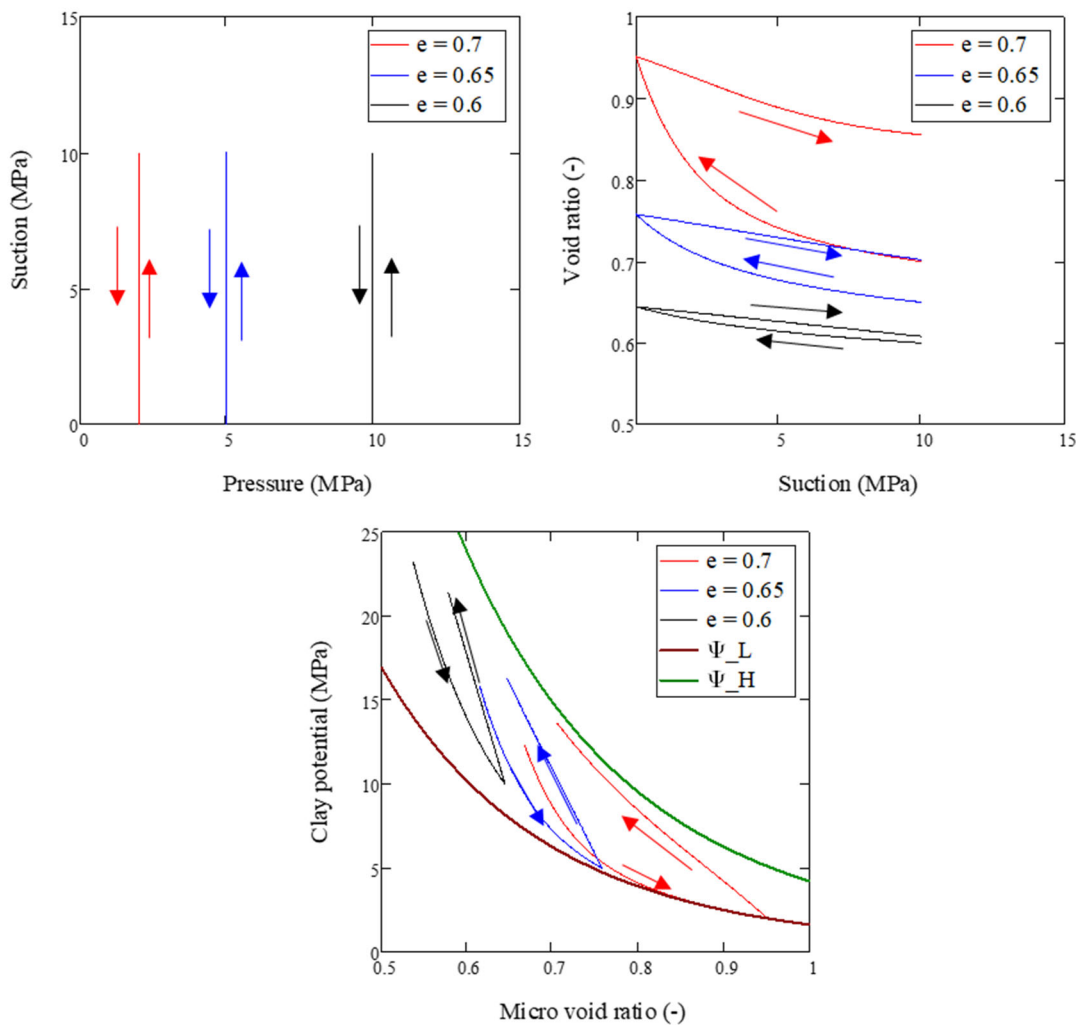


Figure 3-2. Calculated swelling/shrinkage paths at constant load. In s - p plane (upper left), as void ratio versus suction (upper right), and as clay potential versus micro void ratio (lower).

3.3 Behaviour during swelling stress test. Dependence of swelling pressure on the dry density.

These tests were performed from initially unsaturated conditions. Three void ratios were chosen (0.65, 0.75 and 0.85) and the initial pressure and the f value were both set to zero. The initial suction value was set to 55 MPa.

The pressure evolution was calculated by keeping e constant, by decreasing s , and successively integrating p with Eq (3-4) and e_μ with Eq (3-1) (f remained constant). The calculated stress path in the $s - p$ plane is shown in Figure 3-3 (upper graph). Suction is also shown as a function of the degree of saturation (i.e. e_μ/e), which illustrates that the water retention curve is inherent from the material model (lower left). Finally, the final swelling pressure values are plotted against the dry density and shown together with the mid-line of the clay potential (Ψ_M) (lower right). This shows that the model displays a behaviour in which the swelling pressure is influenced by the dry density.

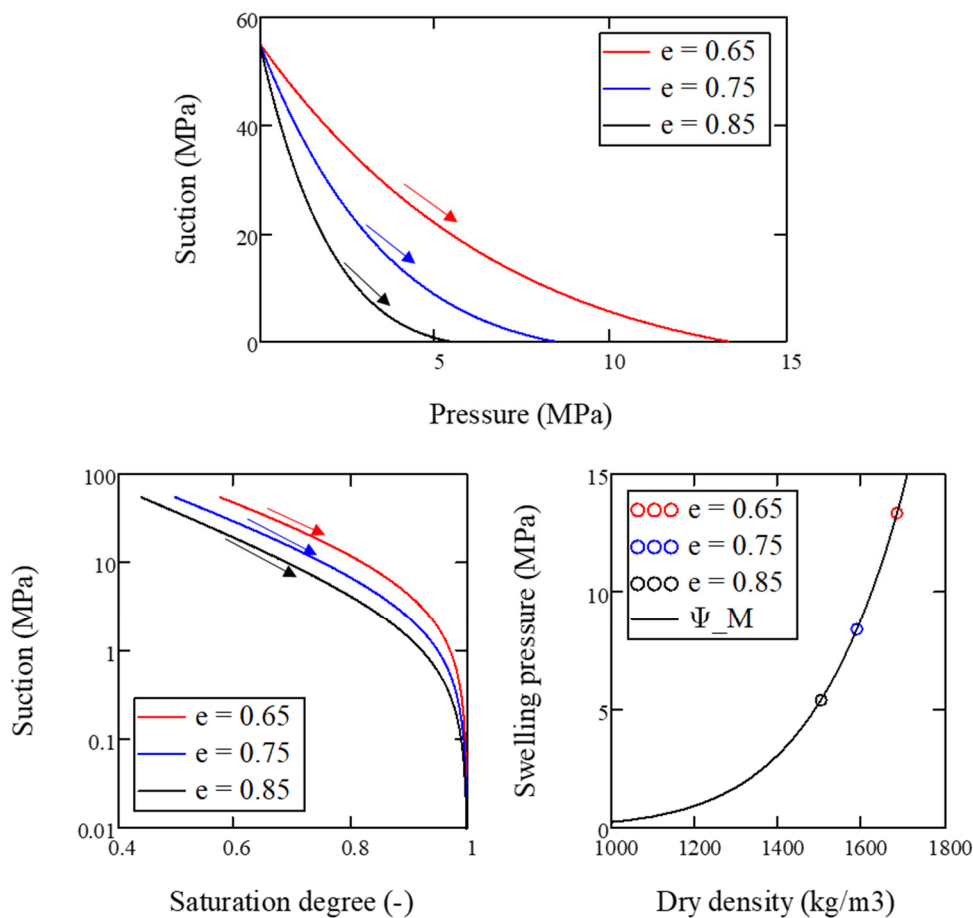


Figure 3-3. Calculated stress path in $s-p$ plane for three different void ratios (upper). Evaluated water retention curves for the same test cases (lower left). Final pressure vs dry density compared with the mid-line of the clay potential (lower right).

3.4 Stress path dependence from an unsaturated to a saturated state

These tests were performed from initially unsaturated conditions. The initial suction and pressure were set to 50 and 1 MPa respectively. The initial void ratio was set to 0.6. Three different stress paths were analysed: i) by decreasing suction (to zero) at constant pressure, followed by increasing pressure (to 10 MPa) at constant suction; ii) by increasing pressure at constant suction, followed by decreasing suction (to zero) at constant pressure; and iii) by decreasing suction at constant void ratio, followed by unloading at constant suction.

The stress path evolution was calculated by integrating either Eq (3-3), Eq (3-4) or Eq (3-5). For each increment e_μ was integrated with Eq (3-1), and for increments with changing void ratio f was integrated with Eq (3-6). Results show that the different stress paths resulted in different final void ratios (Figure 3-4 upper right). Path 1 displayed the most extensive swelling/compression cycle (lower graph), which meant that the final void ratio (0.79) was significantly higher than for Path 2 and 3, which were quite similar regarding the final void ratio (0.63-0.64). This shows that the model displays a stress path dependence from an unsaturated to a saturated state.

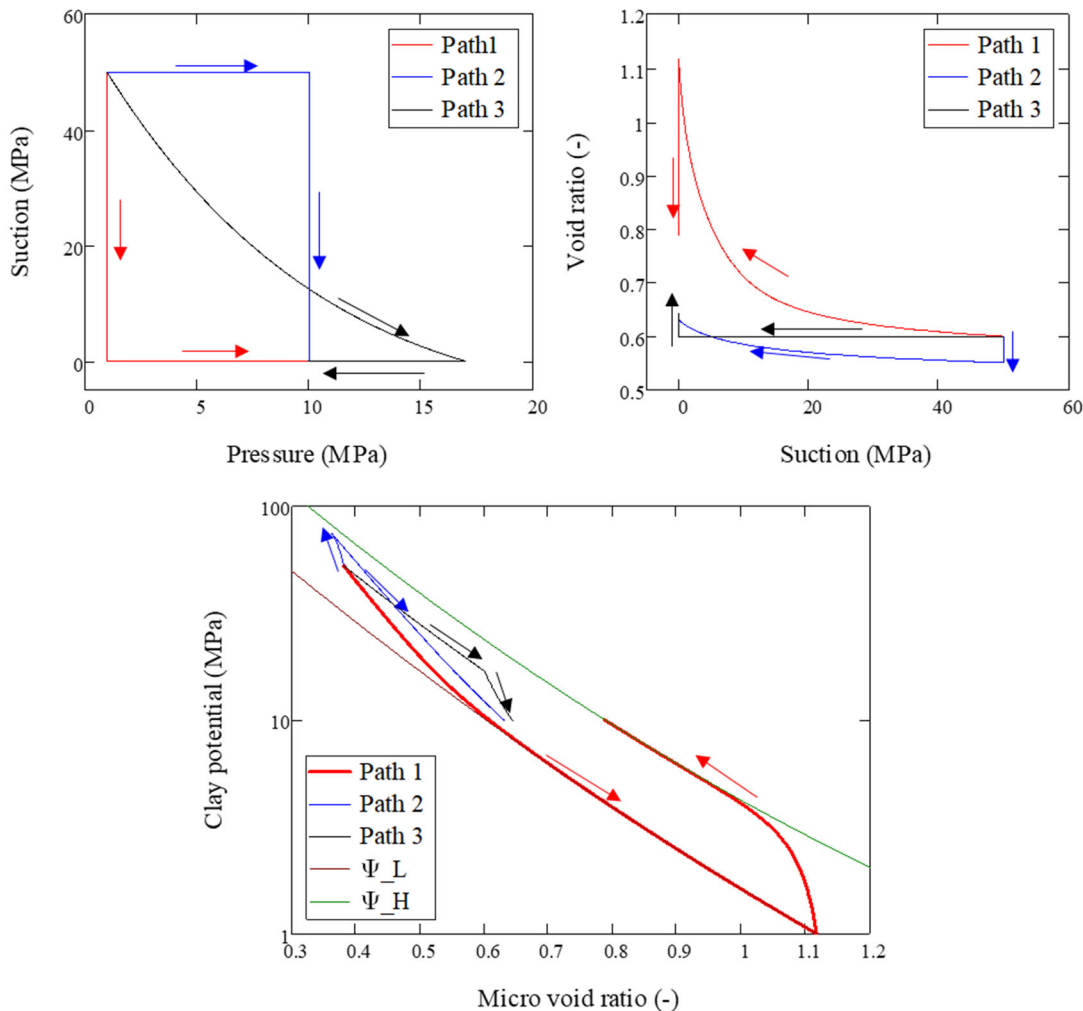


Figure 3-4. Different stress paths from unsaturated to saturated conditions. In s-p plane (upper left), as void ratio versus suction (upper right), and as clay potential versus micro void ratio (lower).

3.5 Stress path dependence from a saturated to an unsaturated state

These tests were performed from initially saturated conditions (i.e. with $e_\mu = e$). The initial suction and pressure were 0 and 1 MPa, respectively, and the initial f value was set to zero. With the used clay potential function this meant that the initial void ratio was about 1.3. Two different stress paths were analysed: i) by increasing suction (to 10 MPa) at constant pressure, followed by increasing pressure (to 10 MPa) at constant suction; ii) by increasing pressure at constant suction, followed by increasing suction at constant pressure

The stress path evolution was calculated by integrating either Eq (3-3) or Eq (3-5). For each increment, e_μ and f was integrated with Eq (3-1) and (3-6), respectively. Results show that the different stress paths resulted in quite similar final void ratios, but with a slightly higher value for Path 1 as compared with Path 2 (Figure 3-5, upper right). This is a consequence of a lower saturation degree (and e_μ value) in the case with Path 1 (lower graph). This shows that the model displays a stress path dependence from a saturated to an unsaturated state.

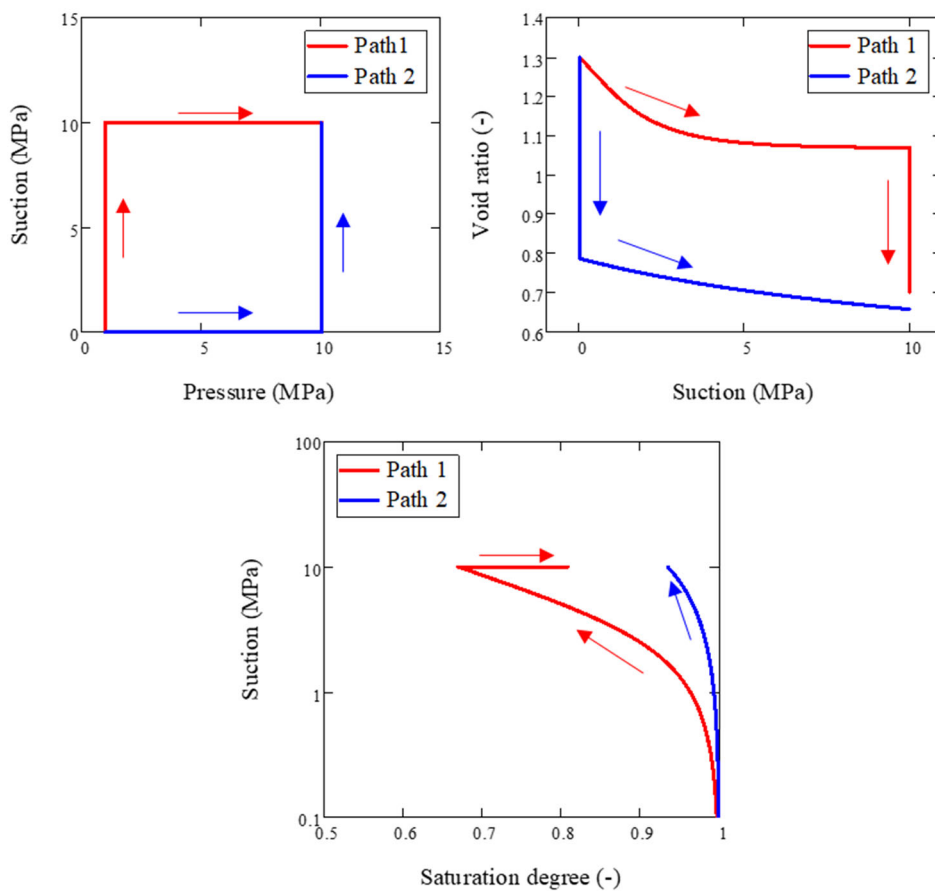


Figure 3-5. Calculated stress paths for two different dehydration paths. In s - p plane (upper left), as void ratio versus suction (upper right), and as suction versus degree of saturation (lower).

3.6 Feature table

All the analysed stress paths and their investigated dependences and irreversible behaviour have yielded affirmative answers which are compiled in the feature table below.

Table 3-1 Requested feature table for the HBM model.

Name of the constitutive law:		Hysteresis Based Material model	
Behaviour feature	D3.1	D3.3	Remarks
Mechanical behaviour			
Dependence of swelling strain on applied stress (at the same dry density) (Figure 1)	Y	Y	New calculations performed with developed model.
Dependence of swelling stress on dry density (at the same stress) (Figure 1)	Y	Y	New calculations performed with developed model.
Irreversibility of strains in wetting/drying cycles (Figure 2)	Y	Y	New calculations performed with developed model.
Dependence of swelling pressure on dry density (Figure 4)	Y	Y	New calculations performed with developed model.
Stress path dependence from an unsaturated to a saturated state (Figure 5)	-	Y	No analysis was performed in D3.1. New calculations performed with developed model.
Stress path dependence from a saturated to an unsaturated state (Figure 6)	N	Y	Analysis in D3.1 was treated as water-saturated throughout the changing state. New calculations performed with developed model.
Double structure/porosity considered?	Y	Y	For unsaturated conditions there are two pore spaces.
Are temperature effects considered in the model?	Y	Y	First and foremost, through the thermal expansion of water.
Dependence of strains developed in a temperature cycle (increase/decrease) on OCR (or stress) (Figure 7)	Y	Y	No new calculation apart from one in the D3.1 report.
Hydraulic behaviour (retention curve)			
Hysteresis	Y	Y	Inherent from the HBM model
Dependence on void ratio	Y	Y	Inherent from the HBM model
Double structure/porosity considered?	Y	Y	Micro pores water-filled and meso pores gas-filled at unsaturated states.

4 Task 3.3

This section describes the work concerning WP3 Task 3 focusing on the influence of two different hydro-mechanical stress paths on the final state of MX-80 bentonite. The two hydro-mechanical paths both consist of a wetting phase which is followed by a consolidation phase. The difference between the two paths is that the wetting phase takes place under:

Path 1 (P1): free swelling conditions (at constant axial stress) and
Path 2 (P2): confined conditions (at constant volume).

When carrying out the simulations an axisymmetric one-dimensional representation was first used since measured time evolutions of strain and stress were available to compare with. A point-model was then also developed since responses from such a model were requested as well.

The model description is given in section 4.1, where geometry, time scale, initial and boundary conditions as well as parameter values are given. Section 4.2 contains results and discussion. The results shown and discussed are stress – void ratio responses and time evolutions of strain and stress.

4.1 Model description

An axisymmetric geometry with radius = 17.5 mm and height = 12.5 mm was used. The used formulation is one-dimensional, i.e. a line-model, the radial dimension will not influence the solution. The geometry was discretized using a mesh with 10×1 elements in the axial \times radial direction. Both simulations were split into two phases of equal length, $t^* = 32$ days:

- Wetting phase (A - B) and (A - B'): $t = 0 \dots t^*$
- Consolidation phase (B -) and (B' -): $t = t^* \dots 2t^*$

t^* was chosen long enough as to ensure equilibrium at full saturation at the end of the wetting phase and enable a "quasi-static" process during the consolidation phase, i.e. no significant pore water pressure build-up.

As an alternative to the axially discretized model, the experiment was also reduced to be represented by a single point. In that case the geometry was discretized into a single element and the water balance was not included, the suction evolution was instead prescribed directly.

4.1.1 Initial conditions, boundary conditions, and parameter values

The initial conditions are listed in Table 4-1, where the quantities indicated by a tilde are functions defined in the theory section. The boundary conditions are defined in Table 4-2, Table 4-3 and Figure 4-1.

Table 4-1 Initial conditions.

Void ratio:	$e_0 = 0.85$
Water content:	$w_0 = 0.065$
Solid density:	$\rho_s = 2780 \text{ kg/m}^3$
Total stress:	$\sigma_0 = \sigma_0 \mathbf{1}$ where $\sigma_0 = -0.02 \text{ MPa}$
Suction:	$s_0 = 110 \text{ MPa}$
Micro void ratio:	$e_\mu^0 = 0.19$ Given by $e_\mu^0 = \frac{\rho_s}{\bar{\rho}_l(s_0)} w_0$
Path variable:	$f_0 = -0.73959 \mathbf{1}$ Given by $-\sigma_0 = \tilde{\alpha}(e_0, e_\mu^0)(\tilde{\Psi}_M(e_\mu^0)\mathbf{1} + \tilde{\Psi}_\Delta(e_\mu^0)f_0 - s_0\mathbf{1})$

Table 4-2 Mechanical boundary conditions at top boundary ($t^* = 32 \text{ days}$)

P1	(A-B):	Vertical stress 20 kPa	if $t < t^*$
	(B-):	Vertical stress ramping from 20 kPa to 20 MPa	if $t > t^*$
P2	(A-B'):	No vertical displacements	if $t < t^*$
	(B'-):	Prescribed vertical displacements	if $t > t^*$

Table 4-3 Boundary conditions identical for P1 and P2 models

Hydraulic:	No flow at the vertical boundary
	Inflow at top and bottom = $10^{-3} \left[\frac{\text{kg}}{\text{m}^3 \cdot \text{s} \cdot \text{MPa}} \right] \cdot \text{s}$ with an initial ramping during 1 h
Mechanical:	Rollers at the bottom and vertical boundary

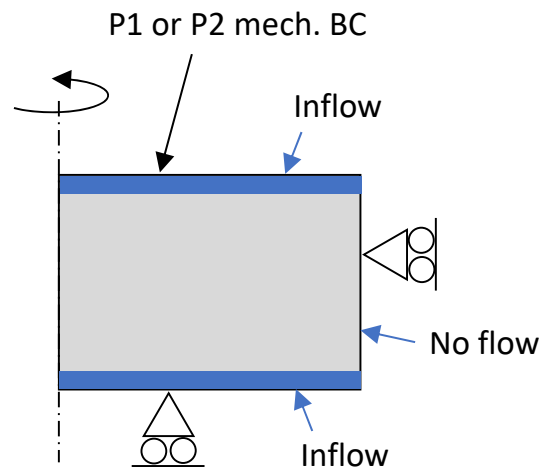


Figure 4-1. Schematic drawing of the axisymmetric geometry with hydraulic and mechanical boundary conditions indicated.

Table 4-4 Hydraulic parameters

Parameter	Value	Source
ρ_l^0	998 kg/m ³	Beacon D5.1.2 (Test 1B)
α	4.5 · 10 ⁻¹⁰ 1/Pa	Beacon D5.1.2 (Test 1B)
μ	1 · 10 ⁻³ Pa · s	Handbook value
e_{ref}	1	Åkesson et. al. (2010)
β	5.33	Åkesson et. al. (2010)
k_{ref}	2.4 · 10 ⁻²⁰ m ²	Åkesson et. al. (2010)
λ	3	Åkesson et. al. (2010)

Table 4-5 HBM parameters

Parameter	Value	Source
c_0^{low}	5.7035	Beacon D5.1.2 (Test 1B) (see below for the expression)
c_1^{low}	-6.3234	Beacon D5.1.2 (Test 1B) (see below for the expression)
c_2^{low}	1.1904	Beacon D5.1.2 (Test 1B) (see below for the expression)
c_3^{low}	-0.0838	Beacon D5.1.2 (Test 1B) (see below for the expression)
c_0^{high}	6.6008	Beacon D5.1.2 (Test 1B) (see below for the expression)
c_1^{high}	-6.6382	Beacon D5.1.2 (Test 1B) (see below for the expression)
c_2^{high}	1.6239	Beacon D5.1.2 (Test 1B) (see below for the expression)
c_3^{high}	-0.1463	Beacon D5.1.2 (Test 1B) (see below for the expression)
$\Psi_{high \& low}^0$	10 ⁶ Pa	For conversion to Pa (see below for the expression)
γ	7	Beacon D3.1
K_{aa}	40	Beacon D5.1.2 (Test 1B)
K_{ab}	40	$K_{ab} = K_{aa}$ (has no effect in the present case)
R	0.9	Beacon D5.2.2 (obtained from studying small example problems)
e_{step}	0.05	Beacon D5.2.2 (obtained from studying small example problems)

In this task the clay potential contributions Ψ_M and Ψ_Δ were expressed using functions,

$$\tilde{\Psi}_\beta(e_\mu) = \Psi_\beta^0 \exp(c_0^\beta + c_1^\beta e_\mu + c_2^\beta e_\mu^2 + c_3^\beta e_\mu^3) \text{ where } \beta = high, low, \quad (4-1)$$

according to,

$$\Psi_M = \frac{\Psi_{high} + \Psi_{low}}{2} \quad \text{and} \quad \Psi_\Delta = \frac{\Psi_{high} - \Psi_{low}}{2}. \quad (4-2)$$

4.2 Results and discussion

In Figure 4-2 void ratio is given as a function of total vertical (compressive) stress. Both experimental and model data are plotted as well as the high and low clay potential functions used in the model. In the experiment as well as the models the void ratio was calculated from knowing the initial value of the void ratio and the displacement of the top surface.

The model generally agrees well with the experiments. There is, however, a difference between the P1 experiment and P1 model during the first part of the consolidation. The experiment indicates a stiffer response at the first part of the consolidation. This takes the measured response outside of the range allowed in the model, roughly defined as between the high and low clay potential functions. Later in the consolidation process of P1 however, the measured and calculated responses converge and agree well.

One cause for the difference could be that the assumption adopted in the model of insignificant effect from wall friction is incorrect. Another cause could be that the high clay potential function is not representative for the material at high void ratios.

It should, however, be remembered that only one set of measurements, from one of the P1-tests (P1-3), is given. The issue of reproducibility, how well the given data represents an ideal or average P1-test, is unknown. To get some information about this, in Figure 4-3, P1-3 measurements, $e(0.5 \text{ MPa}) = 2.2$, $e(1.0 \text{ MPa}) = 1.72$, and $e(2.0 \text{ MPa}) = 1.28$, have been plotted together with results from a compression test reported in Börgesson et. al. (1995). A comparison gives that the two experimental data sets do not agree very well. Thus, an uncertainty exists.

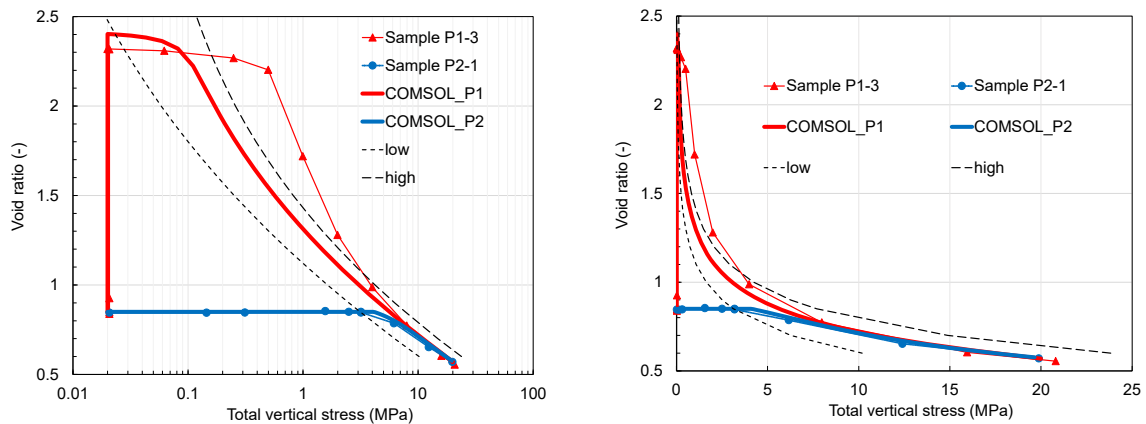


Figure 4-2. Measured (Sample...) and computed (COMSOL...) responses in void ratio – total vertical (compressive) stress space. The high and low clay potential functions used in the model are also plotted. In the left graph stress is plotted on a logarithmic scale and in the right graph stress is plotted on a linear scale.

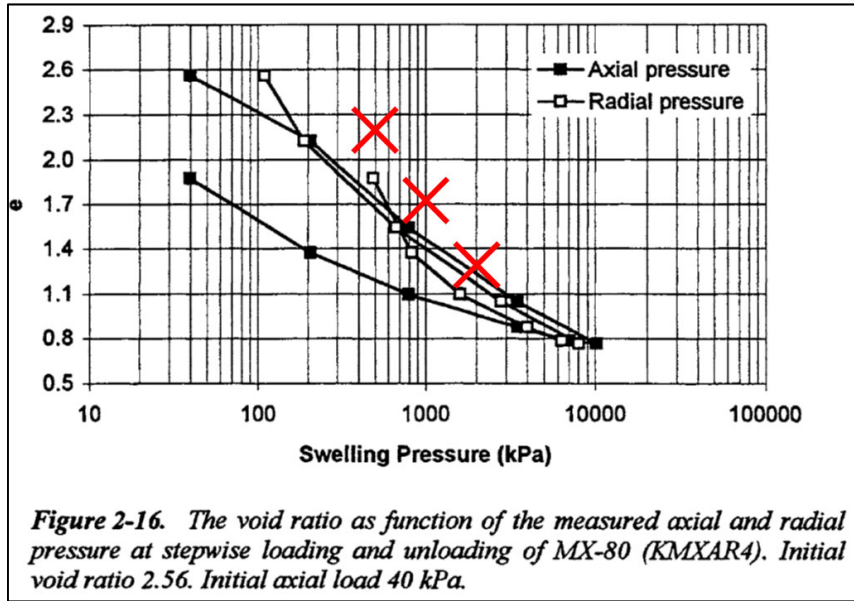


Figure 4-3. Original graph taken from Börgesson et. al. (1995). Some P1-3 measurements recorded under the compression phase have been plotted for comparison.

Results from reducing the model domain to a single point, using a single element, were also requested. For the point-model, the water mass balance was not solved for, instead the suction evolution was prescribed directly. In Figure 4-4 the output from the point-model can be compared with the output from the line-model. The results of the models agree well.

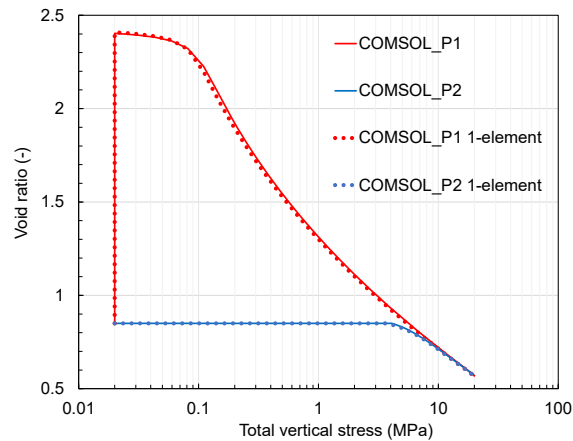


Figure 4-4. Void ratio – total vertical stress space responses obtained from using the line-model (10 elements) and the point-model (1 element).

Since the line-model incorporates the water mass balance and simulates the water uptake process, time evolutions of vertical strain and vertical swelling pressure can be compared with what was measured in the experiments, see Figure 4-5 and Figure 4-6, respectively.

In Figure 4-5 three experimental vertical strain responses during the water-uptake phase for P1 tests are shown together with the corresponding simulated response. When comparing measurements and computations, the build-up of strain is faster in the model, but the final level of strain agrees well with what was measured.

One reason for the overestimation in strain build-up rate could be that the water uptake rate is overestimated. This could in turn be due to that the used hydraulic boundary condition,

$$\text{influx} = 10^{-3} \left[\frac{\text{kg}}{\text{m}^3 \cdot \text{s} \cdot \text{MPa}} \right] \cdot s, \quad (4-3)$$

is unrepresentative of the conditions in the experiment and/or from representing the material as too permeable, i.e. use of

$$\tilde{\kappa}(e, e_\mu) = \kappa_{ref} \left(\frac{e}{e_{ref}} \right)^\beta \left(\frac{e_\mu}{e} \right)^\lambda, \quad (4-4)$$

results in too high values. It could be mentioned that half the value of κ_{ref} used here has been found suitable for some simulations, e.g. Task 1a in WP5.

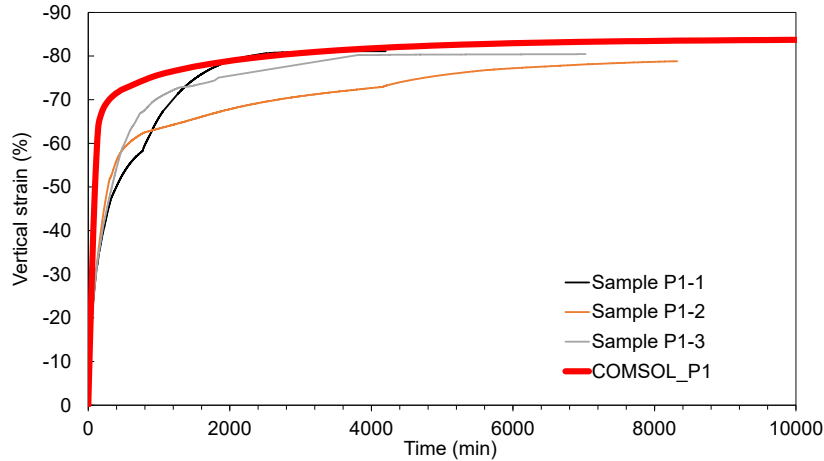


Figure 4-5. Measured and computed vertical strain for P1 tests.

In Figure 4-6 three experimental vertical swelling pressure responses during water uptake for P2 tests are shown together with the corresponding simulated response. The build-up of stress is somewhat faster in the model and the calculated final level of stress, about 4.1 MPa, is too high as compared to what was measured, from 3.12 MPa to 3.55 MPa.

Reasons why the build-up rate of stress is overestimated can be found in the section above discussing the build-up rate of strain.

To investigate why the model overestimates the swelling pressure at the end of the saturation process it can be used that, at zero suction and full saturation, the model reduces to,

$$-\sigma = \Psi_M(e)\mathbf{1} + \Psi_\Delta(e)\mathbf{f}. \quad (4-5)$$

If evaluating the swelling pressure at $e = 0.85$ and using $\mathbf{f} = -\mathbf{1}$, a value of 3.12 MPa is obtained. This is in line with what was measured in the P2 experiments where the swelling pressure ranged from 3.12 MPa to 3.55 MPa. This indicates that the high stress level (about 4.1 MPa) obtained from the model at the end of the saturation process is not a consequence of using unrepresentative clay potential functions. They allow for suitable swelling pressures at the initial void ratio.

One reason for obtaining a higher value of swelling pressure could come from the adopted initial state. If using $f_0 = -0.74$ in the equation above, the value used in the simulations, the evaluated swelling pressure is 3.71 MPa. This exactly corresponds to what was obtained from the point-model which shows that the implementation behaves as wanted. It should be noted that the initial value of the path variable is given by what is described in Table 4-1. Thus, with the current model setup and choices made concerning the initial state ($\sigma_0 = -0.02 \mathbf{1}$ MPa, $s_0 = 110$ MPa, and $\mathbf{f}_0 = f_0 \mathbf{1}$) the value of f_0 is given.

The remaining difference from 3.71 MPa to 4.1 MPa then comes from expanding the point-model to a line-model. The expansion enables the void ratio and path variable fields to change from the initial state during the saturation phase from state A to state B', see Figure

4-7. For the case studied here, this gives rise to a vertical stress of higher magnitude as compared to if the void ratio and path variable remain at their initial values.

Another reason for the difference in swelling pressure could be that wall friction contributes significantly to the behavior of the system. As can be seen in Figure 4-7, despite the confined conditions at a “global” scale, the mechanics in material points are not constrained by this condition “locally”, the void ratio field changes when going from state A to state B'. Thus, if friction was to be introduced, the behavior at the local scale could be affected.

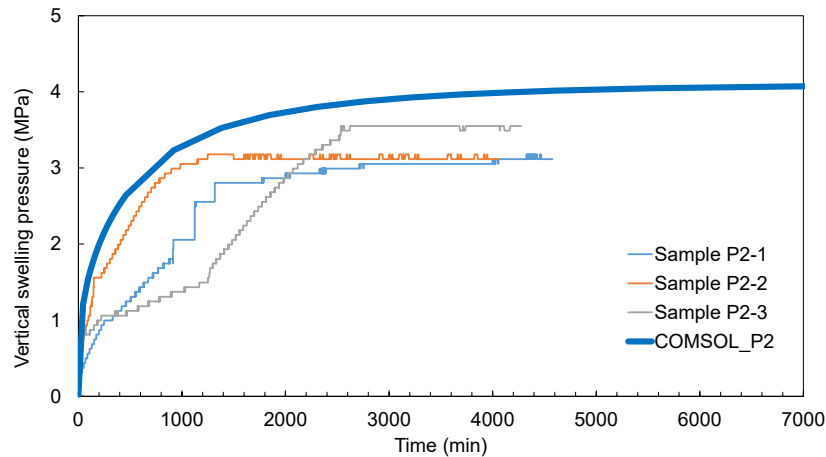


Figure 4-6. Measured and computed vertical swelling pressure for P2 tests.

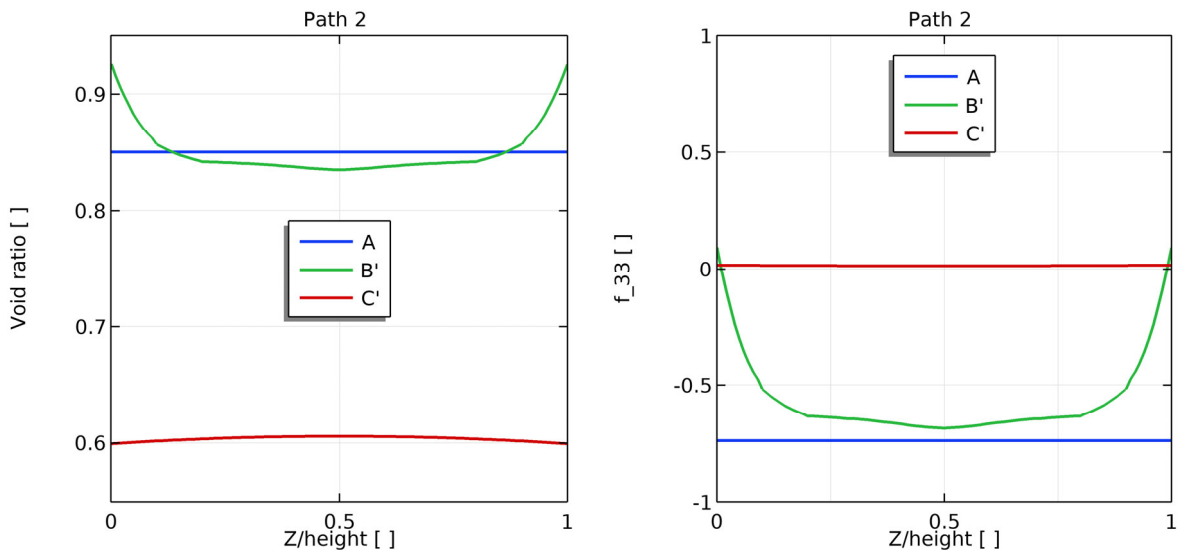


Figure 4-7. Vertical profiles of void ratio (left) and vertical component of the path variable (right) at states A, B', and C' for the P2 model.

5 Performance of the model and assessment of predictive power

As shown in section 3, the HBM model, initially developed to represent compacted bentonite, can using a single set of parameters, produce representative solutions for a large range in the variables it is expressed in. Using a proper coupling between mechanical and hydraulic variables and a formulation which enables generality makes the model very versatile. Versatile in the sense that material characteristics such as retention, swelling pressure and deviatoric stress at failure always correspond to each other, but also in the sense that the

material system may be viewed from different aspects or be exposed to very different conditions, without losing validity of the representation provided by HBM. A firm basis in a thermomechanical framework, relevant for our application, is also considered a strength when assessing the capabilities to make predictions. The formulation can be characterised as being rigid in the sense that excessive tweaking of the parameters is very limited. This is of course positive from a perspective of performing predictive analyses. Once set up properly, one can use the same parameterisation to perform calculations of very different cases.

The clay potential function, which is dependent on the void ratio and the path dependent variable, lies at the very heart of HBM and governs much of the fundamental behaviour of the model. To enable valid simulations, it is therefore vital to define this function with care to match experimental data accurately over a large range of void ratios. During Beacon it has become evident that much effort should be put into obtaining an accurate parametrisation and fit to the experimental data: unconfined retention, swelling pressure and deviatoric stress at failure.

Limits to the generality of the original HBM formulation became evident when bentonite buffer components in other forms than compacted blocks, such as pellet filled gaps or granular filling as in WP5.3, were represented using the model. This is not surprising since such changes of the bentonite buffer leads to changes in the material structure, which in turn affects the material behaviour/properties. In WP5.3 this was pragmatically addressed by designing a new contact area function and using a different permeability for the granular filling, but for some cases there might be a need to go back and revisiting the material structure assumptions and reformulate the material model from there.

Another issue which could limit the predictive capacity is whether HBM can be implemented in a numerically cheap/stable version. As for now the model has been implemented in Comsol Multiphysics. It is using this implementation that most of the modelling reported in Beacon has been carried out. It has, however, often been difficult to achieve converge and produce results. On some occasions simpler representations of the model setup, such as simplifying the geometry or omitting features such as wall friction, were necessary. If this comes from properties of the formulation (such as high nonlinearity) or the method used when implementing the model (or both) is hard to determine at this stage. To enable simulation of larger and more complex systems, such as including wall friction or many buffer constituents with different properties, it is first a necessity to make simulations of small and simple systems more numerically efficient than is currently the case.

6 Concluding remarks

The HBM formulation has progressed significantly during the Beacon project. At the very beginning it only covered isotropic and saturated conditions and now it has been generalised as to incorporate general hydraulic and mechanical states. The numerical solution of the model has also progressed. To begin with a math software such as MathCad could be utilised, but when the tasks grew in complexity the model was implemented in the general-purpose finite element solver Comsol Multiphysics. The Comsol implementation was also changed significantly when the unsaturated formulation was incorporated.

One of the main insights gained from WP3 is that the HBM model agrees well with how bentonite behaves for a variety of different scenarios using a single set of parameters for one type of bentonite. There is no need to “tweak” the parameters for different cases in order for the model to give representative responses.

Furthermore, we have understood the importance of availability of suitable and accurate experimental data (swelling pressure curves, deviatoric stress at failure, and unconfined

retention) when fitting the clay potential present in HBM. Another side of this is the importance of using a suitable parametrisation of the clay potential.

When developing the implementation and working with the tasks provided in WP3 and WP5 we have gained in knowledge about solution of multi-physical and highly coupled models. Even though much effort has gone into trying to improve the Comsol implementation it is presently lacking somewhat in numerical performance regarding stability and efficiency.

References

Börgesson L, Johannesson L-E, Sandén T, Hernelind J, 1995. Modelling of the physical behaviour of water saturated clay barriers. Laboratory tests, material models and finite element application. SKB TR-95-20, Svensk Kärnbränslehantering AB.

D3.3



Annex D

Contribution to Deliverable 3.3

DELIVERABLE (D3.3) EPFL Report

Author(s): Jose A. Bosch, Alessio Ferrari, Lyesse Laloui

Reporting period: 01/06/20 – 31/05/22

Date of issue of this report: **24/08/21**

Start date of project: **01/06/17**

Duration: 60 Months

This project receives funding from the Euratom research and training programme 2014-2018 under grant agreement No 745 942		
Dissemination Level		
PU	Public	X
RE	Restricted to a group specified by the partners of the Beacon project	
CO	Confidential, only for partners of the Beacon project	

REVIEW

Name	Internal/Project/External	Comments
All Beacon partners	Project internal	

DISTRIBUTION LIST

Name	Number of copies	Comments
Seifallah BEN HADJ HASSINE (EC)	Digital	
Beacon partners	Digital	

Abstract

Briefly describe the activity that has been performed and results that have been obtained (include significant nonconformities from activity plan and method description)

Content

2	Introduction	5
3	Description of the model.....	5
4	Basic capabilities of the model	9
5	Task 3.3	10
6	Performance of the model and assessment of predictive power	13
7	Concluding remarks.....	16
	Acknowledgments	17
	References	17
	Appendix 1.....	Error! Bookmark not defined.

2 Introduction

This report summarizes the stress-strain model developed by EPFL in the context of the BEACON project. In the deliverable D3.1, ACMEG-TS was presented as the model available at the start of the project. It consists of a stress-strain constitutive model that comprises soil behaviour under unsaturated and non-isothermal conditions (François and Laloui, 2008). The model was formulated based on experimental evidence of non-active soils and therefore the main objective of EPFL has been to enhance and extend ACMEG-TS formulation to better model highly active soils such as compacted bentonite.

The water retention curve and the loading collapse curve were identified in report Beacon D3.1 as the points on which ACMEG-TS could be subjected to modifications for a better description of the behaviour of compacted bentonite. The model has been substantially modified with respect to the version available at the start of the project. A new version of the model, incorporating a new water retention and loading collapse formulations was presented in Deliverable D3.2.

As in ACMEG-TS, Bishop effective stress using the degree of saturation as pore pressure averaging parameter is used as the variable conjugated to elastic strains, while now the degree of saturation is used as the variable that expresses the increase of yield stress with suction, defining a loading collapse curve. The degree of saturation is computed from the new water retention model, which takes explicitly into account the existence of adsorbed water and the dependency of free water on the dry density. In addition, the elastic domain is expressed as a function of temperature in order to consider the possibility of thermo-plastic behaviour. In addition, within the WP3, the constitutive model has been implemented in the finite element code Lagamine (Charlier 1987) for the analysis of boundary value problems.

In this report the complete Thermo-Hydro-Mechanical formulation is presented. A verification exercise, corresponding to two stress paths on granular MX80 bentonite is included. Afterwards, based on the results obtained within WP5, an assessment of the model capabilities is given.

3 Description of the model

The model is formulated in the framework of a generalised effective stress and elastoplasticity. The elastic domain evolves with the stress history, the degree of saturation and the temperature. A water retention model that takes explicitly into account the existence of adsorbed water is used to predict the evolution of the degree of saturation with suction.

The total strain tensor ϵ is divided into elastic and plastic strains:

$$\epsilon = \epsilon^e + \epsilon^p \quad (1)$$

where the superscripts e and p denote elastic and plastic strains respectively. The following Bishop-type expression is used for the effective stress σ' (Nuth and Laloui 2008):

$$\sigma' = \sigma - [p_a - (p_a - p_w)S_r]\mathbf{I} \quad (2)$$

where σ is the total stress tensor and p_a is the pore air pressure. The equations of the model are written in terms of the stress invariants $p' = \frac{1}{3}\text{tr}(\sigma')$, $q = \sqrt{3}J$ and $\sin(3\theta) = 3\sqrt{3}\det \mathbf{s}/2J^3$, where $\mathbf{s} = \sigma' - p'\mathbf{I}$ and $J = \sqrt{\frac{1}{2}\text{tr}(\mathbf{s}^2)}$. Likewise, the strain invariants $\epsilon_v = \text{tr}(\epsilon)$ and $\epsilon_d = \sqrt{\frac{1}{3}\text{tr}(\boldsymbol{\gamma}^2)}$, where $\boldsymbol{\gamma} = \epsilon - \frac{1}{3}\epsilon_v\mathbf{I}$, are defined.

The thermo-elastic relationships are established as:

$$d\epsilon_v^e = \frac{p'}{\kappa} dp' + \frac{1}{3} [\beta_{T0} + \beta_{T1}(T - T_r)] dT, \quad d\epsilon_d^e = \frac{9(1-2\nu)p'}{2(1+\nu)\kappa} dq \quad (3 a, b)$$

where κ is the elastic volumetric compressibility parameter, ν is the poisson ratio, T_r is a reference temperature and β_{T_0}, β_{T_1} are thermo-elastic parameters (Laloui and François, 2009). The yield surface, f_Y in the stress space takes the following form (Collins and Kelly, 2002):

$$f_Y = q^2 - M^2 \left[\alpha + (1 - \alpha) \left(\frac{2p'}{p_Y} \right) \right]^2 (p'_Y - p')p' = 0 \quad (4)$$

where M is the critical stress ratio, α is a material parameter that controls the shape of the yield surface as well as the flow rule and p'_Y is the yield pressure, which depends on the plastic strains, S_r and T . A stress path dependent strength on Lode's angle θ is incorporated by taking M as (van Eekelen, 1980; Vilarassa et al. 2017):

$$M(\theta) = M_c \left[\frac{1 + b_L \sin(3\theta)}{1 + b_L} \right]^{-0.229} \quad (5)$$

where:

$$b_L = \frac{\left(\frac{M_c}{M_e} \right)^{1/-0.229} - 1}{\left(\frac{M_c}{M_e} \right)^{1/-0.229} + 1} \quad (6)$$

where $M_c = \frac{6 \sin \phi'_c}{3 - \sin \phi'_c}$, $M_e = \frac{6 \sin \phi'_e}{3 + \sin \phi'_e}$ and ϕ'_c and ϕ'_e are the shear strength angles at failure for compression paths and extension paths respectively.

In the previous version, the loading collapse curve, which was formulated in terms of suction, presented some disadvantages in capturing consistently swelling under low stress and swelling stress paths. In the new formulation, the loading collapse curve depends on the degree of saturation:

$$\frac{p'_Y}{p'_r} = \left(\frac{p'_{TY}}{p'_r} \right)^{\frac{\lambda_s - \kappa}{\lambda(S_r) - \kappa}} \quad (7)$$

where p'_{TY} is the saturated yield pressure at current temperature, p'_r is a reference stress, λ_s defines the elastoplastic compressibility at saturated states and $\lambda(S_r)$ expresses the evolution of elastoplastic compressibility with S_r :

$$\lambda(S_r) = \lambda_s - r(\lambda_s - \kappa)(1 - S_r^\zeta)^\xi \quad (8)$$

where r , ζ and ξ are material parameters that generally depend on the initial compaction state. Eq. (8) is a modified version of the expression proposed by Zhou et al. (2012). As the unsaturated compressibility largely determines the evolution of swelling pressure during hydration, this expression was found useful to fit different responses exhibited by the bentonite. Also, using the degree of saturation instead of suction, allows to incorporate naturally the transition to saturated states, irrespectively of the current air entry value. This was a shortcoming in the previous formulation as a sharp transition from unsaturated to saturated states was obtained during swelling pressure tests. A representation of the volume change equations is shown in Figure 1.

As in ACMEG-TS the dependency of yield on temperature is the proposed by Laloui and Cekerevac (2003) and Laloui and François (2009):

$$p'_{TY} = p'_{Ys} \left[1 - \gamma_T \ln \left(\frac{T}{T_r} \right) \right] \quad (9)$$

where p'_{Ys} is the hardening variable (corresponding to the yield pressure at $S_r = 1$ and $T = T_r$ for a fixed ϵ'_v) and γ_T is a material parameter. A graphical representation of the yield surface in the (p', q, T) plane is shown in Figure 2.

The ratio of plastic strain increments is given by the following flow rule (Collins and Kelly, 2002):

$$\frac{d\epsilon_d^p}{d\epsilon_v^p} = \frac{q}{M^2(p' - p'_Y/2) \left[\alpha + (1 - \alpha) \left(\frac{2p'}{p'_Y} \right) \right]^2} \quad (10)$$

The saturated yield pressure, p'_{Ys} evolves according to volumetric plastic strains:

$$\frac{dp'_{Ys}}{p'_{Ys}} = \frac{d\epsilon_v^p}{\lambda_s - \kappa} \quad (11)$$

A key modification to ACMEG-TS is a new water retention formulation in order to fit both unconfined and constant volume water retention of bentonite. This is paramount because the degree of saturation controls the mechanical response through the yield surface and the effective stress. The water retention model is formulated in terms of the water ratio, $e_w = e_{w,f} + e_{w,a}$ where $e_{w,f}$ is the free water ratio and $e_{w,a}$ is the adsorbed water. Free water ratio $e_{w,f}$ is modelled using a similar expression to that proposed by Dieudonné et al. (2017) as:

$$e_{w,f} = (e - e_{w,a}) \left[1 + \left(a(e - e_{w,a})^b s \right)^n \right]^{1/n-1} \quad (12)$$

where n , a and b are material parameters and s stands for matric suction. As proposed by Revil and Lu, (2013), $e_{w,a}$ follows a Freundlich isotherm:

$$e_{w,a} = e_{w,a}^c \left[\exp \left(- \frac{M_w}{\rho_{w,a} RT_r} s \right) \right]^{1/m} \quad (13)$$

where $\rho_{w,a}$ is the density of adsorbed water, M_w is the molar mass of water, $e_{w,a}^c$ is the adsorption capacity parameter and m is a material parameter. Note that while free water ratio depends on the current void ratio, the adsorbed water ratio depends solely on suction.

Also in the context of the WP3, the new constitutive equations have been implemented in the FEM code Lagamine. The numerical integration is performed using an explicit scheme with automatic error control (Sloan, 1987; Sheng et al., 2003), incorporating S_r and T as additional stress variables.

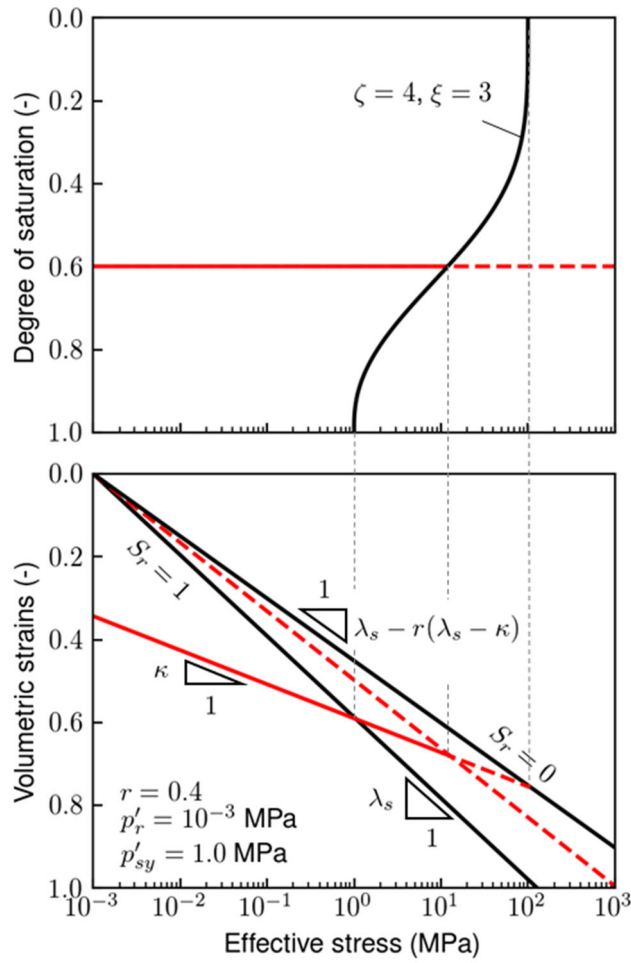


Figure 1. Geometrical significance of the mechanical parameters for volume change behaviour

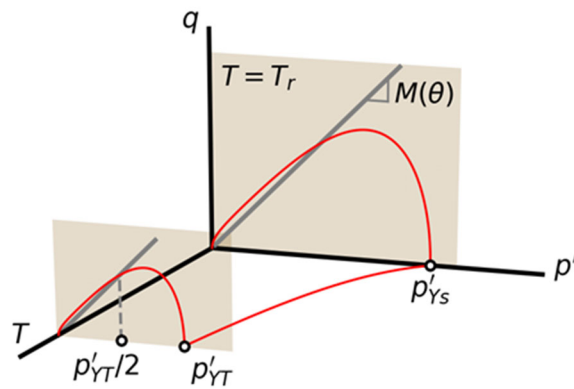


Figure 2. Representation of the yield surface in the space (q, p', T)

Table 1: List of input parameters of the developed model

Mechanical model	Water retention model
κ	a
ν	b
λ_{sat}	n
$\phi'_c = \phi'_e$	m
α	$e_{w,a}^c$
p'_r	$\rho_{w,a}$
r	
ζ	
ξ	
β_{T0}	
β_{T1}	
γ_T	

4 Basic capabilities of the model

Table 2 summarises the features of the model. The capabilities of the new model for the different stress paths were evaluated in D3.2, except for the thermo-mechanical part which has remained unchanged from the one reported in D3.1.

Table 2. Updated table of model capabilities.

Name of the constitutive law: ACMEG-TS			
Behaviour feature	D3.1	D3.3	Remarks
Mechanical behaviour			
Dependence of swelling strain on applied stress (at the same dry density)	Yes	Yes	Swelling strain under low stress is more consistent with experimental evidence in the new version
Dependence of swelling strain on dry density (at the same stress)	Yes	Yes	
Irreversibility of strains in wetting/drying cycles	Yes/no	Yes	Previous version: Final state not consistent with initial OCR New version: Consistent with experimental evidence

Dependence of swelling pressure on dry density	Yes	Yes	In the new version the stress collapse during swelling pressure can be controlled through specific input parameters
Stress path dependence from an unsaturated to a saturated state	Yes	Yes	In the new version the stress path dependence is an effect of different radial stress development during wetting
Stress path dependence from a saturated to an unsaturated state	Yes	Yes	
Double structure/porosity considered?	No	No	
Are temperature effects considered in the model?	Yes	Yes	
Dependence of strains developed in a temperature cycle (increase/decrease) on OCR (or stress)	Yes	Yes	
Hydraulic behaviour (retention curve)			
Hysteresis	Yes	No	
Dependence on void ratio	Yes	Yes	The dependency has been revised in the new model to better predict bentonite behaviour
Double structure/porosity considered?	No	Yes	In the new model: division between free water and adsorbed water

5 Task 3.3

The results of simulating the stress path tests performed on granular MX80 bentonite, using the developed model, are presented in this section. In the context of WP3, the simulations are performed using a single gauss point, therefore no transient (flow) conditions are considered. This allows to clearly assess the capabilities of the stress-strain constitutive model. The initial state considered in the simulations is presented in Table 3.

Table 3. Initial state of the samples

Vertical stress (MPa)	Void ratio	Water content (%)	Degree of saturation (%)	Dry density (g/cm ³)	Density of the solid phase (g/cm ³)	Suction (MPa)
0.021	0.85	6.6	21	1.48	2.74	100

The calibration of the parameters has been made on the basis of the water retention tests by Seiphooori et al. (2014) and the two stress path tests. The water retention curve has been fitted based on the free swelling data provided by Seiphooori et al. (2014) The model fit is shown in Figure 3.

Once the water retention model is calibrated, the effective stress can be predicted, and the mechanical parameters can be calibrated. The elasticity parameter κ has been set in order to fit the final value of swelling strains upon wetting under constant load. The Poisson ratio ν has

been set to $\nu = 0.25$. The elastoplastic compressibility λ_s is determined on the basis of the slope of the normal compression line. This value has been chosen to be representative of the range of stress close to the swelling pressure. The shear strength angle is set the same for compression as extension, $\phi'_c = \phi'_e = 12^\circ$ based on the data from triaxial tests on saturated MX80 block bentonite reported by Dueck and Nilson (2010). The parameter α is set to $\alpha = 1$ which implies that the yield surface in the deviatoric plane is equivalent to the Modified Cam Clay model and that the flow rule is assumed to be associated. The parameters defining the elastoplastic compressibility under unsaturated states, i.e. r , ζ , ξ are defined in order to give a similar trend of the development of swelling pressure (given the already defined parameters) as shown in Figure 4. In order to do so at the single element level, the simulated evolution of swelling pressure in terms of suction has been compared to the measured evolution of swelling pressure in terms of time. The values for the input parameters used to model the tests are summarized in Table 4.

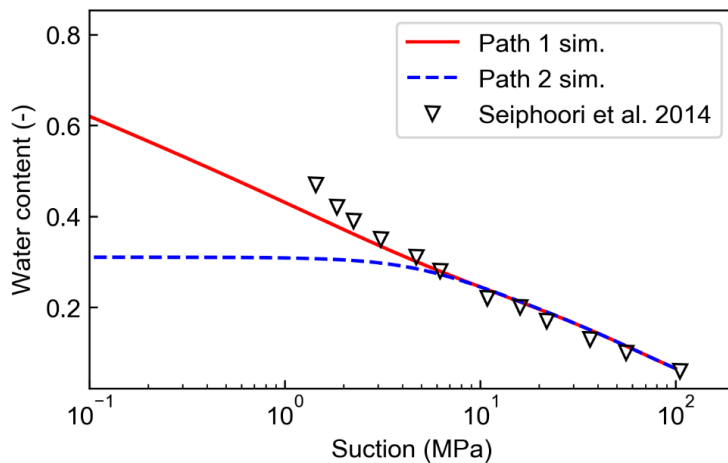


Figure 3. Water retention model calibration. The experimental data corresponds to free swelling conditions obtained by Seiphoori et al. (2014).

The model results in the plane vertical stress - void ratio of the two stress paths are shown in Figure 5. The model captures the overall response consistently for the two stress paths, despite quantitative discrepancies in the first loading stage of the path 1 (B-C), and a slight overprediction of swelling pressure. In line with the experiments, the normal compression line is not affected by the stress path followed to saturate the sample.

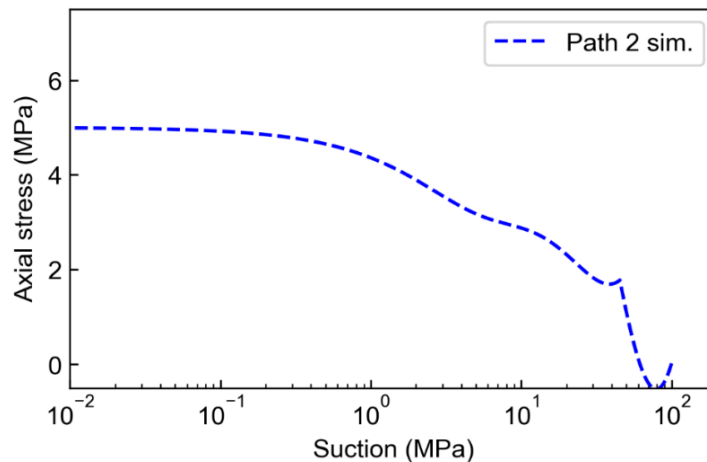


Figure 4. Results of the swelling pressure stage in Path 2 in terms of suction-vertical stress.

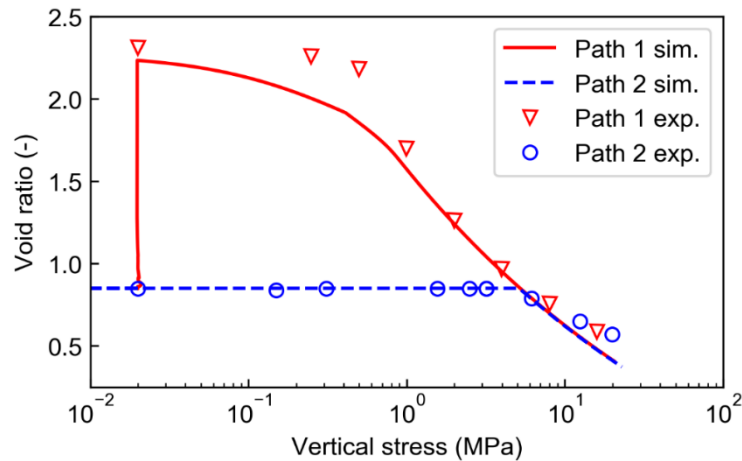


Figure 5. Results of the two stress paths simulated in the vertical stress – void ratio plane.

Table 4. Input parameters used for the simulations (isothermal).

Mechanical model		Water retention model	
Parameter	Value	Parameter	Value
κ	0.087	a	0.9 MPa^{-1}
ν	0.25	b	1.5
λ_{sat}	0.20	n	1.8
$\phi'_c = \phi'_e$	12°	m	0.57
α	1.0	$e_{w,a}^c$	0.55
p'_r	10^{-4} MPa		
r	0.25		
ζ	1.5		
ξ	0.65		

The model can reproduce reasonably well the two stress paths in terms of void ratio and vertical stress. The result is overall satisfactory in the sense that the same parameters for the two stress paths have been used, giving confidence in its use for boundary value problems. One of the merits of the model is that requires relatively few parameters that can be derived from conventional tests as the present case. There are some discrepancies at specific stress levels in both stress paths, the expected causes of which are exposed in the following.

For Path 1 it is believed that one limitation concerns the hypothesis of small strains which are certainly beyond limits, given that the strains in both swelling and compression reach about 80 %. The non-linearity of the compression line might be better reproduced if large strains in the constitutive equations are taken into account. Additionally, as a result of the significant swelling, probably induced by a high radial stress, an anisotropic rearrangement of the fabric was observed from the SEM experiments. This could be a factor that explains the initial stiffness of the saturated bentonite at the initial stage of the compression. As no microstructural features have been incorporated to the model at this stage, this behaviour has not been attempted to be reproduced.

In the case of Path 2, it is observed that the vertical swelling pressure is overestimated. This is, at least partly, because of the one-element simulation that results in the development of isotropic swelling pressure. The experience from modelling swelling pressure tests in WP5 indicates that when the swelling pressure path is modelled as a boundary value problem, the development of radial stress is higher than the axial stress. Afterwards, the compression stage involves a gradual change of the stress-state towards higher axial stress than radial stress until reaching the virgin compression line, that coincides in both paths.

6 Performance of the model and assessment of predictive power

In this section the results obtained with the model in the context of WP5 (application to boundary value problems) are summarised. In particular, the FEBEX insitu test was successfully simulated using the newly developed constitutive model. The results were reported in the Beacon deliverable D5.2.2 and they allow for an assessment of the model performance and predictive power.

The water and heat flow parameters were based on prior studies performed by EPFL, without significant adjustments, and for conciseness the thermo-hydraulic results are not going to be reported here. The mechanical model has been exclusively calibrated with laboratory tests, therefore the results in terms of stress, dry density and water content, can be considered predictions. Because of its importance, the calibration of the model parameters is briefly reported in this section.

The water retention curve was calibrated with the data presented by Lloret et al. (2003) which is shown in Figure 6. The tests consisted in wetting paths, performed under constant volume conditions and at dry densities that are representative of that in the Febex test. The water retention is seen to be rather independent on dry density for suctions above 10 MPa, which suggests that water at high suction is held by means of surface adsorption.

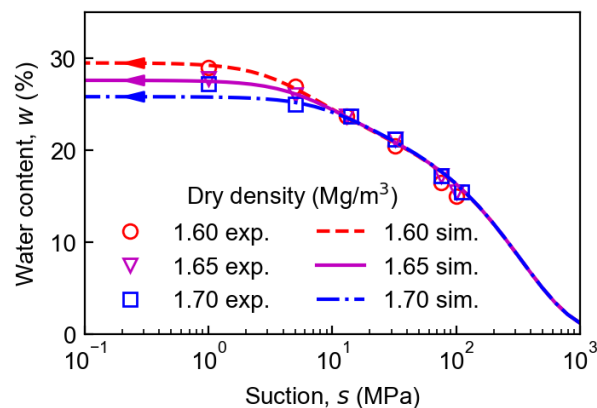


Figure 6. Calibration of the water retention curve of FEBEX bentonite for wetting under constant volume conditions at three different dry densities. Experimental data from Lloret et al. (2003).

As shown in Task 3.3, one of the key parameters to be calibrated in order to ensure reliable predictions is the slope and position of the saturated normal compression line. This determines the value of swelling pressure and void ratio at saturation. For the FEBEX test, this calibration was performed with data obtained by Lloret et al. 2003 from suction-controlled oedometric tests as shown in Figure 7 (test at $s = 0$)

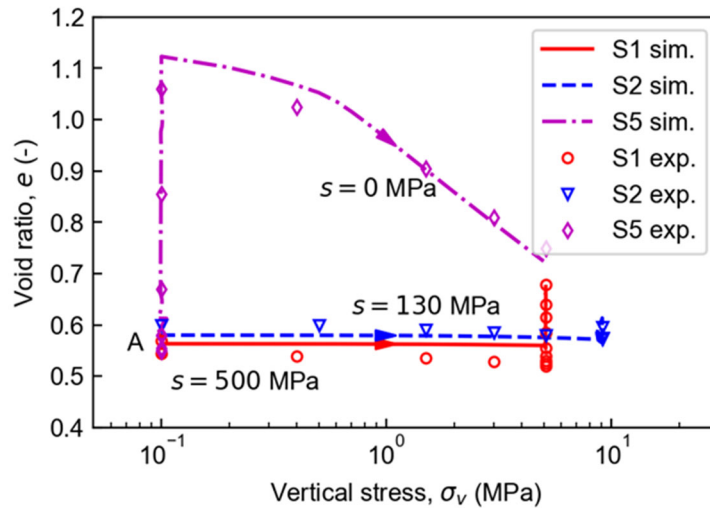


Figure 7. Calibration of the mechanical parameters against suction controlled oedometer tests performed by Lloret et al. (2003).

The loading collapse curve determines the evolution of swelling pressure during hydration. Accordingly, parameters ζ and ξ were calibrated using the swelling pressure tests reported by Lloret et al. (2003), with a dry density close to 1.6 Mg/m^3 , which represents the density of the overall buffer, including the existence of gaps between blocks. This is because this stress path is more sensitive to these parameters than those of wetting under constant load. The calibration with these swelling pressure tests is shown in Figure 8.

The simulation involved all construction and operation stages, including the dismantling operations, which affected the final measurements of bentonite variables, especially dry density and water content. Figure 10 shows the results in two sections (hot and cold section respectively) in terms of total stress. The predicted magnitude of total stress developed in the long term is in agreement with that measured in the field. Figure 10 shows the final profiles of dry density and Figure 11 the profiles in terms of water content. Both are compared to the post-mortem measurements obtained after the 18 years of test operation. In general, the evolution and the final state of the barrier were well captured by the model, despite some discrepancy close to the heater. It should be noted that the dry density at section B2 was already lower at the beginning of the test operation due to the shape of the tunnel front, and this was not considered in the present model. The overall performance of the constitutive model has been satisfactory and shows a good potential for the predictive analysis of similar problems for which results of laboratory tests are available.

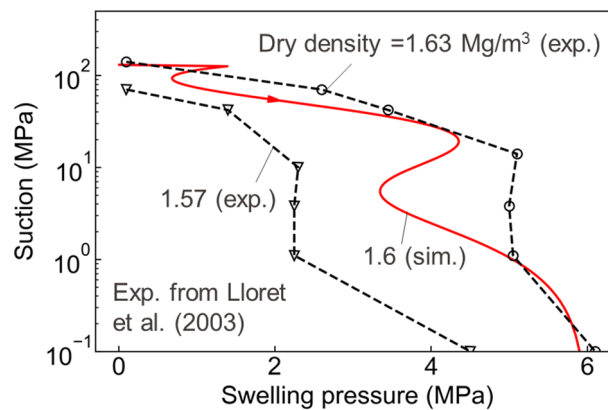


Figure 8. Model calibration of the swelling pressure developed at a dry density representative of the overall buffer. Experimental data obtained by Lloret et al. (2003).

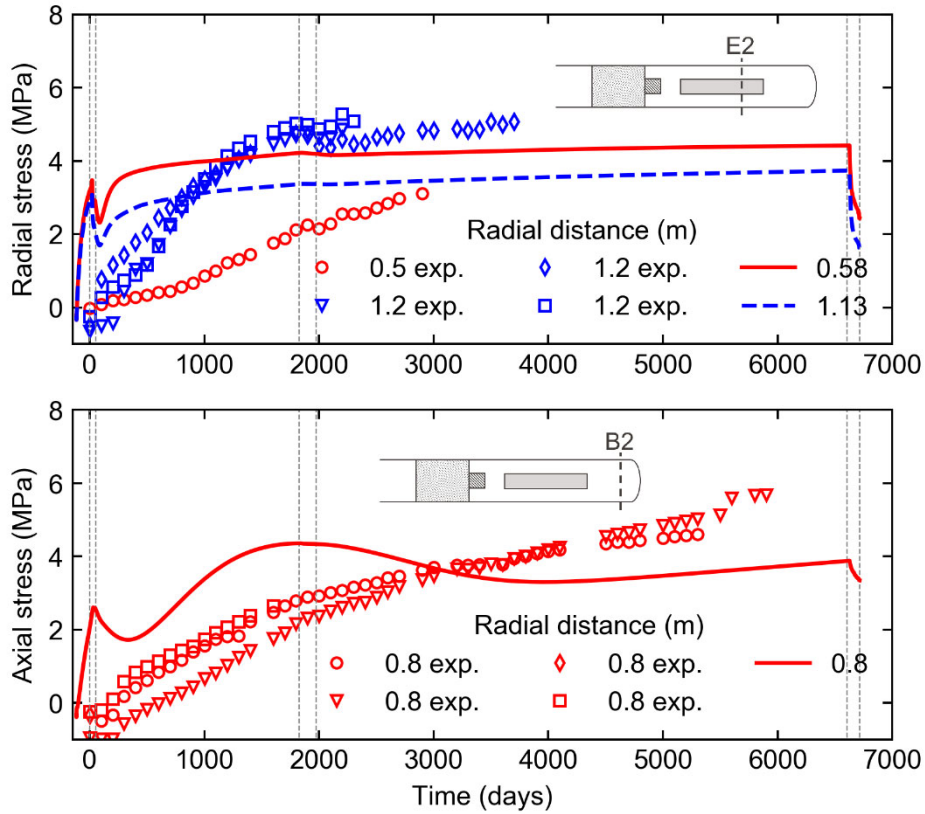


Figure 9. Model results of total stress evolution at the requested locations corresponding to 2 sections. Closest monitored values (exp.) are shown for comparison. Grey-dashed vertical lines indicate transition between phases.

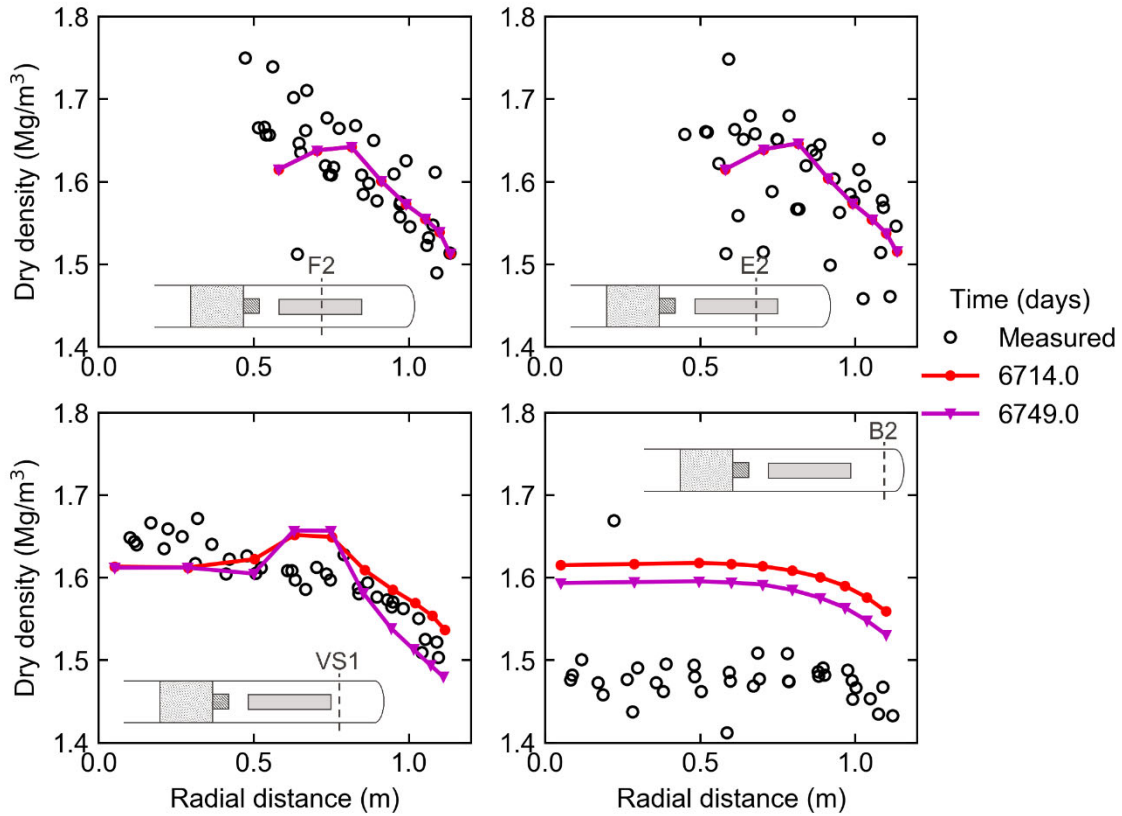


Figure 10. Model results of the dry density distribution before (day 6714) and after (day 6749) dismantling in the four sections of interest.

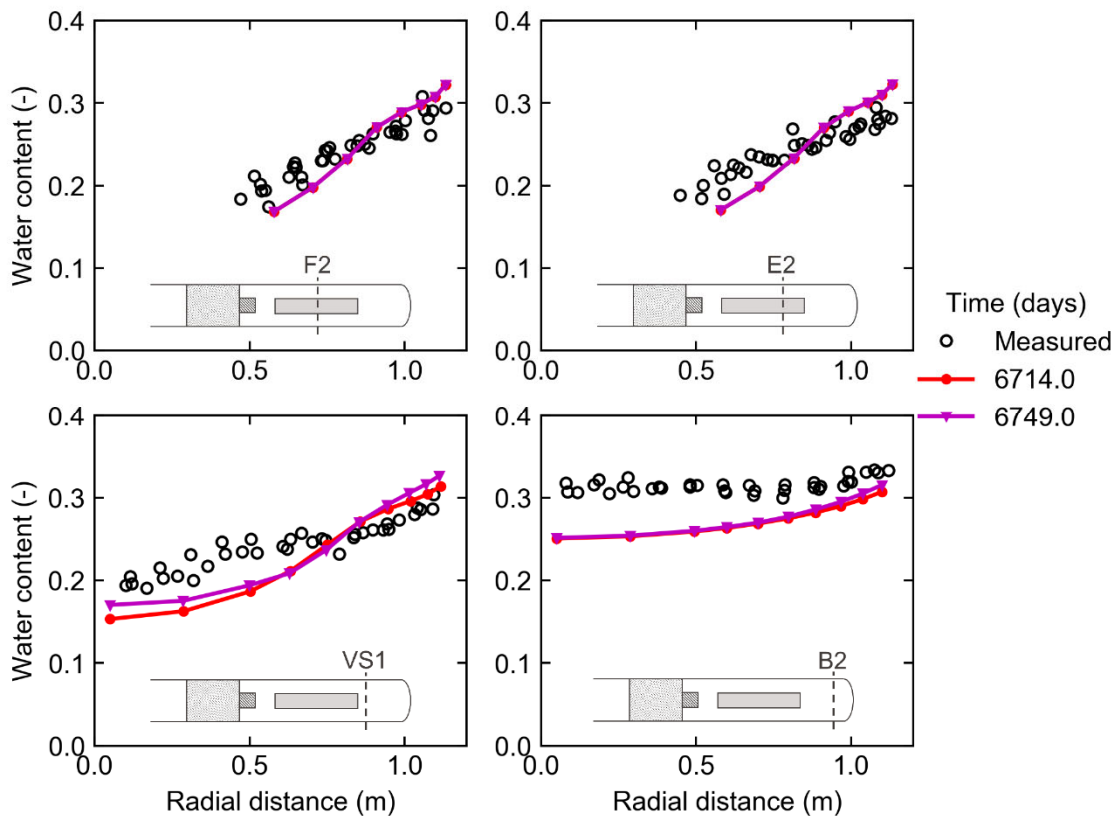


Figure 11. Model results of the water content distribution, in the four sections of interest, before (day 6714) and after (day 6749) dismantling.

The limitations of the model are mainly in modelling pellets mixtures at low densities (less than 1.4 Mg/m^3), such as those used in the CIEMAT tests that were modelled in the context of WP5. In particular an excessive collapse was predicted by the model for that application. Further development would be necessary to increase the confidence in similar cases of applications.

7 Concluding remarks

Within the Beacon project, the THM constitutive model ACMEG-TS has been enhanced for a better reproduction of bentonite behaviour. In particular, a new water retention model and a modified loading collapse formulation are the most significant modifications to the original model. The new water retention model accounts for the different behaviour of adsorbed water and free water while the loading collapse curve is a function of the degree of saturation instead of suction. Furthermore the model has been implemented in the computer code Lagamine for the analysis of boundary value problems.

The application of the model to the stress path tests has shown a good quantitative agreement with the experimental results, with the exception of the final value of swelling pressure that has been slightly overestimated. Nevertheless, the two stress paths have been reproduced with the same set of parameters and the overall behaviour has been well captured.

The model has been used in several application cases within the WP5. Among them, the FEBEX test has been simulated, which was a field scale that reproduced a repository under realistic conditions of operation. In order to test the predictive capability of the constitutive model, the input parameters were calibrated using laboratory tests. The results have been overall satisfactory, giving confidence to the predictive capability of the model.

Future directions of development could include the incorporation of hysteresis in the new water retention model and to increase its performance with bentonites employed at relatively low density.

Acknowledgments

References

[Please refer only to official publications.]

Charlier, R. (1987) : Approche unifiée de quelques problèmes non linéaires de mécanique des milieux continus par la méthode des éléments finis. PhD Thesis, Université de Liège in Department ArGEnCo, Liège, Belgium

Collin, F. (2003) : Couplages thermo-hydro-mécaniques dans les sols et les roches tendres partiellement saturés. PhD Thesis, Université de Liège in Department ArGEnCo, Liège, Belgium.

Collins, I.F. and Kelly, P.A., 2002. A thermomechanical analysis of a family of soil models. *Geotechnique*, 52(7), pp.507-518.

Dieudonne, A.C., Della Vecchia, G. and Charlier, R., 2017. Water retention model for compacted bentonites. *Canadian Geotechnical Journal*, 54(7), pp.915-925.

Dueck, A. and Nilsson, U., 2010. Thermo-Hydro-Mechanical properties of MX-80. Results from advanced laboratory tests (No. SKB-TR-10-55).

François, B. & Laloui, L. (2008): ACMEG-TS: A constitutive model for unsaturated soils under non-isothermal conditions. *International Journal for Numerical and Analytical Methods in Geomechanics* 32, 1955–1988. doi:10.1002/nag.712

Laloui, L. and Cekerevac, C., 2003. Thermo-plasticity of clays: an isotropic yield mechanism. *Computers and Geotechnics*, 30(8), pp.649-660.

Laloui L, Francois B. 2009 ACMEG-T: Soil Thermoplasticity Model. *Journal of Engineering Mechanics*; 135(9):932–944.

Lloret, A., Villar, M. V., Sánchez, M., Gens, A., Pintado, X. & Alonso, E. E. (2003). Mechanical behaviour of heavily compacted bentonite under high suction changes. *Géotechnique* 53, No. 1, 27–40.

Nuth, M. & Laloui, L. (2008). Effective stress concept in unsaturated soils: Clarification and validation of a unified framework. *International Journal for Numerical and Analytical Methods in Geomechanics* 32, 771–801. doi:10.1002/nag.645

Seiphoori, A., Ferrari, A. and Laloui, L., 2014. Water retention behaviour and microstructural evolution of MX-80 bentonite during wetting and drying cycles. *Géotechnique*, 64(9), pp.721-734.

Van Eekelen, H.A.M., 1980. Isotropic yield surfaces in three dimensions for use in soil mechanics. *International Journal for Numerical and Analytical Methods in Geomechanics*, 4(1), pp.89-101.

Vilarrasa, V., Parisio, F. and Laloui, L., 2017. Strength evolution of geomaterials in the octahedral plane under nonisothermal and unsaturated conditions. *International Journal of Geomechanics*, 17(7), p.04016152.

Zhou, A.N., Sheng, D., Sloan, S.W. and Gens, A., 2012. Interpretation of unsaturated soil behaviour in the stress–saturation space, I: volume change and water retention behaviour. *Computers and Geotechnics*, 43, pp.178-187.

D3.3



Annex E

Contribution to Deliverable 3.3

DELIVERABLE (D3.3) ICL Report

Author(s): Lidija Zdravkovic, Giulia Ghiadistri, Giuseppe Pedone, David Potts, Katerina Tsiampousi

Reporting period: 01/06/20 – 31/05/22

Date of issue of this report: 31/08/21

Start date of project: **01/06/17**

Duration: 60 Months

This project receives funding from the Euratom research and training programme 2014-2018 under grant agreement No 745 942		
Dissemination Level		
PU	Public	X
RE	Restricted to a group specified by the partners of the Beacon project	
CO	Confidential, only for partners of the Beacon project	

REVIEW

Name	Internal/Project/External	Comments
All Beacon partners	Project internal	

DISTRIBUTION LIST

Name	Number of copies	Comments
Seifallah BEN HADJ HASSINE (EC)	Digital	
Beacon partners	Digital	

Abstract

This report presents a contribution to the final Deliverable 3.3 for WP3 from Imperial College London (ICL), summarising the formulation and capabilities of the constitutive modelling approach for compacted bentonite used during the BEACON project.

Content

1	Introduction	5
2	Background to ICDSM model development	5
3	Scope and hypotheses.....	5
	3.1 Double-porosity structure.....	5
	3.2 Stress variables.....	6
4	Formulation of double structure model.....	7
	4.1 Yiled surfaces.....	7
	4.2 Elastic behaviour.....	8
	4.3 Hardening laws.....	9
	4.4 Adiditional elements for double porosity formulation.....	9
	4.5 Formulation of the β -mechanism.....	11
	4.6 Hydraulic modelling.....	15
5	Basic capabilities of the model.....	16
	5.1 Dependency of swelling strain on applied stress and on dry density.....	16
	5.2 Irreversibility of strains in wetting/drying cycles.....	17
	5.3 Dependence of swelling pressure on dry density.....	18
	5.4 Stress path dependence from an unsaturated to a saturated state.....	18
	5.5 Stress path dependence from a saturated to an unsaturated state.....	20
6	Report on Task 3.3.....	21
7.	Performance of the model.....	23
8.	Final remarks.....	24
	References	25
	Appendix 1: Finite element implementation.....	26
	Appendix 2: Report on WP3 Task 3.3	29

1 Introduction

This report forms a contribution to BEACON Deliverable 3.3 from Imperial College London (ICL). It describes the modelling capabilities of this project partner in representing the hydro-mechanical behaviour of bentonite buffers at the end of the BEACON project. The constitutive model at the start of the project was the Imperial College Double Structure Model (ICDSM, Ghiadistri et al., 2018; Ghiadistri 2019). The model was implemented in the bespoke finite element code ICFEP (Potts & Zdravkovic, 1999), which has been used for all finite element analyses performed during the BEACON project. It should be noted that, while minor numerical adjustments have been applied in the model during the course of the project, the main formulation has remained the same. This report summarises the background to model development and its main hypotheses, its brief mathematical formulation and input parameters, main steps of finite element implementation, as well as the main aspects of its performance.

2 Background to ICDSM model development

The double-structure model for unsaturated highly expansive clays, ICDSM, was developed in the framework of elasto-plasticity and critical state-based soil mechanics. The model is an extension of a single structure model, ICSSM, developed for unsaturated moderately expansive clays, and described in Georgiadis et al. (2003), (2005); Tsiampousi et al. (2013). The latter model (ICSSM) is a modified and generalised version of the Barcelona Basic Model (BBM, Alonso et al., 1990), while the former model (ICDSM) adopts the conceptual basis of the Barcelona Expansive Model (BExM, Gens & Alonso, 1992; Sanchez et al., 2005). Both ICSSM and ICDSM were implemented in the Imperial College Finite Element Program (ICFEP), Potts & Zdravkovic (1999).

3 Scope and hypotheses

3.1 Double-porosity structure

The formulation of ICDSM adopts the concept of double porosity in the structure of compacted clays. One level of porosity is the void space between the clay aggregates, defined as macro- or inter-aggregate porosity (as sketched in Figure 3-1). The second level of porosity is the void space within an aggregate, defined as micro- or intra-aggregate porosity (Figure 3-1). Macro-porosity is associated with the evolution of negative pore water pressures (suctions) in the clay, while micro-porosity governs the physico-chemical processes associated with the clay mineralogy. It is believed that the interaction between the two levels of structure upon hydration of compacted clays contributes to their swelling potential, which is the principal mechanism of developing a protective clay layer around nuclear waste canisters.

The existence of this structure is evidenced by the electro-scanning micrographs (ESEMs) of compacted clay and/or mercury intrusion porosimetry (MIP) tests performed on samples of compacted clay (e.g. Romero et al., 1999; Sanchez et al., 2005; Monroy et al., 2010; Seiphoori et al., 2014). Example graphs in Figure 3-2(a) show a clear dual concentration of pore sizes in compacted FEBEX bentonite, with the dominant intra-aggregate (micro) pore size of ~ 10 nm, and the inter-aggregate (macro) pore size greater than ≥ 10 μm . The figure also shows the dependency of the macro-porosity on the dry density, ρ_d , of the compacted clay, with a larger value of ρ_d ($= 1.8$ Mg/m^3) generating smaller and lower quantity of macro-pores, compared to the sample of lower ρ_d ($= 1.5$ Mg/m^3). Figure 3-2(b) shows a very similar double porosity initial structure for compacted MX-80 bentonite ("as compacted" curve). Additionally, it also shows that, upon full hydration, the macro-pores seem to disappear, leaving a higher concentration of micro-pores ("fully saturated" curve). This interaction creates a low-permeability buffer, which should prevent the escape of radionuclides into the surrounding ground.

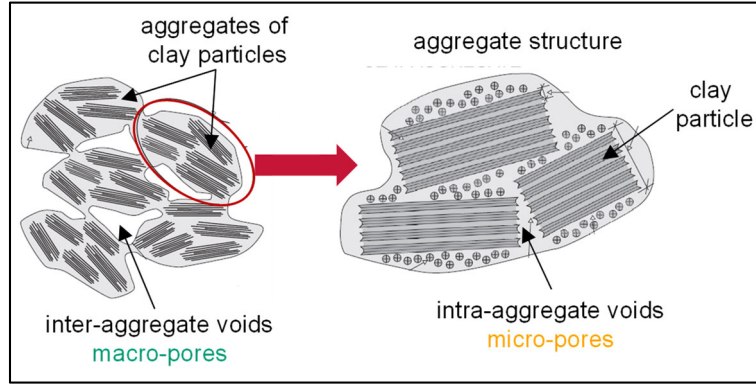


Figure 3-1: Conceptual illustration of a double-porosity structure in compacted clays

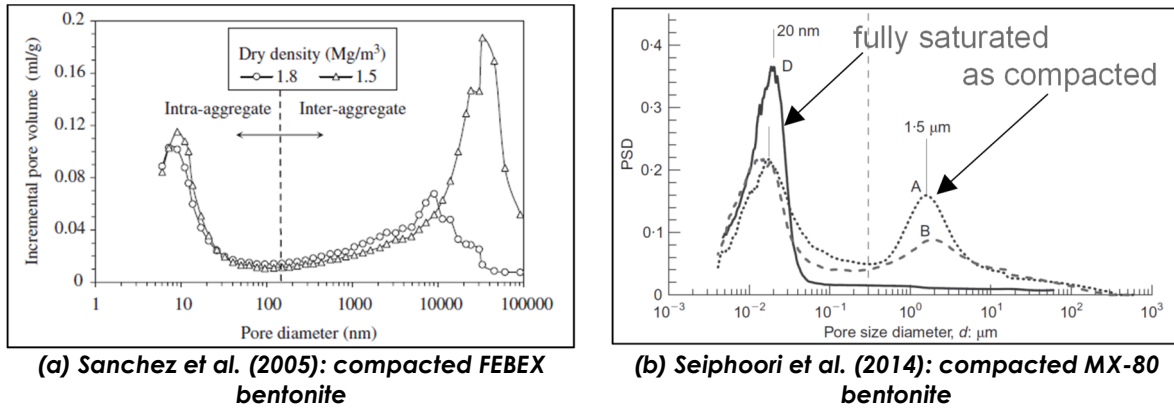


Figure 3-2: MIP evidence of a double-porosity structure in compacted clays

3.2 Stress variables

The mathematical formulation of the ICDSM adopts two independent stress variables to describe the mechanical behaviour of unsaturated soils: the matric suction, $s = u_{air} - u_w$, defined as the difference between the air pressure, u_{air} , and water pressure, u_w , in the macro pores; and net stress, $\bar{\sigma} = \sigma_{tot} - u_{air}$, defined as the difference between the total stress, σ_{tot} , and the pore air pressure. Additionally, to enable a seamless transition from saturated to unsaturated states, and vice versa, the model introduces the equivalent suction, $s_{eq} = s - s_{air}$, where s_{air} is the air-entry value of suction. This necessarily leads to the introduction of equivalent stress, $\sigma = \bar{\sigma} + s_{air}$.

The model is generalised in the $J - p - \theta - s_{eq}$ space, as an extension of the IC SSM model, where p is the mean equivalent stress (Equation 3-1), J is the generalised deviatoric stress (Equation 3-2), and θ is the Lode's angle (Equation 3-3).

$$p = \frac{\sigma_x + \sigma_y + \sigma_z}{3} \quad (3-1)$$

$$J = \left(\frac{1}{6} [(\sigma_x - \sigma_y)^2 + (\sigma_y - \sigma_z)^2 + (\sigma_x - \sigma_z)^2] + \tau_{xy}^2 + \tau_{xz}^2 + \tau_{yz}^2 \right)^{1/2} \quad (3-2)$$

$$\theta = -\frac{1}{3} \cdot \sin^{-1} \left[\frac{3\sqrt{3}}{2} \cdot \frac{\det \mathbf{s}}{J^3} \right] \quad (3-3)$$

where

$$\det \mathbf{s} = \begin{vmatrix} \sigma_x - p & \tau_{xy} & \tau_{xz} \\ \tau_{xy} & \sigma_y - p & \tau_{yz} \\ \tau_{xz} & \tau_{yz} & \sigma_z - p \end{vmatrix} \quad (3-4)$$

Similarly, the strain invariants ε_{vol} (volumetric strain) and E_d (generalised deviatoric strain) are calculated as:

$$\varepsilon_{vol} = \varepsilon_x + \varepsilon_y + \varepsilon_z \quad (3-5)$$

$$E_d = \left(\frac{1}{6} [(\varepsilon_x - \varepsilon_y)^2 + (\varepsilon_y - \varepsilon_z)^2 + (\varepsilon_x - \varepsilon_z)^2] + \gamma_{xy}^2 + \gamma_{xz}^2 + \gamma_{yz}^2 \right)^{1/2} \quad (3-6)$$

4 Formulation of Double Structure Model

The model formulation described in Sections 4.1 to 4.3 is common to both single (ICSSM) and double (ICDSM) structure models implemented in ICSEP. Sections 4.4 and 4.5 introduce additional elements of the formulation for the double porosity structure.

4.1 Yield surfaces

Versatile primary yield, F_{LC} , and plastic potential, G_{LC} , surfaces (Figure 4-1) in the $p - J$ plane adopt the expression of Lagioia et al. (1996) instead of the Modified Cam Clay (MCC) ellipse of the original BBM, hence enabling a more realistic representation of strength for overconsolidated clays:

$$\frac{F_{LC}}{G_{LC}} = \frac{p + k \cdot s_{eq}}{p_0 + k \cdot s_{eq}} - \frac{\left(1 + \frac{\eta}{K_2(\alpha, \mu)} \right)^{K_2(\alpha, \mu) / \beta_f(\alpha, \mu)}}{\left(1 + \frac{\eta}{K_1(\alpha, \mu)} \right)^{K_1(\alpha, \mu) / \beta_f(\alpha, \mu)}} = 0 \quad (4-1)$$

Model input parameters α and μ in Equation (4-1) control the shape of the yield (α_F and μ_F) and plastic potential (α_G and μ_G) surfaces independently, hence allowing the modelling of non-associated plasticity, but can also reproduce the basic MCC ellipse. Tsiampousi et al. (2013a) introduced the Hvorslev surface on the dry side of the critical state as a further flexibility of the generalised yield and plastic potential surfaces. The cohesion increase parameter, k , can be either a constant (original BBM), or set equal to the degree of saturation, therefore allowing a more limited and non-linear increase of the apparent cohesion with suction in the $p - s_{eq}$ plane.

The shape of the primary yield surface in the $p - s_{eq}$ plane (Figure 4-1) defines the Load-Collapse (LC) curve, as in the original BBM:

$$p_0 = p_c \cdot \left(\frac{p_0^*}{p_c} \right)^{[\lambda(0) - \kappa] / [\lambda(s_{eq}) - \kappa]} \quad (4-2)$$

introducing as input parameters: p_c – the characteristic pressure; $\lambda(0)$ – the fully saturated compressibility coefficient; and κ – the compressibility coefficient along elastic paths.

Furthermore, p_0^* is the equivalent fully saturated isotropic yield stress and $\lambda(s_{eq})$ is the unsaturated compressibility coefficient:

$$\lambda(s_{eq}) = \lambda(0) \left[(1-r) e^{-\beta s_{eq}} + r \right] \quad (4-3)$$

Equation (4-3) introduces two additional input parameters, r and β , which also contribute to the definition of the shape of the LC curve. Georgiadis et al. (2005) proposed an alternative definition of the LC curve when formulating the single structure model, which assumes a constant ratio p_0^*/p_c in Eq. (4-2). This assumption was shown to reproduce more accurately the experimental behaviour of soils subjected to high confining stresses (Georgiadis et al., 2003).

Finally, the model adopts the Matsuoka & Nakai (1975) shape of the yield and plastic potential surfaces in the deviatoric plane, which simulates a more realistic and experimentally-observed variation of soil strength in non-triaxial compression loading, compared to the circular shape of the original BBM.

The secondary yield surface in the $p - s_{eq}$ plane, called the Suction Increase (SI) surface (Figure 4-1), is the same as in the original BBM:

$$F_{SI} = \frac{s_{eq}}{s_0} - 1 = 0 \quad (4-4)$$

where s_0 is an input parameter representing the yield value of equivalent suction.

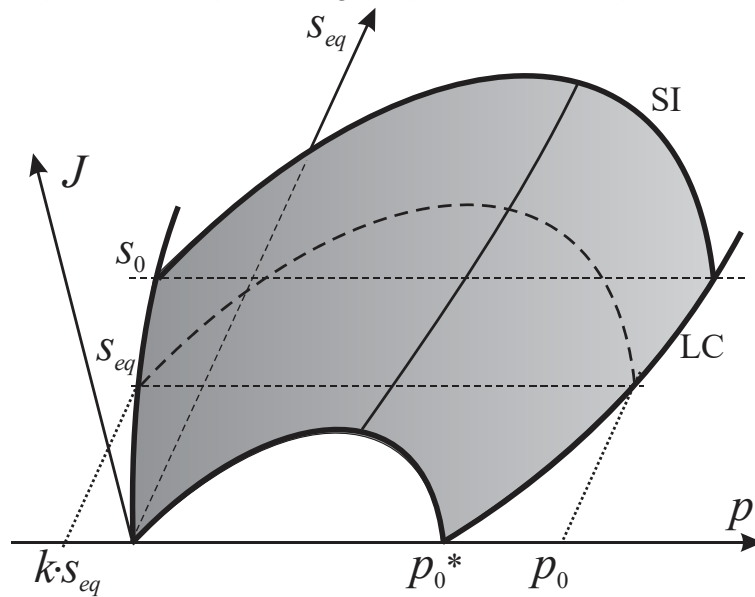


Figure 4-1: Schematic presentation of yield surface in $p - s_{eq} - J$ space

4.2 Elastic behaviour

As in the original BBM, the stress space inside the yield surfaces in a single structure model is assumed elastic, with an increment of elastic volumetric strain, $\Delta \epsilon_v^e$, calculated from changes in both the mean equivalent stress, Δp , and equivalent suction, Δs_{eq} :

$$\Delta \varepsilon_v^e = \frac{\kappa}{\nu \cdot p} \Delta p + \frac{\kappa_s}{\nu (s_{eq} + p_{atm})} \Delta s_{eq} \quad (4-5)$$

where ν is the specific volume. From the above equation, the elastic bulk modulus has two components: K_p due to changes in mean equivalent stress, Δp ; and K_s due to changes in equivalent suction, Δs_{eq} . The shear modulus, G , is evaluated either from a prescribed Poisson's ratio, ν , and the calculated value of K_p , or is input independently as a function of the isotropic equivalent yield stress, p_0 , or prescribed as a constant value.

4.3 Hardening laws

The hardening laws for the primary and secondary yield surfaces are calculated, respectively, as:

$$\Delta p_0^* = p_0^* \frac{\nu}{\lambda(0) - \kappa} \Delta \varepsilon_v^p \quad (4-6)$$

$$\Delta s_0 = (s_0 + p_{atm}) \frac{\nu}{\lambda_s - \kappa_s} \Delta \varepsilon_v^p \quad (4-7)$$

where κ_s and λ_s are input parameters defining the compressibility coefficients at constant mean equivalent stress for elastic and elastoplastic changes in equivalent suction, respectively, and $\Delta \varepsilon_v^p$ is the incremental plastic volumetric strain.

4.4 Additional elements for double-porosity formulation

The model introduces two levels of structure: the macro-structure, which is assumed unsaturated and defined by the ICSSM framework; and the micro-structure, which is assumed to be elastic, volumetric and fully saturated (in agreement with e.g. Gens & Alonso, 1992; Sanchez et al., 2005). The assumption of full saturation implies that the micro-structure can be expressed in terms of effective stresses, where:

$$p' = p + s_{eq} \quad (4-8)$$

p' being the mean effective stress. From the remaining two assumptions, the change in the mean effective stress triggers elastic volumetric micro-strains, $\Delta \varepsilon_{v,m}^e$:

$$\Delta \varepsilon_{v,m}^e = \frac{\Delta p'}{K_m} \quad (4-9)$$

where the micro-structural bulk modulus, K_m , is defined as:

$$K_m = \frac{1 + e_m}{\kappa_m} p' \quad (4-10)$$

κ_m being the elastic compressibility parameter of the micro-structure and e_m the micro-structural void ratio. For consistency, the following condition must always be satisfied:

$$e = e_M + e_m \quad (4-11)$$

e_M being the macro-structural and e the overall void ratio of the material, respectively. The new bulk modulus K_m is additional to the bulk moduli associated with the macro-structure and

defined by the ICSSM formulation in Equation (4-5). The principal difference is that the specific volume term in Equation (4-5) must now be distinguished in terms of the macro-void ratio (i.e. $v_M = 1 + e_M$):

$$K_{s,M} = \frac{1 + e_M}{\kappa_s} (s_{eq} + p_{atm}) \quad (4-12)$$

$$K_{p,M} = \frac{1 + e_M}{\kappa} p \quad (4-13)$$

$K_{s,M}$ being associated with equivalent suction and $K_{p,M}$ with mean equivalent stress. The three bulk moduli components define the overall elastic behaviour of the material in the double-structure formulation.

The next change to the existing modelling framework is that the pre-failure behaviour of the material is no longer purely elastic. Although the micro-structural volumetric deformation is elastic, it is assumed to contribute to the macro-structural volumetric plastic strains, $\Delta \varepsilon_{v,\beta}^p$, introducing an additional plastic mechanism (defined as the β -mechanism, in agreement with Sanchez et al., 2005):

$$\Delta \varepsilon_{v,\beta}^p = f_\beta \cdot \Delta \varepsilon_{v,m}^e \quad (4-14)$$

where f_β is the interaction function between the two levels of structure. With reference to Figure 4-2, this function is defined by expanding the expression suggested by Sanchez et al. (2005), to account for the possibility of a negative mean equivalent stress:

$$f_\beta = \begin{cases} \begin{cases} c_{c1} + c_{c2} \left(\frac{Pr}{p_0} \right)^{c_{c3}} & \text{if } \frac{Pr}{p_0} \geq 0 \\ c_{c1} & \text{if } \frac{Pr}{p_0} < 0 \end{cases} & \text{micro-compression} \\ \begin{cases} c_{s1} + c_{s2} \left(1 - \frac{Pr}{p_0} \right)^{c_{s3}} & \text{if } \frac{Pr}{p_0} \geq 0 \\ c_{s1} + c_{s2} & \text{if } \frac{Pr}{p_0} < 0 \end{cases} & \text{micro-swelling} \end{cases} \quad (4-15)$$

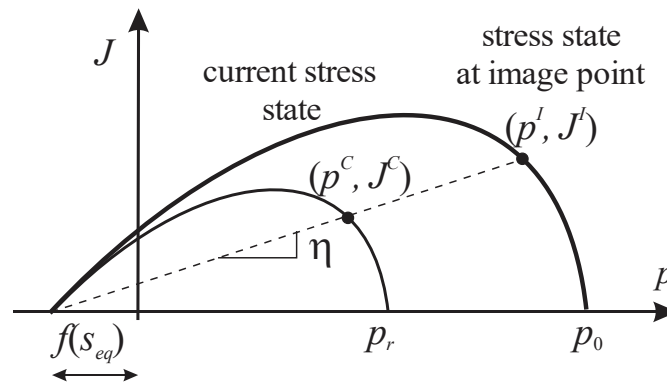


Figure 4-2: ICDSM primary yield surface projection in $p - J$ plane; definition of parameters describing structural interaction, f_β , and plastic straining of the β -mechanism

In Equation (4-15) c_{c1}, c_{c2}, c_{c3} and c_{s1}, c_{s2}, c_{s3} are coefficients defining the shape of the interaction function, f_β , upon compression and swelling, respectively (see example in Figure 4-3), while the ratio p_r/p_0 expresses the degree of openness of the structure (Gens & Alonso, 1992) in terms of the distance of the current stress state to the yield surface, p_0 being the isotropic equivalent yield stress and p_r the isotropic equivalent stress related to the current stress state. If the micro-structure compresses, the f_β can become negative when p_r/p_0 is close to or less than zero, creating a very dense material which has undergone the swelling of the macro-structure. Conversely, if the micro-structure swells, the f_β can become negative when p_r/p_0 is close to unity, creating a loose material that has undergone the compression of the macro-structure.

Finally, the ICDSM formulation introduces the void factor, VF , which enables the quantification of the micro-structural evolution. Defined as the ratio of the micro-void ratio to the total void ratio

$$VF = \frac{e_m}{e} \quad (4-16)$$

this parameter expresses the degree of dominance of each structural level in the overall clay fabric.

Overall, four model inputs are introduced in the ICDSM by the double-porosity formulation, in addition to ICSSM parameters. These are the micro-structural compressibility, κ_m ; void factor, VF ; coefficients c_{s1}, c_{s2}, c_{s3} for the micro-swelling interaction function, f_β ; and coefficients c_{c1}, c_{c2}, c_{c3} for the micro-compressing f_β . All model parameters are summarised in Table 4-1, together with an indication of how they could be determined.

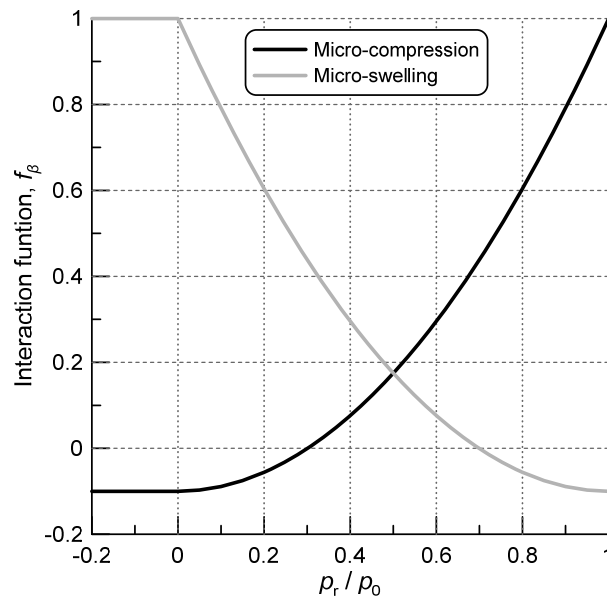


Figure 4-3: Generic form of interaction functions f_β

4.5 Formulation of the β -mechanism

4.5.1 Micro-structural changes

The ICDSM model formulation introduces the “neutral line”, NL, in the $p - s_{eq}$ plane (Figure 4-4) as a means of determining the direction of the micro-structural change (Sanchez et al., 2005).

The neutral loading implies $\Delta p' = 0$ and, consequently, a stress state moving along the NL induces zero deformation of the micro-structure. The equation of the NL is:

$$F_{NL} = \frac{p'}{p'_{NL}} - 1 = 0 \quad (4-17)$$

where p'_{NL} is the mean effective stress on the neutral line. If $\Delta p' > 0$, meaning that $F_{NL} = (p' + \Delta p')/p'_{NL} - 1 > 0$, the micro-structure is being loaded and induces elastic volumetric compressive strains. Conversely, $\Delta p' < 0$ indicates unloading of the micro-structure, generating elastic volumetric swelling strains.

As introduced earlier, elastic volumetric micro-structural strains, $\Delta \varepsilon_{v,m}^e$, are assumed to induce plastic volumetric macro-structural strains in the material through the β -mechanism, $\Delta \varepsilon_{v,\beta}^p$. In the most general case, if both the primary, F_{LC} , and the secondary, F_{SI} , yield surfaces are mobilised, the respective plastic volumetric macro-structural strains, $\Delta \varepsilon_{v,LC}^p$ and $\Delta \varepsilon_s^p$, together with $\Delta \varepsilon_{v,\beta}^p$ strains, contribute to the total volumetric plastic macro-strains, $\Delta \varepsilon_{v,M}^p$:

$$\Delta \varepsilon_{v,M}^p = \Delta \varepsilon_{v,LC}^p + \Delta \varepsilon_s^p + \Delta \varepsilon_{v,\beta}^p \quad (4-18)$$

To reflect the coupling between the two structures, the hardening law of the primary yield surface in Eq. (4-6) becomes:

$$\Delta p_0^* = p_0^* \frac{1 + e_M}{\lambda(0) - \kappa} \Delta \varepsilon_{v,M}^p \quad (4-19)$$

while that of the secondary yield surface in Eq. (4-7) becomes:

$$\Delta s_0 = (s_0 + p_{atm}) \frac{1 + e_M}{\lambda_s - \kappa_s} \Delta \varepsilon_{v,M}^p \quad (4-20)$$

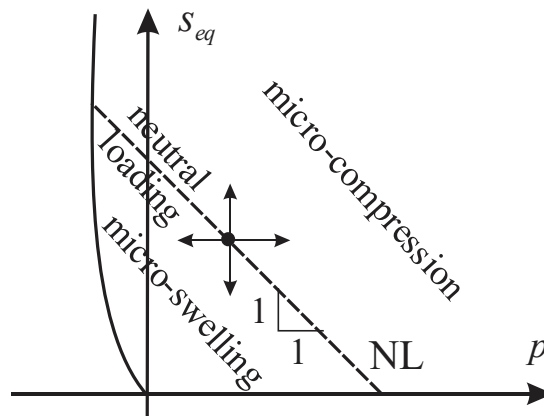


Figure 4-4: Loading changes for the micro-structure

As a consequence of these assumptions, the constitutive model has to enable the following states of structural interaction, if the material is initially unsaturated:

- (a) plasticity is generated only by the micro-structure; $\Delta p' \neq 0$ and the stress state remains inside the yield surfaces F_{LC} and F_{SI} ;

- (b) plasticity is generated by both the micro- and the LC -macro-structure; $\Delta p' \neq 0$ and only the primary yield surface, F_{LC} , is mobilised;
- (c) plasticity is generated by both the micro- and the SI -macro-structure; $\Delta p' \neq 0$ and only the secondary yield surface, F_{SI} , is mobilised;
- (d) plasticity is generated by both the micro- and the macro-structure; $\Delta p' \neq 0$ and both the primary and secondary yield surfaces, F_{LC} and F_{SI} , are mobilised;

As the double-porosity structure evolves into a single-porosity structure upon first full saturation and subsequently remains irreversible (Seiphoori et al., 2014), the contribution of the β -mechanism ceases to exist. The control of the plastic volumetric straining reverts to the primary and secondary yield surfaces. The constitutive model has to enable the following states for the material that has already been saturated once:

- (e) elastic behaviour, if the stress state is inside the yield surfaces F_{LC} and F_{SI} ;
- (f) plasticity is generated only by the yielding of the primary yield surface, F_{LC} ;
- (g) plasticity is generated only by the yielding of the secondary yield surface, F_{SI} ;
- (h) plasticity is generated by the yielding of both F_{LC} and F_{SI} .

The formulation of states (e) to (h) corresponds to the ICSSM framework. The focus here is on the formulation of states (a) to (d), when the micro-structure, and hence the β -mechanism, is active. As the β -mechanism does not involve classical yield and plastic potential surfaces, the generalised plasticity theory (Pastor et al., 1990) is employed in its formulation, introducing plasticity by defining the direction of a loading vector, a flow rule and a plastic modulus.

4.5.2 Direction of loading vector

The loading vector defines the direction of the micro-structural change in the β -mechanism:

$$\frac{\partial F_{\beta}}{\partial p} = \omega_{\beta} \frac{\partial F_{NL}}{\partial p} \quad (4-21)$$

where $\omega_{\beta} = 1$ for the case of micro-compression (loading) and $\omega_{\beta} = -1$ for the case of micro-swelling (unloading). However, assigning a value to ω_{β} is not straightforward, as the stress change $\Delta p'$ (and its sign) is not known at the beginning of a loading step in a finite element analysis. In effect, stress changes are calculated from changes in total strains and the constitutive behaviour of the material and are known only at the end of the loading step. Consequently, an alternative condition (i.e. an estimate of the stress change) to determine the direction of the loading vector is adopted here. This uses an estimate of the change in mean effective stress, $\Delta p'_e$, calculated assuming that the material behaves elastically. Having determined the direction of loading, the full elasto-plastic behaviour can then be evaluated.

4.5.3 Flow rule

The flow rule defines the direction of plastic straining for the β -mechanism. Not having its own yield surface, the radial mapping depicted in Figure 4-2, with a constant stress ratio, η , is applied to the current stress state, (p^C, J^C) , to determine the stress state at the image point (p^I, J^I) on the primary yield surface, F_{LC} , in the $p - J$ plane. While the two invariant stresses at the image point can be easily determined, it is impossible to uniquely define the full stress tensor at the image point, σ^I , for model implementation in a general finite element software. As an infinite number of stress tensors correspond to the same set of invariants, a new assumption is introduced in the ICDSM which scales all component stresses at the current stress state, $(\sigma_x^C, \sigma_y^C, \sigma_z^C, \tau_{xy}^C, \tau_{yz}^C, \tau_{xz}^C)$, by the ratio $(p^I + f(s_{eq}))/(p^C + f(s_{eq}))$ to obtain the corresponding component stresses at the image

point, $(\sigma_x^I, \sigma_y^I, \sigma_z^I, \tau_{xy}^I, \tau_{yz}^I, \tau_{xz}^I)$. It can be shown that such a tensor is unique for the applied assumption. The derivatives of the plastic potential, G_{LC} , at the image point can now be calculated and used to express the plastic potential of the β -mechanism:

$$G_\beta = \text{sign}(f_\beta) \cdot \omega_\beta \cdot |G_{LC}| \quad (4-22)$$

and its flow rule:

$$\left\{ \frac{\partial G_\beta}{\partial \sigma} \right\} = \text{sign}(f_\beta) \cdot \omega_\beta \cdot \left\| \left\{ \frac{\partial G_{LC}}{\partial \sigma^I} \right\} \right\| \quad (4-23)$$

4.5.4 Plastic modulus

The plastic modulus for the β -mechanism, H_β , which appears in the calculation of the scalar, Λ_β , that multiplies the plastic potential derivatives calculated by Equation (4-23), must ensure the validity of Equation (4-14). From Pastor et al. (1990) the following equation can be written:

$$\Lambda_\beta = \frac{\left\{ \frac{\partial F_\beta}{\partial \sigma} \right\}^t \{ \Delta \sigma \} + \left\{ \frac{\partial F_\beta}{\partial s_{eq}} \right\}^t \{ \Delta s_{eq} \}}{H_\beta} \quad (4-24)$$

Thus, considering Equation (4-24), the volumetric plastic strains from the β -mechanism, for the changing micro-structure, can be calculated as follows:

$$\Delta \varepsilon_{v,\beta}^p = \Lambda_\beta \frac{\partial G_\beta}{\partial p} = \frac{\left\{ \frac{\partial F_\beta}{\partial \sigma} \right\}^t \{ \Delta \sigma \} + \left\{ \frac{\partial F_\beta}{\partial s_{eq}} \right\}^t \{ \Delta s_{eq} \}}{H_\beta} \frac{\partial G_\beta}{\partial p} \quad (4-25)$$

For Equation (4-25) to be equivalent to Equation (4-14), the plastic modulus must have the following form:

$$H_\beta = \frac{K_m}{f_\beta} \frac{\partial F_\beta}{\partial p} \frac{\partial G_\beta}{\partial p} \quad (4-26)$$

Equation (4-26) differs from that reported by Sanchez et al. (2005):

$$H_\beta = \frac{K_m}{f_\beta} \left\| \frac{\partial G_\beta}{\partial p} \right\| \quad (4-27)$$

where $\| \cdot \|$ is the Euclidean norm, as Equation (4-27) does not guarantee the equivalence of Equation (4-25) and Equation (4-14).

With all the necessary ingredients for the β -mechanism now defined, the constitutive equations can be written in a form suitable for implementation in a finite element code. The case (d) above, where both the micro- and the macro-structure are inducing plasticity and the latter mobilises both the primary and secondary yield surfaces, has the most general formulation and is presented In Appendix 1. Cases (a) to (c) are special instances of the case (d), with further details provided in Ghiadistri (2019).

Table 4-1: Summary of ICDSM model parameters

	Parameter	Source
Input parameters for IC SSM	Parameters controlling the shape of the yield surface, α_F, μ_F	Triaxial compression; relationship between dilatancy and J/p ratio
	Parameters controlling the shape of the plastic potential surface, α_G, μ_G	Triaxial compression
	Generalized stress ratio at critical state, M_J	Triaxial compression, related to the angle of shear resistance ϕ'_{cs}
	Characteristic pressure, p_c (kPa)	Limiting confining stress at which $p_0 = p_0^* = p_c$
	Fully saturated compressibility coefficient, $\lambda(0)$	Fully saturated isotropic loading
	Elastic compressibility coefficient, κ	Fully saturated isotropic unloading
	Maximum soil stiffness parameter, r	Isotropic compression tests at constant value of suction
	Soil stiffness increase parameter, β 1/kPa)	Isotropic compression tests at constant value of suction
	Elastic compressibility coefficient for changes in suction, κ_s (kPa)	Drying test and constant confining stress
	Poisson ratio, ν	Triaxial compression test
	Plastic compressibility coefficient for changes in suction, λ_s	Drying test and constant confining stress
	Air-entry value of suction, s_{air} (kPa)	From the retention curve
	Yield value of equivalent suction, s_0 (kPa)	Usually a high value if it is not to be mobilised
Additional input for double structure	Microstructural compressibility parameter, κ_m	No direct test
	Void factor, VF	No direct test – potentially from MIP interpretation
	Coefficients for the micro swelling function, c_{s1}, c_{s2}, c_{s3}	No direct test – potentially from MIP interpretation
	Coefficients for the micro compression function, c_{c1}, c_{c2}, c_{c3}	No direct test – potentially from MIP interpretation

4.6 Hydraulic modelling

The ICDSM simulates the mechanical behaviour of highly expansive clays. The simulation of their hydraulic behaviour is achieved by coupling the mechanical model with a soil water retention (SWR) model and with a permeability / hydraulic conductivity model.

4.6.1 Soil water retention (SWR) model

A non-hysteretic Van Genuchten-type (van Genuchten, 1980) SWR model was adopted for all simulations on the BEACON project, formulated in terms of the degree of saturation, S_r , and the matric suction (Melgarejo Corredor, 2004):

$$S_r = \left[\frac{1}{1 + [\alpha \cdot (v - 1)^\psi \cdot s_{eq}]^n} \right]^m \cdot (1 - S_{r0}) + S_{r0} \quad (4-28)$$

In the above equation, S_{r0} is the residual degree of saturation, while α , m and n are fitting parameters controlling the shape of the retention curve; ψ is the parameter controlling the effect of the specific volume, v .

4.6.2 Hydraulic conductivity (permeability) model

The variable permeability model (Potts & Zdravkovic, 1999; Nyambayo & Potts, 2010) adopted in all analyses assumes the permeability (hydraulic conductivity) to vary with matric suction according to the expression:

$$\log k = \log k_{sat} - \frac{s - s_1}{s_2 - s_1} \cdot \log \frac{k_{sat}}{k_{min}} \quad (4-29)$$

where k_{sat} is the saturated value of permeability (m/s), k_{min} its minimum value reached after the prescribed change in matric suction from s_1 to s_2 .

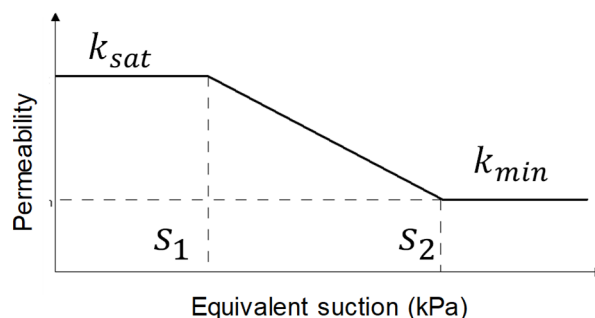


Figure 4-5: Variable permeability model

5 Basic capabilities of the model

To demonstrate the general performance of the IC DSM model, a cylindrical bentonite specimen was considered, 50 mm in diameter and 12 mm high, with generic ICDSM properties. The analyses simulated the wetting of bentonite in oedometric conditions, allowing either a free swelling (restraining vertical displacements along the bottom boundary and horizontal displacement along the vertical boundary of the specimen, but not restraining the top specimen boundary), or constant volume swelling (with top boundary of the specimen being also restrained from displacing vertically). The ability of the model to reproduce the correct response of compacted bentonite under some of the basic paths is summarised in Table 5-1.

5.1 Dependence of swelling strain on applied stress and on dry density

A wetting path under free swelling, changing the suction in the specimen from 10 MPa to 0, was applied at two stress levels (0.1 and 0.5 MPa), as shown in Figure 5-1, and at two values of initial dry density, ρ_d . The resulting swelling strains, ε_y , upon wetting are plotted against the total vertical stress, σ_y , in Figure 5-2(a) for the bentonite specimen with $\rho_d = 1.6 \text{ Mg/m}^3$ and in Figure 5-2(b) for the specimen with $\rho_d = 1.1 \text{ Mg/m}^3$.

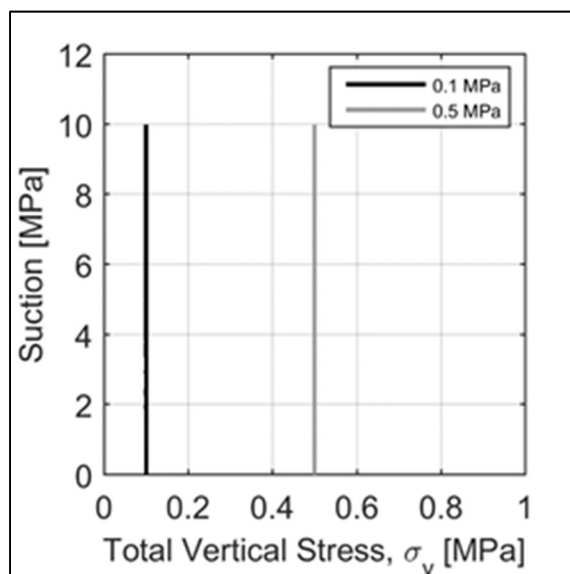


Figure 5-1: Applied change in suction at constant stress

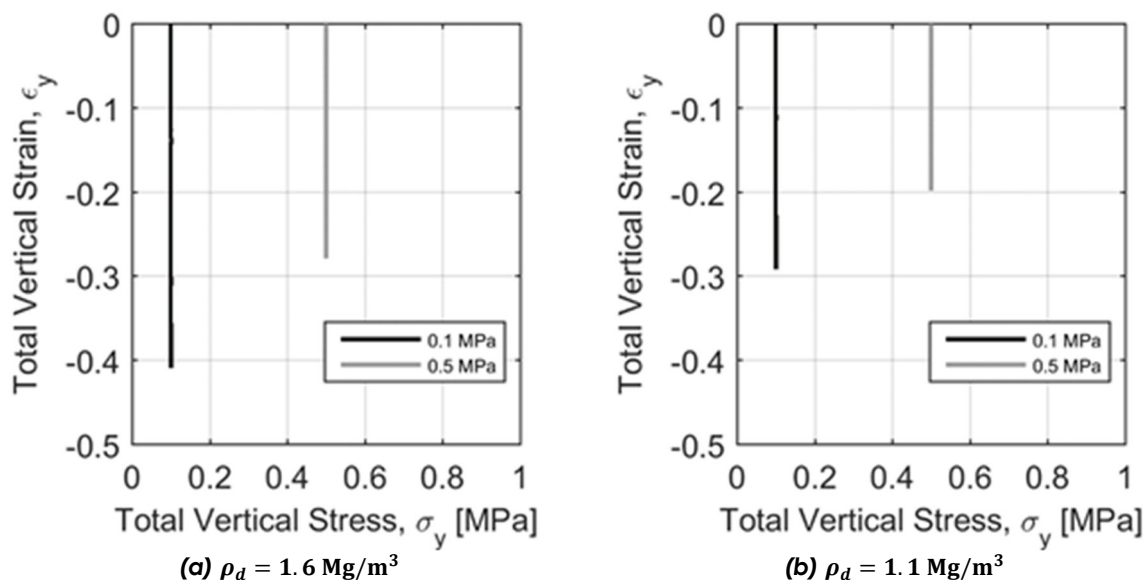


Figure 5-2: Swelling strain upon wetting at constant stress

For each value of ρ_d the model predicts smaller swelling strains when a larger stress is applied to the specimen. Furthermore, the predicted total swelling strains are smaller in magnitude for the lower bentonite density. This is in agreement with experimental findings.

5.2 Irreversibility of strains in wetting/drying cycles

The paths similar to those in Figure 5-1 were simulated next, but this time involving first a reduction in suction from 10 MPa to 0, followed by suction increase from 0 to 10 MPa, under two different levels of vertical stress. A single dry density of $\rho_d = 1.6 \text{ Mg/m}^3$ was considered.

Figure 5-3 shows the resulting evolution of the vertical total strains with changing suction, demonstrating irreversible deformations. The strains are larger at smaller applied stress, which is consistent with the results in the previous section.

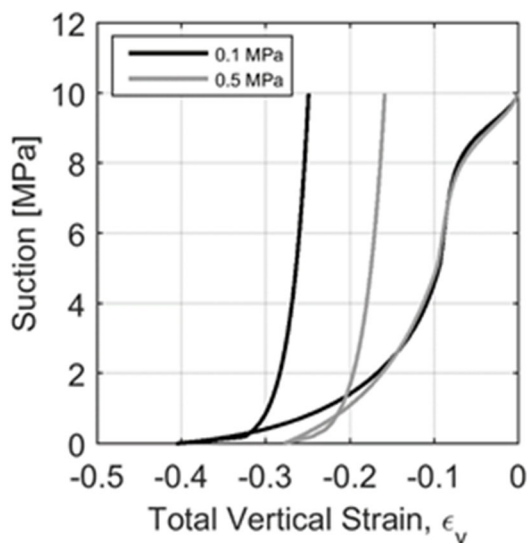


Figure 5-3: Irreversibility of vertical strain during wetting and drying (-ve swelling)

5.3 Dependence of swelling pressure on dry density

Two swelling stress tests were simulated for two values of dry density, under the condition of constant volume, both starting from a total vertical stress, $\sigma_y = 0.5$ MPa, and reducing the suction from 10 MPa to 0. It is assumed that the contribution of the micro-structure is more significant in the denser sample ($\rho_d = 1.6$ Mg/m³), which is deemed reasonable considering the implications of the compaction effort and the formation of the double porosity structure discussed in Section 4.

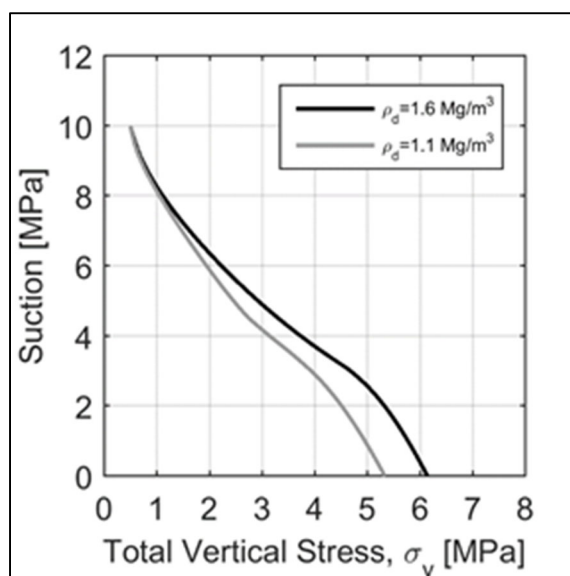


Figure 5-4: Evolution of the swelling pressure in a confined volume wetting test for different dry density

Figure 5-4 shows the evolution of the swelling pressure, in terms of the total vertical stress, σ_y , for initially looser ($\rho_d = 1.1$ Mg/m³) and denser ($\rho_d = 1.6$ Mg/m³) samples. Higher values of σ_y are predicted for the denser sample, which is consistent with the usual experimental findings.

5.4 Stress path dependence from an unsaturated to a saturate state

Three different stress paths, depicted in Figure 5-5, were simulated for this exercise, starting from the same initial unsaturated conditions of suction (10 MPa) and vertical stress (0.5 MPa), and

finishing at the same saturated state, with 0 MPa suction and vertical stress at 3.5 MPa. The relative density for all three paths is $\rho_d = 1.6 \text{ Mg/m}^3$. The stress path 1 involves initial wetting to 0 suction at $\sigma_y = 0.5 \text{ MPa}$, followed by loading at zero suction to $\sigma_y = 3.5 \text{ MPa}$. The stress path 2 is loading first to $\sigma_y = 3.5 \text{ MPa}$ at constant suction of 10 MPa, followed by wetting to 0 suction at constant σ_y . The final stress path, no. 3, involves confined swelling to zero suction, followed by the reduction at 0 suction of total vertical stress, σ_y , to 3.5 MPa.

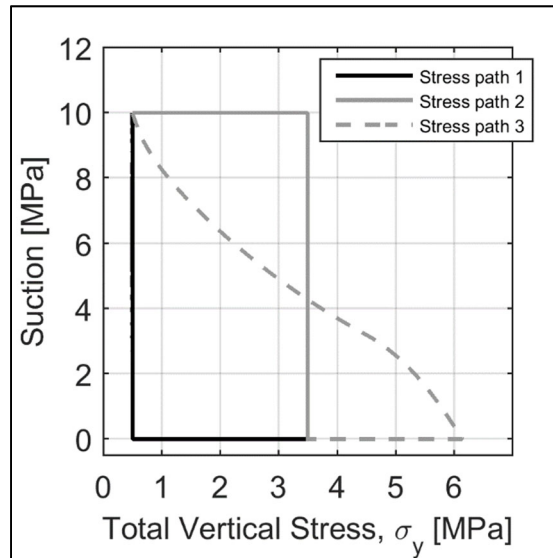


Figure 5-5: Stress paths for simulated changes from unsaturated to saturated stress state

The predicted evolutions of the total vertical strain for each of the applied stress paths are presented in Figure 5-6 against the total vertical stress and are entirely plausible. Initial full hydration in stress path 1 results in a swelling (tensile) strain, which reduces subsequently under the applied compressive vertical stress. Stress path 2 yields initial compressive strain under the applied compressive stress, followed by the swelling (tensile) strain under a constant vertical stress. Finally, the initial confined hydration results in zero vertical strain, followed by a tensile (swelling) strain due the reduction in the vertical stress. The magnitude of the ϵ_y strain at the end of each of the three paths is different, thus further highlighting the ability of the model to capture the stress path dependency in the soil.

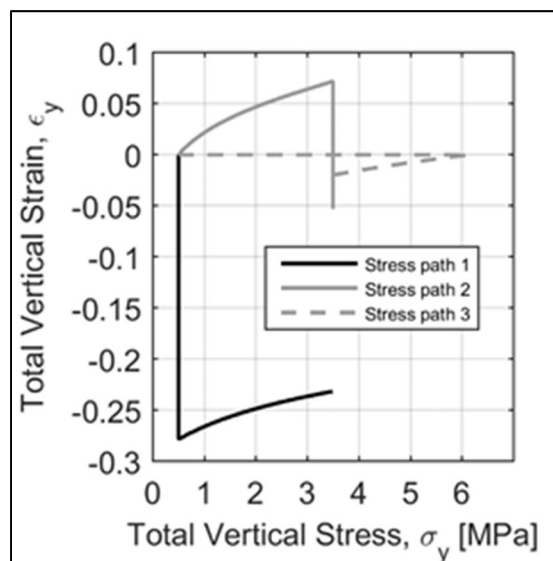


Figure 5-6: Predicted evolution of total strain for changes from unsaturated to saturated stress state

5.5 Stress path dependency from a saturated to an unsaturated state

Two different stress paths, depicted in Figure 5-7, were simulated for this exercise, starting from the same initial saturated conditions of 0 suction and 0.5 MPa vertical stress, and finishing at the same unsaturated state, with 10 MPa suction and vertical stress at 3.5 MPa. The relative density for both paths is $\rho_d = 1.6 \text{ Mg/m}^3$. The stress path 1 involves initial increase in suction (drying) to 10 MPa at $\sigma_y = 0.5 \text{ MPa}$, followed by loading at 10 MPa suction to $\sigma_y = 3.5 \text{ MPa}$. The stress path 2 applies the loading first to $\sigma_y = 3.5 \text{ MPa}$ at 0 suction, followed by increase in suction to 10 MPa at constant σ_y .

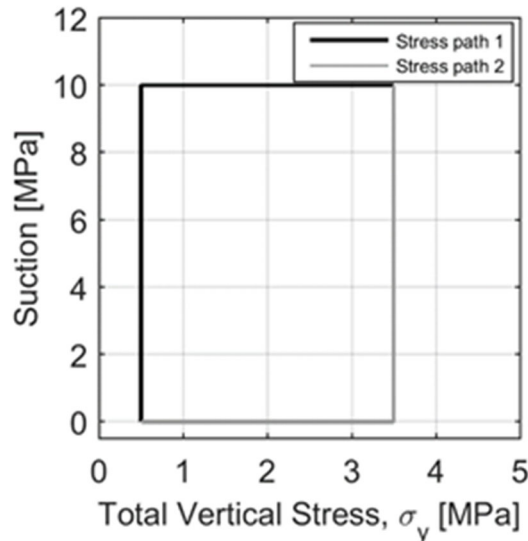


Figure 5-7: Stress paths for simulated changes from saturated to unsaturated stress state

The predicted evolution of total strains from the two stress paths is shown in Figure 5-8. Stress path 1 results initially in shrinking (compressive) vertical strain, which further increases with the applied compressive stress. Stress path 2 initially produces a compressive strain under the applied compressive stress, followed by further compression due to increase in suction (shrinkage). Again, stress path dependency is captured by the model.

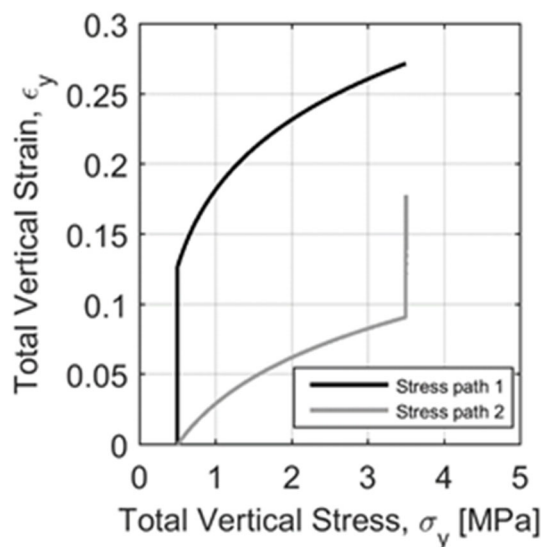


Figure 5-8: Predicted evolution of total strain for changes from saturated to unsaturated stress state

Table 5-1: Summary of basic model capabilities

Name of the constitutive law: Imperial Colle Double Structure Model			
Behaviour feature	D3.1	D3.3	Remarks
Mechanical behaviour			
Dependence of swelling strain on applied stress (at the same dry density) (Figure 5-2(a))	Y	Y	
Dependence of swelling strain on dry density (at the same stress) (Figure 5-2(b))	Y	Y	
Irreversibility of strains in wetting/drying cycles (Figure 5-3)	Y	Y	
Dependence of swelling pressure on dry density (Figure 5-4)	Y	Y	
Stress path dependence from an unsaturated to a saturated state (Figure 5-6)	Y	Y	
Stress path dependence from a saturated to an unsaturated state (Figure 5-8)	Y	Y	
Double structure/porosity considered?	Y	Y	
Are temperature effects considered in the model?	N	N	
Dependence of strains developed in a temperature cycle (increase/decrease) on OCR (or stress) (Figure 7)	N	N	
Hydraulic behaviour (retention curve)			
Hysteresis	Y	Y	
Dependence on void ratio	Y	Y	
Double structure/porosity considered?	N	N	

Y – yes; N – no

6 Report on Task 3.3

As part of the work package 3 (WP3), a set of experiments conducted during the BEACON project was selected for numerical simulation and further testing of modelling capabilities among project partners. The experiments included two oedometer test performed at EPFL on MX80 compacted bentonite, starting from the same initial stresses. One MX-80 specimen was wetted under free swelling, followed by loading, while the other was wetted under constant volume, followed by loading.

The experiments were simulated using the ICDSM model and the finite element software ICPEP. The analyses procedure, model parameters and results are summarised in the report submitted for this task and added here in Appendix A2. The results showed that the numerical model was capable of reproducing reasonably well the hydro-mechanical behaviour of MX80 bentonite observed in these experiments.

7 Performance of the model

The hydro-mechanical modelling tools summarised above were used for all simulations performed as part of Beacon's WP3 and WP5. These have included a range of experiments, from laboratory to large scale in-situ tests, and two types of bentonite, MX80 and Febex.

The examination of basic capabilities of the mechanical (ICDSM) model in Section 5 has demonstrated that such an advanced model is capable of simulating the stress path dependency of bentonite's stress-strain response, which is characteristic of most soils.

Both mechanical (ICDSM) and hydraulic (SWR and permeability) models were calibrated from experimental evidence found in the literature for the two types of bentonite. Two derived sets of model parameters, one each for MX80 and Febex materials, were used throughout the project in their respective analyses. Adjustments were made mainly to micro-structural parameters and SWR curves in some simulations, to reflect the changes in the initial dry density, ρ_d .

Simulations of laboratory tests

With respect to simulated laboratory tests, which involved only hydro-mechanical (HM) coupling and either confined or free swelling, the constitutive model was shown capable of reproducing reasonably well the maximum values of swelling pressures (Tests 1a, 1b; Task 3.3). The model is isotropic in its formulation, hence predicting similar magnitudes of axial and radial swelling pressures measured in constant volume experiments, while the measurements showed these values to be different. It was difficult to assess whether measured data were a result of some inherent anisotropy in specimens of compacted bentonite (which is reasonable to expect to exist), as there also existed some uncertainty of the initial stresses in specimens before the start of their hydration. The simulations also under-estimated the initial rate of the swelling pressure rise (both axial and radial), which could be attributed to possible inadequate variation of permeability at the start of the experiment.

The post-mortem analyses of bentonite states at the end of laboratory tests showed that the model was capable of reproducing the correct trends and close magnitudes of the evolved void ratio / water content / dry density profiles interpreted experimentally.

Laboratory hydration tests under constant volume with mixed bentonite samples (half compacted block, half pellets, Test 1c, Task 5.3) showed fairly homogenised profiles of the evolved void ratio / water content / dry density at the end of experiments. The model was able to simulate the correct magnitudes of changes in these parameters (between the initial values and those at the end of the test) in both parts of the specimen (block and pellets), but still showing a distinction (jump-change) between the two parts. This was again attributed to inadequate permeability modelling especially at the start of the experiment.

Large scale in-situ tests

The large scale in-situ tests simulated as part of Task 5.2 (FEBEX and CRT) involved thermal coupling in addition to hydro-mechanical coupling. The constitutive model is not formulated in terms of temperature, but appropriate parameters for thermal conductivity and coefficients of thermal expansion were applied to bentonite buffer and the surrounding host rock, as well as appropriate temperature / thermal flux boundary conditions at the canister / buffer interface. In both cases the buffer was constructed from compacted bentonite blocks involving Febex bentonite in the Febex experiment and MX80 bentonite in the CRT experiment. The model parameters in both cases were the same as calibrated for the simulations of laboratory tests, the objective being to examine whether such model calibration can be extended for application to a large scale boundary value problem.

The numerical model was shown to reproduce very well the evolution of the temperature field in the buffer. The field tests involved essentially confined hydration (as buffer is entrapped

between the canister and the host rock). The model reproduced very well the mobilised maximum swelling pressures measured at different cross-sections and in different rings of the buffer. The important part of comparison was also the interpretation of field measurements with respect to their operational time of the experiment, in particular in the case of the Febex test which spanned 18 years.

What was not well reproduced in simulations was the rate of wetting in the buffer rings interfacing the host rock, as near 100% relative humidity (RH) in those was measured within the first three years of the Febex experiment, whereas this was around nine years in the simulation. The agreement between the numerical results and measurements of RH evolution was improving for inner rings, given the scatter in measurements. Similar to laboratory experiments discussed above, this shortcoming of the simulation was attributed to inadequate permeability modelling at the start of the experiment.

The post-mortem examination of void ratio / water content / dry density radially across the buffer, after the Febex experiment was dismantled, showed very satisfactory agreement with measurements taken in different cross-sections of the buffer.

8 Final remarks

The principal objective of the modelling work on the Beacon project has been to assess the ability of the available / newly developed modelling tools to simulate the evolution of hydro-mechanical processes in compacted bentonite over a period time, when bentonite specimens are subjected to wetting. Some of the modelled large scale tests additionally exposed bentonite buffers to elevated temperature and therefore drying.

The modelling approach at ICL was to firstly apply the Barcelona Basic single-structure type of a constitutive model (BBM) in the modelling of bentonite, which showed that such a model was not capable of reproducing the measured high swelling pressures. The adopted modelling framework was therefore changed to a double-structure extension of the BBM, introducing two distinct levels of micro and macro porosity in the form of an IC Double Structure Model (ICDSM).

For each of the bentonite types used in the actual experiments, the parameters for ICDSM were derived from model calibration on appropriate laboratory experiments found in literature, different from those simulated for Beacon. It should be noted that some parameters could not be derived directly from any experiments, but were instead derived from simulations of the experiments used in the calibration process.

The objective of this approach was to examine the predictive capabilities of such calibration, by employing independently derived model parameters in the simulations of experiments selected for various stages of the Beacon project. Additionally, appropriate initial stresses / void ratio / dry density in the bentonite material were initialised at the start of each simulation.

Analysing the results from simulations at all scales (laboratory and field) and recognising some of the modelling shortcomings, it may be concluded that the applied modelling approach was shown broadly capable of reproducing the observed patterns of bentonite's THM response and in some cases reasonable agreements between simulations and measurements. There is still a scope for more robust tuning and development of the modelling framework.

References

- Alonso E.E., Gens A., Josa A. (1990).** A constitutive model for partially saturated soils. *Geotechnique* 40 (3), pp. 405-430.
- Bosch J.A., Baryla P., Ferrari A. (2019).** BEACON project. Modelling specifications for Task 3.3: Performance of constitutive models developed in the project. EPFL, July 2019.
- Gens A., Alonso E.E. (1992).** A framework for the behaviour of unsaturated expansive clays. *Canadian Geotechnical Journal* 29 (6), pp. 1013-1032.
- Georgiadis, K., Potts, D. M. & Zdravković, L. (2003).** The influence of partial soil saturation on pile behaviour. *Géotechnique* 53 (1), 11–25.
- Georgiadis, K., Potts, D. M. & Zdravković, L. (2005).** Three-dimensional constitutive model for partially and fully saturated soils. *Int. Jnl. Geomech.* 5 (3), 244–255.
- Ghiadistri G.M. (2019).** Constitutive modelling of compacted clays for applications in nuclear waste disposal. PhD Thesis, Imperial College London, UK.
- Ghiadistri G.M., Potts D.M., Zdravkovic L., Tsiampousi A. (2018).** A new double structure model for expansive clays. 7th Int. Conf. on Unsaturated Soils, UNSAT 2018, 3-5 August 2018, Hong Kong.
- Lagioia, R., Puzrin, A. M. & Potts, D. M. (1996).** A new versatile expression for yield and plastic potential surfaces. *Comput. Geotech.* 19, No. 3, 171–191.
- Matsuoka, H. & Nakai, T. (1974).** Stress-deformation and strength characteristics of soil under three different principal stresses. *Proc. JSCE* No. 232.
- Melgarejo Corredor M.L. (2004).** Laboratory and numerical investigations of soil retention curves. PhD Thesis, Imperial College, University of London, UK.
- Nyambayo V.P., Potts D.M. (2010).** Numerical simulation of evapotranspiration using root water uptake model. *Computers & Geotechnics* 37, pp. 175-186.
- Pastor, M., Zienkiewicz, O. C. & Chan, A. H. C. (1990).** Generalized plasticity and the modelling of soil behaviour. *Int. J. Numer. Anal. Meth. Geomech.* 14, No. 2, 151–190.
- Potts D.M. & Zdravkovic L. (1999).** Finite element analysis in geotechnical engineering: theory. Thomas Telford Publishing, London, UK.
- Sanchez, M., Gens, A., do Nascimento Guimaraes, L. & Olivella, S. (2005).** A double structure generalized plasticity model for expansive materials. *Int. J. Numer. Anal. Meth. Geomech.* 29, 751–787.
- Seiphoori A., Ferrari A., Laloui L. (2014).** Water retention behaviour and microstructural evolutions of MX-80 bentonite during wetting and drying cycles. *Geotechnique* 64 (9), pp.721-734.
- Tang A.M. & Cui Y.J. (2010).** Experimental study on hydro-mechanical coupling behaviours of highly compacted expansive clay. *Journal of Rock Mechanics and Geotechnical Engineering* 2 (1), pp. 39-43.
- Tsiampousi, A., Zdravković, L. and Potts, D.M. (2013a).** A new Hvorslev surface for critical state type unsaturated and saturated constitutive models. *Computers and Geotechnics* 48, 156–166.
- van Genuchten M.T. (1980).** A closed-form equation for predicting the hydraulic conductivity of unsaturated soils. *Soil Science Society of America Journal*, 44, pp. 892-898.

Appendix 1

Finite element implementation

For the macro (F_{LC} and F_{SI}) and micro (β) plastic mechanisms acting simultaneously, the constitutive relationship:

$$\{\Delta\sigma\} = [D] \cdot \{\Delta\varepsilon^e\} \quad (\text{A-1})$$

where $[D]$ is the elastic constitutive matrix and $\{\Delta\varepsilon^e\}$ is the vector of incremental elastic strains, can be expressed as:

$$\{\Delta\sigma\} = [D] \left(\{\Delta\varepsilon\} - \{\Delta\varepsilon_s^e\} - \{\Delta\varepsilon_s^p\} - \{\Delta\varepsilon_{LC}^p\} - \{\Delta\varepsilon_\beta^p\} \right) \quad (\text{A-2})$$

In the above equation $\{\Delta\varepsilon_s^e\}$ and $\{\Delta\varepsilon_s^p\}$ are the vectors of incremental elastic and plastic strains caused by changes in equivalent suction, while the incremental plastic strains $\{\Delta\varepsilon_{LC}^p\}$ and $\{\Delta\varepsilon_\beta^p\}$ result from the macro-structural changes that violate the primary yield surface, F_{LC} , and from the micro-structural changes associated with the β -mechanism, respectively. Consequently:

$$\{\Delta\sigma\} = [D] \left[\{\Delta\varepsilon\} - \{\Delta\varepsilon_s^e\} - \{\Delta\varepsilon_s^p\} - \Lambda_{LC} \left\{ \frac{\partial G_{LC}}{\partial \sigma} \right\} - \Lambda_\beta \left\{ \frac{\partial G_\beta}{\partial \sigma} \right\} \right] \quad (\text{A-3})$$

where Λ_{LC} is the plastic multiplier corresponding to the LC macro-structural plasticity. In order to determine the two unknown plastic multipliers, two conditions must be met:

1. the *macro-structural condition*, according to which the macro-structural plasticity is governed by the primary yield surface, F_{LC} , and therefore has to satisfy the consistency condition (Potts & Zdravkovic, 1999):

$$dF_{LC} = \left\{ \frac{\partial F_{LC}}{\partial \sigma} \right\} \{\Delta\sigma\} + \left\{ \frac{\partial F_{LC}}{\partial s_{eq}} \right\} \{\Delta s_{eq}\} + \frac{\partial F_{LC}}{\partial p_0^*} \Delta p_0^* = 0 \quad (\text{A-4})$$

Substituting Equation (A-3) and Equation (4-19) into Equation (A-4), and rearranging the terms, the following equation containing the plastic multipliers is derived:

$$\begin{aligned} & \left\{ \frac{\partial F_{LC}}{\partial \sigma} \right\} [D] \left[\{\Delta\varepsilon\} - \{\Delta\varepsilon_s^e\} - \{\Delta\varepsilon_s^p\} - \Lambda_{LC} \left\{ \frac{\partial G_{LC}}{\partial \sigma} \right\} - \Lambda_\beta \left\{ \frac{\partial G_\beta}{\partial \sigma} \right\} \right] + \\ & \frac{1+e_M}{\lambda(0)-\kappa} p_0^* \frac{\partial F_{LC}}{\partial p_0^*} \left(\Lambda_{LC} \frac{\partial G_{LC}}{\partial p} + \Lambda_\beta \frac{\partial G_\beta}{\partial p} \right) + \\ & \left\{ \frac{\partial F_{LC}}{\partial s_{eq}} \right\} \{\Delta s_{eq}\} = 0 \end{aligned} \quad (\text{A-5})$$

2. the *micro-structural condition*, given by Equation (4-24) from general plasticity, according to which:

$$\Lambda_{\beta} = \frac{\left\{ \frac{\partial F_{\beta}}{\partial \sigma} \right\} \{ \Delta \sigma \} + \left\{ \frac{\partial F_{\beta}}{\partial s_{eq}} \right\} \{ \Delta s_{eq} \}}{H_{\beta}} \Rightarrow \{ \Delta \sigma \} = \frac{H_{\beta} \Lambda_{\beta} - \left\{ \frac{\partial F_{\beta}}{\partial s_{eq}} \right\} \{ \Delta s_{eq} \}}{\left\{ \frac{\partial F_{\beta}}{\partial \sigma} \right\}} \quad (\text{A-6})$$

Substituting Equation (A-6) into Equation (A-3) and rearranging the terms, the following is obtained:

$$\Lambda_{LC} \left\{ \frac{\partial F_{\beta}}{\partial \sigma} \right\} [D] \left\{ \frac{\partial G_{LC}}{\partial \sigma} \right\} + \Lambda_{\beta} \left(H_{\beta} + \left\{ \frac{\partial F_{\beta}}{\partial \sigma} \right\} [D] \left\{ \frac{\partial G_{\beta}}{\partial \sigma} \right\} \right) = \left\{ \frac{\partial F_{\beta}}{\partial \sigma} \right\} [D] \left(\{ \Delta \varepsilon \} - \{ \Delta \varepsilon_s^e \} - \{ \Delta \varepsilon_s^p \} \right) + \left\{ \frac{\partial F_{\beta}}{\partial s_{eq}} \right\} \{ \Delta s_{eq} \} \quad (\text{A-7})$$

Adopting the notation from Potts & Zdravkovic (1999) when two plastic mechanisms are concurrently active, Equation (A-5) and Equation (A-7) form a two by two (2x2) system of equations that can be written in a short form as follows:

$$\begin{aligned} \Lambda_{LC} L_{11} + \Lambda_{\beta} L_{12} &= T_1 \\ \Lambda_{LC} L_{21} + \Lambda_{\beta} L_{22} &= T_2 \end{aligned} \quad (\text{A-8})$$

The two solutions of Equation (A-8) are then:

$$\begin{aligned} \Lambda_{LC} &= \frac{L_{22} T_1 - L_{12} T_2}{L_{11} L_{22} - L_{12} L_{21}} \\ \Lambda_{\beta} &= \frac{L_{11} T_2 - L_{21} T_1}{L_{11} L_{22} - L_{12} L_{21}} \end{aligned} \quad (\text{A-9})$$

thus enabling the calculation of the macro- and micro-plastic strains. The full expressions for each term of Equation (A-9) are given at the end of this appendix. It is worth noting that for the case (a) above, when only the micro-structure is active and induces plasticity, then $\Lambda_{LC} = 0$ and terms $L_{12} = L_{21} = T_1 = 0$. Consequently, the multiplier Λ_{β} is simply obtained from $\Lambda_{\beta} L_{22} = T_2$.

Finally, to determine the stress changes $\{ \Delta \sigma \}$ in Equation (A-3), the elastic and plastic strains from the change in equivalent suction must be defined. The latter is part of the F_{SI} macro-mechanism, resulting from the mobilisation of the secondary yield surface and is defined by the ICSSM formulation (Georgiadis et al., 2005):

$$\{ \Delta \varepsilon_s^p \} = \frac{\lambda_s - \kappa_s}{3(1 + e_M)(s_{eq} + p_{atm})} \{ \Delta s_{eq} \} \quad (\text{A-10})$$

The elastic strains due to changes in equivalent suction have contributions from both levels of structure, which are weighted by the void factor, VF . This presents a new parameter in the ICDSM model formulation:

$$\{\Delta \varepsilon_s^e\} = \left(\frac{VF}{K_m} + \frac{1-VF}{K_{s,M}} \right) \cdot \{\Delta s_{eq}\} \quad (A-11)$$

where K_m and $K_{s,M}$ were defined by Equation (4-10) and Equation (4-12), respectively. In a similar manner, the global bulk modulus due to changes in equivalent mean stress also has contributions from both levels of structure, defined in the following form:

$$K_{bulk} = \frac{1}{\frac{VF}{K_m} + \frac{1-VF}{K_{p,M}}} \quad (A-12)$$

where $K_{p,M}$ was defined by Equation (4-13). As the purpose of introducing the void factor is to monitor and quantify the evolution of the micro-void ratio, this becomes an additional state parameter in the ICDSM formulation, with its change defined as:

$$\Delta VF = \frac{\Delta e}{e} \frac{\Delta p'}{K_m \cdot \Delta \varepsilon_v} \quad (A-13)$$

The terms that appear in Equation (A-9) are defined as follows:

$$\begin{aligned} L_{11} &= \left\{ \frac{\partial F_{LC}}{\partial \sigma} \right\} [D] \left\{ \frac{\partial G_{LC}}{\partial \sigma} \right\} + H_{LC} \\ L_{12} &= \left\{ \frac{\partial F_{LC}}{\partial \sigma} \right\} [D] \left\{ \frac{\partial G_{\beta}}{\partial \sigma} \right\} + \frac{1+e_M}{\lambda(0)-\kappa} p_0^* \frac{\partial F_{LC}}{\partial p_0^*} \frac{\partial G_{\beta}}{\partial p} \\ L_{21} &= \left\{ \frac{\partial F_{\beta}}{\partial \sigma} \right\} [D] \left\{ \frac{\partial G_{LC}}{\partial \sigma} \right\} \\ L_{22} &= \left\{ \frac{\partial F_{\beta}}{\partial \sigma} \right\} [D] \left\{ \frac{\partial G_{\beta}}{\partial \sigma} \right\} + H_{\beta} \\ T_1 &= \left\{ \frac{\partial F_{LC}}{\partial \sigma} \right\} [D] \left(\{\Delta \varepsilon\} - \{\Delta \varepsilon_s^e\} - \{\Delta \varepsilon_s^p\} \right) + \left\{ \frac{\partial F_{LC}}{\partial s_{eq}} \right\} \{\Delta s_{eq}\} \\ T_2 &= \left\{ \frac{\partial F_{\beta}}{\partial \sigma} \right\} [D] \left(\{\Delta \varepsilon\} - \{\Delta \varepsilon_s^e\} - \{\Delta \varepsilon_s^p\} \right) + \frac{\partial F_{\beta}}{\partial s_{eq}} \Delta s_{eq} \end{aligned} \quad (A-14)$$

where the plastic modulus, H_{LC} , of the macro-structure is defined by the primary yield surface in the ICSSM formulation (Georgiadis et al., 2005):

$$H_{LC} = \frac{1+e_M}{\lambda(0)-\kappa} \cdot p_0^* \cdot \frac{\partial F_{LC}}{\partial p_0^*} \cdot \frac{\partial G_{LC}}{\partial p} \quad (A-15)$$

Appendix 2

Report for WP3 Task 3.3

Task 3.3 - ICL contribution

Author(s):

Giuseppe Pedone, Lidija Zdravkovic, David Potts, Aikaterini Tsiampousi

Reporting period: e.g. 01/06/17 – 13/04/21

Date of issue of this report: **14/04/2021**

Start date of project: **01/07/17**

Duration: 48 Months

This project receives funding from the Euratom research and training programme 2014-2018 under grant agreement No 745 942		
Dissemination Level (choose)		
PU	Public	
RE	Restricted to a group specified by the partners of the Beacon project	
CO	Confidential, only for partners of the Beacon project	CO

REVIEW

Name	Internal/Project/External	Comments

DISTRIBUTION LIST

Name	Number of copies	Comments
Athanasios Petridis (EC) Christophe Davies (EC) Beacon partners		

Abstract

This report presents the contribution to the Deliverable D3.3 from Imperial College London (ICL), describing the finite element (FE) analyses carried out to reproduce the oedometer tests performed at EPFL during the BEACON project.

Content

1	Introduction	32
2	Description of the models	32
3	Geometry and discretisation	32
4	Input parameters	33
5	Initial and boundary conditions	35
6	Results	35
6.1	Test P1-3	35
6.2	Test P2-1	37
7	Conclusions	38
	References	38

1 Introduction

This report presents the contribution to the Deliverable D3.3 from Imperial College London (ICL), describing the finite element (FE) analyses carried out to reproduce the oedometer tests performed at EPFL (Bosch et al., 2019).

A brief description of the models adopted in the analyses is first reported, making reference to the Deliverable D3.1, where a more extensive summary of the constitutive model adopted by ICL in the BEACON project is provided. The FE meshes generated for the analyses are subsequently introduced, together with the model parameters and the boundary conditions adopted. A comparison between experimental and numerical results is then shown, and conclusions are finally drawn.

2 Description of the models

To simulate the mechanical behaviour of the MX80 bentonite in the experiments associated with the Task 3.3, the ICL team has applied the constitutive model presented in the Beacon Deliverable D3.1, produced as part of the WP3 of the Beacon project.

The model is an extended and modified version of the Barcelona Basic Modelling (BBM) framework (Alonso et al., 1990), adopting a double-porosity structure (Gens & Alonso, 1992) and the formulation with net stress and suction as two independent stress variables (Ghiadistri et al., 2018; Ghiadistri, 2019).

The soil water retention (SWR) model used in the simulations is a form of a non-hysteretic van Genuchten-type (van Genuchten, 1980) model, formulated in terms of the degree of saturation and matric suction, and accounting for the variation of the specific volume (Melgarejo Corredor, 2004).

The adopted hydraulic conductivity (permeability) model (Potts & Zdravkovic, 1999; Nyambayo & Potts, 2010) assumes logarithmic variation of permeability with matric suction.

All models were implemented in the finite element software ICFEP (Potts & Zdravkovic, 1999), which has been used by the ICL team in all numerical simulations for the Beacon project.

3 Geometry and discretisation

The numerical simulations undertaken were hydro-mechanically fully coupled. Given that very large deformations (around 80% volumetric strains) were expected in 1 of the 2 tests analysed (i.e. Test P1-3), the large displacement formulation was adopted for that test.

Due to the axisymmetric nature of the experiments under investigation (i.e. Tests P1-3 and P2-1), 2 two-dimensional (2D) axisymmetric FE simulations were undertaken. The domains analysed (radius of 17.5 mm, height of 12.5 mm) were discretised using 8-noded quadrilateral displacement-based elements, with 4 pore pressure degrees of freedom at the corner nodes. The meshes generated are shown in Figure 3.1, together with the mechanical boundary conditions adopted in the 2 stages of each test.

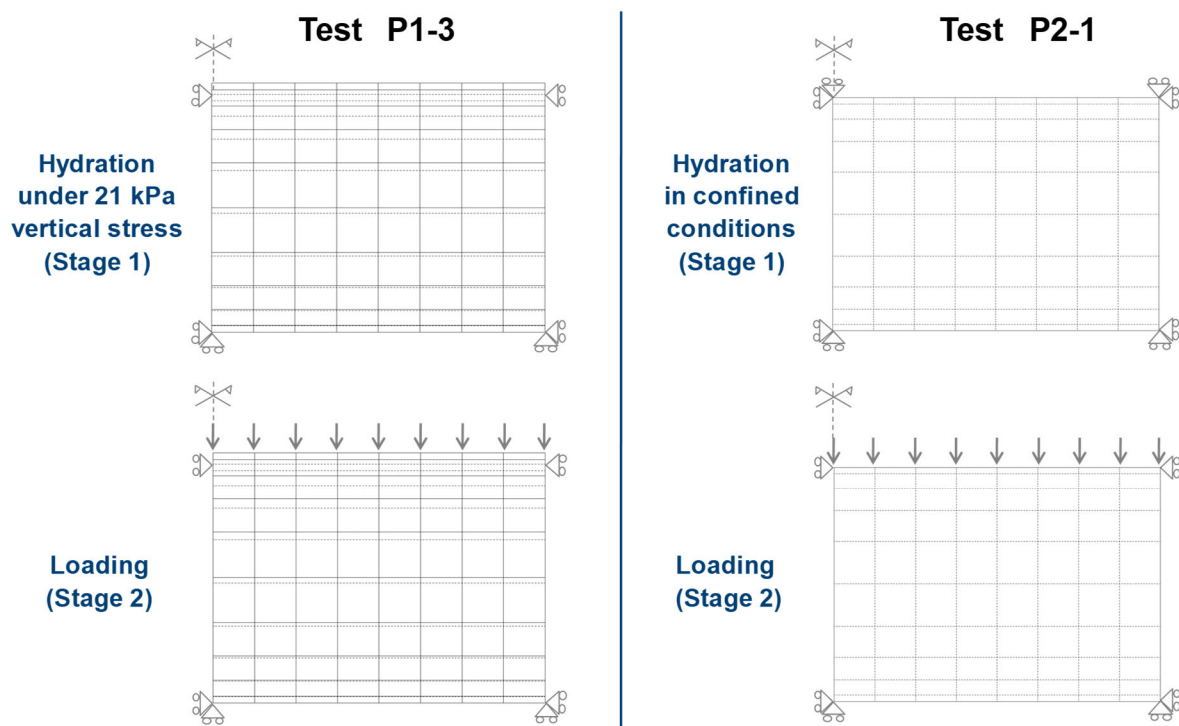


Figure 3.1: Meshes generated and mechanical boundary conditions adopted

4 Input parameters

The model parameters used in both analyses are reported in Tables 4.1, 4.2, and 4.3, with reference to the Imperial College Double Structure Model (IC DSM), the Soil Water Retention (SWR) model, and the Hydraulic Conductivity Function (HCF), respectively.

All parameters were derived from the laboratory data reported in Marcial et al. (2008), Dueck & Nilsson (2010), Tang & Cui (2010), and Seiphoori et al. (2014), except from the values reported in bold (in Table 4.1). The latter were directly based on the EPFL data (Bosch et al., 2019), therefore selected to maximise the model predictive capabilities, as discussed in Section 6.

It is worth highlighting that the parameters reported in Table 4.3 did not influence the results of the analyses given that fully drained conditions were simulated, as mentioned in Section 5.

Table 4.1: Input parameters for IC DSM model

Parameter	Value
Parameters controlling the shape of the yield surface, M_F, α_F, μ_F	0.495, 0.4, 0.9
Parameters controlling the shape of the plastic potential surface, α_G, μ_G	0.4, 0.9
Generalized stress ratio at critical state, M_J	0.495
Characteristic pressure, p_c (kPa)	80.0
Specific volume at unit pressure for initial equivalent suction, $v_1(s_{eq})$	4.684
Fully saturated plastic compressibility coefficient, $\lambda(0)$	0.5154
Elastic compressibility coefficient, κ	0.0087
Maximum soil stiffness parameter, r	0.800
Soil stiffness increase parameter, β (1/kPa)	0.000085
Elastic compressibility coefficient for changes in suction, κ_s	0.1415
Poisson's ratio, ν	0.3
Plastic compressibility coefficient for changes in suction, λ_s	0.5660
Air-entry value of suction, s_{air} (kPa)	0.0
Yield value of equivalent suction, s_0 (kPa)	10^6
Micro-structural compressibility parameter, κ_m	0.3600
Void factor, VF	0.341
Coefficients for the micro swelling function, c_{s1}, c_{s2}, c_{s3}	-0.20, 1.20, 3.00
Coefficients for the micro compression function, c_{c1}, c_{c2}, c_{c3}	-0.20, 1.20, 3.00

Table 4.2: Input parameters for SWR model

Parameter	Value
Fitting parameter, α (1/kPa)	0.0001
Fitting parameter, m	0.47
Fitting parameter, n	1.90
Fitting parameter, ψ	2.0
Residual degree of saturation, S_{r0}	0.05

Table 4.3: Input parameters for HCF model

Parameter	Value
Saturated hydraulic conductivity, k_{sat} (m/s)	3×10^{-13}
Minimum hydraulic conductivity, k_{min} (m/s)	3×10^{-14}
Suction, s_1 (kPa)	100.0
Suction, s_2 (kPa)	40000.0

5 Initial and boundary conditions

The initial conditions assumed in both analyses are reported in Table 5.1. They correspond to the as-poured and hygroscopic conditions provided in Bosch et al. (2019).

The 2 FE analyses conducted were divided into two main stages:

- *Stage 1*: during which hydration was simulated, either under a constant vertical stress of 21 kPa (Test P1-3) or under constant-volume conditions (Test P2-1), as shown in Figure 3.1. Hydration up to full saturation was simulated by imposing homogeneous and gradual suction reductions across the entire mesh. The suction reductions were assumed to take place under fully drained conditions, and, therefore, the evolution of total stresses, void ratios, suctions and degrees of saturation with time was not investigated.

- *Stage 2*: during which vertical total stresses were increased up to 20 MPa in the analysis of Test P1-3 and 5 MPa in the analysis of Test P2-1 (the latter stopped earlier because very small void ratios were attained).

The mechanical boundary conditions applied during both Stages are shown in Figure 3.1.

Table 5.1: Initial conditions adopted for both analyses

Vertical stress (MPa)	OCR* (-)	Void ratio e (-)	Water content w (%)	Degree of saturation S_r (%)	Dry density ρ_d (g/cm ³)	Soil density ρ_s (g/cm ³)	Suction (MPa)
0.021	50.0	0.850	6.266	19.79	1.481	2.740	110.000

*Over-Consolidation Ratio, OCR, defined in terms of mean equivalent stresses

6 Results

The results of the analyses undertaken to simulate Tests P1-3 and P2-1 are summarised in Tables 6.1 and 6.2, respectively. The same results are also shown in Figure 6.1, in comparison with the laboratory data reported by Bosch et al. (2019).

6.1 Test P1-3

The swelling strain predicted in Test P1-3 during *Stage 1* is very similar to the one observed in the laboratory (see path A-B in Figure 6.1). Such a large swelling strain was obtained by adopting a micro-structural compressibility, κ_m , equal to 0.360. This value is almost 3 times larger than the value that could be derived from the laboratory data shown by Tang & Cui (2010).

Table 6.1: FE analysis results for Test P1-3

Test P1-3 (A-B-C-D)				
	Vert. stress (MPa)	e (-)	Suction (MPa)	S_r (%)
Initial (A)	0.021	0.850	110.000	19.79
<i>Stage 1</i>	0.024	0.931	66.500	24.56
	0.023	1.002	41.000	31.05
Swelling (A-B)	0.022	1.245	9.500	60.97
	0.021	1.503	2.000	91.49
	0.022	1.748	0.400	99.19

	0.021	2.029	0.100	99.90
	0.021	2.412	-0.002	100.00
Stage 2 Compression (B-C-D)	0.061	2.409	-0.002	100.00
	0.251	2.402	-0.002	100.00
	0.521	2.397	-0.002	100.00
	0.836	2.388	-0.002	100.00
	0.871	2.368	-0.002	100.00
	1.021	2.286	-0.002	100.00
	2.021	1.933	-0.002	100.00
	4.021	1.578	-0.002	100.00
	8.021	1.222	-0.002	100.00
	16.023	0.866	-0.002	100.00
	20.024	0.751	-0.002	100.00

Table 6.2: FE analysis results for Test P2-1

Test P2-1 (A-B'-C')				
	Vert. stress (MPa)	e (-)	Suction (MPa)	S _r (%)
Initial (A)	0.021	0.850	110.000	19.79
Stage 1 Swelling pressure (A-B')	0.249	0.850	107.000	20.15
	0.489	0.850	105.500	20.34
	0.777	0.850	104.000	20.53
	1.032	0.850	102.950	20.67
	1.501	0.850	45.540	36.31
	1.999	0.849	3.215	97.34
	2.275	0.848	-0.005	100.00
Stage 2 Compression (B'-C')	3.076	0.704	-0.005	100.00
	4.048	0.562	-0.005	100.00
	5.004	0.453	-0.005	100.00
	5.460	0.407	-0.005	100.00

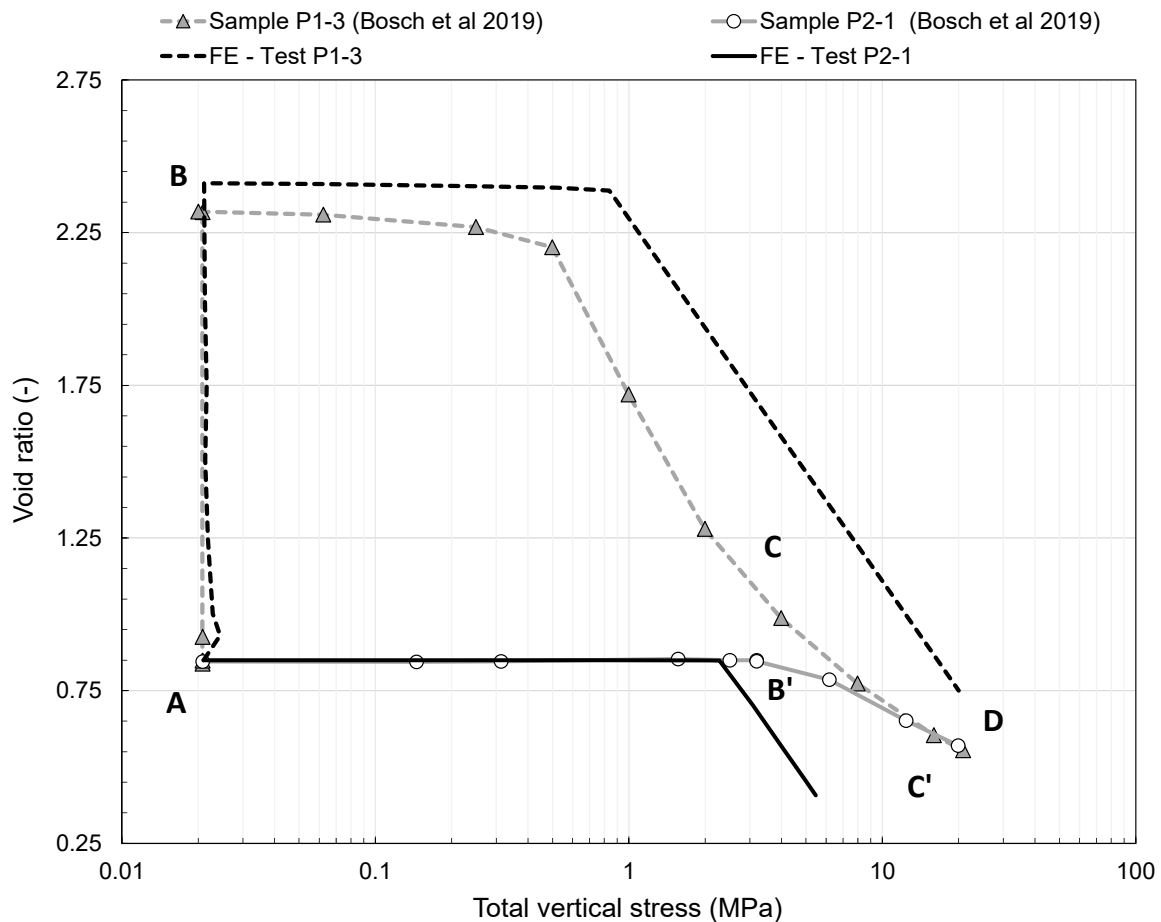


Figure 6.1: Comparison between FE results and laboratory data for Tests P1-3 and P2-1

At the end of *Stage 1*, the material becomes fully saturated (Table 6.1), and, therefore, the void ratio, V_f , in the ICDSM model is automatically set to zero (Ghiadistri et al., 2018; Ghiadistri, 2019). As a consequence, during *Stage 2*, the double-porosity structure is not active and the hydro-mechanical behaviour follows the framework of the original single-structure model.).

The pre-yield response in *Stage 2* is well reproduced, even though a behaviour stiffer than the one measured is predicted close to yielding, but this results from the use of a constant compressibility value, κ . After yielding, as expected, the numerical results show a linear compressibility response (in the logarithmic scale), while the laboratory data indicate a non-linear behaviour post-yield (which the model could only reproduce if the sample remained unsaturated).

The slope of the virgin compression line at full saturation used in the analyses (Table 4.1) is different from the one suggested by Tang & Cui (2010), and was selected to match the average post-yield compressibility observed during Test P1-3. The selected virgin compression line allowed to obtain a final void ratio close to the one measured at the end of the test (Figure 6.1).

6.2 Test P2-1

During *Stage 1*, hydration takes place under confined conditions, so the void ratio remains constant and equal to the initial value of 0.85 (Figure 6.1). A significant increase in vertical total stresses is predicted during this stage, in accordance with the laboratory data provided by Bosch et al. (2019).

As shown in Table 6.2, the analysis tends to under-predict the swelling pressure at the end of *Stage 1*. The measured value is close to 3 MPa, while the predicted one is around 2.3 MPa. However, it is worth recalling that in Test P2-1, before hydration, Bosch et al. (2019) applied an additional vertical stress in the range of 0.12 to 0.31 MPa, with the aim of ensuring good contact between sample and top piston. This additional loading was not modelled in the FE analysis in order to maintain constant-volume conditions, so a swelling pressure under-estimation in the range of 0.12 to 0.31 MPa was expected.

During *Stage 1*, the swelling pressure exceeds the yield stress, hence, at the beginning of *Stage 2*, the stress state lies already on the virgin compression line of the material. As a consequence, the compressibility behaviour predicted in *Stage 2* of Test P2-1 corresponds to the one predicted, post-yield, during *Stage 2* of Test P1-3 (Figure 6.1).

7 Conclusions

The report describes the FE analyses carried out to reproduce the oedometer tests performed at EPFL. A description of the analyses is provided, together with a brief summary of the models used in the simulations. A comparison between experimental and numerical results is also reported, showing that the numerical models can reproduce reasonably well the hydro-mechanical behaviour of the MX80 bentonite when subjected to different hydration processes (confined and unconfined) and subsequent loading.

The results suggest that, when the parameter values listed in Tables 4.1, 4.2 and 4.3 are used, the swelling strain in oedometric conditions is well predicted (*Stage 1*, Test P1-3). However, when the same set of parameter values is adopted, the swelling pressure developing in confined conditions is under-predicted by around 0.5 MPa (*Stage 1*, Test P2-1). Swelling pressure predictions could be refined by enhancing the coupling effects between micro-structure and macro-structure (e.g. by modifying the coupling functions regulating the β interaction mechanism).

After hydration, when loading takes place (*Stage 2*), both analyses show a linear compressibility response (in the logarithmic scale), due to the de-activation of the double-porosity structure occurring at the end of *Stage 1*. The predicted compressibility behaviour is representative of the material response, but it appears to be simpler than the one observed in the laboratory, where a non-linear variation of the void ratio with the logarithm of the vertical stress was observed. The predictive capabilities of the model, in this respect, could be further improved by maintaining a double-porosity structure also in fully saturated conditions, as suggested by the Mercury Intrusion Porosimetry (MIP) data reported in Bosch et al. (2019).

References

- Alonso E.E., Gens A., Josa A. (1990). A constitutive model for partially saturated soils. *Geotechnique* 40 (3), pp. 405-430.
- Bosch J.A., Baryla P., Ferrari A. (2019). BEACON project. Modelling specifications for Task 3.3: Performance of constitutive models developed in the project. EPFL, July 2019.
- Dueck A. & Nilsson U. (2010). Thermo-Hydro-Mechanical properties of MX-80 - Results from advanced laboratory tests. SKB, Technical Report TR-10-55. December 2010.
- Gens A., Alonso E.E. (1992). A framework for the behaviour of unsaturated expansive clays. *Canadian Geotechnical Journal* 29 (6), pp. 1013-1032.
- Ghiadistri G.M. (2019). Constitutive modelling of compacted clays for applications in nuclear waste disposal. PhD Thesis, Imperial College London, UK.

Ghiadistri G.M., Potts D.M., Zdravkovic L., Tsiampousi A. (2018). A new double structure model for expansive clays. 7th Int. Conf. on Unsaturated Soils, UNSAT 2018, 3-5 August 2018, Hong Kong.

Marcial D., Delage P., Cui Y.J. (2008). Hydromechanical couplings in confined MX80 bentonite during hydration. 1st Eur. Conf. on Unsaturated Soils, E-UNSAT 2008, 2-4 July 2008, Durham, UK.

Melgarejo Corredor M.L. (2004). Laboratory and numerical investigations of soil retention curves. PhD Thesis, Imperial College, University of London, UK.

Nyambayo V.P., Potts D.M. (2010). Numerical simulation of evapotranspiration using root water uptake model. *Computers & Geotechnics* 37, pp. 175-186.

Potts D.M. & Zdravkovic L. (1999). *Finite element analysis in geotechnical engineering: theory*. Thomas Telford Publishing, London, UK.

Seiphoori A., Ferrari A., Laloui L. (2014). Water retention behaviour and microstructural evolutions of MX-80 bentonite during wetting and drying cycles. *Geotechnique* 64 (9), pp.721-734.

Tang A.M. & Cui Y.J. (2010). Experimental study on hydro-mechanical coupling behaviours of highly compacted expansive clay. *Journal of Rock Mechanics and Geotechnical Engineering* 2 (1), pp. 39-43.

van Genuchten M.T. (1980). A closed-form equation for predicting the hydraulic conductivity of unsaturated soils. *Soil Science Society of America Journal*, 44, pp. 892-898.

D3.3



Annex F

Contribution to Deliverable D3.3

DELIVERABLE (D3.3) LEI Report

Author(s): dr. A. Narkuniene
prof. P. Poskas
dr. D. Justinavicius

Reporting period: 01/06/20 – 31/05/22

Date of issue of this report: 31/08/21

Start date of project: **01/06/17**

Project duration: 60 Months

This project receives funding from the Euratom research and training programme 2014-2018 under grant agreement No 745 942		
Dissemination Level		
PU	Public	X
RE	Restricted to a group specified by the partners of the Beacon project	
CO	Confidential, only for partners of the Beacon project	

REVIEW

Name	Internal/Project/External	Comments
All Beacon partners	Project internal	

DISTRIBUTION LIST

Name	Number of copies	Comments
Seifallah BEN HADJ HASSINE (EC)	Digital	
Beacon partners	Digital	

Abstract

This report presents a Lithuanian Energy Institute (LEI) contribution to the Deliverable 3.3. It describes the current state of the modelling capabilities of LEI available for modelling the hydro-mechanical behaviour of bentonite material within the frame of the Beacon project. The hydromechanical (HM) model is based on Richards equation to represent water flow through unsaturated material and elastic deformation to represent wetting induced swelling. HM model include important couplings to consider the impact of mechanical deformations on porosity change and subsequently on change of water balance, specific moisture capacity, storage coefficient and permeability. Plastic deformations of bentonite were not considered within this model. The non-linear elastic HM model was implemented in the numerical tool COMSOL Multiphysics. During the project the model development were tested by modelling EPFL test within WP3, meanwhile model application was analysed by modelling different experiments in WP5. One of the test (test1a01) was re-run with the final formulation and is presented in this report. The obtained results within WP3 and WP5 showed that model's predictive capabilities are limited for some analyzed cases. The model output could be treated more as indicator of trends (e. g., full saturation time under same hydration conditions, tendency of occurrence/absent of homogenization) but not the absolute values. In order to increase the predictive capacity of the model, the hydromechanical behavior of bentonite under different material layouts, hydration conditions should be explored further experimentally and numerically. Further model developments are needed with the main focus of the consideration of friction (for laboratory scale experiments), the representation of irreversible strains.

Content

1	Introduction	5
2	Description of the model.....	5
2.1	Basic hypotheses and scope (hydraulic, thermal, chemical, etc.)	5
2.2	Mathematical description	5
3	Basic capabilities of the model	9
4	Model application	10
4.1	Test1a01	10
4.1.1	Parameters	11
4.1.2	Results and discussion	11
4.2	EPFL test	14
4.2.1	Parameters	14
4.2.2	Results and discussion	15
5	Performance of the model and assessment of predictive power	18
6	Concluding remarks	18
	Acknowledgements.....	19
	References	19

1 Introduction

This report provides the description of current status of Lithuanian Energy Institute (LEI) model development for modelling of bentonite hydro-mechanical behaviour in repository conditions. Modelling was performed with numerical tool COMSOL Multiphysics. COMSOL Multiphysics is general-purpose platform software for modelling engineering applications. It allows conventional physics-based user interfaces and coupled systems of partial differential equations for simulation with finite element method.

Modelling results of some experiments with MX-80 and Febex bentonite obtained through the application of model developments were presented in the proceedings of 29th International Conference Nuclear Energy for new Europe NENE2020, September 7-10, 2020, Portorož, Slovenia (Justinavicius et al., 2020) and in Special issue of Minerals journal (Narkuniene et al., 2021).

2 Description of the model

The Richards equation was considered for the water flow modelling in the bentonite material. It was assumed that bentonite mechanical response in terms of deformation or/and developed swelling pressure are mainly governed by bentonite saturation. Wetting induced swelling was modelled as elastic strain and its impact on porosity change was assessed. The hydro-mechanical (HM) model included couplings to consider the impact of mechanical deformations on porosity change and subsequently on change of water balance, specific moisture capacity, storage coefficient and permeability. Plastic deformations of bentonite were not considered within this model. The non-linear elastic HM model was implemented in the numerical tool COMSOL Multiphysics.

2.1 Basic hypotheses and scope (hydraulic, thermal, chemical, etc.)

Within an unsaturated material, hydraulic properties change as fluids move through the medium, filling some pores and draining others. Therefore, it was assumed that the pore space not filled with liquid contains an immobile fluid (gas) at atmospheric pressure. It was also assumed that bentonite mechanical response in terms of deformation or/and developed swelling pressure are mainly governed by bentonite saturation.

2.2 Mathematical description

Flow model

A simplified formulation of the Richards equation was applied to the model of bentonite hydration with water. Partial differential equations for the liquid phase were solved using the following approach:

$$\rho \left(\frac{C_m}{\rho g} + S_e S \right) \frac{\partial p}{\partial t} + \nabla \cdot \rho \left(-\frac{k_s}{\mu} k_r (\nabla p + \rho g \nabla D) \right) = Q_m \quad (1)$$

where p is the dependent variable (pressure of liquid phase), ρ is density of fluid, C_m is specific moisture capacity, g is acceleration of gravity, S_e is effective saturation, S is storage coefficient, k_s is absolute permeability at saturated conditions, k_r is relative permeability, μ is dynamic viscosity of fluid, D represents elevation and Q_m is fluid source (positive) or sink (negative).

The fluid velocity at Darcy scale is:

$$\mathbf{u} = -\frac{k_s}{\mu} k_r (\nabla p + \rho g \nabla D) \quad (2)$$

where \mathbf{u} is the flux vector (Darcy velocity).

Relative permeability was set as a function of effective saturation:

$$k_{r_liq}(S_e) = S_e^l \left(1 - \left(1 - (S_e)^{1/m} \right)^m \right)^2 \quad (3)$$

or

$$k_{r,liq}(S_e) = S_e^l \quad (4)$$

where l is connectivity factor and can be treated as a fitting parameter of the dependency, the relationship better representing experimental conditions is selected. Material of high density has a higher potential to expand, and after contact with water bentonite particles tend to expand more and quickly close larger pores/channels for water transport, thus water transport is reduced and could be described by lower permeability using van Genuchten relative permeability model, for example. If hydrating water is pressurized, it is pressed into the largest open pores/channels, moves quickly into the bentonite and saturate larger part of material in comparison to saturation with not pressurized water or water vapour.

Water saturation (S_w), which is equal to the fraction of the pore space occupied by a given fluid:

$$S_w = \frac{\theta}{\theta_s} \quad (5)$$

Normalized (effective) saturation (S_e) is defined as follows:

$$S_e = \frac{\theta - \theta_r}{\theta_s - \theta_r} \quad (6)$$

where θ_r is residual volume fraction of liquid phase in porous media then there is no continuous flow of this phase, θ_s is a maximal saturated volume fraction of analysed material.

Water retention

The difference between the pressure potentials of gas and liquid in unsaturated conditions, caused by the action of capillary and adsorption forces, is called capillary pressure (suction):

$$p_{gas} - p_{liq} = p_c(S_e). \quad (7)$$

The suction at the Darcy scale is assumed to be a function of the liquid saturation. This relationship is called broadly a water retention curve (WRC). Among the most known dependencies of suction and relative permeability on effective saturation are those called van Genuchten (for suction) and van Genuchten–Mualem (for relative permeability) as defined below [Van Genuchten M, 1980]:

$$p_c = P_{entry} \left((S_e)^{\frac{1}{m_{VG}}} - 1 \right)^{1/n_{VG}} \quad (8)$$

$$S_e = \left(1 + \left(\frac{p_c}{p_0} \right)^{n_{VG}} \right)^{-m_{VG}} \quad (9)$$

$$m_{VG} = 1 - \frac{1}{n_{VG}} \quad (10)$$

where P_{entry} is a pressure scaling parameter (air entry pressure), n_{VG} and m_{VG} are van Genuchten fitting parameters. Air entry pressure is related to the average size of the pores and its value approximately corresponds to the position of the inflection point at the capillary curve.

Modified van Genuchten WRC

In HM model the air entry pressure was implemented as function of void ratio:

$$P_{entry} = A \cdot \Psi \quad (11)$$

Ψ - total suction at saturation, A – fitting parameter.

Ψ as a function of void ratio was derived in [Seiphoori A, et al, 2014] for MX-80 granular bentonite:

$$\Psi(e) = 248.21 \cdot \exp(-4.78 \cdot e) \quad (12)$$

For modelling experiments in WP5 van Genuchten water retention model was prescribed in LEI HM model with implemented air entry pressure as function of void ratio (eq. 12). This relation

was derived based on the experimental data on samples of different void ratio $e=0.83$, $e=0.66$, $e=0.53$, but it is not clear whether this relation is valid for much higher void ratio (>1).

EPFL WRC

The thorough analysis of EPFL test procedure and the measured properties of MX-80 bentonite sample (void ratio, strains, swelling pressure) was performed. The analysis showed that sample void ratio undergoes large changes: from the initial 0.83 to 2.32 in case of free swelling step, and decrease to 0.56 after compression step. Keeping this in mind it was necessary to define water retention curve (WRC) applicable for such large void ratios. It was difficult to calibrate water retention model based on van Genuchten relation, void ratio dependent air entry pressure (eq. 10), van Genuchten parameter $n=1.66$ for confined volume and free swelling conditions (Figure 2-1).

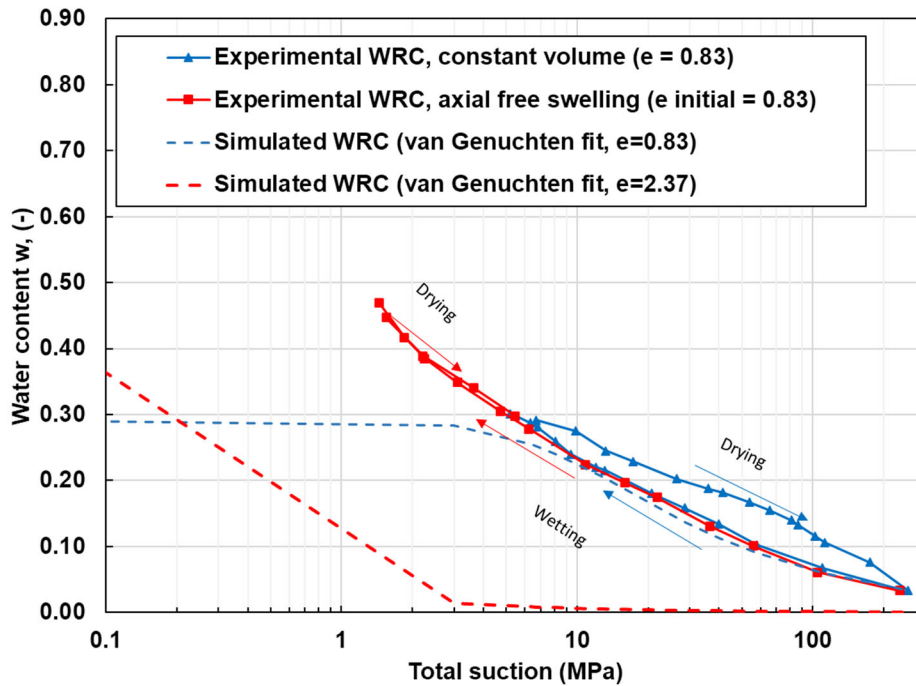


Figure 2-1. Experimental and simulated water retention curves based on van Genuchten relation and void ratio dependent air entry pressure for confined volume and free swell conditions

In order to apply the same WRC for modelling both paths of EPFL test, the water retention model proposed by EPFL [Gens, 2019. Annex D] was analyzed. In this model water ratio e_w (ratio of water volume with respect to volume of solids) is divided into capillary water ratio $e_{w,c}$ (volume of non-adsorbed water with respect to volume of solids) and adsorbed water ratio $e_{w,a}$ (volume of adsorbed water with respect to volume of solids) [Gens, 2019. Annex D]:

$$e_w = e_{w,c} + e_{w,a} \quad (13)$$

The evolution of capillary water ratio $e_{w,c}$ is described with the expression proposed by van Genuchten:

$$e_{w,c}(s, e) = (e - e_{w,a})[1 + (\alpha s)^n]^{1/n-1}, \quad (14)$$

where e is a total void ratio, s – suction, n – van Genuchten parameter. Parameter α is related to air entry pressure as follows:

$$\alpha = a(e - e_{w,a})^b \quad (15)$$

The adsorbed water ratio $e_{w,a}$ is a function of relative humidity, RH following a Freundlich isotherm:

$$e_{w,a}(s) = e_{w,a}^c (RH)^{1/m} = e_{w,a}^c \left(\exp\left(-\frac{M_w}{RT\rho_w} s\right) \right)^{1/m} \quad (16)$$

Where M_w is molecular mass of water, ρ_w is water density, R is universal gas constant, T is temperature, m is fitting parameter.

WRC calibration has been done with the assumption that maximum absorbed water ratio is a function of void ratio instead of constant. This assumption is in line with knowledge that at highly compacted bentonite (low void ratio) the number of water monolayers in the clay platelets is limited and the number of water monolayers is increasing at higher sample void ratio. Parameters for EPFL proposed WRC are presented and compared to parameters to be used in LEI model for EPFL test (Table 2-1).

Table 2-1 Parameters for EPFL proposed WRC model

Parameter		EPFL [Annex D in D3.2.]	Values to be used in LEI model
Coefficient related to air entry value [1/MPa]	a	1.5	0.9
Evolution of air entry value with void ratio	b	1.5	1
Shape of the capillary water retention model	n	1.8	1.8
Parameter controlling the kinetics of adsorption	m	1.2	0.57
Maximum adsorbed water ratio	$e_{w,a}^c$	0.55	$0.7-0.08/e^2$

Experimental WRC and simulated WRC are presented in Figure 2-2. Simulated WRC were in line with the maximum water content at saturation which would be attained in a sample of large void ratio.

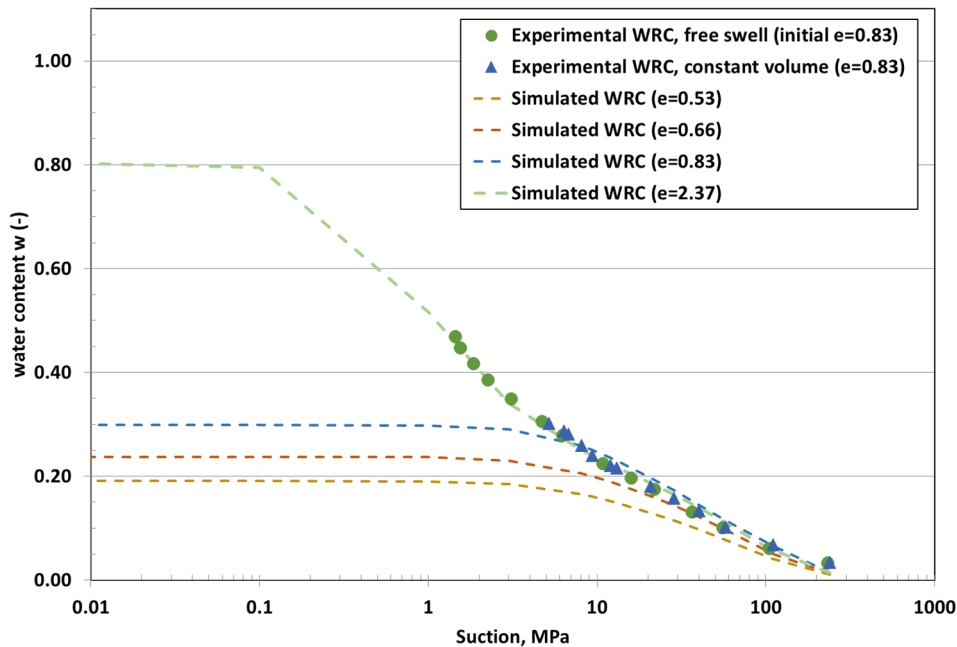


Figure 2-2. Water retention curves for modelling EPFL test with MX-80 bentonite

Swelling model

It is well-known that the bentonite-based material swells after absorption of water. Under free swell conditions it will result in the volume change, while under confined conditions the swelling pressure builds up against the retaining cell walls. The mechanical behaviour of bentonite was

represented using a pure elastic constitutive model based on generalized Hooke's law complemented with hydration (swelling)-induced strain in analogy with thermally-induced strain in [Wang et al, 2015]:

$$\sigma_{ij} = \mathbf{C}_{ijkl}^e \cdot (\varepsilon_{kl} - \varepsilon_{kl}^{sw}) \quad (17)$$

Where σ_{ij} is the stress tensor, ε_{kl} is total strain tensor, ε_{kl}^{sw} swelling strain tensor, \mathbf{C}_{ijkl}^e are the components of the fourth-order stiffness tensor of material properties. It can be determined by the Young's modulus E and Poisson ratio ν in elasticity. Young's modulus E is as follows:

$$E = 3K(1 - 2\nu) \quad (18)$$

where K is the bulk modulus. Young's modulus was assumed to be dependent on changing void ratio, but it is not allowed to become less than prescribed minimum value. Such definition meant to represent overall material behaviour in terms of increased resistance to external load during the compression:

$$E = \max\left(\frac{A}{e^2}, E_{min}\right) \quad (19)$$

A – fitting parameter, e – void ratio, E_{min} – Young modulus corresponding to minimum bulk modulus. This relationship was assumed to be nonlinear and need an experimental verification. The elastic swelling model [Rutquist J et al, 2014] was adopted to model experiments, where the swelling strain was modelled as proportional to the change of saturation:

$$\varepsilon_{ij}^{sw} = \beta^{sw} n \Delta S_w \delta_{ij} \quad (20)$$

where β^{sw} is a moisture swelling coefficient for isotropic material, n is porosity, ΔS_w is change of water saturation, δ_{ij} – Kronecker-delta. Swelling coefficient depends on bentonite type, sample form, porewater composition, experimental conditions (confined volume, unconstrained swelling conditions), etc. Due to lack of experimental database covering a full range of these important aspects, the functional relationship has not been derived and the parameter was calibrated for modelling particular test.

Porosity change

With assumption of slow deformation of solid [Abed A. et al, 2017] the porosity change was evaluated as a function of volumetric strain ε_v ($\varepsilon_v = \varepsilon_{11} + \varepsilon_{22} + \varepsilon_{33}$):

$$\frac{\partial n}{\partial t} = (1 - n) \cdot \frac{\partial \varepsilon_v}{\partial t} \quad (21)$$

Couplings

The following couplings were considered in this hydro-mechanical (HM) model:

- feedback on water mass balance through water source/sink due to change of porosity [Abed A et al., 2016]:

$$Q_m = (1 - n) \cdot S_e \cdot \rho_w \cdot \frac{\partial \varepsilon_v}{\partial t} \quad (22)$$

- porosity change impact on flow equation parameters C_m (specific moisture capacity), S (storage coefficient):

$$C_m = n \cdot \frac{\partial S_e}{\partial h} \quad (23)$$

$$S = n \cdot \chi_f + (1 - n) \cdot \chi_p \quad (24)$$

where χ_f - water compressibility, χ_p - matrix compressibility, h – pressure head.

3 Basic capabilities of the model

Table 3-1 Basic capabilities of Simplified Hydromechanical model developed by LEI.

Name of the constitutive law: Behaviour feature	Simplified Hydromechanical Model		
	D3.1	D3.3	Remarks
Mechanical behaviour			
Dependence of swelling strain on applied stress (at the same dry density)	-	yes	
Dependence of swelling stress on dry density (at the same stress)	-	Yes	Swelling strains depend on swelling coefficient which differ for samples of different dry density and is calibrated
Irreversibility of strains in wetting/drying cycles	-	No	Due to elasticity, strains are reversible
Dependence of swelling pressure on dry density	-	Yes	Swelling pressure is dependent on mechanical properties (bulk modulus), which defined as a function of void ratio (dry density)
Stress path dependence from an unsaturated to a saturated state	-	No	
Stress path dependence from a saturated to an unsaturated state	-	No	
Double structure/porosity considered?	-	-	Not implemented yet
Are temperature effects considered in the model?	-	-	Not implemented yet
Dependence of strains developed in a temperature cycle (increase/decrease) on OCR (or stress)	-	-	Not implemented yet
Hydraulic behaviour (retention curve)			
Hysteresis	No	No	
Dependence on void ratio	No	Yes	For water retention curve based on van Genuchten model, the dependence of air entry pressure on total void ratio is prescribed
Double structure/porosity considered?	No	Yes, partially	For water retention curve based on EPFL WRC model, capillary and absorbed water ratio could be related to macro and microporosity

4 Model application

4.1 Test1a01

Model development proceeded gradually together with model applications for modelling experiments in WP5 and EPFL test within the framework of WP3. The first results of test1a01 modelling performed with the very first model formulation is presented in deliverable D5.1.2 [Talandier, 2019]. LEI results reported showed limited agreement with experimental data. By the end of project, Test1a01 was re-run with the final model formulation to present improvements in model capabilities and obtained results. More detailed description of the test is provided in deliverable D5.1.1 [Talandier, 2018].

4.1.1 Parameters

The parameters used in the modelling of Test1a01 test are summarized in Table 4-1.

Table 4-1 Parameters used for modelling

Parameter	Value
Dry density, kg/m ³	1655
Porosity, -	0.4
Initial void ratio, -	0.68
Initial water content, %	13
Initial saturation, %	53
Hydraulic conductivity, m/s	$K(e) = K_0 \left(\frac{e}{e_0}\right)^\eta$, $K_0 = 2.4 \cdot 10^{-13}$, $e_0 = 1$, $\eta = 5.3$
Relative permeability, -	Van Genuchten, $m = 0.38$, $n = 1.6$, $l = 0.5$
Water retention curve, -	Van Genuchten, $m_{VG} = 0.38$, $n_{VG} = 1.6$, $l = 0.5$, $P_{entry} = f(e)$
Young modulus, MPa	$\max(E = \frac{A}{e^2}, E_{min})$, $A = 13$
Minimum bulk modulus, MPa	20
Poisson ration, -	0.35
Swelling coefficient, -	0.5*S _e (step 1) 0.36*S _e (step 2)

For the 1st step („saturation phase“) the initial water pressure was set to correspond to the degree of saturation of 0.53 based on water retention curve. No initial stresses and strains were assumed. Constant water pressure of 2 kPa was set on the top boundary and no-flow boundary conditions were set to the side and bottom of model domain. Roller type boundary conditions were accepted for all boundaries as no displacements were allowed in normal direction and no friction on the wall.

For the 2nd step („swelling phase“) the initial conditions of variables were obtained from preceding step. The hydraulic boundary conditions were set the same as in the step 1. For the top boundary the prescribed displacement of 2.9 mm was set as a function over short time (~1 min).

4.1.2 Results and discussion

Modelling results are presented in Table 4-1. As it could be seen from the Figure 4-1, the material was not fully saturated by the end of simulation (after 30 days).

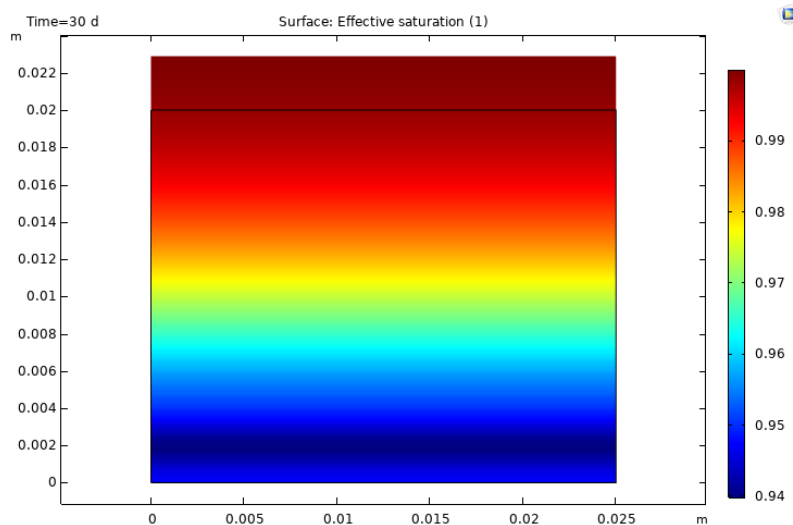
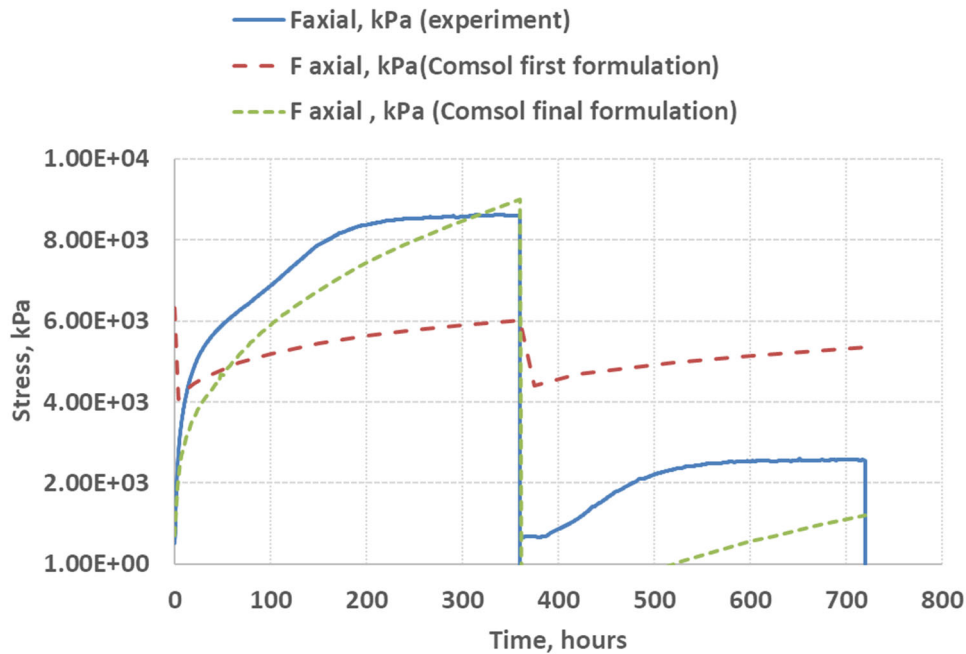
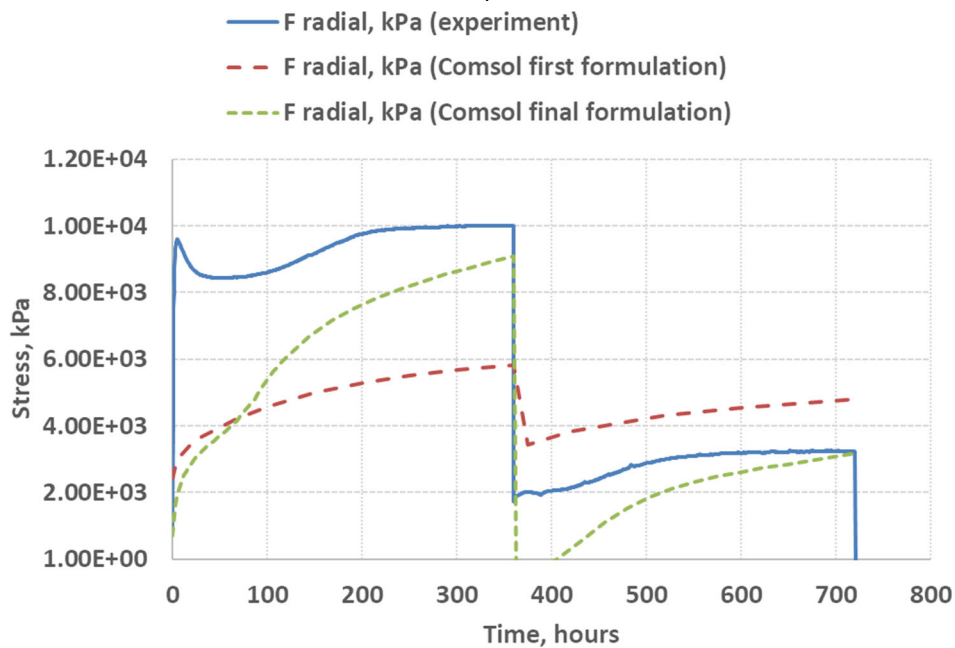


Figure 4-1. Results of water saturation distribution by the end of simulation (after 30 days)

Modelling results of axial and radial stresses (swelling pressure) with a final model formulation are presented in Figure 4-2 a) and b), respectively. The results of the first model formulation presented in [Talandier, 2019] are indicated too. As it could be seen from the figure the trend of non-linearly increasing pressure during step 1 and step 2 was observed. Modelled maximum swelling pressure was higher at the end of step 1 than of step 2. The same trend was observed in the results obtained with first model formulation.



a)



b)

Figure 4-2. Results of swelling pressure evolution modelling and experimental results: a) axial stress, b) radial stress

With a first model formulation, modelling results showed underestimated axial and radial stresses during step 1 and overestimated axial and radial stresses during step 2 in comparison to experimental results. Meanwhile with a final model formulation, the modelled stresses were not overestimated for step 2. The axial swelling pressure was slightly overestimated for step 1,

but differences were larger for step 2. In case of radial swelling pressure, the modelling results were underestimating measured values to some extent for step 1, but at the end of experiment it is good correlation with experiment. The instant initial peak of radial stress was not predicted by model output. The reason of measured instant peak of radial stress is not very clear. It could be related to the heterogeneities in the sample, fast hydration of sample side. The technological gap between sample and cell were not reported, but it was stated that cell walls were lubricated.

Modelling results of void ratio at particular points of specimen after 30 days (step 2) are presented in Figure 4-3. The figure contains the results of modelling with the first model formulation also. As it could be seen from the figure, in the later case the void ratio at height $z=7.5$ mm was in agreement with experimental data, but the void ratio was slightly overestimated in the upper part of specimen and underestimated in the lower part of specimen with the first model formulation. Meanwhile with updated model formulation more points were in line with experimental data (void ratio at height $z < 12.5$ mm). However, the void ratio was underestimated in the upper part of specimen. This could be related to irreversible strains which could take place, however current model formulation is limited to reversible strains only.

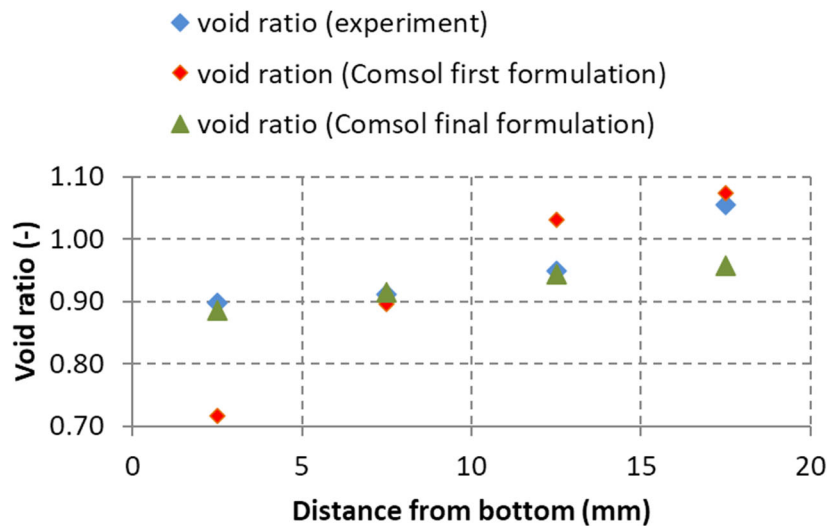


Figure 4-3. Modelling results of void ratio at particular points of specimen and experimental data

Modelling results of water content at particular points of specimen after step 2 are presented in Figure 4-4. The figure contains the results of modelling with the first model formulation also. In this later case, modelled water content at height of 17.5 mm was in line with experimental data, but differed from experimental ones at other heights. The largest difference was observed close to the bottom of specimen. The water content obtained with updated model formulation led to qualitatively better alignment with experimental data, the trend on increasing water content from the bottom to the top was captured. The largest difference was observed close to the upper part of specimen. The reason could be related to irreversible changes of void ratio here as the sample was flooded in the upper part at the beginning of second step. This part experienced an unconstrained swelling condition for certain time period and large changes in material state could be induced (i.e. becoming a gel). However, there is no experimental data on time evolution of void ratio in the sample.

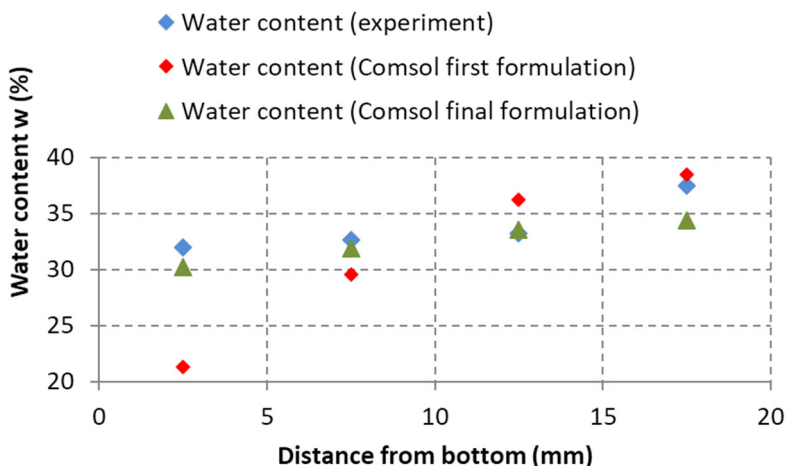


Figure 4-4. Modelling results of water content at particular points of specimen and experimental data

In overall, it could be seen that final model formulation in COMSOL Multiphysics led to underestimated (to some extent) void ratio, water content at different parts of specimen (more significant differences for upper part of specimen). In case of axial swelling pressure, the modelling results were overestimating measured values to some extent for step 1, but largely underestimating the measured one for step 2. Radial swelling pressure was slightly underestimated for step 1, but were in line with experimental data for step 2. The instant initial peak of radial stress was not predicted by model output. Experimental test re-run would be desirable for thorough analysis of this peak and processes determining it.

4.2 EPFL test

Task 3.3 of the Beacon project involved the modelling of a set of oedometer tests, performed at EPFL, comprising various stages of saturation and loading. More detailed description about test is provided in [Bosch et. al., 2019]. The stress paths followed by the tests are depicted in Figure 4-5.

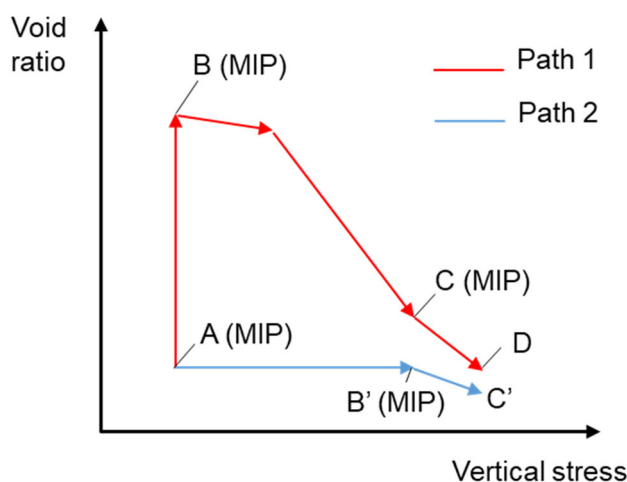


Figure 4-5. Oedometer stress paths followed by the Task tests

4.2.1 Parameters

The parameters used in the modelling of EPFL test are summarized in Table 4-2.

Table 4-2 Parameters used for modelling

Parameter	Value
Dry density, kg/m ³	1529
Porosity, -	0.45
Initial void ratio, -	0.83
Initial water content, %	6
Initial saturation, -	0.2
Hydraulic conductivity, m/s	$K(e) = K_0 \left(\frac{e}{e_0}\right)^\eta$, $K_0 = 2.4 \cdot 10^{-13}$, $e^0 = 1$ $\eta = 5.3$
Relative permeability, -	$k_r(S_e) = S_e^3$
Water retention curve, -	Based on EPFL model, $a=0.9$; $b=1$; $n=1.8$; $m=0.57$; $e_{w,a}^c = 0.7 - \frac{0.08}{e^2}$,
Young modulus, MPa	$\max(E = \frac{A}{e^2}, E_{min})$, $A=13$
Minimum bulk modulus, MPa	20
Poisson ration, -	0.35
Swelling coefficient, -	0.14*S _e (Path 1) 0.33*S _e (Path 2)

For Path 1 the initial water pressure was set to correspond to the degree of saturation of 0.2 based on water retention curve. No initial stresses and strains were assumed. Constant water pressure of 20 kPa was set on the top and bottom boundary and no-flow boundary conditions were set to the side of model domain. For the top boundary the additional equation was solved for displacement as a function of difference mean stress and external load over time.

For the 1st step („saturation phase“ in confined volume conditions) of Path 2 the initial water pressure was set to correspond to the degree of saturation of 0.2 based on water retention curve. No initial stresses and strains were assumed. Constant water pressure of 20 kPa was set on the top and bottom boundary and no-flow boundary conditions were set to the side of model domain. Roller type boundary conditions were accepted for all boundaries as no displacements were allowed in normal direction and no friction on the wall. For the 2nd step („compression phase“) the initial conditions of variables were obtained from preceding step. The hydraulic boundary conditions were set the same as in the step 1. For the top boundary the additional equation was solved for displacement as a function of difference mean stress and external load over time.

4.2.2 Results and discussion

Time dependent evolution of swelling pressure development during saturation under confined volume conditions is presented in Figure 4-6. As it could be seen from the Figure, the time of maximum swelling pressure differed for three samples under the same hydraulic and mechanical conditions. Modelled swelling pressure agreed with experimentally measured swelling pressure of sample P2-2 particularly.

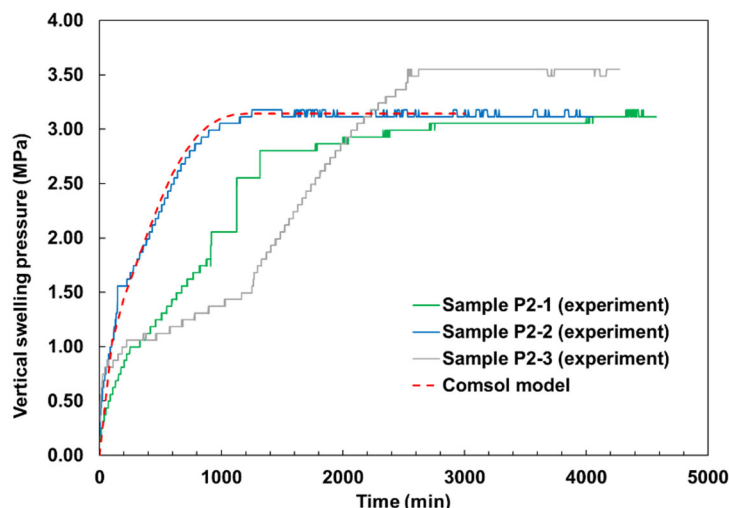


Figure 4-6. Swelling pressure during saturation under confined volume conditions

The evolution of void ratio saturation and compression steps is presented in Figure 4-7.

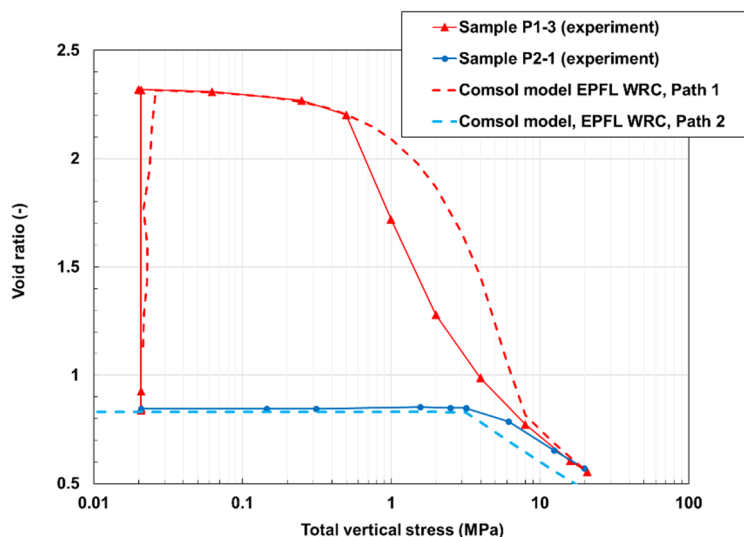


Figure 4-7. Evolution of void ratio during saturation and subsequent compression steps

As it could be seen from Figure 4-7, the modelling results of void ratio evolution during saturation under confined volume conditions followed by compression showed good agreement with the experimental results. For the path 1, modelled void ratio after free swelling step were in line with experimental results. Modelled void ratio evolution during subsequent compression overestimated the void ratio to some extent at vertical stress > 0.5 MPa. The final void ratio for Path 1 conditions was overestimated in the model by ~1 %. The final void ratio for Path 2 was underestimated by ~17 % with final model formulation. The distribution of dry density over sample height has not been reported thus the model capabilities to represent it was not assessed for EPFL test.

Modelling results of sample saturation under confined volume and free swell conditions and subsequent compression are presented in the Table 4-3-Table 4-6.

Table 4-3 Results of the analysis for path A – B – C – D (Path 1)

A – B – C D			
Total vertical stress (MPa)	Void ratio (-)	Suction (MPa)	Degree of saturation (%)

Initial (A)	0.00	0.84	112.9	19
	0.02	1.13	55.6	49
	0.02	1.29	26.2	63
	0.02	1.43	7.2	74
	0.02	1.59	2.3	82
	0.02	1.77	1.0	88
Swelling (AB)	0.02	1.95	0.5	93
	0.02	2.14	0.2	97
	0.03	2.29	0.0	100
	0.03	2.31	0.0	100
	0.03	2.31	0.0	100
	0.03	2.31	0.0	100
	0.03	2.31	0.0	100
	0.03	2.31	0.0	100
	0.50	2.20	0.0	100
	1.01	2.09	0.0	100
	5.98	1.07	0.0	100
Compression (BCD)	7.97	0.82	0.0	100
	11.95	0.70	0.0	100
	15.90	0.62	0.0	100
	18.36	0.59	0.0	100
	20.71	0.56	0.0	100
	20.79	0.56	0.0	100

The evolutions of void ratio, suction and degree of saturation with time (path AB) are presented in Table 4-4.

Table 4-4 Results of the analysis for path A – B

Time (minutes)	A – B		
	Void ratio (-)	Suction (MPa)	Degree of saturation (%)
0	0.84	112.9	19
50	1.13	55.6	49
100	1.29	26.2	63
150	1.43	7.2	74
200	1.59	2.3	82
250	1.77	1.0	88
300	1.95	0.5	93
350	2.14	0.2	97
400	2.29	0.0	100
450	2.31	0.0	100
500	2.31	0.0	100
500	2.31	0.0	100
600	2.31	0.0	100

Table 4-5 Results of the analysis for path A -B' - C'

	A B' C'			
	Total vertical stress (MPa)	Void ratio (-)	Suction (MPa)	Degree of saturation (%)
Initial (A)	0.0	0.83	115.00	20.245
	1.04	0.83	56.46	52
	1.44	0.83	34.89	65
	1.76	0.83	21.08	74
Swelling pressure test (AB')	2.06	0.83	13.28	81
	2.34	0.83	8.59	87
	2.59	0.83	5.73	92
	2.79	0.83	3.94	95
	2.93	0.83	2.72	97
	3.04	0.83	1.79	99
	3.10	0.83	1.02	99

	3.14	0.83	0.36	100
	3.14	0.83	0.00	100
	3.14	0.83	0.00	100
Compression	6.16	0.70	0.00	100
(B'C')	16.10	0.51	0.00	100
	19.81	0.47	0.00	100

Table 4-6 Time dependent results of the analysis for path A – B'

Time (minutes)	A – B'		
	Total vertical stress (MPa)	Suction (MPa)	Degree of saturation (%)
0	0.0	115	20
100	1.04	56.46	52
200	1.44	34.89	65
300	1.76	21.08	74
400	2.06	13.28	81
500	2.34	8.59	87
600	2.59	5.73	92
700	2.79	3.94	95
800	2.93	2.72	97
900	3.04	1.79	99
1000	3.10	1.02	99
1100	3.14	0.36	100
1200	3.14	0.00	100

5 Performance of the model and assessment of predictive power

Within the BEACON project several bentonite materials (MX-80, FEBEX) of different forms (block, pellets, pellet-powder mixture) have been investigated experimentally and numerically. Tests of different scale, different configuration, hydration mode has been performed. A simplified hydro-mechanical model has been developed and tested by LEI team under different hydration conditions. The obtained results within WP3 and WP5 showed that model's predictive capabilities are limited for some analyzed cases. The model output could be treated more as indicatory of trends (e. g., full saturation time under same hydration conditions, tendency of occurrence/absent of homogenization) but not the absolute values. Current model formulation includes some parameters such as swelling coefficient which depend on bentonite type, sample form, density, porewater composition, experimental conditions (confined volume, unconstrained swelling conditions), etc. Due to lack of consistent experimental database covering a full range of these important aspects, it was difficult to derive functional relationship thus the parameter was calibrated for modelling particular test.

In order to increase the predictive capacity of the model, the hydromechanical behavior of bentonite under different material layouts, hydration conditions should be explored further experimentally and numerically. Further model developments are needed with the main focus of the consideration of friction (for laboratory scale experiments), the representation of irreversible strains.

6 Concluding remarks

Within the BEACON project several bentonite materials (MX-80, FEBEX) of different forms (block, pellets, pellet-powder mixture) have been investigated experimentally and numerically. Tests of different scale, different configuration, hydration mode has been performed. A simplified hydro-mechanical model has been developed and tested by LEI team under different

conditions. Despite the limited model capacities for some analysed cases, the model output could be treated more as indicator of trends and subsequently further model developments are needed. Further model development should be supported by experimental data representing wide range of conditions, physical and chemical properties. Compilation of experiment database in sustainable format was started within the project and is of high importance.

Nevertheless, a valuable knowledge on modelling coupled HM processes has been gained by LEI team during the cooperation with partners within the project. Sharing the knowledge on main processes, aspect and challenges in numerical assessment paved the way for further competence development in the prediction of bentonite material behaviour. The understanding and numerical models are essential to support development of geological disposal system.

Acknowledgements

LEI would like to acknowledge to VTT (Finland) research team – prof. Markus Olin, dr. Veli-Matti Pulkkanen, dr. Heidar Gharbieh - for cooperation and exchange of modelling experiences and expertise developing HM model in COMSOL Multiphysics.

References

Abed A, Solowski W T, 2017. A study on how to couple thermo-hydro-mechanical behaviour of unsaturated soils: Physical equations, numerical implementation and examples. *Computers and Geotechnics*, 92, 2017, P.: 132-155.

Abed A, Laitinen M, Lämsä J, Harjupatana T, Sołowski W T, Kataja M, 2016. Hydro-mechanical modelling of MX-80 bentonite: one dimensional study. In proceedings of 3rd European Conference on Unsaturated Soils – “E-UNSAT 2016”, Paris, France, September 12-14, 2016.

Bosch J. A, Baryla P, Ferrari A, 2019. Modelling specifications for task 3.3: performance of constitutive models developed in the project.

Gens A, 2019. Description of improved constitutive models and their implementation and verification. EC H2020 project Beacon report D3.2.

Justinavicius D, Narkuniene A, Poskas P, 2020. Modelling of coupled hydraulic-mechanical behaviour of MX-80 bentonite under hydration with groundwater. In Proceedings of 29th International Conference Nuclear Energy for new Europe NENE2020, September 7-10, 2020, Portorož, Slovenia, 2020, p. 918.

Narkuniene A, Poskas P, Justinavicius D, 2021. The modeling of laboratory experiments with COMSOL Multiphysics using simplified hydromechanical model. *Minerals*, 2021; 11(7):754. <https://doi.org/10.3390/min11070754>

Rutquist J Liange Zheng, Fei Chen, Hui-Hai Liu, Birkholzer J. 2014. Modeling of Coupled Thermo-Hydro-Mechanical Processes with Links to Geochemistry Associated with Bentonite-Backfilled Repository Tunnels in Clay formations. *Rock Mechanics and Rock Engineering*, 47, 2014, P.: 167-186.

Seiphoori A, Ferrari A, Laloui L, 2014. Water retention behaviour and microstructural evolution of MX-80 bentonite during wetting and drying cycles. *Géotechnique*, Volume 64(9), 2014, P.: 721-734.

Talandier J, 2018. Specifications for BEACON WP5: testing, verification and validation of models. Step 1- verification cases. BEACON deliverable report D5.1.1, 2018.

Talandier J, 2019. Synthesis of results from task 5.1. EC H2020 project Beacon report D5.1.2. 2019.

Van Genuchten, M, 1980. A closed form equation for predicting the hydraulic conductivity of unsaturated soils. Soil Sci. Soc. Am. J. 1980, 44, 892–898.

Wang X, Shao H, Wang W, Hesser J, Kolditz O, 2015. Numerical modeling of heating and hydration experiments on bentonite pellets. Eng. Geol. 2015, 198, 94-106.
<http://dx.doi.org/10.1016/j.enggeo.2015.09.009>

D3.3



Annex G

Contribution to Deliverable 3.3

DELIVERABLE (D3.3) Quintessa Report

Author(s): Rebecca Newson, Kate Thatcher, Steve Benbow, Neil Chittenden

Reporting period: 01/06/20 – 31/05/22

Date of issue of this report: 31/08/21

Start date of project: **01/06/17**

Duration: 60 Months

This project receives funding from the Euratom research and training programme 2014-2018 under grant agreement No 745 942		
Dissemination Level		
PU	Public	X
RE	Restricted to a group specified by the partners of the Beacon project	
CO	Confidential, only for partners of the Beacon project	

REVIEW

Name	Internal/Project/External	Comments
All Beacon partners	Project internal	

DISTRIBUTION LIST

Name	Number of copies	Comments
Seifallah BEN HADJ HASSINE (EC)	Digital	
Beacon partners	Digital	

Content

2	Introduction	4
3	Description of the Model	4
3.1	Model Formulation	4
3.2	Boundary Conditions	9
4	Basic capabilities of the Model	10
5	Task 3.3	12
5.1	Parameterisation	12
5.2	Steady state model	13
5.3	Time dependent model	16
5.4	Discussion/Conclusions	20
6	Performance of the Model and Assessment of Predictive Power	20
6.1	Performance of the model for small-scale laboratory tests	20
6.2	Assessment of predictive performance of the model	23
6.3	Performance of the model for full-scale disposal concepts	25
6.4	Discussion	28
7	Code Development and Investigations	29
7.1	QPAC Coupling to Gmsh	29
7.2	COMSOL	33
8	Concluding Remarks	35
	References	36

2 Introduction

The modelling philosophy adopted by Quintessa is to create a model with as few parameters as possible whilst maintaining the ability to fit the key features of experimental data. Where parameters are introduced, they should, as far as possible, be easily determined from available data. The Internal Limit Model (ILM; Thatcher et al., 2016) was developed by Quintessa as part of the DECOVALEX-2015 project. It was inspired by correlations in experimental data that relate stress, suction and failure to dry density and water content. The process models are implemented in the multi-physics finite volume/mixed element code QPAC (Maul, 2013).

During the Beacon project, the main focus has been on applying Quintessa's existing model for bentonite to new experiments and testing its validity, including its predictive capabilities. This process has involved applying the ILM to different types of bentonite (MX-80 and FEBEX), different forms of bentonite (including powder and pellets), and different boundary conditions (including heated experiments, representation of void spaces and non-cylindrical geometries). These applications have necessitated the development of improved material property models, development of friction boundary conditions, and developments to the QPAC code to enable representation of more complex geometries. Alongside this work, Quintessa have also begun to develop capabilities for modelling bentonite in COMSOL Multiphysics® (COMSOL, 2020).

3 Description of the Model

The model used by Quintessa is called the Internal Limit Model (ILM) and is a fully coupled thermo-hydro-mechanical model based on Richards' equation for the hydraulics, momentum balance for the mechanics and the Modified Cam Clay model (MCC; Roscoe and Burland 1968) to represent plastic deformation. Observations from laboratory data are used to define an Internal Limit Curve (ILC), which is used to parameterise both mechanical and hydraulic properties of the bentonite. The process models are implemented in the multi-physics code QPAC which adopts a mixed element approach for the mechanics and a more conventional finite volume approach for the hydraulics.

3.1 Model Formulation

The mechanical problem is expressed in terms of conservation of momentum, which is otherwise referred to as the Navier equation (Howell et al. 2009):

$$\rho \frac{\partial^2 \bar{u}}{\partial t^2} = \nabla \cdot \bar{\sigma} - \rho \bar{g} \quad (1)$$

where ρ (kg/m³) is the solid density, \bar{u} (m) is the displacement vector, t (s) is time, $\bar{\sigma}$ (MPa) is the stress tensor and \bar{g} (m/s²) is the vector of the acceleration due to gravity. The equation effectively ensures a local force balance for pseudo-steady state. The stress vector ($\bar{\sigma}$) assumes a pseudo-steady state and is given by:

$$\bar{\sigma} = \bar{S}(\bar{\varepsilon} - \bar{\gamma}) - P \quad (2)$$

where \bar{S} (MPa) is the elastic stiffness matrix, $\bar{\varepsilon}$ (-) is the strain vector, $\bar{\gamma}$ represents arbitrary additional strains, e.g. swelling strain and plastic strain, and P (MPa) is fluid pressure.

For the applications in Beacon, an isotropic elastic stiffness matrix is used whereby:

$$\bar{S} = \begin{bmatrix} \Lambda + 2\tau & \Lambda & \Lambda & 0 & 0 & 0 \\ \Lambda & \Lambda + 2\tau & \Lambda & 0 & 0 & 0 \\ \Lambda & \Lambda & \Lambda + 2\tau & 0 & 0 & 0 \\ 0 & 0 & 0 & 2\tau & 0 & 0 \\ 0 & 0 & 0 & 0 & 2\tau & 0 \\ 0 & 0 & 0 & 0 & 0 & 2\tau \end{bmatrix} \quad (3)$$

where $\Lambda = \xi * E / (1 + \xi) * (1 - 2\xi)$, $\tau = E / (2(1 + \xi))$, E (MPa) is Young's modulus and ξ (-) is Poisson's ratio. Poisson's ratio is a constant and Young's Modulus is dependent on the average effective stress (κ_0 and κ_1 are constants):

$$E = \kappa_0 + \kappa_1 \left[\frac{1}{3} (\sigma'_{ii} + \sigma'_{jj} + \sigma'_{kk}) \right] \quad (4)$$

For swelling bentonite, it is assumed that there are three additional sources of strain; swelling strains due to changes in water content of the bentonite, plastic strains due to plastic failure of the bentonite, and thermal expansion due to temperature increase of the bentonite. Swelling strains are discussed later as they are coupled to the hydraulics.

Thermal strains are defined by the linear coefficient of thermal expansion in each principal direction α_{nn} :

$$\varepsilon_{nn}^{thermal} = \Delta T \cdot \alpha_{nn} \quad (5)$$

where T is temperature [K]. In Beacon, temperature changes have only been considered in the context of the FEBEX experiment (Task 5.2). For the FEBEX bentonite (ENRESA, 2000), coefficients of linear thermal expansion are assumed to be isotropic and show a temperature dependence:

$$\alpha = -1.256 \cdot 10^{-4} [^{\circ}C] + 6.5 \cdot 10^{-6} [^{\circ}C]T \quad (6)$$

Plastic strains are calculated according to the MCC model. The plastic yield surface is given by:

$$\left[\frac{q}{M} \right]^2 + p'(p' - p_c) = 0 \quad (7)$$

whilst the virgin consolidation line in the MCC model, which describes how the yield surface changes with stress, has the equation:

$$v = \Gamma - \lambda \ln p' \quad (8)$$

where v (-) is the specific volume ($v = 1 + e$, where e (-) is the void ratio), p' (MPa) is the effective confining stress, q (MPa) is deviatoric stress, p_c (MPa) is the pre-consolidation pressure (which is a point on the virgin consolidation line) and M , Γ and λ are all constant parameters. The plastic strain is calculated as the derivative of the plastic yield surface.

The hydraulic problem is expressed in terms of conservation of mass:

$$\frac{\partial}{\partial t} (\theta \rho_f \varphi) = -\nabla \cdot (\rho_f u) + Q \quad (9)$$

where θ (-) is porosity, ρ_f (kg/m³) is fluid density, φ (-) is saturation, u (m/s) is the fluid velocity and Q (kg/m³/s) is a source or sink.

A number of different formulations can be used to represent the fluid migration in the ILM, including full multiphase flow. For the applications in Beacon, Richards' equation is used to represent the fluid migration. Richards' equation can be used where gas flow is very fast compared to water flow, so that gas flow does not need to be solved for in the equations:

$$u = -\frac{k}{\mu} \nabla (P + \rho g z) \quad (10)$$

where u (m/s) is the fluid velocity tensor, k (m²) is the effective permeability tensor, μ (Pa s) is the fluid viscosity and z (m) is height. The intrinsic permeability is a material-dependent function of dry density ρ_{dry} , parameterised separately for FEBEX and MX-80. The saturation-dependent relative permeability (k_{rel}) is given by:

$$k_{rel} = \varphi^4 \quad (11)$$

Water pressure, P_w (MPa), is calculated by subtracting the net suction, Ψ (MPa), from the gas pressure, P_g (MPa):

$$P_w = P_g - \Psi \quad (12)$$

Suction is determined from the Internal Limit Curve (ILC). The ILC is based on the observation of Wang et al. (2012) that for a given composition of bentonite, one can define a log-linear

relationship between the swelling pressure and the void ratio of the bentonite. The ILC curve has the form:

$$p = p_0 * \exp\left(\frac{-e}{\lambda}\right) \quad (13)$$

where p_0 (MPa) and λ (-) are constants calibrated against the data and e is the void ratio, which can be related to the dry density (ρ_{dry}) by:

$$e = \left(1 - \frac{\rho_{dry}}{\rho_{solid}}\right) / \left(\frac{\rho_{dry}}{\rho_{solid}}\right) \quad (14)$$

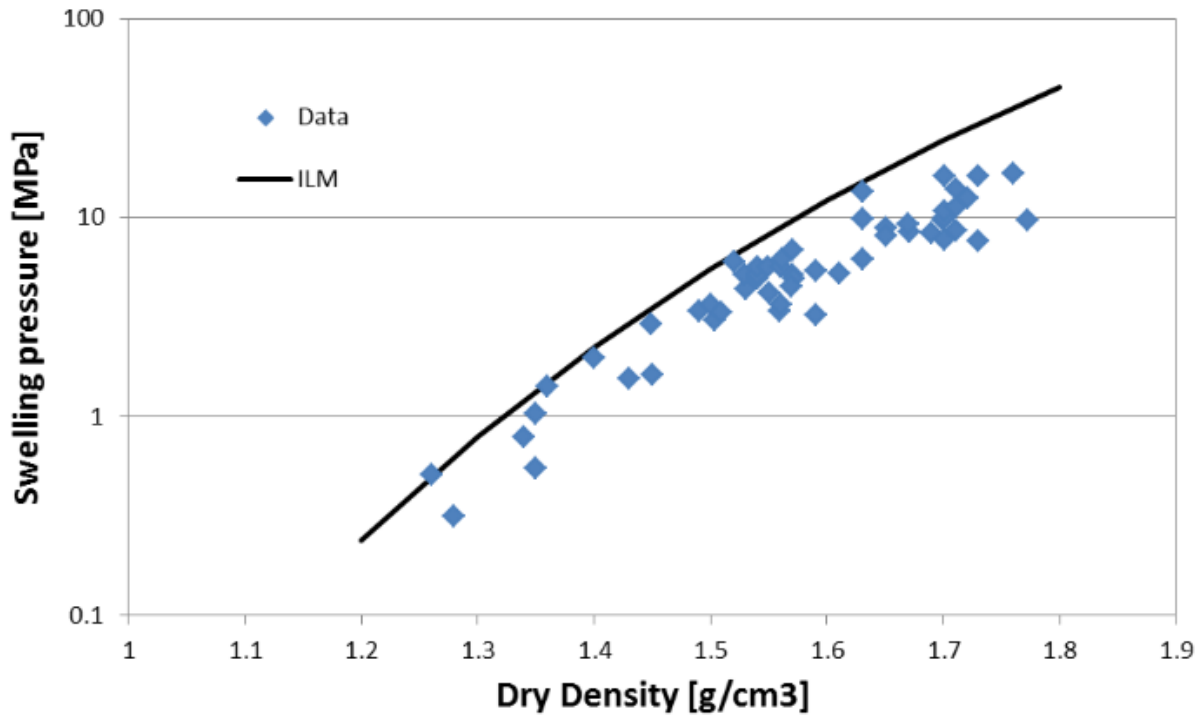


Figure 3-1: Swelling pressure vs dry density data from Lloret et al. (2005) with fitted exponential curve, used to model FEBEX bentonite in Beacon Task 5.2 and 5.3.

This relationship between void ratio and swelling pressure can be plotted with data from oedometer tests and found to coincide with the plastic deformation line (Figure 3-2). The correspondence between swelling pressure and plastic deformation suggests that under swelling conditions, bentonite swells to a stress corresponding to the point of plastic failure. This observation enables the swelling data to be used to parameterise the plastic failure curve at different void ratios using the ILC.

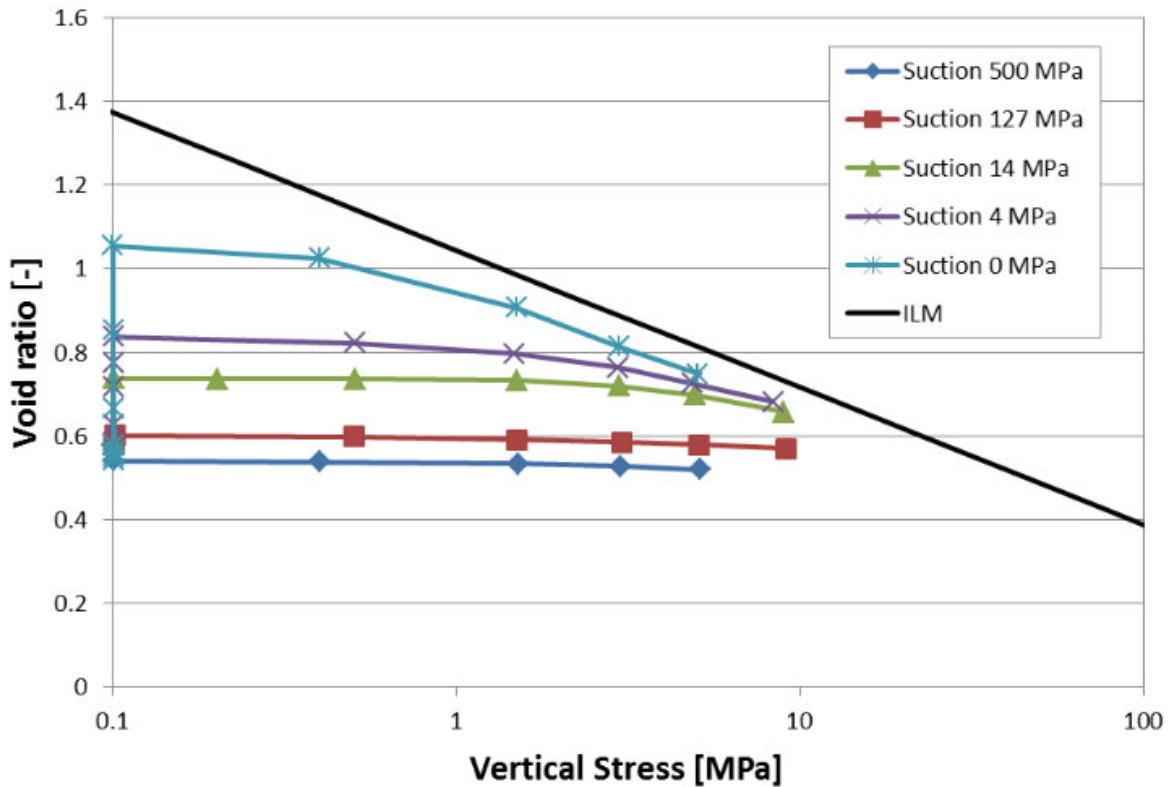


Figure 3-2: Oedometer test data from Lloret et al. (2005) with fitted exponential curve, used to model FEBEX bentonite in Beacon Task 5.2 and 5.3.

Dueck (2004) suggested that the suction of the bentonite (Ψ) could be related to the unconfined (free) suction (Ψ^{free}) for a given water content, and the stress state, such that:

$$\Psi = \Psi^{\text{free}} - \frac{1}{3}(\sigma_{ii} + \sigma_{jj} + \sigma_{kk})e \quad (15)$$

Equation (13) can also be restated in terms of a relationship between water content (assuming all void are filled with water) and free suction (from Equation (15), we see that when suction is zero, free suction must equal stress). When this relationship is plotted against the water retention function, the ILC model shows a close fit to experimental data for the free swell condition and is therefore used to parameterise part of the suction curve for free swelling bentonite (Figure 3-3). For FEBEX bentonite, water retention data show a linear temperature dependence for the ILC (Thatcher, 2017): $p_0 = -7.895[\text{MPa} \cdot ^\circ\text{C}^{-1}] \cdot T + 1674[\text{MPa}]$.

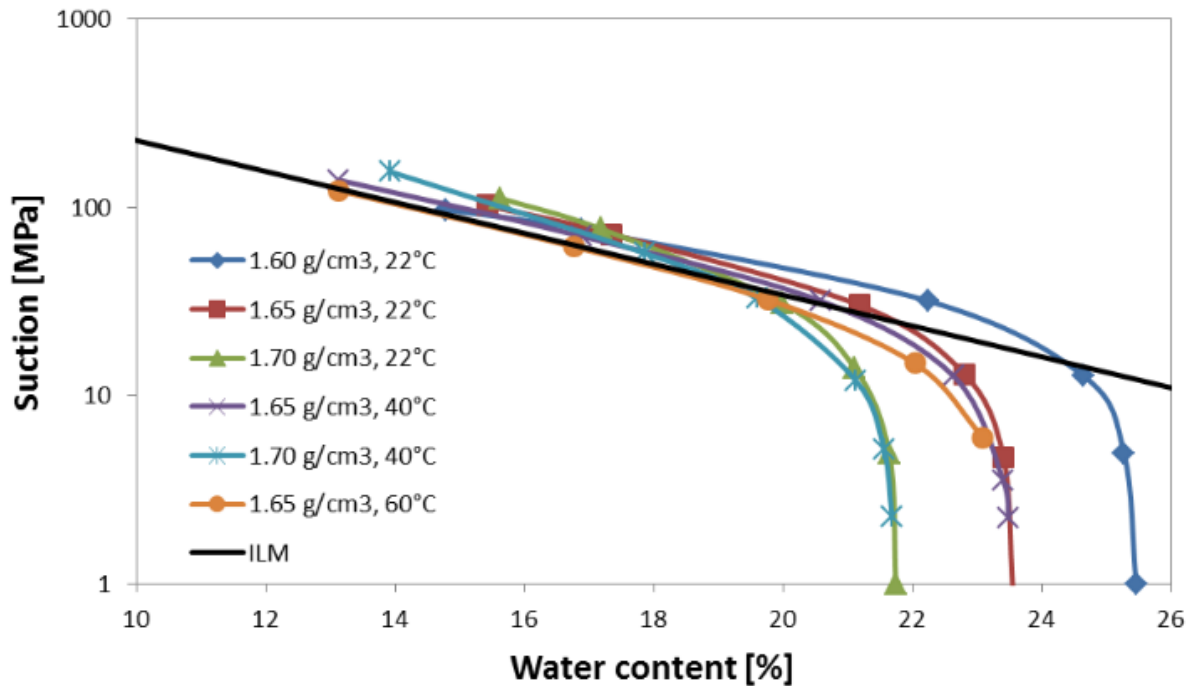


Figure 3-3: Confined water retention data for the FEBEX bentonite at different dry densities and temperatures (Lloret et al., 2005) compared with the calibrated ILM suction curve for unconfined conditions at 60°C.

The observation that three independent sets of data can be described by a single relationship, the Internal Limit Curve, suggests that this relationship could represent a fundamental limit within the material. Swelling pressure cannot exceed the plastic deformation limit because an external energy source would be required to permanently deform the bentonite. If an external energy source is present, e.g. in a loading test, then the sample will deform plastically. Both stress and suction are measures of energy density and the Dueck model suggests that to some extent, energy can be transferred between suction pressure and stress. It would therefore follow that if there is a limiting stress that the sample can support, there is also a limiting suction.

To calculate the net suction when the sample is not swelling freely, an approach modified from that suggested by Dueck (Equation 14) has been adopted. The net suction is the free swell suction minus stress, but localised according to stress direction, following the argument that bentonite interlayers will be constrained in terms of their water content most significantly by the plate normal stress. This is calculated in three principal directions in the model as:

$$\Psi_{nn} = \Psi_{nn}^{free} - \sigma_{nn} \text{ for } n = i, j, k \quad (16)$$

where σ_{nn} is the stress component nn , with the total suction given by:

$$\Psi = \frac{1}{3}(\Psi_{ii} + \Psi_{jj} + \Psi_{kk}) \quad (17)$$

The water content in the three directions is constrained such that the net suction in each of the three directions is equal. The conceptual model behind considering water content and suction in three directions is such that the bentonite grains are oriented in random directions such that a third of the grains are aligned to each principal direction. Note that this suction model is a significant departure from the conventional Richards' model where suction is defined purely as a function of fluid saturation. The approach above allows stress to be coupled into the suction relationship directly, at the expense of always enforcing a strict constraint on volume conservation of the water. Not enforcing such a volume constraint (although local and global mass balance is retained at all times), as one might do for a conventional porous material, is justified on the basis of work which suggests that when water is present as a crystalline phase in the bentonite inter-layers, the density of that water may

depart significantly from the equivalent liquid water density due to the presence of charged ions in the bentonite, allowing water molecules to sit closer together (Jacinto et al., 2012). Hence water saturation can exceed unity in the models in order to obtain the necessary mass in the $\theta\rho_f\varphi$ term in Equation (8), which assumes a fixed fluid density.

In the ILM, swelling strain is calculated based on the change in water content in the bentonite. Swelling strain is calculated in the three principal directions as follows:

$$\varepsilon_{nn}^{swell} = \frac{a(\omega_{nn} - \omega_0)m_s}{3\rho_w V_{comp}} \quad (18)$$

where ω_0 is the initial water content (kg/kg), ω_{nn} is the water content in the direction nn , m_s is the mass of solids (kg), ρ_w is the density of water (kg/m³), V_{comp} is the compartmental volume (m³) and a is a swelling efficiency term which reflects that not all additional water will cause a volume increase, some will just fill void space in the sample. The calculation is considered in three principal directions following the conceptual model that bentonite grains are aligned principally in one of the three directions. The amount of stress in the three principal directions is different, so the free suction, and therefore water content, will be different in the three directions. However, the net suction will be the same.

Movement of heat is represented by conduction and convection (coupled to the flow of water and water vapour) using the equation for heat diffusion with additional fluxes to represent convection.

For the FEBEX bentonite modelled in Task 5.2 of Beacon, a relationship between saturation and thermal conductivity was used (Rutqvist and Tsang, 2003):

$$\lambda_t = 1.28[\text{W/m/K}] - \frac{0.71[\text{W/m/K}]}{1 + \exp\left(\frac{\varphi - 0.65}{0.1}\right)} \quad (19)$$

The vapour transport model is based on the Philip & de Vries (1957) equation for diffusive vapour flux J [kg/y]:

$$J = -D \cdot \nabla \rho_v \quad (20)$$

where D is the coefficient of diffusivity [m²/s] and ρ_v is vapour density [kg/m³]. Following Cleall et al. (2013), this can be expressed as:

$$J = -D_{atm} \cdot \tau_v \cdot \theta \cdot \nabla \rho_v \quad (21)$$

where τ is tortuosity [-], θ is porosity [-] and D_{atm} is the molecular diffusivity of vapour through air [m²/s], described by:

$$D_{atm} = 2.2 \cdot 10^{-5} \cdot \left(\frac{P_{atm}}{P_g}\right) \cdot \left(\frac{T}{T_0}\right)^{1.75} \quad (22)$$

where P_{atm} is atmosphere pressure [Pa], P_g is the pore gas pressure [Pa], T_0 is the reference temperature [K] and T is temperature [K].

3.2 Boundary Conditions

The ILM has been implemented in the multi-physics finite volume/mixed element code QPAC (Maul 2013), together with a variety of boundary conditions to allow it to be applied to a range of bentonite experiments and tests.

On each boundary, there are six possible degrees of freedom (DOFs), three translational and three rotational. The different boundary conditions dictate which DOFs are constrained. The standard mechanical modelling restraint/support boundary conditions of most relevance to the modelling of bentonite experiments are:

- Fixed conditions, in which all six DOFs are constrained so that no translation or rotation is possible at all points on the boundary;

- Roller conditions, which constrain the translational DOF perpendicular to the boundary and the two rotational DOFs that are not in the plane of the boundary and which allow free motion in the other DOFs; and
- Specified stress conditions.

In each case, the boundary condition can be applied directionally, e.g. to allow a roller condition in one direction with a fixed condition in another. This has been used in many of the Beacon test cases to allow translation in the z-direction but not in the angular direction on a curved cylindrical boundary. The boundary conditions are implemented by determining the force that is necessary to hold the DOFs that are constrained in their constrained position. Having determined this constraining force as a function of displacement, it is also possible to specify a fixed displacement boundary condition.

In some bentonite experiments, especially in situ resaturation/homogenisation tests, bentonite will expand/deform along an interface with the experiment vessel or rock boundary. On such boundaries, any motion will be required to overcome the friction force that restricts the motion on the boundary. An additional friction boundary condition has been implemented in QPAC to represent such situations. The friction boundary condition is determined by considering the fixed boundary condition as arising as a consequence of friction, i.e. by assuming that it is friction that fully restricts any motion parallel to the boundary. However, the maximum force that can arise due to friction is limited and so, on friction boundaries, the fixed condition will only persist while the restraining force that is necessary to constrain the displacement is smaller than the force that can be provided due to friction.

If R [N] is the reaction force in the direction perpendicular to the boundary (which can be determined from the stress, $\bar{\sigma}$, in the direction normal to the boundary), then the maximum friction force is given by $F_{max} = \mu R$, where μ is the coefficient of friction. μ will depend upon the bentonite deformation characteristics and the roughness of the boundary surface. If F_{zero} is the force necessary to provide a fixed boundary condition, then the force applied in the plane of the boundary for the friction boundary condition is given by:

$$F = \begin{cases} -F_{max} & F_{zero} \leq -F_{max} \\ F_{zero} & -F_{max} < F_{zero} < F_{max} \\ F_{max} & F_{zero} \geq F_{max} \end{cases} \quad (23)$$

The applied force will result in a displacement of the bentonite in the cases when $|F_{zero}| > F_{max}$, with the magnitude of the displacement depending on the evolving bentonite stresses. To impose the friction boundary condition, it is necessary to specify a coefficient of friction, μ , for the bentonite-boundary contact.

4 Basic capabilities of the Model

Table 4-1 shows the list of basic model capabilities from D3.1, updated for this deliverable.

Quintessa's constitutive model is a single-porosity model. This is a deliberately simplified representation of the bentonite, since double-porosity models require additional parameters which are not always directly available from experimental measurements. Therefore, although a double-porosity model may be more physically representative of the bentonite structure, we have chosen not to introduce this additional uncertainty to our model. In the Beacon project, Quintessa have aimed to test whether a simplified single-porosity model with minimal free parameters can reproduce and predict the observed behaviour of bentonite. The performance of the model is discussed in Section 6.

The formulation of the ILM, in which the water retention curve is parameterised with the same constants as the swelling pressure and virgin consolidation curves, does not currently allow for hysteresis in the retention curve.

All other basic features are able to be represented in Quintessa's constitutive model.

Table 4-1: Table of basic features of the Quintessa's constitutive model at the start and end of Beacon.

Name of the constitutive law:		ILM	
Behaviour feature	D3.1	D3.3	Remarks
Mechanical behaviour			
Dependence of swelling strain on applied stress (at the same dry density) (Figure 1)	✓	✓	
Dependence of swelling stress on dry density (at the same stress) (Figure 1)	✓	✓	
Irreversibility of strains in wetting/drying cycles (Figure 2)	✓	✓	
Dependence of swelling pressure on dry density (Figure 4)	✓	✓	
Stress path dependence from an unsaturated to a saturated state (Figure 5)	✓	✓	
Stress path dependence from a saturated to an unsaturated state (Figure 6)	✓	✓	
Double structure/porosity considered?	X	X	
Are temperature effects considered in the model?	✓	✓	
Dependence of strains developed in a temperature cycle (increase/decrease) on OCR (or stress) (Figure 7)	✓	✓	
Hydraulic behaviour (retention curve)			
Hysteresis	X	X	
Dependence on void ratio	✓	✓	
Double structure/porosity considered?	X	X	

5 Task 3.3

Quintessa modelled the EPFL experiments with two models: a steady state model with prescribed suction in the sample; and a time-dependent model in which the hydration of the sample is represented. The parameters for both models are the same, but the geometry of the grid and the boundary conditions are different.

5.1 Parameterisation

Parameterisation of the ILC curve (see Section 3.1) is by fitting of data provided in Seiphoori (2015). Two different formulations of the ILC curve have been used, one dependent on the void ratio as in Section 3.1 and one dependent on dry density:

$$p = p_0 * \exp\left(\frac{-\rho_{dry}}{\lambda}\right) \quad (24)$$

These two formulations give different curve shapes in void ratio – stress space so are interesting to compare in the models. The dry density formulation fits the data over the whole range better than the void ratio formulation (Figure 5-1). For the void ratio formulation, the four higher dry density data were ignored to ensure a good fit in the range 1.4-1.6 Mg/m³ which is the range that is relevant for the experiments modelled.

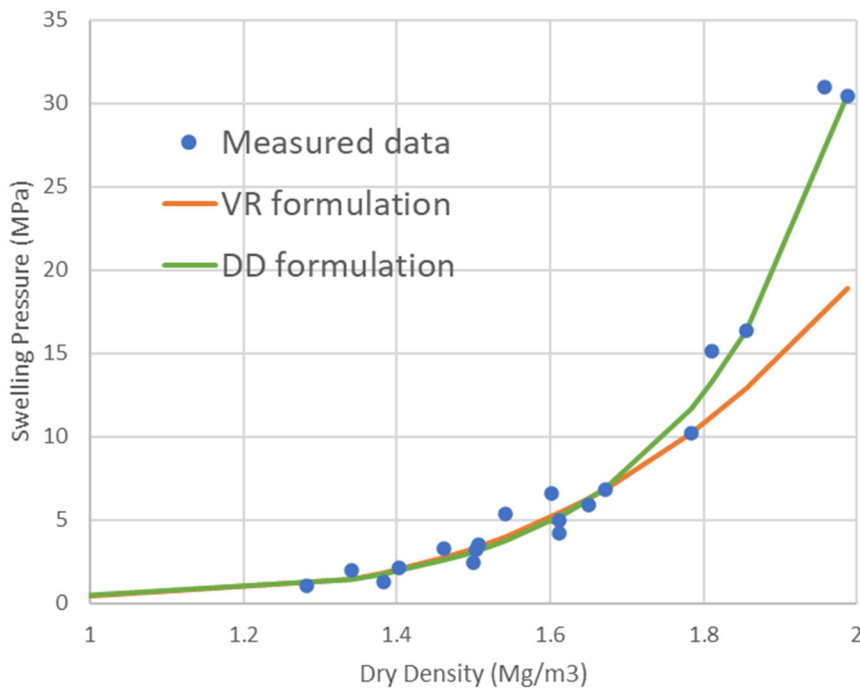


Figure 5-1: Swelling pressure data taken from Seiphoori (2015) with two fitted curves, one using the void ratio formulation and the other using the dry density formulation.

Other than the calibration of the two parameters in the ILC curve to data for MX-80 bentonite, there is no further calibration of the model between model runs or between representing different experiments. Better model fits could be obtained for each experiment by choosing a different set of parameters for each case, but this level of calibration would not benefit the predictive use of this model, nor would it be justified given the uncertainty in the data sets collected (e.g. see Figure 5-7 and Figure 5-10 for examples where an experiment is repeated three times, giving an indication of the amount of uncertainty in the experimental results).

Mechanical parameters are given in Table 5-1 and the initial conditions of the bentonite are given in Table 5-2. Note that the initial suction in the bentonite is determined using the initial water content and the ILC curve, so different values are found for the void ratio (VR) formulation and the dry density (DD) formulation, to remain consistent with the suction curves.

Table 5-1: Mechanical parameters to represent MX-80 bentonite.

Parameter	Value	Reference
Mechanical Parameters		
Poisson's Ratio [-]	0.27	Thatcher, 2017
Initial Bulk Modulus [MPa]	25	
Bulk Modulus Scaling Factor [-]	30	Thatcher, 2017
M (slope of critical state line)	1.25	Thatcher, 2017
Void ratio formulation		
ILM p_0 [MPa]	82.6	Fit to data
ILM $1/\lambda$ [-]	-3.9	Fit to data
Dry density formulation		
ILM p_0 [MPa]	2.60E-3	Fit to data
ILM $1/\lambda$ [m ³ /Mg]	4.7	Fit to data

Table 5-2: Initial conditions of the bentonite

Vertical stress (MPa)	Void ratio	Water content (%)	Degree of saturation (%)	Dry density (g/cm ³)	Density of the solid phase (g/cm ³)	Suction (MPa)
0.021	0.83	0.06	19%	1.5	2.74	43.5 (VR formulation) 167 (DD formulation)

5.2 Steady state model

The steady state model would ideally have a single compartment as there is no need to represent water flow between compartments however in the QPAC implementation of the mechanical equations, two compartments are required (Figure 5-2) in order that displacement gradients are calculated correctly when vertical displacement occurs.

The ILM model is designed to closely couple hydraulic and mechanical effects. In this steady-state model, the hydraulics are represented by values of suction that are prescribed, and the model then calculates the swelling strains associated with that value of suction and hence the stresses and displacements.

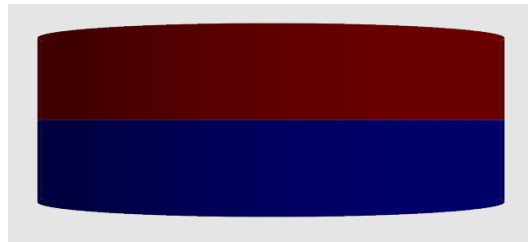


Figure 5-2: Compartment geometry for steady state model.

Modelling results are provided in Table 5-3 and Table 5-4 for Path 1 and Path 2 respectively. The results are also shown in Figure 5-3 and Figure 5-4. For Path 1, Figure 5-3 shows that swelling under a low stress condition is difficult to predict precisely, but the two formulations do bound the observations from the experiment. The void ratio of 2.3 measured in the experiment corresponds to a dry density of 0.83 Mg/m³ which is significantly outside the range of data available to calibrate the ILC curve and the two formulations diverge in estimates of void ratio at high void ratios.

Once loading occurs, the void ratio decreases and the results from the two formulations of curve converge once void ratios are in the range of the available data. The void ratio formulation shows a log-linear increase in vertical stress with reduction in void ratio, following exactly along the ILC curve. The dry density formulation has a curved response, initially with a slow decrease in void ratio with loading and then with a curve that follows the ILC curve.

In the confined swelling test (Path 2), the two models produce very similar results that match the measurements well. Both models show that under confined swelling, the MX-80 bentonite with dry density of 1.5 Mg/m³ will reach a swelling pressure of 3.3 MPa. With continued loading, the void ratio decreases slightly more rapidly in the model than in the data.

Table 5-3: Results of the analysis for path A – B – C – D for the void ratio formulation

	A – B – C – D			
	Total vertical stress (MPa)	Void ratio	Suction (MPa)	Degree of saturation (%)
Initial (A)	0.021	0.826768	43.2	0.20087
Swelling (A-B)	0.021	0.842098	38.89	0.229051
	0.021	0.858846	34.58	0.258622
	0.021	0.876946	30.27	0.2887
	0.021	0.924302	25.96	0.322171
	0.021	0.982949	21.65	0.359568
	0.021	1.05388	17.34	0.40237
	0.021	1.14338	13.03	0.453828
	0.021	1.26472	8.72	0.521199
	0.021	1.45616	4.41	0.627303
	0.021	2.10558	0.1	1.1462
Compression (B-C-D)	0.021	2.10552	0.1	1.16343
	0.06	1.88893	0.1	1.19826
	0.25	1.51479	0.1	1.22286
	0.5	1.32891	0.1	1.2209
	1	1.14205	0.1	1.21142
	1.99	0.956643	0.1	1.19878
	3.99	0.770535	0.1	1.18796
	7.97	0.587393	0.1	1.18881
	15.95	0.405638	0.1	1.22678
	20.81	0.336365	0.1	1.26585

(1) Value of the swelling pressure test in path A-B'-C' (point B')

Table 5-4: Results of the analysis for path A - B' - C' for the void ratio formulation

	A - B' - C'			
	Total vertical stress (MPa)	Void ratio	Suction (MPa)	Degree of saturation (%)
Initial (A)	0.023338	0.826667	43.2	0.200878
Swelling pressure test (A-B')	0.284991	0.826667	40.6651	0.217635
	3.23773	0.826667	30.5235	0.277511
	3.28708	0.826667	20.3822	0.387664
	3.22598	0.826667	10.2412	0.56258
	3.28711	0.826667	5.17059	0.706865
	3.28711	0.826667	2.63528	0.817391
	3.28711	0.826667	0.1	0.990705
	6.17	0.698369	0.1	1.02668
Compression (B'-C')	12.4	0.499088	0.1	1.08522
	16.9912	0.41134	0.1	1.11948

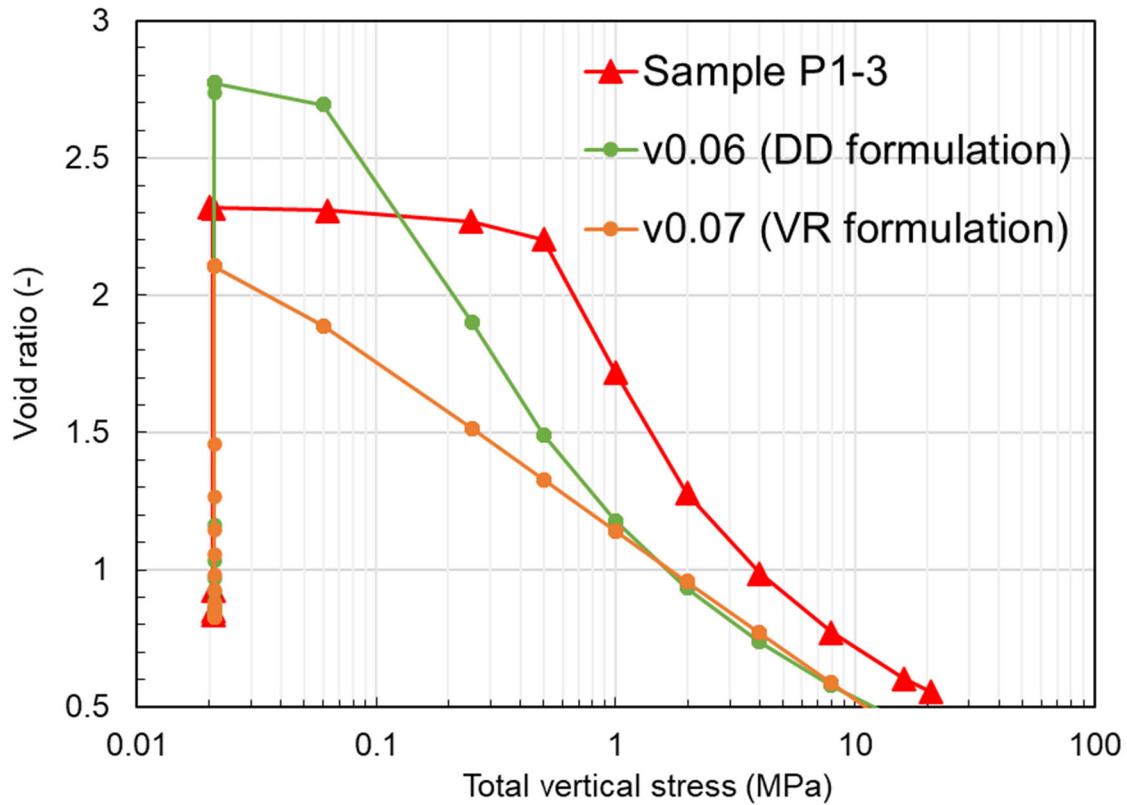


Figure 5-3: Void ratio – stress results for Path 1, showing the data from Sample P1-3 along side model results using the two formulations of ILC curve.

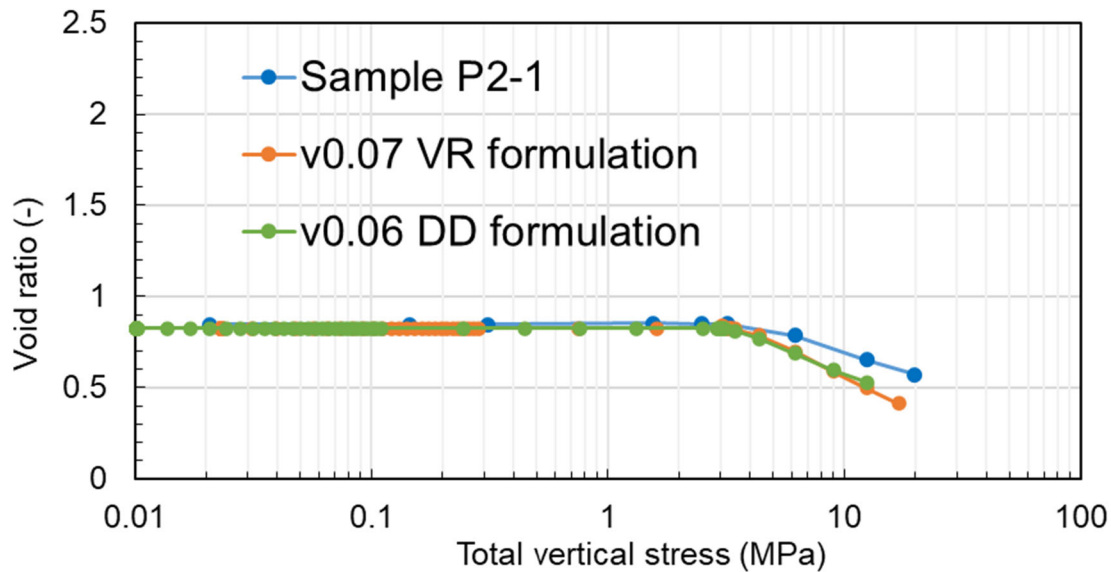


Figure 5-4: Void ratio – stress results for Path 2, showing the data from Sample P2-1 along side model results using the two formulations of ILC curve.

5.3 Time dependent model

In the time dependent model, water enters the sample through boundary conditions and hence more discretisation of the sample is required to represent the hydraulic gradients in the sample to aid calculation of water flows. The updated compartment geometry is shown in Figure 5-5.

Boundary conditions on the outside of the sample are as following:

- Path 1: atmospheric pressure water on the top and bottom surface to allow hydration and a specified stress on the top surface with zero displacement on the bottom surface;
- Path 2: atmospheric pressure water on the top and bottom surface to allow hydration. Zero displacement whilst resaturation occurs and then a specified stress on the top surface with zero displacement on the bottom surface.

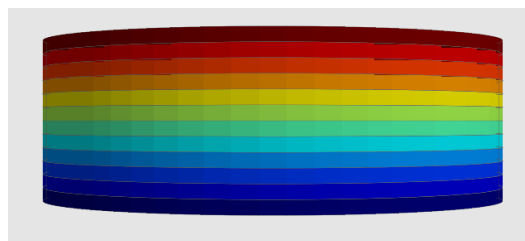


Figure 5-5: Compartment geometry for the time-dependent model, coloured by Z-value.

Modelling results are provided in Table 5-3 and Table 5-4 for Path 1 and Path 2 respectively. The results are also shown in the following figures, this time with time dependent results. Only results for the void ratio formulation are presented for the time dependent model.

For Path 1, the results are very similar to those for the steady state model (Figure 5-6). The maximum void ratio is underestimated and the loading is represented by a straight line that gets closer to the observations as stress increases. The time dependent build-up of vertical stress (Figure 5-7) is a bit slow in the model. This could be improved by calibration of the hydraulic conductivity of the bentonite, but in the interests of minimising calibration to individual experiments, the results are shown without calibration.

For Path 2, the results are again very similar to the steady-state model and also fit the data better than in Path 1 (Figure 5-8). The time dependent behaviour of the model also matches the data well. The data show that the three samples experienced some vertical strains (Figure 5-9), which were not reproduced by the model due to the assumption of constant volume conditions. The build up of axial stress through time (Figure 5-9) is captured well in the model both in terms of the transient phase and the final axial stress before loading.

Table 5-5: Time-dependent results of the analysis for path A – B

A – B			
Time (minutes)	Void ratio	Suction (MPa)	Degree of saturation (%)
0	0.82581	43.4825	0.199077
99.9318	0.856262	35.2215	0.254154
199.8631	0.967468	22.7161	0.349898
399.7262	1.36046	6.25506	0.573894
599.5887	1.5634	2.90306	0.689327
799.4534	1.65788	1.94804	0.747264
999.318	1.72288	1.44851	0.789783
1998.631	1.88226	0.624922	0.90915
2997.949	1.95394	0.391933	0.975003
3997.262	2.00256	0.268691	1.0282
4996.58	2.03864	0.191367	1.07591
5995.887	2.06445	0.14137	1.11827
6995.21	2.08231	0.107971	1.1556
7994.534	2.09439	0.084869	1.18838
8993.857	2.10244	0.068374	1.21706
9993.18	2.10779	0.056265	1.24207

Table 5-6: Time-dependent results of the analysis for path A – B'

A – B'			
Time (minutes)	Total vertical stress (MPa)	Suction (MPa)	Degree of saturation (%)
0	-6.00E-12	43.5039	0.198871
99.9318	0.148571	35.0548	0.255185
199.8631	0.948366	20.8622	0.370188
399.7262	2.48195	0.346259	1.00157
599.5887	2.95733	0.35197	1.01068
799.4534	3.24839	0.315223	1.0178
999.318	3.44394	0.292559	1.02231
1998.631	3.40815	0.074657	1.03157
2997.949	3.39574	0.00635	1.03533

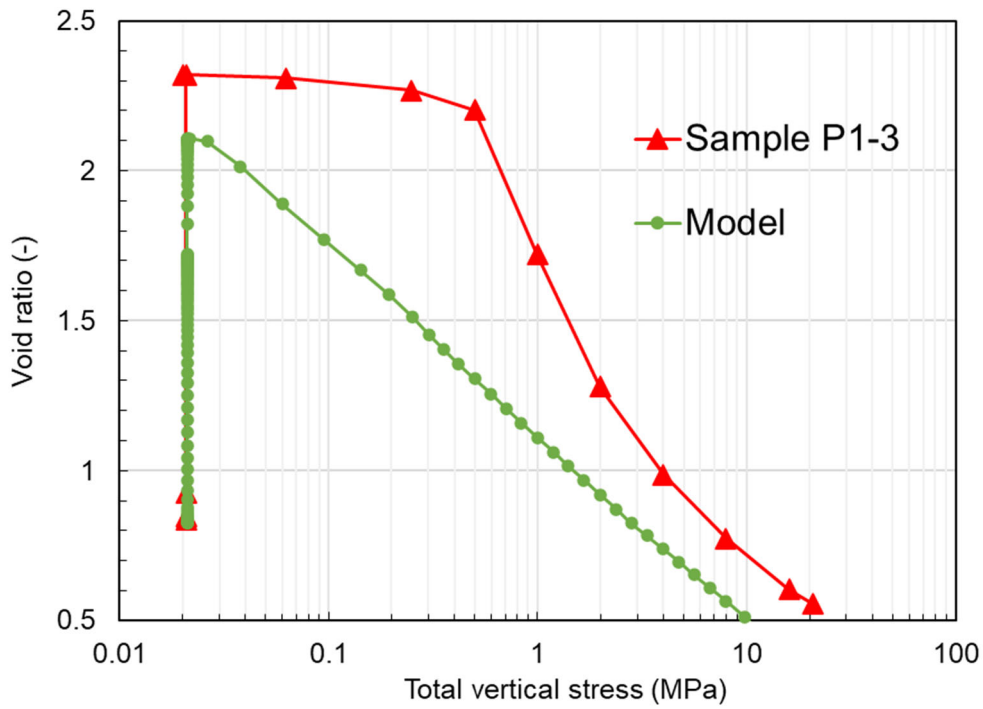


Figure 5-6: Void ratio – stress results for Path 1, showing the data from Sample P1-3 along side the model.

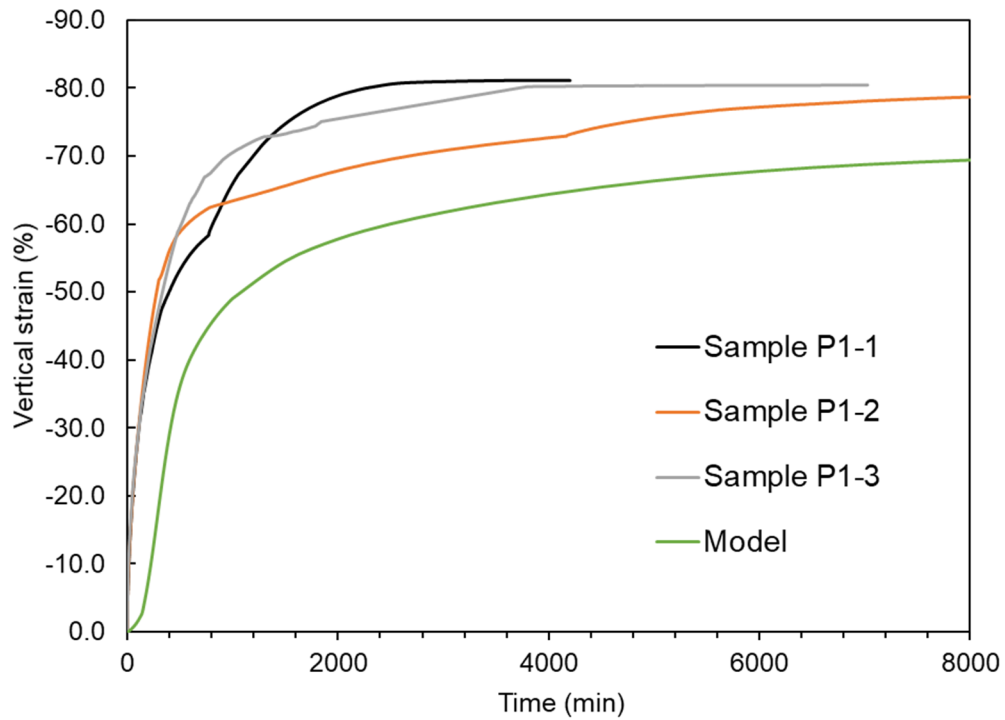


Figure 5-7: Vertical stress through time for Path 1, showing data from three samples alongside the model.

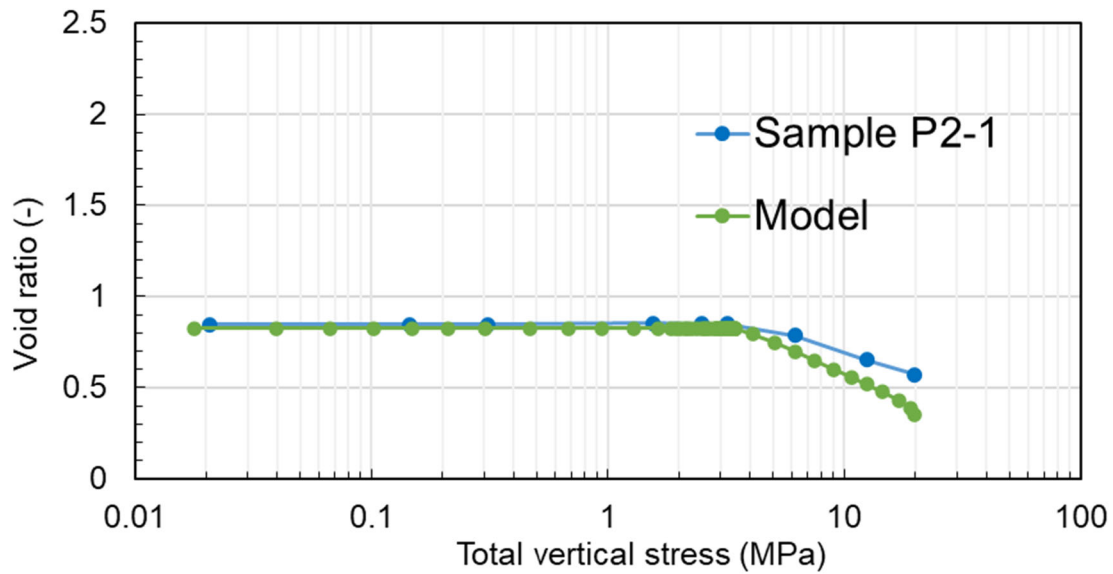


Figure 5-8: Void ratio – stress results for Path 2, showing the data from Sample P2-1 along side the model.

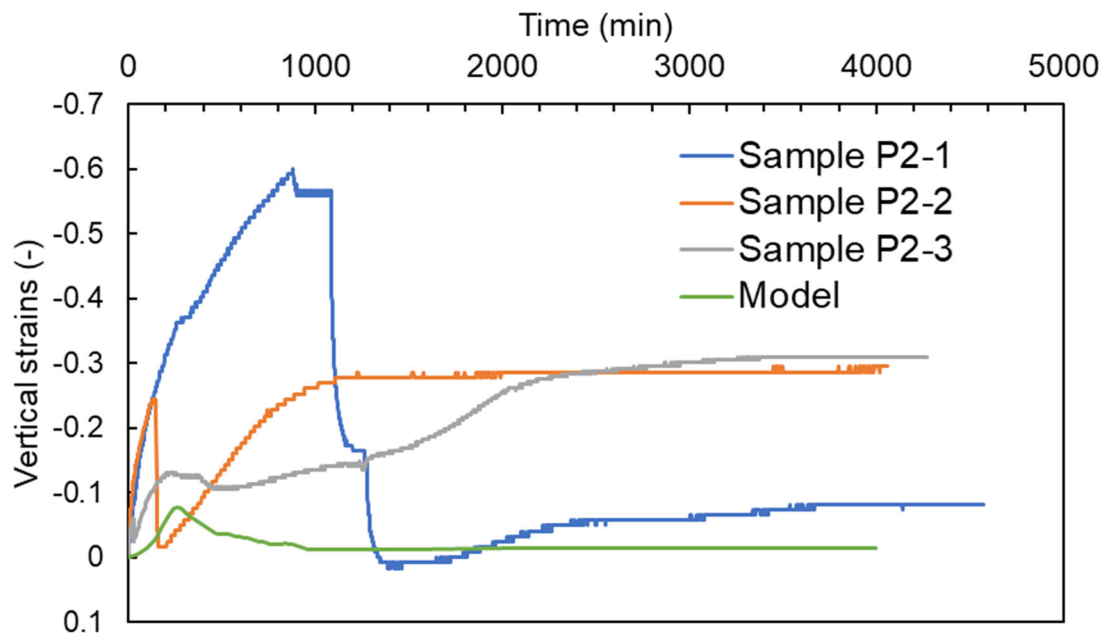


Figure 5-9: Vertical strains through time for Path 2, showing data from three samples alongside the model

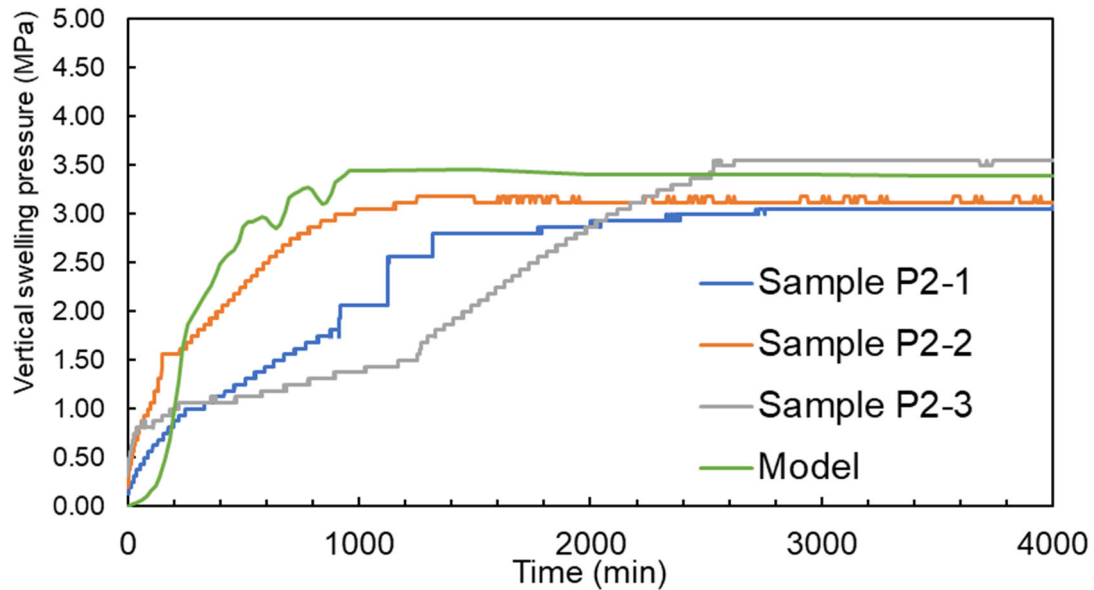


Figure 5-10: Vertical stress through time for Path 2, showing data from three samples alongside the model

5.4 Discussion/Conclusions

Quintessa's model has reproduced most of the features observed in the experiments with no calibration of parameters other than the ILC curve to available swelling data. The model performs particularly well when the dry density of the bentonite is within the range 1.3 – 1.8 Mg/m³, in which data are available to characterise the bentonite. At lower dry density / higher void ratios, the model is less well constrained.

This can make modelling small scale experiments such as those carried out by EPFL challenging. However, for large-scale disposal concepts, the bentonite is required to maintain a specified swelling pressure, so the majority of the bentonite will be with the dry density range in which this model performs well.

There may be regions of lower dry density, such as where bentonite swells into void spaces. This model will be less good at predicting the properties of the bentonite in such situations on the small scale of the void space, but if the majority of the bentonite remains at higher dry density, the model should still give useful estimates of e.g. swelling pressure and resaturation time.

6 Performance of the Model and Assessment of Predictive Power

The performance of Quintessa's model has been tested through participation in Beacon Work Package 5.

6.1 Performance of the model for small-scale laboratory tests

In Task 1, Quintessa modelled a series of small-scale laboratory experiments. These were designed to investigate the evolution of heterogeneities that are also expected to be present in repository concepts, including technological voids and the use of different forms of bentonite (blocks, pellets and powder) with heterogeneous dry densities. Tests 1a01 and 1a02

consider a block of bentonite swelling into a void, test 1b considers saturation of a pellet-powder mixture in a fixed volume, and test 1c considers a bentonite block and pellets in a fixed volume. These small, controlled experiments enable our understanding of the bentonite and behaviour of the model to be tested and provide data for calibrating the model.

Quintessa's models and results for Task 1 are discussed in detail in Beacon Deliverable 5.1.2. The key results of interest are the development of swelling pressures in the tests and the saturation and homogenisation of the bentonite. In the assessment cases, these properties of the bentonite provide key safety functions: high swelling pressures provide mechanical stabilization and limit microbial activity, and saturated bentonite which has filled the available void space will have a low permeability which limits water flow to the waste containers and retards the transport of contaminants.

Figure 6-1 shows the predicted axial and radial stresses in the bentonite, compared with experimental measurements. The model performs reasonably well against data; final values of axial and radial stress are predicted more successfully than the transient behaviour. It is useful to have both axial and radial data to compare against the model since several different combinations of input parameters can result in the same axial stress behaviour, but different corresponding radial stress behaviour.

Void spaces in tests 1a01 and 1a02 are represented with a boundary condition which allows free displacement into the void. This results in an initial delay in stress build-up before the void is filled in the model, whereas the data show an immediate build-up of stress. To investigate and improve our representation of free swelling further, Quintessa are beginning to model a dataset of similar experiments from BGS (documented in Beacon Work Package 4). In full-scale repository systems where bentonite is used as a buffer or plug, any technological voids are likely to be much smaller in proportion to the volume of bentonite. This transient behaviour may therefore be less significant for assessment cases. The calculated final swelling pressure of the bentonite is highly sensitive to dry density (due to the exponential relationship between them) and therefore significantly affected by void space.

The results of test 1c demonstrated that friction was important in the model, resulting in a ~0.5 MPa difference in axial stress between the top and bottom of the bentonite sample. The QPAC model was developed to include a friction boundary condition (described in Section 3.2), which was able to reproduce this behaviour well. However, in full-scale disposal concepts, the surface area to volume ratio of the bentonite will be much lower than in these small samples. Friction may therefore be much less significant in assessment cases.

An identical parameter set was used to model each of the tests in Task 1 (detailed in Deliverable 5.1.2). This enhances the predictive capabilities of the model, since the model does not need to be re-calibrated to each specific test.

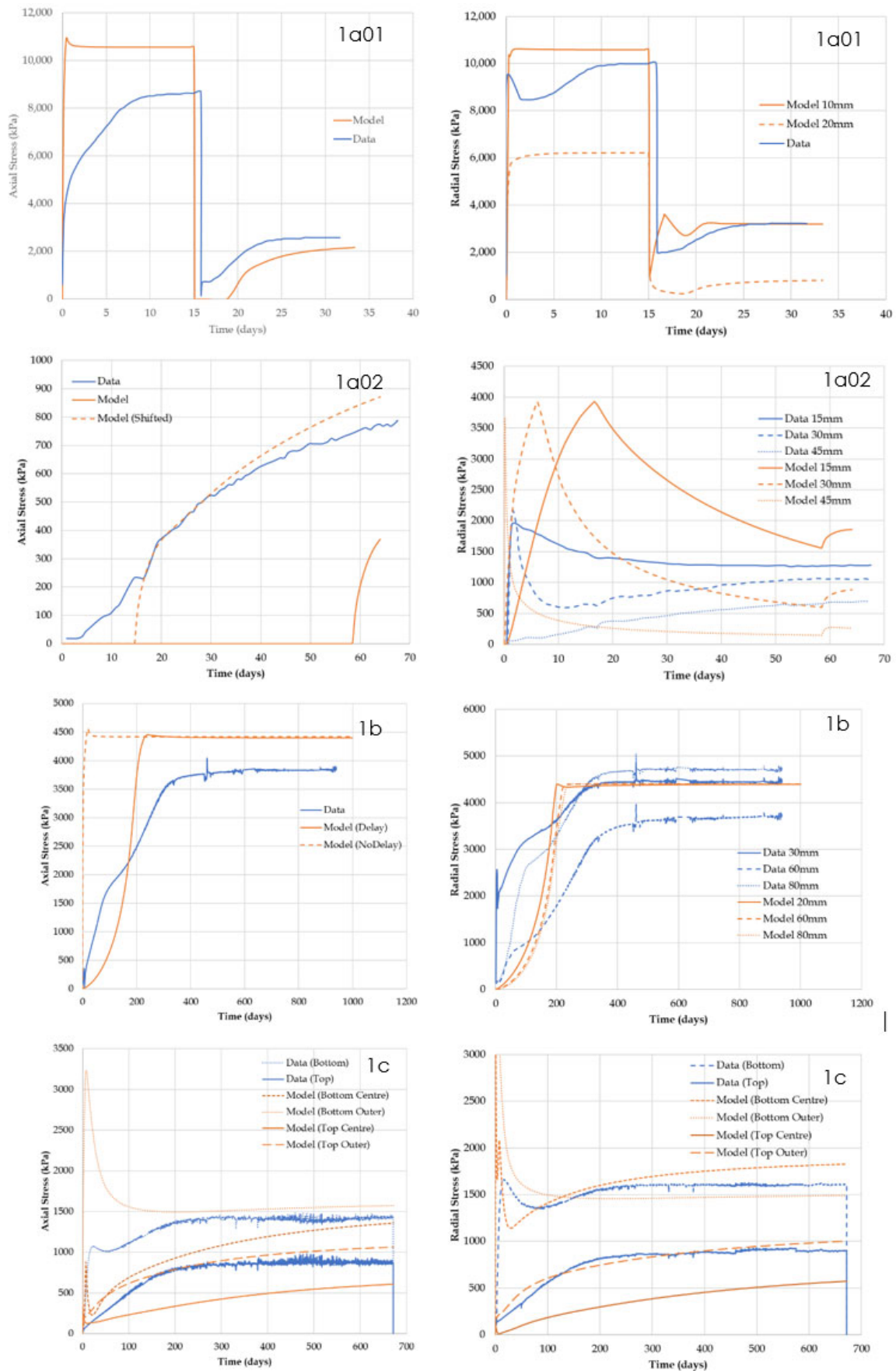


Figure 6-1: Summary of axial and radial stress results from Beacon Tasks 5.1, compared with data.

Figure 6-2 shows the predicted final profiles of void ratio in the bentonite, compared with data. There is generally a good agreement between the model results and the data. All of the tests showed persisting heterogeneity in the bentonite density, even once the sample was fully saturated.

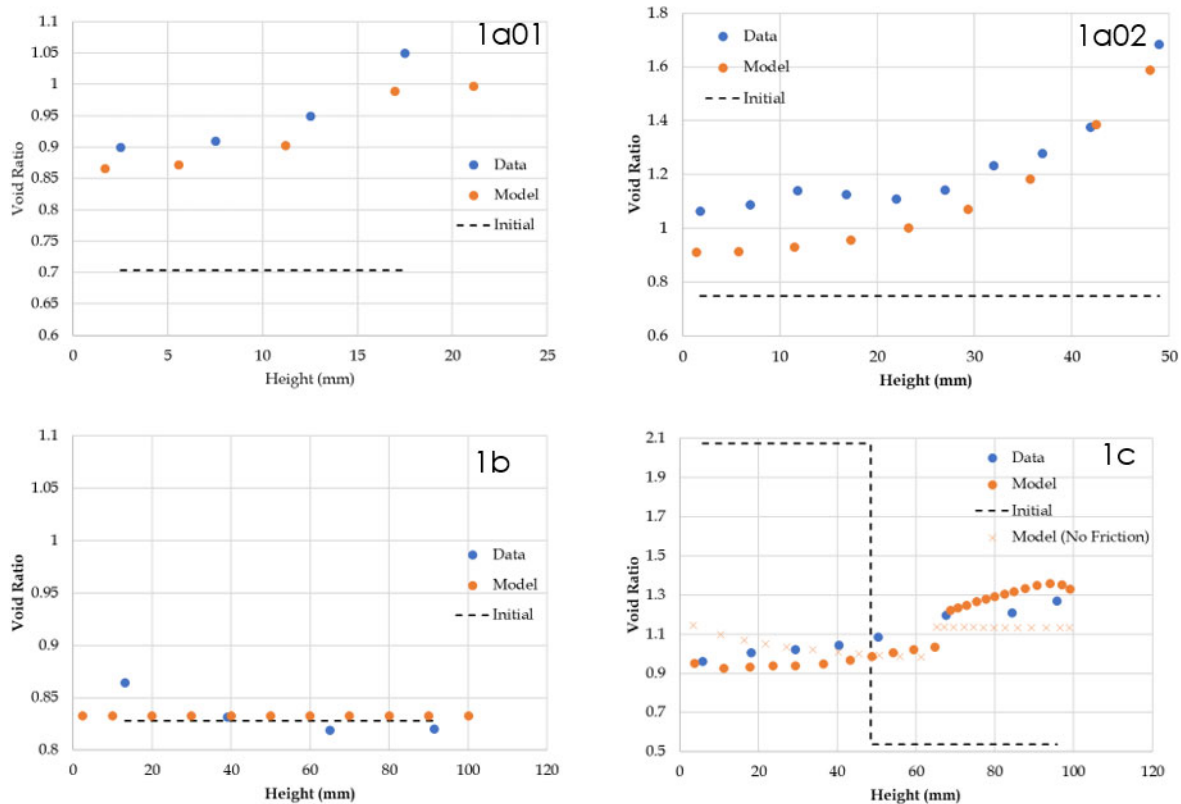


Figure 6-2: Summary of final void ratio profiles from Beacon Tasks 5.1, compared with data.

6.2 Assessment of predictive performance of the model

In Task 3 of WP5, the predictive power of the models was assessed. A series of CIEMAT experiments from WP4 were modelled; data were provided for two of the experiments (MGR22 and MGR23), while the third experiment (MGR27) was modelled 'blind'. Test MGR27 consisted of a bentonite block and bentonite pellets in a fixed volume cylinder, with hydration through the block. Figure 6-3 and Figure 6-4 show the blind predictions from Quintessa's model, compared with the now-available data from the test.

The total water intake during the experiment is well-predicted by the model, although the initial rate of intake is higher than the measured rate. The initial increase in axial stress is therefore also higher than the measurements, but the predicted final stress is ~0.2 MPa lower. The model successfully the relative behaviour of the three tests; notably, it predicted a similar rate of water intake and much lower axial stress measured at the top of test MGR27 compared to test MGR23. The key difference between the two tests is the relative orientation of the bentonite block and pellets; in MGR23, hydration is through the bentonite pellets at the bottom of the test cell, whereas in MGR27 hydration is through the block at the bottom of the test cell. This result suggests that friction is important in the two tests, although as discussed, this is expected to be less important in full-scale experiments. The friction coefficient has not been specifically calibrated to the tests, which may explain some of the discrepancy in the results.

The model predicts a significant degree of homogenisation between the block and pellets but there are notable differences between the predictions and the data. The final dry density and water content profiles are sensitive to friction and to small technological voids in the

experiment. As discussed above, these are expected to be less significant in a full-scale assessment case.

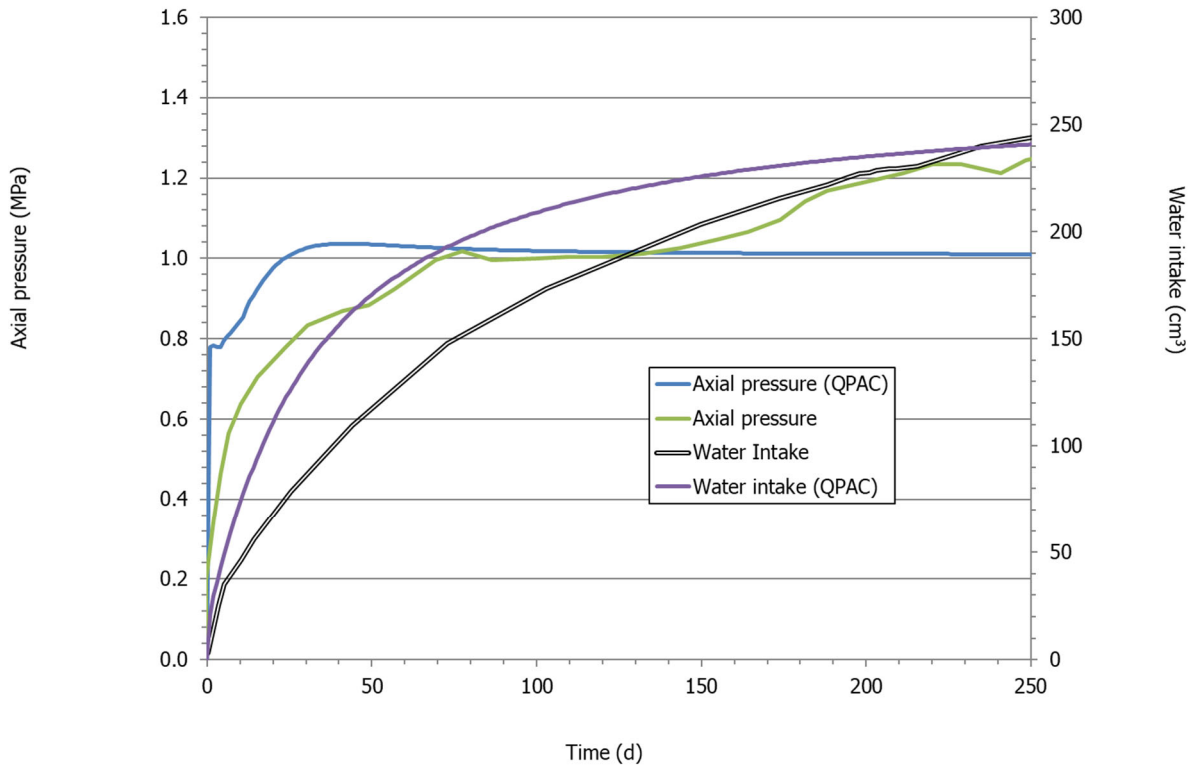


Figure 6-3: Predicted axial pressure and water intake in Task 5.3 test MGR27, compared with data.

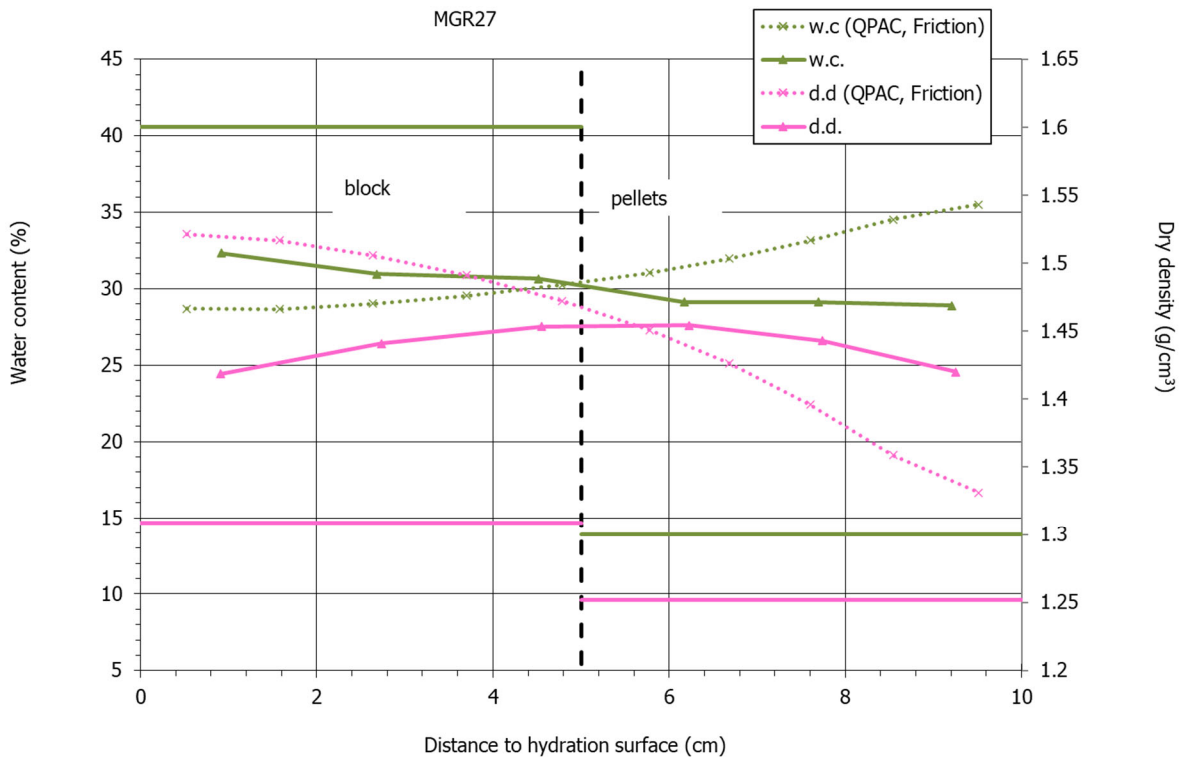


Figure 6-4: Predicted water content and dry density profiles in Task 5.3 test MGR27, compared with data.

6.3 Performance of the model for full-scale disposal concepts

In Task 2 of WP5, Quintessa developed a model of the FEBEX (Full-scale Engineered Barriers) experiment. This experiment was based on the Spanish reference concept, in which the thermal effects of the wastes were simulated with heaters, surrounded by high density compacted bentonite blocks, with natural hydration from the crystalline host rock. Modelling this experiment is therefore a good indication of the performance of the model for a real disposal concept.

The FEBEX experiment is heated, so a THM model was required to model it. The geometry was simplified to a 2D axisymmetric model, with a separate 2D r- θ model used to test axial dependence. QPAC does have the capability to model 3D geometries, but full 3D THM models with fine discretisation are computationally expensive and can take multiple days to run. Quintessa are investigating alternative solvers for QPAC and also developing capability in COMSOL Multiphysics (see Section 7.2) to improve this performance, but it is currently a limitation of the existing code.

The FEBEX bentonite was parameterised using data from lab tests performed as part of the FEBEX experiment. The ILC (p_0 and λ) was calibrated to water retention, swelling and oedometer data. The full parameterisation and details of this model are given in Beacon deliverable 5.2.2. A summary of key model results are presented here.

Figure 6-5 shows temperature evolution in the bentonite compared with data. The model was unable to reproduce the initial heating ramp; with the specified power of 2 kW applied, this resulted in temperature at the heater surface overshooting the 100°C target temperature by 35°C. The initial heat flux therefore had to be calibrated to the results. After this time, the temperature is mostly constant and the model predicts the measured temperature within 5°C. There is notable heterogeneity in the temperatures measured by different sensors at the same radial and axial position (up to 6°C).

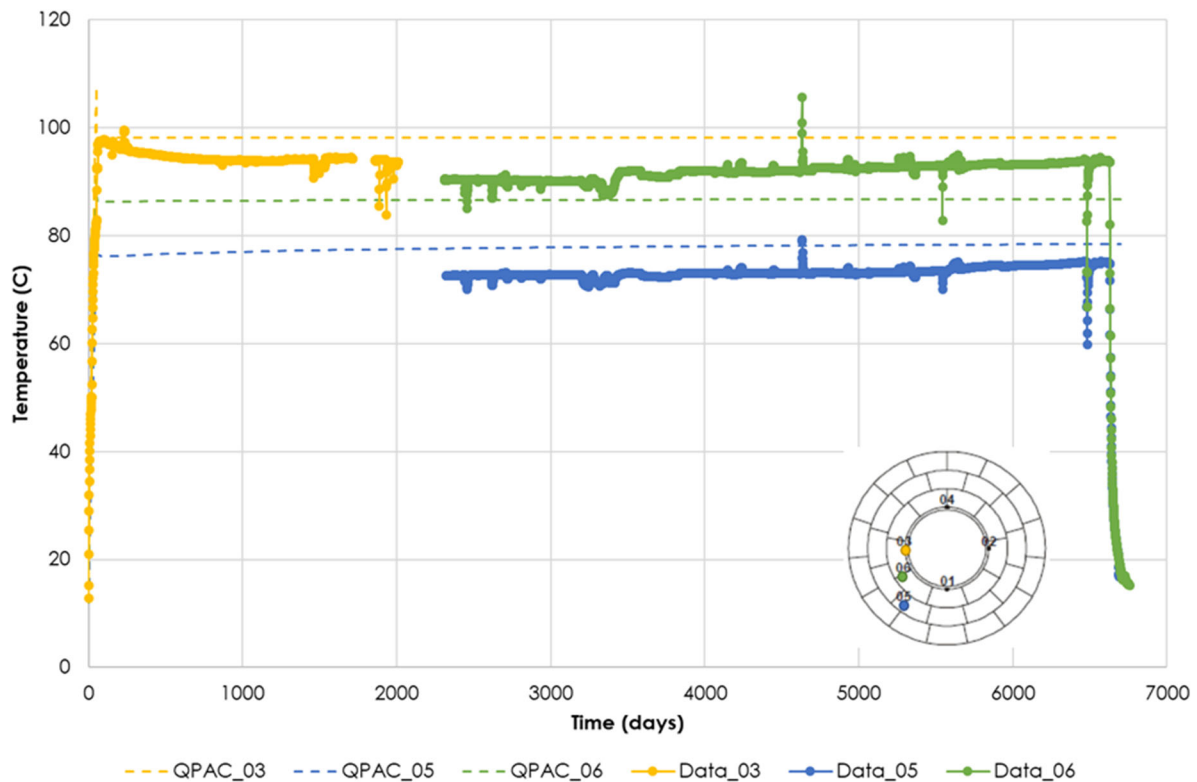


Figure 6-5: Temperature evolution calculated by the 1D model (dashed lines) compared with data (markers) at sensor locations 03 ($r=0.5m$), 05 ($r=0.8m$) and 06 ($r=0.6m$).

Relative humidity evolution results are shown in Figure 6-6. There are limited sensor data but the modelled behaviour is generally consistent with measurements, with 100% relative humidity reached fairly rapidly at the outer bentonite block and more gradually close to the heater. The model initially saturates more rapidly than the experiment but then slows down. The experimental data show a large variation in saturation time between sensors at the same radial distance – taking between 60 and 2450 days to reach 99% relative humidity. The model does not reproduce this behaviour, suggesting heterogeneities such as voids between bentonite blocks or wet spots on the tunnel walls have a significant impact on the transient behaviour.

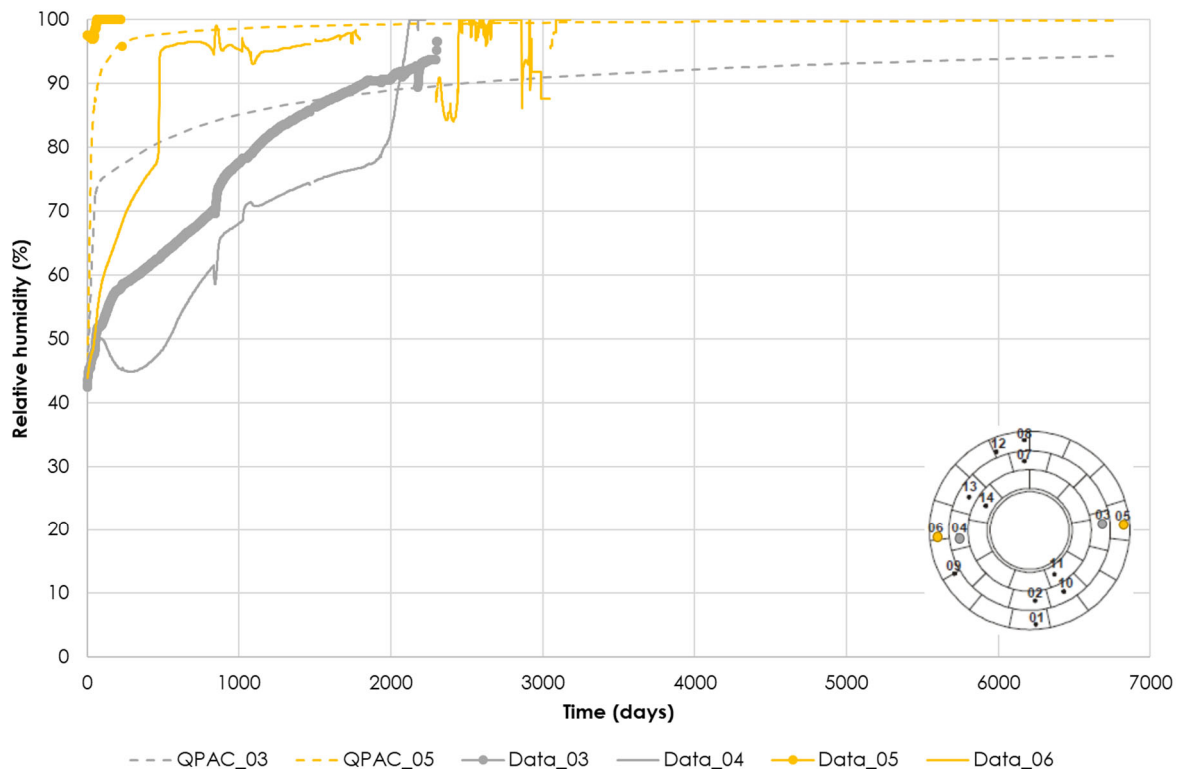


Figure 6-6: Relative humidity evolution calculated by the 1D model (dashed lines) compared with data (markers, solid lines) at sensor locations 03, 04 ($r=0.8m$) and 05, 06 ($r=1.05m$).

Radial stress evolution results are compared with data in Figure 6-7. In general, stresses are overpredicted by the model – particularly close to the heater, where measured stresses are very low. This large difference in measured radial stress between the middle and outside of the bentonite could suggest that friction is important, or hoop stresses are preventing radial collapse of the bentonite. The low measured stresses close to the heater could be an indication of the importance of vapour transport in the system. The final radial stress at the outside of the bentonite (location 01, for which there is complete sensor data) is well-predicted by the model. However, the evolution of stress is less well predicted. The initial spike and collapse in radial stress at the outside of the bentonite during the initial heating period appears to be overpredicted by the model.

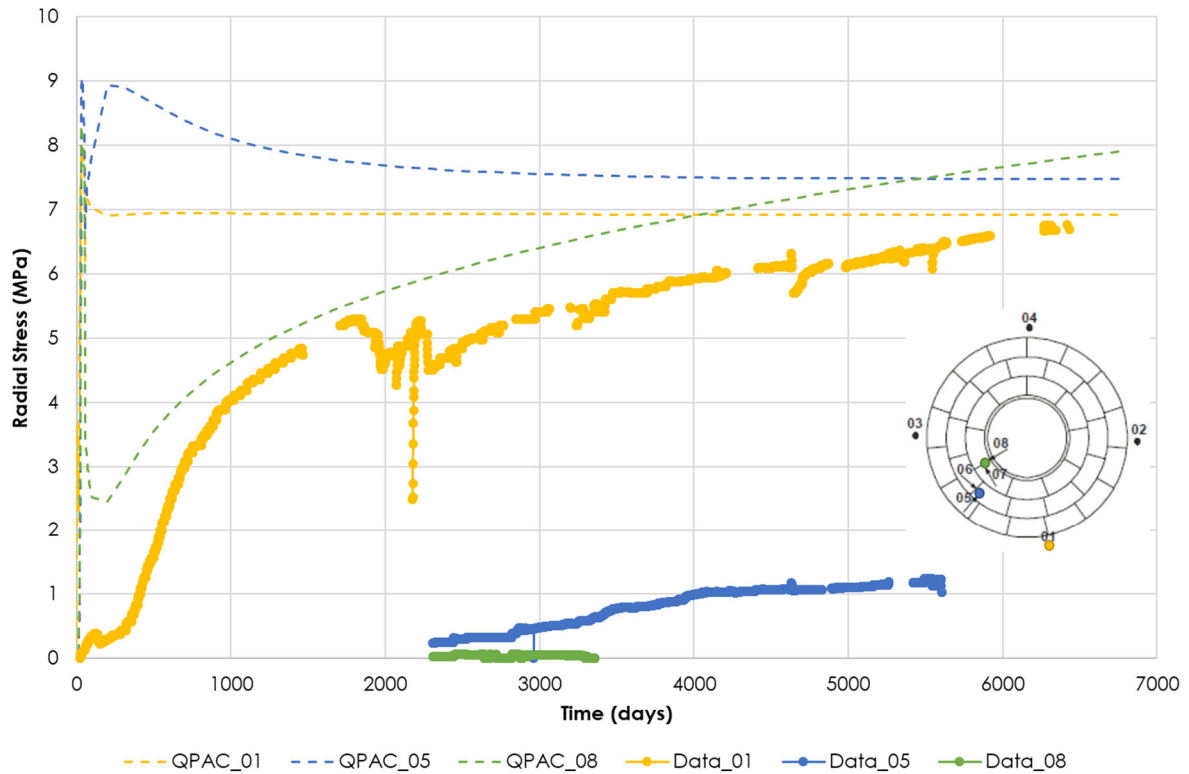


Figure 6-7: Radial stress evolution calculated by the 1D model (dashed lines) compared with data (markers) at sensor locations 01 ($r=1.1m$), 05 ($r=0.8m$) and 08 ($r=0.6m$).

Final radial dry density profiles are compared with data in Figure 6-8. The model predictions lie within the scatter of the measured results from dismantling. Both the model and data show a dry density gradient from the drier and more compact bentonite near the heater, to the wetter bentonite close to the rock. This suggests that water-driven swelling of the bentonite dominates over thermal expansion processes. Towards the heater, the model and data show very similar dry density gradients, whereas the model predicts a flatter gradient in the outer half of the bentonite. This could be because the effect of the void space between the bentonite and the rock is not being fully captured in the model, so the dry density at the edge of the bentonite is overestimated.

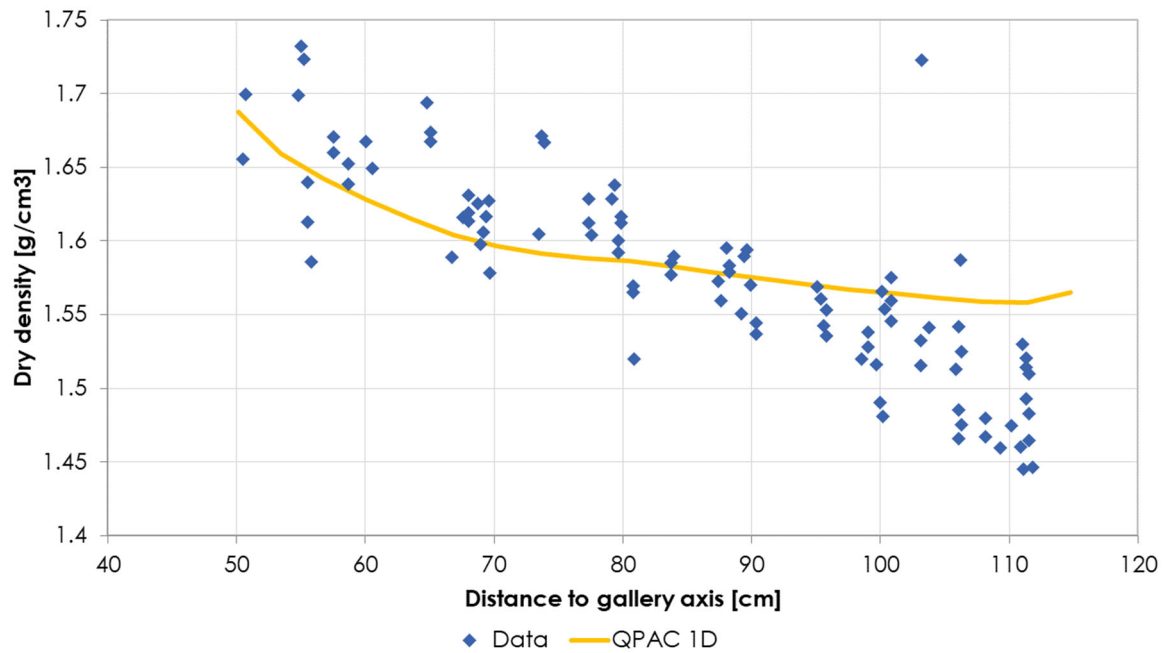


Figure 6-8: Radial dry density profile calculated by the 1D model compared with data.

In general, the model is able to qualitatively represent the behaviour of the full-scale assessment case, including thermal effects of the heater and natural hydration from the host rock. The model predicts that the bentonite will fully saturate with a persisting radial dry density gradient; this behaviour is also seen in the experiment. Without calibrating the model to the observations, the model has reasonable success in predicting the temperatures, relative humidities, stresses and dry densities within the bentonite but there are notable differences in the transient behaviour and in the radial stress measurements in particular. The measurements show much more heterogeneity within the bentonite than is predicted by the model, which may be due to initial heterogeneities in the material itself or due to heterogeneous boundary conditions (void space and heterogeneous hydration). A simple 1D model is able to reproduce much of the behaviour.

In Task 5.4 of Work Package 5, Quintessa are developing a model of Andra's assessment case. In Andra's repository concept, disposal cells (sub-horizontal tunnels containing the waste packages) are excavated in a Callovo-Oxfordian (COx) claystone formation. Bentonite plugs are used to separate the disposal cells from the transfer drifts. The objective of Task 5.4 is to develop a HM model of a 2D cross-section of the bentonite, EDZ and COx. Development of this model is currently in progress. A model has been developed to represent the initial ventilation period before the bentonite is emplaced to provide the initial conditions for the rock. Test models are being developed to compare representation of the rock, EDZ and void spaces as materials in the model, compared to defining them as boundary conditions for the bentonite.

6.4 Discussion

Through participation in Work Package 5, Quintessa's model has demonstrated that it is able to reproduce and predict the behaviour of bentonite in simple laboratory experiments and in a full-scale in-situ experiment with reasonable success. The general THM behaviours of bentonite that are relevant to disposal concepts (e.g. saturation, swelling, homogenisation) can all be modelled. Section 7.1 discusses the geometries of disposal concepts that can be modelled.

A major advantage of Quintessa's model is that it has been developed to require minimal parameters, and these parameters are mostly directly measurable in experiments. The

Internal Limit Curve can be parameterised to readily-available oedometer data and used to parameterise water retention and swelling pressure curves. This greatly strengthens the predictive capabilities of the model, since it requires minimal calibration to each experiment. However, because of the exponential curve used, the model is particularly sensitive to uncertainties in measurements of dry density.

In general, Quintessa's model is able to predict final values of metrics like saturation and swelling pressure better than transient behaviour. This is true for both laboratory experiments and full-scale experiments. Comparison with experimental results can be complicated by uncertainty and heterogeneity in experimental measurements. It is not always clear which features of experimental data are reproducible and which are artefacts, and what the uncertainty is in the measurements. Smaller experiments have more controlled boundary conditions but are also more sensitive to friction and void spaces.

7 Code Development and Investigations

7.1 QPAC Coupling to Gmsh

In Beacon Task 5.4, Quintessa have chosen to develop a model of Andra's assessment case. In Andra's repository concept, disposal cells (sub-horizontal tunnels containing the waste packages) are excavated in a Callovo-Oxfordian (COx) claystone formation. Bentonite plugs are used to separate the disposal cells from the transfer drifts. These plugs consist of a 10-m-diameter bentonite core divided into 3 horizontal layers differentiated by their initial density (Figure 7-1). The objective of Task 5.4 is to develop a HM model of a 2D cross-section of the bentonite, EDZ and COx.

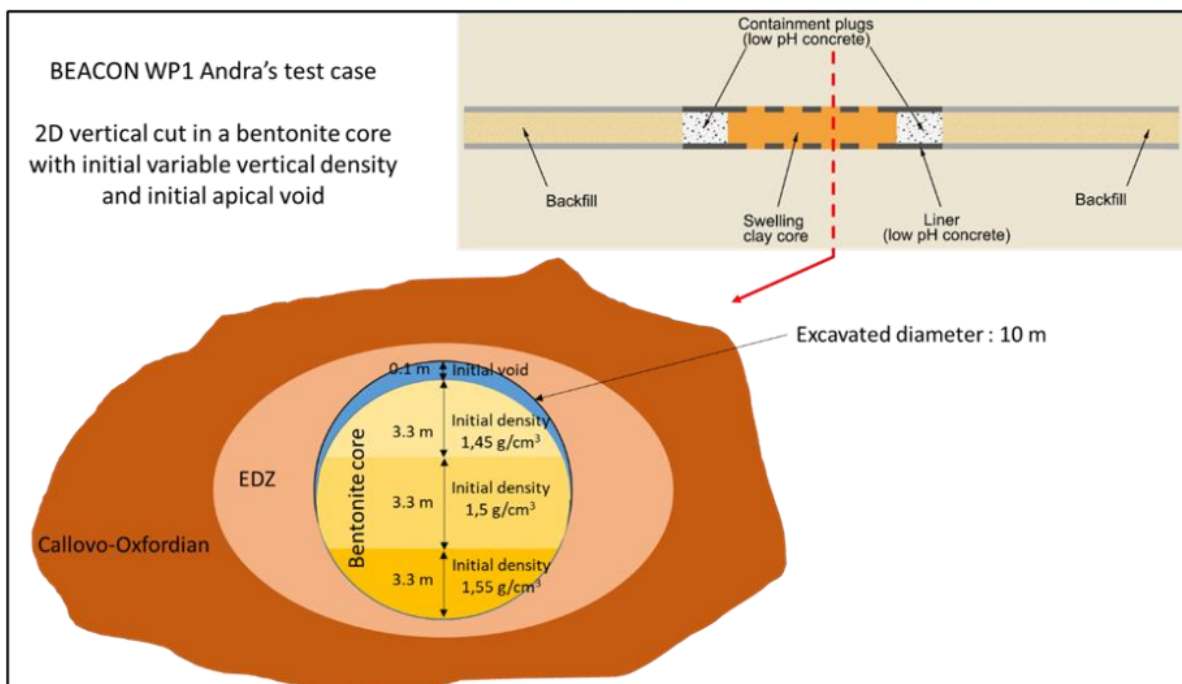


Figure 7-1: Geometry of the bentonite seal in Andra's test case, reproduced from Leupin et al., 2020.

In discussion with other teams in the BEACON project, the geometry depicted in Figure 7-1 has been simplified to that shown in Figure 7-2. Here, the geometry of the void region has been converted to a circular segment to simplify the resulting mesh and avoid extreme small/acute elements that would be needed to discretise the ends of the void 'crescent' in the original geometry.

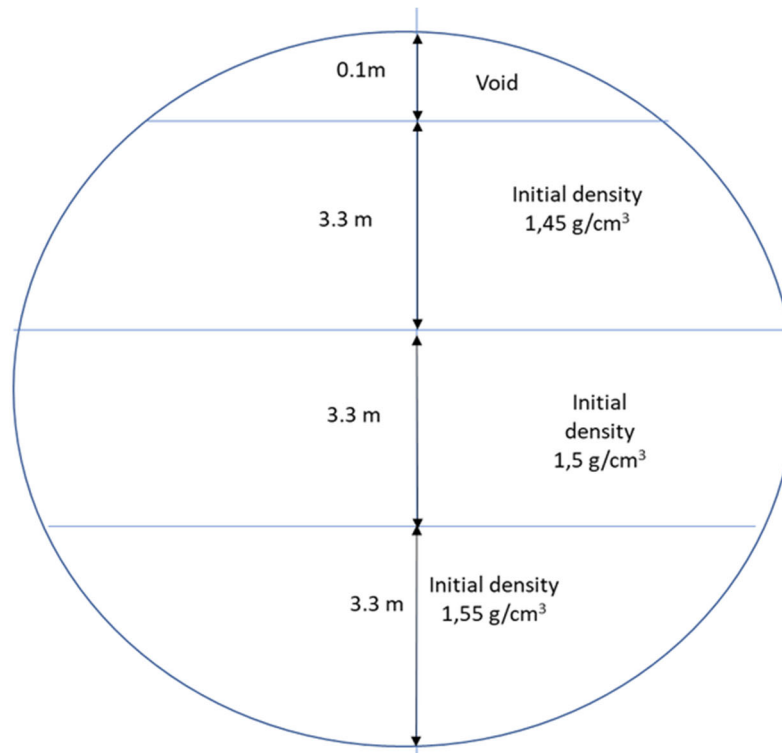


Figure 7-2: Simplified geometry of the bentonite seal to be considered in initial modelling. (Note figure not to scale.)

In QPAC, the model geometry and mesh can only be directly defined using either a Cartesian or cylindrical coordinate system. It is therefore not possible to accurately represent the geometry shown in Figure 7-2 – the circular domain cannot be represented in the Cartesian geometry and the internal boundaries between the bentonite layers cannot be represented in a cylindrical geometry. QPAC supports an alternative 'abstract' representation of the grid, which can be used to directly specify cell locations and cell-cell connection areas and distances that to date has been used when performing abstracted compartmental modelling, but can also be used to define an explicit unstructured grid.

A preprocessor has been developed to allow unstructured 2-D grids developed using the Gmsh mesh generator¹ to be converted to QPAC abstract form. An initial prototype 2-D mesh of the simplified geometry shown in Figure 7-2 using quad elements is shown in Figure 7-3.

The QPAC model in the unstructured grid is still under development, but results are presented for a prototyping calculation in which the void region is assumed to be filled with bentonite of the same density as the upper low density band and zero displacement boundary conditions are applied around the entire boundary, where an external water pressure of 4.5 MPa is applied.

Figure 7-4 shows the evolving dry density of the bentonite. A reduction in dry density is seen around the circumference of the domain due to the ingress of water and subsequent bentonite swelling. There is a corresponding increase in dry density towards the centre of each band due to the resulting compression of the bentonite towards the centre. Figure 7-5 shows the effective stresses that develop in the bentonite after 10 y.

¹ <https://gmsh.info/>

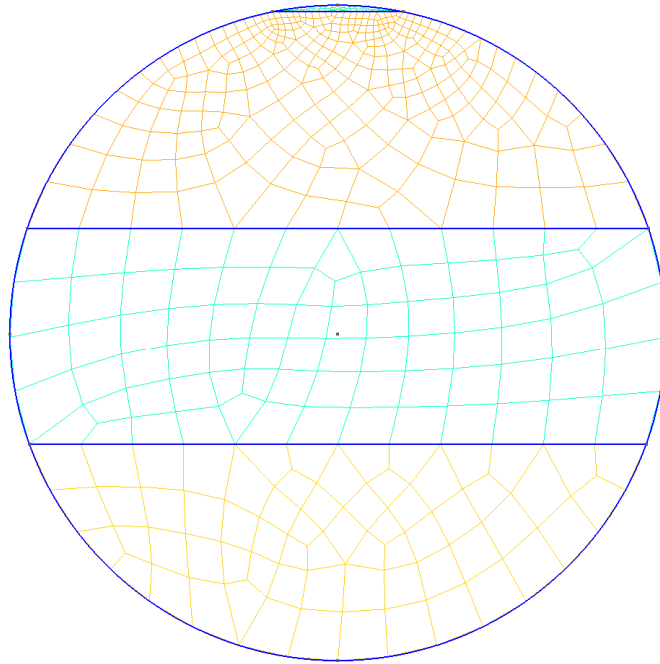


Figure 7-3: Example 2-D meshing of the simplified bentonite seal geometry (Figure 7-2)

The current model is a preliminary prototype and needs further work to correctly simulate the desired simplified system shown in Figure 7-2. Further developments to the model that are required include:

- Treatment of mechanical boundary conditions (the prototype assumes zero displacement conditions throughout);
- Treatment of the void region (the prototype assumes that the void region is filled with bentonite);
- Treatment of the evolving boundary conditions on the boundary that is initially adjacent to the void, but which is subsequently expected to fill with bentonite;
- Grid convergence analysis; and
- General validation of the model.

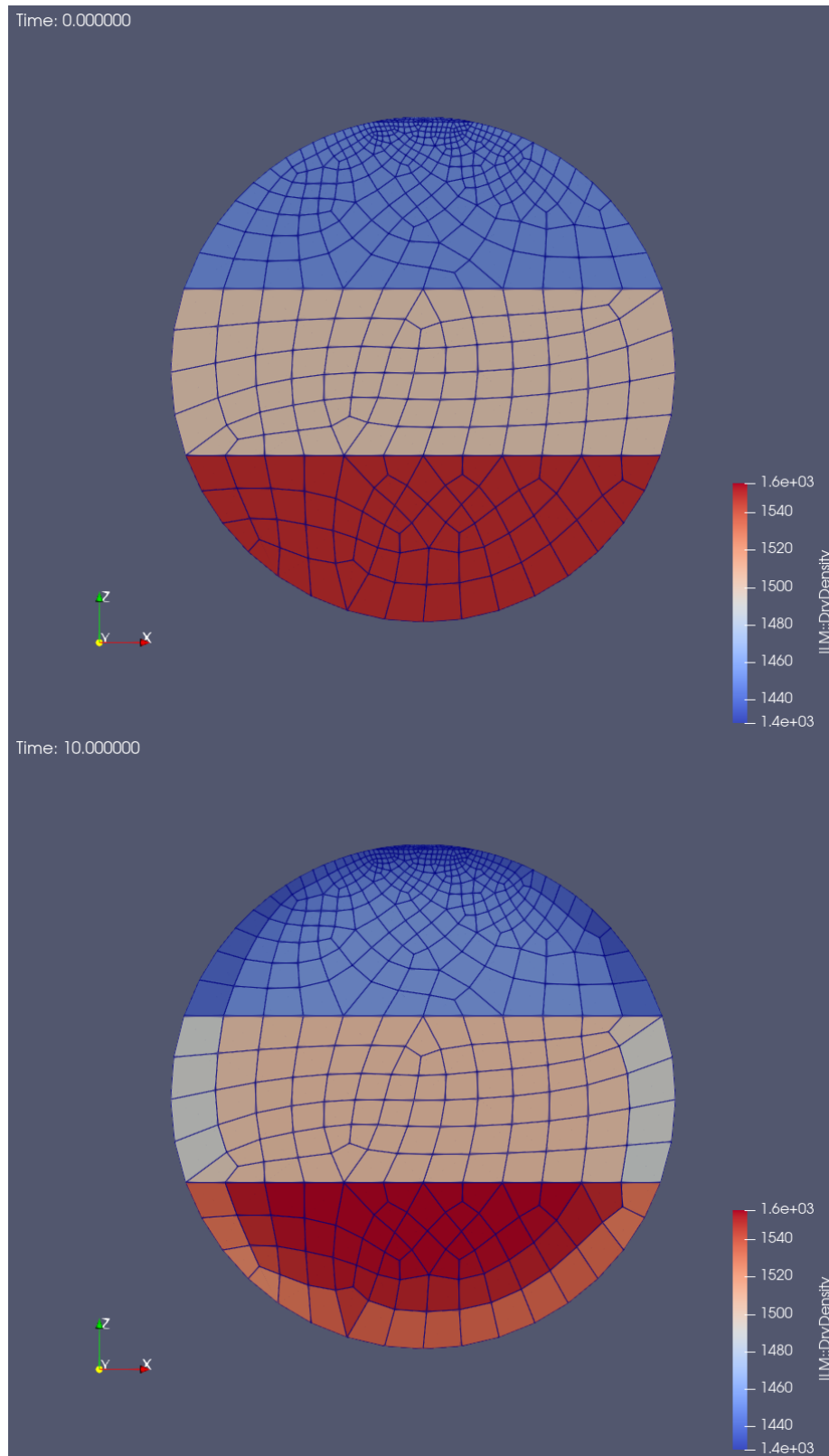


Figure 7-4: Prototyping calculation result showing dry density at 0 y (top) and 10 y (bottom) using the example 2-D meshing shown in Figure 7-3.

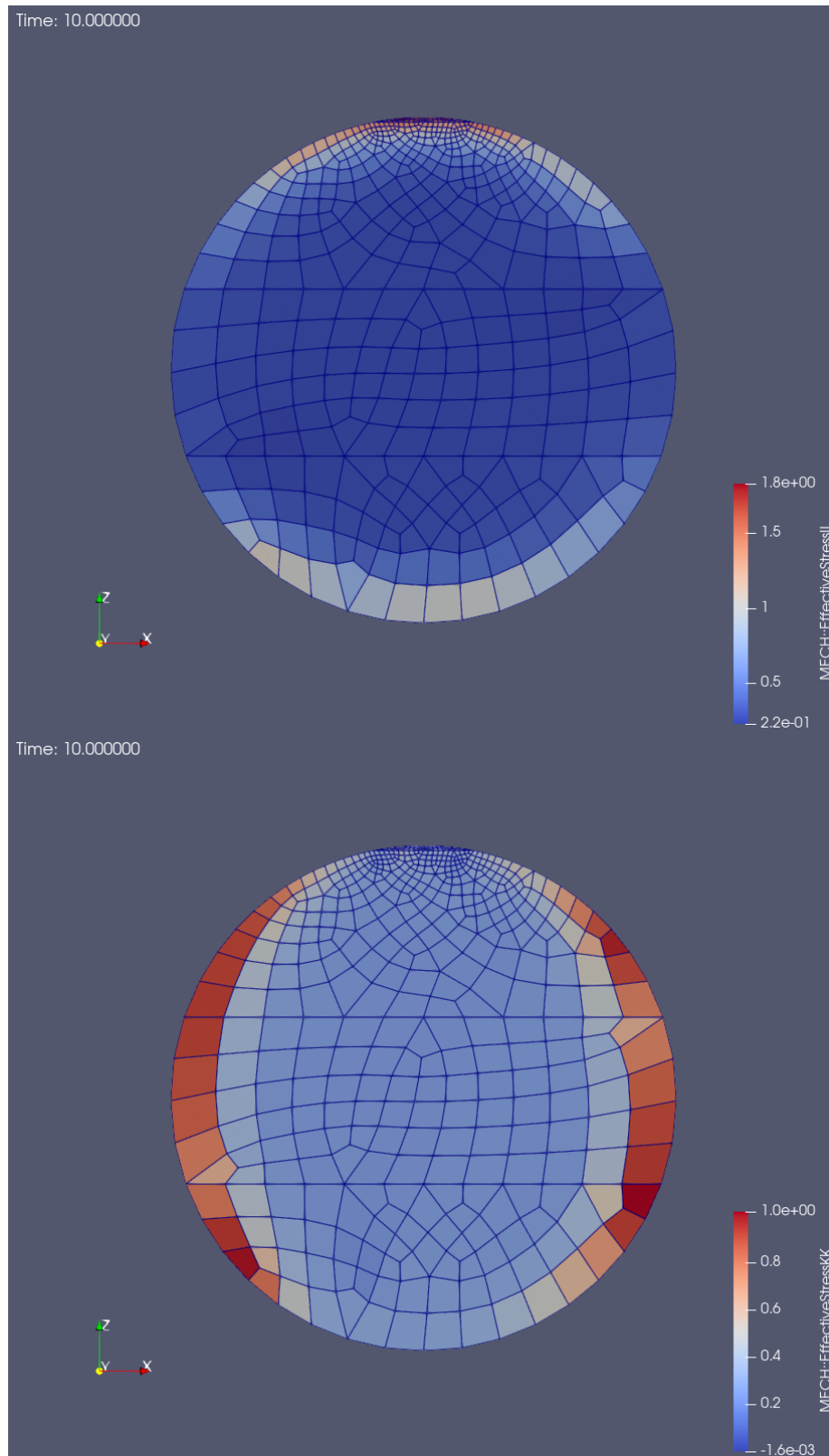


Figure 7-5: Prototyping calculation result showing σ'_{ii} (top) and σ'_{kk} (top) at 10 y using the example 2-D meshing shown in Figure 7-3.

7.2 COMSOL

Alongside modelling work in QPAC, Quintessa have begun to develop capability for modelling bentonite in COMSOL. COMSOL Multiphysics® (COMSOL, 2020) is a commercial finite element code which has inbuilt physics modules (including the Barcelona Basic Model,

BBM). Initial work has focussed on the representation of flow using Richards equation and building an understanding of the BBM and its representation in COMSOL.

The differences between head-based (25) and mixed (26) forms of Richards equation were investigated based on the seminal paper by Celia et al. (1990) for the 1D soil infiltration example, with the different forms implemented in COMSOL using the equation-based modelling interface.

$$C(h) \frac{\partial h}{\partial t} - \nabla \cdot K(h) \nabla h - \frac{\partial K}{\partial z} = 0 \quad (25)$$

$$\frac{\partial \theta}{\partial t} - \nabla \cdot K(h) \nabla h - \frac{\partial K}{\partial z} = 0 \quad (26)$$

Here, h (m) is the pressure head, θ (-) is the volumetric moisture content, $C(h) \equiv \frac{d\theta}{dh}$ (m^{-1}) is the specific moisture capacity function, $K(h)$ ($m \cdot s^{-1}$) is the unsaturated hydraulic conductivity and $\frac{\partial K}{\partial z}$ is the elevation head component where z is the vertical direction in the coordinate system.

Figure 7-6 shows the results of the different forms compared to the reference result from Celia et al. (1990), both using the default solver options and forcing larger timesteps. With larger (30s) time-steps, the head-based form model underpredicts the infiltration depth through the soil at the infiltration front compared with the reference result. The mixed form model matches the reference result well even for this larger time-step. These results illustrate the potential for inaccuracy with the head-based form. Both implementations also exhibited oscillations around the steep infiltration front for early times in the solve which were not observed in a similar implementation using Quintessa's QPAC finite volume code. The inbuilt pressure-based form of Richards equation in COMSOL showed equivalent results to the head-based form described above. This is useful understanding for coupling mechanical models to flow in COMSOL in future.

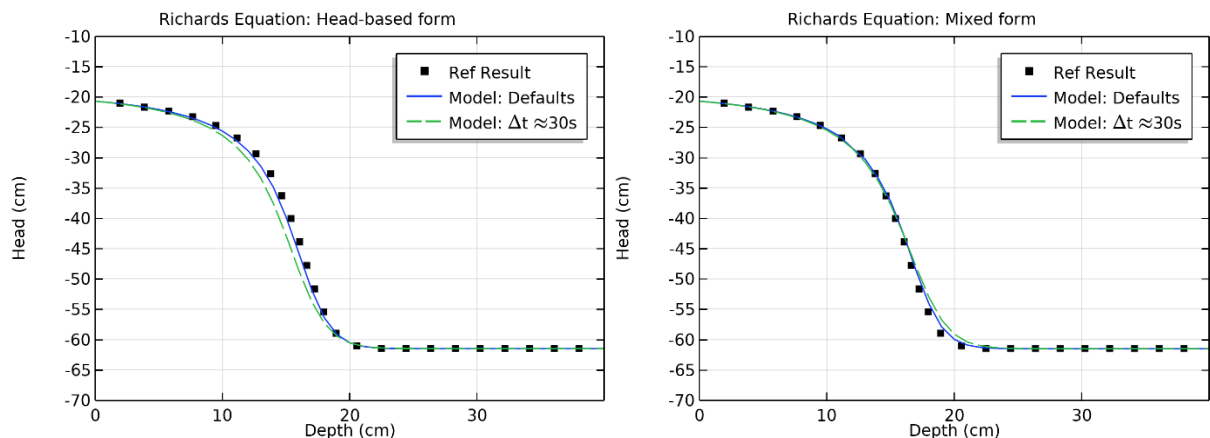


Figure 7-6: Comparison of default solver settings and 30s time-steps for head-based (left) and mixed (right) forms of Richards equation in COMSOL to the reference infiltration depth result, at $t = 360s$.

Some initial work for understanding and applying the inbuilt implementation of the BBM in COMSOL has also been undertaken, using a predefined suction curve from sample moisture content to solve for bentonite swelling. However, models for direct comparison to the task 3.3 experiments have not yet been fully developed.

8 Concluding Remarks

At the start of the Beacon project, Quintessa already had a developed THM model of bentonite which could be used to model bentonite evolution, referred to as the ILM. Throughout the project, Quintessa have been able to test this model in different applications and to develop and improve its capabilities. The model is now able to represent: FEBEX and MX-80 bentonites and bentonite-sand mixtures; blocks, pellets and powdered bentonite; regular and irregular geometries including laboratory and full-scale experiments and Andra's assessment case; heated and isothermal experiments. The model is able to predict and reproduce the main types of qualitative behaviour observed in bentonite evolution.

A key strength of the model is its relatively small parameter set which requires minimal calibration. However, this results in some limitations of the model. The model does not represent the double structure of bentonite, and simplifies representation of pellets. This means that results for the final bulk state of the bentonite are often consistent with experimental measurements, but predictions of transient behaviour and spatial distribution are generally less accurate. Often, closer fits to experimental data could be obtained with further calibration of the model parameters, but this undermines the predictive capabilities of the model. One problem is that there is often a high degree of uncertainty and variability in the properties of the bentonite and boundary conditions of experiments, which can have a significant impact on results. The model is particularly sensitive to the dry density of the sample.

Beyond Beacon, Quintessa hope to make further developments to our model to improve its applicability to safety assessments. We are aiming to model a set of BGS experiments to test and improve our representation of swelling into void spaces. We are also aiming to develop our modelling capabilities in COMSOL, in order to benchmark against our QPAC results and improve our ability to model complex 3D geometries.

References

[Please refer only to official publications.]

Celia MA, Bouloutas ET and Zarba RL (1990). A general mass-conservative numerical solution for the unsaturated flow equation. *Water Resources Research* 26(7): 1483-1496.
doi:10.1029/WR026i007p01483

Cleall P J, Singh R M and Thomas H R, 2013. Vapour transfer in unsaturated compacted bentonite. *Géotechnique* 63, No. 11, 957-964 [<http://dx.doi.org/10.1680/geot.12.P.147>]

COMSOL Multiphysics, 2020. COMSOL Multiphysics Reference Guide, v5.6. www.comsol.com

Dueck A, 2004. Hydro-mechanical properties of a water unsaturated sodium bentonite. PhD thesis, Lund University.

Dueck A, Goudarzi R, Börgesson L, 2014. Buffer homogenization, status report 2. SKB TR-14-25, Svensk Kärnbränslehantering AB.

Enresa, 2000. FEBEX Project. Full-scale Engineered Barriers Experiment for a Deep Geological Repository for High Level Radioactive Waste in Crystalline Host Rock. Final Report. Enresa Report 1/2000, Enresa, Madrid.

Howell P, Kozyreff G and Ockenden J, 2009. *Applied Solid Mechanics*. Cambridge University Press.

Jacinton A C, Villar M, Ledesma A, 2012. Influence of water density on the water retention curve of expansion clays. *Géotechnique* 62(8):657-667.

Leupin O, Talandier J, Sellin P and Lanyon G W, 2020. Assessment Cases for the Evaluation of the Degree of Heterogeneity. Beacon report.

Maul P, 2013. QPAC: Quintessa's general-purpose modelling software. Quintessa report QRS-QPAC-11. www.quintessa.org

Philip J R and de Vries D A, 1957. Moisture Movement in Porous Materials under Temperature Gradients. *Trans., Am. Geophys. Union*, Vol. 38, No. 2, pp. 222-232, p. 594.

Roscoe K H, Burland J B, 1968. On the generalised stress-strain behaviour of 'wet clay'. In Heyman J, Leckie F A (eds), *Engineering Plasticity*. Cambridge University Press, pp 535-609.

Rutqvist J and Tsang C F, 2003. A fully coupled three-dimensional THM analysis of the FEBEX in situ test with the ROCMAS Code: Prediction of THM behaviour in a bentonite barrier. <https://escholarship.org/uc/item/42c6z2nn>

Seiphoori A, 2015. Thermo-hydro-mechanical characterisation and modelling of Wyoming granular bentonite. Nagra Technical Report NTB 15-05.

Thatcher K E, 2017. FEBEX-DP: THM modelling. Quintessa's contribution on behalf of RWM. Contractor Report to RWM QRS-1713A-R2, V1.8.

Thatcher K E, Bond A E, Robinson P C, McDermott C, Fraser Harris A P and Norris S, 2016. A new hydro-mechanical model for bentonite resaturation applied to the SEALEX experiments. *Environmental Earth Sciences* 75:1-17.



Wang Q, Tang A M, Cui Y-J, Delage P, Gatmiri B, 2012. Experimental study of the swelling behaviour of bentonite/clay-stone mixture. *Eng Geol* 123:59-66. [doi:10.1016/j.enggeo.2011.10.003]

D3.3



Annex H

Contribution to Deliverable 3.3

DELIVERABLE (D3.3)
UPC Report

Author(s): Antonio Gens, Ramon B. de Vasconcelos, Carlos Eduardo Rodríguez

Reporting period: 01/06/20 – 31/05/22

Date of issue of this report: 31/08/21

Start date of project: **01/06/17**

Duration: 60 Months

This project receives funding from the Euratom research and training programme 2014-2018 under grant agreement No 745 942		
Dissemination Level		
PU	Public	x
RE	Restricted to a group specified by the partners of the Beacon project	
CO	Confidential, only for partners of the Beacon project	

REVIEW

Name	Internal/Project/External	Comments
All Beacon partners	Project internal	

DISTRIBUTION LIST

Name	Number of copies	Comments
Seifallah BEN HADJ HASSINE (EC)	Digital	
Beacon partners	Digital	

Abstract

This report contains an account of the work of the UPC team in Work Package 3 of the project Beacon.

Content

1	Introduction	5
2	Description of the model.....	5
2.1	General.....	5
2.2	Phase diagrams and basic relationships.....	7
2.3	Additive decomposition of the strain tensor	9
2.4	The local mass transfer mechanism	10
2.5	Balance equations	11
2.5.1	The mass balance of solid.....	11
2.5.2	The mass balance of water	11
2.5.3	The mass balance of air	12
2.5.4	The balance of internal energy	12
2.5.5	The balance of momentum	13
2.6	Constitutive equations	13
2.6.1	Thermal constitutive equations	13
2.6.2	Hydraulic constitutive equations.....	14
2.6.3	Mechanical constitutive equations.....	16
3	Basic capabilities of the model	22
4	Task 3.3	24
4.1	Stress paths of the tests	24
4.2	Modelling features	25
4.2.1	Geometry and boundary conditions.....	25
4.2.2	Initial conditions and model parameters	26
4.3	Results.....	28
4.3.1	Path 1: A-B-C-D.....	28
4.3.2	Path 2: A-B'-C'	30
4.3.3	Full results	31
4.4	Micro-structural evolution	31
5	Performance of the model and assessment of predictive power	34
6	Concluding remarks	36
	References	36
	Appendix 1.....	38

1 Introduction

Work Package 3 of the Beacon project is devoted to the development of the constitutive models for describing the hydro-mechanical and thermo-hydro-mechanical behaviour of bentonite-based highly-swelling materials in an appropriate manner. This document contains the contribution of the UPC team to D3.3, the final Deliverable of the WP. There have been previous contributions to Deliverables 3.1 and 3.2; the present contribution is a summary account of the work carried out within WP3 throughout the project.

This document is structured as follows. A concise description of the THM numerical formulation and constitutive models is presented first. Particular attention is given to the mechanical double structure constitutive model that is a key component for simulating homogenization processes, the main goal of the project. A major development is the inclusion of thermal effects in the double structure formulation, albeit with some simplifications. Although concise, the presentation of the model is comprehensive and contains all the essential aspects of the formulation. The capabilities of the model are addressed afterwards, with particular reference to the developments and improvements carried out during the project. The performance of the model in a verification task, involving oedometer tests with different stress paths, is then described and reviewed. Finally, the performance of the model throughout the project is discussed and reviewed followed by an assessment of its predictive power.

2 Description of the model

2.1 General

A double structure (or double porosity) model that distinguishes between two structural levels (microstructure and macrostructure) has been developed and used in the Beacon project. In such a framework, the porous medium is described by a micro-pore domain, composed by the internal structure of individual particles and aggregates of active clays and their vicinity, and a macro-structural level corresponding to the arrangement of clay aggregates and other large components that leave macro-pores between them (Gens & Alonso, 1992). The conceptual model is illustrated in Figure 2-1. The micro-pore fraction in this double structure formulation includes both the intra- and the inter-particle voids within a clay aggregate (micro- and meso-pores). The consideration of these distinct but overlapping structural media allows the tracking of the evolution of the clay structure during wetting-drying and loading paths. The model has been developed within a generalized elastoplastic framework that considers two different plastic mechanisms.

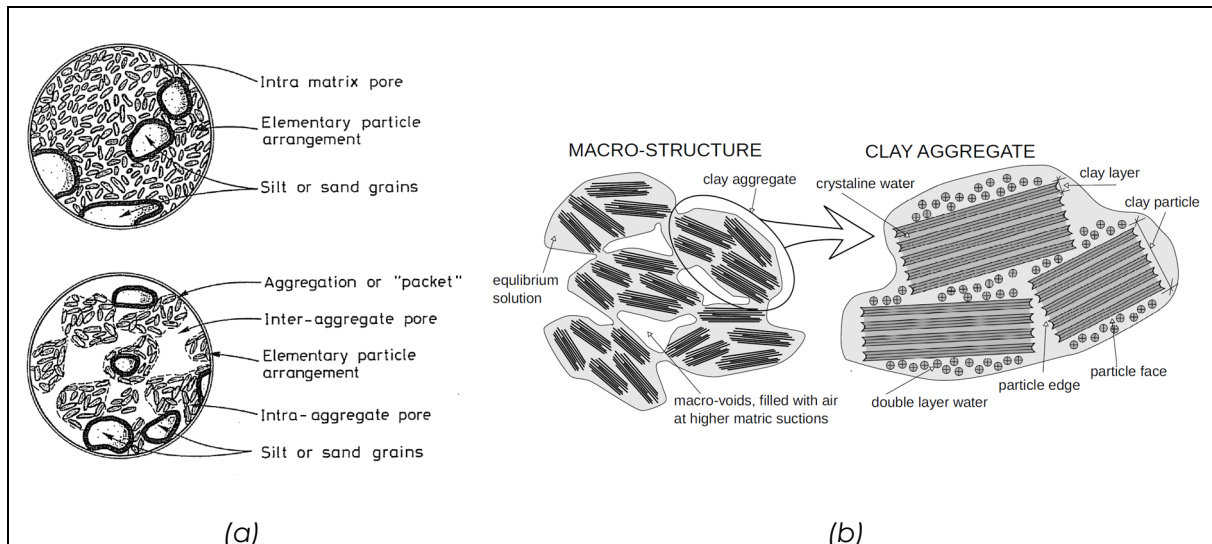


Figure 2-1. (a) Typical soil fabrics in active clays (Gens & Alonso, 1992); (b) Schematic representation of an aggregation of active clays (Mašin & Khalili, 2016).

Some of the main features assumptions of the double porosity model described here are listed below:

- The microstructure may be unsaturated.
- Negligible advective fluxes through micro-pores due to the very low mobility of water and gas in this structural domain.
- Hydraulic equilibrium between microstructure and macrostructure is not assumed. This local difference of the water potential in macro- and micro-pores controls the mass of water exchanged between both pore domains (hydraulic structural coupling).
- Micro-structural deformations are non-linear and fully reversible and purely volumetric.
- Micro-structural behaviour is not affected by the deformation state of macrostructure.
- Plastic macro-structural strains may arise from deformations of the microstructure (mechanical structural coupling).
- No generation of plastic thermal strains is considered at this stage. However, irreversible structural changes due to the thermo-hydromechanical (THM) coupling are possible.
- The theoretical approach based on the small-strain rate theory.

Some of those features and assumptions have been incorporated during the BEACON project.

The THM double porosity model used to carry out the numerical modelling in WP5 has been formulated in a fully coupled way and it has been implemented in the finite element code CODE_BRIGHT (Olivella et al., 1996). The resulting THM formulation requires a set of balance equations and constitutive laws for dealing with the THM coupled processes that take place in geotechnical porous media. This set of basic equations is written in terms of the primary variables (liquid and gas pressures, displacement, temperature, ...). When the constitutive equations are incorporated into the balance equations (Olivella et al., 1994), a system of partial differential equations is generated that must be solved numerically in a fully coupled way.

The mathematical formulation described herein is based on the general approach proposed by Olivella et al. (1994; 1996) and Olivella (1995), applied to both isothermal and non-isothermal problems in double structure unsaturated media. For a better understanding of the mathematical description of the governing equations, the notation used is detailed in Table 2-1.

Table 2-1. General variable notation for the mathematical description of the double porosity formulation

$(\dot{\blacksquare})$	Incremental (or rate) form of a generic variable.
$(\blacksquare)_{\alpha}, (\blacksquare)_{\beta}, (\blacksquare)_{\alpha\beta}$	Subscripts used to identify the structural level (" $\beta \equiv m$ " for microstructure; " $\beta \equiv M$ " for macrostructure) and/or phases (" $\alpha \equiv s$ " for solid; " $\alpha \equiv l$ " for liquid; " $\alpha \equiv g$ " for gas).
$(\blacksquare)^{\gamma}$	Superscript used to identify the species present in the porous medium (" $\gamma \equiv s$ " for solid grains (mineral); " $\gamma \equiv w$ " for water; " $\gamma \equiv a$ " for air).
$V_s; V_{\alpha\beta}; V$	Volume of the solid species/phase; volume of the α phase (liquid or gas) in the β -structural medium; total volume of the porous medium.
$V_p; V_{p,\beta}$	Total volume of pores in the soil; volume of pores in the β -structural medium.
$(\blacksquare)_{\beta}; (\overline{\blacksquare})_{\beta}$	Variable evaluated respect to the volume occupied by the β -structural level; variable evaluated respect to the total volume of the soil.
$\phi; \phi_{\beta}$	Total porosity; porosity of the β -structural medium respect to its actual volume.
$\bar{\phi}_{\beta}$	Pore volume fraction of the β -structural medium.
$\rho_s; \rho_{\alpha\beta}$	Local density of the solid; local density of the α phase in the β -structural medium.
$\omega_{\alpha\beta}^{\gamma}$	Mass fraction of the γ species (solid, water or gas), in the α phase, in the β -structural medium.
$\theta_{\alpha\beta}^{\gamma}$	Partial density of the γ species, in the α phase, in the β -structural medium.
$m_{\alpha\beta}; m_{\alpha\beta}^{\gamma}$	Mass of the α phase in the β -structural medium; mass of the γ species (solid, water or gas), in the α phase, in the β -structural medium.
$S_{\alpha}; S_{\alpha\beta}$	Degree of saturation of the α phase in the soil; degree of saturation of the α phase in the β -structural medium.
s_{β}	Suction at the β -structural level.
E_{α}	Specific internal energy of the α phase.
$\mathbf{j}^{\gamma}_{\alpha\beta}$	Flux of the γ species, in the α phase, in the β -structural medium respect to the solid skeleton.
$\mathbf{q}_{\alpha\beta}$	Advective flux of the α phase in the β -structural medium.
\mathbf{i}_c	Conductive heat flux.
$\boldsymbol{\sigma}, \boldsymbol{\sigma}_{\beta}; \sigma_t$	Effective stress tensor for the whole porous medium and for the β -structural medium; total stress tensor.

2.2 Phase diagrams and basic relationships

An unsaturated soil can be treated as a porous multi-phase medium composed by solid grains, water (as liquid water or vapour in the gas phase) and air (as dry air or dissolved in the liquid phase) (Olivella et al., 1996). In order to define some basic volume-mass relationships commonly used in geotechnical problems, it is useful to depict the phase diagram that shows all the phases – solid (s), liquid (l) and/or gas (g) – present in the porous medium. Three-phase diagrams representing a soil element as a double-porosity medium are shown in Figure 2-2. From the phase diagram, it can be easily noted that the volume of voids in the soil (V_p) is the sum of the volume occupied by macro-pores ($V_{p,M}$) and micro-pores ($V_{p,m}$). The volume of microstructure (V_m) includes the volume of the intra-aggregate pores (micro-pores) and the volume occupied by the solid phase (V_s). Variables defined with the sub-index " m " are related

to the micro-structural level (solid particles and micro-pores) while the sub-index “M” refers to variables defined for the macrostructure. Variables defined for the soil (the whole porous medium) are not labelled with any subscript.

Porosities (ϕ and ϕ_m) and void ratios (e and e_m) for the two porous media (the soil and the clay aggregate) are defined as:

$$\phi = \frac{V_p}{V} \quad (2-1)$$

$$\phi_m = \frac{V_{p,m}}{V_m} \quad (2-2)$$

$$e = \frac{V_p}{V_s} = \frac{V_p}{V - V_p} = \frac{\phi}{1 - \phi} \quad (2-3)$$

$$e_m = \frac{V_{p,m}}{V_s} = \frac{V_{p,m}}{V_m - V_{p,m}} = \frac{\phi_m}{1 - \phi_m} \quad (2-4)$$

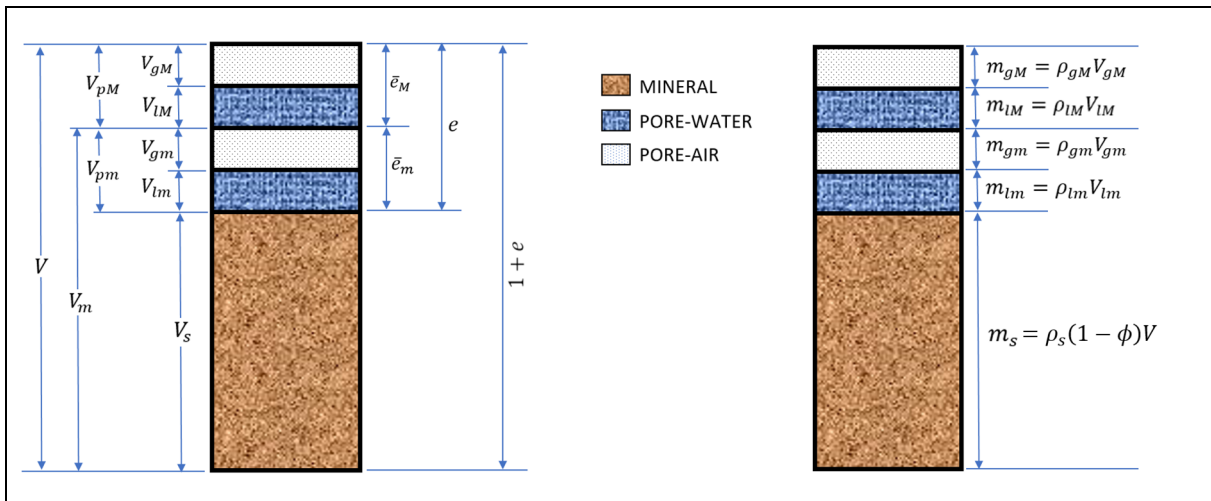


Figure 2-2. Phase diagrams relating volumes (left) and mass of species (right) in each structural level (Vasconcelos, 2021).

Two additional porosity variables need to be introduced in order to describe the “natural” additive decomposition of the total porosity (ϕ),

$$\phi = \frac{V_p}{V} = \frac{V_{p,m}}{V} + \frac{V_{p,M}}{V} = \bar{\phi}_m + \bar{\phi}_M \quad (2-5)$$

where $\bar{\phi}_m$ and $\bar{\phi}_M$ are the pore volume fractions associated with microstructure and macrostructure, respectively. These variables are helpful for establishing the mathematical development of the double porosity formulation. The “aggregate porosity” (ϕ_m), or simply the “micro porosity”, can be also evaluated in terms of the macro-pore ($\bar{\phi}_M$) and the micro-pore ($\bar{\phi}_m$) volume fractions according to the following relationship:

$$\phi_m = \frac{V_{p,m}}{V_m} = \frac{V_{p,m}}{V} \cdot \frac{V}{V_m} = \frac{V_{p,m}}{V} \cdot \left(\frac{V}{V - V_{p,M}} \right) = \bar{\phi}_m \left(\frac{1}{1 - \bar{\phi}_M} \right) \quad (2-6)$$

The relationship in Equation (2-5) combined with Equation (2-3) leads to the definition of a “micro” void ratio (\bar{e}_m) and a “macro” void ratio (\bar{e}_M), expressed as follows:

$$\bar{e}_m = \frac{\bar{\phi}_m}{1 - \phi} \quad (2-7)$$

$$\bar{e}_M = e - \bar{e}_m = \frac{\bar{\phi}_M}{1 - \phi} \quad (2-8)$$

It is important to mention that the substitution of Equation (2-6) into Equation (2-4) results in $e_m = \bar{e}_m$.

The saturation state in the porous medium “ β ” by the α phase, $S_{\alpha\beta}$, is defined as:

$$S_{\alpha\beta} = \frac{V_{\alpha\beta}}{V_{p,\beta}} \quad (2-9)$$

where $V_{\alpha\beta}$ denotes the fraction of the volume of voids in the β -structural medium ($V_{p,\beta}$) filled with the α phase. The compositional approach used in CODE_BRIGHT to describe the unsaturated porous medium (Olivella et al., 1996) requires the definition of the mass fraction (ω) and the partial density (θ) for each fluid species in the soil in order to also account for the dissolved air in the liquid phase and the water vapour in the gas phase. In the context of double porosity media, the mass fraction of the γ species (“ w ” for water and “ a ” for air) in the α phase, in the β -structural medium is given by:

$$\omega_{\alpha\beta}^{\gamma} = \frac{m_{\alpha\beta}^{\gamma}}{m_{\alpha\beta}} \quad (2-10)$$

while the partial density of each fluid species, in each fluid phase and for each structural level is expressed as:

$$\theta_{\alpha\beta}^{\gamma} = \frac{m_{\alpha\beta}^{\gamma}}{V_{\alpha\beta}} = \omega_{\alpha\beta}^{\gamma} \cdot \rho_{\alpha\beta} \quad (2-11)$$

where $m_{\alpha\beta}^{\gamma}$ and $m_{\alpha\beta}$ are the mass of the γ species in the α phase and the total mass of the α phase in the β -structural medium, respectively; $\rho_{\alpha\beta} = \frac{m_{\alpha\beta}}{V_{\alpha\beta}}$ is the local density for the fluid phases in each pore-structural level.

2.3 Additive decomposition of the strain tensor

The explicit consideration of two structural levels in the double structure approach and the definition of the micro- and macro-pore volume fractions in Equation (2-5) lead to the assumption of an additive decomposition of the strain rate tensor ($\dot{\boldsymbol{\epsilon}}$) into a micro- and a macro-strain component according to:

$$\dot{\boldsymbol{\epsilon}} = \dot{\boldsymbol{\epsilon}}_m + \dot{\boldsymbol{\epsilon}}_M \quad (2-12)$$

In terms of volumetric components, such a relationship is given by:

$$\dot{\epsilon}^v = \dot{\epsilon}_m^v + \dot{\epsilon}_M^v \quad (2-13)$$

where the volumetric strain rate ($\dot{\epsilon}^v$) and its micro ($\dot{\epsilon}_m^v$) and macro ($\dot{\epsilon}_M^v$) components are defined as:

$$\dot{\epsilon}^v = \frac{\dot{V}}{V} = \frac{\dot{V}_s + \dot{V}_p}{V} = \frac{\dot{V}_s + \dot{V}_{p,m}}{V} + \frac{\dot{V}_{p,M}}{V} \quad (2-14)$$

$$\dot{\epsilon}_m^v = \frac{\dot{V}_s + \dot{V}_{p,m}}{V} \quad (2-15)$$

$$\dot{\epsilon}_M^v = \frac{\dot{V}_{p,M}}{V} \quad (2-16)$$

It is important to emphasize the distinction between the “micro” component of the volumetric strains, shown in Equation (2-15), which is defined in terms of the total volume of the porous medium (V) and the actual volumetric deformation of the clay aggregate ($\dot{\epsilon}_m^v$), which is related to the volume occupied by the microstructure (V_m). However, these two micro-structural deformations are related by the following expression:

$$\dot{\epsilon}_m^v = \frac{\dot{V}_m}{V_m} = \frac{\dot{V}_s + \dot{V}_{p,m}}{V_m} = \frac{V}{V_m} \cdot \frac{\dot{V}_s + \dot{V}_{p,m}}{V} = \frac{V}{V_m} \cdot \dot{\epsilon}_m^v = \frac{1+e}{1+e_m} \cdot \dot{\epsilon}_m^v \quad (2-17)$$

where the phase diagram relating volumes in Figure 2-2 has been used to establish the relationship in Equation (2-17).

In the elastoplastic framework, it is useful to split the strain rate tensor into its elastic ($\dot{\epsilon}^e$) and plastic ($\dot{\epsilon}^p$) strain components. In the context of a double porosity formulation, it is reasonable to assume that micro-structural strains are purely volumetric and fully reversible (Sánchez et al., 2005) although non-linear. Consequently, the elastic portion of the deformation in active clays can be given by its micro ($\dot{\epsilon}_m^e$) and macro ($\dot{\epsilon}_M^e$) strain components, while the plastic component of strains only takes into account the structural changes occurring at the macro-structural domain ($\dot{\epsilon}_M^p$). Thus, Equation (2-12) can also be expressed, in terms of elastic and plastic strain components, as follows:

$$\dot{\epsilon} = \dot{\epsilon}^e + \dot{\epsilon}^p = (\dot{\epsilon}_m^e + \dot{\epsilon}_M^e) + \dot{\epsilon}_M^p \quad (2-18)$$

2.4 The local mass transfer mechanism

Hydraulic equilibrium between the two structural levels is not assumed, which leads to a local exchange of mass of water and air between micro- and macro-pores. It is assumed that the pore-water transferred between microstructure and macrostructure (Γ^w) is proportional to the difference in micro (s_m) and macro (s_M) suctions (or potentials), that is,

$$\Gamma^w = \gamma^w (s_m - s_M) \quad (2-19)$$

where suction in the β -structural medium, s_β , is defined as:

$$s_\beta = \max(P_{g\beta} - P_{l\beta}, 0) \quad (2-20)$$

where $P_{g\beta}$ and $P_{l\beta}$ are the gas and liquid pressures, respectively, in each pore domain. The leakage parameter, γ^w , is related to geometric characteristics of the porous media (Sánchez, 2004). If the gas mobility between the two continua is considered high enough to assume the

equilibrium between the gas pressures in both porous media, the water mass transfer given by Equation (2-19) is only driven by the difference between the liquid pressures (suctions) in each structural level.

2.5 Balance equations

The compositional approach used in CODE_BRIGHT implies that the mass balance equations are solved for the species (mineral, water and air) rather than the phases (solid, liquid and gas) while the equation for the balance of internal energy is solved for the porous medium as a whole. These equations, together with the constitutive laws, lead to the set of governing equations that describe the THM response of a wide range of geotechnical materials and boundary conditions commonly found in practical engineering problems.

The general expressions for the mass balance of each species in each structural level, the balance of internal energy and the momentum balance for the porous medium are shown in the following sections. In such equations, $\frac{D_s(\blacksquare)}{Dt}$ represents the material derivative with respect to the solid phase. The main state variables (unknowns) adopted in the statement of these balance equations are shown in Table 2-1. A detailed mathematical description of the general balance equations for deformable porous media can be found in Olivella (1995). For further information on the mathematical development of such equations in the context of a double structure formulation, see Vasconcelos (2021).

Table 2-1. Balance equations for a double porosity approach (in CODE_BRIGHT) and their unknowns.

Balance equations	Unknowns
Solid mass balance (Section 2.5.1)	$\bar{\phi}_\beta$ - Pore-volume fractions
Water mass balance for macrostructure (Section 2.5.2)	P_{lM} - Liquid pressure at macro-structural level
Water mass balance for microstructure (Section 2.5.2)	P_{lm} - Liquid pressure at micro-structural level
Air mass balance for macrostructure (Section 2.5.3)	P_{gM} - Gas pressure at macro-structural level
Air mass balance for microstructure (Section 2.5.3)	P_{gm} - Gas pressure at micro-structural level
Balance of internal energy (Section 2.5.4)	T - Temperature
Momentum balance (Section 2.5.5)	\mathbf{u} - Solid velocity

2.5.1 The mass balance of solid

The mass balance of solid in porous media characterized by the existence of two distinct pore domains is expressed as:

$$\frac{D_s \phi}{Dt} = \frac{D_s \bar{\phi}_m}{Dt} + \frac{D_s \bar{\phi}_M}{Dt} = \frac{(1 - \bar{\phi}_m - \bar{\phi}_M) D_s \rho_s}{\rho_s} + (1 - \bar{\phi}_m - \bar{\phi}_M)(\dot{\epsilon}_m^v + \dot{\epsilon}_M^v) \quad (2-21)$$

which relates the variation of porosity to the changes in solid density (ρ_s) and to the volumetric deformation at each structural level.

2.5.2 The mass balance of water

Water is present in soils in liquid phase and/or evaporated in the gas phase (as water vapour). In double structure porous media, water is found both in macro- and micro-pores. Consequently, it is necessary to write a balance equation to account for the mass of macro-structural water, expressed as:

$$\frac{D_s(\theta_{lM}^w S_{lM} + \theta_{gM}^w S_{gM})}{Dt} \bar{\phi}_M + (\theta_{lM}^w S_{lM} + \theta_{gM}^w S_{gM}) \dot{\bar{\epsilon}}_M^v + \nabla \cdot (\mathbf{j}'_{lM} + \mathbf{j}'_{gM}) = -\Gamma^w \quad (2-22)$$

and another to compute the mass of water in micro-pores, whose simplified form is given as follows:

$$\begin{aligned} \frac{D_s(\theta_{lm}^w S_{lm} + \theta_{gm}^w S_{gm})}{Dt} \bar{\phi}_m + (\theta_{lm}^w S_{lm} + \theta_{gm}^w S_{gm}) \dot{\bar{\epsilon}}_m^v \\ = \Gamma^w - (\theta_{lm}^w S_{lm} + \theta_{gm}^w S_{gm})(1 - \phi) \frac{\dot{\rho}_s}{\rho_s} \end{aligned} \quad (2-23)$$

where \mathbf{j}'_{lM} and \mathbf{j}'_{gM} are the macro-structural fluxes of water in liquid and gas phases, respectively, respect to the solid skeleton. Γ^w is the local water exchange term that represents the hydraulic coupling between the two pore domains (see Section 2.4). In the current double structure formulation, a positive value of this term implies that differences in the local water potential lead to a water mass transfer from macro- to micro-pores, while a negative value means that the water exchange occurs in the opposite direction.

It is important to highlight that Equation (2-23) assumes that the water mobility through micro-pores is very low and, consequently, the micro-structural water does not participate to the Darcien advective flux (Romero, 1999). Therefore, the divergence term of the advective flux in the mass balance of micro-structural water can be neglected, that is, $\nabla \cdot (\mathbf{j}'_{lm} + \mathbf{j}'_{gm}) \approx 0$. This assumption allows the treatment of the liquid pressure at micro-structural level (P_{lm}) as a history variable to be updated during the constitutive integration of stresses.

2.5.3 The mass balance of air

The mass balance of air present in macro-pores, as gas or dissolved in the liquid phase, is given by the following expression:

$$\frac{D_s(\theta_{lM}^a S_{lM} + \theta_{gM}^a S_{gM})}{Dt} \bar{\phi}_M + (\theta_{lM}^a S_{lM} + \theta_{gM}^a S_{gM}) \dot{\bar{\epsilon}}_M^v + \nabla \cdot (\mathbf{j}'_{lM} + \mathbf{j}'_{gM}) = -\Gamma^a \quad (2-24)$$

while the mass balance of air present in the micro-structural domain, under the assumption of negligible gas mobility through micro-pores, can be written as:

$$\begin{aligned} \frac{D_s(\theta_{lm}^a S_{lm} + \theta_{gm}^a S_{gm})}{Dt} \bar{\phi}_m + (\theta_{lm}^a S_{lm} + \theta_{gm}^a S_{gm}) \dot{\bar{\epsilon}}_m^v \\ = \Gamma^a - (\theta_{lm}^a S_{lm} + \theta_{gm}^a S_{gm})(1 - \phi) \frac{\dot{\rho}_s}{\rho_s} \end{aligned} \quad (2-25)$$

If it is also assumed the local equilibrium between the pore-air pressures, the air mass transfer between micro- and macro-pores (Γ^a) can be neglected, that is, $\Gamma^a \approx 0$.

2.5.4 The balance of internal energy

The assumption of local thermal equilibrium among the phases implies that the equation for the internal energy balance is established for the porous medium as a whole by accounting for the energy stored in each phase. In the context of a double porosity approach, the energy balance equation is given by:

$$\begin{aligned}
 & \frac{D_s(E_s\rho_s)}{Dt}(1-\phi) + \frac{D_s(E_l\rho_{lm}S_{lm} + E_g\rho_{gm}S_{gm})}{Dt}\bar{\phi}_m + \frac{D_s(E_l\rho_{lM}S_{lM} + E_g\rho_{gM}S_{gM})}{Dt}\bar{\phi}_M \\
 & + (E_l\rho_{lm}S_{lm} + E_g\rho_{gm}S_{gm})\dot{\bar{\epsilon}}_m^v + (E_l\rho_{lM}S_{lM} + E_g\rho_{gM}S_{gM})\dot{\bar{\epsilon}}_M^v \\
 & + \nabla \cdot (\mathbf{i}_c + E_l\rho_{lM}\mathbf{q}_{lM} + E_g\rho_{gM}\mathbf{q}_{gM}) \\
 & = f^Q - (E_l\rho_{lm}S_{lm} + E_g\rho_{gm}S_{gm} - E_s\rho_s)(1-\phi)\frac{\dot{\rho}_s}{\rho_s}
 \end{aligned} \tag{2-26}$$

where E_α is the specific internal energy of the α phase; f^Q is an internal/external energy supply per unit volume of soil; \mathbf{i}_c represents the heat flux by conduction through the porous medium and \mathbf{q}_{lM} , \mathbf{q}_{gM} are the macro-structural advective fluxes of the liquid and gas phases with respect to the solid phase, respectively. The energy transport by the fluid motion through the micro-pores has been neglected in the formulation of the energy balance expressed in Equation (2-26).

2.5.5 The balance of momentum

The balance of momentum reduces to the equilibrium of stresses in the porous medium. In the context of a double porosity formulation, the momentum equilibrium equation is expressed as follows:

$$\nabla \cdot \boldsymbol{\sigma}_t + (\rho_s(1-\phi) + (\rho_{lm}S_{lm} + \rho_{gm}S_{gm})\bar{\phi}_m + (\rho_{lM}S_{lM} + \rho_{gM}S_{gM})\bar{\phi}_M)\mathbf{g} = \mathbf{0} \tag{2-27}$$

where $\boldsymbol{\sigma}_t$ is the total stress tensor and \mathbf{g} is the gravity vector. The vector of body forces, represented by the second term on the left-hand side of Equation (2-27), takes into account the weight of the liquid and gas phases in both structural media.

2.6 Constitutive equations

The mathematical formulation for solving THM problems also requires a set of constitutive equations that provides the coupling among the main thermal, hydraulic and mechanical phenomena that take place in geotechnical porous media. The THM constitutive equations relate the independent variables (the unknowns of the coupled THM problems) with the dependent ones (fluxes of liquid and gas phases, heat fluxes, degree of saturation, liquid and gas densities, stress tensor, etc.).

In the following sections, a brief description of the general expressions of the THM constitutive laws used in the current double porosity model is presented. A detailed explanation of such equations can be found in Olivella (1995) (for single-porosity media) and in Sánchez (2004), and Vasconcelos (2021), among others.

2.6.1 Thermal constitutive equations

Heat conduction through the soil (\mathbf{i}_c) is driven by temperature gradients (∇T) and described by Fourier's law according to:

$$\mathbf{i}_c = -\lambda \cdot \nabla T \quad (2-28)$$

where the global thermal conductivity of the porous medium (λ) is usually expressed as a function of the thermal conductivity of each phase in the soil (λ_α), porosity (ϕ) and degree of saturation (S_l), that is,

$$\lambda = f(\lambda_\alpha, \phi, S_l) \quad (2-29)$$

In double porosity media, the thermal conductivity becomes dependent not only on the water content in the two pore-structure domains but also on the pore volume fraction in each structural medium. Thus, the global thermal conductivity is evaluated in terms of an “average” degree of saturation (S_l), which is defined as:

$$S_l = \frac{\bar{\phi}_m}{\phi} S_{lm} + \frac{\bar{\phi}_M}{\phi} S_{lM} \quad (2-30)$$

2.6.2 Hydraulic constitutive equations

In the current double porosity approach, the volumetric advective fluxes are only formulated for the macro-structural domain, since the liquid and gas advective fluxes through micro-pores have been neglected. Therefore, the generalized Darcy's law ($\mathbf{q}_{\alpha M}$) for the α phase (liquid, l ; gas, g) in active clays can be expressed as:

$$\mathbf{q}_{\alpha M} = -\mathbf{k}_M \frac{k_{r\alpha M}}{\mu_{\alpha M}} (\nabla P_{\alpha M} - \rho_{\alpha M} \mathbf{g}) \quad (2-31)$$

The intrinsic permeability tensor for the macrostructure, \mathbf{k}_M , only depends on its pore structure, according to the modified Kozeny-Carman equation:

$$\mathbf{k}_M = \mathbf{k}_{0,M} \frac{\bar{\phi}_M^3}{(1 - \bar{\phi}_M)^2} \frac{(1 - \bar{\phi}_0)^2}{\bar{\phi}_0^3} \quad (2-32)$$

or by means of an empirical exponential expression:

$$\mathbf{k}_M = \mathbf{k}_{0,M} \exp\left(b(\bar{\phi}_M - \bar{\phi}_0)\right) \quad (2-33)$$

In those relationships, $\bar{\phi}_0$ is the pore fraction for which the reference intrinsic permeability tensor $\mathbf{k}_{0,M}$ is estimated and b is a fitting parameter of the model.

The phase relative permeability, $k_{r\alpha M}$, expresses the hydraulic permeability on the degree of saturation of the macrostructure. The decrease in the water permeability with the reduction of the liquid saturation in macro-pores is defined through the following exponential function:

$$k_{r_{lM}} = A_{rl} (S_{el,M})^{\lambda_r} \quad (2-34)$$

where the effective degree of saturation of macrostructure, $S_{el,M}$, is defined by:

$$S_{el,M} = \frac{S_{lM} - S_{lr,M}}{S_{ls,M} - S_{lr,M}} \quad (2-35)$$

in which S_{IM} , $S_{lr,M}$, $S_{ls,M}$ are the current, the residual and the maximum degree of saturation of the macrostructure, respectively; A_{rl} , λ_r are model parameters.

The dependence of the dynamic viscosities of fluid species in macro-pores ($\mu_{\alpha M}$) on temperature is also considered in the current THM formulation – see Vasconcelos (2021).

The water retention curve (WRC) of a porous medium relates its water content (or degree of saturation) to the pore-water potential (suction). Due to the assumption that micro-pores may be unsaturated, it is also necessary to define hydraulic constitutive laws for the microstructure by the definition of a WRC for this pore domain as well. In CODE_BRIGHT the water retention capacity of a porous medium is described by a modified van Genuchten law. In the current double structure formulation, such empirical relationship is defined for the β -structural medium as follows:

$$S_{el,\beta} = \left(1 + \left(\frac{P_{g\beta} - P_{l\beta}}{P} \right)^{\frac{1}{1-\lambda_{rc}}} \right)^{-\lambda_{rc}} \cdot \left(1 - \frac{P_{g\beta} - P_{l\beta}}{P_{d,\beta}} \right)^{\lambda_d} \quad (2-36)$$

in which the thermal effect on the WRC can be taken into account by means of the following relationship proposed in Olivella & Gens (2000):

$$P = P_0 \cdot \frac{\sigma(T)}{\sigma_0(T_0)} \quad (2-37)$$

where P and P_0 are model parameters related to the pore-air entry value at the current temperature (T) and at a reference temperature (T_0), respectively. Surface tension, σ (in N/m) is a function of temperature and σ_0 is its value at the same temperature at which P_0 is measured. λ_{rc} and λ_d are model parameters and $P_{d,\beta}$ is the suction value at fully dry conditions. The main differences between the retention curves at each structural domain, that is, the distinct pore-air entry pressures and desaturation rates, can be clearly noted in Figure 2-3. The water storage capacity of the whole porous medium (the average WRC in Figure 2-3) can be determined by taking into account the water potential and the pore volume fractions in each structural domain.

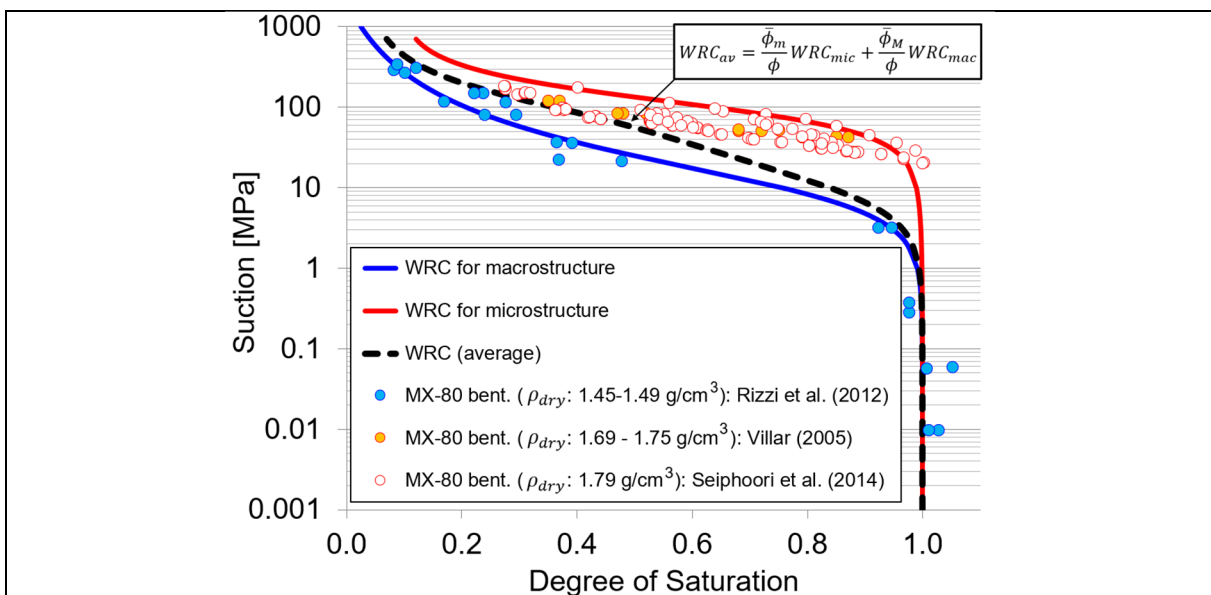


Figure 2-3. Water retention curves (WRC) for the macro- and micro-structural domains of compacted samples of MX-80 bentonite

2.6.3 Mechanical constitutive equations

A direct consequence of assuming the expansive clay as two distinct but interacting continuum media is the possibility of establishing different stress-strain constitutive relationships for each structural level. The coupling between these two porous media is accomplished through mass transfer processes and strain coupling mechanisms that account for the portion of macro-structural strains arising from the deformations that occur at particle level (microstructure). The description of the mechanical model below also includes the incorporation of thermal effects.

The generalized stress-strain relationship for the β -structural domain can be expressed by:

$$\dot{\boldsymbol{\sigma}}_{\beta} = [\mathbf{D}_{\beta}] \dot{\boldsymbol{\epsilon}}_{\beta} + \mathbf{h}_{l\beta} \dot{P}_{l\beta} + \mathbf{h}_{g\beta} \dot{P}_{g\beta} + \mathbf{h}_{T\beta} \dot{T} \quad (2-38)$$

where $\dot{\boldsymbol{\sigma}}_{\beta}$ is the constitutive stress rate vector, $\dot{\boldsymbol{\epsilon}}_{\beta}$ is the strain rate vector, $[\mathbf{D}_{\beta}]$ is the constitutive stiffness matrix, $\mathbf{h}_{l\beta}$, $\mathbf{h}_{g\beta}$ are the generic constitutive vectors relating changes in liquid and gas pressures, respectively, to stress increments and $\mathbf{h}_{T\beta}$ is a constitutive vector relating stress to temperature changes.

As mentioned before, it is assumed that the macro-pore structure can be affected by the micro-structural deformations (Gens & Alonso, 1992; Alonso et al., 1999; Sánchez et al., 2005). Consequently, it is reasonable to define a macro-structural strain component that expresses such a mechanical coupling ($\dot{\boldsymbol{\epsilon}}_{m \rightarrow M}$). In contrast, it is assumed that the micro-structural behaviour is not affected by the deformations of the macrostructure. Therefore, the plastic changes in the soil fabric are attributed to the loading-collapse mechanism (LC mechanism) and to the micro-macro structural coupling mechanism (beta mechanism). The more relevant features of the elastic and the plastic behaviour described by the current double porosity model are briefly presented in the following sections. Further and detailed information on the mechanical constitutive behaviour of double structure media can be found in Vasconcelos (2021).

Elastic behaviour

Taking into account the strain decomposition given in Equation (2-18), the elastic behaviour of the expansive soil is completely described by its micro-structural and macro-structural strain components. In the context of THM analyses, the elastic strain component associated with the microstructure, $\dot{\boldsymbol{\epsilon}}_m^e$, can be split into a hydro-mechanical component, $(\dot{\boldsymbol{\epsilon}}_m^e)_{\Delta\sigma, \Delta P_{\alpha}}$, and a thermal component, $(\dot{\boldsymbol{\epsilon}}_m^e)_{\Delta T}$, as follows:

$$\dot{\boldsymbol{\epsilon}}_m^e = (\dot{\boldsymbol{\epsilon}}_m^e)_{\Delta\sigma, \Delta P_{\alpha}} + (\dot{\boldsymbol{\epsilon}}_m^e)_{\Delta T} \quad (2-39)$$

where

$$(\dot{\boldsymbol{\epsilon}}_m^e)_{\Delta\sigma, \Delta P_{\alpha}} = [\bar{\mathbf{D}}_m^e]^{-1} \dot{\boldsymbol{\sigma}}_m = [\bar{\mathbf{D}}_m^e]^{-1} \dot{\boldsymbol{\sigma}} + \frac{1}{3\bar{K}_m} \cdot \mathcal{H}(S_{lm}, P_{lm}, P_{gm}, T) \mathbf{m} \quad (2-40)$$

$$(\dot{\boldsymbol{\epsilon}}_m^e)_{\Delta T} = \frac{1 + e_m}{1 + e} \cdot (\dot{\boldsymbol{\epsilon}}_m^e)_{\Delta T} \quad (2-41)$$

In such expressions, $[\bar{\mathbf{D}}_m^e]$ and $\dot{\boldsymbol{\sigma}}_m$ are the elastic constitutive stiffness matrix and the generalized Bishop effective stress vector for the microstructure; \bar{K}_m is the volumetric elastic modulus of the micro-structural medium; $\dot{\boldsymbol{\sigma}}$ is the net effective stress vector (for the soil); \mathcal{H} represents a non-linear function of temperature, the saturation and the fluid pressures in micro-pores; and $\mathbf{m} = [1 \ 1 \ 1 \ 0 \ 0 \ 0]^t$ is an auxiliary vector. Equation (2-17) has been recalled in order to

establish the relationship between the thermal component of the micro-structural strain, $(\dot{\boldsymbol{\epsilon}}_m^e)_{\Delta T}$, and the elastic thermal expansion of each clay particle/aggregate (actual microstructure), $(\dot{\boldsymbol{\epsilon}}_m^e)_{\Delta T}$, as given in Equation (2-41).

The elastic deformations of the solid skeleton (macrostructure), $\dot{\boldsymbol{\epsilon}}_M^e$, can be also described by means of a hydro-mechanical component, $(\dot{\boldsymbol{\epsilon}}_M^e)_{\Delta\sigma, \Delta P_\alpha}$, and a thermal strain component, $(\dot{\boldsymbol{\epsilon}}_M^e)_{\Delta T}$:

$$\dot{\boldsymbol{\epsilon}}_M^e = (\dot{\boldsymbol{\epsilon}}_M^e)_{\Delta\sigma, \Delta P_\alpha} + (\dot{\boldsymbol{\epsilon}}_M^e)_{\Delta T} \quad (2-42)$$

with

$$(\dot{\boldsymbol{\epsilon}}_M^e)_{\Delta\sigma, \Delta P_\alpha} = [\bar{\mathbf{D}}_M^e]^{-1} \dot{\boldsymbol{\sigma}} + \frac{1}{3\bar{K}_s} \dot{s}_M \mathbf{m} + (\dot{\boldsymbol{\epsilon}}_{m \rightarrow M}^e)_{\Delta\sigma, \Delta s_M} \quad (2-43)$$

$$(\dot{\boldsymbol{\epsilon}}_M^e)_{\Delta T} = (\dot{\boldsymbol{\epsilon}}_{m \rightarrow M}^e)_{\Delta T} = \dot{\boldsymbol{\epsilon}}_{\Delta T}^e - (\dot{\boldsymbol{\epsilon}}_m^e)_{\Delta T} \quad (2-44)$$

where $[\bar{\mathbf{D}}_M^e]$ is the elastic constitutive matrix for the macrostructure; \bar{K}_s is the volumetric elastic modulus related to changes in the macro-structural suction, \dot{s}_M ; $\dot{\boldsymbol{\epsilon}}_{\Delta T}^e$ is the elastic thermal expansion of the soil (as a whole), defined as:

$$\dot{\boldsymbol{\epsilon}}_{\Delta T}^e = \frac{1}{3K_T} \dot{T} \mathbf{m} \quad (2-45)$$

where K_T is the thermal bulk modulus of the porous medium. The assumption of fully reversible thermal strains in the mathematical formulation of the current double porosity model implies that the porous skeleton must undergo the same thermal expansion as that experienced by the solid particles (clay particle/aggregate) when temperature changes (Khalili et al., 2010). In other words, $\dot{\boldsymbol{\epsilon}}_{\Delta T}^e = (\dot{\boldsymbol{\epsilon}}_m^e)_{\Delta T}$. Consequently, the macro-structural component of the elastic thermal strains in Equation (2-44) can be given by:

$$(\dot{\boldsymbol{\epsilon}}_M^e)_{\Delta T} = \bar{\phi}_M \dot{\boldsymbol{\epsilon}}_{\Delta T}^e = \frac{\bar{\phi}_M}{3K_T} \dot{T} \mathbf{m} \quad (2-46)$$

The elastic bulk moduli, \bar{K}_M , \bar{K}_s and K_T , are defined by the following expressions:

$$\bar{K}_M = \frac{(1 + e_M)p}{\bar{\kappa}_M} \quad (2-47)$$

$$\bar{K}_s = \frac{(1 + e_M)(s_M + p_{atm})}{\bar{\kappa}_s} \quad (2-48)$$

$$K_T = \frac{1}{\alpha_0 + 2\alpha_2 \Delta T} \quad (2-49)$$

where p is the net mean effective stress, p_{atm} is the atmospheric pressure and $\bar{\kappa}_M$, $\bar{\kappa}_s$, α_0 and α_2 are model parameters. It is important to remark that the "macro" void ratio parameter in such expressions (e_M) is not equal to the macro void ratio defined in Equation (2-8). In Equations (2-47) and (2-48), e_M is estimated without taking into account the fraction of pores within the clay particles/aggregates, that is,

$$e_M = \frac{\bar{\phi}_M}{1 - \bar{\phi}_M} \quad (2-50)$$

The assumption of no fabric changes in the elastic range entails a geometrical restriction that links the elastic moduli of the microstructure (\bar{K}_m) and of the macrostructure (\bar{K}_M). Consequently, this coupling between the elastic parameters leads to the following relationships:

$$K = K_m = \left(\frac{1 + e}{1 + e_m} \right) \bar{K}_m \quad (2-51)$$

$$K = \bar{\phi}_M \bar{K}_M \quad (2-52)$$

$$\bar{K}_m = \left(\frac{e - e_m}{1 + e_m} \right) \bar{K}_M \quad (2-53)$$

where K and K_m are the bulk moduli of the expansive soil and the individual clay particle/aggregate, respectively.

Plastic Loading-Collapse (LC) mechanism

The plastic loading-collapse (LC) mechanism of the double porosity formulation is fully defined by the same set of equations and parameters that describe the single-porosity, thermo-elastoplastic Barcelona Basic Model (BBM). A complete description of the evolution of the yield surface in the stress space and its dependence on the stress state, history variables and (macro) suction can be found in Alonso et al. (1999), Sánchez (2004) and Vasconcelos (2021). Only the main mathematical ingredients characterizing this plastic mechanism are given below.

The yield surface for a general state, expressed in terms of the stress invariants (p, J, θ), is expressed by:

$$F_{LC} = 3J^2 - \left(\frac{g_F(\theta, \alpha_F)}{g_F\left(-\frac{\pi}{6}, \alpha_F\right)} \right)^2 \cdot M_F^2 \cdot (p + p_s) \cdot (p_0 - p) = 0 \quad (2-54)$$

where M_F is the slope of the critical state line, g_F is a function of Lode's angle (θ), α_F is a model parameter and p_s expresses the dependence of the shear strength on macro suction and temperature (Gens, 1995), according to:

$$p_s = p_{s0} + k_s \cdot s_M \cdot \exp(-\rho_T \cdot \Delta T) \quad (2-55)$$

where p_{s0} is the tensile strength in saturated conditions; k_s and ρ_T are model parameters that computes the dependence of p_s on the macro suction and temperature, respectively. The apparent non-saturated pre-consolidation pressure (p_0), that defines the locus of activation of irreversible deformations due to loading increments or macro-structural collapse, is given by:

$$p_0 = p_c \cdot \left(\frac{p_{0,T}^*}{p_c} \right)^{\frac{\lambda_{(0)} - \bar{\kappa}_M}{\lambda_{(sM)} - \bar{\kappa}_M}} \quad (2-56)$$

where:

$$p_{0,T}^* = p_0^* + 2(\alpha_1 \cdot \Delta T + \alpha_3 \cdot \Delta T \cdot |\Delta T|) \quad (2-57)$$

$$\lambda_{(s_M)} = \lambda_{(0)} \cdot [r + (1 + r) \cdot \exp(-\beta \cdot s_M)] \quad (2-58)$$

where $\lambda_{(0)}$ and $\lambda_{(s_M)}$ is the macro-structural compressibility at saturated conditions and for a given macro suction, s_M , respectively; p_0^* is the pre-consolidation pressure at saturation and p_c is a reference pressure. α_1 and α_3 are model parameters that control the size of the BBM surface for a temperature increment (ΔT); r and β are model parameters that expresses the dependence of the size and evolution of the LC curve on the macro suction. A three dimensional representation of the BBM yield surface is given in Figure 2-4.

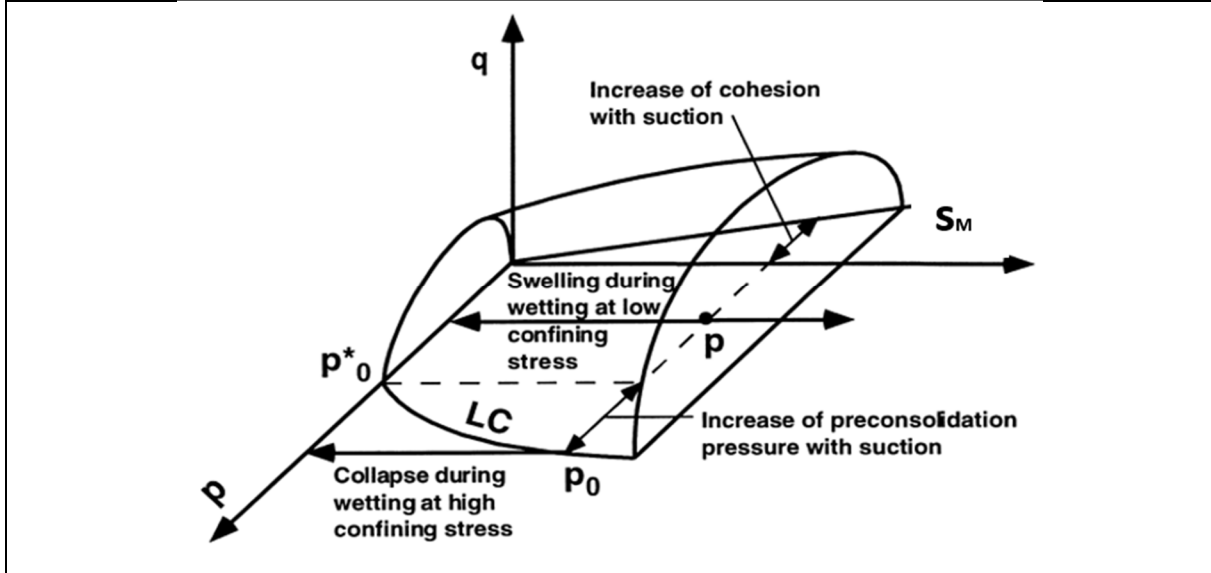


Figure 2-4. Three-dimensional representation of the BBM yield surface (modified from Alonso et al., 1999)

The generation of macro-structural plastic deformations when the LC mechanism is activated is governed by the plastic flow rule, which is given by the following expression:

$$\dot{\epsilon}_{M,LC}^p = \dot{\lambda}_{LC} \frac{\partial G_{LC}}{\partial \sigma} \quad (2-59)$$

where the magnitude of the plastic deformation rate is determined by the scalar plastic multiplier, $\dot{\lambda}_{LC}$. The plastic potential function of the LC mechanism, G_{LC} , is expressed as:

$$G_{LC} = 3 \cdot \alpha_{LC} \cdot J^2 - \left(\frac{g_F(\theta, \alpha_F)}{g_F\left(-\frac{\pi}{6}, \alpha_F\right)} \right)^2 \cdot M_F^2 \cdot (p + p_s) \cdot (p_0 - p) = 0 \quad (2-60)$$

in which α_{LC} is the non-associativity parameter.

Plastic Beta (β) mechanism

Although it has been assumed that micro-structural behaviour is not affected by the macro-structural state, the volumetric deformations of microstructure may induce plastic strains at the macro-structural level (Gens & Alonso, 1992). The magnitude of these macro-structural deformations ($\dot{\epsilon}_{M,\beta}^p$) is taken as proportional to the micro-structural elastic strains (Gens & Alonso, 1992; Alonso et al., 1999; Sánchez et al., 2005):

$$\dot{\epsilon}_{M,\beta}^p = f_\beta \cdot \dot{\epsilon}_m^e \quad (2-61)$$

where f_β represents a pair of micro-macro coupling functions that distinguishes between the stress paths characterized by a **micro-structural contraction** (MC paths) and those paths in which a **micro-structural swelling** (MS paths) occurs. The following general expression has been used in the current double porosity approach:

$$f_\beta = \begin{cases} f_{MC}^{(1)} + (f_{MC}^{(0)} - f_{MC}^{(1)}) \cdot (1 - \mu_\beta)^{n_{MC}} & \text{if } \dot{p}_m > 0 \\ f_{MS}^{(1)} + (f_{MS}^{(0)} - f_{MS}^{(1)}) \cdot (1 - \mu_\beta)^{n_{MS}} & \text{if } \dot{p}_m < 0 \end{cases} \quad (2-62)$$

where μ_β is a parameter that accounts for the degree of compactness of the macrostructure and \dot{p}_m is the rate of the mean effective stress at the micro-structural domain. $f_{MC}^{(0)}$, $f_{MC}^{(1)}$, n_{MC} and $f_{MS}^{(0)}$, $f_{MS}^{(1)}$, n_{MS} are model parameters that define the structural coupling function in MC paths and MS paths, respectively. A general representation of the micro-macro coupling functions, including the main behaviour features expected during wetting and drying paths are shown in Figure 2-5.

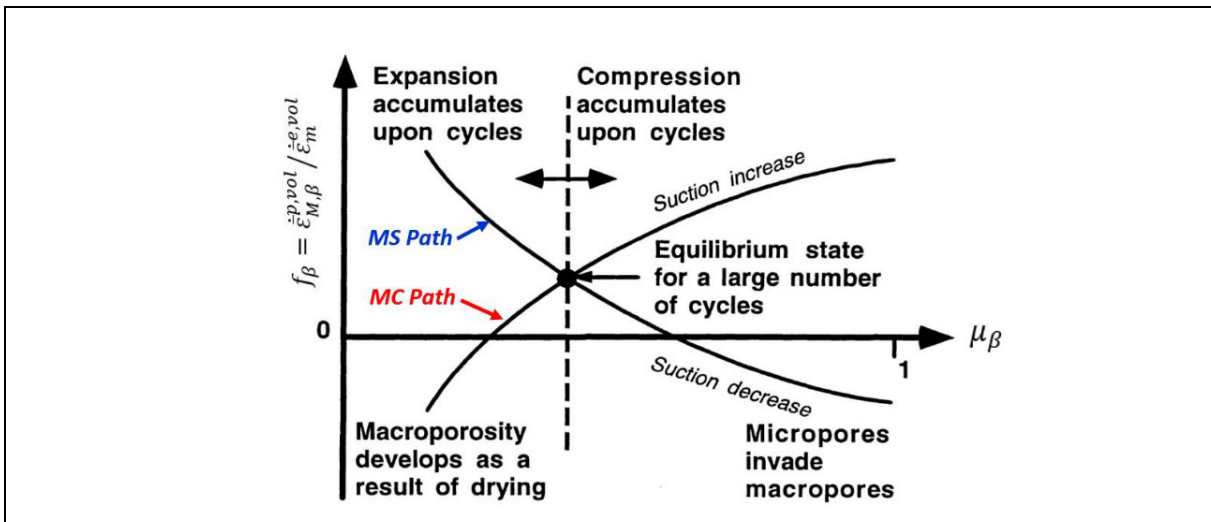


Figure 2-5. Micro-macro pore interaction mechanisms and the structural coupling functions (Alonso et al., 1999).

A modification of Equation (2-61) is required to ensure the simplifying assumption of elastic thermal deformations at both structural levels in non-isothermal analyses. In such conditions, the thermal expansion of the microstructure does not generate any irreversible structural changes (as a thermal collapse) in the soil skeleton. Consequently, the thermal component of the micro-structural deformations must be discounted from the total micro-structural strains:

$$\dot{\tilde{\epsilon}}_{M,\beta}^p = f_\beta \cdot \left(\dot{\tilde{\epsilon}}_m^e - (\dot{\tilde{\epsilon}}_m^e)_{\Delta T} \right) \quad (2-63)$$

When isothermal analyses are performed, $(\dot{\tilde{\epsilon}}_m^e)_{\Delta T} = \mathbf{0}$, and Equation (2-61) is recovered.

Hardening rule

Finally, the hardening of the double porosity medium is given by the evolution of the isotropic yield stress due to the contribution of both plastic mechanisms considered in the current formulation. Thus, the evolution of the saturated pre-consolidation pressure (the hardening parameter of this model), \dot{p}_0^* , is given as follows:

$$\dot{p}_0^* = p_0^* \cdot \left(\frac{1 + e_M}{\lambda_{(0)} - \bar{\kappa}_M} \right) \cdot \left(\dot{\tilde{\epsilon}}_{M,LC}^{p,v} + \dot{\tilde{\epsilon}}_{M,\beta}^{p,v} \right) \quad (2-64)$$

where $\dot{\varepsilon}_{M,LC}^{p,v}$ is the volumetric plastic strain induced by the yielding of macrostructure due to the LC mechanism and $\dot{\varepsilon}_{M,\beta}^{p,v}$ is the volumetric component of macro-structural strains due to the plastic β -mechanism.

In non-isothermal problems, the evolution of this hardening parameter, $\dot{p}_{0,T}^*$, can also become dependent on the temperature changes. In such conditions, the general expression for the hardening rule of the double structure model is given as follows:

$$\dot{p}_{0,T}^* = p_{0,T}^* \cdot \left(\frac{1 + e_M}{\lambda_{(0)} - \bar{\kappa}_M} \right) \cdot \left(\dot{\varepsilon}_{M,LC}^{p,v} + \dot{\varepsilon}_{M,\beta}^{p,v} \right) + 2(\alpha_1 \pm 2\alpha_3 \cdot \Delta T) \cdot \dot{T} \quad (2-65)$$

Model parameters

The full list of model parameters together with a brief description is presented in Table 2-2.

Table 2-2. Model parameters

Constitutive Law	Input Parameters	Description
Bishop parameter for the microstructure (Bishop effective stress)	p_k	Input parameter for the dependence of the Bishop coefficient on the saturation state of the microstructure – see Vasconcelos (2021).
	q_k	Input parameter for the dependence of the Bishop coefficient on the saturation state of the microstructure – see Vasconcelos (2021).
Non-linear elasticity for the macrostructure	$\bar{\kappa}_M$	Elastic slope for specific volume – mean stress. See Equation (2-47).
	$\bar{\kappa}_s$	Elastic slope for specific volume – macro suction. See Equation (2-48).
	$\bar{K}_{M,min}$	Minimum bulk modulus for changes in the macro-structural mean stress.
	$\bar{K}_{s,min}$	Minimum bulk modulus for changes in the suction at macrostructure.
	ν	Poisson's ratio.
Plastic LC Mechanism (BBM) for the macrostructure	φ	Friction angle.
	p_0^*	Pre-consolidation pressure at saturated conditions.
	p_c	Reference pressure.
	$\lambda_{(0)}$	Slope of void ratio – mean stress at saturation.
	r	Parameter defining the maximum soil stiffness. See Equation (2-58).
	β	Parameter controlling the rate of increase of stiffness with macro suction. See Equation (2-58).
	k_s	Parameter that takes into account the increase of tensile strength due to macro suction. See Equation (2-55).
	α_{LC}	Non-associativity parameter. See Equation (2-60).
Mechanical micro-macro coupling	$f_{MS}^{(0)}$	Value for the interaction function (MS paths) when $\mu_\beta = 0$.
	$f_{MS}^{(1)}$	Value for the interaction function (MS paths) when $\mu_\beta = 1$.
	n_{MS}	Model parameter (MS paths).

(interaction functions): Equation (2-62)	$f_{MC}^{(0)}$	Value for the interaction function (MC paths) when $\mu_\beta = 0$.
	$f_{MC}^{(1)}$	Value for the interaction function (MS paths) when $\mu_\beta = 1$.
	n_{MC}	Model parameter (MC paths).
Hydraulic micro-macro coupling (water mass transfer)	γ^w	Leakage parameter. See Equation (2-19).
Water retention curve (WRC): Equation (2-36)	$P_{0,\beta}$	Pore-air entry value at 20°C for the β -structural medium. See Equation (2-37).
	σ_0	Surface tension at 20°C. See Equation (2-37).
	λ_{rc}	Shape parameter for the WRC.
	$S_{lr,\beta}$	Residual saturation for the β -structural medium.
	$S_{ls,\beta}$	Maximum saturation for the β -structural medium.
	$P_{d,\beta}$	Pressure related to the suction at zero degree of saturation of the β -structural medium.
	λ_d	Model parameter.
Intrinsic permeability for the macrostructure	$k_{0,M}$	Intrinsic permeability (isotropic tensor).
	$\bar{\phi}_0$	Reference porosity.
Thermal conductivity coefficient for the flux of heat (Fourier's law): Equation (2-28)	λ_{sat}	Thermal conductivity of the dry porous medium.
	λ_{dry}	Thermal conductivity of the water saturated porous medium.
Thermal parameters for the elastoplastic response of the porous medium	α_0	Parameter for the elastic thermal volumetric strain. See Equation (2-49).
	α_1	Parameter for the plastic thermal strain. See Equation (2-57) and Equation (2-65).
	α_2	Parameter for the elastic thermal volumetric strain. See Equation (2-49).
	α_3	Parameter for the plastic thermal strain. See Equation (2-57) and Equation (2-65).
	T_{ref}	Reference temperature.
	ρ_T	Parameter that takes into account the reduction of tensile strength due to temperature. See Equation (2-55).

3 Basic capabilities of the model

A basic capability of the double structure model is the possibility of tracking and predicting changes in the microstructure of the material under loading and saturation changes. This capability is strikingly demonstrated in the modelling of Task 3.3 (section 4).

In addition, at the time of submitting Deliverable 3.1, it was demonstrated, by appropriate single element calculations, that the model possessed a number of capabilities deemed essential to model properly homogenization processes. They were:

- Dependence of swelling strain on applied stress (at the same dry density)
- Dependence of swelling strains on dry density (at the same stress)

- Irreversibility of strains in wetting/drying cycles
- Dependence of swelling pressure on dry density
- Differential stress path dependence from depending on saturation/unsaturation direction

This is reflected in the first column of Table 3- 1. Although not explicitly reflected in the Table, there have been a number of developments and improvements carried out on the isothermal formulation of the constitutive model during the BEACON project. The main ones are:

- a more consistent definition of porosity and volume fractions
- the microstructure may be unsaturated
- hydraulic equilibrium between microstructure and macrostructure is not assumed
- The micro-macro transfer of liquid (or, sometimes, gas) is governed by a linear law between flow and micro-macro potential difference
- clarification of the physical meaning of the interaction functions via DEM simulations
- examination of the relationship between the micro and macro elastic components leading to a direct relationship between the two sets of elastic parameters
- advective flow occurs only in the macrostructure
- variations of permeability depend only on the macro porosity
- separate retention curves are defined for each structural level, as the microstructure may now be unsaturated.

A significant development that is reflected in Table 3- 1 is the inclusion of the thermal component in the current double porosity model as described in this contribution to Deliverable 3.3. Although more work is required for the full development of the thermo-elasto-plastic model, the double structure formulation has already been modified to incorporate the new variables in a consistent way and the model is already operational although under some restricted conditions.

Table 3- 1. . Summary table of the basic capabilities of the enhanced THM double structure model

Name of the constitutive law:		Enhanced Double Porosity Model (DPM)	
Behaviour feature	D3.1	D3.3	Remarks
Mechanical behaviour			
Dependence of swelling strain on applied stress (at the same dry density)	YES	YES	The location of the stress state respect to the LC curve generates this dependence.
Dependence of swelling strain on dry density (at the same stress)	YES	YES	Swelling strain is implicitly dependent on the dry density. This dependence is modelled by a suitable choice of the saturated pre-consolidation pressure (p_0^*), which is a user-defined (input) parameter of the model, so that the higher the dry density, the higher the swelling strain (for the same stress state).
Irreversibility of strains in wetting/drying cycles	YES	YES	The irreversible strains are generated in wetting/drying paths that cross the current LC curve.
Dependence of swelling pressure on dry density	YES	YES	At the same initial conditions, stress state and suction, different values of the isotropic yield stress for saturated conditions p_0^* (the higher the dry density, the higher the pre-consolidation

			pressure) generate different kinetics and final values of swelling pressure.
Stress path dependence from an unsaturated to a saturated state	YES	YES	This feature comes from the HM constitutive formulation. Numerical testing requires an additional effort related to the numerical implementation. The transition of saturated to unsaturated (or vice-versa) is not a trivial issue with the net stress as stress variable.
Stress path dependence from a saturated to an unsaturated state	YES	YES	
Double structure/porosity considered?	YES	YES	The expansive clay is considered as a multi-phase porous media composed by arrangement of clay aggregates and micro- and macro-pores.
Are temperature effects considered in the model?	NO	YES	Elastic thermal expansion/contraction is considered. Plastic thermal collapse can be introduced by the activation of the dependence of p_0^* on thermal changes (see Equation (2-57)). Thermal expansion of water in both pore levels and the dependence of the macro- and micro-structural water properties on temperature are also included in the current double-porosity model.
Dependence of strains developed in a temperature cycle (increase/decrease) on OCR (or stress)	NO	NO	Irreversible thermal strains arising from the structural coupling between micro and macro media are not taken into account (see Equation (2-63)). However, structural changes might occur during a temperature cycle because of the fully coupled THM formulation of the double-porosity model, since the thermal effects on the HM variables may generate irreversible strains.
Hydraulic behaviour (retention curve)			
Hysteresis	NO	NO	
Dependence on void ratio	NO	NO	It has not been considered so far. However, an explicit dependence of the pore-air entry value (P_0 in Equation (2-37)) and the shape parameter λ_{rc} of the water retention curve (WRC) for each structural level on the evolution of macro and micro void ratios could be easily implemented into the present double-porosity formulation.
Double structure/porosity considered?	YES	YES	Macro- and micro-structural hydraulic responses are related to different WRC, each of them associated with a distinct pore level.

4 Task 3.3

4.1 Stress paths of the tests

This task focuses on the effect of two different hydro-mechanical (HM) stress paths on the final state of granular MX80 bentonite. The task is based on laboratory tests performed at EPFL in which two different hydration procedures (free-swelling and constant-volume) were applied; both tests were continued with a compression path to a similar value of vertical total stress (Figure 4-1). Results of the oedometric compression tests after saturation under constant axial stress (Path-1) and constant volume conditions (Path-2).

The tests were performed under oedometric conditions. Micro-structural analyses using Mercury Intrusion Porosimetry (MIP) were performed to assess the evolution of the micro-structural features of the material along with the different HM loadings.

Path 1 (**A–B–C–D**) consisted of the following two stages:

- **A–B**: Hydration under constant vertical stress of 21 kPa. The stage finished once swelling strains stabilized with time.
- **B–C–D**: Increase vertical stress in steps up to 20 MPa.

Path 2 (**A–B'–C'**) consisted of the following two stages:

- **A–B'**: Hydration under constant-volume conditions. Vertical stress was increased according to the observed displacements to maintain as much as possible isochoric conditions. This stage finished once swelling pressure stabilized with time.
- **B'–C'**: Increase of vertical stress in steps up to 20 MPa.

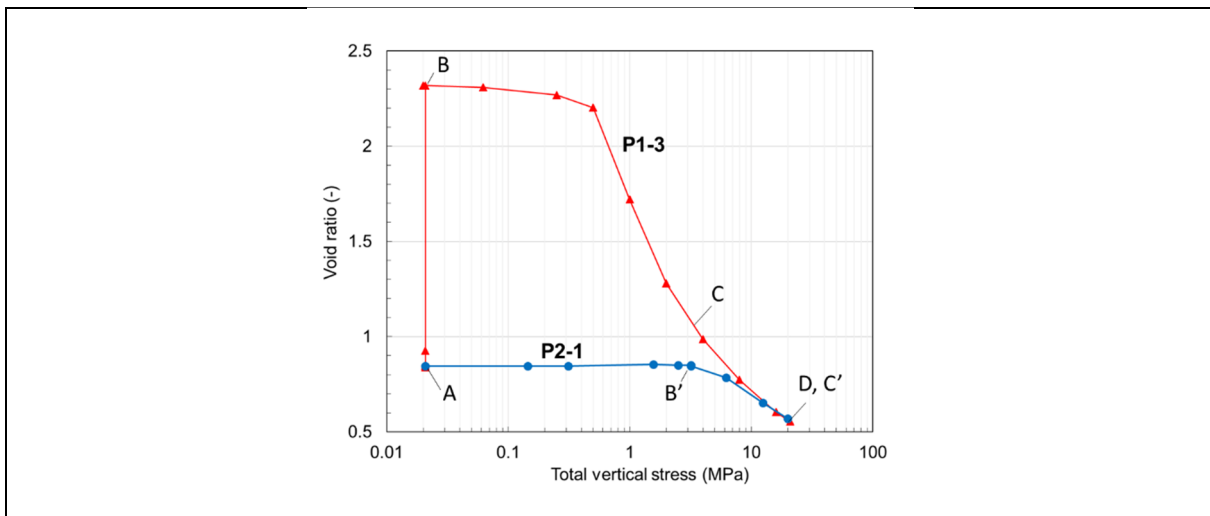


Figure 4-1. Results of the oedometric compression tests after saturation under constant axial stress (Path-1) and constant volume conditions (Path-2).

4.2 Modelling features

4.2.1 Geometry and boundary conditions

A cubic sample of soil, with a volume of 1.0 cm³, was selected to act as a single-element test. The generated mesh is composed of 125 identical hexahedral elements. In accordance with the goal of the Task, only the constitutive response of the model is evaluated. To this end, in the hydration stages, the suction is changed simultaneously in the entire domain of analysis.

In the wetting path at constant load conditions (“free swelling”), the confining pressure is applied on the upper surface and on the four lateral surfaces. Under such condition, vertical displacements (in the z-axis direction) are not allowed at the lower surface. In contrast, in the isochoric condition path, the vertical displacements are restricted in all surfaces of the volume until the suction is reduced to a value of 0.

The FE mesh and three orthogonal views with the applied mechanical boundary conditions for wetting path under unconfined (free swelling) and confined (isochoric) conditions are displayed in Figure 4-2.

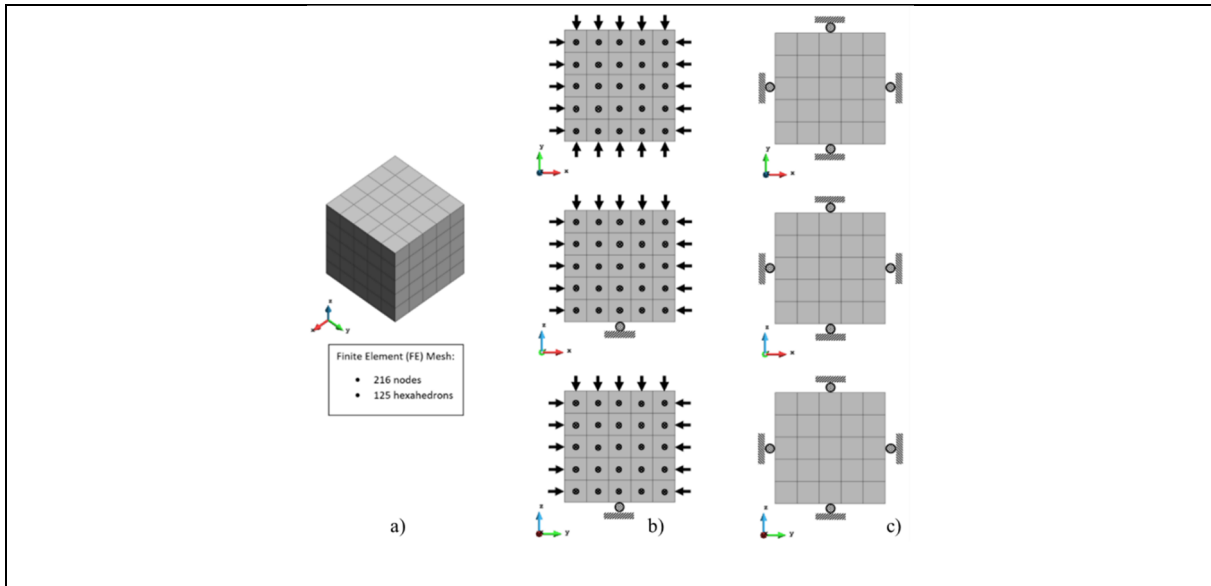


Figure 4-2. (a) Schematic representation of the modelled geometry (FE mesh) of a cubic element of soil together with the mechanical boundary conditions under (b) unconfined and (c) confined swelling/shrinkage evolution (Vasconcelos, 2021)

4.2.2 Initial conditions and model parameters

The current double-porosity model requires the definition of a different retention curve for each structural level. Retention curves are based on Seiphooori et al. (2014) who investigated the water retention behaviour of compacted MX-80 (Wyoming) granular bentonite. The overall retention curve of the specimen is given by the superposition of the micro and macro Van Genuchten curves, as shown Figure 4-3a. Also, the mechanical micro-macro coupling (β -mechanism) was simulated by defining the shape of the interaction functions (f_β), whose mathematical expression is given in Equation (2-62). The pair of micro-macro interaction functions are also plotted in Figure 4-3b. The parameters defining the initial LC curve (i.e. r , β , $\lambda_{(0)}$, p_0^* , p_c) were defined according to the results obtained by Seiphooori (2015) resulting in the curve presented in Figure 4-3c. The non-linear elasticity parameters ($\bar{\kappa}_M$ and $\bar{\kappa}_s$) were determined according to the results of laboratory swelling pressure tests. The Poisson ratio ν and the shear strength angle (φ) have been set to a value of 0.3 and 25 respectively. Finally, the initial macro and micro-pore volume were determined from the MIP observations of bentonite pore sizes (Figure 4-3d). Hydraulic equilibrium between structural levels was assumed to ensure that the constitutive model predictions were obtained. For this purpose, the leakage parameter adopted (γ^w) is high enough to maintain this equilibrium state during the stress-suction paths. Table 4-1 shows the input parameters and initial conditions considered in the analysis.

Table 4-1. Input parameters

Constitutive Law	Input Parameter			Description
	Symbol	Unit	Value	
Bishop parameter for the microstructure (Bishop effective stress)	p_k	-	0.7	Input parameter for the dependence of the Bishop coefficient on the saturation state of the microstructure – see Vasconcelos (2021).
	q_k	-	100	Input parameter for the dependence of the Bishop coefficient on the saturation state of the microstructure – see Vasconcelos (2021).

Non-linear elasticity for the macrostructure	$\bar{\kappa}_M$	-	2.5e-05	Elastic slope for specific volume – mean stress. See Equation (2-47).
	$\bar{\kappa}_S$	-	2.8e-03	Elastic slope for specific volume – macro suction. See Equation (2-48).
	ν	-	0.3	Poisson's ratio.
Plastic LC Mechanism (BBM) for the macrostructure	φ	°	25	Friction angle.
	p_c	MPa	0.5	Reference pressure.
	$\lambda_{(0)}$	-	0.3	Slope of void ratio – mean stress at saturation.
	r	-	0.65	Parameter defining the maximum soil stiffness. See Equation (2-58).
	β	MPa ⁻¹	0.02	Parameter controlling the rate of increase of stiffness with macro suction. See Equation (2-58).
	k_s	-	0.01	Parameter that takes into account the increase of tensile strength due to macro suction. See Equation (2-55).
	α_{LC}	-	1	Non-associativity parameter. See Equation (2-60).
Mechanical micro-macro coupling (interaction functions): Equation (2-62)	$f_{MS}^{(0)}$	-	4	Value for the interaction function (MS paths) when $\mu_\beta = 0$.
	$f_{MS}^{(1)}$	-	0	Value for the interaction function (MS paths) when $\mu_\beta = 1$.
	n_{MS}	-	2	Model parameter (MS paths).
	$f_{MC}^{(0)}$	-	0	Value for the interaction function (MC paths) when $\mu_\beta = 0$.
	$f_{MC}^{(1)}$	-	4	Value for the interaction function (MC paths) when $\mu_\beta = 1$.
	n_{MC}	-	2	Model parameter (MC paths).
Hydraulic micro-macro coupling (water mass transfer)	γ^w	$\frac{\text{kg}}{\text{s} \cdot \text{m}^3 \cdot \text{MPa}}$	5.0e-03	Leakage parameter. See Equation (2-19).
	P_0	MPa	90	Pore-air entry value at 20°C. See Equation (2-37).
Water retention curve (WRC) for the micro-structural medium: Equation (2-36)	σ_0	N/m	0.072	Surface tension at 20°C. See Equation (2-37).
	λ_{rc}	-	0.65	Shape parameter for the WRC.
	$S_{lr,m}$	-	0.3	Residual saturation.
	$S_{ls,m}$	-	1.0	Maximum saturation.
	$P_{d,m}$	MPa	1.0e27	Pressure related to the suction at zero degree of saturation.
	λ_d	-	0.8	Model parameter.
Water retention curve (WRC) for the macro-structural medium: Equation (2-36)	P_0	MPa	12	Pore-air entry value at 20°C.
	σ_0	N/m	0.072	Surface tension at 20°C.
	λ_{rc}	-	0.55	Shape parameter for the WRC.
	$S_{lr,M}$	-	0.01	Residual saturation.
	$S_{ls,M}$	-	1.0	Maximum saturation.
	$P_{d,M}$	MPa	1.0e27	Pressure related to the suction at zero degree of saturation.

	λ_d	-	3.9	Model parameter.
Intrinsic permeability for the macrostructure	$k_{0,M}$	m ²	4.0e-21	Intrinsic permeability (isotropic tensor).
	$\bar{\phi}_0$	-	0.20	Reference porosity.
Initial conditions	p_0^*	MPa	2.5	Pre-consolidation pressure at saturated conditions.
	ϕ	-	0.460	Total porosity.
	$\bar{\phi}_m$	-	0.324	Micro-pore volume fraction.
	P_{lM}	MPa	-110	Liquid pressure at the macro-structural level.
	P_{lm}	MPa	-110	Liquid pressure at the micro-structural level.
	P_g	MPa	0.1	Gas pressure (atmospheric pressure).

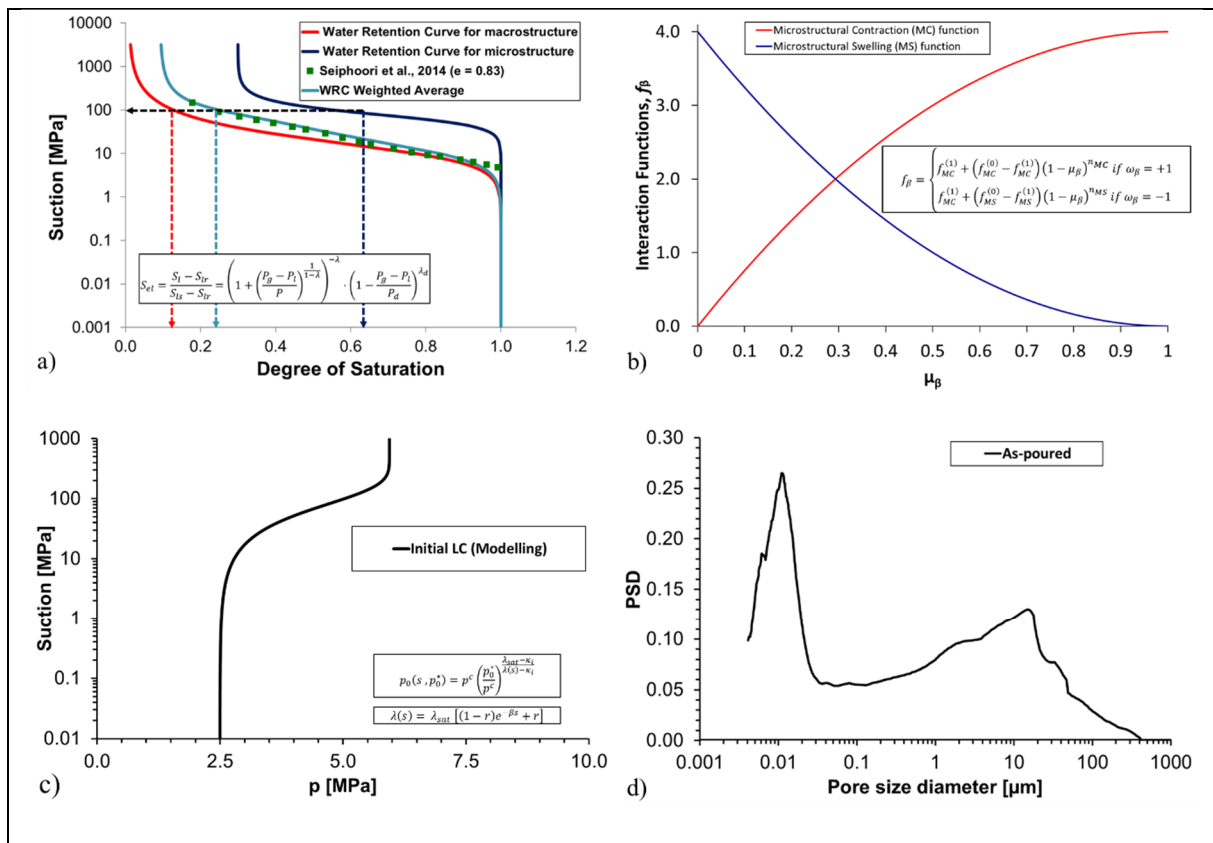


Figure 4-3. a) Water retention curve for macro and microstructure, b) Interaction functions, c) Initial LC curve, and d) Pore size distribution

4.3 Results

4.3.1 Path 1: A-B-C-D

In path A-B, the swelling of the clay aggregates leads to an increase macro porosity, which produces a global expansion of the soil element (increase in total porosity). Some of the positions of the LC yield curve during the performance of Path 1 (free swelling and loading) are shown in Figure 4-4a. It can be seen that during this stage, the LC curve moves to the left in response to the plastic swelling strains taking place in the macrostructure. This is due to the low

isotropic stress ratio p/p_0 . When this ratio is low, it implies a dense packing of the clay aggregates and, under this condition, the micro-structural swelling (MS path) affects strongly the global arrangements of clay aggregates, inducing large macro-structural plastic strains and a macro-structural softening.

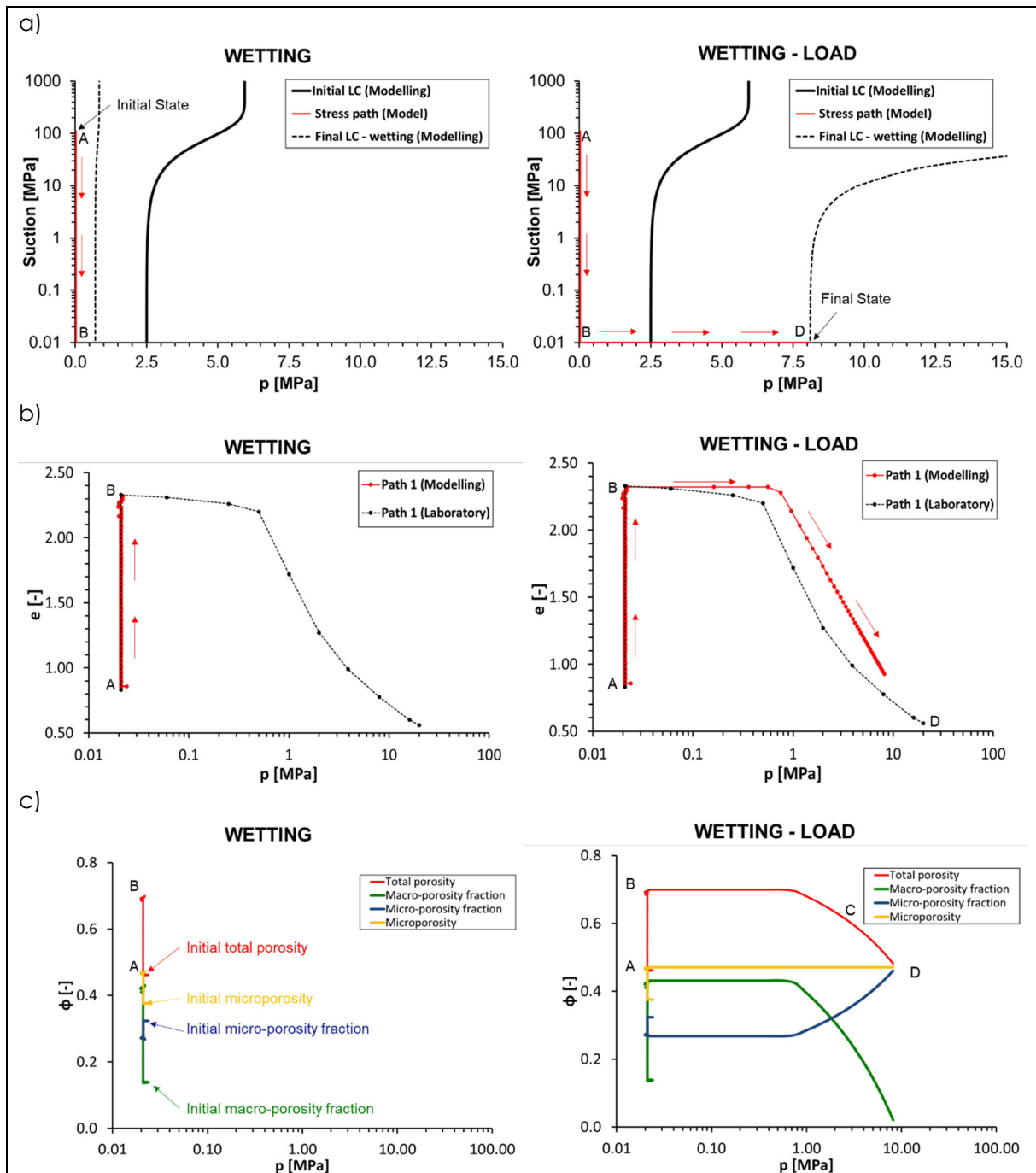


Figure 4-4. Schematic representation of Path 1 a) the wetting at constant confining pressure and a subsequent load (in the $p:s_M$ plane), b) evolution of void ratio (in the plane $e:p$) and c) evolution of the different porosities considered in the model.

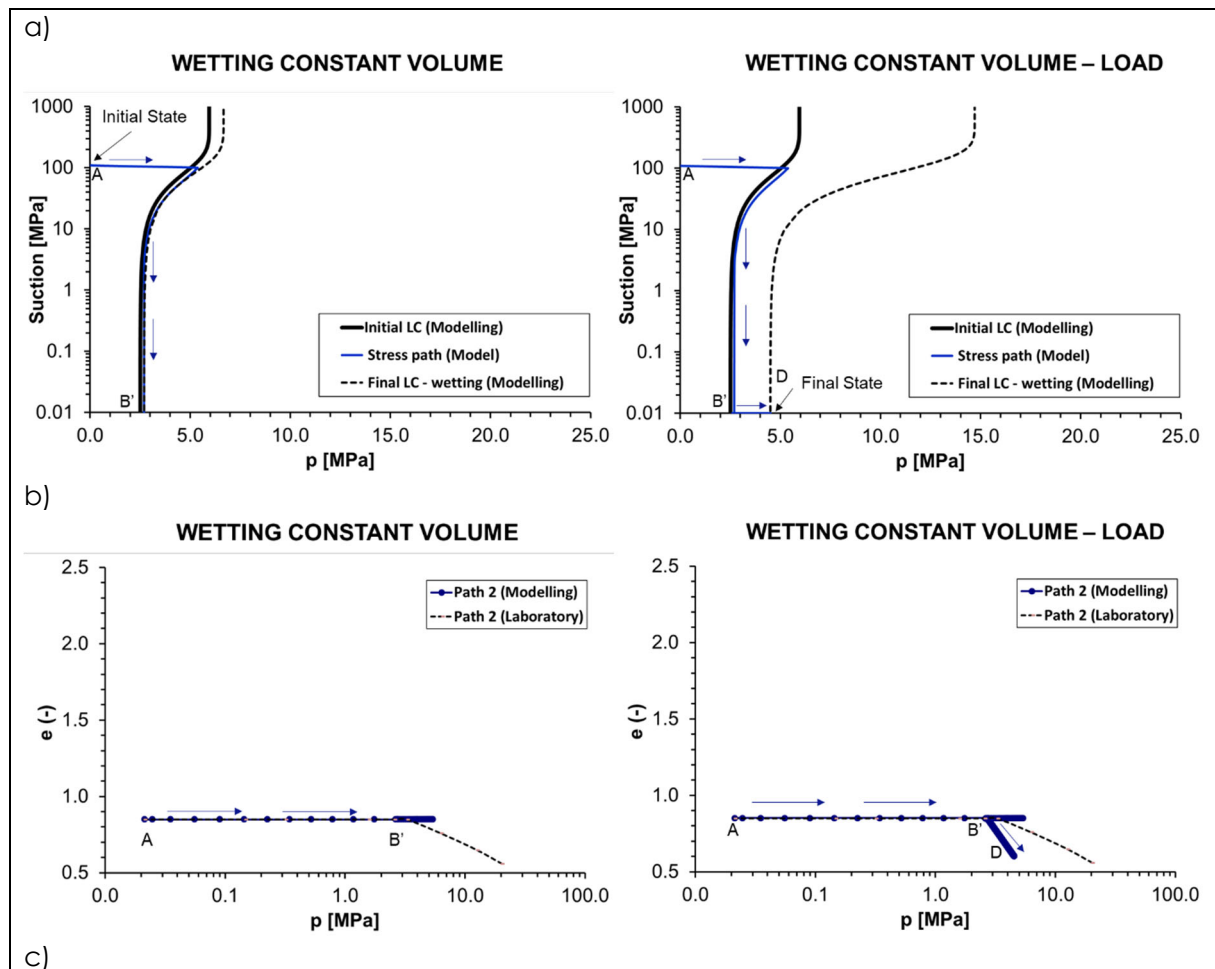
Comparing the numerical predictions with the experimental results in path A-B, a good agreement is obtained in terms of the void ratio against vertical stress (Figure 4-4b). After saturation, the subsequent loading (B-D) takes the LC again to the right to the final load value of approximately 8.0 MPa. Figure 4-4. Schematic representation of Path 1 a) the wetting at

constant confining pressure and a subsequent load (in the p : s M plane), b) evolution of void ratio (in the plane e : p) and c) evolution of the different porosities considered in the model. Figure 4-4c shows the evolution of the micro-structural and macro-structural void ratio computed for Path 1. During the subsequent loading (B-D), under saturated conditions, the deformation of the macrostructure is significant but it is not due to micro-structural strains that are now quite small. The evolutions of total vertical stress, void ratio, suction and degree of saturation for path 1 are listed in Table A1-1 (Appendix 1).

4.3.2 Path 2: A-B'-C'

The initial location of the LC curve is presented along with the different positions of the LC yield curve during the performance of this test (Figure 4-5a). Initially, the stress increases due to the development of swelling pressure. Once the LC yield surface is reached, the vertical stress drops to compensate for the tendency of the macrostructure to collapse so that the sample volume is maintained constant. It can be seen that during the wetting stage (A-B') the LC curve moves slightly to the right in response to macro-structural hardening. In the final stage (B'-D), the reduction of macro-pores can be observed; it is related to the progressive increase of vertical stress (Figure 4-5c).

Table A1-2 in Appendix 1 contains the evolutions of total vertical stress, void ratio, suction and degree of saturation of path 2.



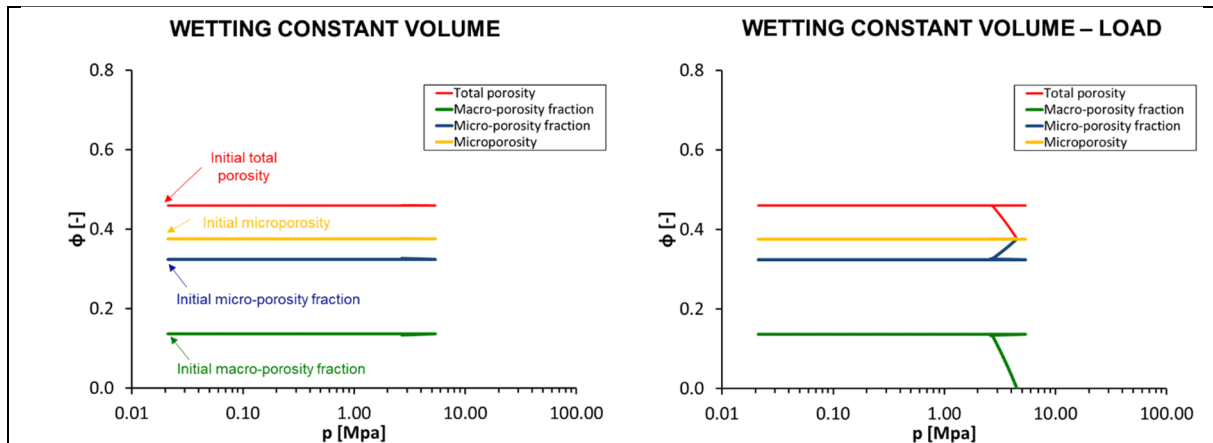


Figure 4-5. Schematic representation of Path 2 a) the wetting at constant volume conditions and a subsequent load (in the $p:s_M$ plane), b) evolution of total porosity (in the plane $e:p$) and c) evolution of the different porosities considered in the model.

4.3.3 Full results

Figure 4-6. Variation of void ratio in stress paths 1 and 2. Computed and experimental results

shows the comparison between model and experimental results for paths 1 and 2. As can be seen, the agreement with experimental data is reasonably satisfactory although some departures from observations can be noted. Specifically, the following features have been correctly reproduced:

- large swelling strains upon wetting under low applied stresses
- a clearly defined yield point when loading after wetting
- stress path dependency comparing the swelling pressure test and the swell-load test (although the void ratio difference is overestimated by the model)
- a realistic value of swelling pressure is obtained.

In contrast, the convergence of the loading compression lines is not captured by the model.

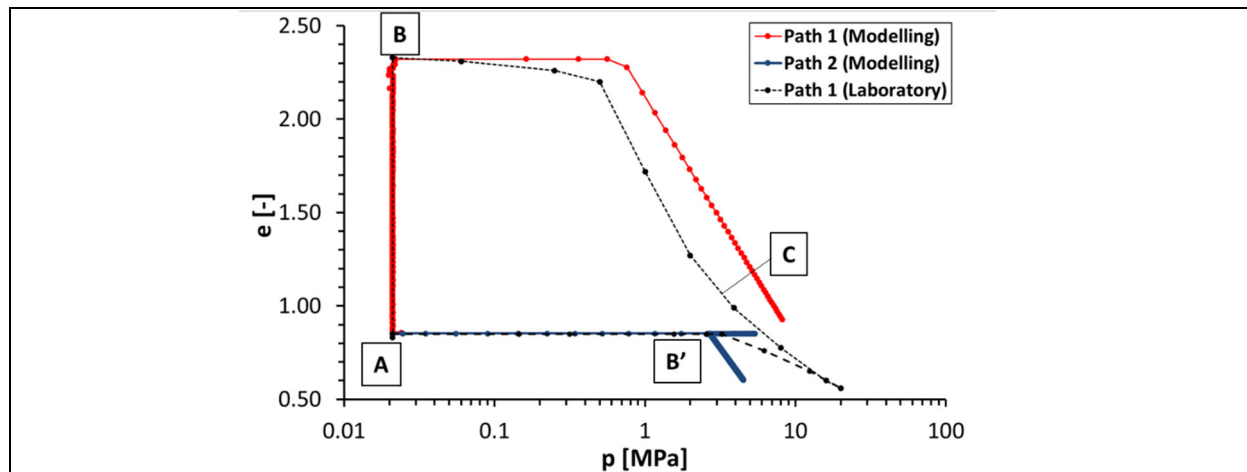


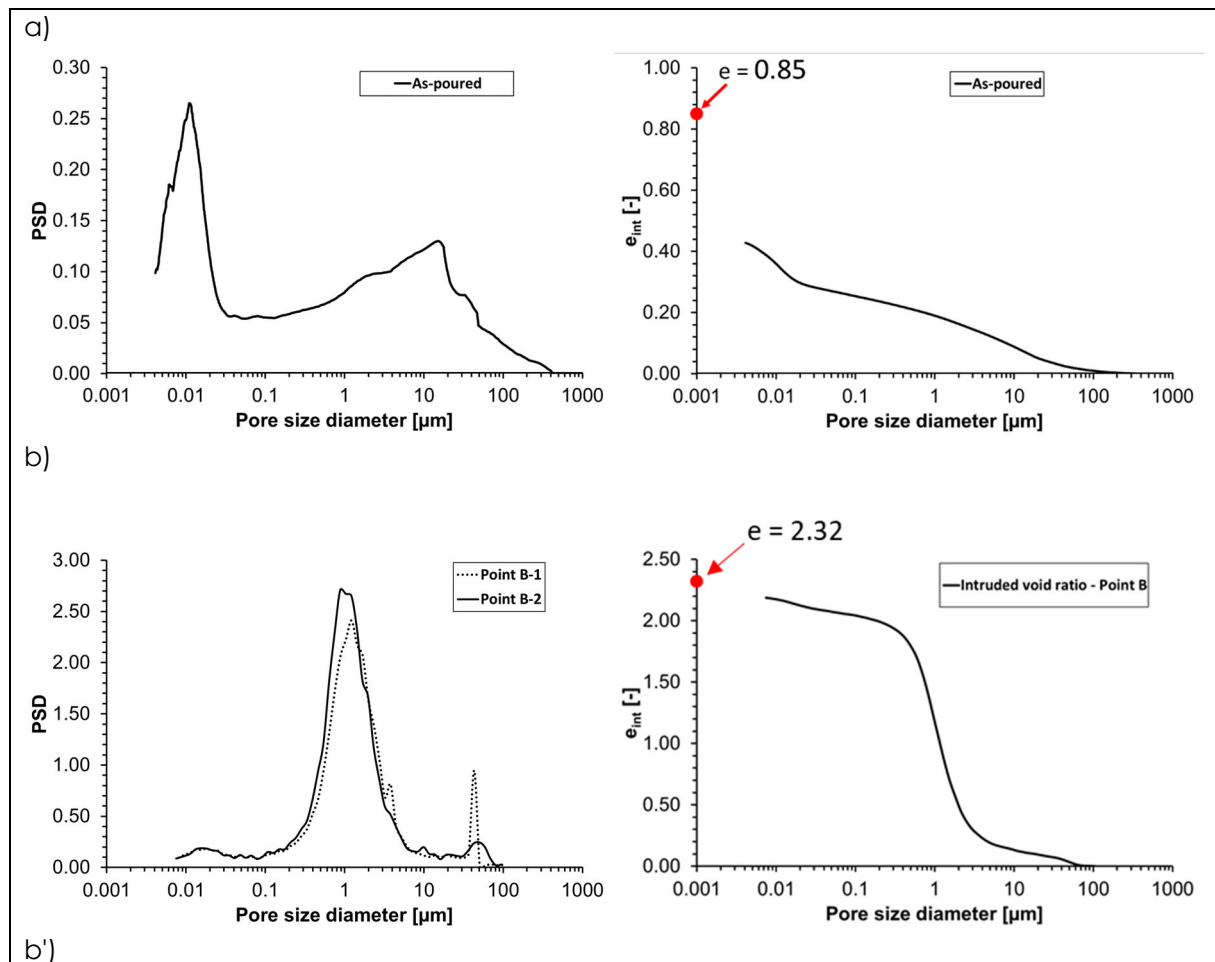
Figure 4-6. Variation of void ratio in stress paths 1 and 2. Computed and experimental results

4.4 Micro-structural evolution

The microstructure of a soil changes when subjected to mechanical or hydraulic actions. These changes are especially relevant in the case of expansive clays. One of the advantages of adopting a double structure constitutive model is that allows the consideration of micro-structural changes, albeit in an approximate manner.

In the set of tests used in this Task, pore size distributions were determined using Mercury Intrusion Porosimetry (MIP) at points A, B, C and B', indicated in Figure 4-1. The MIP results in terms of the pore size distribution and intruded void ratio are shown in Figure 4-7 for the four points examined. Such observations provide an opportunity to check the performance of the constitutive model with respect to the evolution of the microstructure. Note that the intruded volume is less than the total pore volume because mercury does not penetrate when the pore size is less than a minimum threshold, around 4-7 nm. In Figure 4-7, the total void ratio of the sample is indicated with a red dot; in this way the pore volume below the penetration threshold can be readily observed.

The MIP data corresponding to the initial state (point A) indicates a clear double porosity arrangement with two separate predominant pore sizes. However, after swelling under low stresses a uni-modal pore size distribution emerges (point B). Romero et al. (2011) advocated that the dominant peak of the PSD function determined by MIP after wetting provided a good criterion to distinguish between micro-porosity and macro-porosity. In the present case, this criterion yields a size of about 0.8-1.2 μm (Figure 4-7b). Using this delimiting threshold, the micro and macro void ratios from the MIP determinations are listed in Table 4-2. The values derived from the application of the double structure model are also presented in the same Table.



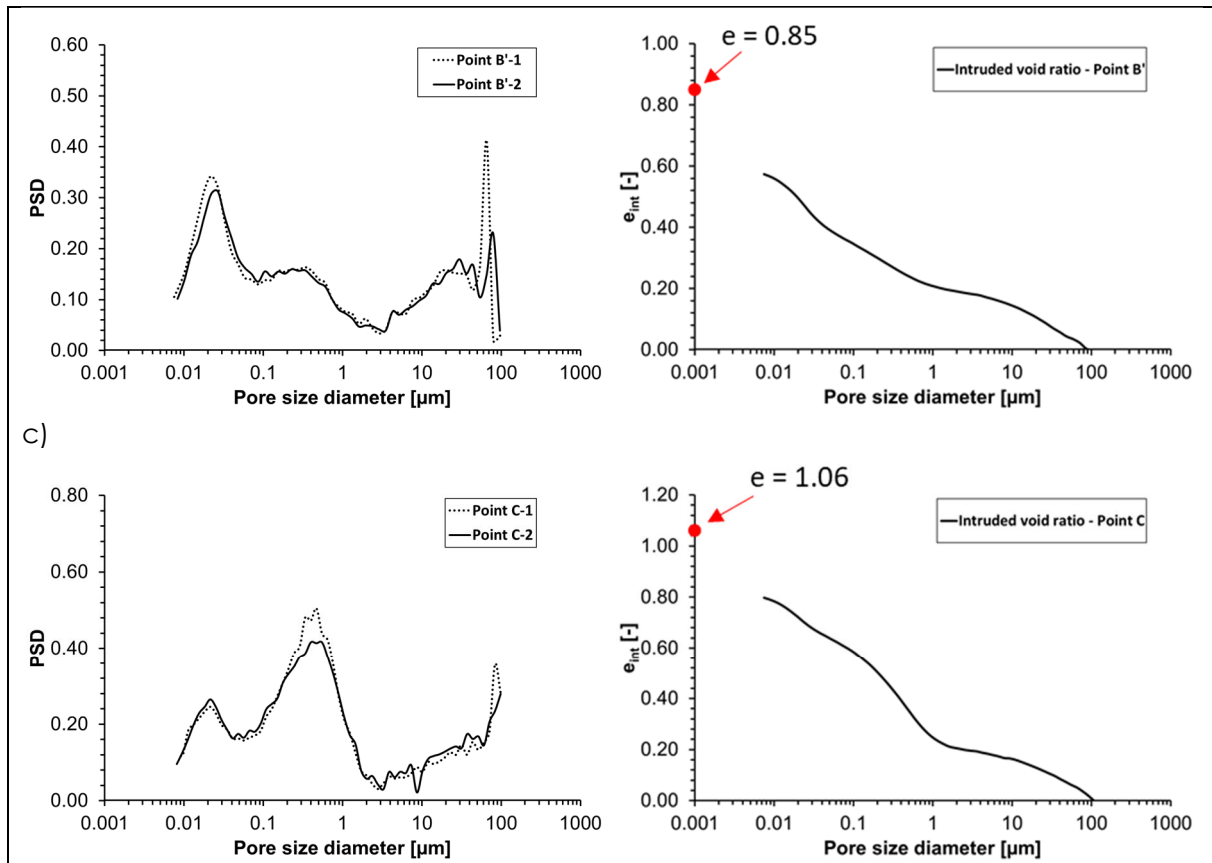


Figure 4-7. MIP results in terms of pore size distribution (left column) and intruded void ratio (right column). a) Initial conditions, b) after axial swelling (Point B), b') after isochoric wetting up to saturation (Point B') and c) After axial swelling and subsequent compression under saturated states at 3.24 MPa

Table 4-2. Total, micro and macro void ratios using Romero et al. (2011) criterion. Experimental and model results

Point	Experimental void ratios			Model void ratios		
	Total	Micro	Macro	Total	Micro	Macro
A	0.85	0.60	0.25	0.85	0.60	0.25
B	2.32	1.15	1.17	2.32	0.89	1.43
C	1.06	0.82	0.24	1.46	0.89	0.57
B'	0.85	0.64	0.21	0.85	0.605	0.245

Considering first the swelling under low applied stresses (path A-B), it can be noted that there is the expected significant increase in the micro void ratio but, also, even a larger one of the macro void ratio. This is due to the large effect of micro-structural strains on the macrostructure; the model represents well this interaction.

The effects of loading can be examined in path BC. It can be observed that the experimental results reveal that most of the void ratio reduction affects the macrostructure. The same type of behaviour is predicted by the model, although the reduction of micro void ratio is severely underestimated, suggesting an area for potential model improvement. It should also be noted that the model predicts a higher overall void ratio at point C compared to the experimental result. It can be easily inferred that additional loading would lead to further reductions in macro

void ratio. Finally, the swelling pressure test (path A-B') results in quite limited variation of micro and macro void ratios; an observation also reproduced by the model.

Thus, it can be concluded that the double structure model is capable of representing successfully the micro-structural evolution of the material, at least for the stress paths considered in this Task.

5 Performance of the model and assessment of predictive power

The double constitutive model presented appears to fulfil most of the criteria required for an adequate modelling of the processes underlying homogenizations identified in WP3. When applied to the case of Task 3.3, The constitutive model has been able to represent correctly most of the observed features of behaviour: development of large swelling strains at low confining stresses, occurrence of a sharp yield during saturated compression, stress path dependency and a realistic value of swelling pressure. However, the model does not yield the convergence of consolidation lines at large stresses. The evolution of micro and macro porosity obtained from the model appears consistent with porosimetry results, although it also highlights the difficulty of defining precisely the boundary between the two levels of porosity.

The model has been applied to a variety of boundary value problems, involving different homogenization cases within the framework of WP5 that is structured in four steps. Step 1 includes a series of deceptively simple laboratory tests structured in three different sets of tests: bentonite swelling into a void performed by Clay Technology (1a), a constant-volume swelling test on a pellets mixture carried out by CEA (1b) and the hydration of a specimen composed by pellets poured on top of a bentonite block, performed by POSIVA (1c). The performance of the model was generally highly satisfactory not only in terms of the final state of the sample but also regarding its transient evolution. The main exception is the axial pressure of case 1c. As friction was not included in the analysis, the different axial pressures at both ends of the sample measured in the test could not be reproduced.

Step 2 refers to large scale tests; UPC selected the EB experiment for analysis. The EB test involves the artificial hydration of an engineered barriers that include bentonite blocks and granular bentonite (pellets). The practically complete homogenization between blocks and pellets is successfully reproduced by the analysis. There are more differences between observations and model results regarding the transient hydration period. However, it should be pointed out that the degree of control of the process of artificial hydration was not high and the level of instrumentation in the barrier was rather sparse. In addition, a sensitivity analysis was performed to check on the effects of two of the most uncertain components of the formulation: retention curve and interaction functions.

Step 3 is based on a series of isochoric oedometer hydration tests performed by CIEMAT on samples constituted by bentonite pellets and a compacted bentonite block. Different hydration conditions were applied. Three tests were selected for the step, two of them intended for calibration and the third one for blind prediction. The UPC work in this step was delayed because of the Covid-19 pandemic. It coincided with a change of personnel and the necessary training of new researchers was hindered by lockdown restrictions. For this reason, the UPC results of this step were only partially reported in Deliverable 5.6; the analyses of this step have now been completed and are fully reported in Deliverable 5.7. The spirit of blind prediction has been kept by using for test MGR27 the same parameters as for the two calibration tests without any modification. In all cases, there has been a quite large degree of axial homogenization between pellets and block that has been well captured by the analyses. The type of evolution and final value of the swelling pressure is also well reproduced by the model but there are significant departures concerning the time evolution of the hydration and of the pressure development during the transient period. Also, the non-consideration of lateral

friction prevents a good prediction of the swelling pressure value in the MGR27 test. The development of interface formulations for friction modelling is under way, based on thin finite elements, but they are not fully implemented yet. Micro and macro porosity results obtained from the double structure model appear largely consistent with observations.

Finally, Step 4 refers to the analyses of assessment cases; UPC has analysed that proposed by NAGRA. It involves an engineered barrier made up of bentonite blocks and pellets subjected to heating and natural hydration from the rock. The goal is to examine the evolution of the dry density of the barrier during the initial thermo-hydro-mechanical transients. Because of the non-isothermal nature of the case, the model including thermal effects has been used. Because the development of the formulation is still not fully complete, there are a number of convergence difficulties and the final time of the analysis (10000 years) has not been yet achieved at the time of writing this contribution.

The general conclusion is that the formulation and constitutive model are able to simulate satisfactorily the set of isothermal benchmarks that have been proposed. The final state of the specimens is correctly reproduced including the high degree of homogenization that has been observed in both laboratory samples and engineered barriers (EB test) that started from a highly heterogeneous situation (presence of voids, combination of blocks and pellets). Final values of swelling pressure are also adequately predicted except in the cases where friction is dominant. It seems that the same basic constitutive model can be used for bentonite pellets and bentonite blocks, by choosing appropriate parameters.

The adoption of a double structure model that distinguishes between microstructure and macrostructure allows a modelling closer to the physical reality and provides enlightening insights on the progress of the saturation of the bentonite and of the associated mechanical effects. Comparison with MIP data has confirmed that the model does follow the observed fabric change trends correctly.

The success in reproducing the transient behaviour of the bentonite is more variable, good agreement with experimental observations in some cases are in contrast with other instances that exhibit significant differences between predictions and test results. Since transient behaviour is largely controlled by hydraulic phenomena, it may be simply the result of the high sensitivity of hydraulic processes to small variations of hydraulic conductivity, relative permeability and retention curves. This implies that perhaps more efforts should be made to determine precisely those model components. But it may also be necessary to accept that transient behaviour will always be subject to a higher degree of uncertainty. Sensitivity analysis may be the best way to bound those uncertainties.

Considering the model performance overall, it can be stated the formulation and constitutive model are both robust and operative. Against those advantages, it is necessary to weigh, however, the added complexity and cost of using a double structure model instead of a single porosity one. In this respect, the work performed and reported in the Beacon project provides relevant information for reaching a rational decision when designing the numerical analysis of a new problem.

The predictive power of the model that has not been explored in depth during the project. There has been a predictive exercise in WP5 that has met with a fair degree of success but the prediction case was quite similar to the tests used for calibration. The predictive power for other cases and across of a wider span of conditions remains basically unproved. It is expected that the predictive power will be higher with regard to the more robust results (swelling pressure, final degree of homogenization) than for more sensitive phenomena such as transient hydration.

6 Concluding remarks

The work within Beacon's WP3 has focused on the development, improvement and application of a double structure model described in this contribution. A significant development has been the incorporation of thermal effects in this type of framework, although at a simplified level so far. Overall, the model has proved capable of simulating satisfactorily the set of benchmarks that have been proposed in the project; in particular, the process of homogenization, the main goal of Beacon, is especially well captured. On the other hand, some differences with observations can be noted, in some cases, when modelling transient hydration phenomena. The double structure model provides information on the evolution of the microstructure during hydration and loading. Although the amount of experimental data in this regard is limited, the comparison of model results and MIP observations are encouraging. The model performed well in the only predictive exercise undertaken but its predictive power is largely unproven at this point.

References

- Alonso, E. E., Vaunat, J. & Gens, A., 1999.** Modelling the mechanical behaviour of expansive clays, *Engineering Geology*, 54, pp. 173–183.
- Gens, A., 1995.** Constitutive laws. In: *Modern issues in non-saturated soils. Edited by A. Gens, P. Jouanna & B. Schrefler. Springer-Verlag.* pp. 129-158.
- Gens, A. & Alonso, E. E., 1992.** A framework for the behaviour of unsaturated expansive clays, *Canadian Geotechnical Journal*, 29, pp. 1013–1032.
- Khalili, N., Uchaipichat, A. & Javadi, A.A., 2010.** Skeletal thermal expansion coefficient and thermo-hydro-mechanical constitutive relations for saturated homogeneous porous media, *Mechanics of Materials*, 42, pp. 593-598.
- Mašín, D. & Khalili, N., 2016.** Swelling phenomena and effective stress in compacted expansive clays, *Canadian Geotechnical Journal*, 53 (1), pp. 134-147.
- Olivella, S., 1995.** Nonisothermal multiphase flow of brine and gas through saline media. *PhD Thesis, Technical University of Catalonia.* Barcelona, Spain.
- Olivella, S. & Gens, A., 2000.** Vapour transport in low permeability unsaturated soils with capillary effects, *Transport in Porous Media*, 40, pp. 219-241.
- Olivella, S., Carrera, J., Gens, A. & Alonso, E.E., 1994.** Non-isothermal multiphase flow of brine and gas through saline media, *Transport in Porous Media*, 15, pp. 271-293.
- Olivella, S., Gens, A., Carrera, J. & Alonso, E.E., 1996.** Numerical formulation for a simulator (CODE_BRIGHT) for the coupled analysis of saline media, *Engineering Computations*, 13 (7), pp. 87-112.
- Romero, E., 1999.** Characterisation and thermo-hydro-mechanical behaviour of unsaturated Boom Clay: an experimental study. *PhD Thesis, Technical University of Catalonia.* Barcelona, Spain.
- Romero, E., Della Vecchia, G. & Jommi, C., 2011.** An insight into the water retention properties of compacted clayey soils, *Géotechnique*, 61 (4), pp. 313–328. doi: 10.1680/geot.2011.61.4.313.
- Sánchez, M., 2004.** Thermo-hydro-mechanical coupled analysis in low permeability media. *PhD Thesis, Technical University of Catalonia.* Barcelona, Spain.
- Sánchez, M., Gens, A., Guimarães, L. do N. & Olivella, S., 2005.** A double structure generalized plasticity model for expansive materials, *International journal for numerical and analytical methods in geomechanics*, (January 2004), pp. 751–787. doi: 10.1002/nag.434.
- Seiphoori, A., 2015.** Thermo-hydro-mechanical characterisation and modelling of Wyoming granular bentonite. *Technical Report 15-05.* Laussane.

Seiphoori, A., Ferrari, A. & Laloui, L., 2014. Water retention behaviour and microstructural evolution of MX-80 bentonite during wetting and drying cycles, *Géotechnique*, 64(9), pp. 721–734.

Vasconcelos, R., 2021. A double-porosity formulation for the THM behaviour of bentonite-based materials. *PhD Thesis, Technical University of Catalonia*. Barcelona, Spain.

Appendix 1

This appendix contains the tables of the model results for paths A-B-C-D and A-B'-C'.

Table A1-1. Results of the analysis for path A – B – C – D

	Total vertical stress (MPa)	Void ratio (-)	Suction (MPa)	Degree of saturation macro (%)	Degree of saturation micro (%)
Initial (A)	0.02	0.85	110.10	0.077	0.665
Swelling (A-B)	0.02	1.02	99.19	0.085	0.709
	0.02	1.23	83.59	0.103	0.779
	0.02	1.33	75.19	0.115	0.819
	0.02	1.43	66.79	0.132	0.858
	0.02	1.53	58.79	0.151	0.893
	0.02	1.62	51.19	0.177	0.923
	0.02	1.72	43.19	0.213	0.950
	0.02	1.83	35.19	0.266	0.971
	0.02	1.92	28.39	0.334	0.984
	0.02	2.01	21.19	0.445	0.993
	0.02	2.20	7.56	0.849	1.000
Compression (B-C-D)	0.02	2.32	0.01	1.000	1.000
	0.36	2.32	0.01	1.000	1.000
	0.56	2.32	0.01	1.000	1.000
	0.76	2.28	0.01	1.000	1.000
	0.96	2.14	0.01	1.000	1.000
	1.16	2.03	0.01	1.000	1.000
	2.18	1.68	0.01	1.000	1.000
	2.78 (1)	1.54	0.01	1.000	1.000
	4.16	1.31	0.01	1.000	1.000
6.76	1.04	0.01	1.000	1.000	
8.15	0.93	0.01	1.000	1.000	

(1) Value of the swelling pressure test in path A-B'-C' (point B'); Swelling pressure (Model) = 2.69 MPa

Table A1-2. Results of the analysis for path A – B' – C'

	Total vertical stress (MPa)	Void ratio (-)	Suction (MPa)	Degree of saturation macro (%)	Degree of saturation micro (%)
Initial (A)	0.02	0.85	110.10	0.077	0.665
Swelling pressure test (A-B')	0.14	0.85	109.75	0.077	0.666
	0.78	0.85	108.48	0.078	0.671
	1.75	0.85	106.80	0.079	0.677
	2.62	0.85	105.40	0.080	0.683
	5.37	0.85	100.63	0.084	0.703
	4.42	0.85	52.93	0.170	0.917
	3.71	0.85	30.91	0.306	0.980
	3.18	0.85	16.23	0.560	0.997
	3.05	0.85	12.56	0.671	0.998
	2.79	0.85	5.22	0.925	1.000
	2.71	0.85	2.62	0.982	1.000
	2.69	0.85	0.01	1.000	1.000
Compression (B'-C')	2.70	0.85	0.01	1.000	1.000
	3.28	0.76	0.01	1.000	1.000
	4.14	0.65	0.01	1.000	1.000
	4.50	0.60	0.01	1.000	1.000

Annex I

Contribution to Deliverable 3.3

DELIVERABLE (D3.3) ULg Report

Author(s):

Reporting period: 01/06/20 – 31/05/22

Date of issue of this report: 04/10/21

Start date of project: **01/06/17**

Duration: 60 Months

This project receives funding from the Euratom research and training programme 2014-2018 under grant agreement No 745 942		
Dissemination Level		
PU	Public	X
RE	Restricted to a group specified by the partners of the Beacon project	
CO	Confidential, only for partners of the Beacon project	

REVIEW

Name	Internal/Project/External	Comments
All Beacon partners	Project internal	

DISTRIBUTION LIST

Name	Number of copies	Comments
Seifallah BEN HADJ HASSINE (EC)	Digital	
Beacon partners	Digital	

Abstract

Briefly describe the activity that has been performed and results that have been obtained (include significant nonconformities from activity plan and method description)

Content

2	Ulg models	5
2.1	The LAGAMINE version of the Barcelona Basic Model	5
2.1.1	Description of the model	5
2.1.2	Basic capabilities of the model	9
2.1.3	Parameters calibration on oedometer test results	10
2.1.4	Validation of the BBM constitutive model	15
2.1.5	Parameters dependency on density	21
2.1.6	Alternative formulation for compressibility coefficient for change in suction	24
2.1.7	Task 3.3	26
2.2	Mohymar – A new double structure model	31
2.2.1	Description of the model	31
2.2.2	Basic capabilities of the model	33
2.2.3	Task 3.3	34
2.2.4	Performance of the model and assessment of predictive power	38
2.2.5	Concluding remarks	39

2 ULg models

Two constitutive models have been used for bentonite. The first one is an improved BBM, that was mostly existing at the project beginning. It has been extensively used. Its parameters calibration is largely discussed in this section. The second model has been developed during the project last year and has only be few used for the benchmark. This is a tool that will be much validated in the near future.

For some benchmarks, ULg has also used an interface finite element and constitutive model, that allows taking into account both unilateral contact and friction. This has helped to improve significantly our modelling capabilities. However, this model was still existing before the Beacon project beginning, and it has not been necessary to modify it for Beacon benchmarks.

2.1 The LAGAMINE version of the Barcelona Basic Model

2.1.1 Description of the model

The Barcelona Basic Model (BBM) was selected in order to describe the mechanical behaviour of low to moderate activity unsaturated soils such as bentonite based materials. This mechanic constitutive model will be adopted in all the numerical analyses presented in this thesis.

It was proposed by Alonso (Alonso, Gens, and Josa 1990), who pioneered the development of mechanical constitutive models for partially saturated soils. Most of the existing models for unsaturated soils rely indeed on the concepts developed in the BBM. The idea behind the model is the extension of the existing model for saturated soils to unsaturated conditions.

Accordingly, the behaviour of unsaturated soils should be modelled consistently and full saturation has to be considered as a limiting case. Therefore, the Barcelona Basic Model consists in the extension of the Modified Cam-Clay Model (Roscoe and Burland 1968) to unsaturated conditions, by using suction as an additional stress variable. It is formulated adopting net stress σ and suction s as stress variables.

It is worth reminding the definition of net stress σ :

$$\sigma = \sigma_T - u_a \mathbf{I} \quad \text{Eq. 2.1}$$

With σ_T the total stress tensor, u_a the air pressure for $s > 0$ and \mathbf{I} the identity tensor.

The model is first formulated for isotropic stress states and then it is progressively extended to triaxial and three-dimensional stress states.

Isotropic stress states

Volumetric behaviour

Mean net stress $p = \sigma_i$ and suction s are used to describe the mechanical state under isotropic stress conditions ($\sigma_1 = \sigma_2 = \sigma_3$).

As the Barcelona Basic Model corresponds to the Modified Cam-Clay Model (Roscoe and Burland 1968) in full saturated state, it belongs to the family of elastoplastic strain-hardening models.

Accordingly, the total volumetric strain increment of the soil $d\varepsilon_v$ is written as the sum of the elastic $d\varepsilon_v^e$ and plastic $d\varepsilon_v^p$ incremental volumetric strain components:

$$d\varepsilon_v = d\varepsilon_v^e + d\varepsilon_v^p \quad \text{Eq. 2.2}$$

In the elastic domain, the increment of volumetric strain associated to changes in mean net stress dp and suction ds is calculated as:

$$d\varepsilon_v^e = d\varepsilon_{vp}^e + d\varepsilon_{vs}^e = \frac{\kappa}{1+e} \frac{dp}{p} + \frac{\kappa_s}{1+e s + u_{atm}} \frac{ds}{s} = \frac{dp}{K} + \frac{ds}{K_s} \quad \text{Eq. 2.3}$$

Where $d\varepsilon_{vp}^e$ and $d\varepsilon_{vs}^e$ represent respectively the elastic volumetric strain associated to the change in net stress and the one related to the change in suction, e is the void ratio, u_{atm} is the atmospheric pressure and κ and κ_s are the elastic coefficients for change in net stress and suction, defining the slope of the elastic loading-unloading line in the $(p - e)$ space and of the wetting drying line in the $(s - e)$ space. In LAGAMINE BBM implementation and in the following numerical analyses, the elastic coefficient for change in net stress κ is considered constant, whereas a number of relations

have been proposed to define the elastic coefficient for change in suction κ_s , as it will be discussed in Section 4.4.5.

The Modified Cam-Clay Model considers non-linear elasticity. Namely, the bulk moduli K and K_s are respectively written as functions of the void ratio e and the mean net stress p and of the void ratio e and suction s summed to the atmospheric pressure u_{atm} according to:

$$K = \frac{(1+e)p}{\kappa} \quad K_s = \frac{(1+e)(s+u_{atm})}{\kappa_s} \quad \text{Eq. 2.4}$$

The plastic volumetric strain increment $d\varepsilon_v^p$ develops when the preconsolidation pressure $p_0(s)$ or/and the suction yield locus s_0 are reached, according to the increments dp and ds . The corresponding hardening law reads:

$$d\varepsilon_v^p = \frac{\lambda(s) - \kappa}{1+e} \frac{dp_0(s)}{p_0(s)} + \frac{\lambda_s - \kappa_s}{1+e} \frac{ds_0}{s_0 + u_{atm}} \quad \text{Eq. 2.5}$$

Where $\lambda(s)$ and λ_s are the plastic coefficients respectively for change in net stress and suction, defining the slope of the virgin compression line in the $(p - e)$ space and of the drying line in the $(s - e)$ space.

The slope $\lambda(s)$ of the virgin compression line and the yield stress $p_0(s)$ are functions of suction (Fig. 2.1 and Fig. 2.2). The plastic coefficient $\lambda(s)$ is calculated as:

$$\lambda(s) = \lambda(0)[(1-r)\exp(-\omega s) + r] \quad \text{Eq. 2.6}$$

with r and ω material parameter respectively related to the maximum stiffness of the soil ($\lambda(s) = r \times \lambda(0)$ when $s \rightarrow \infty$) and to the rate of the soil stiffness increase with suction.

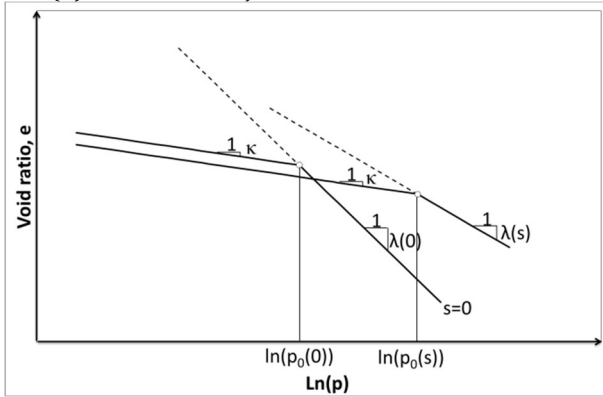


Fig. 2.1: Compression curves for saturated and unsaturated states (Alonso, Gens, and Josa 1990).

Yield surfaces and hardening laws

The BBM considers two yield loci in the plane $(s - p)$, for increase in suction (i.e. drying) and increase in net stress (i.e. loading). These latter are denoted SI (suction increase) and LC (loading collapse) curves (Fig. 2.2).

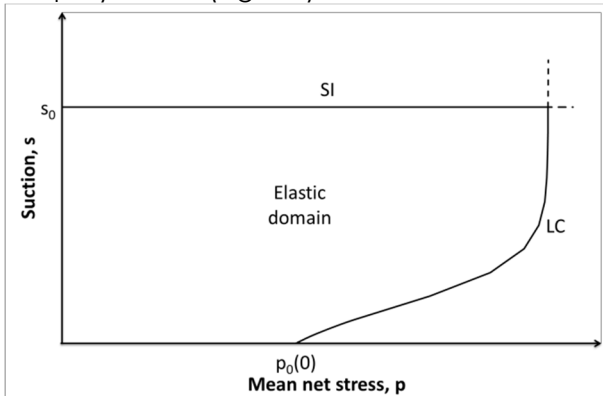


Fig. 2.2: Yield curves of the Barcelona Basic Model for isotropic stress states: Loading-Collapse (LC) and Suction Increase (SI) curves.

The evolution of the LC curve, in other terms “preconsolidation pressure $p_0(s)$ ” suction dependence, is modelled consistently with the concept of increasing the elastic domain with increasing suction, whereas the SI does not depend on net stress.

$$p_0(s) = p_c \left(\frac{p_0(0)}{p_c} \right)^{\frac{\lambda(0)-\kappa}{\lambda(s)-\kappa}} \text{Eq. 2.3} \quad f_{SI} \equiv s = s_0 \quad \text{Eq. 2.7}$$

where p_c is a reference net pressure and s_0 defines a threshold value of suction after which irreversible plastic strain develops for a given drying path. Irreversible plastic strains control the position of the LC and SI yield surfaces as follows:

$$\frac{dp_0(0)}{p_0(0)} = \frac{1+e}{\lambda(0)-\kappa} d\varepsilon_V^p \quad \frac{ds_0}{s_0 + u_{atm}} = \frac{1+e}{\lambda_s - \kappa_s} d\varepsilon_V^p \quad \text{Eq. 2.8}$$

Accordingly, the hardening of both yield surfaces is coupled because the total increment of plastic volumetric strain ε_V^p appears in both equations. Depending on the sign of the volumetric plastic strain, hardening or softening of the yield surface will take place.

Loading collapse curve

Two samples presenting initial state s_1 and p_1 in the $(p - s)$ plane are considered (Fig. 2.3). The stress states lay on the yielding curve LC_1 . The first sample is loaded from p_1 to p_2 at constant suction, following the path denoted L . Volumetric plastic strain is developed and the material undergoes hardening according to Eq. 2.8. The second sample is subjected to suction decrease at constant mean net stress. The material stress state evolves following the stress path denoted C . On the path C , elastic swelling and plastic collapse are computed. If the plastic collapse overcomes the elastic swelling, hardening occurs according to Eq. 2.8. In this latter case, the LC curve evolves similarly to the first case and irreversible volumetric plastic strain is obtained. As a result, the Loading-Collapse curve principle enables consistent modelling of compressive strains due to loading and collapse strains due to wetting.

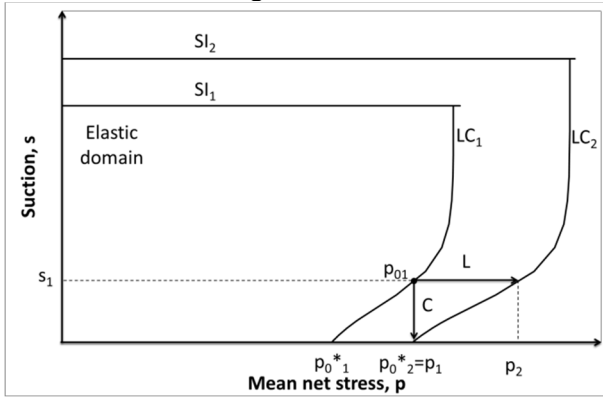


Fig. 2.3: Effects of loading at constant suction (L) and wetting at constant mean net stress (C) on the LC curve

Triaxial test stress states

Under triaxial test conditions ($\sigma_1 \neq \sigma_2 = \sigma_3$), the mechanical stress state can be described by the mean net stress p , suction s and the deviatoric stress $q = \sigma_1 - \sigma_3$ (see Fig. 2.4).

Deviatoric behaviour

The deviatoric strain ε_d can be generally defined as:

$$\varepsilon_d = \frac{\sqrt{2}}{3} \sqrt{(\varepsilon_1 - \varepsilon_2)^2 + (\varepsilon_1 - \varepsilon_3)^2 + (\varepsilon_2 - \varepsilon_3)^2} \quad \text{Eq. 2.9}$$

In the elastic domain, the deviatoric deformation due to the deviatoric stress is given:

$$d\varepsilon_d^e = \frac{1}{3G} dq \quad \text{Eq. 2.10}$$

where $d\varepsilon_d^e$ is the deviatoric strain elastic increment and G is the shear modulus.

This modulus can be set as a constant value or as a function of the bulk modulus K , as shown below:

$$G = \frac{3(1-2\nu)K}{2(1+\nu)} \quad \text{Eq. 2.11}$$

Yield surfaces and hardening laws

In the $(p - q)$ plane, the yield surface is expressed (see Fig. 2.4):

$$f_{LC} \equiv q^2 - M_\theta^2(p + p_s)(p_0 - p) = 0 \quad \text{Eq. 2.12}$$

M_θ is the critical state line slope, p_s is the yield surface left intercept and p_0 is the apparent preconsolidation pressure at a suction s .

The friction angle φ is related to the slope of the critical state line M_θ via:

$$M_\theta = \frac{6 \sin \varphi}{3 - \sin \varphi} \quad \varphi = \arcsin \frac{3M_\theta}{6 + M_\theta} \quad \text{Eq. 2.13}$$

The left intercept of yield surface p_s increases with increasing cohesion. It can be given as a function of suction:

$$p_s(s) = \frac{c(s)}{\tan \varphi} = \frac{c(0) + ks}{\tan \varphi} \quad \text{Eq. 2.14}$$

with $c(0)$ the cohesion under saturated conditions and k a parameter controlling the increase of cohesion with suction.

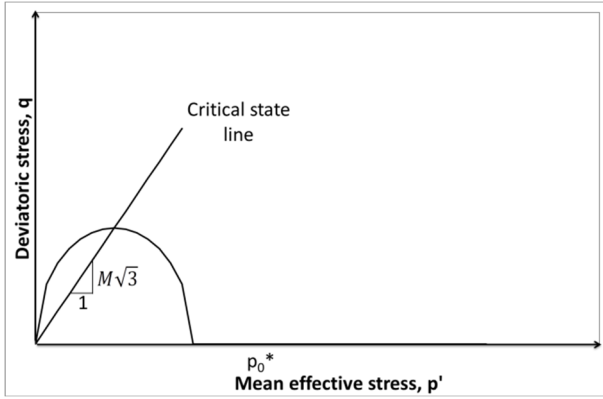


Fig. 2.4: Modified Cam-Clay Model.

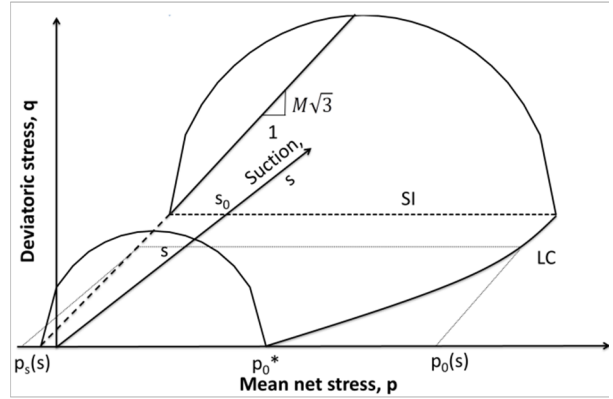


Fig. 2.5: Barcelona Basic Model.

A non-associated flow rule completes the Barcelona Basic Model's triaxial formulation. The following non-associated flow rule reads:

$$\frac{d\varepsilon_d^p}{d\varepsilon_v^p} = \frac{2q\alpha}{M_\theta^2(2p + p_s - p_0)} \quad \text{Eq. 2.15}$$

where α is set so that Eq. 2.15 predicts zero lateral strain for stress states corresponding to Jacky's K_0 values, i.e.:

$$\alpha = \frac{M_\theta(M_\theta - 9)(M_\theta - 3)}{9(6 - M_\theta)} \frac{1}{1 - \frac{\kappa}{\lambda(0)}} \quad \text{Eq. 2.16}$$

As a result, the flow surface is equal to:

$$g_{LC} \equiv \alpha q^2 - M_\theta^2(p + p_s)(p_0 - p) = 0 \quad \text{Eq. 2.17}$$

Three dimensional stress states

The mechanical stress state is represented under three-dimensional conditions the mean net stress p , suction s , the second invariant of the deviatoric stress tensor J_2 and the Lode's angle θ , which are given by:

$$J_2 = \sqrt{\frac{1}{2} \mathbf{s} : \mathbf{s}} \quad \theta = -\frac{1}{3} \sin^{-1} \left(\frac{3\sqrt{3} J_3}{2 J_2^2} \right) \quad J_3 = \frac{1}{3} \sigma_{ij} \sigma_{jk} \sigma_{ki} \quad \text{Eq. 2.18}$$

where \mathbf{s} is the deviatoric stress tensor given by $\mathbf{s} = \boldsymbol{\sigma}_T - p\mathbf{I}$, the Lode's angle θ gives the direction of the stress path in the deviatoric plane and J_3 the third invariant of the deviatoric stress tensor.

The stress increment is connected to the strain and suction increments in the elastic domain via:

$$d\boldsymbol{\sigma} = \mathbf{D}^e : d\boldsymbol{\varepsilon}^e + \boldsymbol{\alpha}_s ds \quad \text{Eq. 2.19}$$

where \mathbf{D}^e is the global elastic tensor and $\boldsymbol{\alpha}_s$ is the elastic tensor for suction changes, and they are calculated as follows:

$$D_{ijkl}^e = 2G\delta_{ik}\delta_{jl} + \left(K + \frac{2}{3}G\right)\delta_{ij}\delta_{kl} \quad \boldsymbol{\alpha}_s = \frac{1}{K_s}\mathbf{D}^e : \mathbf{I} \quad \text{Eq. 2.20}$$

Where K , G and K_s have already been discussed in the previous section.

Yield surfaces and hardening laws

The yield surface that limits the elastic domain is represented as shown in:

$$f_{LC} \equiv 3J_2^2 - M_\theta^2(p + p_s)(p_0 - p) = 0 \quad \text{Eq. 2.21}$$

where M_θ is the slope of the critical state line, p_s considers the dependence of shear strength on suction and p_0 is the apparent preconsolidation pressure at a suction s .

The slope of the critical state line M_θ in three-dimensional stress states is a function of the Lode angle θ and defines the shape of the failure surface in the deviatoric plane. The van Eekelen (van Eekelen 1980) model is used to approximate the Mohr-Coulomb failure criterion. As a result, the critical state line slope M_θ is equal to:

$$M_\theta = a(1 + b\sin 3\theta)^n \quad \text{Eq. 2.22}$$

where the parameter n is a constant that determines the convexity of the failure surface in the deviatoric plane and it is set to -0.229 to ensure the convexity of the surface ((van Eekelen 1980), (Barnichon 1998)) and a and b are proportional to the triaxial compression and extension friction angles φ_C and φ_E

$$a = \frac{r_C}{(1+b)^n} \quad b = \frac{\left(\frac{r_C}{r_E}\right)^{1/n} - 1}{\left(\frac{r_C}{r_E}\right)^{1/n} + 1} \quad \text{Eq. 2.23}$$

$$r_C = \frac{2\sin\varphi_C}{\sqrt{3}(3 - \sin\varphi_C)} \quad r_E = \frac{2\sin\varphi_E}{\sqrt{3}(3 + \sin\varphi_E)}$$

where r_C and r_E are the reduced radii for axisymmetric triaxial stress paths of compression and extension.

The expression of the SI yield surface remains:

$$f_{SI} \equiv s = s_0 \quad \text{Eq. 2.24}$$

With flow surface corresponding to the LC surface as:

$$g_{LC} \equiv \alpha 3J_2^2 - M_\theta^2(p + p_s)(p_0 - p) = 0 \quad \text{Eq. 2.25}$$

2.1.2 Basic capabilities of the model

The model is able to reproduce the essential aspects of the behaviour of unsaturated clays: swelling/shrinkage upon hydration/drying; macrostructural swelling resulting from microstructural swelling; evolution of strength and stiffness with suction; plastic collapse upon wetting.

Regarding the hydromechanical behaviour of compacted bentonite, capabilities of the model are detailed in Table 3.

Table 1. Model capabilities

Name of the constitutive law:		BBM-ULiege
Behaviour feature	D3.3	Remarks
Mechanical behaviour		
Dependence of swelling strain on applied stress (at the same dry density)	Y	
Dependence of swelling stress on dry density (at the same stress)	Y	
Irreversibility of strains in wetting/drying cycles	N	
Dependence of swelling pressure on dry density	Y	
Stress path dependence from an unsaturated to a saturated state	Y	
Stress path dependence from a saturated to an unsaturated state	Y	
Double structure/porosity considered?	N	
Are temperature effects considered in the model?	N	
Dependence of strains developed in a temperature cycle (increase/decrease) on OCR (or stress)	-	Temperature effects not considered
Hydraulic behaviour (retention curve)		
Hysteresis	N	Only if irreversible change in void ratio occurs
Dependence on void ratio	Y	
Double structure/porosity considered?	Y	

2.1.3 Parameters calibration on oedometer test results

Oedometer swelling consolidation tests are often preferred to triaxial (i.e. isotropic) ones due to their more simple feasibility in laboratory conditions (Gens and Alonso 1992). However, one major disadvantage of this type of test is that radial pressure is not generally measured and is thus ignored in the studies. In this paragraph, taking advantage of BBM framework, some experimental observations are analysed and compared accounting for the possible influence of this latter feature.

(A. Dueck and Nilsson 2010) performed numerous swelling at constant vertical stress in oedometer conditions on compacted MX80 samples. Test labelled 02_0705 is accounted as example (Fig. 2.6, Fig. 2.7 and Fig. 2.9). The sample is compacted presenting initial diameter $D=34.64$ mm, void ratio equal to $e=0.58$, water content equal to $w=9.55\%$ and saturation equal to $S_r=46.18\%$. It is successively placed in an oedometer ring and let it stabilise in order to obtain diameter $D=35$ mm, void ratio equal to $e=0.61$, water content equal to $w=9.55\%$ and saturation equal to $S_r=43.7\%$.

Hydration at constant vertical stress path is analysed. Axial and radial stresses, together with axial deformation (i.e. void ratio) and relative humidity and temperature (i.e. suction) are continuously measured. Radial stress and void ratio time and suction evolutions are reported respectively in Fig. 2.6 and Fig. 2.7. While full contact with the cell wall is established, radial stress quickly increases upon suction decrease up to $s=70$ MPa, then it reaches a peak value and starts to decrease. The void ratio continuously increases upon hydration. Axial stress remains constant at about 3 MPa.

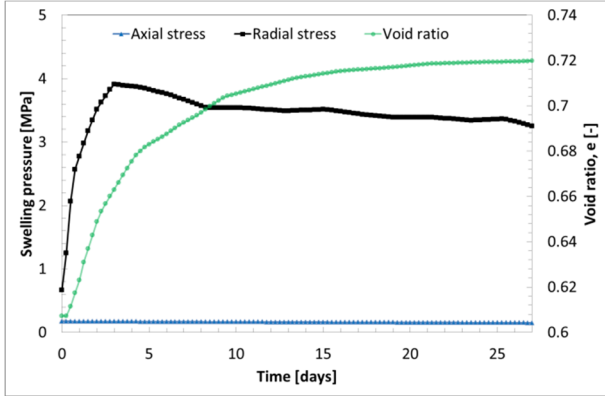


Fig. 2.6: Axial and radial stress and void ratio time evolution. Experimental results on compacted MX80 (A. Dueck and Nilsson 2010).

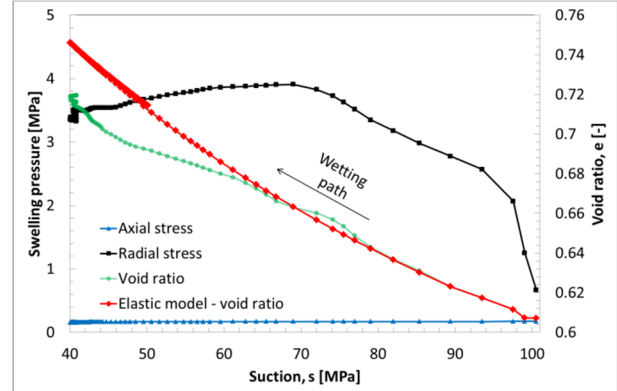


Fig. 2.7: Axial and radial stress and void ratio suction evolution. Experimental results on compacted MX80 modified after (A. Dueck and Nilsson 2010) and elastic model.

Taking advantage of the elastoplastic framework formulated in the BBM, further observations can be done in the $(p - s)$ (Fig. 2.8) and in the $(p - q)$ plane (Fig. 2.9). Mean stress increases from 0.5 MPa to 1.6 MPa at about constant suction until full contact between the bentonite sample and the cell ring takes place (Fig. 2.8). After that, the mean (radial) stress increase becomes more evident for suction decrease. The mean (radial) stress development is increasing until the elastic limit (i.e. yielding surface), then it decreases, possibly following the yielding surface, while remaining almost constant. The radial swelling pressure at suction $s=40$ MPa is equal to 3.5 MPa, whereas the void ratio $e=0.70$. The resulting water content is equal to $w=16.18\%$ (and saturation $S_r=64.19\%$). The test conditions (i.e. oedometric swelling at constant and low axial stress) result in the development of high stress deviator (Fig. 2.9). Due to the radial stress development at constant axial stress, the deviatoric stress q reaches 4 MPa with slope equal to 1.5 in the $p - q$ plane. The stress deviator successively decreases until 3 MPa with slope equal to 1.5 (but always related to oedometer conditions).

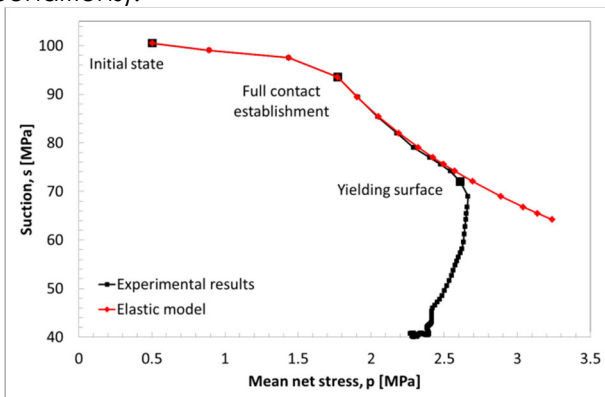


Fig. 2.8: Stress path in the $(p - s)$ plane. Comparison between experimental data and elastic model results modified after (A. Dueck and Nilsson 2010)

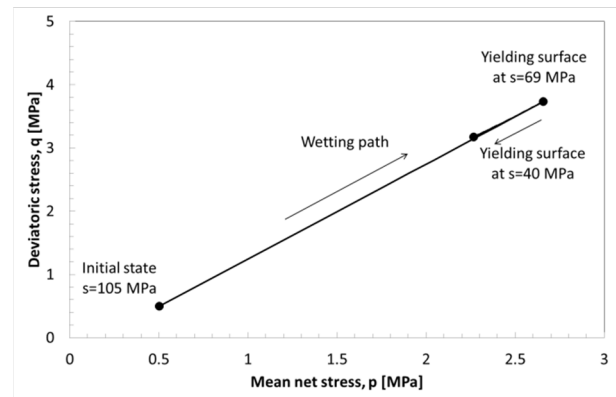


Fig. 2.9: Stress path in the $(p - q)$ plane. Experimental data modified after (A. Dueck and Nilsson 2010).

The elastic radial stress development resulting from BBM (see APPENDIX A for complete analytical development) during wetting at constant vertical stress reads as follows:

$$\sigma_{rB} = \frac{1}{2} \left[(\sigma_{a,0} + 2\sigma_{rA}) \left(\frac{S_A + u_{atm}}{S_B + u_{atm}} \right)^{\frac{\kappa_s}{\kappa} \frac{2(1-2\nu)}{3(1-\nu)}} - \sigma_{a,0} \right] \quad \text{Eq. 2.26}$$

It can be seen that it is function of the elastic compressibility coefficient of change in net stress κ , of the elastic compressibility coefficient of change in suction κ_s and of the Poisson's ratio ν . On the other hand, the void ratio evolution in elastic domain is obtained via:

$$e_B = -\kappa_s \frac{(1 + \nu)}{3(1 - \nu)} \ln \left(\frac{s_A + u_{atm}}{s_B + u_{atm}} \right) + e_A \quad \text{Eq. 2.27}$$

Being function of κ_s and ν only.

Eq. 2.27 is similar to Eq. 2.28, which would be obtained by the integration of Eq. 2.3 in the case of wetting at constant isotropic stress.

$$e_B = -\kappa_s \ln \left(\frac{s_A + u_{atm}}{s_B + u_{atm}} \right) + e_A \quad \text{Eq. 2.28}$$

It follows that the elastic volume increase upon wetting obtained in oedometer conditions (i.e. constant vertical stress) is smaller with respect to the one which would result under wetting at constant isotropic stress (Fig. 2.10).

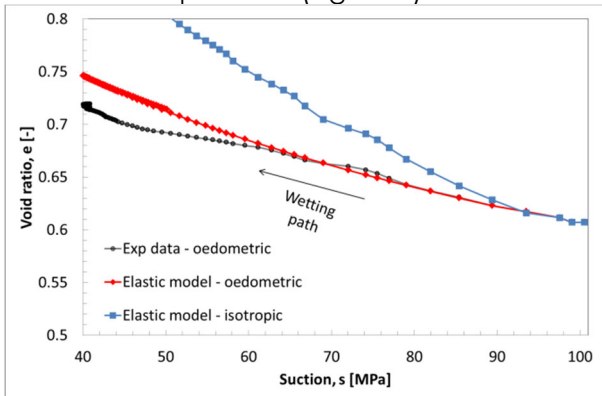


Fig. 2.10: Void ratio suction evolution. Comparison between experimental data modified after (A. Dueck and Nilsson 2010) and elastic model responses in oedometer and isotropic conditions.

It can be seen that for increasing Poisson coefficient, increasing deformation and decreasing radial swelling pressure development are obtained. For $\nu = 0.2$ the exponents of Eq. 2.26 and Eq. 2.27 are both divided by a factor 2 (i.e. multiplied by 0.5). It means that the developed elastic radial swelling stress is half with respect to the one that would be computed during hydration in constant volume conditions and the swelling deformation is half with respect to the one that would be obtained during hydration at constant isotropic stress.

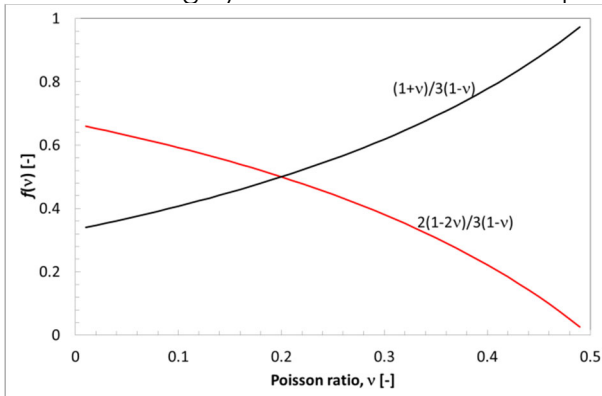


Fig. 2.11: Eq. 2.26 and Eq. 2.27 function dependency on Poisson ratio ν (for constant κ and κ_{s0}).

Finally, it can be assumed that the simultaneous analyses of radial stress, suction and deformation measurements upon wetting at constant stress allow evaluating the parameters triplet of κ , κ_s and ν that can be used in the BBM.

The analysis of the presented experimental test conducted on MX80 bentonite compacted at initial dry density equal to $\rho_d = 1.70 \text{ Mg/m}^3$ permits determining the following triplet: $\kappa = 0.085$, $\kappa_s = 0.300$ and $\nu = 0.23$.

Let us now consider the second phase of the classic oedometer swelling consolidation tests: the vertical compaction phase. For this purpose, the axial stress is increased from 0.1 MPa to 8 MPa at

constant suction $s=40$ MPa. At the same time, radial stress and axial deformation are measured (Fig. 2.12).

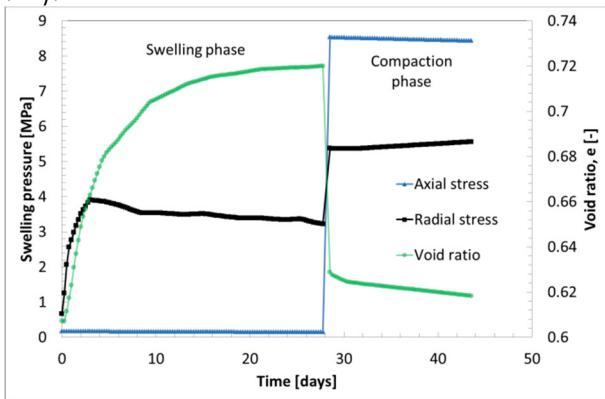


Fig. 2.12: Axial and radial stress and void ratio time evolution. Experimental results on compacted MX80

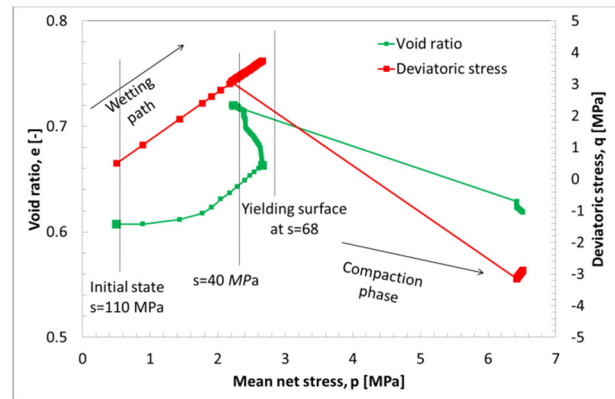


Fig. 2.13: Void ratio and deviatoric stress as function mean net stress. Experimental results on compacted MX80 modified after (A. Dueck and Nilsson 2010).

The deviatoric stress q evolution with respect to mean net stress p follows the slope of -1.5 for axial stress increase accordingly to oedometer compaction conditions (Fig. 2.13).

It is possible to obtain from the $(p - e)$ plane (Fig. 2.13) the slope of the compaction curve, which corresponds to $\kappa = 0.085$, namely the value computed via the elastic model.

Moreover, if oedometric compaction path is considered, the ratio between the horizontal and vertical stresses depends on the Poisson ratio only via Eq. 2.29.

$$\frac{\sigma_h}{\sigma_v} = \frac{\nu}{1 - \nu} \qquad \frac{\Delta\sigma_h}{\Delta\sigma_v} = \frac{\nu}{1 - \nu} \qquad \text{Eq. 2.29}$$

By analysing the axial and radial stress measurements, it is possible to validate the Poisson's ratio value $\nu = 0.23$ determined in the swelling at constant vertical stress phase.

The stress values accounted in these test are relatively low with respect to the suction level, thus it is not possible to determine an additional point of the yielding surface in the $(p - q)$ and $(p - e)$ planes, which would help to define the size of the elastic domain.

For sake of completeness, void ratio evolution as function of vertical net stress is presented in Fig. 2.14. The slope of the elastic path results much lower with respect to the results obtained by considering the mean net stress (i.e. the material looks stiffer). Hence, it is worth reminding that when radial stress measurements are not available, oedometer compaction tests need to be read carefully and the elastic compressibility coefficient has to be modified consistently.

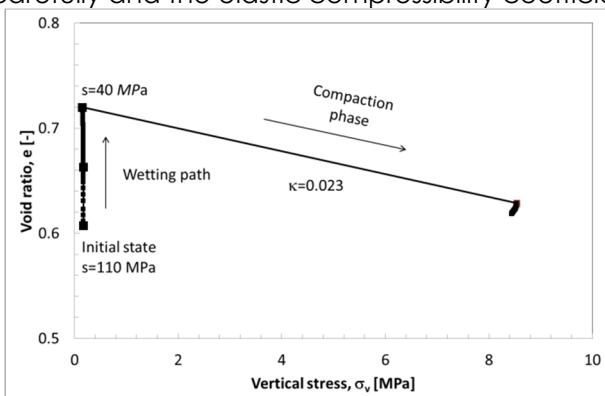


Fig. 2.14: Void ratio as function vertical net stress. Experimental results on compacted MX80 (A. Dueck and Nilsson 2010).

The above computed triplet of elastic parameters is applied to predict the elastic behaviour of MX80 bentonite investigated by (Villar 2005). This further comparison is given in order to assess the reliability of the above presented parameters determination procedure.

(Villar 2005) performed suction controlled oedometer tests to study one-dimensional compressibility of compacted MX80 bentonite. The specimens were obtained by uniaxial compaction of the clay directly in the oedometer ring. The clay was previously mixed with deionised water to reach water

content equal to $w=17\%$. The initial height of the specimen was $H=1.20$ cm with diameter $D=4.95$ cm and dry density $\rho_d=1.69$ g/cm³. The compaction pressure required to achieve this dry density was 32 MPa. The tests were performed at a constant temperature of $T=20^\circ\text{C}$. The samples have been subjected to hydration under a low vertical load and, once saturated, they have been loaded.

Fig. 2.15 shows the void ratio evolution as function of suction and the elastic model response with the parameters $\kappa_s = 0.300$ and $\nu = 0.23$. Information with respect to radial stress development is not provided, thus no further validation on the proposed procedure can be given.

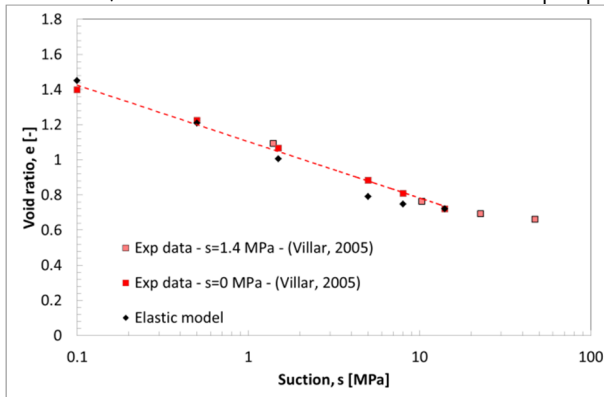


Fig. 2.15: Void ratio suction evolution. Experimental results on compacted MX80 (Villar 2005) and elastic model.

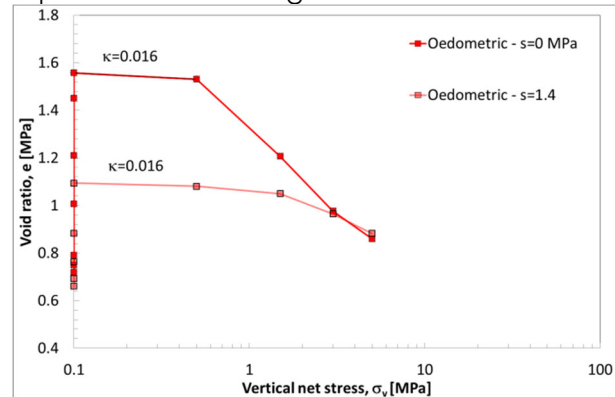


Fig. 2.16: Void ratio as function vertical net stress. Experimental results on compacted MX80 (Villar 2005)

For sake of completeness, the compaction phase results are given in Fig. 2.16. The elastic compressibility coefficient for change in stress can be computed considering the slope of the elastic loading path. The obtained value is equal to 0.016, which is much lower with respect to $\kappa = 0.085$ (i.e. the slope in the space $(p - e)$), but much closer to 0.023 (given in the $(\sigma_v - e)$ of Fig. 2.14). Information on the elastic domain size is provided in this case (Fig. 2.16). The change of slope allows determining the limit of the space in which the material elastic-reversible behaviour is shown (i.e. yielding surface) and the plastic compressibility coefficient for change in net stress λ at the analysed suction levels.

The one-dimensional compressibility behaviour of the compacted MX80 is compared to the isotropic one in Fig. 2.17. For this purpose, experimental swelling-isotropic consolidation tests by (Tang and Cui 2010) are presented. The sample was obtained via static compaction under an isotropic pressure of 40 MPa and suction $s=110$ MPa. After compaction, the soil specimen was placed in a chamber at a relative humidity of 44% and a temperature of 20°C . This procedure allowed obtaining compacted soil specimens with a dry density $\rho_d=1.78\pm 0.3$ Mg/m³ and a void ratio $e = 0.55\pm 0.3$.

Fig. 2.17 shows the above-mentioned discrepancies on the elastic paths of the analysed specimens (i.e. different slope). On the other hand, with respect to the elastoplastic behaviour, it is possible to see that at saturation the compressibility is nicely comparable. Hence, oedometric plastic compressibility can be adopted for isotropic models. One final remark on the yield loci determined in oedometer conditions is necessary. It may appear that the elastic limit is larger with respect to the isotropic one (Fig. 2.17). However, as Eq. 2.29 reports, the radial stress and consequentially the mean net stress are always smaller than the vertical one.

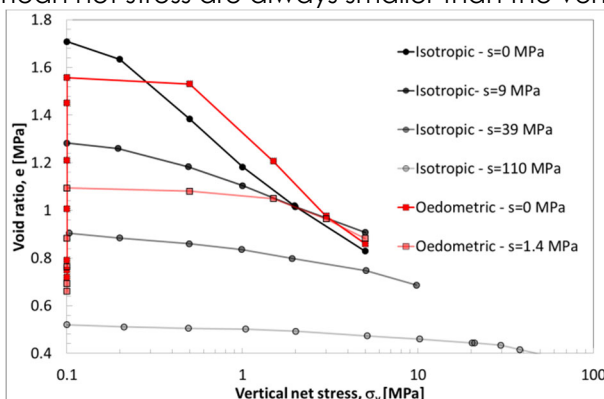


Fig. 2.17: Void ratio as function vertical net stress. Experimental results for oedometer compaction (Villar 2005) and isotropic compaction (Tang and Cui 2010) on compacted MX80.

2.1.4 Validation of the BBM constitutive model

The Barcelona Basic Model is validated against experimental data on bentonite-based materials from the literature. Three types of bentonites are considered, namely Febex (compacted and pellets mixtures), MX80 and sand mixture and pure MX80 (compacted and pellets mixture). In addition, based on experimental observations, the mechanic parameters for pure MX80 at a different dry density are also determined. The BBM mechanical parameters can be found in Table 2.2.

Febex bentonite

Compacted Febex

(Lloret et al. 2003) performed suction-controlled oedometer tests on compacted Febex bentonite. The samples were compacted at an initial dry density of $\rho_d = 1.70 \pm 0.02 \text{ Mg/m}^3$ and water content equal to $w = 13.55 \pm 0.65\%$. Suction levels equal to 127 MPa, 14 MPa, 4 MPa and 0 MPa were taken into account in order to consider the compressibility properties evolution. With respect to the experimental procedure: each sample reaches the given level of suction under a vertical load of 0.1 MPa, it is successively compacted. The experimental data and the model response correspond remarkably well (Fig. 2.18). Swelling strain increases and plastic compressibility and preconsolidation pressure decrease as the suction reduces, both in experimental and numerical cases. Calibrated parameters for the BBM are reported in Table 2.2.

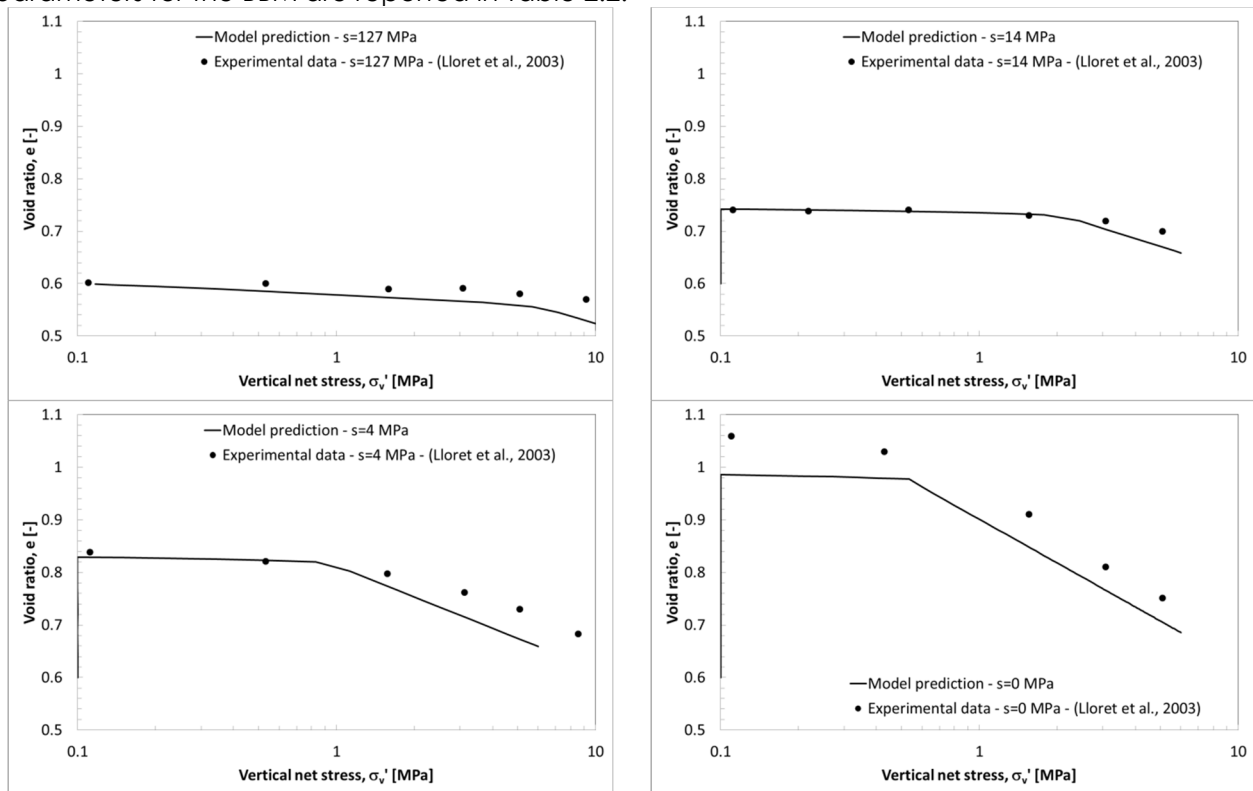


Fig. 2.18: Controlled-suction oedometer tests on compacted Febex bentonite. Comparison between experimental data (Lloret et al. 2003) and model responses on loading paths.

Table 2.2: Parameters for Barcelona Basic Model for commercial bentonites.

			Compacted Febex	Pellet Febex	MX80/Sand	Pellet MX80	Compacted MX80	Compacted MX80
ρ_d	[Mg/m ³]	Dry density	1.60	1.28	1.69	1.50	1.69	1.50
κ	[-]	Elastic compressibility coefficient for changes in mean net stress	0.012	0.074	0.025	0.06	0.007	0.03
κ_s	[-]	Elastic compressibility coefficient for changes in suction	0.12	0.075	0.073	0.08	0.340	0.220
α_p	[Pa ⁻¹]	Parameter controlling the stress dependency of the swelling strain for change in suction	4.4×10^{-8}	3×10^{-6}	2.6×10^{-7}	2.6×10^{-7}	1.5×10^{-7}	3.5×10^{-7}
p_0^*	[MPa]	Pre-consolidation pressure for saturated state	1.6	0.65	1.4	1.86	0.15	0.3
p_c	[MPa]	Reference pressure controlling the shape of the LC curve	0.395	0.325	0.01	0.93	0.02	0.086
$\lambda(0)$	[-]	Slope of the saturated virgin consolidation line	0.12	0.20	0.12	0.20	0.25	0.25
r	[-]	Parameter defining the minimum soil compressibility	0.55	0.70	0.80	0.75	0.32	0.32
ω	[MPa ⁻¹]	Parameter controlling the soil stiffness	0.25	0.008	0.09	0.10	0.051	0.051
ϕ	[°]	Friction angle	20	26	25	25	10	20
ν	[-]	Poisson ratio	0.25	0.35	0.35	0.40	0.17	0.17
$c(0)$	[MPa]	Cohesion in saturated conditions	0	0	0.1	0.1	0.1	0.10
k	[-]	Parameter controlling the increase of cohesion of increase of suction	0.0046	0.0046	0.046	0	0	0.0046

Febex Pellets

Febex pelletized material was exhaustively investigated by (Alonso, Hoffmann, and Romero 2010) in the context the EB test (Chapter 7). Suction controlled oedometer tests were performed on the typical bentonite dry densities obtained via pneumatic injection techniques equal to $\rho_d=1.30 \text{ Mg/m}^3$ and $\rho_d=1.50 \text{ Mg/m}^3$. In this thesis, Febex pellets material at $\rho_d=1.30 \text{ Mg/m}^3$ will be considered in the framework of the EB test analysis, thus attention is focused on this one. Fig. 2.19 presents oedometer compression at suction $s=60 \text{ MPa}$. The numerical response well reproduces the experimental data. Compressibility and swelling properties are calibrated in order to reproduce reference work experimental results (Hoffmann, Alonso, and Romero 2007). The calibrated data can be found in Table 2.2.

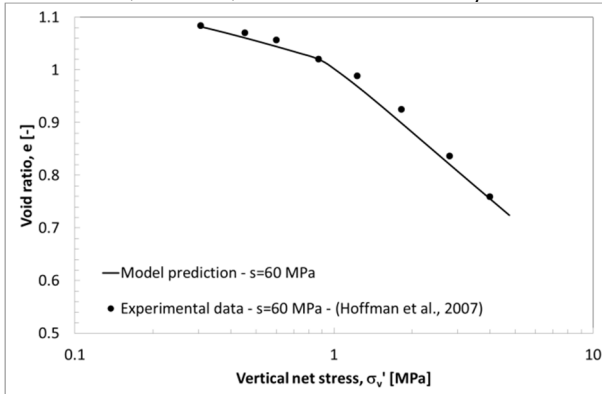
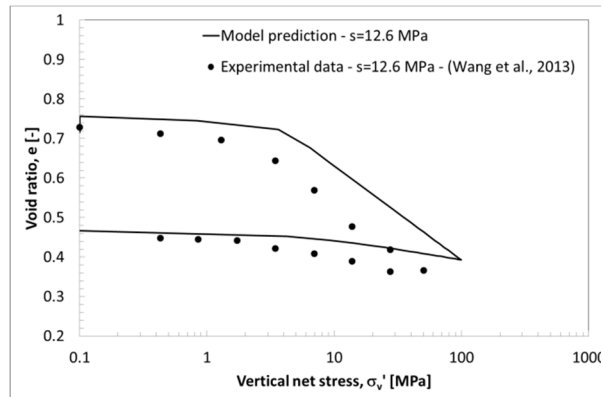
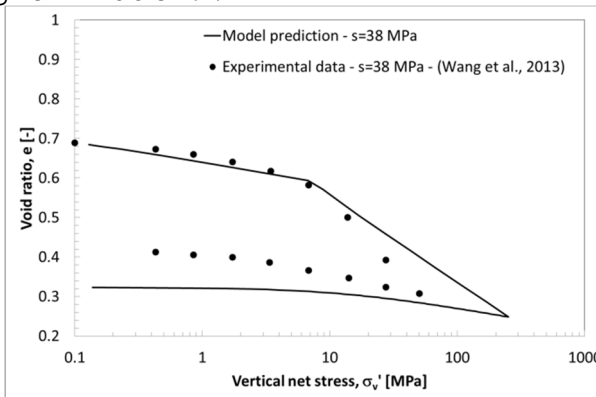


Fig. 2.19: Controlled-suction oedometer tests on Febex pellets bentonite. Comparison between experimental data (Hoffmann, Alonso, and Romero 2007) and model responses on loading paths.

Compacted MX80 and sand mixture

(Wang, Tang, et al. 2013) performed suction-controlled oedometer tests on MX80 bentonite-sand mixture with respective proportion of 70/30 in dry mass. The samples were compacted at an initial dry density of $\rho_d=1.67 \text{ Mg/m}^3$ and water content equal to $w=11\%$. The suction values taken into account are 4.2 MPa, 12.6 MPa and 38 MPa. With respect to the experimental procedure: each sample reaches the given level of suction under a vertical load of 0.1 MPa, it is successively compacted to a vertical stress of 50 MPa and finally unloaded.

The experimental data and the model response are represented in Fig. 2.20. The model is able to well reproduce the swelling deformation during the hydration together with the compaction strain obtained upon loading. It is possible to tackle the increase of stiffness with increasing suction as well as the increase of preconsolidation pressure with increasing suction. The calibrated mechanical parameters obtained for the numerical modelling of this test are given in Table 2.2.



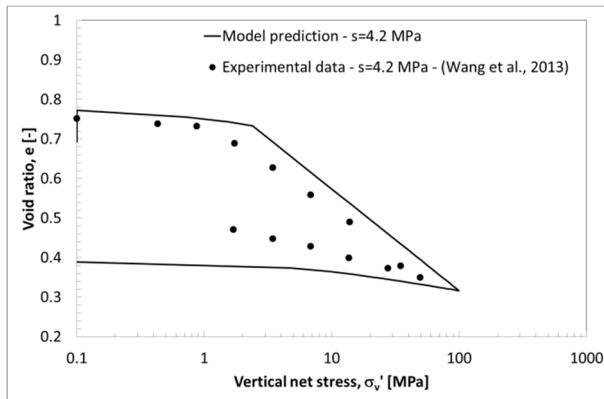


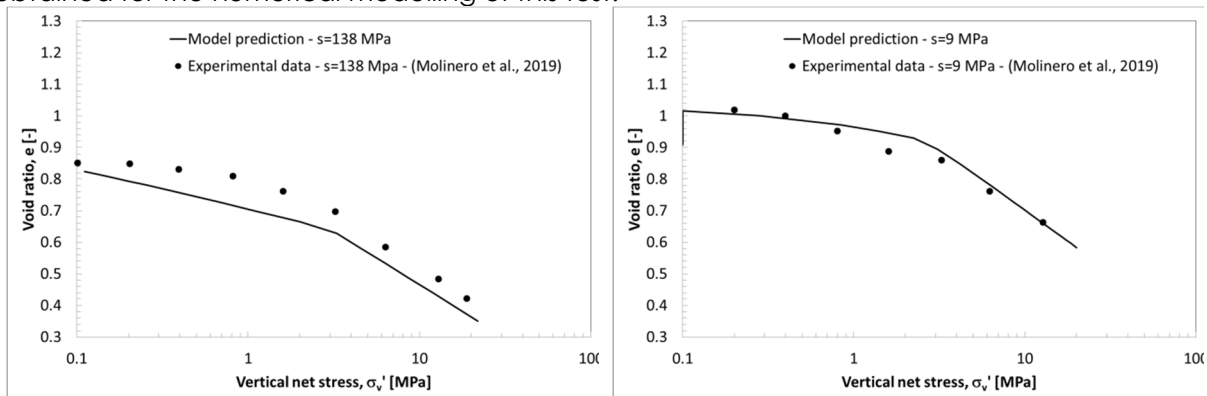
Fig. 2.20: Controlled-suction oedometer tests on MX80/sand mixture bentonite (proportion 70/30). Comparison between experimental data (Wang, Tang, et al. 2013) and model responses on loading and unloading paths.

**Pure MX80
MX80 Pellets**

(Molinero et al. 2019) investigated the hydro-mechanical behaviour of MX80 bentonite pellet/powder mixture at a proportion of 80/20 in dry mass via swelling-consolidation tests. Pellets were produced in the Laviosa-MPC company by instantaneously compacting MX80 bentonite in a mould of 7mm in diameter and 7 mm in height. The fabrication water content was $w=6.0 \pm 1.0\%$ and the dry density was $\rho_d=2.06 \pm 0.06 \text{ Mg/m}^3$ with initial suction ($s=135 \pm 3 \text{ MPa}$). The MX80 bentonite powder was produced by crushing pellets just after their fabrication. The maximum size of grains was 2 mm and the portion of the grains smaller than $80 \mu\text{m}$ was 5%. An initial water content of $w=3.2 \pm 1.0\%$ was found in the laboratory by oven-drying at $105 \text{ }^\circ\text{C}$ for 24 h, corresponding to an initial suction $s=191 \text{ MPa}$.

The mixture was prepared by filling the cell by packets corresponding to one layer of pellets spread over the base of the cylinder, with the corresponding amount of powder, respecting the proportion of 80-pellets/20-powder. The global dry initial density of the mixture thus prepared was 1.49 Mg/m^3 . The analysed compressibility properties are related to suction values equal to 0, 9 and 138 MPa, applying the selected value of relative humidity with vapour. Swelling strains upon wetting were recorded as well as the compressive strain due to the applied loading.

Fig. 2.21 depicts the experimental data and the model response. The model reproduces the swelling deformation that appears during hydration, as well as the compaction strain that develops during loading. Increasing stiffness and preconsolidation pressure are both well addressed for increasing suction also in this case of initial heterogeneous macrostructure and dry density distribution. Table 2.2 summarizes the calibrated mechanical parameters obtained for the numerical modelling of this test.



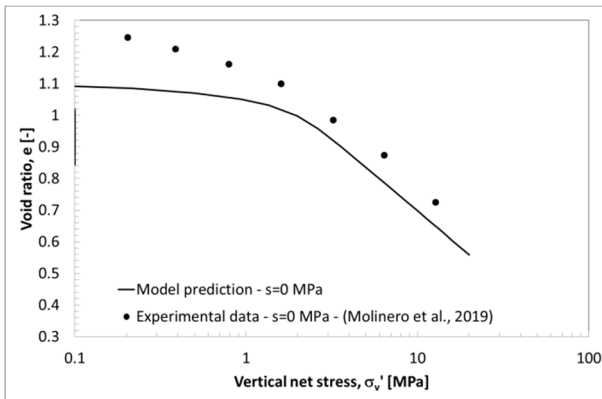


Fig. 2.21: Controlled-suction oedometer tests on MX80 pellets bentonite. Comparison between experimental data (Molinero et al. 2019) and model responses on loading paths.

Compacted MX80

(Tang, Cui, and Barnel 2008) performed suction-controlled isotropic compression tests on pure MX80 compacted bentonite. Prior to utilization, the clay was sieved at 2 mm and dried at 44% of relative humidity, which corresponded to a suction $s=110$ MPa at temperature $T=20$ °C. After reaching equilibrium, the soil water content was $w=10\% \pm 2\%$. Then the soil was statically compacted under an isotropic pressure of 40 MPa. After compaction, the soil specimen was placed in a chamber at a relative humidity of $RH=44\%$ and a temperature of $T=20$ °C. This procedure allowed obtaining compacted soil specimens with a dry density $\rho_d=1.78 \pm 0.3$ Mg/m³ and void ratio $e=0.55 \pm 0.3$. The considered suction levels were 110 MPa, 39 MPa and 9 MPa. The comparison between the experimental data and the model predictions is shown in Fig. 2.22. The numerical predictions are in good agreement with experimental data.

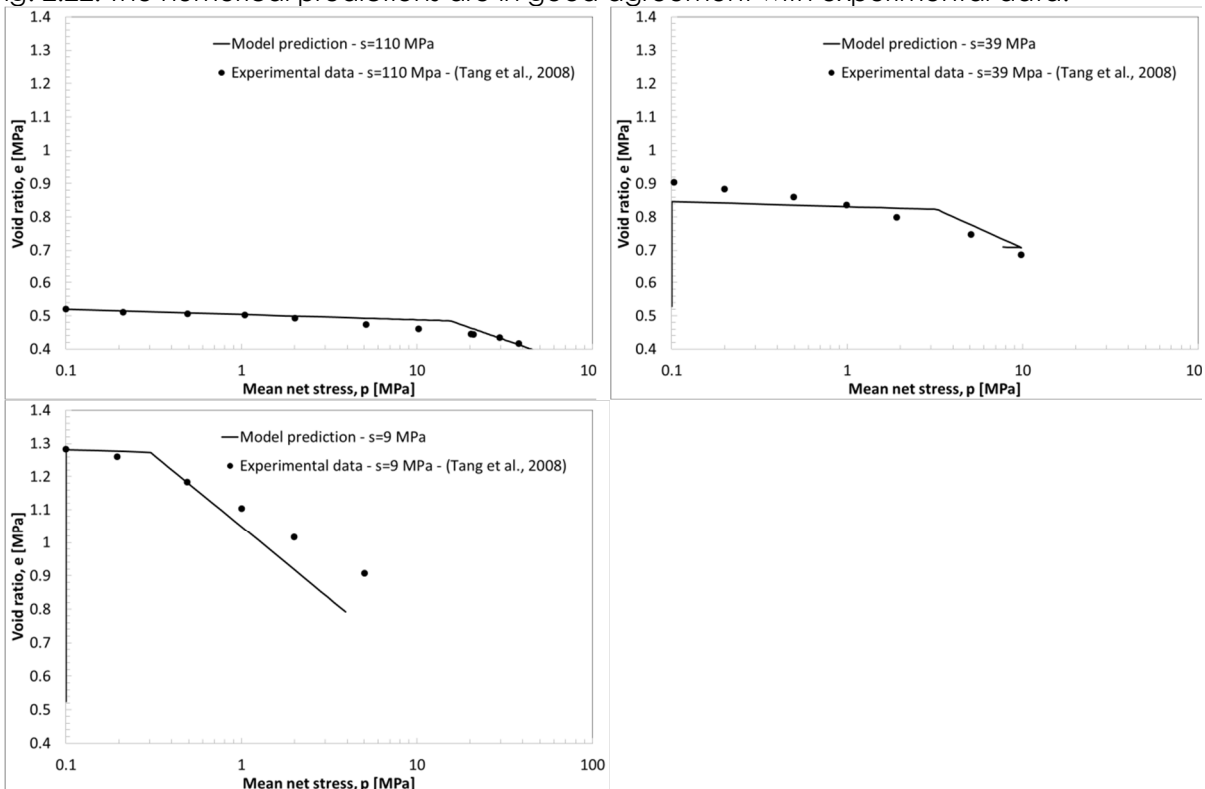


Fig. 2.22: Controlled-suction isotropic tests on pure MX80 compacted bentonite. Comparison between experimental data (Tang, Cui, and Barnel 2008) and model responses on loading paths.

Data extrapolation for a different dry density

The widespread use of bentonite in nuclear waste disposals facilities requires the evaluation of specific swelling capacities, which have to be sufficiently high to enable the sealing of technological gaps, while remaining low enough not to exceed the host-rock strength resistance. These characteristics are inextricably related to the dry density of the bentonite material (Fig. 2.23 and Fig. 2.24). However, given the difficulty and the important time required to perform laboratory tests, experimental characterisations on compacted bentonite are limited and not always available for any dry density and type. Thus, collecting data from available experimental campaigns (and dry densities) and adapting them for the particular purpose becomes important for numerical modelling. In this paragraph, parameters for the BBM are extrapolated from experimental results presented by (Tang, Cui, and Barnel 2008) for pure MX80 compacted at dry density equal to $\rho_d=1.69 \text{ Mg/m}^3$ for the same material compacted at the lower dry density equal to $\rho_d=1.50 \text{ Mg/m}^3$. Among other parameters, the swelling capacity upon suction decrease for BBM is mostly defined by the elastic compressibility coefficient for change in suction κ_s . The κ_s coefficient controls the slope of the stress paths in free swelling conditions in the $(s - e)$ (Fig. 2.23) and respectively in $(p - s)$ planes for constant stress and constant volume conditions, where it affects the final swelling pressure. Consequentially, it is selected in order to fit the experimental evidences concerning swelling capacity dry density dependence. Namely, upon hydration (i.e. suction decrease) numerical results have to show lower swelling deformation with respect to an initially more compacted bentonite (red line Fig. 2.23). At the same time, the swelling pressure developed during hydration at constant volume conditions must to be lower than the one presented by a denser material and higher with respect to the one of a looser one (red square Fig. 2.24). The value at zero stress that fits these requirements is equal to $\kappa_{s0} = 0.220$ for MX80 at $\rho_d=1.50 \text{ Mg/m}^3$ (instead of $\kappa_{s0} = 0.310$ for MX80 $\rho_d=1.69 \text{ Mg/m}^3$) and the parameters controlling its dependency on the stress value equal to $a_p = 0.035 \text{ MPa}^{-1}$ (instead of $a_p = 0.015 \text{ MPa}^{-1}$) (as it will be discussed in the following).

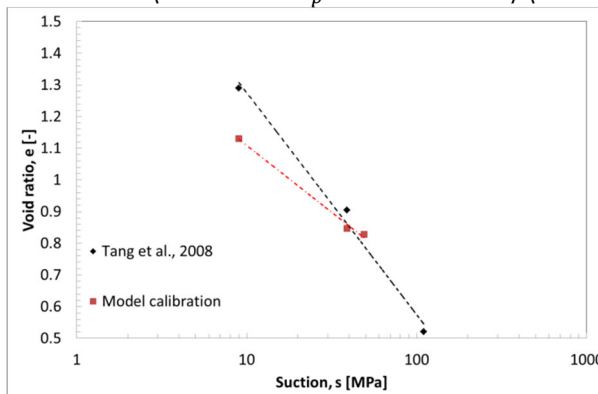


Fig. 2.23: Influence of suction changes and initial bentonite dry density on the volumetric behaviour of compacted bentonite-based materials, under free swelling conditions. Comparison between experimental data (Tang, Cui, and Barnel 2008) and model response.

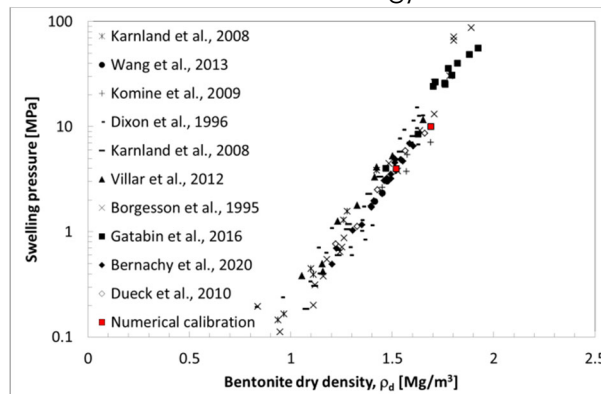


Fig. 2.24: Evolution of the swelling pressure with effective bentonite dry density. Comparison between experimental data (isochoric swelling) and model responses.

Accordingly, the compressibility properties (and coefficients) for change in net stress have to be reasonably similar to the ones of the same material. It is necessary to remind that the elastic and plastic compressibility coefficients for change in net stress κ and λ do not affect remarkably the swelling deformation upon wetting under constant stress conditions. On the other hand, in the BBM framework, these control both the stress path and the shape of the yielding surface with its evolution. In general, these parameters are not considered being dry density dependent. Nevertheless, it can be observed in Fig. 2.22 (but also Fig. 2.20 and Fig. 2.21), especially with respect to the elastic coefficient κ , that for higher void ratio (i.e. lower dry density), the elastic compressibility of the material slightly increases. Thus, according to this evidence the elastic compressibility coefficient for change in net stress concerning MX80 at $\rho_d=1.50 \text{ Mg/m}^3$ is selected equal to $\kappa = 0.030$ (instead of $\kappa = 0.007$ for MX80 compacted at

$\rho_d = 1.69 \text{ Mg/m}^3$). The plastic compressibility coefficient for change in net stress λ , that is assumed suction dependent, corresponds to the one of MX80 bentonite compacted at dry density $\rho_d = 1.69 \text{ Mg/m}^3$. The calibrated data for MX80 at $\rho_d = 1.50 \text{ Mg/m}^3$ are compared to the ones related to the experimental suction-controlled isotropic compression performed by (Tang, Cui, and Barnel 2008) (Fig. 2.25). At suction $s = 38 \text{ MPa}$, the void ratios (i.e. dry densities) and the compressibility of the experimental and numerical responses correspond quite well. The void ratios are strikingly different at $s = 9 \text{ MPa}$ due to the different swelling capabilities related to the initial dry density difference, but the compressibility are comparable for the numerical and experimental cases.

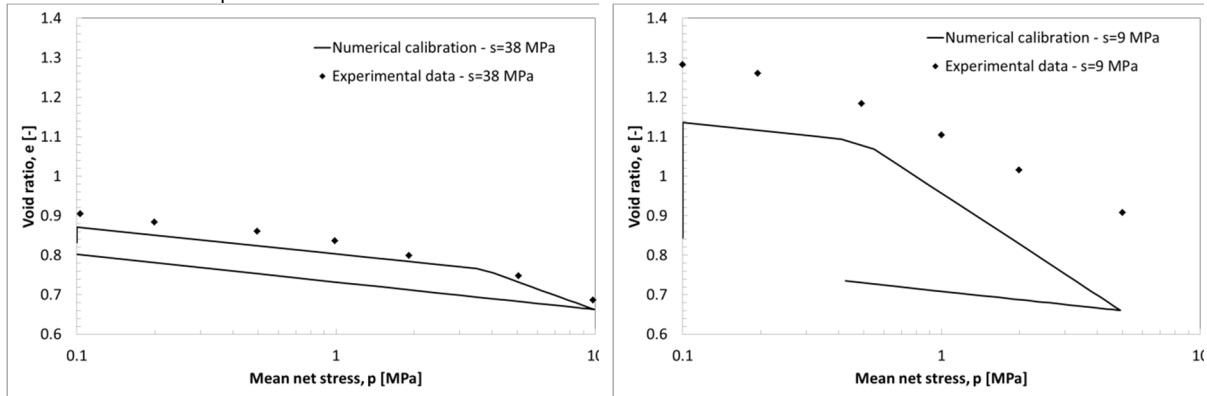


Fig. 2.25: Controlled-suction isotropic tests on pure MX80 compacted bentonite. Comparison between experimental data for initial dry density $\rho_d = 1.70 \text{ Mg/m}^3$ (Tang, Cui, and Barnel 2008) and model responses for initial dry density $\rho_d = 1.50 \text{ Mg/m}^3$ on loading paths.

It was not possible to extrapolate the shape of the yielding surface from experimental data. Hence, the parameters defining the LC curve were determined in order to fit the swelling pressure development in constant volume conditions.

2.1.5 Parameters dependency on density

BBM parameters of the five different materials presented in the previous section are summarized in the follow. Table 2.3 recalls symbols (square and circle respectively for compacted and pellet mixtures) and colours (black, white and grey respectively for Febex, pure MX80 and MX80 and sand) adopted for each type of considered bentonite. For sake of completeness, the “extrapolated” parameters calibrated for a different dry density of MX80 are also reported (red triangle).

Table 2.3: Distinction adopted in the following plots with dry density.

	Compacted		Pellets	
Febex	■	$\rho_d = 1.60$ Mg/m^3	●	$\rho_d = 1.28$ Mg/m^3
Pure MX80	□	$\rho_d = 1.69$ Mg/m^3	○	$\rho_d = 1.50$ Mg/m^3
MX80 and sand	■	$\rho_d = 1.69$ Mg/m^3		
Pure MX80 (Extrapolated)	▲	$\rho_d = 1.50$ Mg/m^3		

The following representations are given in terms of “effective bentonite dry density” (obtained via Eq. 2.30 (Gatabin et al. 2006)).

$$q_{d \text{ clay}} = \frac{p_{\text{clay}}}{q_{d \text{ mixture}} - \frac{p_{\text{component}}}{q_{d \text{ component}}}} \quad \text{Eq. 2.30}$$

p_{clay} and $p_{component}$ are respectively the bentonite and the second component proportions in the mixture, $\rho_{d\ mixture}$ and $\rho_{d\ component}$ are respectively the dry densities of the mixture and of the second component.

This distinction is done in order to consider the clay dry density in materials such as MX80 and sand mixtures, which is the responsible for the swelling capabilities of the overall assembly. In addition, even though the following analyses are given in terms of “initial/dry” bentonite dry density, it becomes necessary to distinguish the “final/saturated” bentonite dry density, due to the important volume changes occurring upon hydration.

Fig. 2.26 and Fig. 2.27 show the evolution of the elastic compressibility coefficients κ (for change in net stress) and κ_{s0} (for change in suction) with initial effective bentonite dry density. The parameter κ is considered constant for a given dry density, whereas a pressure dependence relation is adopted for κ_{s0} (section 2.1.6), whose value is considered at null stress. The elastic parameter κ seems to be in general inversely proportional to the bentonite dry density (Fig. 2.26). The lowest value (related to higher material stiffness) equal to $\kappa=0.003$ is found for dry density equal to $\rho_d=1.69\text{ Mg/m}^3$ and the higher one (higher compressibility) equal to $\kappa=0.074$ is found for dry density equal to $\rho_d=1.28\text{ Mg/m}^3$. Compacted bentonite materials show in general lower compressibility for change in net stress (between 0.003 and 0.012), whereas pellets mixture look more compressible (values between 0.06 and 0.074). This tendency can also be observed in the calibration of the experimental data from Fig. 2.18 to Fig. 2.22. The elastic constant parameter κ fits remarkably well the initial dry densities (i.e. lower void ratios) and less precisely the lower ones.

The evolution of the elastic compressibility coefficient for change in suction at null stress κ_{s0} as function of dry density is given in Fig. 2.27. Data calibrated on experimental tests clearly present proportionality with the dry density. For the higher dry density $\rho_d=1.69\text{ Mg/m}^3$, $\kappa_{s0}=0.330$ is observed and for the lowest $\rho_d=1.28\text{ Mg/m}^3$, $\kappa_{s0}=0.075$ is given. The minimum $\kappa_{s0}=0.072$ is found for MX80 and sand mixture at $\rho_d=1.44\text{ Mg/m}^3$, but the discrepancy is very low.

These observations allow concluding that bentonite-based materials elastic compressibility coefficients for change in stress, κ , and in suction, κ_s , are respectively inversely and directly proportional with dry density. Namely, the denser material corresponds to the stiffer behaviour for change in stress, as well as, the denser material corresponds to the more swelling behaviour for suction increase. These conclusions are confirmed by numerous experimental observations. However, further experimental campaigns would allow determining a more precise tendency for a wider dry density range.

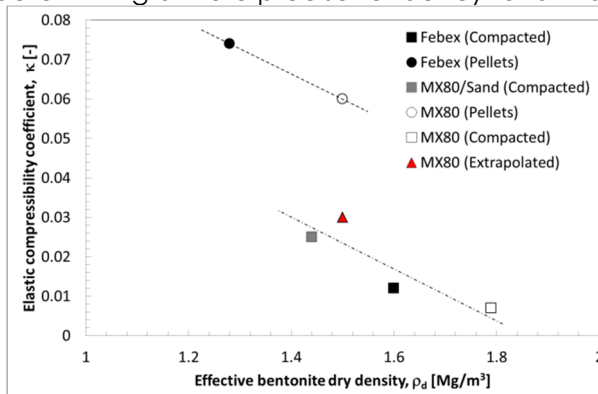


Fig. 2.26: Evolution of elastic compressibility coefficient for change in net stress κ of five bentonites with dry density.

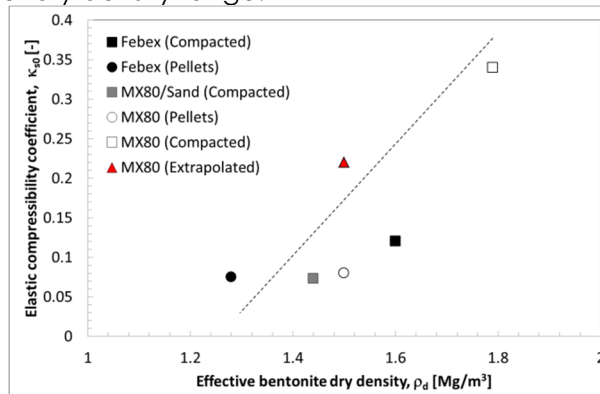


Fig. 2.27: Evolution of elastic compressibility coefficient for change in suction κ_{s0} at zero stress of five bentonites with dry density.

Fig. 2.28 and Fig. 2.29 show the plastic compressibility coefficient λ for change in stress as function of initial dry density. As Eq. 2.6 suggests, this parameter decreases for increasing suction (i.e. the material becomes stiffer when dried), thus the values as dry density function are given for the saturated state (Fig. 2.28) and for the dry state ($s=1000\text{ MPa}$, Fig. 2.29). The plastic compressibility coefficient in the dry state is in general inversely proportional to the dry

density of the material. Compacted assemblies look stiffer than pellets bentonite mixtures (Fig. 2.29). It does not seem possible to extrapolate a clear tendency with dry density of the plastic compressibility coefficient at the saturated state (Fig. 2.28). However, it is relevant to point out that at saturation, the final dry density is completely different from the initial one at the dry state (accounted in the plot), due to the important volumetric change occurring during hydration.

Similarly to the elastic compressibility coefficient for change in stress, also the plastic compressibility coefficient evidently evolves with dry density underlining increasing stiffness for increasing compactness.

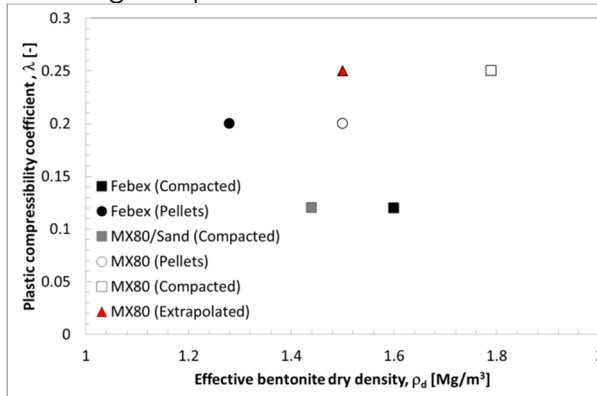


Fig. 2.28: Evolution of plastic compressibility coefficient for change in net stress λ at suction $s=0$ (i.e. saturated state) of five bentonites with initial dry density.

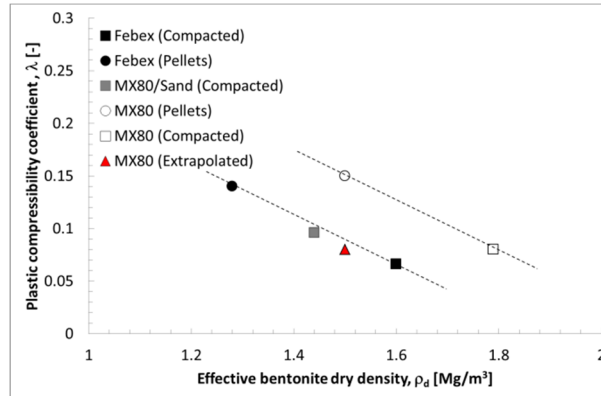


Fig. 2.29: Evolution of plastic compressibility coefficient for change in net stress λ at suction $s=\infty$ (i.e. dry state) of five bentonites with initial dry density.

Similarly to Fig. 2.28 and Fig. 2.29, Fig. 2.30 and Fig. 2.31 show the preconsolidation pressure p_c as function of initial dry density. The preconsolidation pressure, i.e. the elasticity threshold, increases for increasing suction (Eq. 2.7), namely calibrated values are reported for saturated state (i.e. $s=0$, Fig. 2.30) and the dry state (i.e. $s=1000$ MPa, Fig. 2.31). Remarkable proportionality can be observed between the preconsolidation pressure at the dry state and the dry density, with compacted assemblies generally stiffer than pellet mixtures. The sand component may increase the stiffness of the mixture. For the saturated state (Fig. 2.30), it is not possible to extrapolate a clear tendency. Also in this case, it is relevant to point out that at saturation, the final dry density is completely different from the initial one at the dry state (accounted in the plot), due to the important volumetric change occurring during hydration. This occurrence was also considered in Darde et al numerical model (Dardé 2019) and may allow a more reasonable analysis of the experimental data.

It was not possible to present similar analyses on experimental data characterising the deviatoric behaviour (such as friction angle and cohesion) due to the scarcity of experimental evidences at the present state.

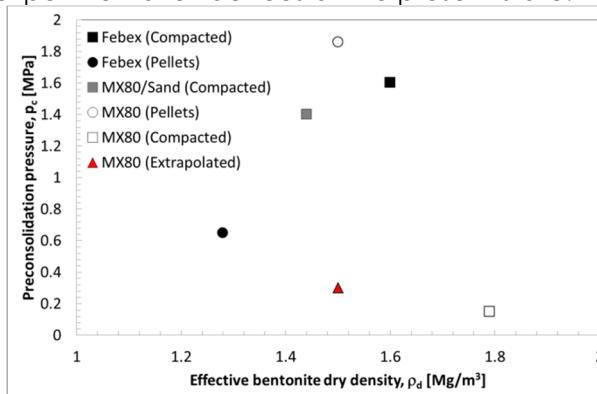


Fig. 2.30: Evolution of preconsolidation pressure at suction $s=0$ (i.e. saturated state) of five bentonites with initial dry density.

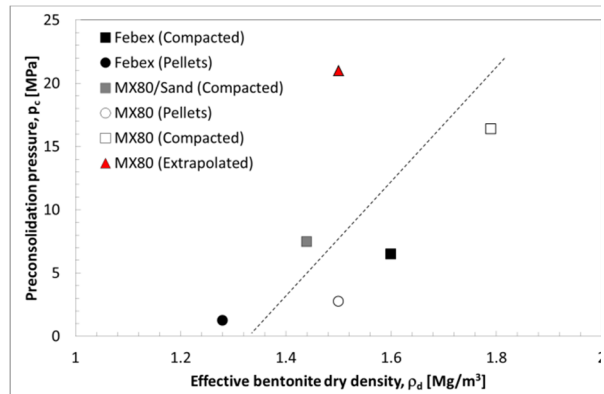


Fig. 2.31: Evolution of preconsolidation pressure suction $s=\infty$ (i.e. dry state) of five bentonites with initial dry density.

2.1.6 Alternative formulation for compressibility coefficient for change in suction

Even though, the Barcelona Basic Model is able to reproduce a wide range of phenomena taking place during bentonite hydration, an important drawback is represented by the significant swelling pressure overestimation when isochoric wetting tests are modelled (Gens and Sanchez 2014).

When the BBM is selected to model swelling clays during saturation in constant volume conditions, the swelling stress can be obtained by integrating equation Eq. 2.3. Thus, under isotropic and elastic conditions, the resulting stress increment reads as follows:

$$p(s) = p_A \left(\frac{S_A + u_{atm}}{S_B + u_{atm}} \right)^{\frac{\kappa_s}{\kappa}} \quad (\text{Elastic state}) \quad \text{Eq. 2.31}$$

The stress increment is an exponential function of the ratio between the elastic compressibility parameters for change in suction (κ_s) and change in net stress (κ). In the hypothesis of isothermal conditions and stress paths mainly based on suction decrease (as reported in the analyses of this work), the elastic parameter κ accounts for the evolution of the yielding surface (Eq. 2.7) and irreversible plastic deformation development (Eq. 2.5), apart from the elastic volumetric evolution upon loading (Eq. 2.3). On the other hand, the parameter κ_s controls only volumetric changes upon hydration (Eq. 2.3). Thus, in order to limit the swelling pressure overestimation and to keep the following analysis straightforward, it is decided to evaluate only the effect of the parameter κ_s . Three strategies are presented:

1. Original constant elastic compressibility coefficient for change in suction κ_s (Alonso, Gens, and Josa 1990) (Eq. 2.32).

$$\kappa_s = \text{constant} \quad \text{Eq. 2.32}$$

Even though the classic BBM formulation results into an overestimation of swelling pressure while modelling isochoric wetting tests, (Alonso, Gens, and Josa 1990) already introduced u_{atm} in Eq. 2.3 to avoid the infinitive swelling that occurs when null suction value is approached.

2. Constant elastic compressibility coefficient for change in suction κ_s for saturation values below a given threshold (Dieudonné 2016) (Eq. 2.33);

$$\kappa_s = \kappa_{s0} \text{ if } S_r < S_r^* \ \& \ \kappa_s = 0 \text{ if } S_r \geq S_r^* \quad \text{Eq. 2.33}$$

(Dieudonné 2016) proposes Eq. 2.33 considering the experimental tests performed by (Agus et al. 2013) on Calcigel bentonite and quartz mixtures. This model is formulated assuming that swelling pressure maintains a steady value when saturation is reached. Considering the high air entry values that bentonite based materials present (i.e. suction levels the material is able to sustain without desaturating), it is obvious that saturation is reached when suction is still high (Seiphoori, Ferrari, and Laloui 2014). Thus a threshold saturation value S_r^* is introduced beyond which the swelling capacity of the material (i.e. κ_s coefficient) is null. This assumption provides remarkable results when isochoric conditions are modelled, however it contradicts other experimental observations stating that most of the swelling deformation takes place when incredibly low suction values are approached (Seiphoori et al. 2016).

3. Elastic compressibility coefficient for change in suction κ_s pressure dependence (Eq. 2.34) (employed thanks to Dieudonné' suggestion);

$$\kappa_s(p) = \kappa_{s0} * \exp(-\alpha_p * p) \quad \text{Eq. 2.34}$$

Where κ_{s0} is the elastic compressibility parameter for change in suction at null stress and α_p is a parameter controlling its dependency on the stress level. The swelling upon wetting at constant stress is strongly linked to the applied stress level. (A. Dueck and Nilsson 2010) also observe this behaviour on compacted MX80 bentonite samples hydrated at constant vertical load (Fig. 2.32). It is clear that for increasing applied stress, decreasing swelling capacity is obtained, with possible wetting collapse according to (Lloret, Romero, and Villar 2004) and as the BBM modelling suggests. Differently from the other two formulations, this modelling strategy allows reducing the influence of initial stress conditions on the development of swelling pressure upon hydration as it will be clearly explained in the following. Moreover, Eq. 2.34 does not present abrupt coefficient variations such as Dieudonné' strategy. Thus, swelling

pressure evolution evolves smoothly, without pressure drops that could affect numerical stability.

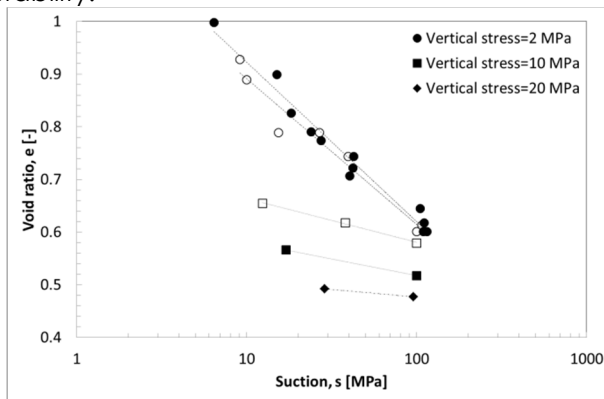


Fig. 2.32: Void ratio evolution with suction at constant vertical stress on MX80 compacted bentonite samples (A. Dueck and Nilsson 2010). White and black points differ for loading paths conditions before swelling.

The performances comparison between the three strategies is conducted on the experimental test adopted to calibrate the MX80 and sand mixture of paragraph 0. The model parameters are given in Table 2.2 and coincide for the three strategies, which evolves only for the κ_s formulation. For Eq. 2.33 the saturation threshold value is selected equal to $S_r^* = 0.98$.

Initial state is equal to suction $s=38$ MPa and confining net stress equal to $p=0.10$ MPa.

Fig. 2.33 shows the stress paths and the unique LC curve in the $(p - s)$ plane for wetting under isochoric conditions for the three numerical strategies. Eq. 2.33 and Eq. 2.32 result into completely overlapping stress paths up to $S_r^* = 0.98$. Indeed Eq. 2.32 can be read as Eq. 2.33 with $S_r^* = 1$. In the elastic domain, the stress increment is related to the constant ratio $\frac{\kappa_s}{\kappa}$ (Eq. 2.31) and it results into a straight line into the log-log $(p - s)$ plane. Consequentially, among other factors, the initial conditions (i.e. initial suction and confining stress) affect remarkably the point in which the yielding surface is touched and the computed final swelling pressure value. On the other hand, with respect to Eq. 2.34 strategy, it can be observed that the stress path slope is decreasing, as a result of the κ_s decrease for increasing net stress (Fig. 2.34). For this modelling strategy, the stress increase and the κ_s evolution are coupled according to Eq. 2.31 and Eq. 2.34. This significantly reduces the impact of the initial conditions on the stress path and computed swelling pressure development and final value.

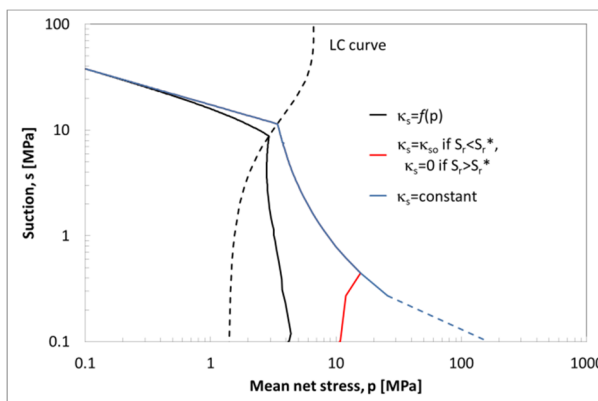


Fig. 2.33: Stress paths and LC curves in the $(p - s)$ plane for wetting under isochoric conditions. Comparison between numerical strategies.

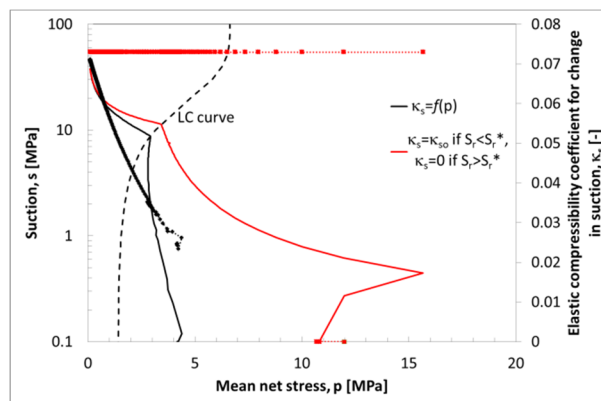


Fig. 2.34: Stress paths and LC curves in the $(p - s)$ plane for wetting under isochoric conditions and κ_s evolution with mean net stress. Comparison between numerical strategies presented by Eq. 2.34 and Eq. 2.33.

The elastoplastic swelling pressure development does not depend only on the κ_s parameter, but also on the yielding surface evolution. However, as Fig. 2.33 shows, the stress paths given by Eq. 2.33 and Eq. 2.32 diverge when $S_r \geq S_r^*$, resulting in final swelling pressure values respectively equal to ~ 10 MPa (Eq. 2.33) and ~ 110 MPa (Eq. 2.32). With respect to Eq. 2.33 strategy, a stress drop takes place. This is obtained in order to maintain the constant volume conditions without violating the yield criterion. Indeed, further suction decrease does not cause any elastic deformation, but, the preconsolidation pressure is still decreasing with suction. Thus, a decrease in mean net stress is observed. The elasto-plastic stress path related to Eq. 2.34 is somehow similar to the one of Eq. 2.33. However, the excessive swelling pressure development is limited by the decreasing tendency of κ_s (Fig. 2.34). The final swelling pressure value is equal to 4 MPa and it is much more reasonable with respect to experimental observations.

Fig. 2.35 presents the comparison between for the proposed numerical strategies with respect to the void ratio evolution with suction at constant vertical stress. Also in this case, Eq. 2.33 and Eq. 2.32 present overlapping stress paths up to the selected threshold value. The slope of the strategy accounting for Eq. 2.34 is again lower. Fig. 2.36 shows that κ_s decreases for decreasing suction. This phenomenon is mostly related to the development of radial swelling pressure upon hydration at constant stress conditions. However, when the yielding surface is touched, the radial swelling pressure decreases Hence, κ_s increases again. Due to the fact that the radial stress development is limited, the κ_s value does not decrease dramatically. The final void ratio values are quite similar for the three strategies. They range between $e=0.95$ (for Eq. 2.34) and $e=1.05$ (Eq. 2.32). The final swelling deformation difference is negligible with respect to the one related to the swelling pressure development (which ranges between 4 MPa and 105 MPa). This allows concluding that even though Eq. 2.34 requires back analysis calibration for the determination of κ_{s0} and α_p parameters, it provides more accurate results for a larger range of phenomena and stress paths conditions.

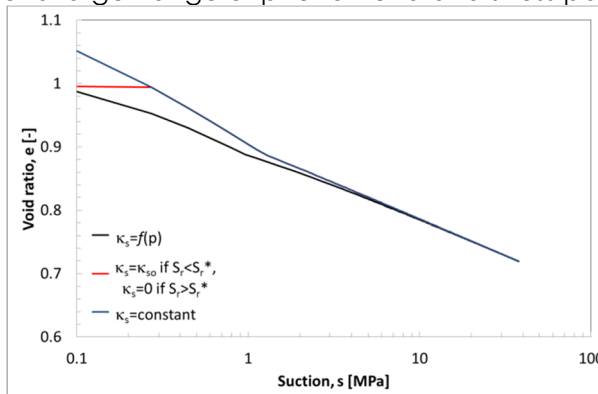


Fig. 2.35: Void ratio evolution at constant vertical stress as function of suction. Comparison between numerical strategies.

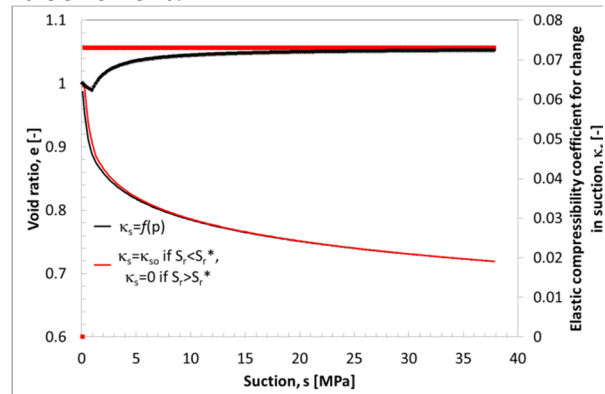


Fig. 2.36: Void ratio at constant vertical stress and κ_s evolutions as function of suction. Comparison between numerical strategies presented by Eq. 2.34 and Eq. 2.33.

2.1.7 Task 3.3

Task 3.3 experiments are simulated using the Lagamine FEM code, in which the model is implemented. Two simulations have been performed, respectively in February 2020 and in November 2020. The material parameters differ slightly.

Model parameters

The selected mechanical parameters are reported in Table 2.4.

	$\lambda(0)$	r	ω	ρ_0^*	ρ_c	K	K_s	α_p	ν	φ	$c(0)$	k
	[-]	[-]	[-]	[MPa]	[MPa]	[-]	[-]	[MPa]	[-]	[°]	[MPa]	[-]
February	0.44	0.50	1e-7	0.50	0.25	0.036	0.17	1.6e-7	0.35	25	0.1	0.046
November	0.44	0.32	1e-7	0.50	0.25	0.036	0.22	5.5e-7	0.25	15	0.1	0.0046
Tang	0.34	0.32	0.5e-7	0.15	0.02	0.007	0.34	1.5e-7	-	-	-	-

Table 2.4: Selected mechanical parameters for WP3.3 (February and November 2020) and calibration for (Tang, et al., 2008).

For the water retention behaviour, the parameters calibrated by (Dieudonne', 2016) for MX-80 are adopted. The comparison between the experimental data provided by EPFL and the model prediction for a MX-80 bentonite of a dry density of $\rho_d=1.50 \text{ g/cm}^3$ is reported in Figure 2..

	ρ_{di}	C_{ads}	n_{ads}	A	n	m	ϵ_{m0}	β_0	β_1
	[g/cm ³]	[MPa ⁻¹]		[MPa]					
February	1.50	0.0075	1.5	0.2	3	0.15	0.31	0.1	0.48
November	1.50	0.0075	1.5	0.2	3	0.15	0.31	0.1	0.28

Table 2.5: Selected hydraulic parameters for WP3.3 (February and November 2020) strategies.

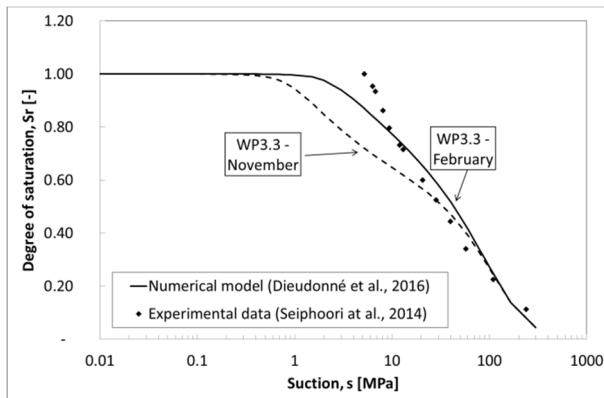


Figure 2.1: Water retention curve in constant volume conditions. Comparison between experimental data (Seiphoori, et al., 2014) and numerical model (Dieudonné, 2016) for MX-80 bentonite of a dry density $\rho_d=1.50 \text{ g/cm}^3$ for WP3.3 (February and November 2020) strategies.

Test 1: free-swelling hydration followed by oedometer test

Geometry and Mesh

The numerical bentonite sample consists in 25 8-node isoparametric elements. The problem is assumed monodimensional and oedometer conditions are considered (Figure 2. and Figure 2.3).

Initial uniform suction is considered with a value equal to 110 MPa.

The hydration of the sample is provided from the top and bottom ends [blue line Figure 2.] applying a constant water pressure equal to 25 kPa.

Finally, the sample is subjected to an initial confining stress values of 0.02 MPa axially (vertically) and 0.02 MPa radially (horizontally) (red arrows Figure 2.).

After the full saturation of the sample, the vertical stress is increased in steps up to a value corresponding to a void ratio $e=0.56$ (Figure 2.3) assuming drained conditions.

In order to reproduce the time evolution kinetics of the hydration process an intrinsic permeability value equal to $K_w=1.6 \times 10^{-19} \text{ m}^2$ is selected for the numerical strategy “November” and $K_w=4.6 \times 10^{-20} \text{ m}^2$ for the strategy “February”.

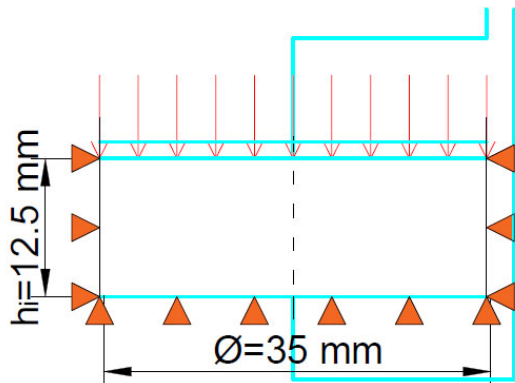


Figure 2.2: Configuration for hydration in free swelling conditions in the vertical direction (stress path A-B).

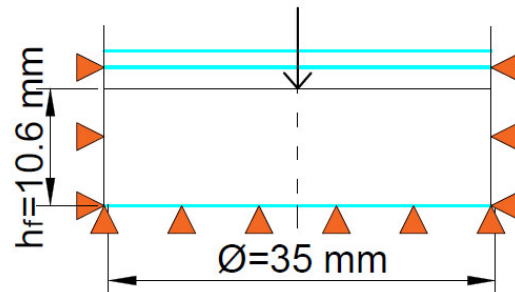


Figure 2.3: Configuration for compression after hydration in free swelling conditions in the vertical direction (stress path B-C-D).

The comparison between the numerical results concerning the sets of parameters calibrated for WP3.3 and the experimental results are reported in Figure 2.4. The final value of vertical swelling deformation is comparable with respect to the experimental results ($\approx 80\%$) for the strategy “November” ($\approx 70\%$), whereas for the strategy “February” a strong underestimation is obtained ($\approx 20\%$).

Also the time evolution kinetics is different. The “November” strategy with constant intrinsic permeability equal to $K_w=1.6 \times 10^{-19} \text{ m}^2$ reproduces well the experimental time evolution. The permeability value selected for the “February” strategy equal to $K_w=4.6 \times 10^{-20} \text{ m}^2$ delays the final stabilisation time.

These results were obtained thanks to a sensitivity analysis of the mechanical parameters κ_s , α_p , p_0^* , p_c , v , ϕ , $c(0)$ and k , which affect the stress path in the elastic domain and the size and evolution of the yielding surface.

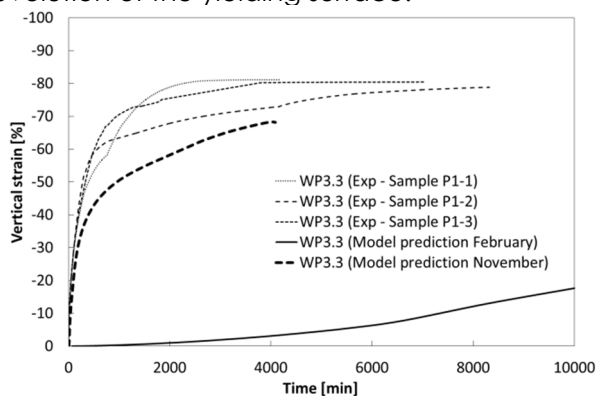


Figure 2.4: Vertical swelling deformation time evolution. Comparison numerical with WP3.3 strategies and experimental data.

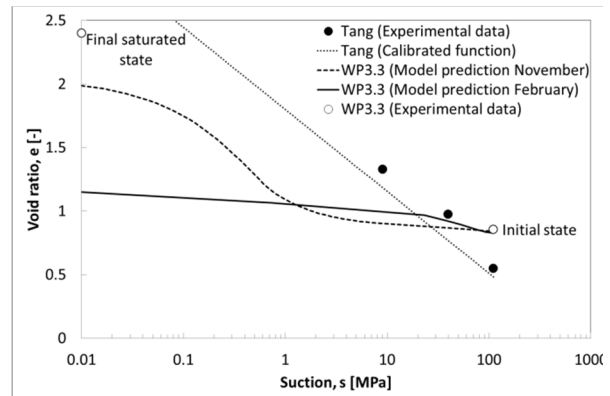


Figure 2.5: Void ratio evolution with suction. Comparison between WP3.3 strategies functions.

Figure 2.6 reports the comparison between experimental and numerical results for WP3.3 parameters for stress path B-D (compression after hydration in free swelling conditions in the vertical direction) in the void ratio-total vertical stress plane.

The numerical and experimental starting points are different but the three curves are parallel in the elastic and plastic branches.

It means that the selected compressibility coefficients for change in stress κ and $\lambda(0)$ provide realistic results.

The discrepancies between the experimental and numerical results are due to the different swelling deformation in the case of the numerical prediction “February” (20% instead of experimental 80 %) and due to the pre-consolidation pressure in saturated conditions ($p_0^*=2$ MPa instead of experimental $p_0^*\approx 0.5$ MPa) for the numerical prediction “November”. The parameter pre-consolidation pressure in saturated conditions p_0^* affects the results in terms of swelling pressure in constant volume hydration and swelling deformation at constant axial pressure swelling tests. The value equal to $p_0^*=2$ MPa was selected in order to obtain a reasonable compromise between the two.

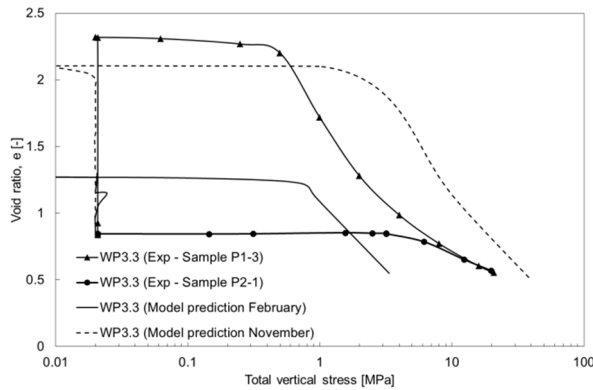


Figure 2.6: Void ratio evolution with total vertical stress. Comparison between experimental and numerical results for WP3.3 strategies for stress path B'-C' (compression after hydration at constant volume).

Test 2: constant-volume hydration followed by oedometer test

The numerical bentonite sample consists in 25 8-node isoparametric elements. The problem is assumed monodimensional and oedometer conditions are considered (Figure 2.7 and Figure 2.8).

Initial uniform suction is considered with a value equal to 110 MPa.

The hydration of the sample is provided from the top and bottom ends [blue line Figure 2.7] applying a constant water pressure equal to 25 kPa.

Finally, the sample is subjected to an initial confining stress values of 0.02 MPa axially (vertically) and 0.02 MPa radially (horizontally).

After the full saturation of the sample, the vertical stress is increased in steps up to a value corresponding to a void ratio $e=0.56$ (Figure 2.8) assuming drained conditions.

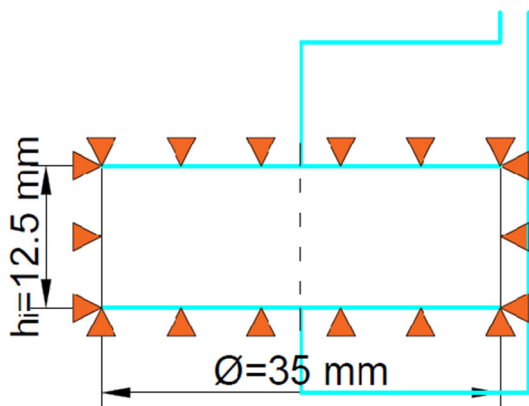


Figure 2.7: Configuration for hydration at constant volume conditions (stress path A-B').

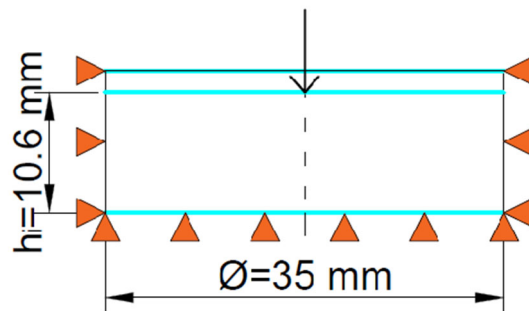


Figure 2.8: Configuration for compression after hydration at constant volume conditions (stress path B'-C').

The comparison between the numerical results concerning the set of parameters calibrated for the two presented strategies for WP3.3 and the experimental results are reported in Figure 2.9. The final value of vertical swelling pressure is comparable in the 2 numerical cases and slightly lower with respect to the experimental ones for the February strategy. A final experimental swelling pressure values variability is observed for the experimental tests. The full saturation time and the stabilization of the swelling pressure occurs at different time due to the different value of intrinsic permeability ($K_{w0}=4.6 \times 10^{-20} \text{ m}^2$ for case WP3.3-February and $K_{w0}=3.6 \times 10^{-20} \text{ m}^2$ for case WP3.3-November). Nevertheless, also in the experimental outcomes, a certain variability in stabilisation times is obtained between the same tests type.

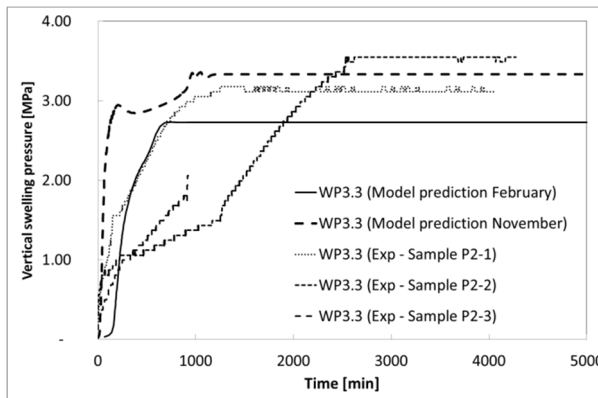


Figure 2.9: Vertical swelling pressure time evolution. Comparison numerical with WP3.3 strategies and experimental data.

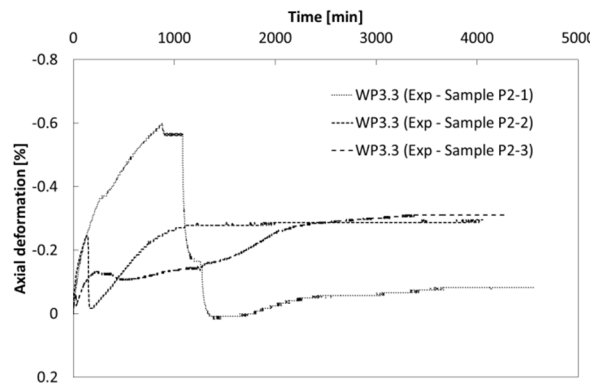


Figure 2.10: Axial deformation of the cell. Experimental records.

Results

Figure 2.11 reports the comparison between experimental and numerical results for WP3 strategies parameters for stress path B'-C' in the void ratio-total vertical stress plane. The results concerning the set of parameters calibrated for February and November underline a plastic compressibility coefficient in saturated conditions $\lambda(0)=0.44$ too high with respect to the experimental results. Indeed, the numerical void ratio decreases too quickly with respect to the experimental evidences reaching a final value of vertical swelling stress equal to 9 MPa instead of 20 MPa for a corresponding void ratio $e=0.56$. The compaction after isochoric hydration follows the same path because the plastic compressibility index for change in pressure in saturated condition $\lambda(0)=0.44$ is the same and the final swelling pressure values are comparable.

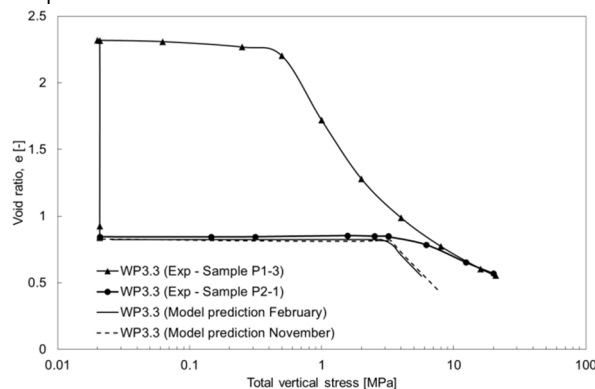


Figure 2.11: Void ratio evolution with total vertical stress. Comparison between experimental and numerical results for WP3.3 parameters for stress path B'-C' (compression after hydration at constant volume).

2.2 Mohymar – A new double structure model

A double structure hydromechanical model for unsaturated clays is presented. The model was developed at the University of Liège (Belgium). The detailed formulation has not been published yet and is currently under review.

A short description of the model is presented in section 3. Basic capabilities of the model are presented in section 4. Results of the simulations of task 3.3 experiments are presented in section 5. Performance of the model and assessment of predictive power are discussed in section 6.

2.2.1 Description of the model

Constitutive approach

The model presented in this section is a double structure hydromechanical model for unsaturated clays. It is formulated in the framework of hardening elastoplasticity. Two independent stress variables are considered: Bishop effective stress and a corrected suction pressure.

Levels of structure

The void ratio, e is equal to the sum of microstructural void ratio, e_m and macrostructural void ratio, e_M :

$$(1) \quad e = e_m + e_M$$

Water retention model

Degree of saturation of the microstructure, S_{rm} is written as a function of water potential (suction in unsaturated state), Ψ and model parameters Ψ_m^* and n_m as follows:

$$(2) \quad S_{rm} = \left(1 + \frac{\Psi}{\Psi_m^*}\right)^{n_m}$$

Degree of saturation of the macrostructure, S_{rM} is written as a function of Ψ and model parameters Ψ_M^* and n_M as follows:

$$(3) \quad S_{rM} = \left(1 + \frac{\Psi}{\Psi_M^*}\right)^{n_M}$$

Degree of saturation is written as a function of e_m , S_{rm} , e_M , S_{rM} and e as follows:

$$(4) \quad S_r = \frac{e_m}{e} S_{rm} + \frac{e_M}{e} S_{rM}$$

Stress variables

The two independent stress variables are (i) the Bishop effective stress with Bishop coefficient taken equal to the degree of saturation of the macrostructure, (ii) a corrected value of Ψ taking into account effects of adsorption at the microstructural level.

Effective mean stress, p_M' , is written as a function of the total mean stress, p and Ψ as follows:

$$(5) \quad p_M' = p - S_{rM} \Psi$$

Corrected suction, p_{fm} , is written as a function of Ψ as follows:

$$(6) \quad \begin{cases} p_{fm} = S_{rm} \Psi & \Psi \leq 0 \\ p_{fm} = 0 & \Psi > 0 \end{cases}$$

Elastic volumetric strains

Total elastic volumetric strain, ε_V^e and microstructural volumetric strain, ε_{Vm} are defined as follows:

$$(7) \quad \begin{pmatrix} d\varepsilon_V^e \\ d\varepsilon_{Vm} \end{pmatrix} = \begin{pmatrix} \frac{1}{K} & -\frac{1 + C_{mM}}{K_{fm}} \\ \frac{C_{pp}}{K_{fm}} & -\frac{1}{K_{fm}} \end{pmatrix} \begin{pmatrix} dp_M' \\ dp_{fm} \end{pmatrix}$$

Where K is the bulk modulus, K_{fm} is a stiffness term related to the influence of adsorption on the volumetric behaviour, C_{pp} is a fabric term and C_{mM} a coupling term between macrostructural and microstructural deformations. These latter are defined as follows:

$$(8) \quad K = \frac{1 + e_0}{[F_M + C_{pp}(1 + C_{mM})F_m]}$$

$$(9) \quad K_{fm} = \frac{1 + e_0}{F_m}$$

$$(10) \quad C_{pp} = \frac{1 + e}{1 + e_m}$$

$$(11) \quad C_{mM} = \frac{e_M}{1 + e_m}$$

With F_M and F_m functions of p_M' and p_{fm} related to macrostructure and microstructure, respectively:

$$(12) \quad F_M = -e_{M0} \beta_M^e \exp(-\alpha_M p_M')$$

$$(13) \quad F_m = -(1 + e_{m0}) \beta_m \exp[-\alpha_m (C_{pp} p_M' - p_{fm})]$$

Where α_M , α_m , β_M^e are model parameters.

Note that ε_{vm} remains elastic.

Plasticity and hardening

The definition of the yield surface, f is as follows:

$$(14) \quad f \equiv q_M^2 - M^2 (p_{Mc}' - p_M') (p_M' - p_{Mc} t) = 0$$

Where q_M is the deviatoric stress, M is a model parameter, p_{Mct}' is a model parameter, and p_{Mc}' is the elastic limit in isotropic compression. p_{Mc}' is defined as a function of p_{fm} as follows:

$$(15) \quad p_{Mc}' = \frac{N_0}{C_{qp} - C_{pp} N_p} - \frac{N_p}{C_{qp} - C_{pp} N_p} p_{fm}$$

Where N_0 and N_p are parameters related to the shear strength of microstructure, and C_{qp} a fabric parameters governing the transmission of the stress state from macrostructure to microstructure.

The hardening law describes the evolution of N_0 with plastic volumetric strain ε_v^p :

$$(16) \quad \frac{\partial N_0}{\partial \varepsilon_v^p} = (C_{qp} - C_{pp} N_p) \left(\frac{1 + e_0}{e_{M0}} \right) \frac{\exp(\alpha_M p_{Mc}')}{\beta_M^{ep} - \beta_M^e}$$

Where β_M^{ep} is a model parameter.

2.2.2 Basic capabilities of the model

The model is able to reproduce the essential aspects of the behaviour of unsaturated clays: swelling/shrinkage upon hydration/drying; macrostructural swelling resulting from microstructural swelling; evolution of strength and stiffness with suction; plastic collapse upon wetting. Original features of the model include: consideration of distinct effects of capillary and adsorption suction; smooth transition to saturated state; ability to reach a minimum void ratio; transmission of macrostructural stress to microstructure related to soil fabric; yielding governed by microstructural phenomena.

Regarding the hydromechanical behaviour of compacted bentonite, capabilities of the model are detailed in Table 3.

Table 6. Model capabilities

Name of the constitutive law:		Mothymar-ULiege
Behaviour feature	D3.3	Remarks
Mechanical behaviour		
Dependence of swelling strain on applied stress (at the same dry density)	Y	
Dependence of swelling stress on dry density (at the same stress)	Y	
Irreversibility of strains in wetting/drying cycles	N	
Dependence of swelling pressure on dry density	Y	
Stress path dependence from an unsaturated to a saturated state	Y	
Stress path dependence from a saturated to an unsaturated state	Y	
Double structure/porosity considered?	Y	
Are temperature effects considered in the model?	N	
Dependence of strains developed in a temperature cycle (increase/decrease) on OCR (or stress)	-	Temperature effects not considered
Hydraulic behaviour (retention curve)		
Hysteresis	N	Only if irreversible change in void ratio occurs
Dependence on void ratio	Y	
Double structure/porosity considered?	Y	

2.2.3 Task 3.3

Task 3.3 experiments are simulated using the Lagamine FEM code, in which the model is implemented.

Test 1: free-swelling hydration followed by oedometer test

Geometry and Mesh

The test is simulated as an axisymmetric problem. The mesh consists in a single 8-node finite element.

Boundary conditions

During the free-swelling hydration, radial displacements are blocked on the left boundary. Axial displacements are blocked on the bottom boundary. Total stress is imposed on the top and right boundaries. During the oedometer test, radial displacements are blocked on the left and right boundaries. Axial displacements are blocked on the bottom boundary. Total stress is imposed on the top boundary.

Boundary conditions for the free-swelling path and the oedometer test are presented in Figure 2.12 a) and b), respectively.

Note that boundary conditions in the simulation of the free-swelling hydration are not exactly the same as in the experiment. To avoid the development of significant radial stresses, boundary conditions describe a true free-swelling experiment instead of hydration in an oedometer cell.

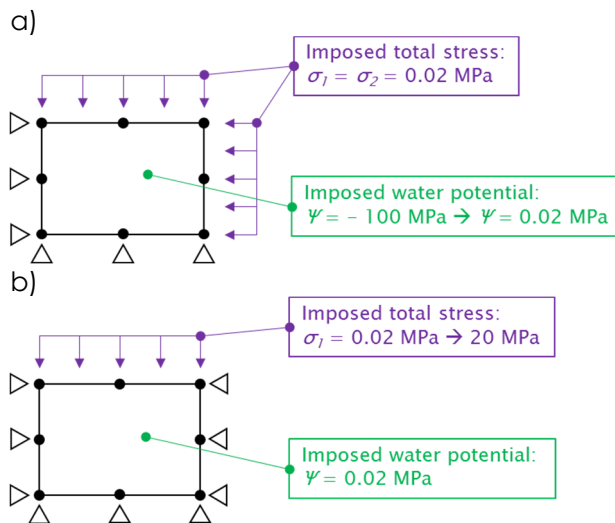


Figure 2.12. Boundary conditions for test 1 of Task 3.3: a) free-swelling, b) oedometer test.

Model parameters

Model parameters are given in Table 7.

Results

Results for the free-swelling hydration and the subsequent oedometer test are presented in Figure 13. Both the evolutions of void ratio and microstructural void ratio are well reproduced in the simulation.

Table 7. Model parameters for MX80 bentonite.

Initial properties of the soil		
e_{m0}	0.300	-
ρ_{d0}	1.50	Mg/m ³
Ψ_0	-100	MPa
Mechanical model		
Macrostructure		
α_M	0.350	MPa ⁻¹
β_{M^e}	0.550	MPa ⁻¹
$\beta_{M^{eP}}$	0.650	MPa ⁻¹
Microstructure		
α_m	0.030	MPa ⁻¹
β_m	0.015	MPa ⁻¹
Plasticity and hardening		
M	0.567	-
$\rho_{Mct'}$	0	MPa
N_p	0.150	-
N_0	0.200	MPa
C_{qp}	0.25	-
Water retention model		
Ψ_M^*	-1.00	MPa
n_M	-1.50	-
Ψ_m^*	-220	MPa
n_m	-1.50	-

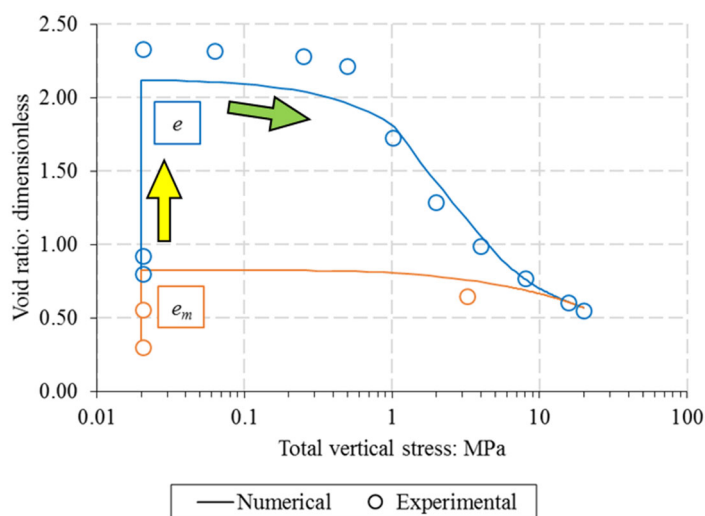


Figure 13. Comparison between experimental and numerical results for test 1. The yellow arrow represents the free-swelling hydration, the green arrow represents the oedometer test.

Test 2: constant-volume hydration followed by oedometer test

Geometry and Mesh

The test is simulated as an axisymmetric problem. The mesh consists in a single 8-node finite element.

Boundary conditions

In the constant-volume hydration test, radial displacements are blocked on the left and right boundaries. Axial displacements are blocked on the top and bottom boundaries. In the oedometer test, radial displacements are blocked on the left and right boundaries. Axial displacements are blocked on the bottom boundary. Total stress is imposed on the top boundary.

Boundary conditions for the constant-volume hydration and the oedometer test are presented in Figure 14 a) and b), respectively.

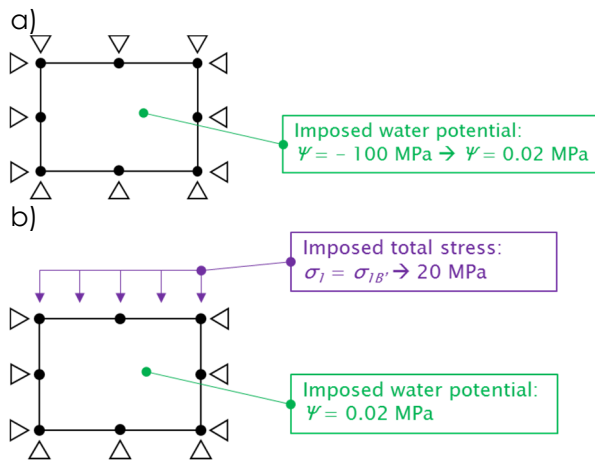


Figure 14. Boundary conditions for test 1 of Task 3.3: a) free-swelling, b) oedometer test.

Model parameters

Model parameters are given in Table 7.

Results

Results for the constant-volume hydration and the subsequent oedometer test are presented in Figure 15. Both the evolutions of void ratio and microstructural void ratio are well reproduced in the simulation.

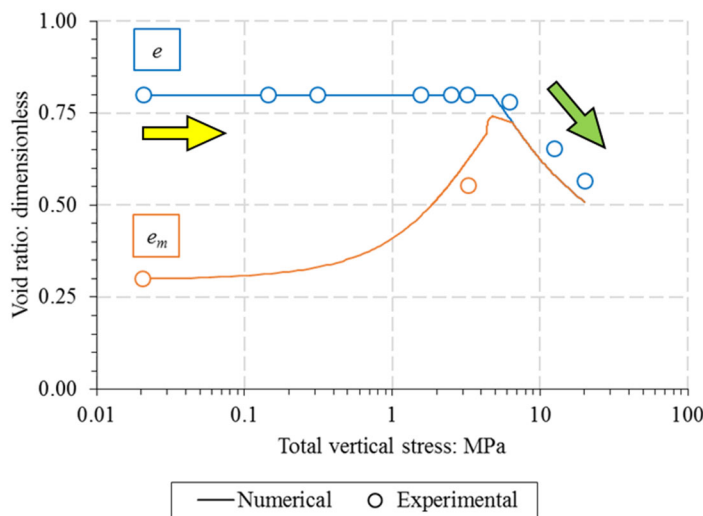
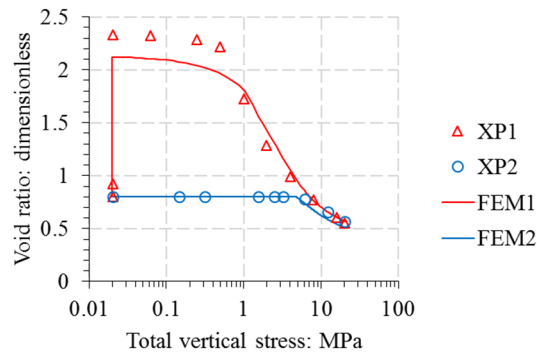


Figure 15. Comparison between experimental and numerical results for test 2. The yellow arrow represents the constant-volume hydration, the green arrow represents the oedometer test.

2.2.4 Performance of the model and assessment of predictive power

The formulation was able to satisfactorily reproduce the evolutions of void ratio and microstructural void ratio during various hydration/loading paths, using a single set of parameters. Figure 16 a) and b) summarizes the results. The comparison of FEM results with experimental results demonstrates that, despite some simplifications of the material behaviour, the mechanical and hydraulic models are relevant under the hydromechanical conditions addressed in this study.

a)



b)

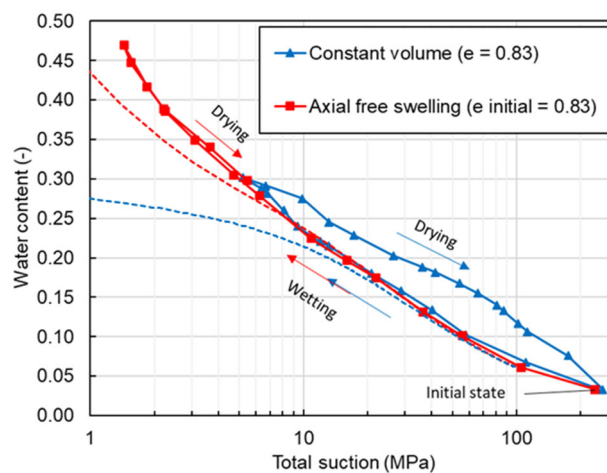


Figure 16. Comparison of numerical results and experimental results: a) void ratio as a function of vertical stress for tests 1 and 2, b) water content as a function of suction for free-swelling hydration and constant-volume hydration.

Some perspectives for future work can be identified:

- Detail an experimental program for the determination of the model parameters;
- Improve the hydraulic model to consider hysteresis;
- Consider temperature effects.

Only single-element simulations were performed. In order to perform boundary-value problems of bentonite seals/engineered barriers under repository conditions, the proposition of a permeability law can be regarded as a relevant perspective as well.

2.2.5 Concluding remarks

A new double structure hydromechanical model was presented. Its performance was evaluated by simulation of Task 3.3 experiments. In general, the model was able to reproduce the evolution of void ratio, microstructural void ratio, and water content well.

Only single-element simulations were performed. In order to evaluate the model performance under repository conditions, boundary value problems should be simulated. In this regard, interesting perspectives include the proposition of a permeability law, improve the hydraulic model to consider hysteresis, improve the mechanical model to consider temperature effects.